

AD-A225 971

DTIC FILE COPY

AFOSR-TR- 90 0897

2

FINAL TECHNICAL REPORT

for

AFOSR GRANT 86-0165

During the Period

April 15, 1986 to October 15, 1989

on

COUPLED EXPERIMENTAL AND THEORETICAL INVESTIGATIONS
OF INSTABILITY, CHAOS AND TURBULENCE
IN AN AXISYMMETRIC JET FLOW

by

Thomas C. Corke

Hassan M. Nagib

and

Simon Rosenblatt

*Fluid Dynamics Research Center
Armour College of Engineering
Illinois Institute of Technology
Chicago, Illinois*

IIT/FDRC

July, 1990

1990 08 15
1990 08 15

Full release:
unlimited.

Information Division
1990 08 15

UNCLASSIFIED

SECURITY CLASSIFICATION OF THIS PAGE

REPORT DOCUMENTATION PAGE

1a. REPORT SECURITY CLASSIFICATION unclassified			1b. RESTRICTIVE MARKINGS		
2a. SECURITY CLASSIFICATION AUTHORITY			3. DISTRIBUTION/AVAILABILITY OF REPORT unlimited		
2b. DECLASSIFICATION/DOWNGRADING SCHEDULE					
4. PERFORMING ORGANIZATION REPORT NUMBER(S)			5. MONITORING ORGANIZATION REPORT NUMBER(S)		
6a. NAME OF PERFORMING ORGANIZATION Illinois Institute of Technology		6b. OFFICE SYMBOL (If applicable) IIT	7a. NAME OF MONITORING ORGANIZATION AFOSR		
6c. ADDRESS (City, State and ZIP Code) MAE Dept. and FDRC 10 W. 32nd Street Chicago, IL 60616			7b. ADDRESS (City, State and ZIP Code) AFOSR/NA Bolling Air Force Base Washington, DC 20332-6448		
8a. NAME OF FUNDING/SPONSORING ORGANIZATION AFOSR		8b. OFFICE SYMBOL (If applicable) NA	9. PROCUREMENT INSTRUMENT IDENTIFICATION NUMBER AFOSR-86-0165		
8c. ADDRESS (City, State and ZIP Code) AFOSR/NA Bolling Air Force Base Washington, D.C. 20332-6448			10. SOURCE OF FUNDING NOS.		
			PROGRAM ELEMENT NO.	PROJECT NO.	TASK NO.
					WORK UNIT NO.
11. TITLE (Include Security Classification) Coupled Exp. and Theor. Investigations OF INSTABILITY, CHAOS, 61102F 2307 A 2 + TURBULENCE IN AN AXISYMMETRIC JET FLOW					
12. PERSONAL AUTHOR(S) T. C. Corke, H. M. Nagib and S. Rosenblatt					
13a. TYPE OF REPORT Final Technical		13b. TIME COVERED FROM 4/86 TO 10/89		14. DATE OF REPORT (Year, Month, Day) 90/7/16	
				15. PAGE COUNT 396	
16. SUPPLEMENTARY NOTATION					
17. COSATI CODES			18. SUBJECT TERMS (Continue on reverse if necessary and identify by block number)		
FIELD	GROUP	SUB-GROUP	Jets, Instability, Turbulence, Chaos, Feedback, Dynamical Systems, Experimental, Theoretical, Critical Value, Hopf, Bifurcation, Global Instability		
19. ABSTRACT (Continue on reverse if necessary and identify by block number)					
<p>This work focused on instability, routes to chaos, and transition to turbulence in an axisymmetric jet. The research focused on three basic tasks. The first involved the search for evidence of low dimensional strange attractors in a naturally excited condition. The theoretical analog was the construction of low-dimensional model equations for this flow. The second involved 3-D (non-axisymmetric) periodic forcing of the jet to lead to the enhanced growth of 3-D modes. This was to focus on natural resonant mechanisms involving natural instability modes of the shear layer and jet core. The theoretical analysis for this part was to preedict the conditions for the most resonant interactions, which would maximize our ability to control the jet outcome. The third task was to integrate the previous tasks to exploit important mode interactions which lead to strong nonlinear regimes and or random or chaotic states. In this phase, we accomplished this through intrinsic forcing of the jet by "enhanced feedback". The results of the work have covered all these tasks, and yielded many new fundamental results basic to dynamical systems with feedback.</p>					
20. DISTRIBUTION/AVAILABILITY OF ABSTRACT UNCLASSIFIED/UNLIMITED <input checked="" type="checkbox"/> SAME AS RPT. <input type="checkbox"/> DTIC USERS <input type="checkbox"/>			21. ABSTRACT SECURITY CLASSIFICATION Unclassified		
22a. NAME OF RESPONSIBLE INDIVIDUAL Dr. James McMichael			22b. TELEPHONE NUMBER (Include Area Code) (202) 767-4936		22c. OFFICE SYMBOL AFOSR/NA

TABLE OF CONTENTS

	Page
1. SUMMARY	v
1.1 Task A.....	vi
1.2 Task B.....	ix
1.3 Task C.....	xii
1.4 Ice Storage Chill Water System for NDF.....	xv
1.5 References.....	xv
2. COPIES OF PUBLISHED PAPERS	1
2.1 Global Instability in an Axisymmetric Jet with Enhanced Feedback	1
2.2 Mode Selection and Resonant Phase Locking in Unstable Axisymmetric Jets.....	112
2.3 The Dynamics of Low Initial Disturbance Turbulent Jets.....	219
2.4 Control of Two and Three-Dimensional Modes in the Initial Region of an Axisymmetric Jet.....	232
2.5 Seeding of Helical Modes in the Initial Region of an Axisymmetric Jet.....	245
3. COPIES OF INTERNAL REPORTS	270
3.1 Closed-Loop Excitation of an Air Jet.....	270
4. ABSTRACTS IN BULLETIN OF AMERICAN PHYSICAL SOCIETY	333
4.1 An Experimental Investigation of an Open Flow System with Enhanced Feedback	333
4.2 Global Oscillations and Bifurcations in a Jet with Enhanced Feedback.....	334
4.3 Receptivity of an Axisymmetric Shear Layer to an Azimuthally-Local Sound Source.....	335
4.4 Receptivity Transfer Function of a Round Jet.....	336
4.5 Nonlinear Stability of a Viscous Axisymmetric Jet	337
4.6 Experimental Investigation of Resonant Spatial-Temporal Instability Waves in an Axisymmetric Shear Layer.....	338

5. THESES.....	Page 339
5.1 Hybrid Instability in an Axisymmetric Jet with Enhanced Feedback	339
5.2 Nonlinear Stability of a Viscous Axisymmetric Jet	348
5.3 On the Instability of Thin Circular Shear Layer	357
6. NUMERICAL EXPERIMENTS ON CALCULATING ATTRACTOR DIMENSION	366

Author	
Title	
Code	
Category	
Notes	
Index	
Other	
Remarks	
Signature	
Date	
Initials	
Stamp	
Handwritten: A-1	



1. SUMMARY

In the original proposal of March, 1985 (85-NA-177) and in the letter of December 16, 1985, we had chronologized the direction and focus of an investigation on the instability, routes to chaos and transition to turbulence of an axisymmetric jet flow. As described in the proposal, the choice of performing this investigation in a jet were based on a number of factors including (a) the low disturbance quality of the Jet Facility at IIT, (b) the large amount of data accumulated over the recent years in past AFOSR funded research on instability and transition in jets, (c) the fact that the jet can represent the more general class of open flow systems in which evidence of strange attractor dynamics has not been documented, and (d) a fact which was not pointed out in the original proposal but which now has come to be appreciated, which is that the initial region of the jet can act either as a convectively unstable system, or as a result of feedback resonance, act as a globally unstable system. The implications of the latter fact will be discussed in greater length in a later part in this report.

In those two documents we had detailed three general tasks (A-C) which were intended to be performed in sequential order and which were each to encompass approximately one year of time. Within each general task were a number of subtasks which involved both experimental and theoretical analysis. These were designed to interact, enhance and build in a cumulative effort to reach the general goals of the study.

The first general task (A) involved the basic search for evidence of low-dimensional strange attractors in a naturally (stochastic) excited axisymmetric jet. The theoretical analog was the construction of low-dimensional model equations for this flow which might show period doubling and behavior commensurate with dynamical systems known to have strange attractors. Also part of the effort, was the use of numerical, theoretical and experimental 'exercises' with data series from systems with attractors of known dimensions and characteristics. These exercises were intended to provide a level of confidence for making predictions about the dynamical state of the measured systems as well as provide bench-marks for comparison to other past and ongoing similar investigations in fluid dynamics and to the more prolific number of investigations in the areas of physics and applied mathematics. This was to involve the development of the computational tools for determining such characteristic quantities as the attractor dimension, Lyapunov exponents and phase space distributions.

The second general task (B) involved the 3-D (non-axisymmetric) periodic and random forcing of the jet. This was intended to produce two types of results. The first was meant to consider the basic instability processes which lead to the growth of 3-D modes in jets. The second would attempt to trace the development of quasi-periodic states which might lead to random behavior.

Experimentally this was to involve the use of azimuthally placed disturbance generators capable of producing different axisymmetric and helical mode combinations. A similar approach using heating segments to produce spanwise periodic modes in boundary layers has been a great success in our laboratory. As evidenced by the boundary layer experiments, the detailed documentation of even a small number of possible combinations of controlled states was expected to take considerable time, although, we fully expected it would provide valuable new information about the initial instability and resonance conditions of such growing 2-D and 3-D mode interactions.

The theoretical analysis within task B was intended to predict the conditions for these highly controlled states. The major thrust would deal with the non-linear evolution of disturbances leading to the growth of 3-D modes. This would involve resonance mechanisms and strongly non-linear couplings leading to transition to turbulence. We expected that at this stage of the work there would be frequent comparisons between experiment and analysis in order to pinpoint similarities and differences.

The third task (C) was designed to integrate the initial work and apply it towards the active control of jets. In particular it was intended to build on the experimental and theoretical results to pinpoint important mode interactions which may have been found to lead to strong non-linear regimes and/or to random or chaotic states. Such information would then be used in a detection, feedback and control arrangement.

In the three year period of the grant, our investigations have nearly followed the chronological order laid out in the original proposal. We have addressed most of the experimental and theoretical tasks cited in A and B, as well as some tasks which were not explicitly stated in the original proposal. We have addressed task C through the concept of intrinsic mode forcing through enhanced feedback.

1.1 Task A

During this period, extensive amounts of computer software were developed for performing chaos related data analysis of time series. Some of the results of this work were presented at the 39th Annual Meeting of the American Physical Society Division of Fluid Dynamics.¹ An appendix on this topic taken from the Ph.D. Thesis of Patrick Reisenthel² is included in pages 366 to 379 of this final report. These exercises demonstrated that it was possible to obtain estimates of the dimension of low-dimensional attractors, with known uncertainty, at reasonable computational cost, and established a number of practical limitations which besets higher dimensional estimates. In those exercises, an approximation of the Grassberger-Procaccia dimension of known chaotic and pseudo-periodic signals was calculated. The tests were designed to simulate data series obtained from a single

sensor probe, for example, what might be obtained from a single sensor hot-wire in the initial shear layer region of an axisymmetric jet. The test cases included the Henon and Lorenz attractors, and sine waves with different numbers of incommensurate frequencies. Other parameters that were varied were the relative sampling rate and the number of contiguous sample points. These exercises pointed out the large uncertainties in determining the dimension of systems with more than five degrees of freedom, and in our minds placed strong questions on results which claim to have done so.

Methods for displaying phase space representations of data series with different attractor dimensions were also developed. In particular a highly efficient algorithm based on the singular decomposition method introduced by Broomhead and King³ was used to produce optimum projections in phase space of low and moderate dimension systems. The method is extremely powerful for discerning deterministic behavior which might be masked by non-deterministic (incoherent) processes. As a further means for separating out deterministic behavior, methods using first-return mapping were developed and used in various numerical exercises.

In this phase of the work, measurements were made in the initial shear layer region of the axisymmetric jet under conditions of different Reynolds numbers, with natural forcing as well as with mild forcing of axisymmetric modes using sound. The Reynolds numbers were chosen based on the experience gained in previous studies in this jet (Drubka⁴; Shakib⁵; Corke et al.⁶) to produce conditions with minimum feedback and strong resonant (enhanced) feedback. Measurements were taken at a fixed azimuthal position but with different selected downstream positions where the unstable modes were primarily initial fundamental axisymmetric, primarily initial fundamental helical, a mixture of initial axisymmetric fundamental and subharmonic, and mixture of initial axisymmetric fundamental, subharmonic and fundamental helical modes. In terms of attractor dimensions these respective locations should have produced systems with attractor dimensions of one in the first two cases, one with a subharmonic, and two with a subharmonic. With the addition of far-field acoustic forcing, we could suppress the helical modes and in those cases reduce the dimension by one. Such forcing at the natural axisymmetric mode frequency could also, to some extent, weaken or otherwise alter the feedback and thereby modify the development of the axisymmetric subharmonic mode. Away from the preferred frequency, forcing could produce strong non-linear coupling with sum and difference interactions and a non-exact subharmonic mode. Therefore these cases represented different degrees of complexity and order of attractors under conditions which were well documented and repeatably set.

Under the conditions with natural and enhanced feedback, long highly sampled time-series at the fixed probe locations were acquired and processed using the mathematical tools for analyzing the dynamical systems developed and tested earlier. The results of this experiment constituted Chapter V of Reisenhel's thesis.² Independent measures of attractor dimension were obtained, using the modified

Grassberger-Procaccia⁷ algorithm and the singular decomposition method by Broomhead and King.³ These measures confirmed the low-dimensional nature of the dynamics of shear-layer instability, up to pairing location. The dimension was shown to increase with downstream distance. Mild axisymmetric forcing consistently reduced dimensionality by approximately one. Phase-space representations and Poincare sections were examined in an attempt to evidence more clearly any departure of the data from quasi-periodicity. These underlined the added complexity introduced by the presence of non-axisymmetric modes, and revealed no discernible fine or fractal structure. First return maps calculated from the Poincare sections reinforced these observations. Finally, direct measurements of the largest Lyapunov exponent (K) were performed using two of the available methods, due respectively to Wolf et al.⁸, and Sano and Sawada⁹. Though different in scope these methods gave convergent large positive values of K , but are not trusted as being sufficiently quantitative, owing to their critical sensitivity to various input parameters.

One of the conclusions drawn from these measurements of Task A was the crucial role of "clean" experimental conditions such as core turbulence intensity (approximately 0.05%) and the need for *strongly resonant* axisymmetric instabilities in order to distinguish deterministic non-linear dynamics from noisy quasi-periodicity in the jet. Such conditions may be achieved by examining jet behavior at Reynolds numbers corresponding to the "column instability mode", namely, when the initial axisymmetric wave length is such that an integer number of pairing events coincides with the end of the potential core, and/or alternatively by the use of *controlled external forcing*. The existence of the column instability mode has been known for some time, however in other higher disturbance jet facilities it is only observable with strong axisymmetric forcing. In our case, with the low disturbance levels, we have Reynolds numbers at which the column instability mode exists naturally (Drubka's $Re=42,000$). Therefore one approach to reduce the noisy quasi-periodicity in the jet, that is, the random phase modulations of the periodic initial instabilities would involve operating at Reynolds number conditions where such a natural coupling existed.

There were more profound reasons for setting our operating conditions to be at a strongly resonant state for studying the routes to chaotic behavior in an open fluid flow. During the period of the grant, there appeared a numerical study by Deissler¹⁰ on convective chaos in an open flow system that pointed to the role of non-determinant disturbance imperfections from purely harmonic inputs in the route to chaotic behavior. He stressed the inadequacy of presently available tools in order to study deterministic oscillations in a "true" open system. Such an analysis does not however include considerations of feedback. Therefore, a series of measurements were undertaken that elucidated the role of feedback in an open flow system (Task C), since feedback or forcing can play the role of effective "boundary conditions" with respect to wave dynamics. Early observations of probe feedback

and harmonic spectra indicated that a convectively unstable flow, such as a cold axisymmetric jet, in the presence of feedback, shared some of the features related to absolute instability (closed flows). Such a distinction has profound implications with respect to the possible existence of deterministic chaos in jets, as well as issues of "flow controllability".

The theoretical analog to the experimental work of Task A was a nonlinear stability analysis of a viscous axisymmetric jet to axisymmetric and helical disturbances. These were analyzed with a severely truncated form of a Fourier-eigenfunction model expansion to lead to a low-dimensional system of amplitude equations of the Lorenz-type. The formulation and analysis of these formed the basis of the Ph.D. thesis of Judith Horwitz.¹¹ The abstract and summary of her thesis are contained in pages 348 to 356 of this report.

For the case of axisymmetric disturbances, the 3-D analog of the Lorenz equations which included the fundamental mode and mean flow distortion was obtained. Unlike the Lorenz system, which has chaotic solutions when the Prandtl number is high enough, there are no chaotic solutions for this model of the jet. For $R > R_c$ only globally stable periodic solutions existed. This result was independent of the shape function used.

Adding in the harmonic to produce a 5-D system caused the periodic solution to lose stability to a quasi-periodic solution with two incommensurate frequencies. For one choice of shape functions, the quasi-periodic branch eventually goes through a periodic regime and then becomes intermittent. A different choice of shape functions lead to a homoclinic orbit and unbounded solutions following the quasi-periodic regime. The bifurcation diagram for the axisymmetric case are shown on page 355 of this report.

The case for nonaxisymmetric disturbances lead to a similar sequence of bifurcations. The bifurcation diagram for this case is shown on page 356. In both cases, the feature that distinguishes these low order models, representing an open flow system, from the closed flow system Lorenz model, is that the secondary bifurcation leads to a two-frequency quasi-periodicity rather than to chaos. Thus, the main conclusion is that the low order truncation model for the jet does not lead to chaotic solutions and as such does not give an identifiable path to turbulence. This work however represents the first attempt to proceed beyond the linear stability analysis for the axisymmetric jet, and the first to include three-dimensional disturbances to derive a low order system of amplitude equations.

1.2 Task B

In addition to the far-field acoustic forcing, we had also developed a method to produce azimuthally varying 3-D modes in the jet. This constituted the experimental portion of Task B. This involved placing an azimuthal array of 12

miniature speakers on the face of the jet, in the proximity of the exit lip. The speakers were individually controllable in amplitude and phase to allow different azimuthal wave numbers of helical modes. Measurements of the mean flow character of the exit shear layer, and the Strouhal number dependence on Reynolds number of the dominant natural instability modes showed that the speaker array did not introduce any *passive* modification of the jet conditions. Forcing from a single speaker and 180° phase shifted speaker pairs were used to confirm quasi-two-dimensional linear theory predictions, regarding relative insensitivity of amplification rates to azimuthal wave number. This was further confirmed for all active speakers forcing helical modes of different azimuthal wave numbers. From these results, we have the capability to excite helical modes up to ± 6 , the limit of 12 speakers.

Documentation of this set-up and early measurements is contained in the two papers by Kusek et al.^{12,13} In that work, we take a different approach than others in that we directly seed helical wave *pairs* of both positive and negative azimuthal wave numbers. The reasons for this approach are that linear theory does not distinguish between these, and a helical mode of one sign, interacting with an axisymmetric mode, will otherwise produce the opposite signed helical mode. The latter is important in terms of our applications which deal with helical/axisymmetric mode resonance interactions. We therefore need not wait for the growth to sufficiently large amplitudes before the complete outcome of the mode interactions, we ultimately seek, occurs.

The setup has been used in both active and reactive (enhanced feedback) situations to control simultaneously axisymmetric and pairs of helical modes. Under active control, periodic time series to the speaker array are supplied by a function generator or digital computer. Under reactive control, the forcing input is derived from the analog time series proportional to the velocity fluctuations taken at a point in space in the developing shear layer downstream of the jet exit. Analog circuitry was designed and built to accept these input signals and provide independent control of each speaker output to allow different azimuthal amplitude and phase distributions needed to seed different azimuthal wave number modes, $0 \leq m \leq 6$.

The ability to seed $m = \pm 1$ helical modes has been confirmed over a range of jet diameter Reynolds numbers from 4,000 through 60,000. At the lower Reynolds numbers, where flow visualization is more easily performed, we were able to visually record the characteristic features of these modes (see for example Figures 15 and 16 of reference 12, reproduced on page 242 of this report). These revealed in the nonlinear stages, staggered vortices at the azimuthal positions of amplitude maxima (helical mode pair crossing intersections), and formed 'Y' pattern connections to these. The junction of the 'Y' pattern forms at the location of the azimuthal amplitude minima. This pattern is invariant in the flow direction. Multiple photograph realizations confirmed that these modes were phase locked with the forcing time series.

With helical modes, we have shown that intrinsic forcing of the jet through enhanced feedback provides similar dynamics as for the axisymmetric ($m=0$) modes documented by Reisenthel² (Case C). In this case a highly asymmetric jet spreading was exhibited (see Figure 18 of reference 12, reproduced on page 243), with the greater spreading occurring at the locations of the azimuthal amplitude maxima. This alone, or in combination with $m=0$ modes offers rich possibilities for practically exploiting such controlled resonant growth of these modes. The present setup offers an ideal flexible test bed for examining these approaches.

A recent thesis by Kusek¹⁵ has performed a systematic quantitative measure of the characteristics of the jet for three forcing conditions. The first consisting of a weakly amplified helical mode pair which was essentially superposed onto the natural jet instability modes. This provided a reference to the second case which consisted of the same helical mode pairs along with an axisymmetric mode at the harmonic streamwise wave number. This was designed to lead to the resonant growth of the otherwise weakly amplified subharmonic helical mode. The third case consisted of forcing $m=\pm 1$ helical modes at a streamwise wave number which was close to that of the natural helical mode. The exact streamwise wave number was carefully selected to nonlinearly couple with the jet column instability mode. This occurred through a mode at the frequency of the difference between the forced and natural axisymmetric modes, which equaled the harmonic of the column mode frequency. The result of this lead to numerous discrete sum and difference interacted modes which quickly filled the spectrum.

The data of this study consist of the spatial distribution of energy in the forced and natural modes, as well as linear and quadratic phase coupling between velocity fluctuations in the shear layer and pressure fluctuations at the exit lip of the jet which arise from pressure feedback. For the case of subharmonic resonance, an initial linear growth was verified, which was followed by a sharp change to an enhanced secondary growth. The secondary growth was comparable to that of the higher linear amplification rate of the forced axisymmetric mode. This, combined with a matching of phase speeds of these two modes, confirmed resonance.

Resonance also resulted in an asymmetric growth in momentum thickness, with the largest growth occurring at the azimuthal locations of the helical mode energy maxima. The total (azimuthally summed) growth in this case was 300 percent larger than in the natural jet. Coupling with the column mode produced a 50 percent increase over the natural jet.

The theoretical underpinnings to Task B were provided by the Ph.D. thesis by Azam Ahmadi-Moghadam.¹⁴ The abstract and conclusions have been included in pages 357 to 365 of this report. This considered the temporal and spatial instability of a Blasius shear layer to helical modes of different azimuthal wave number. In particular, the effect of shear layer curvature on amplification rates and phase velocities was examined as a prerequisite to the main focus of resonance mechanisms. A nonaxisymmetric secondary instability for the shear layer through a

Kelly-type parametric resonance was analyzed. This showed the most important case, that is, the one with the strongest contribution to the total growth rate, was the one involving an axisymmetric fundamental disturbance, and two subharmonic modes with opposite but equal azimuthal wave numbers. In this case, the secondary growth rate increased with both increasing azimuthal wave number and curvature effects.

A Craik-like triad interaction involving an axisymmetric fundamental and two subharmonic waves with opposite azimuthal wave numbers was also analyzed. This showed that once the subharmonic disturbance reached a sufficient amplitude so that back-interaction to the fundamental becomes important, an *explosive* growth would occur. This phenomena was found to be relatively insensitive to initial conditions, although the rapid growth was found to occur earlier for larger azimuthal wave numbers and curvature effects. The M.S. thesis of Kusek¹⁵, has verified some of these predictions for $m = \pm 1$ helical modes.

1.3 Task C

The direction of thinking based on the observations from Task A, led to the concept of intrinsic jet forcing which we had termed as enhanced feedback. In terms of the original task, this approach constituted Task C, in that it involved interactive forcing, feedback and control. The results of this formed the basis of a large part of the Ph.D. thesis of Reisenhel.² The abstract, and conclusions from his thesis are included in pages 339-347. A recent paper¹⁶ accepted for publication in the Journal of Fluid Mechanics, which is based on this thesis work, is included in pages 1 to 111. Another publication, partly based on documentation of the mean characteristics of the jet from Reisenhel's thesis, and previously unpublished results from Drubka⁴, has appeared in Physics of Fluids A¹⁷. A copy of that has been included in pages 219-231.

The approach in this task involved using the amplified signal from a hot-wire, placed in the shear layer of the jet, to drive a far-field sound source. Under these conditions, the otherwise wholly convectively unstable system was shown to be governed by a global *temporal* instability. This was observed through exponential amplification or decay of self-sustained oscillations of an eigenmode of the system, produced by closing or opening the feedback loop. The selection of the eigenfrequency was based on the combination of being the most amplified shear layer mode from linear theory, as well as satisfying a feedback criterion requiring an integer number of wavelengths between the jet lip and feedback sensor. The self-excited, highly organized axisymmetric (far-field source) modes were found to share many of the qualitative features such as frequency jumps, and hysteresis, exhibited by the broad class of hydroacoustic problems. The results documented the origin of a critical Reynolds number. At criticality, experimental evidence supports the result

that the flow undergoes a supercritical Hopf bifurcation. The connections with the Landau equation were established.

Because of the controlled feedback conditions of the experiment, threshold effects based on velocity and streamwise flow scale were able to be related to a critical gain. A dual empirical and analytical approach, motivated by observations from this flowfield and based on the concept of a "hybrid" instability, was used to explain the origin of frequency selectivity. The role of this instability was analyzed with phenomenological equations utilizing the results of linear theory to describe in detail the dynamics of feedback, and many of its nonlinear consequences. A primary result was that close to criticality, open flow systems *with feedback* may support global instabilities which grow in time. Analytical considerations suggest that an increasing number of potentially excited modes may be involved as the Reynolds number is further increased.

A key element in systems such as this, where pressure feedback plays a dominant role in the selection of unstable eigenmodes, is the receptivity of the initial shear layer to pressure disturbances. More specifically, the amplitude and phase frequency response are an integral element in the choice of eigenfrequencies of the total system. The important role of feedback in a natural (stochastically forced) jet for the resonant growth of the subharmonic axisymmetric mode has been documented by Corke et al.¹⁸ A copy of this paper, completed during the period of this grant, which is to appear in the Journal of Fluid Mechanics, is included in this final report on pages 112 through 218. Our understanding of the role of feedback gained in this work was the origin in thinking of the enhanced feedback which we exploited under Task C. In all of this, the receptivity process remained an unknown element within this process.

We had looked at the amplitude and phase response at receptivity in a separate experiment. The results of this were reported in the Bulletin of the American Physical Society.¹⁹ This has been included in the final report on page 336. This involved forcing the shear layer of the jet using a far field sound source and monitoring the amplitude and phase response of the unsteady pressure at the exit lip of the jet, and in velocity fluctuations at different downstream positions in the shear layer. At a given Strouhal number, the linear spatial amplification rate and phase development was measured. These were then used to extrapolate back to the point of receptivity at the lip of the jet. A range of jet diameter Reynolds numbers from 40,000 to 80,000 were examined. For these, a range of Strouhal numbers which bracketed the range of most amplified values were used to construct the receptivity transfer function. As a byproduct of this exercise, we also were able to make comparisons to linear theory for the mode amplification rate and phase velocity.

The results showed an approximate 2π phase variation with Strouhal number at receptivity for frequency values close to that of the natural axisymmetric modes. A very gradual increase in the amplitude transfer function with increasing Strouhal number was found above the most amplified value. Below the most amplified

Strouhal number, an almost constant amplitude transfer function, u'/p' , of approximately 2.5 was measured at receptivity.

A secondary issue to the experiment, was the level reached by the forced mode at saturation, and its dependence on Reynolds number and Strouhal number. The outcome of this was a surprising result that the saturation amplitude was not a constant, but appeared to scale with Strouhal number, based on the initial momentum thickness. The highest saturation amplitudes occurred at the Strouhal numbers of the natural axisymmetric modes.

Currently, there is no theory to guide us. Receptivity analysis, in the manner of triple deck approaches, is done on a linear basis. This problem is, clearly *nonlinear* in nature, and cannot be modeled by current approaches. Yet, the receptivity transfer is a fundamental aspect to resonant feedback systems and deserves further attention. Our setup provides an approach to explain some of our observations, and we expect to pursue this in our future research. The results to date are to be submitted as a Technical Note in Physics of Fluids A.

Within Task C, the follow-up work to Patrick Reisenthel's Ph.D. thesis was an experiment to measure the values of the Landau coefficients at different spatial locations in the shear layer for the jet with enhanced feedback. This involved using two hot-wire sensors, one at a fixed spatial location to provide the feedback signal similar to Reisenthel's, and the other, which was moved to different spatial locations, to sample the temporally growing eigenmode produced with a closed feedback loop. The issue here is if the coefficients of the simple Landau amplitude equation model are invariant in space. Phase averaged measurements were obtained by repeated opening and closing of the feedback loop under computer control. At any streamwise position within the shear layer, the temporal growth of a single eigenfrequency was fit to the complex form of the Landau equation. The result of this indicated that although both the real and imaginary parts of the equation appear to be largely independent of space when the flow is almost parallel (approximately 1.5 wavelengths downstream), the Landau coefficient decreases by several orders of magnitude within a fraction of the eigenfrequency wavelength. The implications are that this simple mode is *not sufficient* to predict the behavior of the eigenmode at different points in space.

The results summarized here are contained in the internal report²⁰ (in French) by Nathalie Nivelet, a French exchange student, and Patrick Reisenthel. This has been reproduced, with an abstract in English, in pages 270 through 332. A paper to be submitted to Physics of Fluids A is in progress.

In this experiment when we review the time-series or spectra, we observe the presence of a subharmonic mode. We have documented in our previous work that the fundamental and subharmonic modes are quadratically phase locked, which results in a matching of phase velocities and ultimate energy transfer between them. This is reflected in the enhanced growth of the subharmonic beyond what is predicted from linear theory. The presence of the eigenfrequency subharmonic

suggests that *at minimum* a pair of *coupled* amplitude equations are necessary to model this system. That is, it accounts for the effect of the amplitude of the fundamental eigenmode on the subharmonic, and the subharmonic on the fundamental. The change in the Landau coefficient for the amplitude equation which reflects only the fundamental mode is not the complete picture. As a result, we are currently repeating this experiment to obtain the coefficients of the coupled amplitude model, and from this to determine any spatial dependence on their values.

1.4 Ice Storage Chill Water System for NDF

Work on the 1100 ton-hour ice storage chill water system began March, 1989, with an expected completion date of September, 1989. As a result of numerous delays in the delivery of hardware and in fabrication of the delivery piping system, the ultimate completion date was June, 1990. At that time the system was thoroughly checked and optimized for operation with the cooling-vanes of turns 1 and 3 of NDF. Air temperature surveys downstream of turn 1 showed outstanding spatial uniformity of mean temperatures, with deviations from the mean of less than 0.4 percent. The overall performance of the cooling vanes was in line, or slightly better with the computer model and small scale experiment predictions used to design the full scale turn. Overall we are very pleased with the cooling operation.

1.5 References

1. Reisenhel, P., 1986. Determination of attractor dimension using a laboratory computer. *Bulletin of the American Physical Society*, 31, No. 10, p. 1689.
2. Reisenhel, P., 1988. Hybrid instability in an axisymmetric jet with enhanced feedback. Ph.D. Thesis, Illinois Institute of Technology, Chicago.
3. Broomhead, D.S. and King, G.P., 1986. On the qualitative analysis of experimental dynamic systems. *Nonlinear Phenomena and Chaos*, ed. 5, Sankar, Adam Hilger, Bristol.
4. Drubka, R.E., 1981. Instability in near field of turbulent jets and their dependence on initial conditions and Reynolds number. Ph.D. Thesis, Illinois Institute of Technology, Chicago.
5. Shakib, F., 1985. Evolution and interaction of instability modes in an axisymmetric jet. M.S. Thesis, Illinois Institute of Technology, Chicago.

6. Corke, T.C., Shakib, F. and Nagib, H., 1985. Effects of low amplitude forcing on axisymmetric jet flows. *AIAA Paper No. 85-0573*.
7. Grassberger, P. and Procaccia, I., 1983. Characterization of strange attractions. *Physical Review Letters*, 50, No. 5, pp. 346-349.
8. Wolf, A., Swift, J.B., Swinney, H.L. and Vastano, J.A., 1985. Determining Lyapunov Exponents from a time series. *Physical D*, 16, pp. 285-317.
9. Sano, M. and Sawada, Y., 1983. Experimental study on the Poincare mappings in Rayleigh Benard convection. Proceedings of the IUTAM symposium on turbulence and chaotic phenomena in fluids, Kyoto, Japan
10. Deissler, R.J., 1985. Spatially growing waves, intermittency, and convective chaos in an open flow system. *Report No. 85-4211*, Los Alamos National Laboratory, Los Alamos, New Mexico.
11. Horwitz, J., 1990. Nonlinear stability of a viscous axisymmetric jet. Ph.D. Thesis, Illinois Institute of Technology, Chicago.
12. Kusek, S.M., Corke, T.C. and Reisenhel, P., 1989. Control of two and three dimensional modes in the initial region of an axisymmetric jet. AIAA Shear Flow Control Conference, *AIAA - 89-0968*.
13. Kusek, S.M., Corke, T.C. and Reisenhel, P., 1990. Seeding of helical modes in the initial region of an axisymmetric jet. To appear *Experiments in Fluids*.
14. Ahmadi-Maghadam, A., 1986. On the instability of thin circular shear layers. Ph.D. Thesis, Illinois Institute of Technology, Chicago.
15. Kusek S.M., 1990. Helical instability modes in jets. M.S. Thesis, Illinois Institute of Technology, Chicago.
16. Reisenhel, P., Nagib, H.M. and Corke, T.C., 1990. Global instability in an axisymmetric jet with enhanced feedback. To appear *J. Fluid Mech.*
17. Drubka, R. E., Reisenhel, P. and Nagib, H. M., 1989. The dynamics of low initial disturbance turbulent jets. *Phys. Fluids A*, 1, No. 10, pp1723-1735.
18. Corke, T., Shakib, F. and Nagib, H.M., 1990. Mode selection and resonant phase locking in unstable axisymmetric jets. To appear *J. Fluid Mech.*

19. Ghassemi, M., Xiong, Y-M., Reisenhel, P. and Corke, T.C., 1988. Receptivity transfer function of a round jet. *Bulletin of the American Physical Society*, 33, No. 10 , p. 2271.
20. Nivelet, N., 1989. Closed-loop excitation of an air jet. Fluid Dynamics Research Center Internal Report, Illinois Institute of Technology, Chicago.

Global instability in an axisymmetric jet with enhanced feedback

By P. REISENTHIEL, H. M. NAGIB & T. C. CORKE

Fluid Dynamics Research Center, Illinois Institute of Technology, Chicago, IL 60616, USA

The present experiment considers an axisymmetric jet as a prototypical open flow system, the organization of which has been enhanced by a feedback loop of controllable strength. When the source of feedback is located in the initial shear layer, strong self-sustained oscillations were spontaneously produced past critical conditions. Because of the controlled conditions of the experiment, thresholding effects based on velocity and streamwise flow scale were related to the existence of a critical gain. A dual empirical and analytical approach, motivated by observations from this flowfield and based on the concept of "hybrid" instability, was used to explain the origin of frequency selectivity and the existence of a critical Reynolds number in feedback systems. The primary result of this study is the demonstration that, close to criticality, open flows with feedback may support global instabilities which grow in time. The instability is hybrid, in the sense that it is temporal with respect to the amplitude of global oscillations, but convective with respect to local shear layer dynamics. The role of this instability was analyzed with phenomenological equations utilizing the results of linear theory to describe in detail the dynamics of feedback, and many of its non-linear consequences. Finally, it was experimentally demonstrated that, for Reynolds numbers slightly larger than critical, well-defined limit-cycle behavior is observed. Analytical considerations suggest that an increasing number of potentially excited modes may be involved as the Reynolds number is further increased.

1. Introduction

1.1. *Jet flows: streamwise evolution*

A prototypical open flow system is provided by the axisymmetric jet. Though much knowledge has been gained over the years, in the present investigation we examine this flowfield in light of new methods of excitation motivated by the study of dynamical systems. The large body of work related to jets has been instigated by a number of interests which may be divided into two main categories. The first one is related to the engineering importance of jets: many investigations have been driven by the challenging prospects of controlling turbulent jets. "Control" generally refers to the alteration of global quantities of practical interest, such as spreading rates, mixing, or the production of acoustic noise. Another motivating force, however, is the basic understanding of turbulence generated in free shear flows. The strong, localized receptivity at the lip, the powerful broadband amplification in the shear layer, and pressure feedback associated with the main restructuring events in the shear layer constitute the three principle elements of such flowfields. The early stages of shear layer amplification are quite well predicted by linear stability theory. The mean profile of a jet is inviscidly unstable to small disturbances, which grow exponentially over short distances from the lip. Weakly non-linear aspects have also been analyzed from small perturbations around the neutral point. In particular, the increased growth of a subharmonic frequency leading to pairing has been successfully accounted for by the subharmonic resonance mechanism. Drubka (1981) showed that a subharmonic resonance takes place in the jet at approximately two fundamental wavelengths from the lip.

In addition to their large spatial amplification rates, jet flows are characterized by an unusual sensitivity to low-amplitude acoustic forcing. The phenomenon by which irrotational pressure disturbances are efficiently converted to embryonic vortical fluctuations at the lip is termed "receptivity". Morkovin and Paranjape (1971) examined

the sensitivity of shear layers to acoustic excitation and showed the existence of an "acoustic coupling" proportional to the gradient of the diffracted pressure field at separation.

The downstream evolution and reorganization of flow structures in the jet has been the focus of much analysis. It is somewhat surprising, however, that relatively few attempts have been made to consider the flowfield globally, by incorporating the weak pressure feedback to the lip. Yet, there is clear experimental evidence of the acoustic feedback. Corke et al. (1985) used bicoherence measurements to verify the feedback of energy at the lip, from the sites of first vortex roll up, and pairing respectively. Gutmark and Ho (1983) mention a significant amount of "self-forcing" in jets, due to downstream sources of pressure fluctuation. According to Ho and Huerre (1984), the fluctuating pressure felt at the lip is most likely due to the first two pairing events, which are the most spatially coherent ones. There is also strong experimental evidence of feedback due to the preferred mode. Kibens's (1980) resonant jet clearly exhibited a form of synchronization between initial shear layer and "largest scale information" fed back to the lip. In this way, the "phase randomization" (loss of phase reference) which accounts for spatial jitter in most jets was effectively reduced, due to a phase lock at the point of receptivity.

Under general non-resonant conditions, however, the location of pairing events is not fixed. Monkewitz (1983) examined the weak feedback mechanism associated with pairing interactions and the jet column instability mode. Low-frequency amplitude modulations of the initial shear layer instability were unequivocally shown to correspond to the passage frequency at the end of the potential core, which effectively "organizes" the development of the jet, through receptivity. Even weakly felt at the lip, the low-frequency forcing due to the jet column mode may be essential, since low-frequency modulations have been shown to play a dominant role in the transition process (Miksad

et al., 1982), although the question here is whether the low frequencies can be a bi-product of the detuning in a parametric interaction.

As pointed out by Ho and Huerre (1984), the global understanding of jet dynamics requires the coupling between the initial conditions in the shear layer and the downstream "dominant flow events" which may feed back to the lip through pressure disturbances. Herbert and Morkovin (1980) also stressed the global dependence of the flow on the receptivity and the matching of the shear-layer frequencies with that of the weakly preferred mode.

Although feedback loop considerations bestow upon jet flows an underlying degree of *intrinsic* order, these flows exhibit a remarkable sensitivity to environmental forcing. Gutmark and Ho (1983), for example, compiled data from six jet facilities and found that small facility-dependent spatially coherent perturbations caused large variations in initial Strouhal number, frequency of the preferred mode, and spreading rates (as much as 100%). In contrast to the sharp sensitivity of the shear-layer to initial conditions at the lip, the jet-column mode has been found to be remarkably independent of initial conditions. Hussain and Zaman (1981), in particular, showed that the Strouhal number scaling of the preferred mode was independent of whether exit conditions were laminar or turbulent. They mentioned that the gradual independence from initial conditions is achieved via successive restructurings of the shear layer, evolving to a "terminal structure" at the end of the potential core.

Of importance (among the dominant modes of the jet) is the helical instability mode, which is approximately equally amplified as the fundamental axisymmetric mode. Drubka (1981) showed experimentally the existence of a helical mode having a Strouhal number 23% higher than that of the fundamental axisymmetric mode. Shakib (1984) used the maximum entropy method to document the switching between helical and axisymmetric modes, and concluded that the existence of one effectively suppressed the

presence of the other. A satisfactory explanation of the origin of the switching between these modes has not yet been put forth. It is believed that considerations of the continuing non-linear competition between these dominant modes (including subharmonic and jet-preferred modes), coupled with feedback to the lip, may provide significant insight into the deterministic non-linear dynamics of the jet.

1.2. *Free shear flows with feedback*

In contrast to the weak feedback that naturally occurs in jets (with the exception of the jet-column mode), strong feedback loops can organize free shear flows in spectacular ways. The interest in studying flows which exhibit such resonances stems in part from the fact that their "non-resonant" counter-part (i.e. in the absence of strong phase-locking) may be regarded in most respects as containing the underlying degree of organization which appears when enhanced by feedback. In addition to purely hydrodynamic resonances initiated by "pockets of absolute instability" (Chomaz et al., 1987), self-sustained oscillations are most commonly observed in free shear flows impinging on boundaries.

In their review, Rockwell and Naudascher (1979) stress the four key ingredients that constitute these flows. These are: "inducement" of local vorticity fluctuations at separation, amplification in the shear layer, production of disturbances at impingement, and feedback. The feedback process can be either hydrodynamic (Biot-Savart induction) or acoustic (e.g. vortex straining may act as a pressure source). In air, it is the latter of the two which is predominant. According to Rockwell and Naudascher (1979), the impingement of vortical structures on the downstream body is probably the least understood of the four, although considerable progress has been made in this area, as exemplified by the detailed knowledge of vortex-edge interactions obtained in recent years (see for example Kaykayoglu and Rockwell, 1985). Also, depending on the

geometry, the presence of solid boundaries downstream of separation may either generate the disturbances, or inhibit their upstream influence, thereby breaking the feedback loop. In jets, even though pressure waves may propagate through the core, most of the energy has been shown to be fed back through the ambient fluid.

It is important to classify impinging shear layers in the context of absolute and convective instability. It should first be clarified that these linear concepts refer to local vortical fluctuations, which are not to be confused with the overall degree of organization which may be present in resonant or feedback systems. For instance, in Ho and Nossier's (1981) impinging jet experiment, the location of pairings is fixed and may be predicted using an 'integer number of wave lengths around the loop' criterion. The coherent oscillations of the flow are the result of a "global" instability. This phenomenon is referred to by Huerre (1987) as a "hydroacoustic resonance", as opposed to the purely hydrodynamic resonances that may occur without the presence of a downstream body in some flows containing regions of absolute instability. There is also evidence that the stability properties of the hydrodynamic part of even strong feedback loops remains relatively unaltered by the global instability. Namely, shear-layer tones, flows over cavities and other edge-tone like phenomena are convectively unstable flows. Hussain and Zaman (1978), for instance, found remarkably close agreement between the normal phase distributions and eigenfunction amplitudes associated with the shear layer tone phenomenon, and spatial linear stability theory.

Unlike convectively unstable flows in the absence of feedback loops, hydroacoustic resonances display a clear insensitivity to external disturbances, as far as global oscillations are concerned (see e.g. Ho and Nossier, 1981). Although the insensitivity to external perturbations is a property which is shared by absolutely unstable flows, it should be stressed that the flows under consideration remain locally convectively unstable, as one should expect if the local mean velocity profile is not significantly

affected by the presence of a feedback loop.

The great majority of flows capable of self-sustained oscillations have been shown to share qualitatively similar characteristics. It is believed therefore that they are controlled by a common basic mechanism. Among these shared properties, one of the most striking features is the existence of "frequency stages". The observed frequency of oscillation jumps between stages, and these frequency jumps may or may not be accompanied by hysteresis. In cases of weaker feedback, such as Hussain and Zaman's (1978) shear layer tone experiment, intermittent switching is observed in the vicinity of frequency jumps. However, in flows with a high degree of symmetry, such as in hole tone experiments, there is evidence of strong hysteresis. Within a given frequency stage, the number of cycles in the loop is presumably fixed so that phase information is preserved. The frequency of oscillation increases within a given stage with increasing Reynolds number and decreasing impingement distance from the point of separation.

Depending on the flowfield, various empirical formulae have been used to determine the frequency stages. Although it is believed that these various flowfields must satisfy the same fundamental feedback condition that there be an integer number of periods (N) around the loop, it is not uncommon to observe (among others) criteria involving $(N + 1/4)$ (edge tones) or $(N + 1/2)$ (shear layer tones). Unknown phase changes at the impingement and receptivity stages of the loop might account for these differences. Another common characteristic of hydroacoustic resonances is the existence of a threshold in Reynolds number, in order for self-sustained oscillations to make their appearance. In the case of impinging shear layers, the distance between impingement and separation must also exceed a minimum value. Sarohia (1977) established the existence of a minimum dimensionless length in the case of flow over an axisymmetric cavity, and showed that this number was independent of cavity depth.

As mentioned by Rockwell and Naudascher (1979) and Herbert and Morkovin

(1980), although several frequencies may simultaneously be found near the point of separation, usually only one eventually dominates the flowfield. Indeed, the coexistence of amplified modes of oscillations within the feedback loop appears to be rare, except if several independent loops are present, or if the frequencies are harmonically related. This last case was illustrated by Lucas and Rockwell (1984) for a planar jet impinging upon a wedge, where all frequencies in the spectrum could be related to the interaction of two modes of oscillation whose frequencies were multiple of each other. Knisely and Rockwell (1982) focussed on the presence of a dual subharmonic in the oscillations of a cavity shear layer. They showed that each of the observed modes corresponded to eigenfrequencies of the feedback loop and that the low-frequency modulation was due to the lowest eigenvalue (i.e. one cycle around the loop).

Krothapalli (1985) experimentally investigated a choked underexpanded jet impinging on a flat plate and showed the coexistence of two feedback loops. The first feedback loop corresponded to the classical "screech" tone, whereas the second, "impinging" tone, was shown to correspond to large scale structures convecting at half the jet velocity, in accordance with Ho and Nossie (1981). Thus, both the shock wave and the distance to the flat plate played equivalent roles as feedback flow scales. Umeda et al. (1987) also conjectured a double feedback loop of similar nature in the case of strong discrete tones generated from the interaction of a high speed jet with a circular cylinder. They concluded to the existence of two characteristic length scales for the feedback loop: the shock cell structure, and the nozzle to cylinder distance. An interesting suggestion was also made concerning the practical use of multiple feedback loops to produce wave cancellation, a result which appears to have been successfully demonstrated by Nagel et al. (1983) in the case of supersonic jet screech.

Among the various theories aimed at the prediction of self-sustained oscillations, Powell's (1961) theory of the edge tone is recognized as one of the most complete to

date, despite the fact that it used a somewhat arbitrarily prescribed phase difference between impingement and separation. Most theories revolve around such a postulate, complemented by results of linear stability theory. Powell developed an elegant "unity gain around the loop" criterion from which he derived most of the qualitatively observed features of edge tone phenomena such as velocity and distance thresholds, frequency jumps, and even hysteresis. Woolley and Karamcheti (1974) emphasized more strongly the essential role of shear layer amplification, but claimed that the frequency decrease that was observed with increasing streamwise flow scale was the result of non-parallel effects. Hussain and Zaman (1978) argued that it cannot be so, since the frequency of oscillation does not scale with local momentum thickness. Another deficiency of Woolley and Karamcheti's theory (which is based on the integrated amplitude by application of non-parallel stability theory) is that it does not address the problem of frequency jumps. Tam and Block (1978) developed a complex model based on a rigorous analysis of cavity tones. In their model, the shear layer thickness comes into consideration, along with the aspect ratio of the cavity. Their results illustrate the possibility of a cavity mode resonance at low Mach number.

It is important to realize that the generality of self-sustained oscillations does not apply solely to laminar flows like edge tones, and that coherent oscillations have been obtained via strong feedback loops in fully turbulent flows (Sarohia, 1977). Also, Ho and Nossier (1981) obtained spectacular phase-locking of large scale coherent structures in a high-speed subsonic turbulent jet impinging on a flat plate. Intermittent switching was also observed close to frequency jumps between stages. According to Ho and Nossier, the Strouhal number of the resonant modes was close, on the average, to the "most unstable mode of a free jet column". They concluded that the entire organizing process revolved around the multiple merging of coherent structures or "collective interaction", (similar to Crow and Champagne's, 1971), and stressed the essential role of large scale

structures in the feedback mechanism. As pointed out by Rockwell and Naudascher (1979), the reduction of spatial jitter in spatially developing flows is closely tied to the nature of the highly coherent feedback mechanism which is attainable in both laminar and turbulent flows.

2. Experimental facilities and procedures

2.1. *Experimental facility*

The main facility used in this study was the I.I.T. air jet facility depicted in Figure 1. This facility is essentially unchanged from the configuration used by both Drubka (1981) and Shakib (1984), except for modifications upstream of the settling chamber. The settling chamber is acoustically insulated with foam and contains a series of grids, screens and honeycombs carefully designed to produce a uniform, low turbulence intensity flow at the outlet. The actual details of the settling chamber are reported by Ahmed et al. (1976). During the course of the present investigation, a single test-section configuration was used, corresponding to Drubka's (1981) "1L" case. The test section is made of a 38.1 cm long plexiglass circular cylinder (diameter 15.2 cm) followed downstream by a fifth-order contraction of 9:1 area ratio, and produces a uniform jet with thin laminar exit boundary layers (exit momentum thickness Θ less than 1/200 diameter). The exit diameter is 5.1 cm, and the jet velocity ranged from 10 m/s to 30 m/s. Many of the details of the experimental set up, along with the well documented spatial characteristics of this flowfield, can be found in Nagib et al. (1989). For the purpose of the present manuscript, it suffices to stress that the overwhelming characteristic of this facility is its low freestream turbulence intensity (less than 0.05%). Stepper motors powered the traversing mechanism and provided a positioning accuracy of 10 μm in the streamwise direction and 5 μm in the radial direction (the hot-wire sensor was 3.8 μm in

diameter). The traversing mechanism was used to control the position of the miniature hot-wire probe which was used and described by Drubka (1981). The use of the miniature probe (prong diameter $7.6 \mu\text{m}$) over other available probes was found to be critical, particularly in terms of often unsuspected probe feedback effects (see Hussain and Zaman, 1978 and Reisenthel, 1988). A second (stationary) hot-wire probe was occasionally placed farther downstream and diametrically opposed to the miniature probe, in order to document the spatial structure of the flow field. Both probes were placed at a 45° angle from the flow in order to minimize probe body interference.

2.2. Enhanced feedback configuration

The so-called "enhanced feedback" configuration is depicted in Figure 2. This case of artificial feedback was designed to provide a controlled means of reinjecting disturbances originating at an arbitrary location in the jet, back to the point of shear layer separation. The velocity signal measured by the miniature feedback sensor was amplified, using an adjustable gain analog amplifier, and used as an input to the speaker placed 70 diameters, D , away from the jet exit, therefore generating pressure fluctuations of magnitude proportional to the input velocity fluctuation at the sensor location. The feedback loop is closed by the upstream propagation of these pressure waves, and their coupling with initial fluctuations at the point of receptivity. The strict linearity of the return leg in the loop was documented by Reisenthel (1988). Finally, transient measurements were made possible by the synchronization of A/D and D/A transfers controlling the closure (or the opening) of the feedback loop at specific times during digital data acquisition. This operation relied on fast electronic switches, which were externally controlled by the analog output level of an MC-5500 series Masscomp computer.

3. Non-linear effects of closed-loop excitation

3.1. Gain threshold

The majority of the work described in the present manuscript focuses on the harmonic excitation of the jet by means of enhanced feedback. Although the nature of self-sustained oscillations under these conditions is generally not harmonic (see Reisenthel, 1988), the jet is strongly organized when the feedback hot-wire sensor is positioned at spatial locations for which the flow is both laminar and axisymmetric. In practice, these conditions are reasonably well satisfied up to the first pairing location (approximately four fundamental wave-lengths downstream of the lip), and on the high-speed side of the shear-layer. Self-sustained oscillations with the purest spectral content were obtained by positioning the feedback sensor along similarity lines of constant mean velocity U such that typically: $0.6 < U/U_j < 0.9$.

A typical power spectrum of the streamwise velocity is shown in Figure 3, where the spectra of the natural and excited shear-layer are compared at $Re = 68,000$. This organization of the initial shear layer is present both upstream and downstream of the feedback sensor, as demonstrated in Figure 4. In all cases, no initial forcing was required to start these self-sustained oscillations. In addition, the peaks in the power spectrum of the excited jet (Figure 3) are seen to be apparently unrelated to the natural fundamental axisymmetric mode (frequency f_0).

One of the most striking characteristics of these self-sustained oscillations is their strong dependence on the total *gain level* of the feedback loop. The gain level G is defined as the pressure fluctuation p' measured at the jet lip, per unit velocity fluctuation u'_x at the location of the feedback sensor: $G = p' / u'_x$ (non-dimensional gain:

$$\Gamma = \frac{2p'}{\rho u'_x U_j}).$$

Qualitatively speaking, low gains have little or no effect on the shear-

layer, whereas high values of the gain promote self-sustained oscillation. In the limit of infinitely small gains, one intuitively expects to observe the natural jet behavior (open

system), since no external pressure waves are added to the background sources of excitation (turbulence intensity, environmental conditions, and natural jet feedback). As the gain is slowly increased, low-level acoustic disturbances not unlike "wind noise" start to affect the shear-layer, but with no distinct spectral signature. As the gain is increased further, regular tones make their intermittent appearance (see Reisenthel, 1988). These tones are unsteady and continually switch in an apparently random way. Time-averaged spectra show that the tones correspond to closely spaced frequencies of low amplitude (frequently subaudible), that are simply superimposed on the background spectrum. A very small increase in the gain from this point produces a distinct and dominant frequency, the amplitude of which saturates rapidly, and remains relatively unchanged with further increase of the gain.

The above scenario is quite general and has been repeated at numerous Reynolds numbers and sensor positions (denoted X). Figure 5 illustrates the variation of amplitude with gain, at $Re = 75,700$ and $X/D = 0.132$. Under these conditions of Reynolds number and probe position, the frequency of the self-sustained oscillation was 3320 Hz. The amplitude of the fluctuation "jumps" by at least three orders of magnitude as Γ exceeds a certain *threshold*. It should be stressed, however, that the data points presented here are time averages of the spectral density, and that the smooth transition of the amplitude across the threshold is nothing but the result of the long-time averaging process. In reality, the oscillation has a marked intermittent character, close to the critical point. Therefore, in the neighborhood of the threshold, the mean spectral density reflects the proportion of time for which the amplitude saturates. Additionally, the vertical dashed lines indicated in Figure 5 represent the boundaries of hysteretic behavior: as Γ is rapidly decreased from a state of fully established, saturated self-sustained oscillation, the fluctuation vanishes at a gain value close to Γ_1 . Conversely, the onset of oscillation is delayed until Γ_2 as the gain is rapidly increased. Incidentally, the range $\Gamma_1 < \Gamma < \Gamma_2$

coincides approximately with the intermittent region as the gain is varied across the threshold in a quasi-steady fashion. For these reasons, the curve presented in Figure 5 illustrates the existence of a gain threshold, but does not suggest the actual abruptness with which amplitude changes take place in an instantaneous sense.

Within the region where self-sustained oscillations are possible, there is a sensitive dependence of the threshold location on downstream position of the feedback probe. Figure 6 depicts the peak amplitude of the feedback frequency as a function of gain for four values of X/D . At this Reynolds number ($Re = 61,800$), the oscillation frequency F decreased from 2260 Hz to 2120 Hz with increasing X/D . For a given value of the gain, the generation (or decay) of self-sustained oscillations depends critically on sensor location. Figure 6 illustrates these large variations in threshold value. Specifically, the X/D range considered in Figure 6 represents only 2.2 wave-lengths (λ) of the oscillation, but the corresponding variation in Γ threshold is approximately 500.

3.2. Frequency selectivity

The "intrinsic" response of the shear-layer (under given feedback excitation conditions) represents a substantial departure from the convective instability concepts ordinarily associated with jets and shear layers. Figure 7 illustrates the intrinsic response of the feedback loop at $Re = 64,000$. At this Reynolds number, the frequency of the fundamental axisymmetric mode was $f_0 = 1700$ Hz, while the frequency selected by feedback was $F = 2140$ Hz. In an attempt to "disturb" the feedback process, the jet was also externally forced, using the adder configuration depicted in Figure 2. The forcing frequency was chosen in this case to be $f^* = 2020$ Hz, and the initial forcing level was selected such that the corresponding spectral peak in the velocity signal had an amplitude slightly larger than that of the fundamental axisymmetric mode, as measured by the feedback sensor. This situation was designed to "favor" an initial frequency, and

examine the subsequent shear-layer response as the gain is gradually increased. In this fashion, one alters the initial imprint (or signature) of background jet fluctuations on the feedback process itself. Figure 7 depicts the spectral amplitude of all three frequencies as a function of gain. The gain Γ is shown on a logarithmic scale, and is normalized by the critical gain Γ_c , defined as the value of Γ which characterizes the gain threshold. A more refined definition of Γ_c , based on semi-theoretical considerations is presented in subsequent developments. The intrinsic frequency selected by the feedback (2140 Hz in the present case) is called "eigenfrequency", in accordance with Powell (1961). At the lowest value of Γ , the axisymmetric and forcing frequencies have comparable amplitudes. However, no spectral peak is detected at the eigenfrequency until Γ reaches approximately 60% of Γ_c . As Γ crosses the threshold, the amplitude of the eigenfrequency rises rapidly and saturates, while the two other peaks quickly become indistinguishable from spectral background. This characteristic *selective growth* of the eigenfrequency is a remarkable property, when one considers that all three initial frequencies are fed back with identical gain.

Similarly, Figure 8 illustrates the shear-layer response to white noise forcing in the closed-loop configuration described above. The amplitude of the eigenfrequency (3320 Hz at $Re = 76,300$) is clearly dissociated from the background amplitude, which increases linearly with Γ . Of all possible frequencies initially introduced via white noise forcing, only *one* emerges with a clear spectral peak.

3.3. Hysteresis and band structure

The above results conclusively show the existence of a unique frequency selected by the enhanced feedback, and that the appearance of this self-sustained oscillation depends on a gain threshold. Concerns over the repeatability of excitation conditions (i.e. actual frequency and threshold values) set up by means of enhanced feedback motivated the

measurements presented in this section. The existence and frequency of the self-sustained oscillations was recorded systematically as a function of gain and Reynolds number. The resulting maps constitute the feedback "environment", for a given position of the hot-wire sensor.

Figure 9 depicts successive "slices" of the feedback environment corresponding to different values of the gain. For practical reasons, it is difficult to maintain the non-dimensional gain Γ constant, when varying the Reynolds number. Thus, the gain in these figures is the dimensional gain G , measured in Ns/m^3 . In each graph, the thickest lines are actually collections of closely spaced data points relating the value of the eigenfrequency to the Reynolds number. The absence of data points in certain regions of the (Re, G) parameter space simply indicates that no self-sustained oscillations were present under the particular conditions of Reynolds number and gain setting. In addition, the frequency of the fundamental axisymmetric and linearly most amplified instability modes is indicated as a reference. These correspond to Strouhal numbers $St_{\Theta} = 0.0132$ and $St_{\Theta} = 0.0163$ respectively, as determined experimentally for the present flowfield (see Nagib et al., 1989). Figure 9 reveals several important facts. The first one is the accumulation of the data points along well-defined "stages". Each stage is a well defined entity, with upper and lower bound in Reynolds number, and almost constant frequency. The second observation is the widening of existing stages, as well as the appearance of new stages, with increasing gain. At a given Reynolds number, the appearance of a new stage with increasing gain corresponds to the crossing of a threshold, similar to the case illustrated in Figure 5. Low gain values are typically characterized by disjoint stages. As Re varies, the "crossing" of a given stage is accompanied by a noticeable intermittency in the immediate vicinity of its boundaries. As the boundaries of distinct stages get closer to one another with larger gain, the intermittency takes the form of a switching between competing tones.

With a further increase in the gain, the widening of the stages eventually leads to hysteresis. The hysteresis phenomenon is shown by the overlap of the stages, signifying that at a given Reynolds number two or more self-sustained oscillations are possible. It is important to realize, however, that these possible frequencies are usually mutually exclusive, and that the eigenfrequency that is physically observed depends on the entire *time history* of the flowfield. In the presence of hysteresis, the precise extent of a given stage must be determined by varying the Reynolds number in both directions, using the stage itself as the initial condition. The careful documentation of the position and extent of the various stages in the (Re, G) space is an essential consideration for repeatability issues, thus justifying the terminology "feedback environment".

A more concise and informative way of representing the feedback environment is to focus on the boundaries of a given stage. Figure 10 shows the boundary location of the four principal stages observed in Figure 9, plotted as a function of gain and Reynolds number. The global structure emanating from this representation is a series of overlapping *bands*. Each band is labeled by its characteristic frequency. In reality, the proper characterization of a band is not its frequency (which varies slightly with Re), but a certain integer (see section 4.1). For the present discussion, however, each band of oscillation is tagged by its central frequency. The boundaries of a band can be defined in several different ways. The convention used here is that a band ends when intermittency appears. This operational definition avoids ambiguities in the experimental determination of a stage. If the intermittent region were to be included in the definition of a stage, the bands would be slightly wider with respect to Reynolds number, and the measurement would be subject to more error. The widening of the bands with increasing gain is thus clearly evidenced, and the onset of hysteresis between two adjacent bands at the higher gains is indicated by the crossing of their boundaries. A great number of additional bands can be found using, as controlled initial conditions, the external forcing

of a particular frequency (Reisenthel, 1988).

The most common hysteretic configuration ("simple" hysteresis) refers to the existence of two possible eigenfrequencies at a given Reynolds number. This situation is characterized by frequency jumps at the edges of the region of overlap of the two competing bands. More severe cases of hysteresis include situations where three frequencies compete to feed back. This special case can lead to curious frequency modulation effects, as shown in a later section. The rich band structure underlying the feedback environment is further illustrated in Figure 11. In this case, the feedback probe was positioned farther downstream ($X/D = 0.30$), with a dimensional gain $G = 0.033 \text{ Ns/m}^3$. The increase in the streamwise position of the sensor reveals a large number of bands, particularly at the lower Reynolds numbers. A consistent feature of the eigenfrequencies is the fact that their value generally lies within the interval delimited by the fundamental axisymmetric and most amplified frequencies. Figure 12 presents the various stages at two $(X/D; G)$ conditions using the Strouhal number St_{Θ} based on initial momentum thickness Θ and jet velocity U_j . It is clear that the eigenfrequency associated with feedback does not scale with shear layer thickness. The scaling of the eigenfrequency and the role of the shear-layer instability as a vehicle for the amplification of disturbances are examined section 6.

Hence, a complex band structure controlling hysteresis and frequency jump phenomena underlies the enhanced feedback environment. The dependence on the "path", or "start up" conditions of the flowfield for nominally identical Reynolds number and excitation conditions has been clearly illustrated. The mapping of the eigenfrequency bands was found to be crucial to the understanding of the role of initial conditions in the frequency selection process.

3.4. *Insensitivity to external disturbances*

Earlier results illustrating frequency selectivity have shown the existence of spontaneous oscillations in the feedback loop. The intrinsic nature of this instability was documented using external forcing which altered the initial signature of the jet (Figure 7). In this case, the forcing levels were kept constant, while the feedback gain was varied. Therefore the amplitude of all frequencies was nominally affected by an equal amount. Nevertheless, an increase in the gain was shown to establish a unique self-sustained oscillation that was independent of the nature (i.e. harmonic or white noise) of the initial forcing. In order to evaluate the resilience of the eigenfrequency to external forcing, the results presented in this section examine the case where the total gain is fixed, and the forcing levels are varied. This represents a very stringent test since the proportion of energy of the eigenfrequency F and forcing frequency f^* is now deliberately varied over several orders of magnitude. An additional complication arises from the fact that the forcing frequency is introduced twice in the feedback loop: once by direct input from the signal generator, and once through the hot-wire signal.

Figure 13 depicts the destabilization of the eigenfrequency ($F = 3340$ Hz) with increasing forcing level. The open-loop response of the shear-layer at the forcing frequency ($f^* = 3266$ Hz) is shown for comparison with closed-loop excitation. One can deduce from the average 10 dB increase in the closed-loop response of the external forcing that the fluctuation must be approximately in phase at the adder stage of the feedback loop (see Figure 2). Despite the net increase in the amplitude of the forcing signal, the energy of the eigenfrequency remains constant over two orders of magnitude of the forcing. A similar case of excitation is presented in Figure 14, where the forcing frequency was changed to $f^* = 3222$ Hz. The closed-loop amplitude of the forcing fluctuation is now smaller than the open-loop response. This indicates that the fraction of the forcing signal that is fed back to the adder is out of phase with the signal generator output. With this choice of f^* , it was not possible to disturb the eigenfrequency within

the range of amplitudes that could be generated. Figures 13 and 14 consider the case of fully established self-sustained oscillation, using a non-dimensional gain $\Gamma = 0.0176$. Similar measurements were made closer to the gain threshold at $\Gamma = 0.0044$. These measurements were performed with forcing frequencies chosen such that the excitation was respectively in phase and out of phase at the adder. Predictably, the range of forcing amplitudes at which the eigenfrequency remained insensitive to external forcing was somewhat decreased, as compared to the results of Figures 13 and 14. In any case, it was clear that the intrinsic character of the eigenfrequency is not limited to small excitation levels, since the amplitude of the eigenfrequency remained unaffected for several orders of magnitude in either case. Thus, the combination of enhanced feedback with external forcing provides clear evidence of the *intrinsic nature* of the closed-loop fluctuations. In the following, a few analytical results are derived along with the examination of the spatial and temporal characteristics associated with these global fluctuations.

4. Analysis of feedback constraints based on experimental results

4.1. Eigenfrequency formulation

It was shown that for values of the gain which exceed a certain threshold, self-sustained oscillations take place, the frequency of which does not scale with initial shear-layer thickness. The band structure underlying this phenomenon provides a concise representation of the feedback environment, compatible with the various observed nonlinearities (frequency jumps, hysteresis). Some basic questions remain to be answered, however. For example, what is the origin of this global instability, and how does its frequency scale?

Figures 13 and 14 illustrated the effect of externally forcing the jet, in a closed-loop configuration. The main conclusion drawn from these results pertained to the

relative insensitivity of the feedback instability to external forcing. The experiments described in these figures also revealed that the choice of the forcing frequency f^* , was an important parameter. For certain values of f^* , the closed-loop amplitude increased with respect to the open-loop response, whereas other choices of f^* inhibited the amplitude associated with this frequency of oscillation. It was suggested that the fraction of energy reinjected in the feedback loop in these cases was respectively in phase and out of phase with respect to the forcing signal.

This hypothesis was experimentally verified by systematically varying the forcing frequency in small increments around the value of the feedback frequency. At each frequency, the gain and forcing amplitude were kept constant. From the spectrum of the feedback signal, the relative amplitudes of the fed back (A_F) and forcing (A_{f^*}) frequencies were recorded. Figure 15 presents their ratio as a function of frequency. The data are shown for two values of the gain ($\Gamma = 0.0044$ and $\Gamma = 0.0088$), at $Re = 76,000$. The value of the eigenfrequency was 3330 Hz and 3340 Hz at the low and high gain respectively. Figure 15 demonstrates that the relative amplitude of the two frequencies varies by several orders of magnitude (for $\Gamma = 0.044$), as the forcing frequency scans the range $3000 \text{ Hz} < f^* < 3550 \text{ Hz}$. The sharp dips in the amplitude ratio were experimentally observed to correspond to the simultaneous enhancement of the forcing frequency, and inhibition of the eigenfrequency. These dips may be considered as a form of resonance. Staubli and Rockwell (1987) referred to the above phenomenon as "quenching". Not surprisingly, this behavior was less pronounced at $\Gamma = 0.0088$, owing to the increased resilience associated with higher gains. The regular structure displayed by the results of Figure 15 adds considerable insight to the feedback phenomenon. In particular, it suggests a relatively small frequency increment Δf between adjacent bands. It appears therefore that the permissible bands are much closer to each other than suggested by the results of Figure 9.

Further evidence of the competition between self-sustained oscillations can be obtained in the vicinity of frequency jumps. Figure 16 represents the hysteresis diagram obtained for $X/D = 0.17$, using a dimensional gain $G = 0.045 \text{ Ns/m}^3$. The solid and dashed lines in this figure indicate respectively the observed stages and the location of observed frequency jumps, as a function of Reynolds number. The Reynolds number was varied in both directions from the middle of each stage, to ensure that the bounds of the stage were correctly determined. The configuration illustrated by Figure 16 involves a complex case of three-frequency hysteresis around $Re = 75,000$. Most cases of hysteresis involve only two competing frequencies. In these situations, the self-sustained oscillation is generally a pure tone: the intermittent presence of the other frequency is only felt very close to the jump location and for low gain values. However, no stable quasi-periodicity is ever observed when two frequencies only are in competition. In other words, the "solution" jumps from one limit cycle to the other; i.e., there is no true coexistence of the eigenfrequencies.

The situation is completely different, however, in the proximity of jumps corresponding to three-frequency hysteresis. The small circles in Figure 16 indicate the location where spectral measurements of the streamwise velocity were made. The corresponding power spectra are shown in Figure 17. For Reynolds numbers smaller than 75,000, the feedback signals corresponded to pure tone oscillation, as indicated by their harmonic spectra. Immediately after the jump, however, there is a dramatic change in the character of the velocity signal. The spectrum at $Re = 75,700$ displays a multitude of coexisting peaks. This quasi-periodic band transition was found to be highly repeatable, but critically sensitive to probe positioning (see Reisenthel, 1988). However, the quasi-periodic band transitions of the type illustrated in Figure 17 appear to be the exception more than the rule. Further inspection of the velocity signal revealed a remarkably regular structure in the spectrum; in addition it appeared that the fundamental

frequency of the oscillation was subjected to some form of frequency modulation. Incidentally, the spacing between neighboring peaks is approximately $\Delta f = 80$ Hz, which is the same value that was obtained by the introduction of an additional forcing frequency (Figure 15). The above results support the hypothesis that a regular structure of competing self-sustained oscillations underlies the frequency selection mechanism.

We now examine the relation between the phase of the closed-loop instability and the regular sequence of resonances shown in Figure 15. Before any attempts to quantify this concept, the hypothesis of phase dependence is examined on the basis of physical observation. In particular, phase variations have been suggested by the modification of the forcing amplitude in the closed-loop configuration of Figures 13 and 14. If a steady self-sustained oscillation is to feed back, the instability wave must be "in phase" with itself at any point in the feedback loop. Empirical observation also suggests that these oscillations tend to always maximize their amplitude under proper gain conditions. This is essentially similar to observations made by Powell (1961) regarding the edge tone phenomenon. Conversely, if the wave length of a particular frequency is such that it is "out of phase" with itself after going through the feedback loop once, then its amplitude will be effectively *reduced* by the introduction of feedback. Naturally, this criterion is overly simplistic, since one must consider the evolution of a fluctuating signal as it travels more than once around the feedback loop. It is clear, however, that if the signal is a pure tone, its amplitude will be maximized, under the condition that there be an integer number of wave lengths around the loop.

Assuming a self-sustained oscillation of frequency f , the various phase delays (denoted $\Delta\Phi$) are calculated according to: $\Delta\Phi = 2\pi f \tau$, where τ designates a time delay. The phase origin in the feedback loop being arbitrary, the acoustic delay is first considered. As a pressure wave propagates from the speaker to the lip (distance d), the wave retardation is $\Delta\Phi_a = 2\pi f d / C_0$, where C_0 designates the speed of sound.

Momentarily ignoring phase relations at the point of receptivity, and assuming a constant phase speed C for the hydrodynamic branch of the loop, we express the hydrodynamic phase delay: $\Delta\Phi_h = 2\pi fX/C$. The phase change associated with the electronics of the feedback loop was negligible. Finally, the effect of the speaker itself was determined experimentally. A microphone was placed at the closest possible location from the speaker cone (i.e. approximately 10 mm away), and the transfer function of the speaker was determined using white noise input. The phase of the transfer function was found to vary almost linearly with frequency, indicating a constant time-delay $\tau_s \approx 0.56$ ms. Therefore, if ϕ denotes the phase-lock due to linear coupling at the point of receptivity, between the incident pressure wave and the initial velocity fluctuation, the global feedback condition ($\sum_i \Delta\Phi_i = 2\pi n$) is expressed by the condition:

$$2\pi f \frac{d}{C_0} + 2\pi f \frac{X}{C} + 2\pi f \tau_s + \phi = 2\pi n, \quad n = 1, 2, 3, \dots \quad (1)$$

Note that the above notation does not suggest that ϕ is a constant. More importantly, the simple addition of ϕ to account for the receptivity process is not intuitively obvious. Some encouraging results, however, can be derived from Bechert's (1982) theoretical analysis. Bearing in mind some of the restrictions of Bechert's calculations (inviscid parallel flow, $\Theta = 0$, etc.), it can be shown that in the limit of large X ($X/\lambda > 2$), the phase-delay between the high-speed side Helmholtz-type contribution of the streamwise velocity and the input pressure gradient at the lip is: $(2\pi fX/U_j - 5\pi/8)$. By analogy with equation (1), one deduces in this case: $C = U_j$ and $\phi = 5\pi/8$, for a vortex sheet and small Strouhal numbers. Therefore, it is believed that the introduction of $\phi \neq 0$ in model equation (1) is justified, to a first degree of approximation. For the real shear-layer under investigation ($129 < Re_\Theta < 193$), the possible dependence of ϕ on Strouhal number and various flow parameters is unknown, and its value was arbitrarily set to zero in the

following numerical implementations of equation (1), rather than assuming a functional form for ϕ .

Equation (1) represents an eigenvalue problem, since a solution (the "*eigenfrequency*") to the feedback model equation only exists for integer values of n (the *eigenvalues*). Using equation (1), one can solve for the eigenfrequency:

$$f_n = \frac{n - \frac{\phi}{2\pi}}{\frac{d}{C_0} + \frac{X}{C} + \tau_s} \quad (2)$$

Equation (2) reveals that because of the receptivity term ϕ (and also because of the dispersive nature of instability waves), the eigenfrequencies f_n are *not*, in general, expected to be harmonically related. This means that the feedback competition between a fundamental frequency with some of its harmonics is unlikely. Conversely, should the simultaneous feedback of several eigenfrequencies be observed, issues of frequency locking could play an important role in furnishing insight into the dynamics of these instability waves. Figure 18 constitutes an example of the implementation of equation (2), which is compared with the bands detected at $X/D = 0.128$ using a dimensional gain $G = 0.132 \text{ Ns/m}^3$, and for Reynolds numbers ranging from 45,000 to 85,000. It is clear that the observed stages indeed correspond to eigenfrequencies of the type described by (2). Hence, the eigenfrequencies f_n represent the set of "allowable" frequencies for self-sustained oscillations, but do not offer any explanation for the eigenvalue selection process as a function of Reynolds number. This question is examined in detail in section 4.2, and in the discussion. Further experimental verification of the suggested model was performed by varying the distance d between the speaker and the lip from $d/D = 70.7$ to $d/D = 30.5$ and $d/D = 4.5$. At the closer speaker locations, less quantitative agreement was found between the model and the experimental data. It is clear from equation (2), that acoustic and hydrodynamic delays d/C_0 and X/C play similar roles, as far as phase

is concerned. Figure 19 is a comparison of the predicted eigenfrequencies with the observed bands at $X/D = 0.295$. Once again, there is at least qualitative agreement between prediction and experiment. In particular, the decreased eigenfrequency spacing ($f_{n+1} - f_n$) results in a larger number of observable frequencies. Consecutive stages are still found to correspond to 2π phase jumps, and the small quantitative differences between data and model are principally attributable to an overall phase shift. Since phase changes in a closed-loop configuration always manifest themselves by a shift in the frequency of the fluctuation, small phase changes across the shear-layer can produce sizable frequency variations, depending on the total length of the feedback loop.

Thus, it has been shown that the feedback condition restricts the frequency of self-sustained oscillations to a discrete set of permissible eigenfrequencies. This condition can be regarded as a constraint which effectively "closes" the system.[†] There has been more than one indication at this point that the enhanced feedback configuration makes the flow behave like a closed system, with respect to instability waves. The most striking feature corroborating this view is the global insensitivity to external disturbances. Figure 19 brings to attention a point of interest: in the limit of large delays (speaker at infinity, or large X/D), the eigenfrequencies become infinitely close to one another. One may then expect the resilience of the system to external fluctuations to collapse, since all frequencies are then allowed to feed back. It is tempting to hypothesize that this situation constitutes the open flow limit, although such questions may not be answered by phase considerations alone. Conversely, the above results underline the crucial importance of incidental boundary or feedback conditions in both experimental and numerical investigations of open flows.

[†] *The terminology is inspired by analogy with closed flows, for which resonances occur when particular wave-length conditions are favored by the presence of solid boundaries.*

4.2. Transient amplitude evolution

There are several ways to analyze the time evolution of a closed loop system. The present analysis decomposes the system into two separate parts. First, the open-loop response of the system to external forcing is examined independently. Then, properly formulated feedback constraints are added to the open system in order to determine the global closed-loop response.

Quasi-steady Analysis. The first element of the feedback loop is the hydrodynamic branch, defined as the portion starting from the input pressure fluctuation at the lip, and resulting in an output velocity fluctuation measured at the sensor location. The characteristics of this portion can be examined by determining its non-linear *transfer function*. The transfer function is experimentally measured in a controlled open-loop forcing situation, in which known input pressure fluctuations at the lip (p') result in amplified stream-wise velocity fluctuations u'_x at the sensor location. Owing to the shear-layer amplification characteristics, the transfer function is expected to vary with the frequency of the input disturbance. Three typical transfer functions are shown in Figure 20. These were measured at $x/D = 0.16$ and $Re = 61,600$, for forcing frequencies equal to 2240 Hz, 2500 Hz and 3700 Hz respectively. The open-loop response of the shear-layer is shown over a range of forcing amplitudes covering as many as five decades. Non-dimensional pressure fluctuations smaller than $2 \cdot 10^{-6}$ could not be perceived by the human ear, but had measurable effects on the shear-layer. For reference, it should be noted that the low sound pressure levels used by Shakib (1984) in the same facility corresponded to $p' / \frac{1}{2} \rho U_j^2 = 5 \cdot 10^{-5}$. This level is considered very small, as compared to many of the available investigations on forced shear layers (see Ho and Huerre, 1984), and corresponds to a total amount of input energy equal to the freestream turbulence intensity, concentrated in a single frequency.

The shape of each transfer function can be characterized by three regions. At low

energy inputs, the velocity fluctuation has a constant spectral amplitude, equal to the level of the background spectrum at that frequency. At the largest levels of fluctuation, the velocity fluctuation reaches saturation. For the large intermediate range, however, the slope of the transfer function remains constant. More importantly, all slopes are approximately unity. The unit slopes in Figure 20 indicate the expected proportionality relation between input (p') and output (u'_x) fluctuating amplitudes. This proportionality relation frequently holds over more than three decades of the forcing, although some exceptions were found to exist for forcing frequencies close to the dominant instability modes of the unforced jet (Reisenthel, 1988), for which non-linear interactions presumably play an important role.

Due to the existence of background fluctuations and because of the saturation range, the transfer functions are by essence non-linear. This is to be contrasted to the feedback portion of the loop (from the sensor to the lip), which is strictly linear. The return leg corresponds to the artificial part of the loop. This includes in particular the electronic stages of amplification, and the generation and upstream propagation of acoustic waves. The global gain associated with the enhanced feedback is therefore the mere multiplication of various known transfer functions ($G = \prod_i g_i$). Each of the elements of the loop is linear, and hence the enhanced feedback effect can be simply expressed as:

$$\frac{p'}{\frac{1}{2}\rho U_j^2} = \Gamma \frac{u'_x}{U_j} \quad (3)$$

where Γ is the non-dimensional gain of the loop. Equation (3) is to be regarded as the amplitude counterpart of (2), since these equations govern dual aspects of the feedback problem.

For the remaining of this discussion, the previous notation used to signify non-dimensionalized velocity and pressure rms fluctuations is replaced by the symbols u and

p respectively. For consistency with the orientation of Figure 20, equation (3) is considered in its reciprocal form ($u = \frac{1}{\Gamma} p$), which represents a set of curves parameterized by Γ . These feedback constraints are graphed in Figure 21 as a series of parallel curves, C_Γ , horizontally shifted from ($\Gamma = 1$) by an amount $\ln(\Gamma)$. Geometrically speaking, given the gain Γ , a pair $(u;p)$ must belong to C_Γ in order to represent a self-sustained oscillation. Evidently, the actual value of u or p is undetermined a priori. However, in the closed-loop situation, $(u;p)$ must belong to the open-loop non-linear transfer function curve, as well as to the gain curve C_Γ . The operating point is thus defined as the intersection (if it exists) of both curves. Figure 21 shows the open-loop transfer function corresponding to the eigenfrequency selected by feedback at $Re = 61,600$ and $X/D = 0.16$. Two opposite gain configurations are hypothetically considered: at the high gain value ($\Gamma = 0.01$), the amplitude of the velocity fluctuation must coincide with the saturation amplitude. In contrast, at low gain values (e.g. $\Gamma = 0.001$) the amplitude remains equal to the background value. Furthermore, the quasi-parallelism between the open-loop transfer function and gain curve is recognized as the cause of abrupt amplitude changes, as the gain is increased through a critical value. The documented observation of a gain threshold (Figure 5) can therefore be attributed to the linear portion of the open-loop transfer function.

The above considerations regarding the existence of an "operating point" $(u;p)$ in the feedback loop are steady-state considerations. Empirical observation, however, suggests that transient effects can be quite appreciable. Specifically, it was shown that as the gain is suddenly increased beyond a critical value, the jet starts "ringing". This ringing corresponds to the transient amplitude growth of a well defined eigenfrequency. The observation that shorter transients are associated with larger gains also suggests that the gain participates in some sense in the scaling of the feedback instability.

The quasi-steady increase of the gain through the threshold was shown to generate

a rapid but smooth amplitude variation, the smoothness being an artifact of the long-term averaging. In reality, intermittent ringing is observed for values of Γ close to the threshold. The intermittency factor is related to the near-tangency of the open-loop transfer function and gain curves: close to the point of tangency, infinitesimal disturbances of pressure or velocity can cause the instantaneous operating point $(u;p)$ to move erratically along the gain curve. Hence, at the point of tangency, random *microscopic* noise can result in *macroscopic* fluctuations. In addition to intermittency phenomena, the proximity of the threshold is associated with amplitude hysteresis, as the apparent value of the critical gain is dependent upon whether Γ is increased or decreased. The inset of Figure 21 (bottom graph) illustrates how jump phenomena around the threshold can be related locally to the slight concave curvature of the transfer function. In addition, for slightly supercritical values of the gain, one notices the possibility of a narrow "channel" between the open loop transfer function and the feedback curve. The physical significance of channels in first return maps has been shown by Pomeau and Manneville (1980) and Berge et al. (1984) and was related to so-called "laminar periods" in temporally intermittent regimes. It is not certain at this point whether Pomeau and Manneville's theory might be applicable to the present phenomenon, although the gathering of statistical information of intermittency close to critical gain might prove to be a worthwhile avenue of research in establishing possible connections with their model. This exemplifies how the actual details of the open-loop characteristics can be enhanced temporally by closed-loop feedback.

Critical Gain. Two main questions are addressed in the present section: can the (so far experimentally observed) existence of a critical gain be substantiated on analytical grounds, and what is the physical significance of the critical gain, in relation to the shear layer characteristics?

We first focus on the modeling of the open-loop transfer function. The principal

characteristics of the non-linear transfer functions are: a range of linear dependence of u on p , followed by the saturation of u . In accordance with Miksad (1972), we consider the equation of lowest possible order, capable of displaying the above non-linear character.

Let u' be the rms wave amplitude. Consider the following Stuart-Landau like equation:

$$\frac{d u'^2}{dx} = -2\alpha_i u'^2 + 2\beta u'^4 \quad (4)$$

where the quadratic term $2\beta u'^4$ merely represents the smallest order non-linearity that can act as a limiter of the initially exponential growth of the energy. Note that $-\alpha_i > 0$ is the linear spatial amplification rate of the disturbance.† The term $\beta < 0$ is the so-called Landau coefficient. Dividing (4) by u'^2 , one finds the following analytical solution:

$$u'_x{}^2 = \frac{-\alpha_i e^{-2\alpha_i x}}{\frac{1}{c} - \beta e^{-2\alpha_i x}} \quad (5)$$

where c is an integration constant which can be related to conditions at $x = 0$. Substitution in (5) yields:

$$\frac{u'_x{}^2}{u'_0{}^2} = \frac{-\alpha_i e^{-2\alpha_i x}}{-\alpha_i + \beta u'_0{}^2 (1 - e^{-2\alpha_i x})} \quad (6)$$

Finally, by letting $x \rightarrow +\infty$ in (6), the Landau coefficient β can be expressed as a function

of the saturation amplitude, u'_∞ : $\beta = \frac{+\alpha_i}{u'_\infty{}^2}$. Substitution in (6) yields after non-

dimensionalization by U_j :

$$\frac{u'_x}{U_j} = \frac{u'_0}{U_j} \cdot \frac{e^{-\alpha_i x}}{\left[1 - \left[\frac{u'_0}{U_j} \right]^2 \left[\frac{U_j}{u'_\infty} \right]^2 (1 - e^{-2\alpha_i x}) \right]^{\frac{1}{2}}} \quad (7)$$

† The notation comes from linear stability theory, where α ordinarily represents the complex wave number in the normal mode assumption.

Equation (7) therefore allows us to express u'_x/U_j as a function of u'_0/U_j , knowing the saturation amplitude u'_∞ , the sensor location $x = X$, and the spatial amplification rate $-\alpha_i$. For the Reynolds number and probe position corresponding to the data of Figure 21, the saturation amplitude is approximately $u'_\infty/U_j = 0.08$. At a fixed x , equation (7) represents a set of curves $u'_x/U_j = f(u'_0/U_j)$, parameterized by $-\alpha_i$. In order to make the comparison with the measured open-loop transfer functions more quantitative, the spatial amplification rate was measured directly with open-loop forcing at the feedback frequency ($f^* = F$). The result was then used to find u'_0 , knowing X , U_j and u'_∞ . Figure 22 shows the open-loop transfer functions (u'_x as a function of p') at two frequencies, along with their corresponding Stuart-Landau fits (u'_x as a function of u'_0), with the scale of implied initial conditions u'_0/U_j shown at the top of the graph. As expected, the Stuart-Landau curves appropriately reflect the linearity between u'_x and p' at small to moderate forcing levels, and display saturation at the higher amplitudes. The relation between the two horizontal scales used in Figure 22 is naturally governed by the receptivity phenomenon. Much study has been done on this subject. In particular, Morkovin and Paranjape (1971) conjectured a generalization of Freymuth's (1966) law, from which one can derive (using the current notation) the following general relation:

$$\frac{u'_0}{U_j} = \frac{B L(p)}{\frac{1}{2}\rho U_j^2} \quad (8)$$

where B is the so-called "receptivity constant", which is presumably dependent on St_Θ and geometry. Morkovin and Paranjape's improvement mainly concerns the fact that $L(p)$ is some linear operator of the pressure. The structure of the spatial operator gave insight into the sensitivity of sharp separation edges to sound excitation. Equation (8) is consistent with Freymuth's (1966) measurements which covered the range $61 < Re_\Theta < 334$. For comparison, the present experiment covered the range $123 < Re_\Theta < 193$. It is

clear from equation (8) that for the fixed geometry (i.e. jet nozzle and sound source) under consideration, the "constant" B is proportional to the quantity $R = \frac{1}{2}\rho U_j u'_0/p'$. The dependence of R on freestream velocity, U_j , frequency of the excitation, ω , and amplitude p' , is unknown in general, despite some useful results due to Bechert (1983) that are valid in the limit of negligible momentum thickness and small frequency. Therefore, the point of receptivity will be regarded as a "black box" in the feedback loop, where R is the *receptivity transfer function*.

The parallelism of the Stuart-Landau and transfer function curves reflects the linear coupling between p' and u'_0 . This linearity in amplitude ($\partial R/\partial p' = 0$ for fixed Reynolds number and fixed frequency) was experimentally verified, and R was found to be approximately constant for three decades of the forcing level. These results are consistent with recent measurements by Sreenivasan et al. (1987). The average value of the receptivity transfer function R was used in equation (7) to provide a semi-empirical analytical fit to the open-loop transfer function:

$$\frac{u'_x}{U_j} = \frac{R p'}{\frac{1}{2}\rho U_j^2} \cdot \frac{e^{-\alpha_i x}}{\left[1 - \left[\frac{R p'}{\frac{1}{2}\rho U_j u'_\infty} \right]^2 (1 - e^{-2\alpha_i x}) \right]^{\frac{1}{2}}} \quad (9)$$

In order to express the fact that the fluctuation is a self-sustained oscillation, the additional feedback constraint (3) was introduced in (9) to eliminate p' and yield the amplitude (u'_x/U_j) of the fed back fluctuation as a function of Γ :

$$\frac{u'_x}{U_j} = \frac{u'_\infty}{U_j} \cdot \left[\frac{1 - R^2 \Gamma^2 e^{-2\alpha_i X}}{R^2 \Gamma^2 (1 - e^{-2\alpha_i X})} \right]^{\frac{1}{2}} \quad (10)$$

For $X > 0$ and $-\alpha_i > 0$ this equation admits a physical solution only if the following relation is satisfied:

$$\Gamma > \frac{e^{+\alpha_i X}}{R} = \Gamma_c \quad (11)$$

Equation (11) expresses the fact that no self-sustained oscillations can exist for gains Γ smaller than a "critical gain" Γ_c . Below Γ_c , the fluctuation amplitude remains equal to the background value. Above the critical gain, steady-state closed-loop fluctuations can exist, the amplitude of which is described by equation (10).

The existence of a gain threshold was first evidenced by physical observation. The above results have substantiated and quantified the concept of "critical gain". The implications of a critical gain criterion are now examined in terms of the temporal stability characteristics of self-sustained oscillations. At a fixed Reynolds number and fixed sensor location, consider the feedback frequency and its spatial amplification rate $-\alpha_i$. If the feedback loop (global gain Γ) is suddenly closed at time $t = 0$, and if $\Gamma > \Gamma_c$, the amplitude of the selected eigenfrequency increases from its natural background value to the final saturation amplitude. The final amplitude can be predicted using equation (10), knowing the open-loop behavior of the system, but what can be said about the transient process? We next use standard *first return map* arguments to describe this evolution. The temporal evolution of the system can be described in the following way. At $t < 0$, the velocity fluctuation (u) has background spectral amplitude. The pressure level (p) is undetermined a priori and presumably depends on both the amount of natural feedback of the jet and extrinsic environmental forcing. At $t = 0$, u assumes an initial value u_0 , and a switch is hypothetically closed. Through the feedback loop, this initial velocity fluctuation results in a pressure fluctuation p_1 . This pressure fluctuation; once it is felt at the lip, will generate an initial velocity disturbance through receptivity. This new velocity fluctuation at $x = 0$ undergoes rapid exponential growth in the streamwise direction, generating in turn a new fluctuating amplitude u_1 measured at $x = X$. The entire process is reiterated until convergence is attained. The convergence point $(u_\infty; p_\infty)$ corresponds to

the steady operating point previously defined as the intersection of the feedback curve C_F and the open-loop transfer function.

The above scenario describes a fixed point problem, and the time evolution of the system can be graphically represented using a first return map (i.e. plotting one iterate versus the previous one). The use of such iterated maps is common in the analysis of dynamical systems, where the dynamics of a system are simplified by considering only successive iterates at discrete times. To construct the map, we start with an initial condition $(u_0; p_0)$ on the non-linear transfer curve. The feedback process itself is represented by a horizontal projection onto the gain curve C_F . The combined receptivity and spatial amplification stages (hydrodynamic part of the loop) is represented as the vertical projection of $(u_0; p_1)$ onto the open-loop transfer curve, yielding the new state of the system. This graphical construction (illustrated in Figure 23) is reiterated until a fixed *accumulation point* is reached. Each step in the construction, from $(u_i; p_i)$ to $(u_{i+1}; p_{i+1})$ takes a fixed amount of time τ , equal to the basic "around-the-loop-once" delay of the feedback process.

The introduction of equation (4) was used to obtain an analytical representation of the saturation of the shear-layer open-loop response. It is clear, however, that a simplified estimate for the temporal growth of closed-loop disturbances can be obtained by considering only the linear part of the open-loop transfer function. In other words, the horizontal and vertical projections performed at each time step (see Figure 23) can be approximated respectively by the following relations:

$$p_{i+1} = \Gamma u_i \quad (12)$$

$$u_{i+1} = R p_{i+1} e^{-\alpha_i X} \quad (13)$$

The first equation represents the feedback condition, whereas the second reflects the receptivity process followed by linear spatial amplification. Substitution of (12) into (13)

yields:

$$\frac{u_{i+1}}{u_i} = \frac{\Gamma}{\Gamma_c}, \quad (14)$$

in which use has been made of the expression for the critical gain Γ_c (equation (11)).

Thus, $\{u_i\}$ is a geometric series of ratio (Γ/Γ_c) . At any time step i , the fluctuating

amplitude may therefore be expressed as a function of the initial condition u_0 as:

$u_i = u_0 (\Gamma/\Gamma_c)^i$. The time between successive iterations is equal to the sum of all delays in the loop ($\tau = \tau_a + \tau_h + \tau_s$). Therefore, one may express the discrete times corresponding to the completion of each step as: $t_i = i \tau$. Finally, in the limit of continuous time, one obtains the temporal evolution equation:

$$u(t) = u_0 e^{\frac{\ln(\Gamma/\Gamma_c)}{\tau} t} \quad (15)$$

It should be stressed that the above result holds for small times (i.e. away from saturation), but large number of steps (continuous time approximation). Both restrictions are reconcilable in the limit of Γ/Γ_c ratios of the order of unity.

Thus, the fundamental result implied by the first return map arguments is that the temporal growth of fed back disturbances is, in a first approximation, exponential. Their constant amplification rate, σ , may be expressed as:

$$\sigma = \frac{\ln(\Gamma/\Gamma_c)}{\tau} \quad (16)$$

Equation (16) results from the linearization and built-in time-delay of the feedback loop.

A gain $\Gamma > \Gamma_c$ will cause exponential growth, whereas $\Gamma < \Gamma_c$ guarantees exponential decay. While the exponential growth starts spontaneously due to background fluctuation, the decay may only be evidenced, when started from an artificial initial amplitude away

from equilibrium. The exponential decay of disturbances (in the presence of closed-loop feedback) is to be contrasted with open-loop behavior, for which disturbances convecting past a stationary probe are expected to produce a sudden decay (i.e. on a time scale of the order of the convective time, say λ/U_j). Finally, expressing Γ_c according to (11), the temporal amplification rate may be given as:

$$\sigma = \frac{\ln(\Gamma) - \alpha_i X + \ln(R)}{\tau} \quad (17)$$

Equation (17) therefore relates the *temporal* amplification rate, σ , to the *spatial* amplification rate, $-\alpha_i$. As a first approximation, if the gain Γ of the feedback loop is held constant, this linear relation suggests that at a fixed Reynolds number, the eigenfrequency most likely to be selected by feedback (maximum σ) is that which maximizes the quantity $(-\alpha_i X + \ln(R))$.

5. Global temporal instabilities

5.1. Temporal growth rates

In order to investigate experimentally the instability characteristics of closed-loop oscillations, amplitude transients were obtained by the sudden closure of an electronic switch controlling the feedback loop. The total gain of the loop was carefully selected to be above critical, so that self-sustained oscillations would spontaneously take place after closure of the switch. The proper synchronization of A/D and D/A transfers ensured that the recording of the transients started before the feedback loop was closed, and that the time of closure was perfectly known.

Figure 24a (top) shows the raw velocity data corresponding to the transient growth of the eigenfrequency at $Re = 62,500$, for a gain $\Gamma = 0.00236$. By convention, the origin of time was chosen to correspond to the instant the feedback loop was closed. The

transient behavior displayed in Figure 24a takes place over several hundreds of periods of the eigenfrequency. The sampling frequency was always chosen to be approximately 30 times the fundamental frequency of the feedback instability ($F = 2260$ Hz in the present case). The raw time series was amplitude demodulated using a discrete Hilbert transform, according to the technique described by Wlezien and Way (1979). Because the quality of the amplitude demodulation depends highly upon the filtering around the eigenfrequency, the data were processed in two stages. First the raw time series was decimated after appropriate low-pass filtering. Secondly, the resulting data were convolved with a 58 dB narrow-band finite impulse response filter. The filtered time series was then used as the input to the Hilbert filter. Figure 24b (center) shows the filtered time series with the calculated amplitude. Because of the 10:1 decimation factor, there are only approximately three samples per period in the filtered time series. The fictitious low frequency undulations visible in Figure 24b are merely the visual appearance associated with the low sampling condition after decimation. The presentation of the demodulated amplitude envelope, A , was chosen so that both A and $-A$ are shown about the mean \bar{U} of the time series. In this fashion, it is easy to appreciate how the actual details of the filtered time-series are faithfully reflected in the calculated envelope. Finally, the exponential growth rate, σ (measured in s^{-1}), is determined according to $\sigma = \frac{d \ln(A)}{dt}$. Figure 24c (bottom) shows the logarithm of A as a function of time. Because the data is generally noisy throughout the transient, the slope is determined using a least squares fit. Approximately 400 such transients were recorded and similarly processed, using various conditions of gain, Reynolds number and probe location. An estimate $\Delta\sigma$ of the error on the growth rate was also systematically calculated, based on the length and mean square error of the fit. The globally exponential character of such transients is nevertheless unmistakable, in spite of large uncertainties.

For large growth rates, a noticeable growth of the subharmonic toward the end of

the transient was commonly observed. The digital Hilbert filtering technique was applied to these transients in order to determine the temporal evolution of both fundamental and subharmonic frequencies (see Figure 25). The rapid growth of a subharmonic indicates the pairing which starts near the time when saturation of the fundamental is reached. Temporal amplification rates of the subharmonic were calculated according to the method described above. It was shown (Reisenthel, 1988) that there was no correlation between the growth rates of fundamental and subharmonic frequencies. Whether the sudden appearance of a subharmonic and the existence of a critical gain for the fundamental are related or not to a bifurcation sequence is not known at the present time.

For values of Γ/Γ_c of five or larger, a characteristic step-like ripple was observed in the growth of the demodulated amplitude, corresponding to the discrete steps shown by first return maps such as Figure 23. It can be shown that in spite of the presence of the ripples, the average slope σ corresponding to this geometric progression is still related to the gain according to: $\sigma = \frac{\ln(\Gamma/\Gamma_c)}{\tau}$. Therefore, σ does not always represent a rate of growth associated with true exponential amplification, but is invariably related to both feedback loop (Γ, τ_a) and flow (τ_h, ϕ, Γ_c) characteristics via equation (16). Conversely, (16) can be used to deduce the critical gain Γ_c , from measurements of σ as a function of gain. This equation applies equally to negative amplification rates. Figure 26 depicts a case of exponential decay for the same flow conditions as Figure 24, with a subcritical gain such that $\Gamma/\Gamma_c = 0.76$. The acoustic delay is evidenced by the fact that the exponential decay does not begin until approximately $\tau_a = 10$ ms after the opening of the electronic switch. The initially high amplitude of the fluctuation is obtained by means of external forcing, at the eigenfrequency. The forcing is stopped at $t = 0$, when the switch (K_2 in Figure 2) is opened. It is clear from Figure 26 that a characteristic exponential range persists for a substantial number of periods of the eigenfrequency. In the present case, the decay rate ($\sigma = -14.5 \pm 1.7 \text{ s}^{-1}$), was determined from fitting the amplitude over

approximately 400 cycles of the fundamental. Despite inherent experimental difficulties associated with the measurement of such decays, their exponential characteristic is distinctively symptomatic of feedback, since step-like functions are expected to appropriately describe the shape of amplitude decays in a convectively unstable flow. This also suggests that the proper measurement (e.g. in an anechoic chamber) of these decays in the absence of *enhanced* feedback might give insight into the actual strength of the feedback process occurring in natural shear layers.

Figure 27 shows single realization measurements of the growth rate σ as a function of $\ln(\Gamma)$. For clarity, the uncertainty bars corresponding to $\Delta\sigma$ are not shown in this figure. Despite the experimental scatter, the logarithmic dependence of σ on Γ is clearly demonstrated, in support of equation (16). A least squares fit through the data yields an estimate for the critical gain Γ_c , as well as for the total loop delay τ . The above method for the determination of the critical gain is considerably more accurate than a direct estimate based on the perceived location of the gain threshold, owing to the hysteresis and intermittency phenomena described earlier (see Figure 5). In conclusion, the present experimental measurements demonstrate that under conditions of closed-loop feedback, self-sustained velocity fluctuations may undergo a temporal instability. Furthermore, the temporal growth rates appear to be satisfactorily described by equation (16).

5.2 Spatial independence

The measurements presented thus far have been obtained from the feedback probe itself, namely: the acquired signal at one location in the shear layer was also the forcing signal. In this configuration, the dual functions of the hot-wire sensor as both part of the feedback instrumentation and as a measuring device cannot be dissociated. In order to document the spatial characteristics of the shear-layer during transient growth, these two functions had to be separated, owing to the large sensitivity of self-sustained oscillations to

the actual location of the sensor. Therefore, two hot-wire sensors were used; the first one for spatial sampling, and the second one as the feedback sensor. The positioning of the feedback probe on the opposite side of the jet was chosen so as to minimize probe interference problems, but also in order to provide a means of verifying the axial symmetry of the instability waves. The data presented here were acquired at three Reynolds numbers, one of which ($Re = 42,000$) corresponded to the naturally enhanced jet column mode condition (see Nagib et al., 1989).

The shear layer response was investigated along lines corresponding to y/δ locations of 0.0, -0.5, -0.75 and -1.0, respectively, where δ designates the local shear layer thickness, and y is counted positively outward, from the local position of largest mean shear (see Figure 2). The first two radial locations correspond to the middle and high speed edge of the shear layer respectively, whereas the last two are nominally within the freestream of the unexcited jet. The feedback probe was located at a constant $X/D = 0.2$ for this experiment, while the downstream position of the sampling probe (x) covered the range $0.1 < x/D < 0.4$. At each location of the resulting (x, y) grid, 13 transients were recorded, corresponding to various gain conditions Γ . The signals of both probes were simultaneously sampled, and the transient data were analyzed using the amplitude demodulation technique described previously. Figure 28 is an example of the growth rates obtained at various radial locations, as a function of $\ln(\Gamma)$. As expected, the logarithmic dependence of σ on the gain is verified, within experimental scatter. Figure 28 also illustrates the fact that the temporal growth rates at any given gain appear to be uncorrelated with radial position.

Streamwise Dependence. In order to examine the dependence of temporal growth rates with respect to the streamwise location x of the measurement, the values of σ obtained from each of the two probes are compared to each other for various values of the gain. Figure 29 examines the degree of correlation between σ_1 measured by the

sampling probe, and σ_2 measured by the stationary feedback probe, at various downstream locations of the sampling probe, and includes cases of temporal amplification as well as temporal decay. In this representation, the gain is not explicitly shown, but Γ determines the magnitude of σ_1 and σ_2 . The identity line is indicated as a reference. The correlation coefficient between σ_1 and σ_2 was found to be $R_{\sigma_1\sigma_2} = 0.94$ at $Re = 72,500$ and $R_{\sigma_1\sigma_2} = 0.99$ at $Re = 60,000$. This result indicates that the growth rate σ is not a function of x . Incidentally, the high value of the correlation $R_{\sigma_1\sigma_2}$ confirms the axial symmetry of the instability waves, since the two probes were placed at different azimuthal positions. Thus, over the investigated range of spatial locations ($x \leq 3\lambda$), and for given flow and feedback conditions, the value of σ is independent of downstream distance.

The condition $\partial\sigma/\partial x = 0$ now allows the values of σ_1 acquired at different streamwise locations but same gain to be considered as independent realizations of the same measurement. Therefore, the large uncertainties associated with individual measurements of σ can be reduced by averaging realizations together, for each probe. The resulting mean values of σ_1 and σ_2 can be compared to each other for different values of the feedback gain. By doing so, an excellent correlation was found between the two probes ($R_{\sigma_1\sigma_2} = 1.00$ at $Re = 60,000$, and $R_{\sigma_1\sigma_2} = 0.99$ at $Re = 72,500$), thus constituting supporting evidence that the temporal growth rate σ is not only independent of radial and streamwise positions in the shear layer, but also independent of azimuthal position for the range $x \leq 3\lambda$. The correlations of individual realizations of σ_1 and σ_2 are summarized in Figure 30, for all three Reynolds numbers investigated, over the range of gains $0.87 \times 10^{-4} \leq \Gamma \leq 0.26 \times 10^{-1}$. It may be concluded from these results that the "in place" linear temporal amplification of feedback disturbances is a *global* phenomenon, independent of space.

Returning to the issue of scaling of the growth rate with σ , we now make use of the

previous findings by averaging σ_1 and σ_2 in order to reduce measurement uncertainty. Figure 31 summarizes the scaling of the amplification rates obtained at all three Reynolds numbers. The critical gain (obtained from the intersection of the least squares fits with the line of neutral stability) clearly increases with decreasing Reynolds number. The scaling of Γ_c with Reynolds number is of importance, because this term reflects the role of shear layer characteristics on the global instability.

5.3. Local phase speed measurement

The simultaneous acquisition of velocity signals from the two probes was used to obtain phase information at various spatial locations in the shear layer. For this purpose, the stationary feedback probe was used as a phase reference. Cross-spectral analysis of short data segments was used to calculate the phase difference ($\Phi_1 - \Phi_2$) between hot-wire signals, under steady-state and transient conditions. These measurements indicated that the phase varies linearly with downstream distance. Furthermore, phase distributions were determined during periods of transient growth, transient decay, and during steady-state.

The calculated values of $\frac{d\Phi}{dx}$ all fell within 1.5% of each other. The unequivocally linear variation of phase with downstream distance was used, based on the average of transient growth, transient decay and steady-state cases for all gain configurations investigated, to calculate the phase speed C of the disturbance, knowing the eigenfrequency $f = F$ according to:

$$C = 2\pi f \left[\frac{d\Phi}{dx} \right]^{-1} \quad (18)$$

At $re = 60,000$ ($F = 2120$ Hz ; $U_j = 18.3$ m/s), C/U_j was determined to be 0.49. This value is quite similar to that obtained by other investigators using conventional open-loop forcing (see for example Drubka, 1981). Reisenhelt (1988) confirmed this result by using

various cases of different amplitudes with on/off open-loop excitation of the jet at the same frequency and same Reynolds number as the enhanced feedback measurements presented here, and found a corresponding normalized phase speed $C/U_j = 0.48$. Similar results were found at the two other Reynolds numbers, for which the phase distribution across the shear layer was found to be essentially independent of whether the oscillation undergoes a transient or has reached steady-state behavior. Similarly, a high degree of correlation ($R_{\Phi_T \Phi_S} \approx 1.00$) was measured between the phases Φ_T and Φ_S , obtained during transient growth and steady-state respectively. Thus, the measured constant phase speeds (of the order of half the jet velocity) are the same as those obtained with conventional open-loop forcing at the same frequency. Finally, the high correlation between transient and post-transient phases supports the conjecture that the global temporal growth experienced by the amplitude of the fluctuation does not significantly affect the *local stability properties* of the shear layer.

6. Discussion

6.1. Comparison with theory

Scaling Considerations. It has been shown both analytically and experimentally that the global temporal instability of closed-loop sinusoidal disturbances is controlled by the gain of the feedback loop. This dependence manifested itself in the form of a logarithmic variation of the temporal amplification rate σ , with the gain Γ . It is important to appreciate, however, that the controlling parameter is not Γ , but the ratio Γ/Γ_c . While Γ is purely a property of the return leg of the feedback loop, Γ_c on the other hand is determined by the instability characteristics of the shear layer, the receptivity at the lip, and the feedback sensor position. Because the $\frac{1}{\tau}$ factor in equation (17) acts (to a first degree of approximation) as a passive multiplier in the calculation of the growth rate, the

influence of flow properties on the instability of the feedback loop (i.e. growth, decay or neutral stability) can be studied by considering the sole functional dependence of Γ_c on flow characteristics.

The magnitude of the temporal amplification rate σ is described by equation (16), which states that the conditions for growth, decay, and neutral *temporal* stability can be expressed by the following relations: $\Gamma > \Gamma_c$ (temporal amplification), $\Gamma < \Gamma_c$ (temporal decay), $\Gamma = \Gamma_c$ (neutral stability). The following expression was also obtained for the critical gain: $\Gamma_c = \frac{e^{+\alpha_i X}}{R}$, where X is the feedback sensor position, $-\alpha_i$ is the spatial amplification rate, and R the receptivity transfer function. As previously mentioned, the structure of the receptivity transfer function $R = f(U_j, \omega, \Theta, \dots)$ remains greatly unknown, except for the theoretical results due to Bechert (1982), in the limit of infinitely thin shear layer and low Strouhal number. Nevertheless, it is clear that for fixed flow conditions (i.e. fixed jet velocity U_j , and fixed nozzle geometry), and constant forcing frequency ω , R is a constant, as demonstrated experimentally by Reisenthel (1988) over several decades of the forcing amplitude. Furthermore, since the normalized spatial amplification rate $-\alpha_i \Theta$ scales with the Strouhal number $\omega \Theta / U_j$, it is expected that for fixed flow and forcing conditions, $\ln(\Gamma_c)$ should be proportional to the feedback probe position X , in accordance with (17).

As explained earlier, the empirical estimation of the critical gain Γ_c based on amplitude jumps or intermittency at the threshold is prone to subjectivity. Therefore, it is believed that an unbiased way of determining Γ_c is to calculate a linear fit to numerous realizations of σ versus $\ln(\Gamma)$. This method is quite labour intensive, however, and its use was illustrated in Figure 31 for three Reynolds numbers at one feedback sensor location. Because X was kept constant in these data, we consider instead the closed-loop amplitude results of Figures 5 and 6, and obtain an approximate determination of the threshold gain level for each X . The result is shown in Figure 32, where $\ln(\Gamma_c)$ is

presented as a function of the streamwise position of the feedback probe. Uncertainty boxes reflect the confidence interval (box height) on Γ_c , based on the limits of hysteretic behavior (Γ_1 and Γ_2 in Figure 5), while the width of the boxes indicates the uncertainty on X . Clearly, the expected proportionality between $\ln(\Gamma_c)$ and distance between the lip and the source of feedback appears to be satisfied. This result is the direct consequence of the linear spatial amplification of disturbances in the shear layer.

In order to further substantiate the validity of equation (11), the variation of Γ_c with Reynolds number is now examined. Recalling the results of Figure 31, we consider the three values of Γ_c obtained at a fixed X/D for the three Reynolds numbers considered in this study. These values were calculated from the least squares fit of σ against $\ln(\Gamma)$, and are consequently expected to yield a more accurate determination of the critical gain. Note that as the Reynolds number changes, the receptivity term R is not expected to be a constant. An additional complication rises from the fact that the value of the eigenfrequency itself changes with Reynolds number. Therefore, in order to clarify the issue of scaling with Reynolds number, certain hypotheses must be made.

Consider expression (17) for the temporal amplification rate. If it is assumed that the frequency most likely to be selected by feedback corresponds to the one with the maximum temporal growth rate σ_{\max} , then for given feedback conditions (Γ and X constant) and fixed Reynolds number (τ constant), the eigenfrequency is that which maximizes the quantity $(-\alpha_i X + \ln(R))$. Secondly, we make the simplifying assumption that R is a constant. As will be discussed later, this assumption is naturally incorrect, but instructive approximate results can be derived if one is momentarily willing to make it. In any event, the relative importance of the receptivity term in $(-\alpha_i X + \ln(R))$ can be diminished by choosing X to be large. This simply reflects the fact that the dependence of Γ_c on Reynolds number is exponential through $-\alpha_i$, but only algebraic through the receptivity term R . Under these assumptions, the frequency most likely to be observed is

that with the largest spatial amplification rate. The scaling of $-\alpha_i$ with frequency has been the subject of much study. It has been shown (see for example Ho and Huerre, 1984) that the normalized spatial amplification rate $-\alpha_i \Theta$ scales with Strouhal number based on momentum thickness ($St_\Theta = f \Theta / U_j$). In particular, the maximum spatial amplification rate satisfies: $-\alpha_{i,\max} = \kappa / \Theta$, where κ is a constant depending on the velocity ratio parameter (Monkewitz and Huerre, 1982). Since the initial momentum thickness is proportional to $Re^{-1/2}$, the maximum spatial amplification rate may be expressed as: $-\alpha_{i,\max} = \eta Re^{1/2}$, where η is some positive proportionality constant. According to equation (17), $-\alpha_{i,\max}$ corresponds to maximum temporal amplification under the assumption that R is constant. The total delay τ may be considered constant as a first approximation because of its weak dependence on flow parameters (i.e. by examining orders of magnitude in equation (1)). It is not obvious, however, that the frequency corresponding to $-\alpha_{i,\max}$ should be one of the permissible eigenfrequencies of the system. The likelihood is that it is not. However, we argue that due to the broadness of the spatial amplification curve for shear layers, and to the close spacing of competing eigenfrequencies (for $d \gg D$), the condition $-\alpha_{i,\max} = \eta Re^{1/2}$ ought to be approximately satisfied. If this third assumption is made, then it is justified to replace $-\alpha_i$ in equation (11) by $-\alpha_{i,\max}$, yielding:

$$\ln(\Gamma_c) = -\eta Re^{1/2} X - \ln(R) \quad (19)$$

Figure 33 depicts the exponential dependence of Γ_c on \sqrt{Re} , based on the data of Figure 31, corresponding to the simultaneous variation of both Reynolds number and eigenfrequency. The dashed line represents a least squares fit of $\ln(\Gamma_c)$ versus \sqrt{Re} . It may be concluded from the closeness of the fit that there is good agreement between the predicted trend of equation (19), and the experimental data. It is not completely understood, in fact, why such good agreement is obtained, considering the assumptions

involved (the strongest of which is the constancy of the receptivity transfer function). However, it may be deduced *a posteriori* from these results that R is indeed a weak function of Reynolds number and frequency, as compared to the exponential dependence associated with the $e^{-\alpha_r X}$ term.

Frequency Selection Criteria. Most of the work presented thus far focussed on the description of the temporal growth of the amplitude, assuming a self-sustained oscillation takes place at a well-defined frequency. Also, the expression of phase conditions led to effective frequency constraints on the closed-loop system. Experimental observations, however, suggest that only few of the predicted stages are actually observed. Hence, phase considerations alone do not give a satisfactory explanation of the observed frequencies. The present section examines the role of flow conditions in the frequency selection process. Two main ideas are contrasted. First, arguments suggesting that the temporal instability should scale with flow characteristics are presented. Secondly, some results indicating intrinsic characteristics independent of the initial flow are considered.

Consider the results presented in Figures 9 and 11. The selected eigenfrequencies were shown to depend on both Reynolds number and downstream distance. Within a given band, the eigenfrequency exhibited a weak monotonic increase with Reynolds number, and a decrease with downstream position of the feedback probe. Nevertheless, it was shown that the dependence on Reynolds number did not manifest itself in the form of scaling with Strouhal number St_θ (see Figure 12). This fact does not necessarily imply that the temporal instability does not originate from the shear layer instability. Clearly, the hydrodynamic part of the loop is not only the sole cause of non-linearity, but also the origin of unsteadiness. These considerations imply that the temporal instability of closed-loop fluctuations takes root in the stability characteristics of the shear layer. On the other hand, our experiments documenting the insensitivity of self-sustained oscillations to external disturbances have shown that the closed-loop system behaves in an

intrinsic fashion. In particular, the final selected frequency appeared to be largely independent of the initial spectral content of the jet. If the initial imprint of the jet has no effect on the final, saturated stage, what is the role of flow characteristics in the observed global instability?

Because of the absence of scaling with St_Θ , one may conclude that the feedback instability is not *purely* a shear layer instability mechanism. The role of the initial shear layer characteristics should not be excluded, however, as a possible explanation for both frequency selection and initial seeding of the temporal instability. It is clear from the above results that the hypothesis that the self-sustained oscillations with maximum temporal amplification rate be the ones actually observed, can be used in conjunction with equation (2) to obtain a criterion for frequency selection. In order to handle the $-\alpha_i$ term in numerical calculations, an approximate amplification curve was obtained using a piecewise polynomial fit to the spatial amplification curve obtained according to inviscid linear stability theory (Monkewitz and Huerre, 1982). The curve $-\alpha_i = f(f \Theta/U_j)$ is used in conjunction with the experimentally determined Θ -dependence on Reynolds number, to obtain: $-\alpha_i = \chi(f, Re)$. Therefore, the function χ is the dimensional expression derived from the spatial amplification curve. Substituting in (17) yields:

$$\sigma = \frac{\ln(\Gamma R) + \chi X}{\tau} \quad (20)$$

In order to follow the temporal instability characteristics of a given eigenfrequency f_n , this equation has to be supplemented with the feedback constraint (2), assuming a constant phase speed equal to half the jet velocity (a justified approximation, in view of previous results). Hence, for a given eigenvalue n , the eigenfrequency f_n can be obtained for every Reynolds number. The values of f_n and Re can then be substituted in the spatial growth rate equation. One can then substitute $-\alpha_i$ in (17) to produce σ , knowing Γ . Conversely, the neutral stability curves $\Gamma_c = f(n, Re)$, can be calculated from equation

(20), by setting the condition $\sigma = 0$. The numerical implementation of equation (20) is illustrated in Figure 34a (left), for two eigenvalues ($n = 23$ and $n = 39$), corresponding to two of the most prevalent bands experimentally observed in Figure 9. These bands correspond to the stages labeled "1960 Hz" and "3320 Hz" in these figures, and their corresponding eigenvalues ($n = 23$ and $n = 39$) were obtained from the comparison produced in Figure 18. For this calculation, the receptivity term R was kept constant.

Again, it is believed that this hypothesis can be justified as a first approximation, on the basis of the linear behavior observed in Figure 33. Also, the curves represented in Figure 34a correspond to the boundaries of the "bands" that were experimentally observed (see Figure 10). Each of these curves determines the boundary for stability: inside the band, self-sustained fluctuations are observed ($\sigma > 0$) at the eigenfrequency f_n , whereas outside the band, they are exponentially damped. Quantitative agreement with Figure 10 is not observed, however, since for larger values of Γ the experimental data reveal bands apparently narrower than the calculated widths. This observation underlines the fact that within a band, the feedback behavior is no longer governed by linear equations: finite amplitude oscillations set in, and mode-competition becomes a crucial factor. Nevertheless, the previous agreement between theory and experiment at low gains is not fortuitous, since most of the predictions dealt with the *onset* of self-sustained oscillations (i.e. behavior close to the critical gain).

Depending on whether one considers the stability properties associated with a given eigenfrequency band or the *global* stability of the system, leads to different definitions of the neutral stability curve. Figure 34b (center) depicts the band of stability associated with the eigenvalue $n = 23$. Each line is a curve of constant temporal amplification, and the narrowing of the band with increasing amplification rate is clearly illustrated. On the other hand, if the global stability of the system as a whole is considered, regardless of the selected eigenfrequency, one must examine the most restrictive

condition associated with the stability of each frequency (i.e. find the most unstable eigenfrequency at each Reynolds number). Figure 34c (right) represents the lines of neutral stability corresponding to the eigenvalues $n = 15$ through $n = 50$. The close proximity of the eigenfrequencies thus justifies the use of the third assumption, in the derivation of equation (19), to describe the condition of *global neutral stability*.

Furthermore, the previous results may be used to approximate the location of frequency jumps and to illustrate the possibility of hysteresis. These results show that at any given Reynolds number there exists a most unstable eigenfrequency ideally given by the condition: $\frac{\partial \chi(f_n, Re)}{\partial n} = 0$.

In an experimental situation, if the gain is gradually increased at a fixed Reynolds number, the eigenfrequency most likely to be observed is the one with the largest temporal amplification rate (i.e. lowest critical gain). This hypothesis was substantiated by the data of Figure 33, since the linear behavior is the consequence of the above assumption. On the other hand, if the gain is fixed and the Reynolds number varied, successive bands are crossed. For sufficiently weak gains, all disturbances are damped below a critical Reynolds number (see Figure 34c). As the Reynolds number increases, a first eigenfrequency becomes unstable. As the band is crossed, this eigenfrequency becomes neutrally stable and eventually becomes damped for sufficiently large Reynolds number. However, because of the overlap between adjacent bands, neighboring eigenfrequencies compete with the initial one. This process is essentially analogous to a "bifurcation" sequence. For Reynolds numbers slightly larger than critical, well-defined limit-cycle behavior is observed, with an increasing number of potentially excited modes as the Reynolds number is increased.

A simple minded hypothesis governing the frequency jump phenomenon can be formulated by requiring that the location of the jump be determined according to the crossing of two bands (i.e. requiring that jumps occur instantly, in such a way that σ is

maximized with respect to n at any given Reynolds number). The application of this criterion leads to a multitude of small steps in frequency as Re changes, owing to the proximity of competing eigenfrequencies. Experimental observation, however, suggests that the extent of the stages can be significant (see Figure 9). An additional objection to the above scenario is the fact that it does not account for the frequency hysteresis phenomenon.

In order to remedy this deficiency, the following assumption is made. Consider an already established self-sustained oscillation at a given gain and given Reynolds number. At the point of crossing of two competing bands (i.e. equal amplification rates), the established wave has reached its saturation amplitude, and tends to inhibit the competing frequency. Thus, a simple hypothesis is to consider that in order to overcome the saturated amplitude of the existing oscillation, the new competing frequency must have an amplification rate actually greater than that of the established wave, say by an amount $\Delta\sigma$. This criterion is schematically illustrated in Figure 35. It is clear that the introduction of a minimum $\Delta\sigma$ criterion to overcome the existing frequency allows for hysteresis, since irreversibility has been introduced in determining the points of switching between bands. The numerical implementation of the above criterion was performed (Reisenthel, 1988) and compared to experimental data. It was found that a very minute overamplification ($\Delta\sigma$) is required to generate a noticeable amount of hysteresis. As expected, both the magnitude of the jumps, and the amount of hysteresis (i.e. width of stages) increase with $\Delta\sigma$, although additional study would be required to analyze the dependence of $\Delta\sigma$ on various flow parameters. Hence, the combined use of equations (2) and (20) accounts for the existence of the observed bands in (Re, Γ) parameter space. These equations govern dual aspects of the feedback problem: phase constraints on the one hand, and global temporal instability on the other. Furthermore, the existence of hysteresis and frequency jumps was qualitatively shown from simple hypotheses applied

to the crossing of competing eigenfrequency bands.

Despite the qualitative agreement of these results with experimental observation, it is clear that the regularity of the frequency jumps exhibited with the requirement of a fixed overamplification $\Delta\sigma$ contrasts with the large irregular steps that were measured. Figure 9, for example shows that regular stages were observed for the range of frequencies $1900 \text{ Hz} < f < 2300 \text{ Hz}$, but that a large jump occurs from 2250 Hz to 3280 Hz at $Re = 70,000$. A similar abnormal jump is displayed by the hysteresis diagram of Figure 16. Qualitatively speaking, the experimental data suggests that some bands attract more strongly than others. This feature is clearly not accounted for by the previous considerations.

Although useful insight is gained from the predictions of Figures 34 and 35, it is important to recognize the role of the two main assumptions that were made. The first assumption was that the receptivity term R varied slowly with Reynolds number and frequency, in comparison with $e^{-\alpha_1 X}$. The second assumption concerns the constancy of Γ . It was shown earlier that the gain of the enhanced feedback loop is independent of amplitude ($\partial\Gamma/\partial p' = 0$). This does not imply, however, that in a practical situation the gain is not a function of frequency ($\partial\Gamma/\partial\omega = 0$). In order to extract physical insight from feedback equations (2) and (20), this assumption had to be implicitly made. We now consider its consequences separately, as a perturbation on the previously obtained "basic" criterion for frequency selection.

Because care was taken to ensure that no non-linearities were introduced by the electronic circuitry of the feedback loop, the frequency response of the acoustic branch was investigated. The acoustic branch of the loop includes the speaker and the global path of the sound, including possible reflections, etc. In order to perform this calibration, a white noise input was fed to the speaker. The output signal of a microphone placed close to the lip of the jet (in the absence of flow) was recorded and Fourier analyzed.

The transfer function between input and output signals determined the acoustic frequency response of the system. It was found that the frequency response was independent of forcing amplitude, which is consistent with the result $\partial\Gamma/\partial p' = 0$. No simple analytical expression for the acoustic transfer function could be used, however, since $\partial\Gamma/\partial\omega$ depends, among other things, on the properties of the speaker and acoustical path. Instead, the frequency response is shown as the top trace of Figure 36, shifted by an arbitrary amount for clarity. Large variations in the acoustic response are easily observed with varying frequency. The effect of such imperfections on the amplitude response of the shear layer is illustrated in Figure 36, which represents (from bottom to top) the natural spectrum, the open-loop amplitude response of the shear layer to pure tone forcing, and the acoustic transfer function of the system. The vertical dashed line indicates the eigenfrequency selected by the feedback loop for $Re = 61,600$ and $X/D = 0.17$. Figure 36 clearly shows that the selected eigenfrequency ($F = 2240$ Hz) also corresponds to the frequency maximally amplified by the shear layer. In addition, noticeable dips in the acoustic frequency response are clearly correlated with corresponding dips in the shear layer response. A similar correspondence was observed at other Reynolds numbers. Reisenthel (1988) showed that the details of the acoustic transfer function can influence the location of frequency jumps, by contributing to the isolation of "favorable" eigenfrequency ranges. Hence, apparently small variations in the acoustic frequency response can have important effects (such as incidental frequency jumps) on systems with pressure feedback. This sensitivity is evidently a consequence of the relative flatness of the shear layer amplification curve, and must be accounted for in the interpretation of experimental data with varying frequency of excitation.

Thus, the proper criterion for frequency selection must include effective gain variations with respect to frequency. Therefore, at a given Reynolds number and in the absence of any hysteresis phenomena, the selected eigenfrequency should actually be that

which maximizes the global quantity $(\ln(\Gamma) - \alpha_i X + \ln(R))$. In the limit of infinitely close eigenfrequencies (i.e. large loop delays), this may be expressed symbolically by the condition:

$$\frac{1}{\Gamma} \frac{\partial \Gamma}{\partial \omega} - \frac{\partial \alpha_i}{\partial \omega} X + \frac{1}{R} \frac{\partial R}{\partial \omega} = 0 \quad (21)$$

Finally, we examine the role of the receptivity term in equation (21). Thus far, some light has been shed on the issue of frequency selection by the sole criterion of maximizing the spatial amplification rate $-\alpha_i$, under properly formulated eigenfrequency constraints. It was also shown that discrepancies between experimental observation and prediction of the eigenfrequency could be attributed to the shape of the global acoustic transfer function ($\partial \Gamma / \partial \omega \neq 0$). However, the above criteria relied on the assumption of a constant receptivity R . This assumption was made for the sake of simplicity and in the hope of extracting the principal mechanisms which characterize the enhanced feedback phenomenon. Nevertheless, it may be concluded a posteriori that the predictive ability of the previous criteria supports the conjecture: $R^{-1} \partial R / \partial \omega \ll -\partial \alpha_i / \partial \omega X$.

Recalling the results of Figure 11, it is clear that the selected eigenfrequency has an average tendency of lying between the frequency of maximum spatial amplification ($St_\Theta = 0.163$) and the frequency corresponding to the fundamental axisymmetric mode ($St_\Theta = 0.132$). It is argued that if the receptivity term were a constant, one would expect instead that the stages be *centered* around the frequency of maximum spatial amplification. This argument stems from the fact that apart from a few noticeable dips in the acoustic transfer function, the term $\frac{\partial \ln(\Gamma)}{\partial \omega}$ should be zero "on the average". This means letting $\partial R / \partial \omega = 0$, averaging equation (21) over all frequencies (notation: $\langle \rangle$), and setting $\langle 1/\Gamma \partial \Gamma / \partial \omega \rangle = 0$. The result ($\langle \partial \alpha_i / \partial \omega \rangle = 0$) implies that on the average, the value of the eigenfrequency should coincide with the frequency of maximum spatial

amplification. This result is clearly contradicted by experimental observation. Thus, it is suggested that the receptivity term is responsible for this discrepancy. In order to evaluate the validity of this hypothesis, we consider Bechert's (1982) theoretical work in the limit of plane, parallel, inviscid, incompressible flow and infinitely thin shear layer. Bechert's results suggest that for a fixed freestream velocity, (transposing to current notation) R should be proportional to $\omega^{-1/2}$. If we now make the assumption that the range of validity of this result may be extended to the case of finite Reynolds number, finite momentum thickness, and moderate Strouhal numbers, the relation:

$$\frac{\partial \ln(R)}{\partial \omega} = -\frac{\gamma}{2} \frac{1}{\omega} \quad (22)$$

may be substituted in equation (21), where γ is a positive constant, presumably dependent upon Reynolds number and geometry. The main point of equation (22) is that $\partial \ln(R)/\partial \omega$ is always *negative*. Therefore, even in the averaged sense considered previously (i.e. $\langle \frac{\partial \ln(\Gamma)}{\partial \omega} \rangle = 0$), the frequency corresponding to maximum spatial amplification cannot satisfy the frequency selection criterion expressed in (21). In particular, assuming a perfectly flat acoustic transfer function ($\partial \Gamma/\partial \omega = 0$) for simplicity, the frequency selection criterion: $-\frac{\partial \alpha_i}{\partial \omega} X + \frac{\partial \ln(R)}{\partial \omega} = 0$ implies that: $-\partial \alpha_i/\partial \omega > 0$. Therefore, since $\partial \alpha_i/\partial \omega = 0$ corresponds to a *maximum* in the linear amplification curve, it is clear that the selected eigenfrequency should be "on the average" *lower* than the frequency with maximum spatial amplification. The term "on the average" is used in order to eliminate pseudo-random contamination caused by the acoustic transfer function, but also to put aside considerations of frequency hysteresis.

In summary, the present data agree well with the predicted scaling of the critical gain with X and with Reynolds number. Moreover, a properly expressed criterion based on the maximization of the *temporal* amplification rate has been suggested. This

criterion was complemented with the knowledge of the acoustic frequency response of the system to yield quantitative agreement between prediction and experiment. Finally, the correction suggested from the application of Bechert's (1982) calculations is found to be consistent with the trends experimentally observed.

6.2 *Hybrid instability*

Two apparently contradicting properties are associated with the stability characteristics of closed-loop fluctuations with enhanced feedback. The first one is the fact that under given feedback conditions, the frequency of the jet appears to be an intrinsic characteristic. Measurements demonstrating the presence of frequency bands and the insensitivity to external disturbances support the argument of a global instability. In order to validate this conjecture, direct measurements of temporal growth rates were made. It was shown that the amplitude of the selected eigenfrequency (which depends on shear layer characteristics) grows "in place", and that the associated temporal amplification rate is not a function of space. It would be tempting to conclude to an absolute instability of the flow, based on the sole consideration of the above symptoms. However, the concept of absolute instability is a local one, and concerns vortical waves with zero group velocity (Bechert, 1985). It was shown unequivocally that the feedback instability does not scale on local momentum thickness, but scales instead with an array of mixed terms associated with both the feedback loop itself, and the spatial stability characteristics of the shear layer. From the scaling experiments, the role of the shear layer was clearly assessed as a "vehicle" for selective amplification of disturbances, rather than the origin of the instability. Unmistakably, the role of the initial shear layer fluctuations as a seed for the global instability should also be appreciated. Furthermore, the overall agreement of analysis (which was based solely on monochromatic waves with positive group velocity) and experimental observation suggests that the present phenomenon is a global instability

through pressure feedback. In other words, the present enhanced feedback experiment falls under the category of "hydroacoustic" flow resonances (Huerre, 1987).

Similarly to the natural jet, the instability waves in the enhanced feedback configuration maintain their convective character. Hence, the frequency selectivity and apparent insensitivity to external disturbances are the consequence of the closed feedback loop. The usual broadband amplification characteristics of open flow systems apply locally, but one must consider the conditions under which a disturbance is "allowed" to self-sustain. In effect, all modes picked up by the sensor are fed back to the lip and are subsequently amplified or damped by the shear layer, but only a discrete number of them satisfy the proper criteria leading to large amplitudes integrated over time. The obtainment of pure limit cycle behavior has been recognized as a precondition to the identification of bifurcation sequences and possible routes to chaos in fluid flows. Consequently, much attention in recent years has naturally been directed toward absolutely unstable flows, such as in the near wake of bluff bodies and variable density jets (Sreenivasan et al., 1987), for which resonances may be initiated by purely hydrodynamic means. A major difficulty associated with the study of such flows, however, arises from the necessary exclusion of intrusive measurement techniques. As pointed out by Huerre (1987), such may also be the case for convectively unstable flows with hydroacoustic resonances caused by the presence of a downstream body. The enhanced feedback configuration described in the present manuscript, however, does not require the presence of a downstream body, so that disturbances introduced by the presence of the hot-wire probe are convected downstream without consequence on the global instability.

The high degree of similarity between open-loop forcing on the one hand and *feedback* excitation on the other was also demonstrated for steady-state conditions of matched frequency and amplitudes (i.e. rms levels). This similarity was argued on the

basis of both mean centerline decay measurements and spectral measurements close to the lip (Reisenhel, 1988). Given the constraints imposed by feedback, it is natural to ask oneself what differentiates these two modes of excitation, if the local instability properties are unchanged. In order to compare open-loop forcing to excitation via feedback, Reisenhel (1988) also estimated equivalent temporal growth rates for the case of on/off excitation. In this configuration, an electronic switch was closed to produced the sudden open-loop harmonic excitation of the jet. The amplitude growth was recorded and processed for a variety of frequencies and amplitudes. It was found that the equivalent growth rates obtained by open-loop forcing were frequently two orders of magnitude larger than the corresponding amplification rates associated with feedback, and that these growth rates were not correlated with the sound pressure level of the excitation. While the temporal amplification of fed back disturbances reflects the global instability phenomenon, the step-like amplitude growth generated by transient external forcing, on the other hand, corresponds to the initial wave front convecting past a stationary probe.

Further evidence that the jet remains locally convectively unstable under enhanced feedback conditions is given by phase speed measurements. It was shown that the measured phase speeds were constant and approximately equal to half the jet velocity. In particular, the phase speeds calculated from closed-loop feedback excitation and by transient forcing differed by less than two percent. The top graph of Figure 37 shows the measured normalized phase speed, C/U_j , of the eigenfrequency at all three Reynolds numbers investigated herein. These phase speeds were calculated from cross-spectral analysis between two velocity probes placed at various downstream locations. In contrast, an inferred propagation speed, ζ , of the amplitude envelope is presented in the lower graph of Figure 37. The convection speed ζ was calculated in the following way. Recalling the expression for the temporal amplification rate: $\sigma = \frac{\ln(\Gamma/\Gamma_c)}{\tau}$, one obtains from the least squares fits of σ versus $\ln(\Gamma)$ a value for Γ_c , but also an estimate of the total loop delay

τ . Knowing the acoustic delay τ_a and the probe position X , it is possible to obtain the inferred hydrodynamic delay $\tau_h = \tau - \tau_a$, and an equivalent normalized convection speed:

$$\zeta = \frac{1}{U_j} \frac{X}{\tau - \tau_a} \quad (23)$$

A very puzzling result is the fact that ζ appears to be an order of magnitude smaller than C/U_j . Many rigorous verifications were performed to ensure that the values of Γ_c and τ were being properly calculated. The uncertainty bars shown in Figure 37 are obtained from the mean square error of the fit and represent confidence intervals on ζ . Within experimental error, ζ remains independent of Reynolds number ($\zeta \approx 0.035$). It is conjectured that a possible explanation for this discrepancy may lie in a time delay associated with the transient receptivity for finite Reynolds numbers and finite shear layer thickness. This delay would have to be comparable to the convection time of the spatial instability over a few wave lengths to adequately confirm the explanation. The similar trend of scatter between the values of C/U_j and ζ is consistent with this explanation. It is important to appreciate that ζ does not represent the actual local phase speed of the instability wave, but an equivalent propagation speed at which the amplitude information is communicated downstream of the lip. It is also most interesting to realize that this information therefore does not travel with the self-sustained oscillation, as might be intuitively expected. Indeed, the distinction between the dynamics of the hydrodynamic instability wave ($\omega, C, -\alpha_i$) and the temporal growth of its amplitude (characterized by $\Gamma, X, -\alpha_i$ and ζ) is a key factor in the representation of the feedback instability. On the one hand, the hydrodynamic instability wave has a local phase speed approximately equal to half the jet velocity, and phase changes across the shear layer that are typical of the usual Kelvin-Helmholtz instabilities. On the other hand, the temporal amplification of the amplitude is the result of a global instability. This global instability was shown to have a

time scale several orders of magnitude larger than the period of the wave itself. These two components of the enhanced feedback qualify the instability of the present jet configuration as being "hybrid", in the sense that it appears to be a temporal instability with respect to global amplitude, but a spatial instability with respect to local shear layer dynamics.

6.3 *Relation to other self-sustained oscillations*

The concept of critical gain is now examined in relation to previous experiments. In particular, it has been reported in the literature (see for example Rockwell and Naudascher, 1979) that in most shear layer tone and edge tone experiments, there exists a minimum (threshold) distance between the edge (or point of impingement) and the point of separation, in order for self-sustained oscillations to make their appearance. In the present experiment, the equivalent of the edge location is the feedback position X . We have shown that under quite general conditions the gain had to satisfy the following inequality:

$$\Gamma > \frac{e^{-\eta X \text{Re}^{1/2}}}{R} \quad (24)$$

in order to obtain self-sustained oscillations. This expression determines a threshold value $X_{\min} = -\frac{\ln(\Gamma R)}{\eta \text{Re}^{1/2}}$. Conversely, for a fixed distance between points of separation and feedback, it is a common observation that there is a threshold in Reynolds number; e.g., "ringing" is only observed above a critical velocity. In particular, similar observations pertain to the problem of the "singing plate" (see Nagib et al., 1975), where a critical Reynolds number remained unexplained in a supposedly convectively unstable flow. Some similarity to the near wake problem (see Huerre, 1987) may exist in this flow made of a multiple array of jets. For given feedback conditions, the Reynolds number

threshold is expressed by the inequality:

$$\text{Re} > \left[\frac{\ln(\Gamma R)}{\eta X} \right]^2 \quad (25)$$

Sarohia (1977) considered the tones generated by an axisymmetric cavity, and found that for fixed upstream conditions:

$$X_{\min} \cdot \sqrt{\text{Re}} = \text{constant} \quad (26)$$

This result is evidently analogous to equations (24) and (25). Equation (26) simply reflects the fact that an amplitude threshold must be reached by the location of feedback, and that this amplitude is the result of linear spatial amplification ($-\alpha_{i,\max} = \eta \sqrt{\text{Re}}$) over a distance X . Clearly, much work remains to be done on the modeling of the effective gain Γ in flows with naturally occurring pressure feedback. Nevertheless, it may be inferred by analogy with equations (24) and (25), that the product (ΓR) was approximately constant in the case of Sarohia's experiment.

An elegant analysis of feedback was given by Powell (1961), who used a control-system type approach to describe the edge tone phenomenon. Powell claimed that a condition of unity gain around the loop had to be satisfied to obtain steady-state self-sustained oscillations. From this criterion, amplitude and phase constraints were derived, similar to the dual aspects expressed by equations (1) and (3) of the present manuscript. In the present work, most of Powell's results have been qualitatively recovered using first return map arguments. This simple approach was inspired by the study of dynamical systems (see for example Mees, 1986), and in addition gave physical insight into the transient temporal growth of disturbances. Also, the role of the spatial stability characteristics of the shear layer as a vehicle for the amplification of disturbances has been clearly demonstrated.

The present study provides a general frame of work which relates the notion of

"critical gain" to the instability characteristics of the shear layer in a simple fashion. Moreover, the introduction of a controllable gain provides the added dimension that allows us to unify the results of various tone experiments. Fundamental differences were claimed, for instance, between the shear layer tone (or probe feedback) and the edgetone phenomena (see Hussain and Zaman, 1978), partly on the basis of the absence of hysteresis in the former. In light of the present findings, the two phenomena fall under the same category of flow systems which may support self-sustained oscillations, due to pressure feedback. It is conjectured that the qualitative differences between tone experiments are largely attributable to differences in their effective gains, which must include receptivity considerations. For example, it was shown that as the gain was increased, the width of the eigenfrequency bands increased, causing hysteretic behavior past the point of crossing of competing bands. Clearly, the effective gain associated with natural feedback experiments is more difficult to quantify than in the explicitly controlled feedback configuration developed in this study. However, it may be inferred from the literature (Rockwell and Naudascher, 1979, and Hussain and Zaman, 1978) that the higher effective gains appear to be associated with the more symmetric configurations, such as flow over axisymmetric cavities, and hole tones.

It is believed that focusing on the notions of gain and "critical gain" should help future modeling of the feedback process. Such modeling, complemented with an increased understanding of the receptivity problem would lead to significant progress in the prediction of open flows with pressure feedback, including turbulent flows.

Reisenthel (1988) established that in presence of mild probe feedback, the dimensionality of attractors, reconstructed from long time series of the velocity signal at a given point in space, indicate an increase in both the dimension and the sensitivity to initial conditions, with downstream distance. In addition, low-level axisymmetric acoustic forcing was found to reduce the dimension by approximately one. Although these findings are in

good agreement with our physical understanding of the present well-documented jet (see Nagib et al., 1989), it is conjectured that the loss of phase reference in an open flow may have precluded further characterization, i.e. deviation from periodic behavior. In the presence of enhanced feedback, however, strong temporally developing disturbances dominate the flowfield, past a *critical* value of the Reynolds number. Therefore, it is anticipated that the jet in the enhanced feedback configuration may circumvent some of the previous difficulties encountered in open flows, and provide us with the opportunity to test the dynamical systems approach as a *tool* to analyze empirical findings.

7. Conclusions

The role of feedback in a convectively unstable axisymmetric jet has been experimentally investigated using a controlled means of enhanced self-excitation. It was found that under general conditions, the upstream propagation of pressure fluctuations and their coupling with the initial shear-layer instability spontaneously produced strong self-sustained oscillations past critical conditions. This special open flow configuration was investigated with an eye towards the potential use of dynamical systems in transition and turbulence.

These self-excited, highly organized instabilities were found to share many of the qualitative features exhibited by a broad class of hydroacoustic phenomena. Because of the controlled conditions of the experiment, thresholding effects based on velocity and streamwise flow scale were related to the existence of a critical gain. Furthermore, using the concept of "hybrid" instability, we explained the origin of a critical Reynolds number in feedback or resonant systems. Model phenomenological equations utilizing linear stability theory were used to describe in detail the dynamics of feedback and many of its

nonlinear consequences. This dual empirical and analytical approach allowed us to explain the observed frequencies and their inter-relation in more complete and rigorous ways than in previous studies. The present data agree well with the predicted scaling of the critical gain with downstream position of the source of feedback and with Reynolds number. Specifically, it was demonstrated that frequency stages are embedded within a band structure. The width of these attracting bands and their possible overlap was determined to bear close ties with phenomena of intermittent switching and hysteresis between competing eigenfrequencies. Clear evidence was presented that these effects should be viewed as being part of a unified structure controlled by the overall gain of the feedback loop, including receptivity.

Most importantly, the exponential amplification or decay of self-sustained oscillations close to criticality was shown to be governed by a global temporal instability. This instability has a time scale several orders of magnitude larger than the period of the oscillation itself. The growth rates at the onset of resonance were measured experimentally and found to be independent of space. These global intrinsically driven oscillations were found to be insensitive to external disturbances for a substantial range of forcing levels and initial conditions, although all indications were that the flow remained locally convectively unstable. The role of the shear layer as a vehicle for the amplification of disturbances within the feedback loop was clearly established by connecting temporal growth rates of the global instability with the linear spatial amplification rates of the initial shear layer. These two components of the enhanced feedback effect qualify the instability as being "hybrid", in the sense that it is temporal with respect to the global amplitude of oscillations, but convective with respect to local shear layer dynamics.

By considering issues of frequency competition based on the *temporal* growth rates of global oscillations, an explanation was proposed for the frequency selection process in a closed-loop configuration, and for the observed frequency hysteresis. It was also

shown experimentally that, for Reynolds numbers slightly larger than critical, well-defined limit-cycle behavior is observed, with an increasing number of potentially excited modes of oscillation as the Reynolds number is increased. The related existence of a critical streamwise flow scale for the appearance of self-sustained oscillations in various "tone" experiments was also established. Greater insight into the role of receptivity in feedback systems has been gained through the examination of related frequency selection criteria. Finally, it is believed that the present measurements of receptivity constitute a wealth of new results that pertain to the excitation of free shear layers, under both steady-state and transient conditions. Comparison with theoretical estimates based on the application of linear stability theory revealed that while the location and magnitude of frequency jumps only agreed in a qualitative sense, excellent agreement was found in predicting the *onset* of oscillations.

ACKNOWLEDGMENT

The authors greatly acknowledge the support of this work by the Air Force Office of Scientific Research under grant number 86-0165 which was monitored by Dr. J. McMichael.

REFERENCES

- Ahmed, M., Wigeland, R. A. & Nagib, H. M. 1976 Generation and management of swirling flows in confined streams. Interim Report No. ARO-ITR-76-1, Illinois Institute of Technology, Chicago.
- Bechert, D. W. 1983 A model of the excitation of large scale fluctuations in a shear layer. AIAA Paper No. 83-0724. Proceedings of the AIAA 8th Aeroacoustics Conference, Atlanta.
- Bechert, D. W. 1985 *Z. Flugwiss. Weltraumforsch.* **9**, 356-361.
- Bechert, D. W. 1988 *J. Fluid Mech.* **186**, 47-62.
- Berge, P., Pomeau, Y. & Vidal, C. 1984 *L'Ordre Dans le Chaos*. Hermann.
- Chomaz, J. M., Huerre, P. & Redekopp, L. G. 1987 *Phys. Rev. Lett.* **60**, No. 1, 25-28.

- Chomaz, J. M., Huerre, P. & Redekopp, L. G. 1987 Models of hydrodynamic resonances in separated shear flows. Proceedings of the 6th Symposium on Turbulence Shear Flows, Toulouse.
- Corke, T. C., Shakib, F. & Nagib, H. M. 1985 Effects of low amplitude forcing on axisymmetric jet flows. AIAA Paper No. 85-0573. Proceedings of AIAA Shear Flow Control Conference, Boulder.
- Corke, T. C., Shakib, F. & Nagib, H. M. 1989 Mode selection and resonant phase locking in unstable axisymmetric jets. Submitted to *J. Fluid Mech.*
- Crow, S. C. & Champagne, F. H. 1971 *J. Fluid Mech.* **48**, 547-591.
- Drubka, R. E. 1981 Instability in near field of turbulent jets and their dependence on initial conditions and Reynolds number. Ph.D. thesis, Illinois Institute of Technology, Chicago.
- Freythuth, P. 1966 *J. Fluid Mech.* **25**, 683-704.
- Gutmark, E. & Ho, C. M. 1983 *Phys. Fluids* **26**, 2932-2938.
- Herbert, T. & Morkovin, M. V. 1980 In *Laminar-Turbulent Transition* (ed. R. Eppler & H. Fasel), Springer-Verlag.
- Ho, C. M. & Nossier, N. S. 1981 *J. Fluid Mech.* **105**, 119-142.
- Ho, C. M. & Huerre, P. 1984 *Ann. Rev. Fluid Mech.* **16**, 365-424.
- Hussain, A. K. M. F. & Zaman, K. B. M. Q. 1978 *J. Fluid Mech.* **87**, 349-383.
- Hussain, A. K. M. F. & Zaman, K. B. M. Q. 1981 *J. Fluid Mech.* **110**, 39-71.
- Huerre, P. 1987 In *Instabilities and Nonequilibrium Structures* (ed. E. Tirapegui & D. Villarroel), Reidel.
- Kaykayoglu, R. & Rockwell D. 1985 *J. Fluid Mech.* **156**, 439-461.
- Kibens, V. 1980 *AIAA J.* **18**, 434-441.
- Knisely, C. & Rockwell, D. 1982 *J. Fluid Mech.* **116**, 157-186.
- Krothapalli, A. 1985 *AIAA J.* **23**, 1910-1915.
- Lucas, M. & Rockwell, D. 1984. *J. Fluid Mech.* **147**, 333-352.
- Lucas, M. & Rockwell, D. 1987. *J. Sound & Vib.* **116**, 355-369.
- Mees, A. 1986 In *Chaos* (ed. A. Holden), Princeton University Press.
- Miksad, R. W. 1972 *J. Fluid Mech.* **56**, 695-719.
- Miksad, R. W., Jones, F. L., Powers, E. J., Kim, Y. C. & Khadra, L. 1982 *J. Fluid Mech.* **123**, 1-29.
- Monkewitz, P. A. & Huerre, P. 1982 *Phys. Fluids* **25**, 1137-1143.
- Monkewitz, P. A. 1983. *Phys. Fluids* **26**, 3180-3184.
- Morkovin, M. V. & Paranjape, S. V. 1971 *Z. Flugwiss* **19**, 328-335.
- Nagel, R. T., Denham, J. W. & Papathanasiou, A. G. 1983 *AIAA J.* **21**, 1541-????.
- Nagib, H. M., Way, J. L. & Tan-Atichat, J. 1975 *Prog. in Astr. & Aero.* **37**, 503-520.

- Nagib, H. M., Drubka, R. E. & Reisenthel, P. 1989 *Phys. Fluids* (submitted).
- Pomeau, Y. & Manneville, P. 1980 *Comm. Math. Phys.* **74**, 189-197.
- Powell, A. 1961 *J. Acous. Soc. Am.* **33**, 395-409.
- Reisenthel, P. 1988 Hybrid instability in an axisymmetric jet with enhanced feedback.
Ph.D. thesis, Illinois Institute of Technology, Chicago.
- Rockwell, D. & Naudascher, E. 1979 *Ann. Rev. Fluid Mech.* **11**, 67-94.
- Sarohia, V. 1977 *AIAA J.* **15**, 984-991.
- Shakib, F. 1984 Evolution and interaction of instability modes in an axisymmetric jet.
M.S. thesis, Illinois Institute of Technology, Chicago.
- Sreenivasan, K. R., Raghu, S. & Kyle, D. 1987 Absolute instability in variable density jets. Internal Report, Yale University, New Haven.
- Staubli, T. & Rockwell, D. 1987. *J. Fluid Mech* **176**, 135-167.
- Tam, C. K. W. & Block, P. J. W. 1978 *J. Fluid Mech.* **89**, 373-399.
- Umeda, Y., Maeda, H. & Ishii, R. 1987 *Phys. Fluids* **30**, 2380-2388.
- Wlezien, R. W. & Way, J. 1979 *AIAA J.* **17**, 563-570.
- Woolley, J. P. & Karamcheti, K. 1974 *AIAA J.* **12**, 1457-1458.

LIST OF FIGURES

FIGURE 1. Schematic of the I.I.T. air jet facility.

FIGURE 2. Schematic describing enhanced feedback excitation.

FIGURE 3. Comparison of streamwise velocity spectra with and without enhanced feedback excitation, at $X/D = 0.26$ and $Re = 68,000$.

FIGURE 4. Variation of velocity spectra with downstream distance under feedback conditions, at $Re = 69,800$ and $y/\delta = 0$.

FIGURE 5. Typical variation of spectral amplitude of the feedback frequency as a function of gain ($X/D = 0.132$, $Re = 75,700$).

FIGURE 6. Variation of spectral amplitude of the feedback frequency as a function of gain and downstream distance at $Re = 61,800$.

FIGURE 7. Variation of spectral amplitude with gain, for fundamental axisymmetric frequency, feedback frequency, and externally added pure tone forcing.

FIGURE 8. Variation of spectral amplitude as a function of gain, with externally added white noise forcing.

FIGURE 9. Representation of eigenfrequency stages as a function of Reynolds number for $G = 0.055 \text{ Ns/m}^3$, 0.066 Ns/m^3 , 0.132 Ns/m^3 , and 0.263 Ns/m^3 , at $X/D = 0.17$.

FIGURE 10. Principal eigenfrequency bands as a function of non-dimensional gain, Γ , and Reynolds number.

FIGURE 11. Representation of eigenfrequency stages as a function of Reynolds number for $G = 0.033 \text{ Ns/m}^3$ and $X/D = 0.30$.

FIGURE 12. Representation of eigenfrequency stages at $X/D = 0.30$ and $X/D = 0.17$, illustrating the absence of scaling with St_θ .

FIGURE 13. Variation of the amplitude of feedback and forcing frequencies as a function of "in phase" forcing level, at $\Gamma = 0.0176$, $Re = 75,800$, and $X/D = 0.13$.

FIGURE 14. Variation of the amplitude of feedback and forcing frequencies as a function of "out of phase" forcing level, at $\Gamma = 0.0176$, $Re = 75,800$, and $X/D = 0.13$.

FIGURE 15. Variation of relative amplitude of feedback and forcing frequencies as a function of forcing frequency, at $Re = 76,000$ and $X/D = 0.13$.

FIGURE 16. Eigenfrequency hysteresis diagram, at $X/D = 0.17$ and $G = 0.045 \text{ Ns/m}^3$. Letters indicate positions corresponding to the spectra in Figure 17.

FIGURE 17. Spectral variation of the streamwise velocity with Reynolds number, in the vicinity of three-frequency hysteresis, for $X/D = 0.17$ and $G = 0.045 \text{ Ns/m}^3$.

FIGURE 18. Comparison of frequency stages observed at $G = 0.132 \text{ Ns/m}^3$, with calculated eigenfrequencies for $X/D = 0.17$, $d/D = 70.7$, and $\phi = 0$.

FIGURE 19. Comparison of frequency stages observed at $G = 0.033 \text{ Ns/m}^3$, with calculated eigenfrequencies for $X/D = 0.30$, $d/D = 70.7$, and $\phi = 0$.

FIGURE 20. Open-loop transfer functions using harmonic forcing at 2240 Hz, 2500 Hz, and 3700 Hz, for $X/D = 0.16$ and $Re = 61,600$.

FIGURE 21. Open-loop transfer function of the feedback frequency including gain curves, for $X/D = 0.16$ and $Re = 61,600$: (top) high and low operating points far from critical gain, (bottom) illustration of intermittency and hysteresis (inset) close to critical gain.

FIGURE 22. Open-loop transfer functions and their analytical approximation at 2240 Hz and 1000 Hz, for $X/D = 0.16$ and $Re = 61,600$.

FIGURE 23. Illustration of closed-loop temporal evolution of the eigenfrequency amplitude for $X/D = 0.16$, $Re = 61,600$, and $\Gamma/\Gamma_c = 3.25$.

FIGURE 24. Comparison of time series (a), amplitude demodulation (b), and exponential growth (c) of the eigenfrequency mode at $Re = 62,500$, $X/D = 0.17$, and $\Gamma = 0.007$.

FIGURE 25. Comparison of demodulated amplitudes of fundamental and subharmonic frequencies for $\Gamma = 0.0032$, $Re = 62,850$, and $X/D = 0.17$.

FIGURE 26. Comparison of time series (a), amplitude demodulation (b), and exponential decay (c) of the eigenfrequency mode at $Re = 62,500$, $X/D = 0.17$, and $\Gamma = 0.002$.

FIGURE 27. Scaling of temporal amplification rates with gain, at $Re = 62,500$ and $X/D = 0.17$.

FIGURE 28. Scaling of temporal amplification rates with gain, for various radial positions at $Re = 72,500$.

FIGURE 29. Correlation of temporal amplification rates between two velocity probes at $Re = 60,000$.

FIGURE 30. Correlation of individual temporal amplification rates between two velocity probes at $Re = 72,500$, $Re = 60,000$, and $Re = 42,000$.

FIGURE 31. Scaling of mean temporal amplification rates with gain, at $Re = 72,500$, $Re = 60,000$, and $Re = 42,000$.

FIGURE 32. Variation of critical gain with downstream distance at $Re = 61,850$.

FIGURE 33. Variation of critical gain with Reynolds number at $X/D = 0.17$.

FIGURE 34. Calculated curves of constant temporal amplification rates at $X/D = 0.17$; (a) neutral stability curves for eigenfrequencies corresponding to $n = 23$ and $n = 39$; (b) detail of the amplification band for $n = 23$; (c) neutral stability curves for eigenfrequencies corresponding to $n = 15$ through $n = 50$.

FIGURE 35. Schematic illustrating the frequency hysteresis phenomenon resulting from Reynolds number variation at fixed gain; (a) neutral stability curves for $n = 23$ and $n = 39$; (b) temporal amplification rates, σ , experienced along constant G line; (c) resulting frequency hysteresis.

FIGURE 36. Effect of acoustic transfer function on shear layer response to monochromatic excitation at $Re = 61,600$, $X/D = 0.17$.

FIGURE 37. Comparison of phase speed and envelope convection speed of the feedback frequency, as a function of Reynolds number.

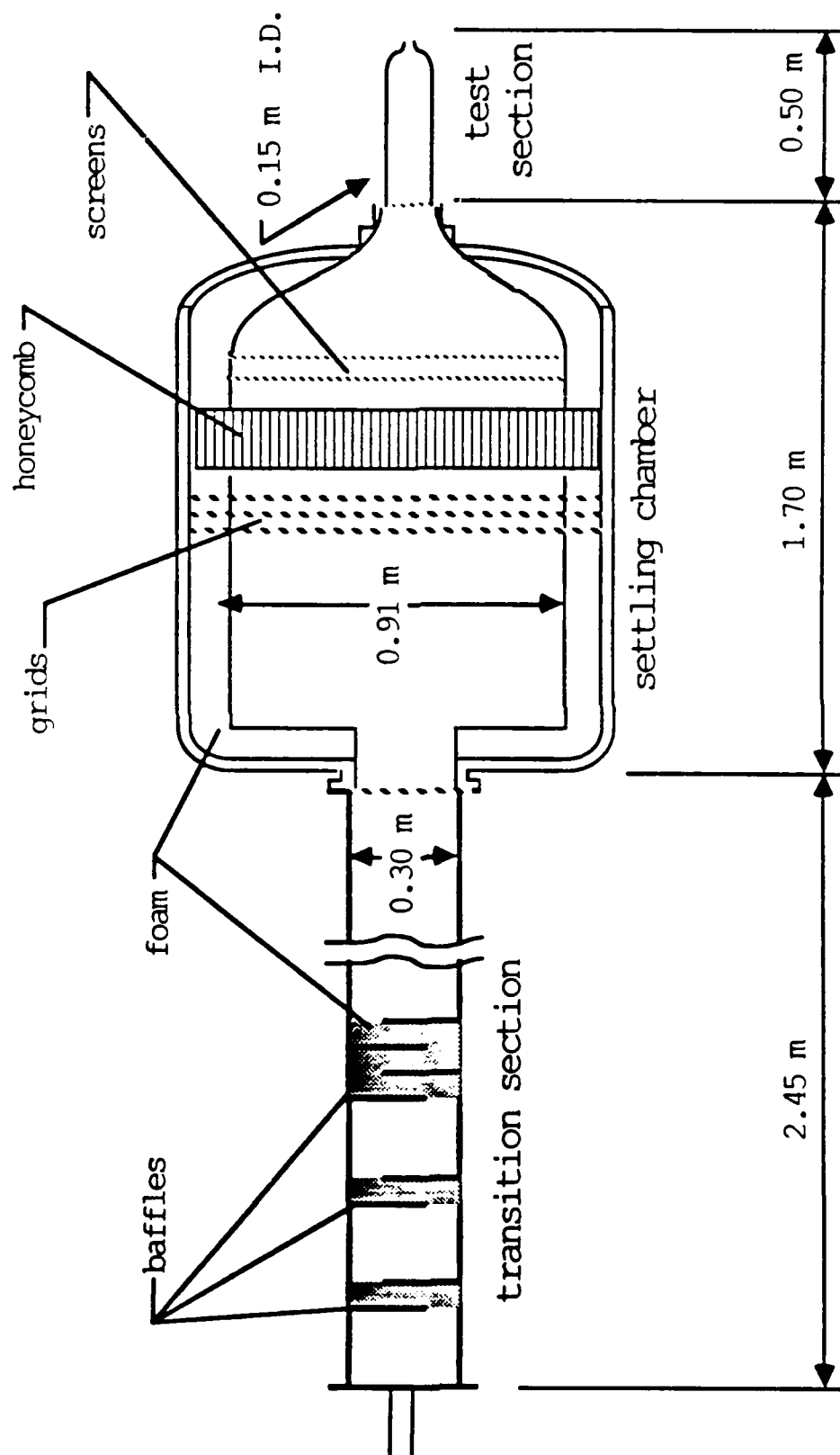


Figure 1. Schematic of the I.I.T. Air Jet Facility

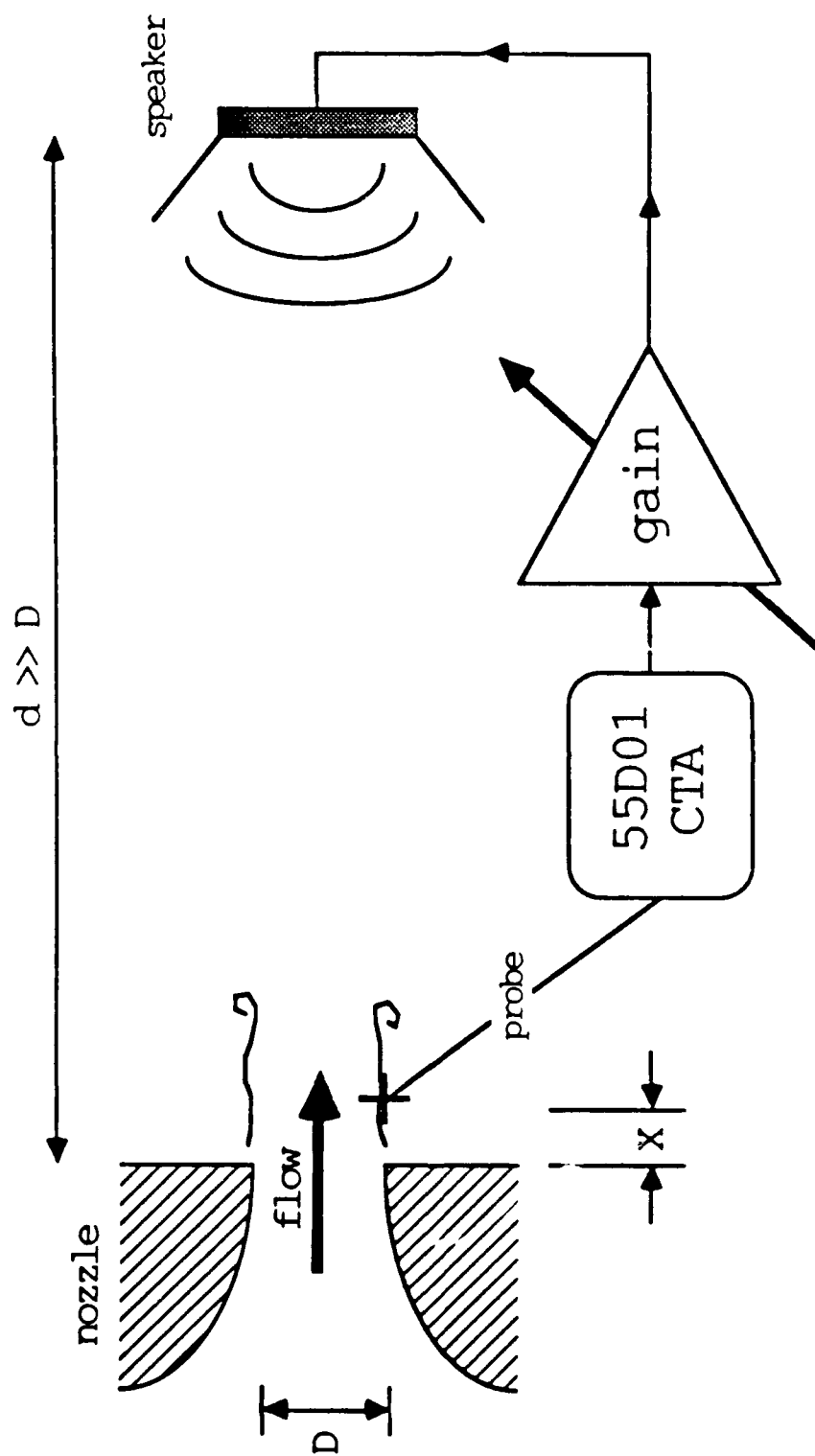


Figure 2. Schematic Describing Enhanced Feedback Excitation

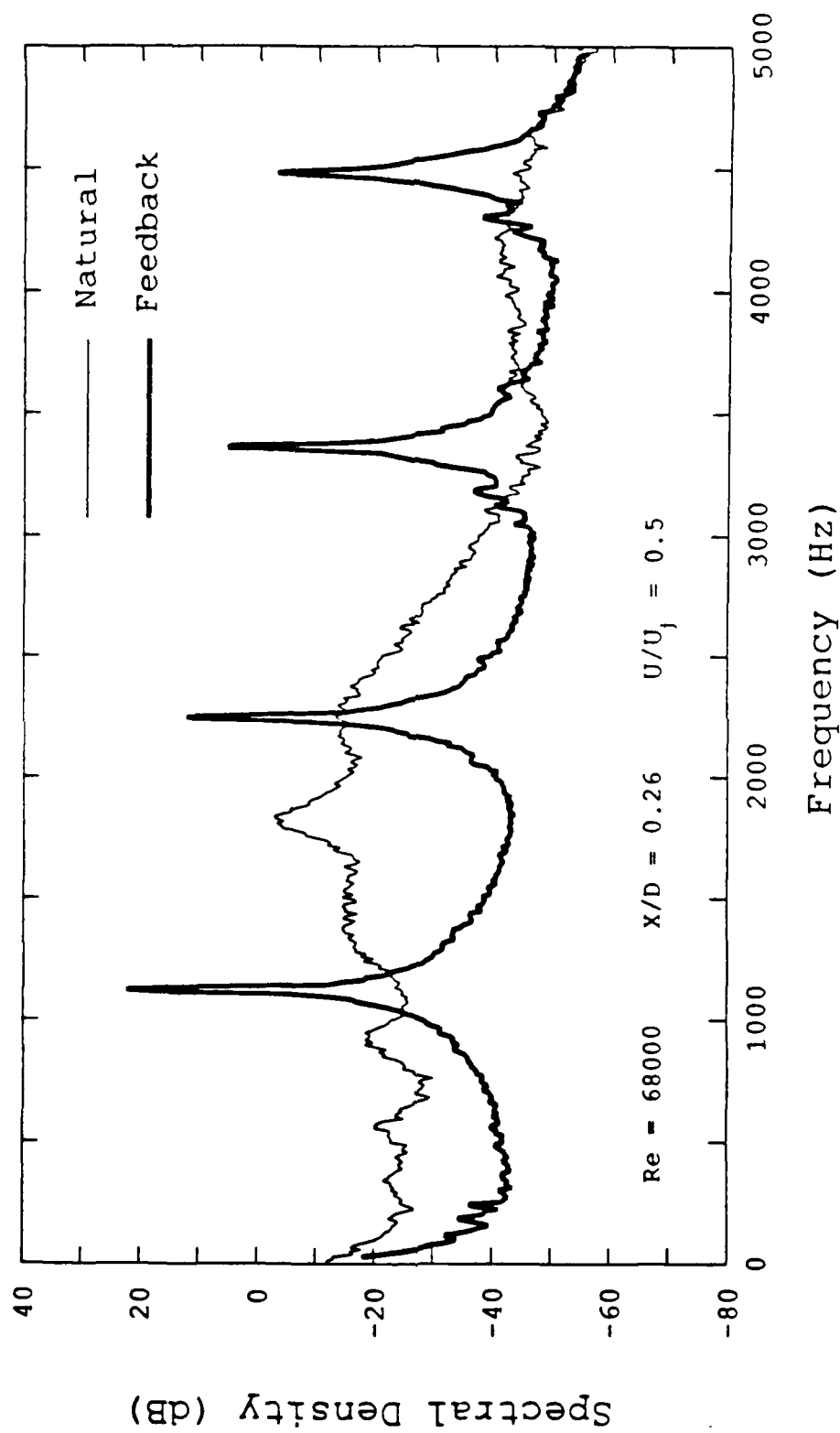


Figure 3. Comparison of Streamwise Velocity Spectra With and Without Enhanced Feedback Excitation, at $X/D = 0.26$ and $Re = 68,000$

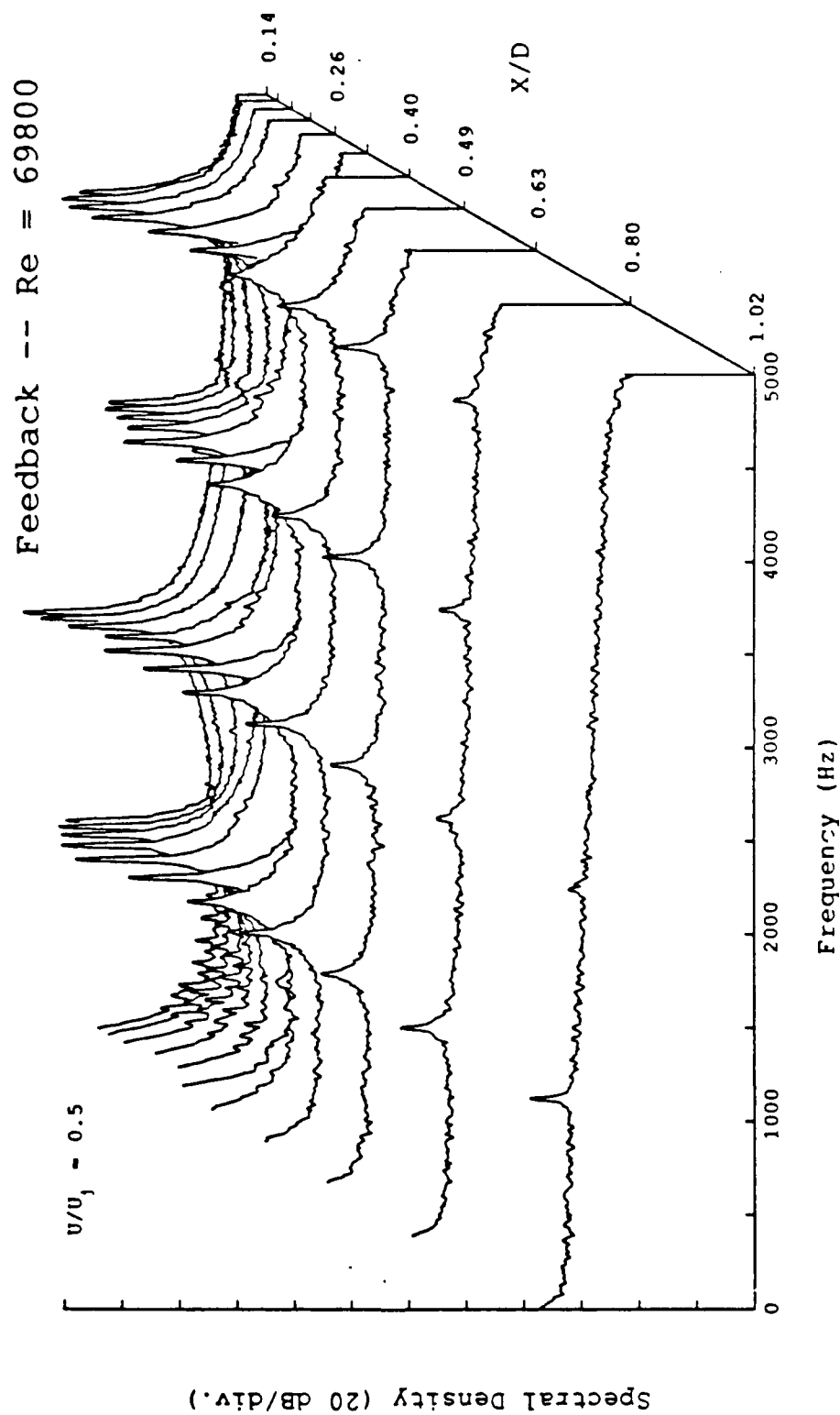


Figure 4. Variation of Velocity Spectra with Downstream Distance under Feedback Conditions, at $Re = 69,800$ and $Y/\delta = 0$

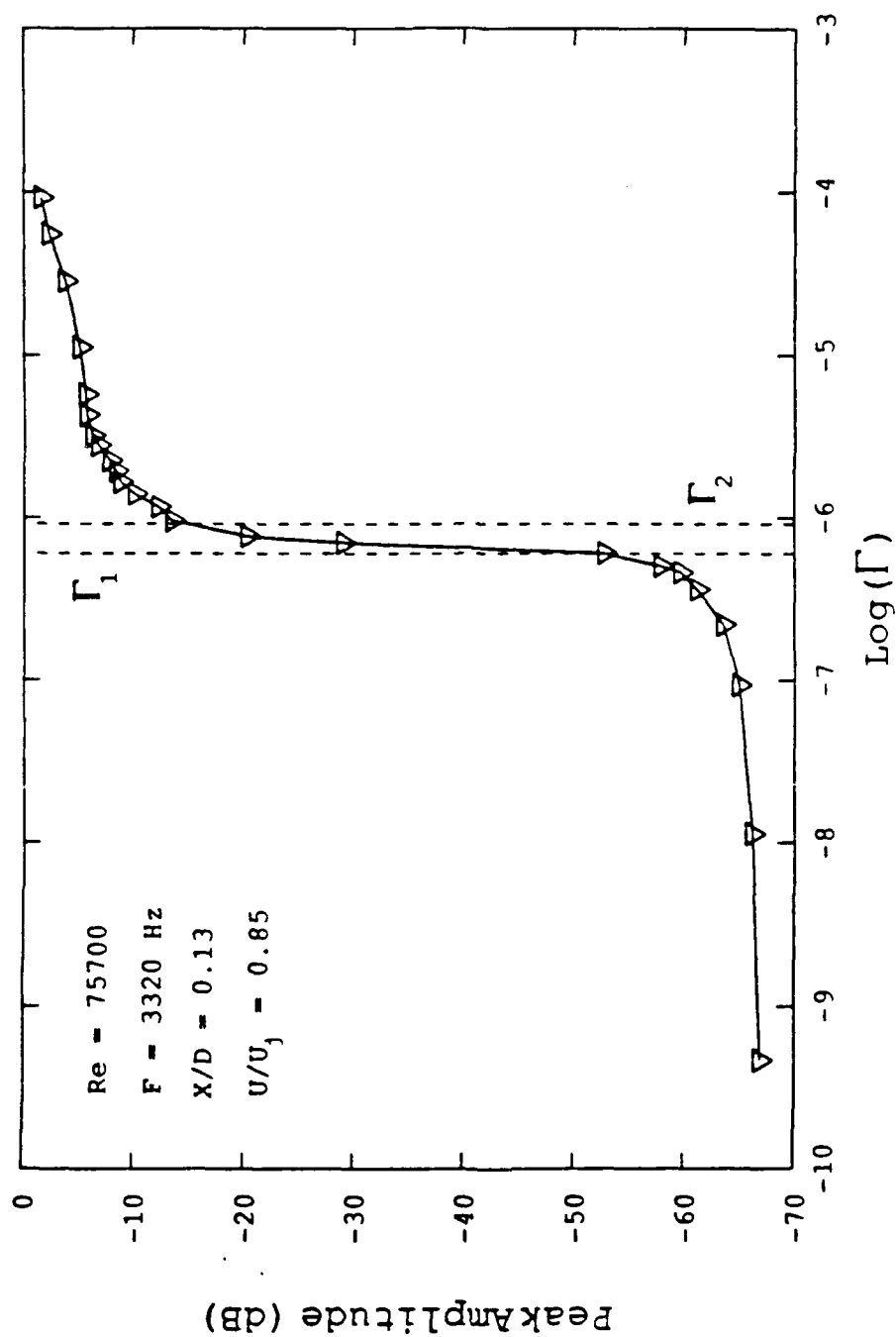


Figure 5. Typical Variation of Spectral Amplitude of the Feedback Frequency as a Function of Gain ($X/D = 0.132$, $Re = 75,700$)

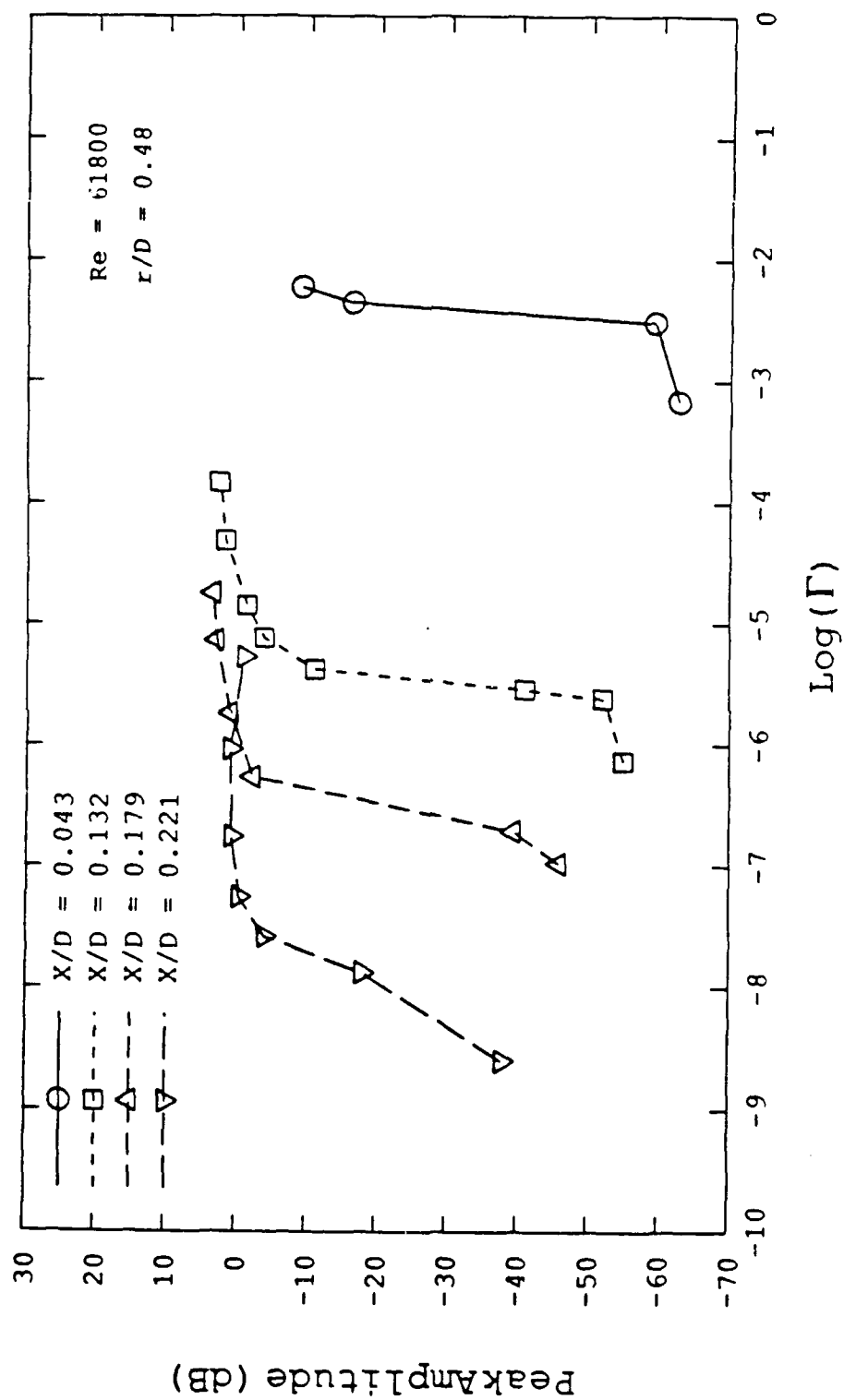


Figure 6. Variation of Spectral Amplitude of the Feedback Frequency as a Function of Gain and Downstream Distance at $Re = 61,800$

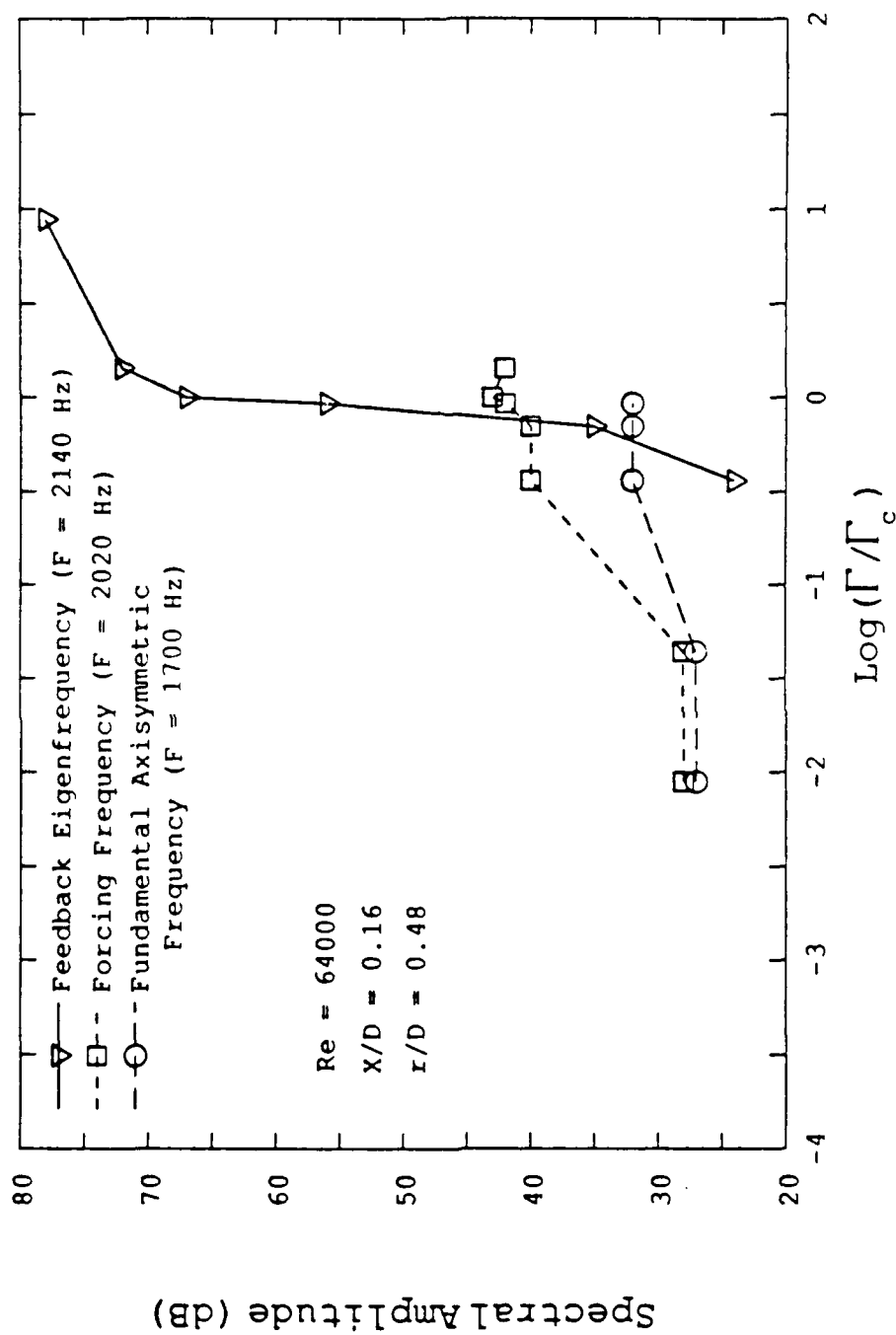


Figure 7. Variation of Spectral Amplitude with Gain, for Fundamental Axisymmetric Frequency, Feedback Frequency, and Added Pure Tone Forcing

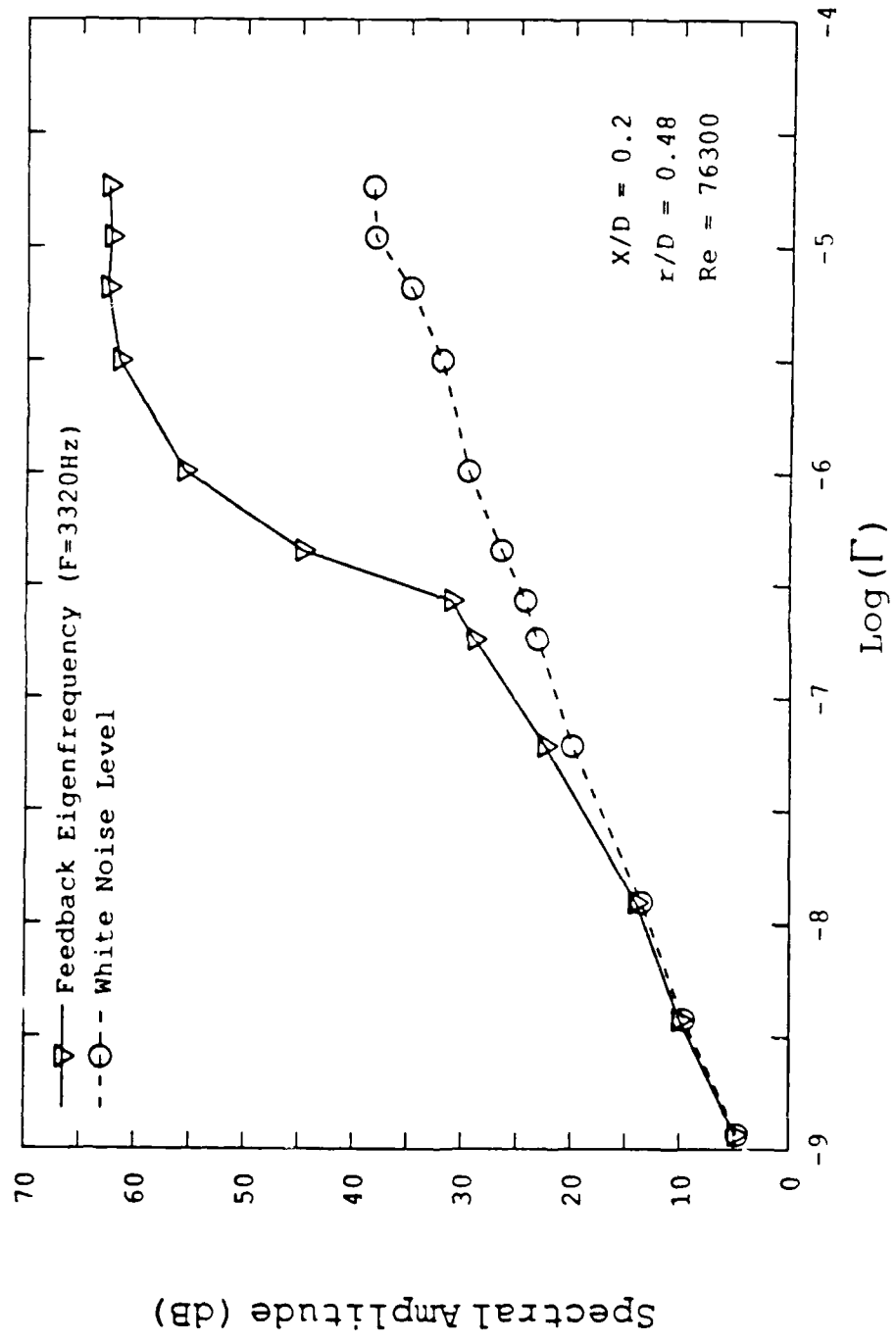


Figure 8. Variation of Spectral Amplitude as a Function of Gain, with Added White Noise Forcing

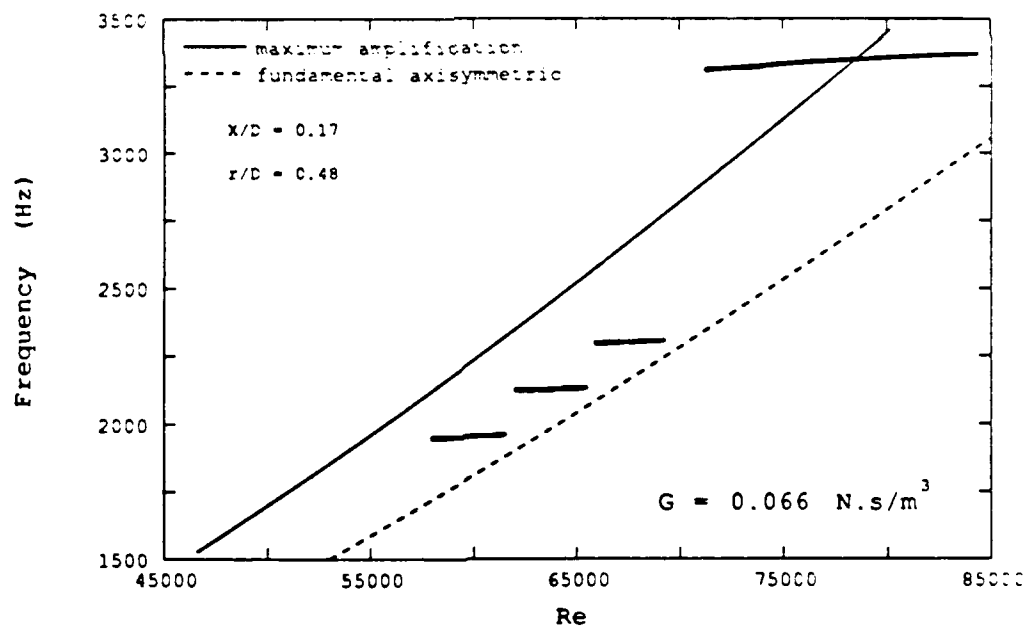
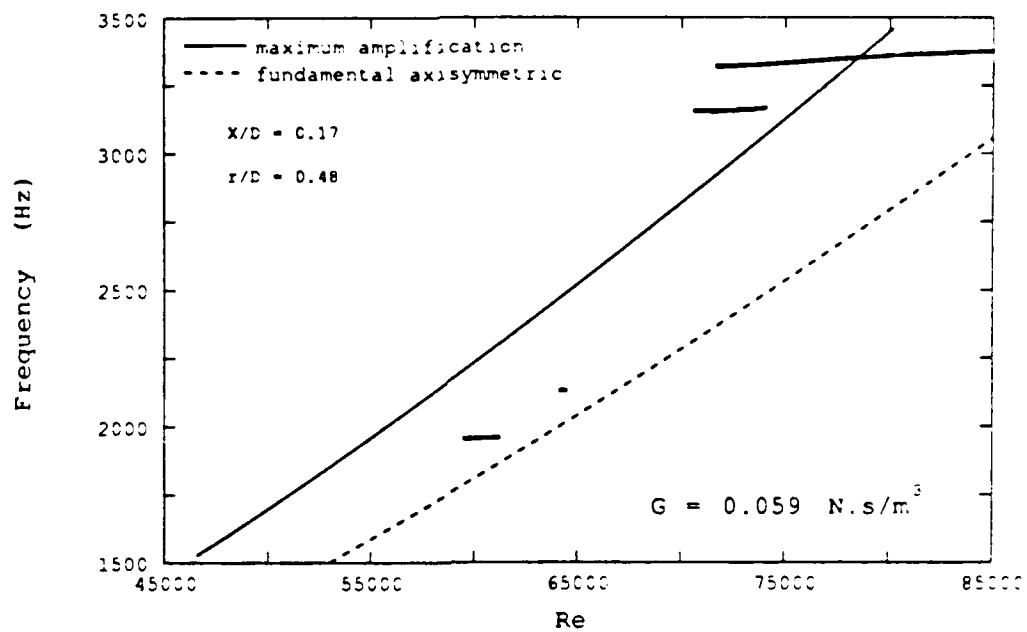


Figure 9a. Representation of Eigenfrequency Stages₃ as a Function of Reynolds Number for $G = 0.059 \text{ N.s/m}^3$ and $G = 0.066 \text{ N.s/m}^3$ at $X/D = 0.17$

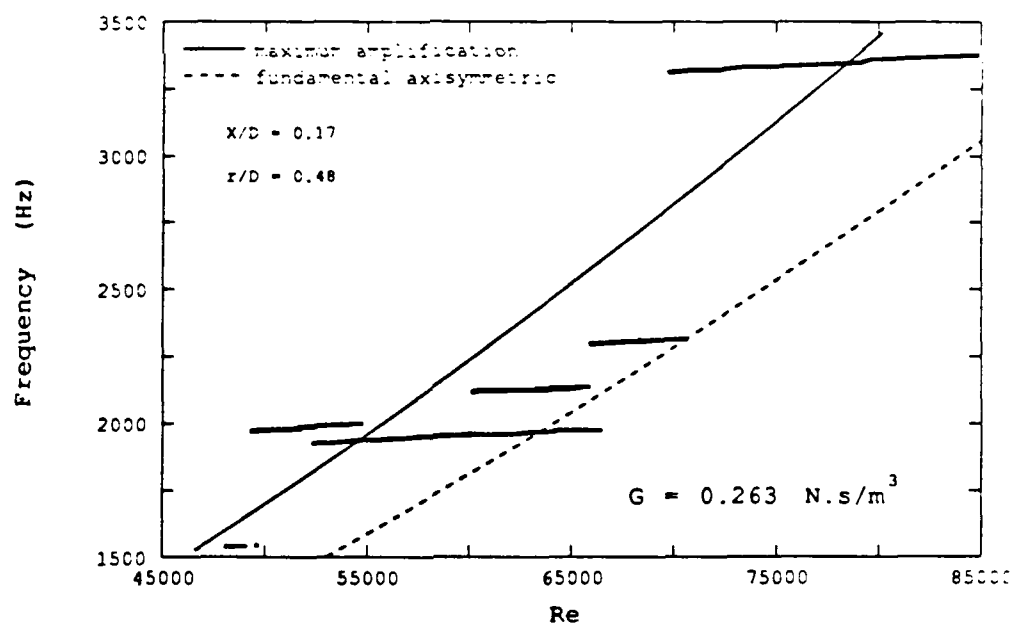
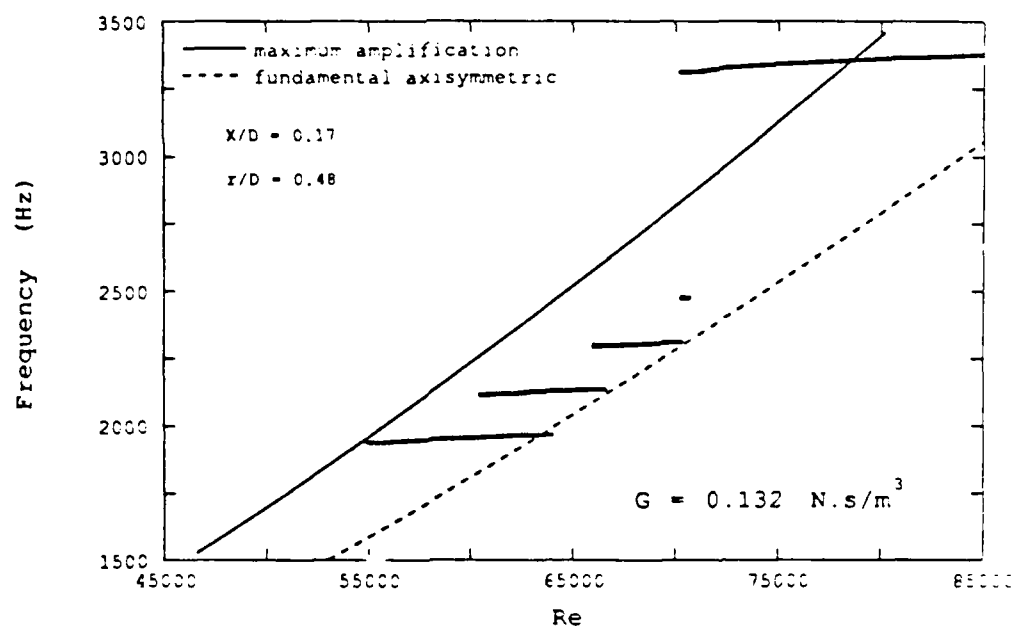


Figure 9b. Representation of Eigenfrequency Stages, as a Function of Reynolds Number for $G = 0.132 \text{ N.s/m}^3$ and $G = 0.263 \text{ N.s/m}^3$ at $X/D = 0.17$

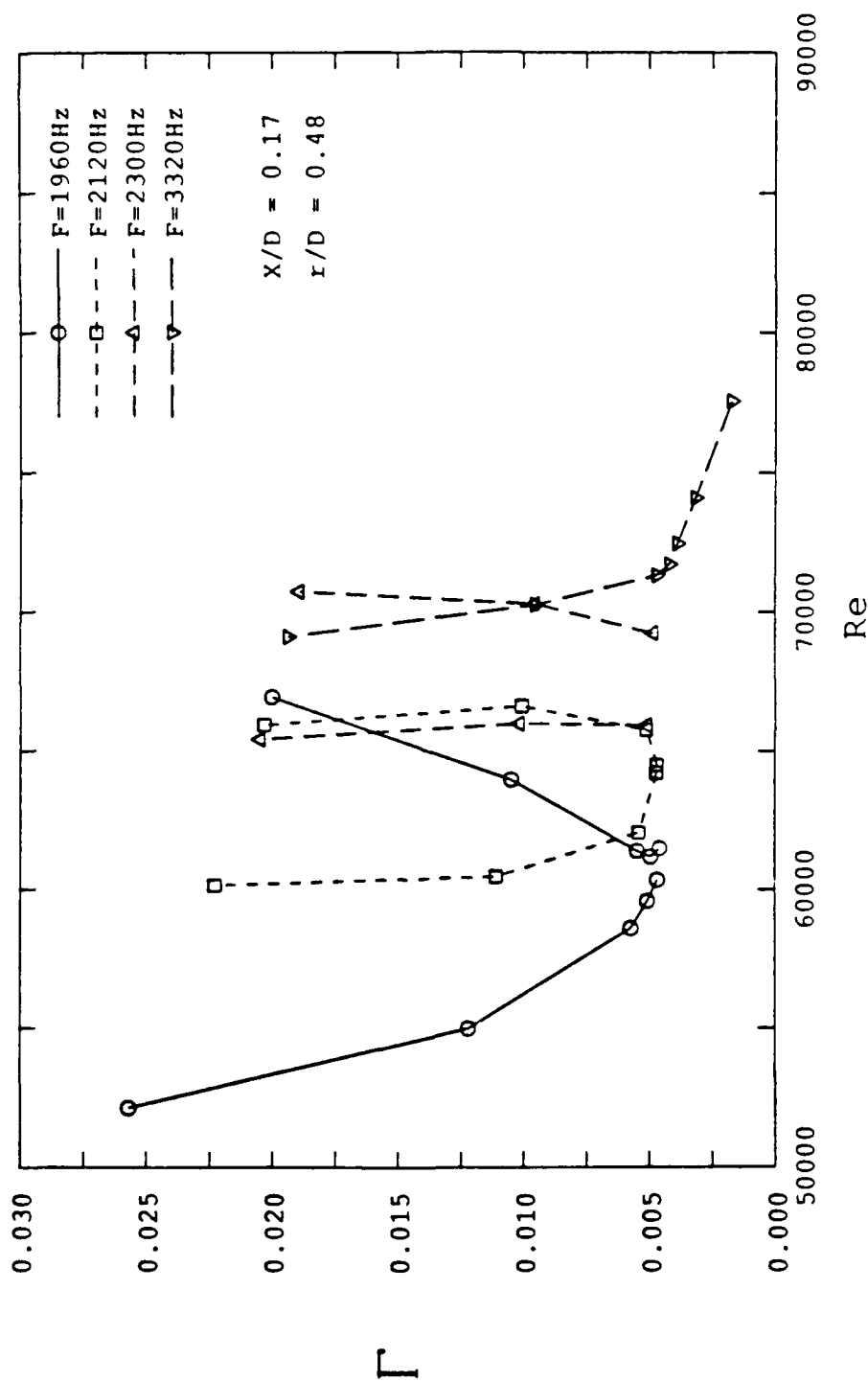


Figure 10. Principal Frequency Bands as a Function of Non-Dimensional Gain (Γ) and Reynolds Number, Determined by Reynolds Number Variation at $X/D = 0.17$

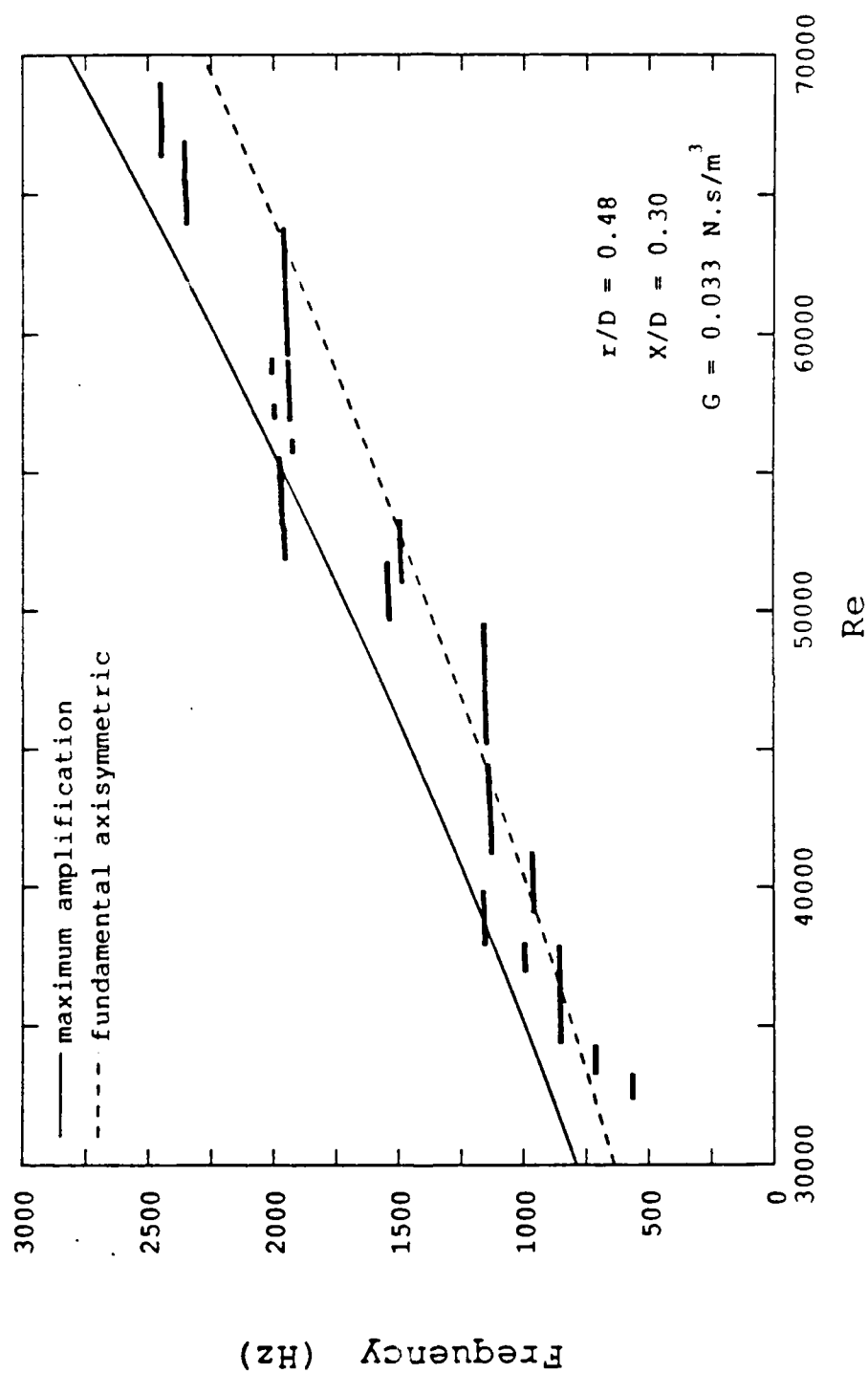


Figure 11. Representation of Eigenfrequency Stages as a Function of Reynolds Number for $G = 0.033 \text{ N.s/m}^3$ and $X/D = 0.30$

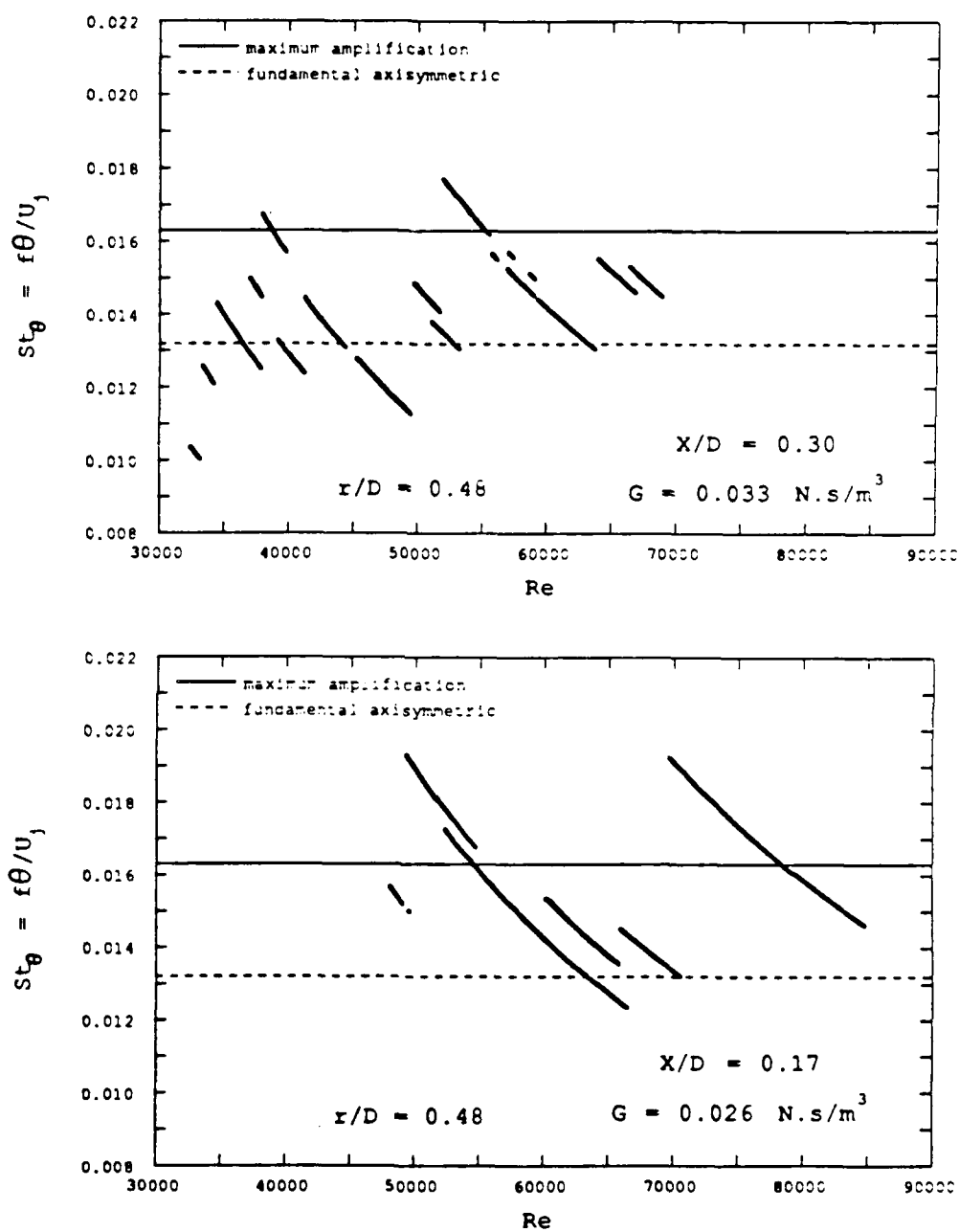


Figure 12. Representation of Eigenfrequency Stages
Illustrating the Absence of Scaling with St_θ , at
 $X/D = 0.30$ and $X/D = 0.17$

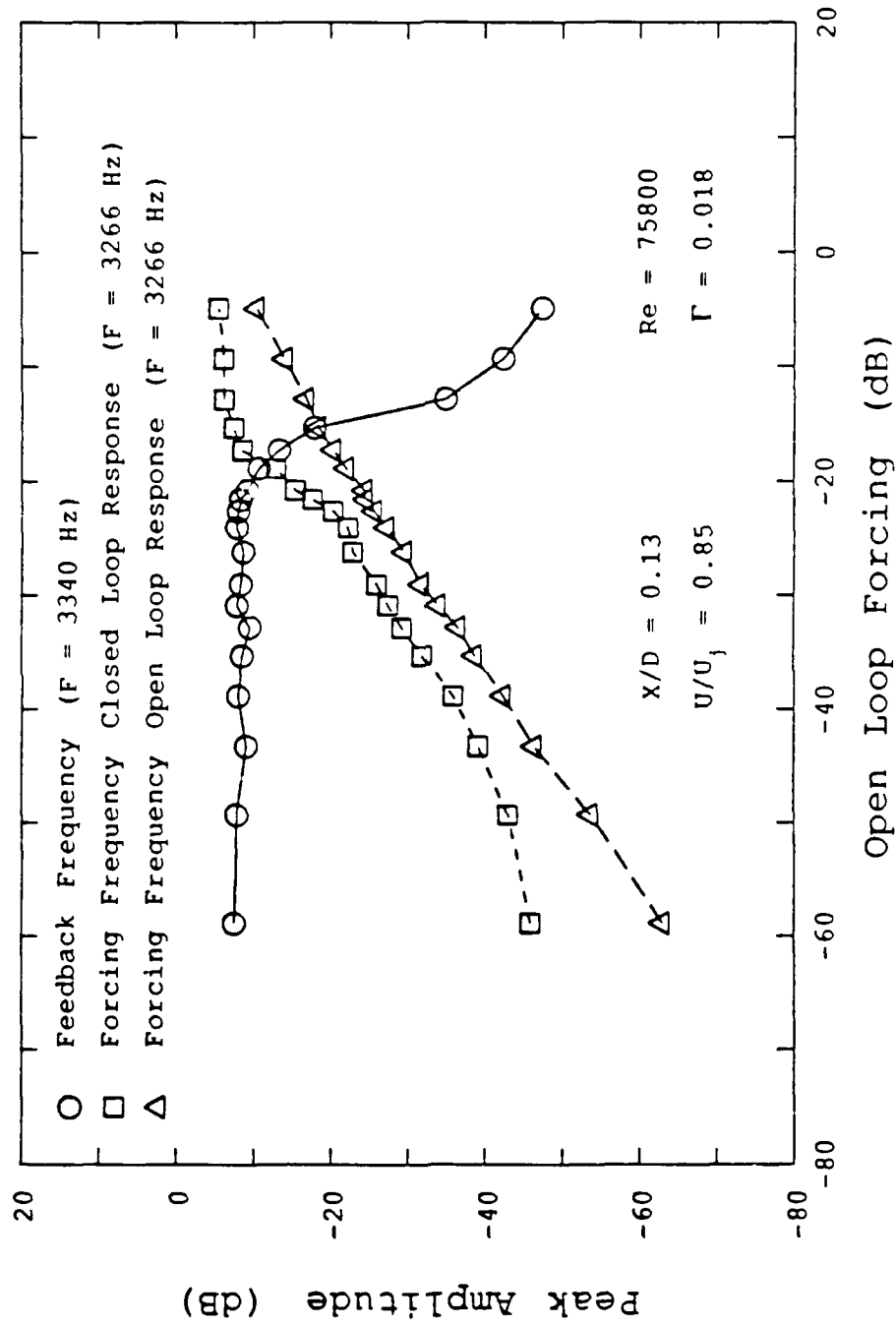


Figure 13. Variation of the Amplitude of Feedback and Forcing Frequencies as a Function of "In Phase" Forcing Level at $r = 0.0176$, $Re = 75,800$ and $X/D = 0.13$

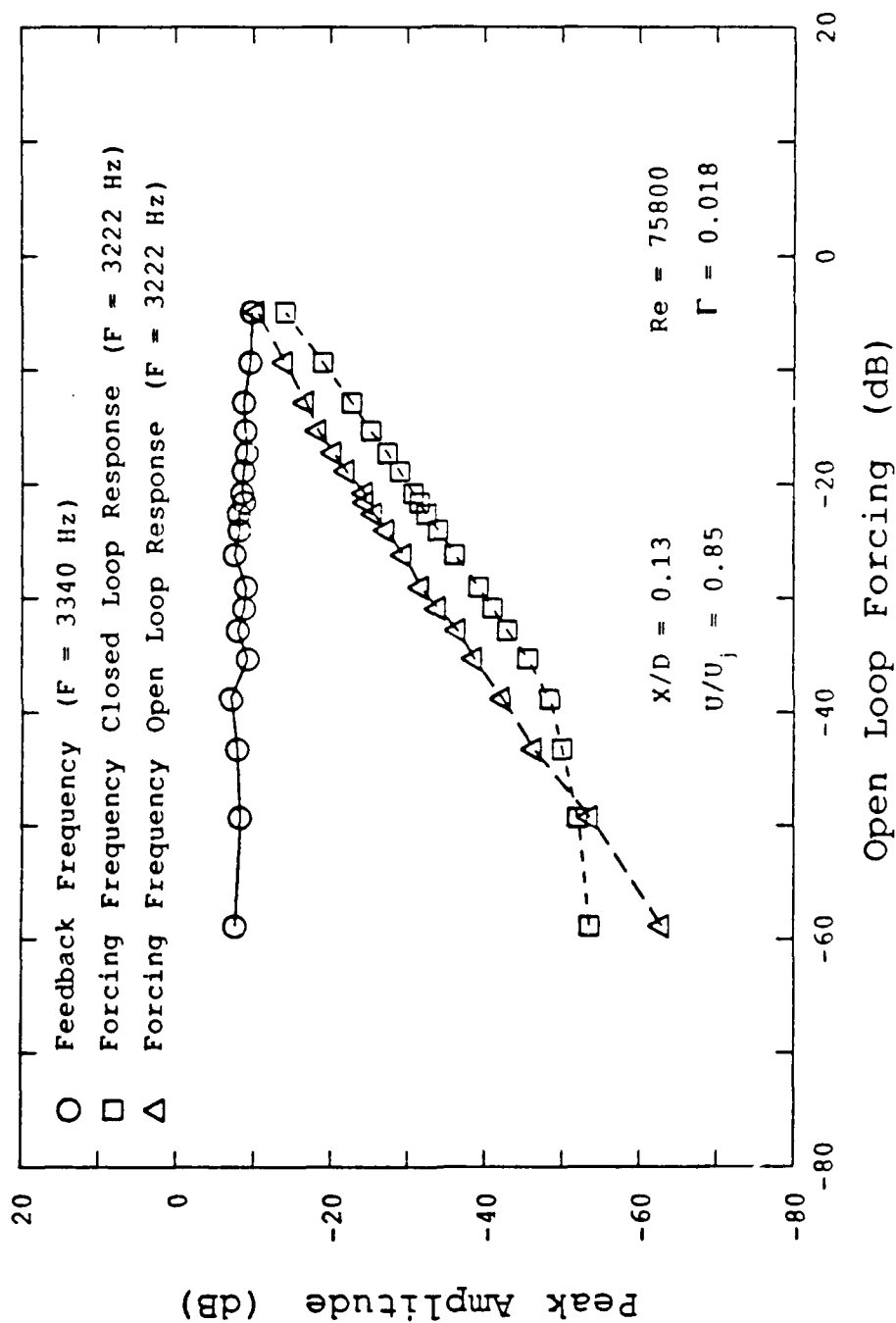


Figure 14. Variation of the Amplitude of Feedback and Forcing Frequencies as a Function of "Out of Phase" Forcing Level at $\Gamma = 0.0176$, $Re = 75,800$ and $X/D = 0.13$

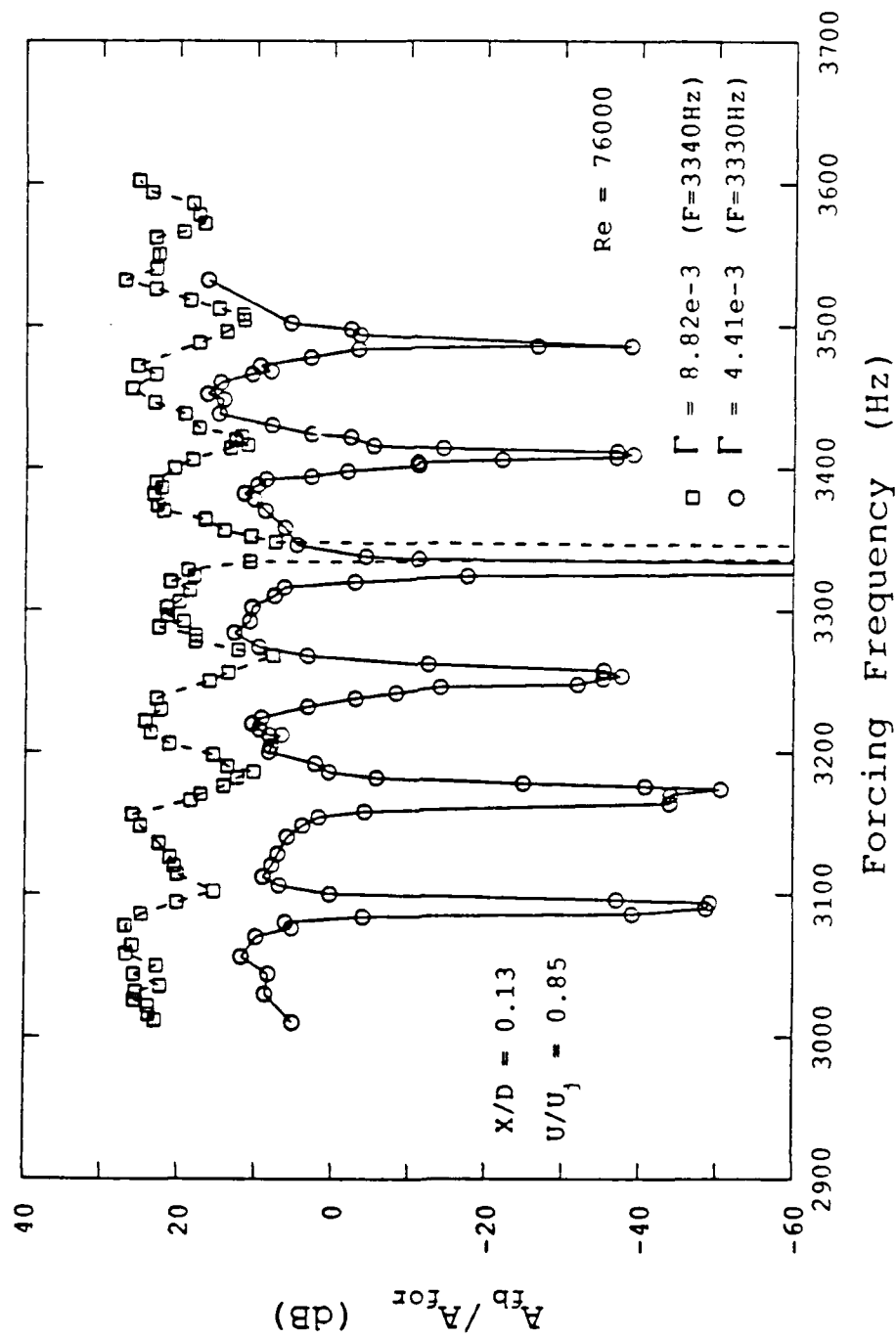


Figure 15. Variation of Relative Amplitude of Feedback and Forcing Frequencies as a Function of Forcing Frequency at $Re = 76,000$ and $X/D = 0.13$

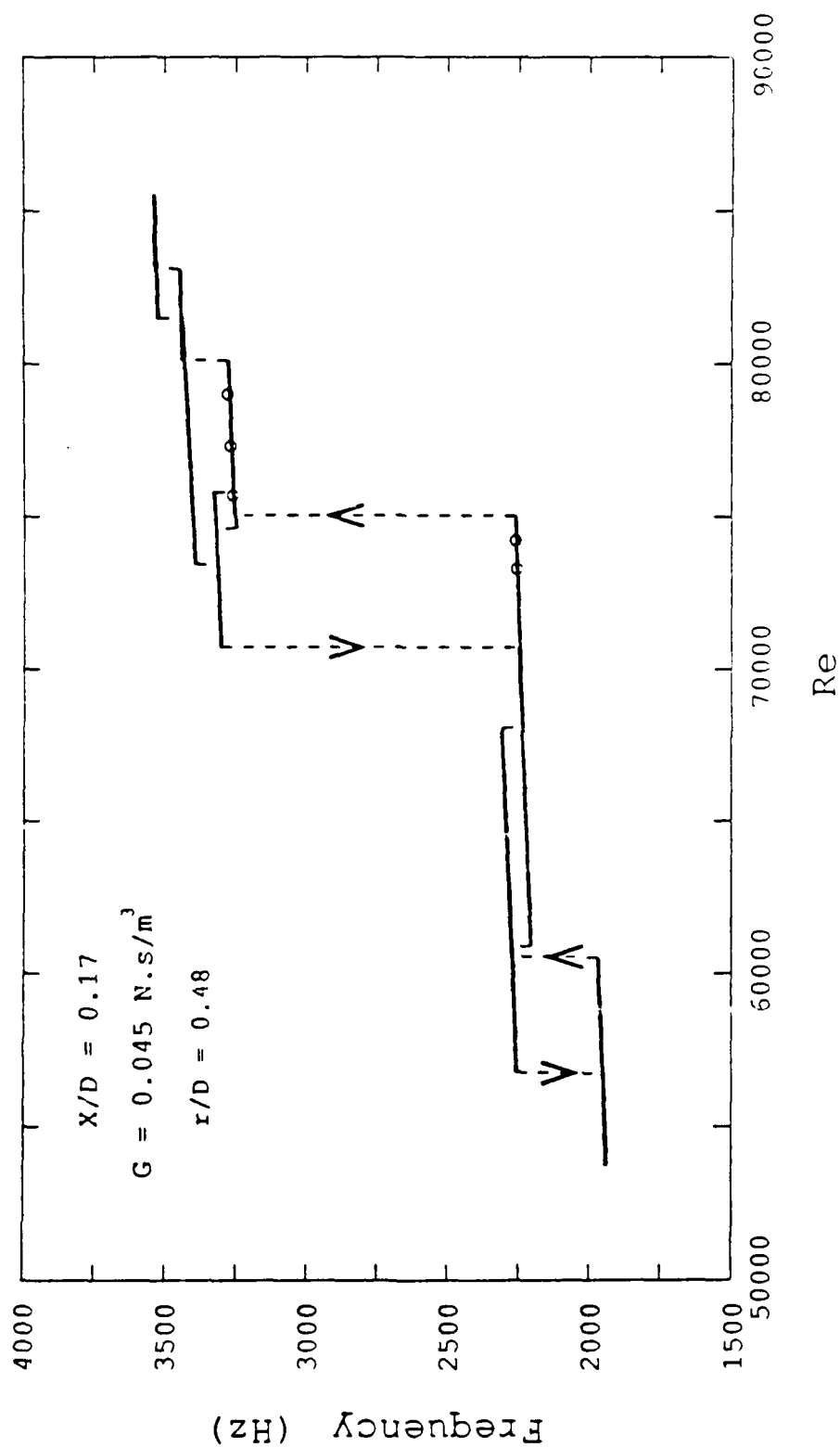


Figure 16. Eigenfrequency Hysteresis Diagram at $X/D = 0.17$ and $G = 0.045 \text{ N.s/m}^3$

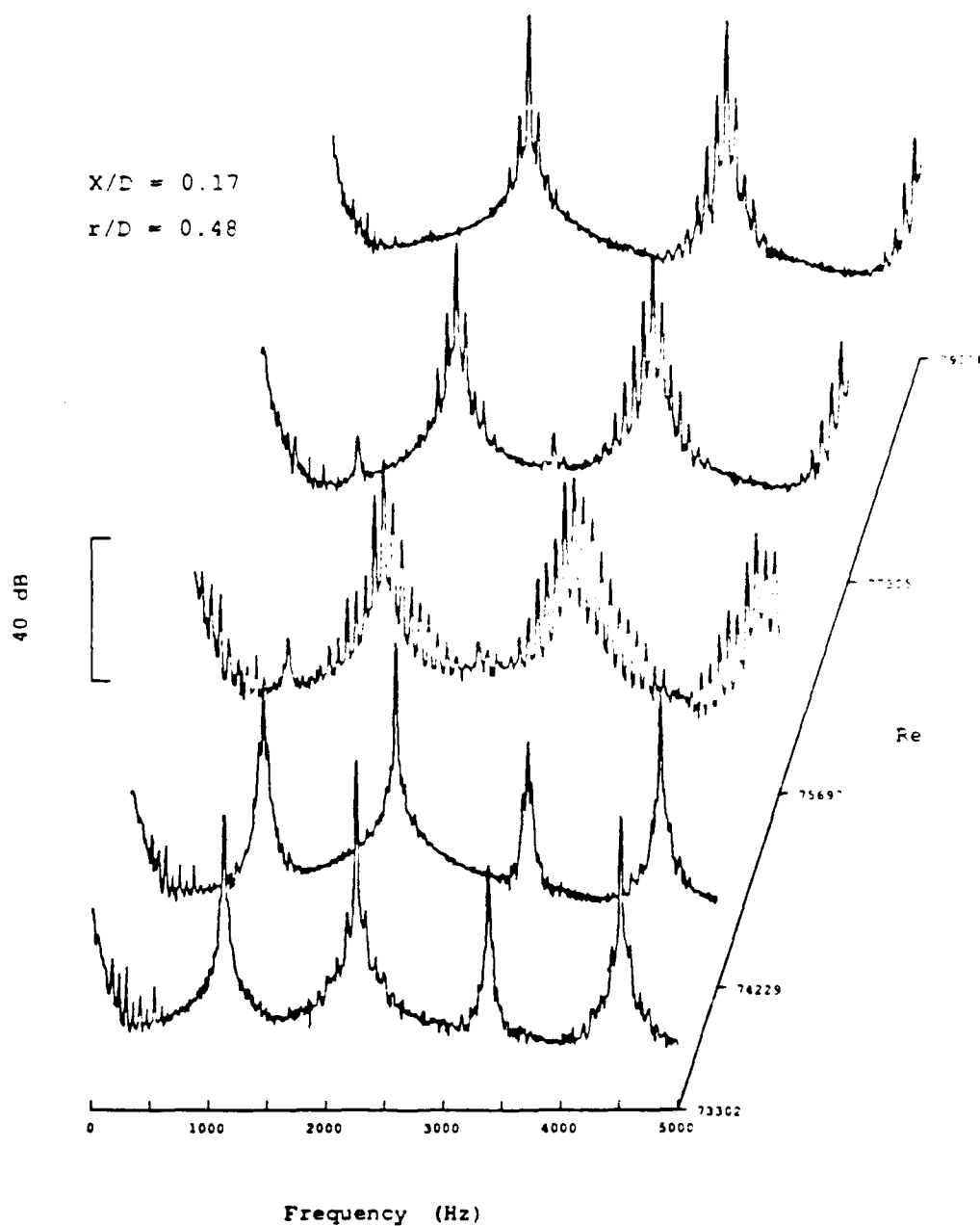


Figure 17. Spectral Variation of the Streamwise Velocity
 with Reynolds Number, in the Vicinity of
 Three-Frequency₃ Hysteresis for $X/D = 0.17$ and
 $G = 0.045 \text{ Ns/m}$

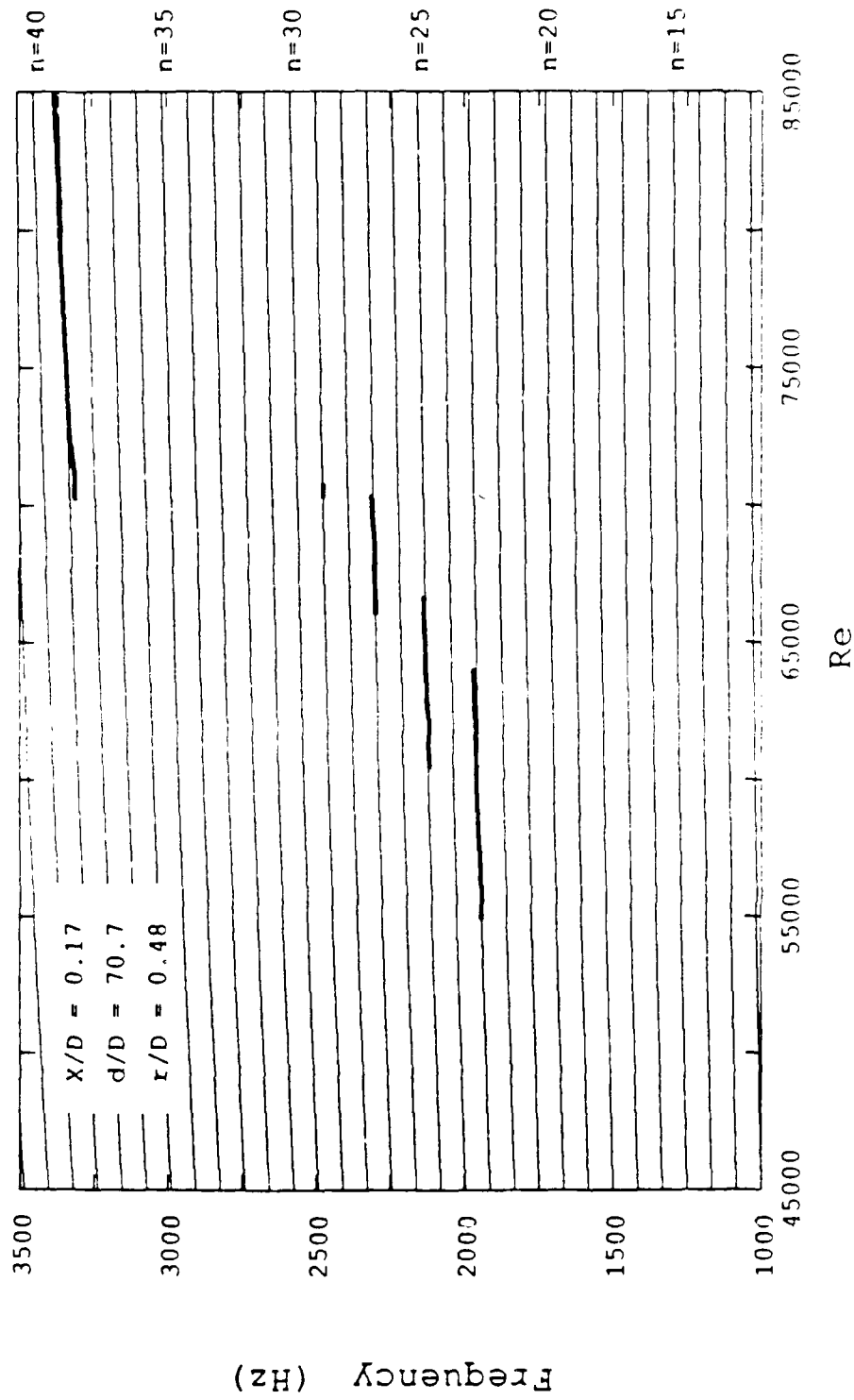


Figure 18. Comparison of Frequency Stages Observed at $G = 0.132 \text{ Ns/m}^3$, with Calculated Eigenfrequencies for $X/D = 0.17$, $d/D = 70.7$ and $\varphi = 0$

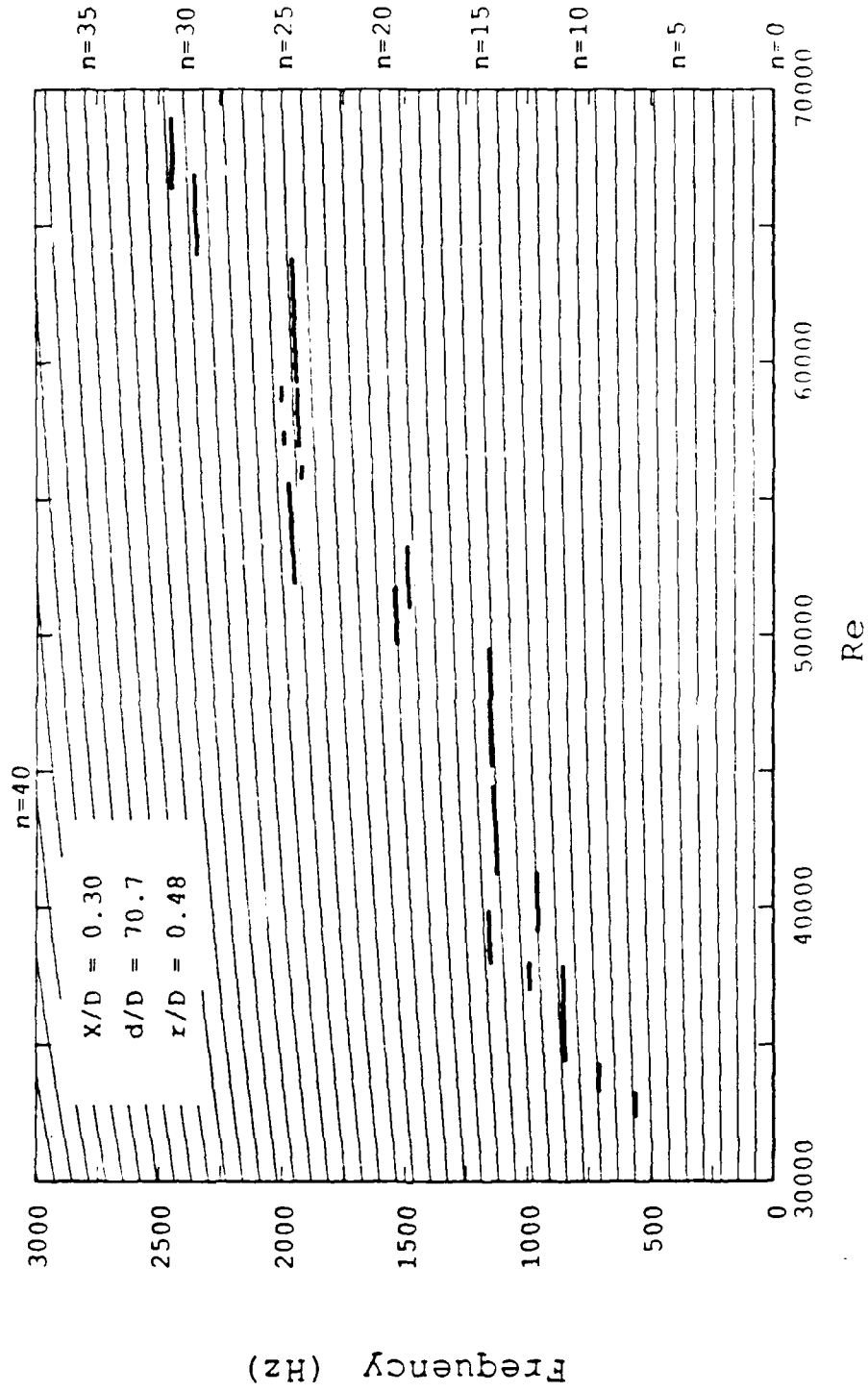


Figure 19. Comparison of Frequency Stages Observed at $G = 0.033 \text{ N}_2/\text{m}^3$, with Calculated Eigenfrequencies for $X/D = 0.30$, $d/D = 70.7$ and $\phi = 0$

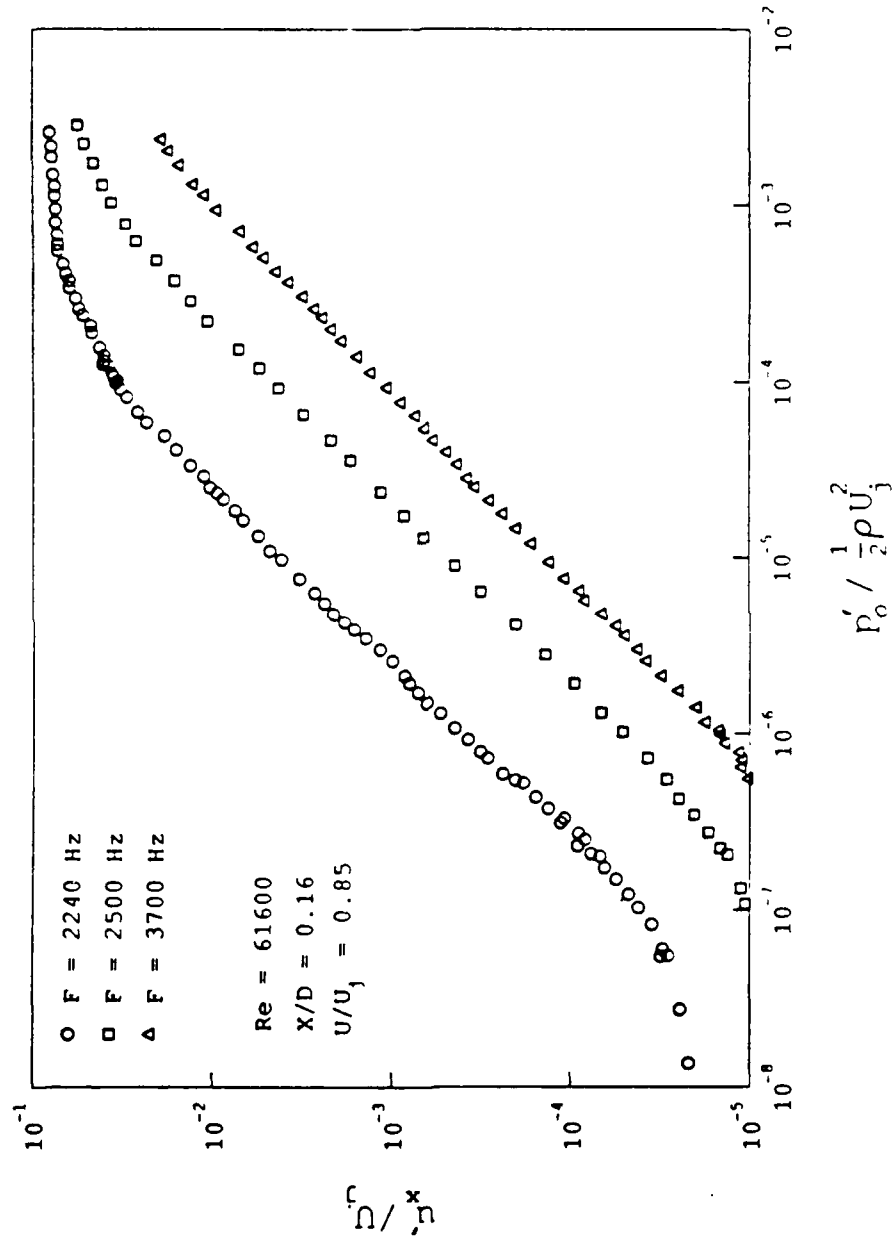


Figure 20. Open-Loop Transfer Functions Using Harmonic Forcing at 2240 Hz, 2500 Hz and 3700 Hz, for $X/D = 0.16$ and $Re = 61,600$

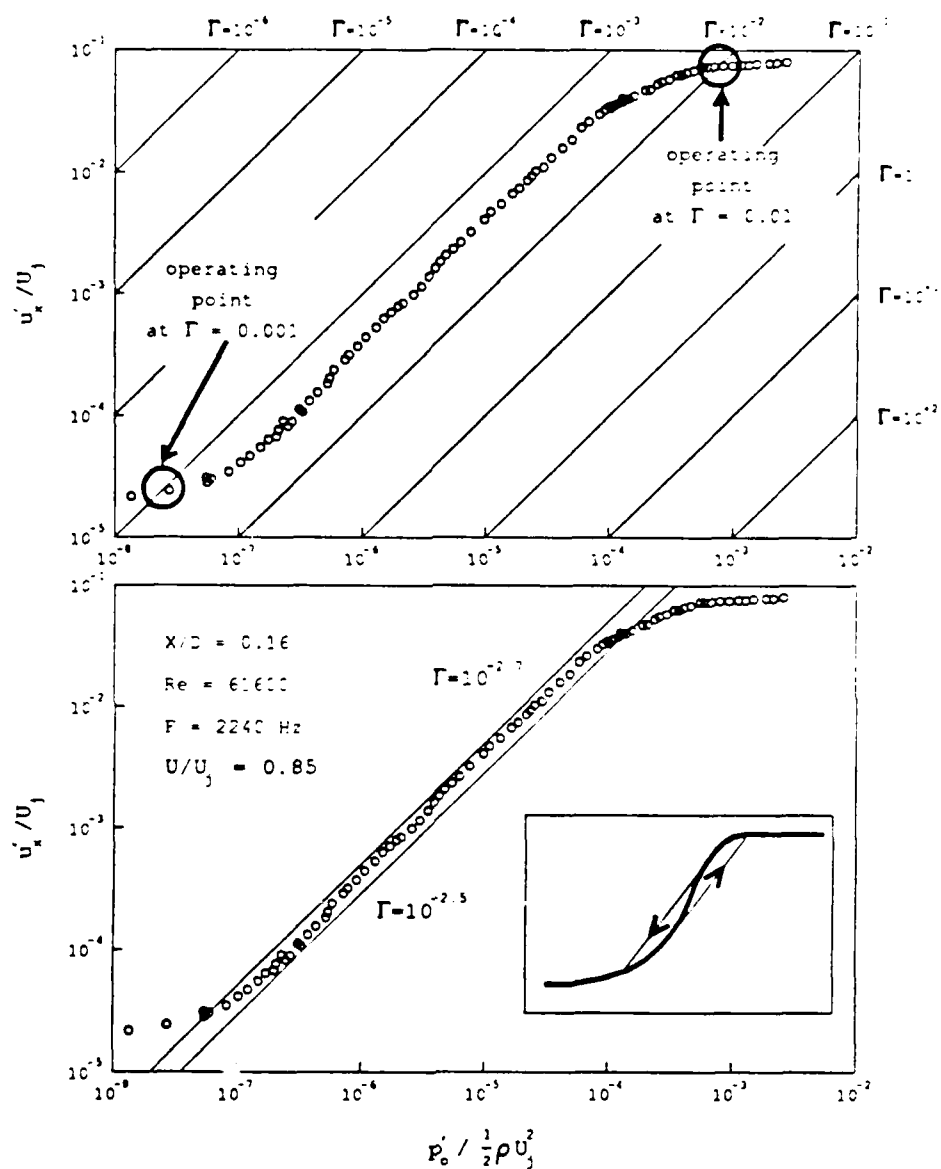


Figure 21. Open-Loop Transfer Function of the Feedback Frequency including Gain Curves for $X/D = 0.16$ and $Re = 61,600$: (a) High and Low Operating Points Far from Critical Gain, (b) Hysteresis Close to Critical Gain

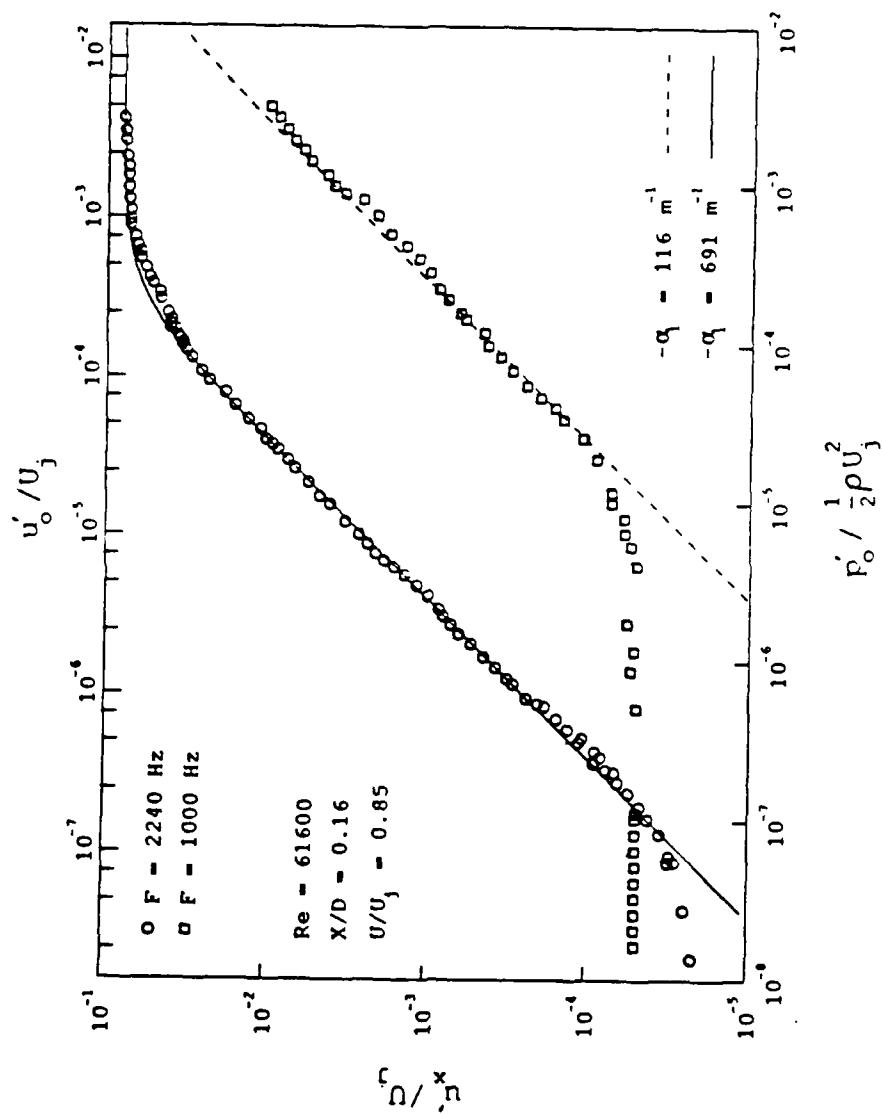


Figure 22. Open-Loop Transfer Functions and their Analytical Approximation at 2240 Hz and 1000 Hz, for $X/D = 0.16$ and $Re = 61,600$

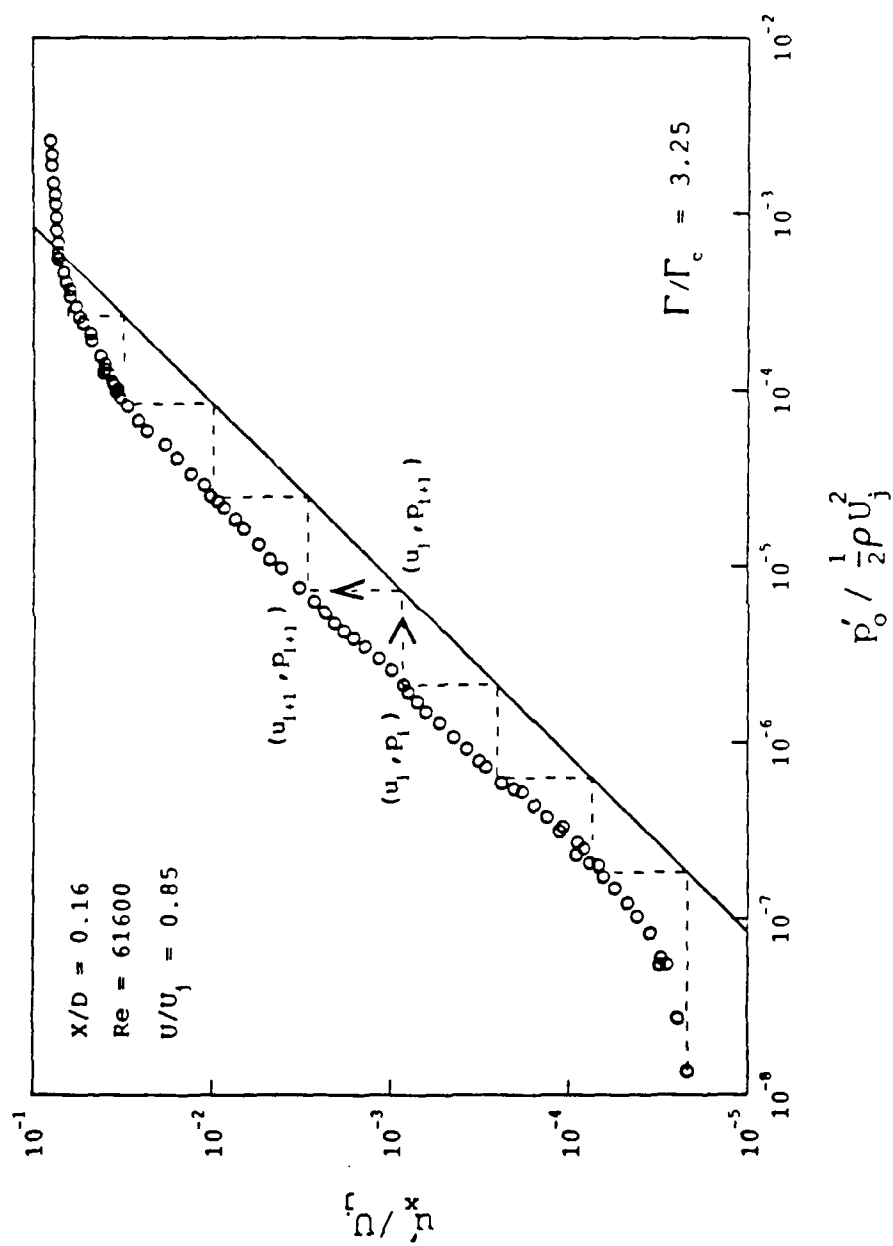


Figure 23. Illustration of Closed-Loop Temporal Evolution of the Eigenfrequency Amplitude for $X/D = 0.16$, $Re = 61,600$ and $\Gamma/\Gamma_c = 3.25$

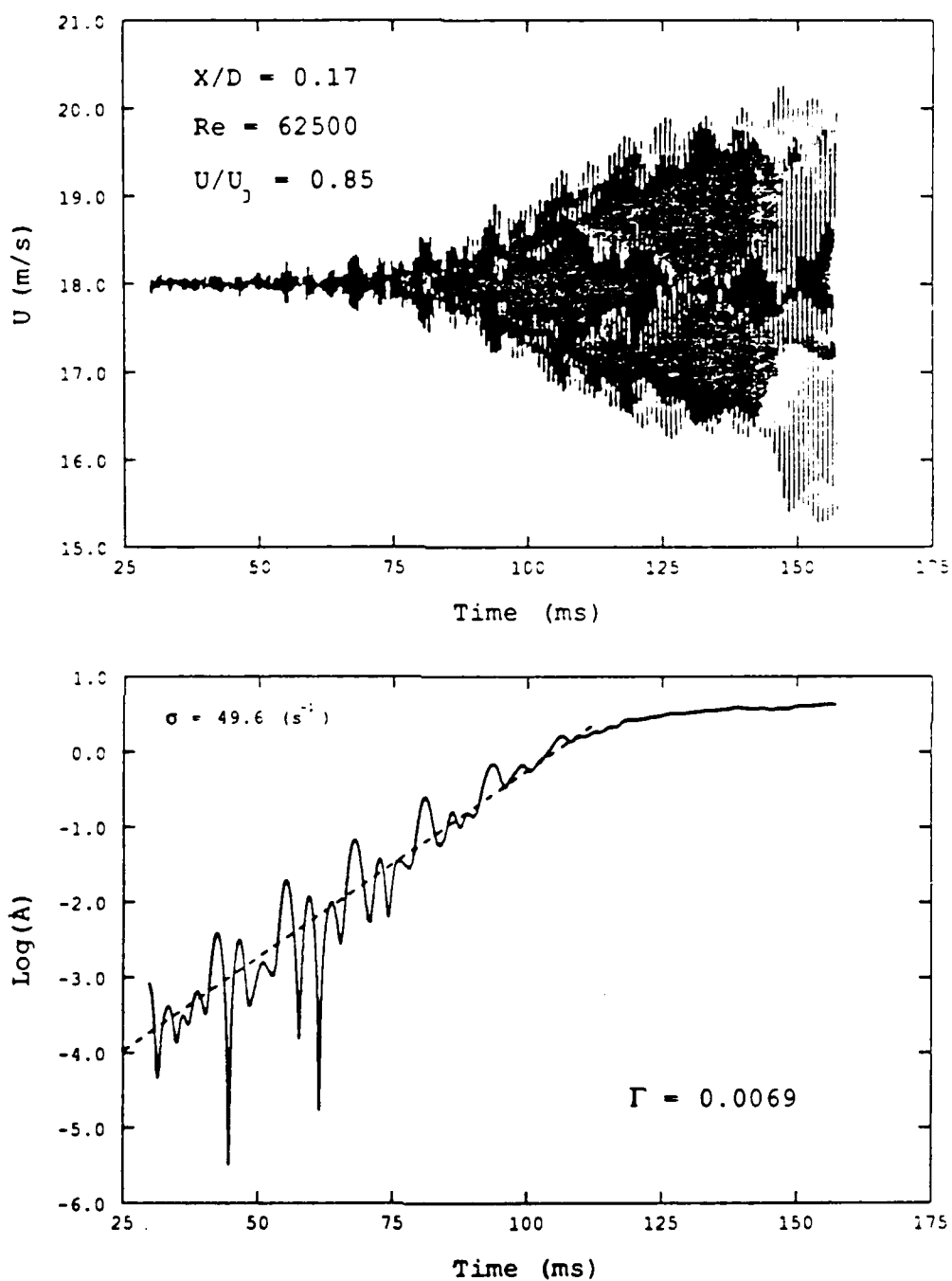


Figure 24. Time Series and Exponential Growth of the Demodulated Amplitude at $Re = 62,500$, $X/D = 0.17$, and $\Gamma = 0.007$

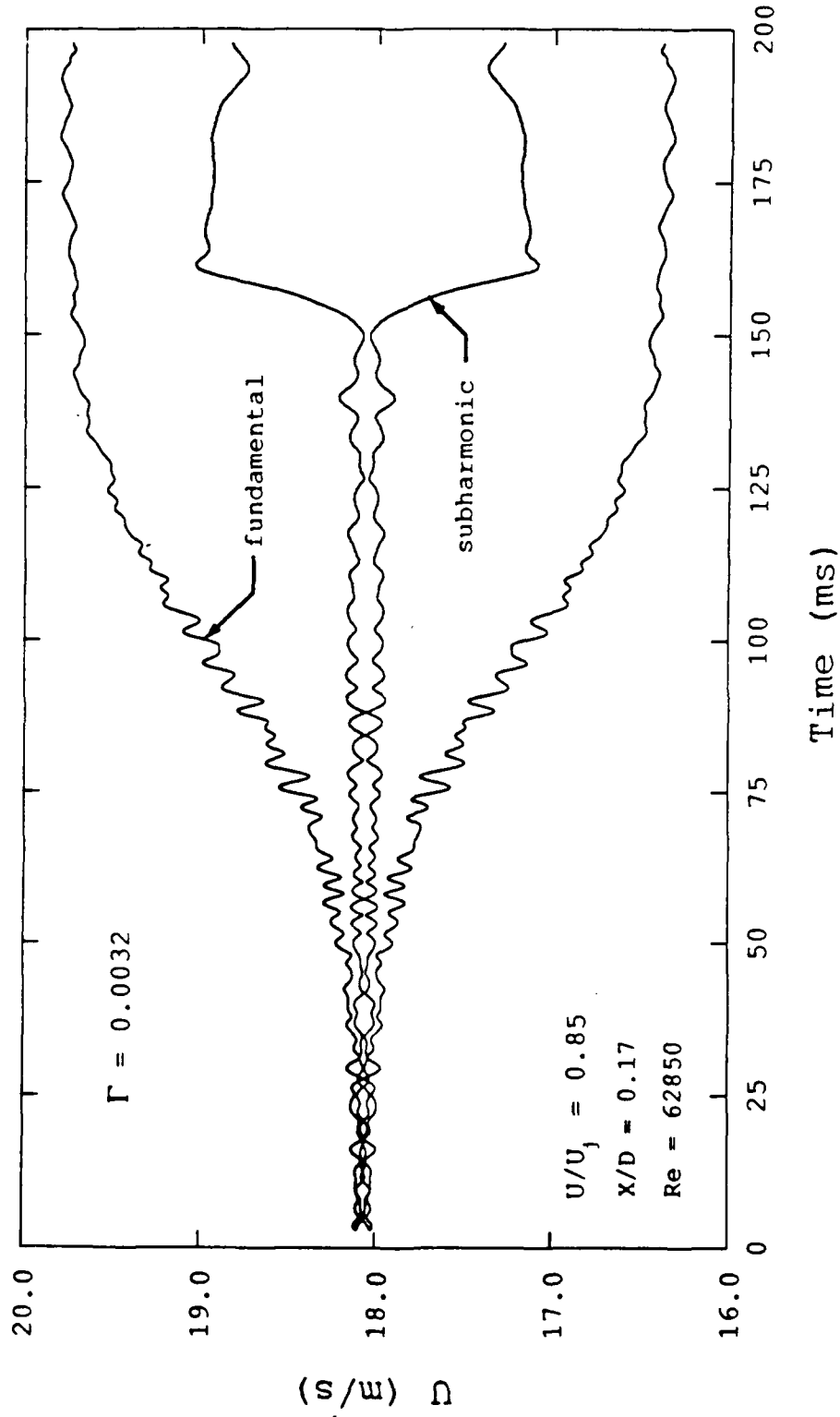


Figure 25. Comparison of Demodulated Amplitudes of Fundamental and Subharmonic Frequencies for $\Gamma = 0.0032$, $Re = 62,850$ and $X/D = 0.17$

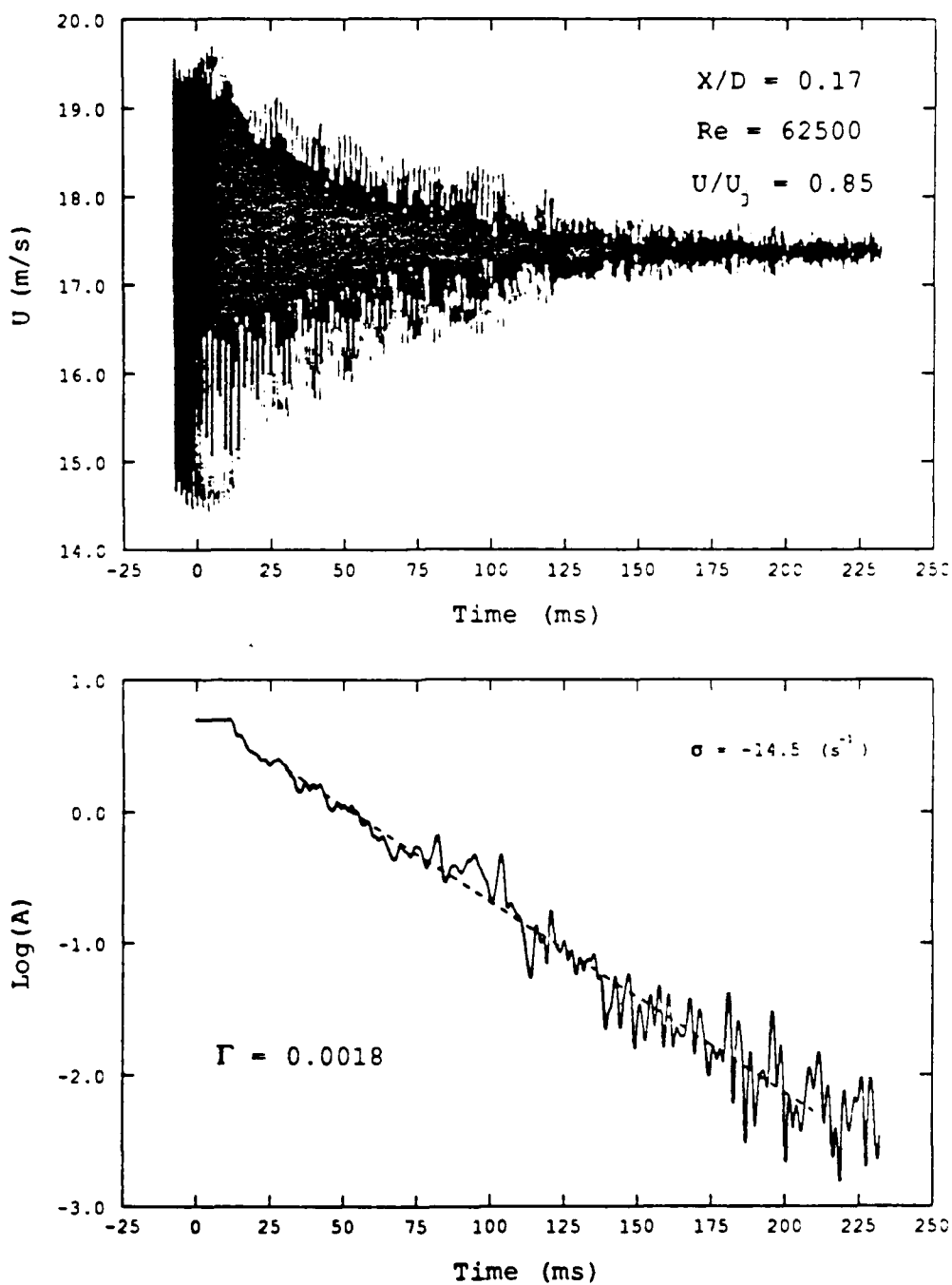


Figure 26. Time Series and Exponential Growth of the Demodulated Amplitude at $Re = 62,500$, $X/D = 0.17$, and $\Gamma = 0.002$

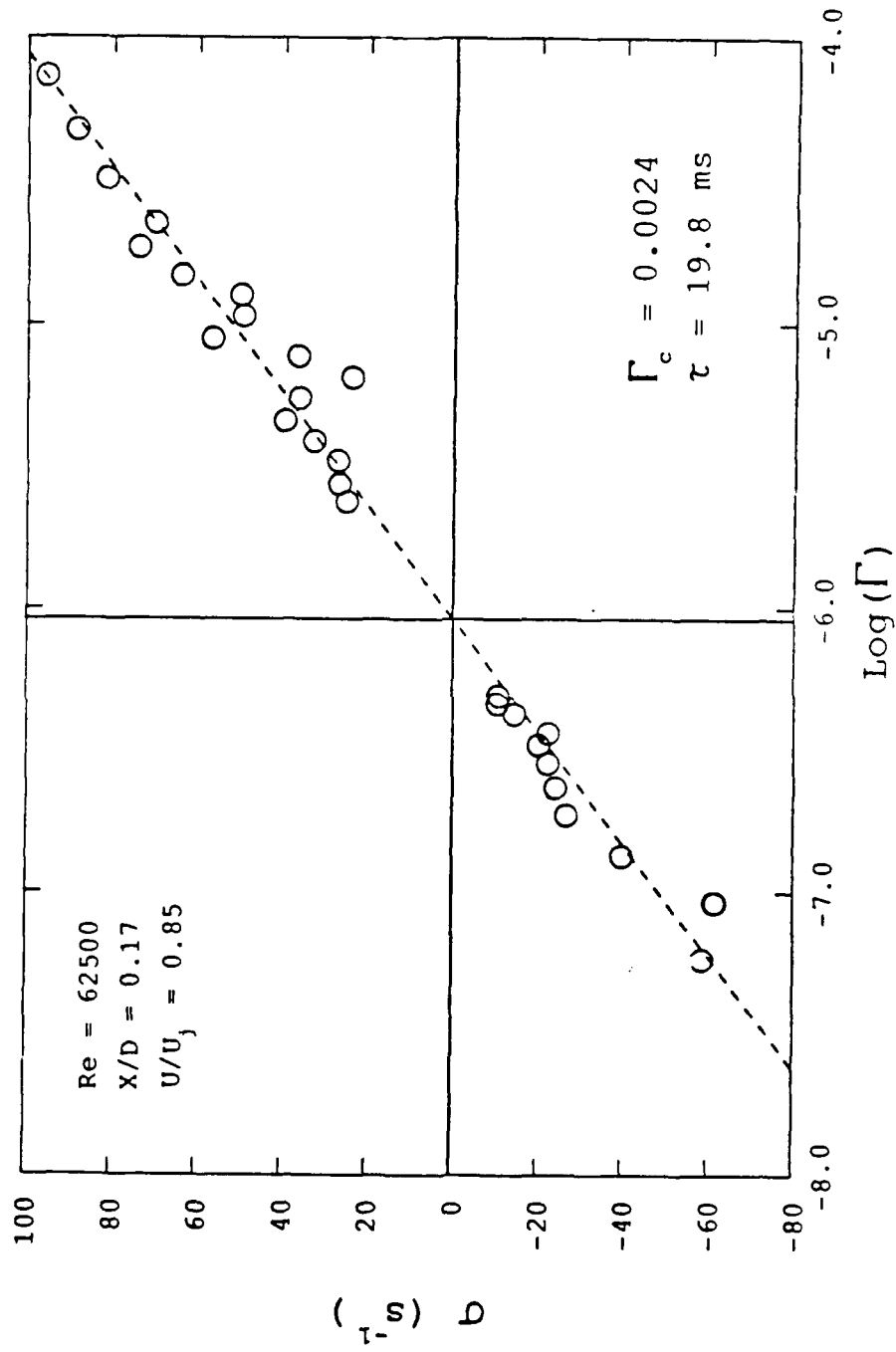


Figure 27. Scaling of Temporal Amplification Rates with Gain at $\text{Re} = 62,500$ and $X/D = 0.17$

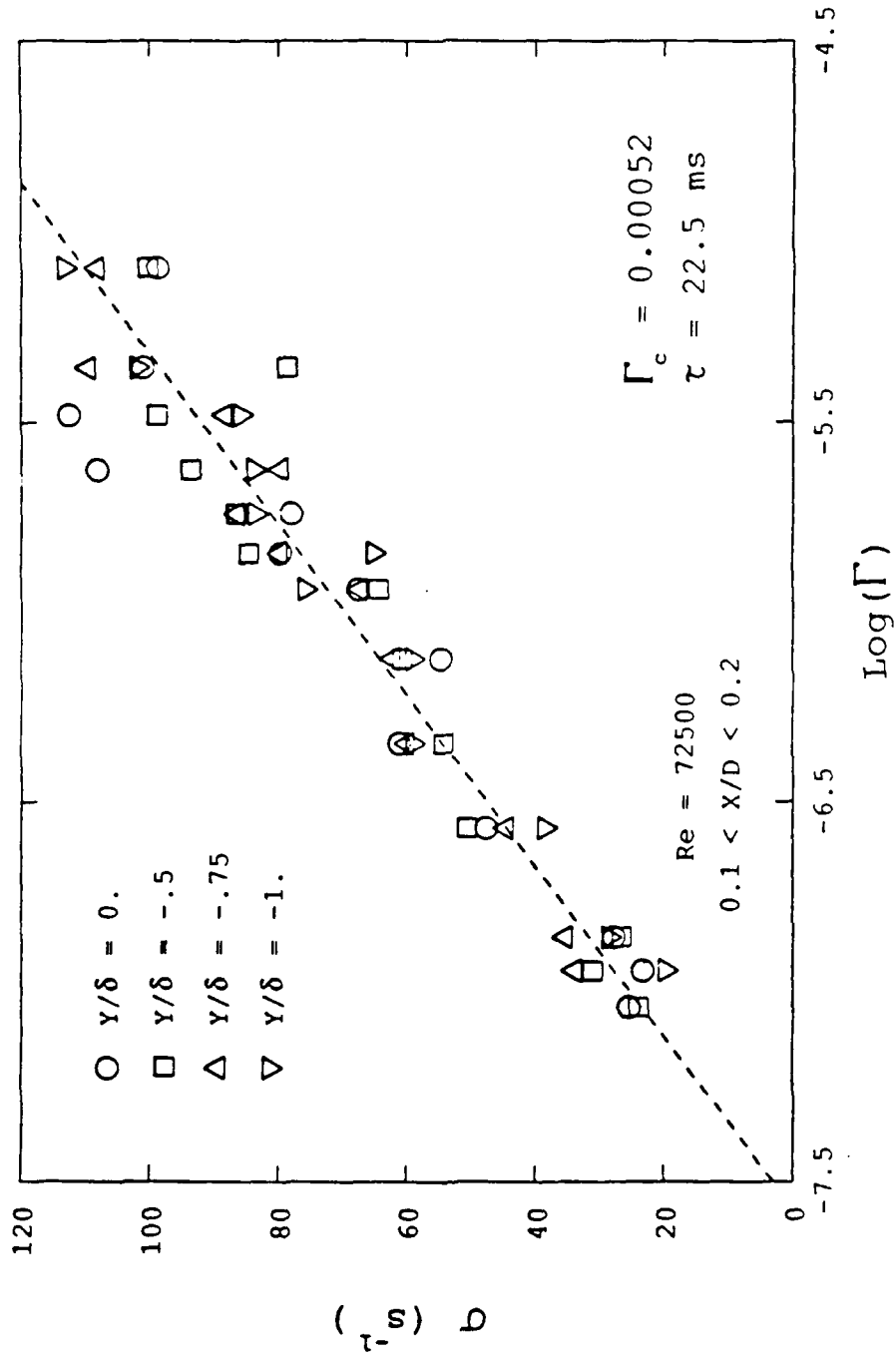


Figure 28. Scaling of Temporal Amplification Rates with Gain, for various Radial Positions at $Re = 72,500$

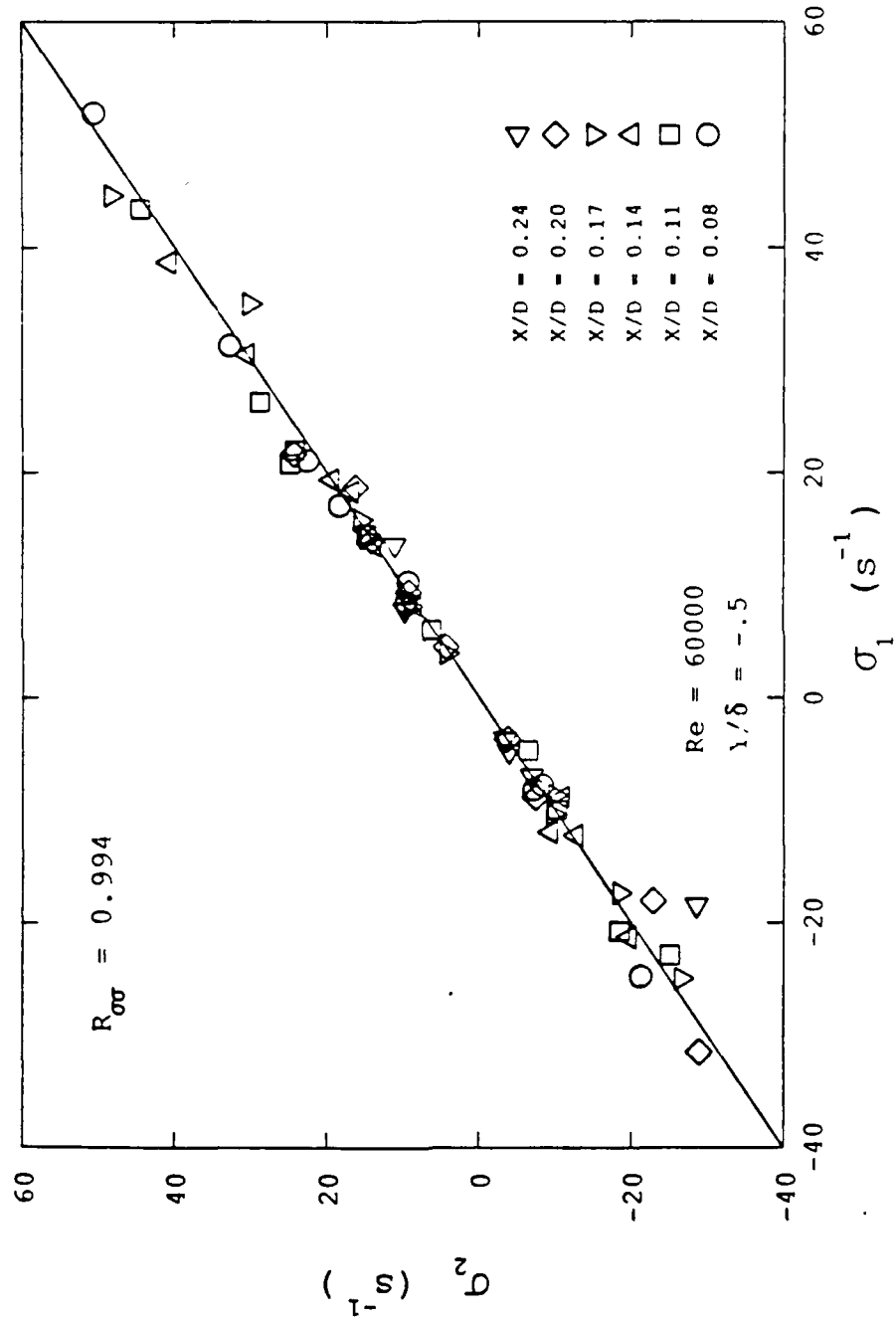


Figure 29. Correlation of Temporal Amplification Rates between Two Velocity Probes at $Re = 60,000$

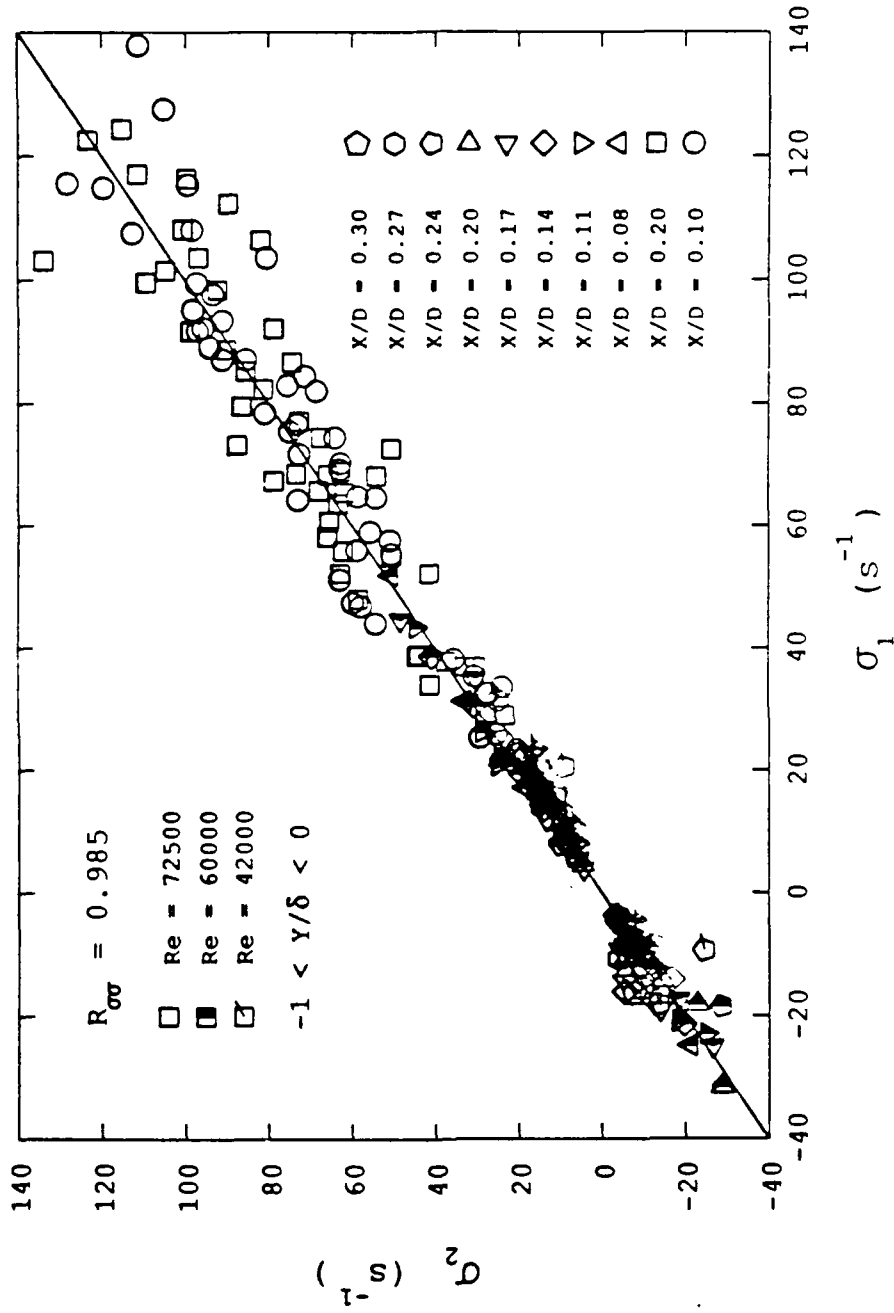


Figure 30. Correlation of Individual Temporal Amplification Rates between Two Velocity Probes at Re = 72,500, Re = 60,000 and Re = 42,000

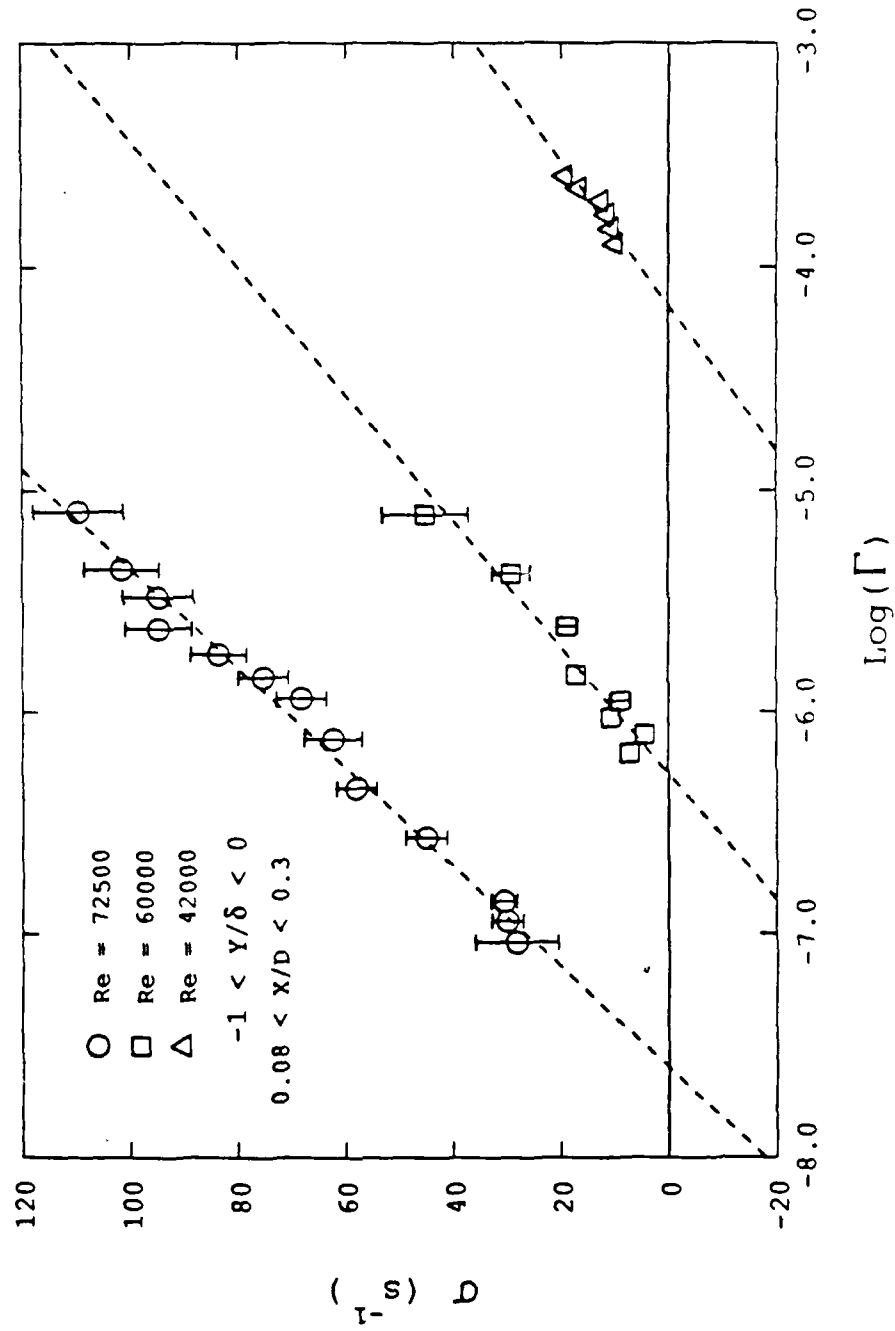


Figure 31. Scaling of Mean Temporal Amplification Rates with Gain at
 $Re = 72,500$, $Re = 60,000$ and $Re = 42,000$

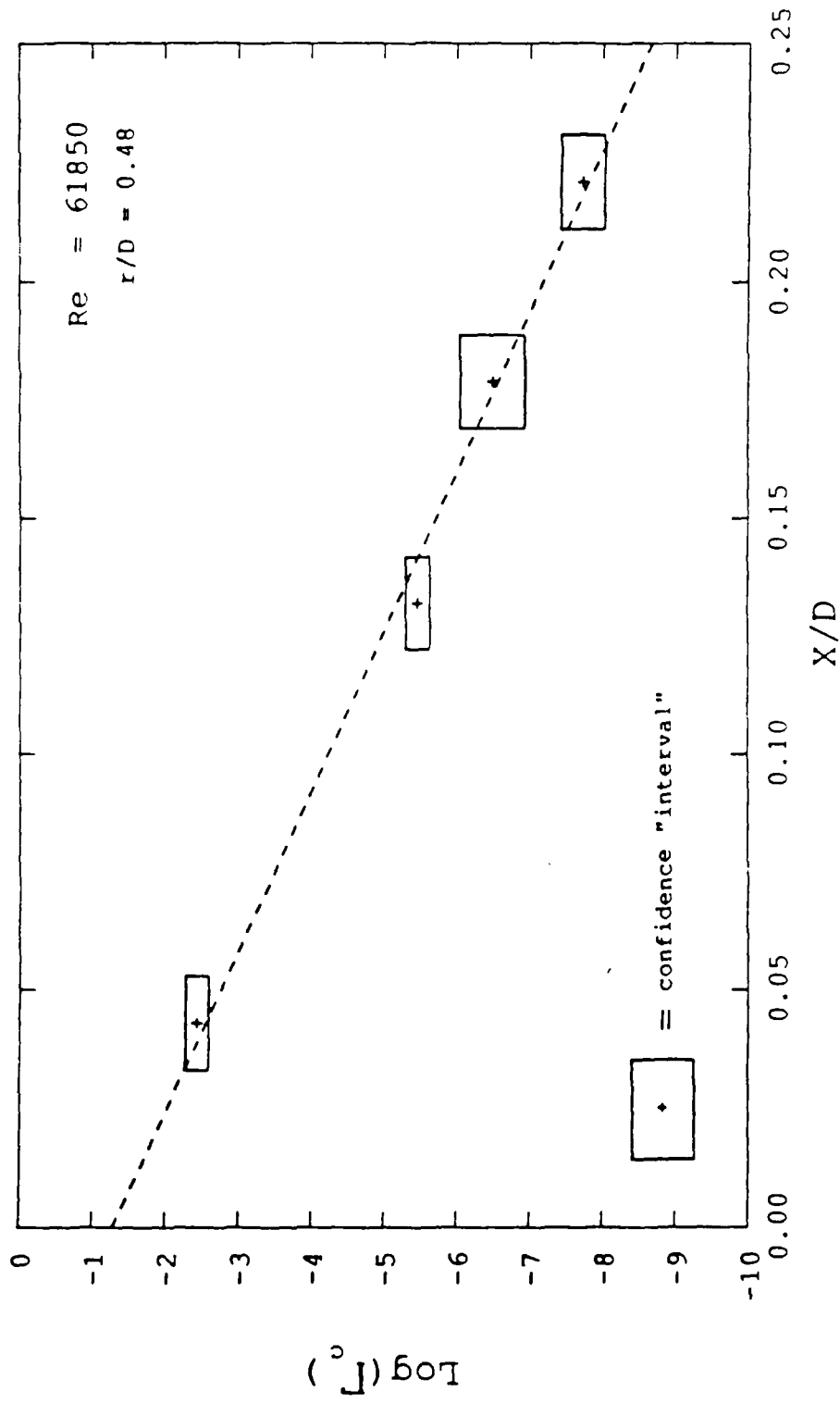


Figure 32. Variation of Critical Gain with Downstream Distance at
Re = 61,850

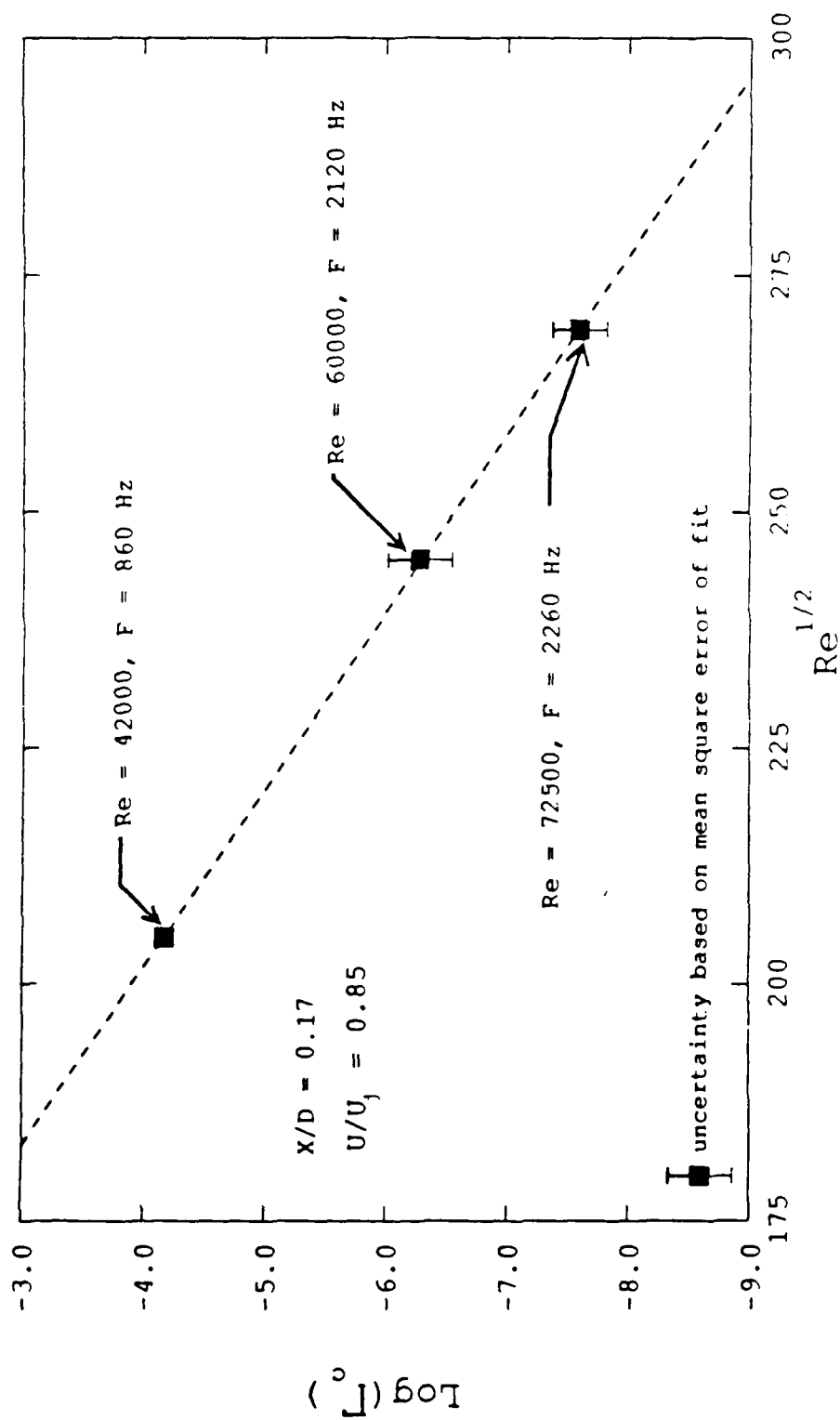


Figure 33. Variation of Critical Gain with Reynolds Number at $X/D = 0.17$

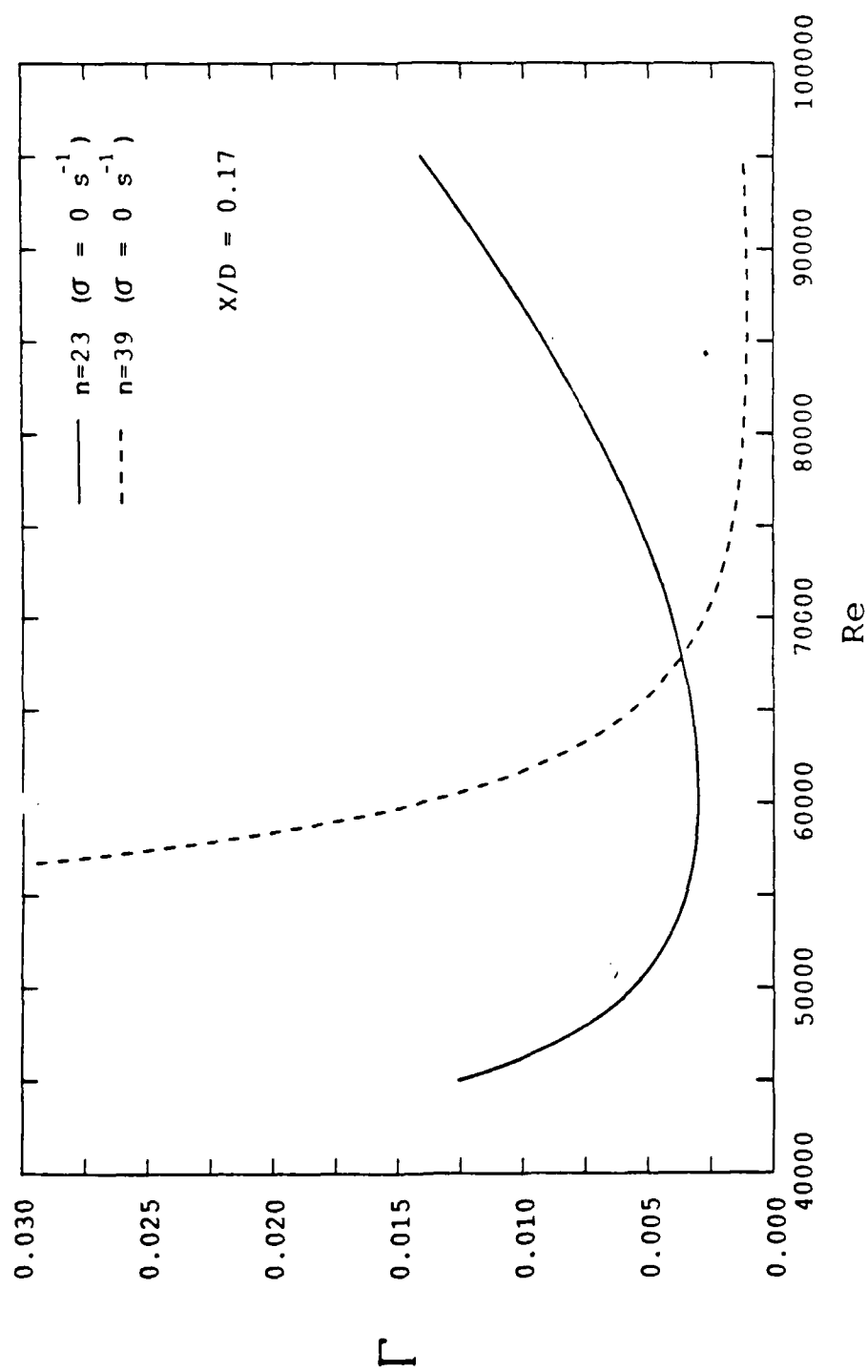


Figure 34a. Calculated Neutral Stability Curves for the Eigenfrequencies Corresponding to $n = 23$ and $n = 39$, using $X/D = 0.17$

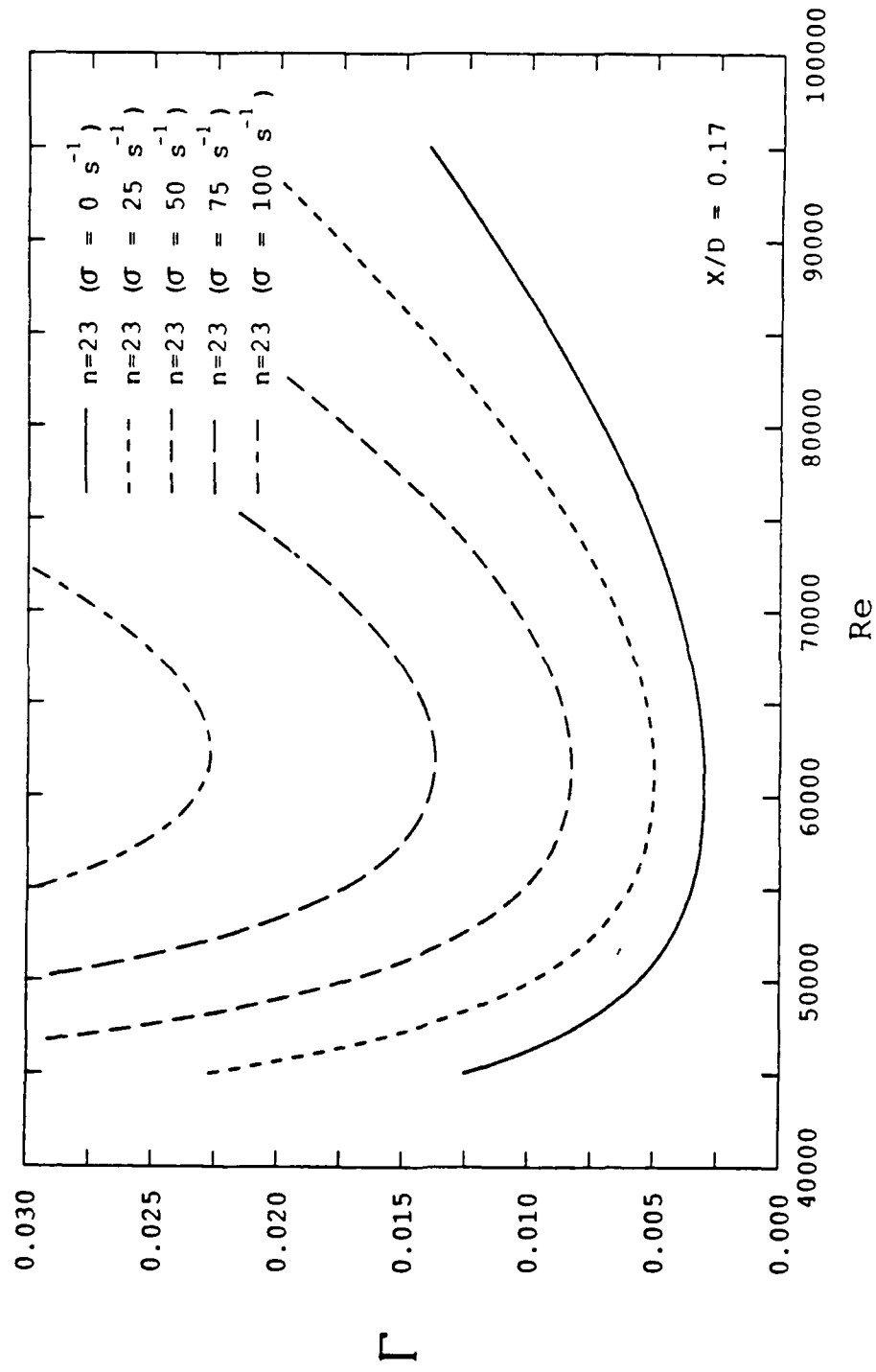


Figure 34b. Calculated Curves of Constant Temporal Amplification Rate for the Eigenfrequency Corresponding to $n = 23$, using $X/D = 0.17$

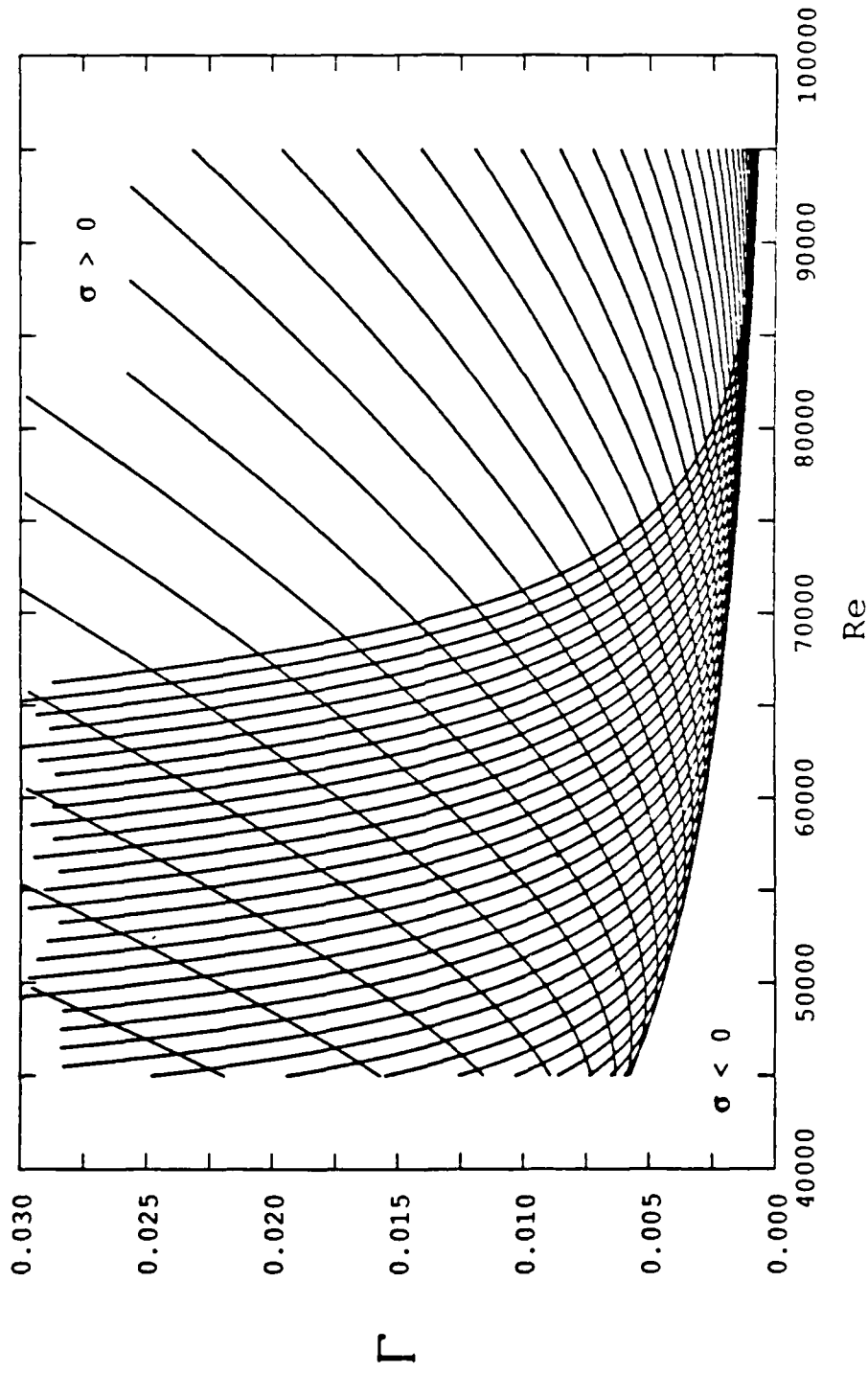


Figure 34c. Calculated Neutral Stability Curves for Eigenfrequencies
Corresponding to $n = 10$ through $n = 50$, using $X/D = 0.17$

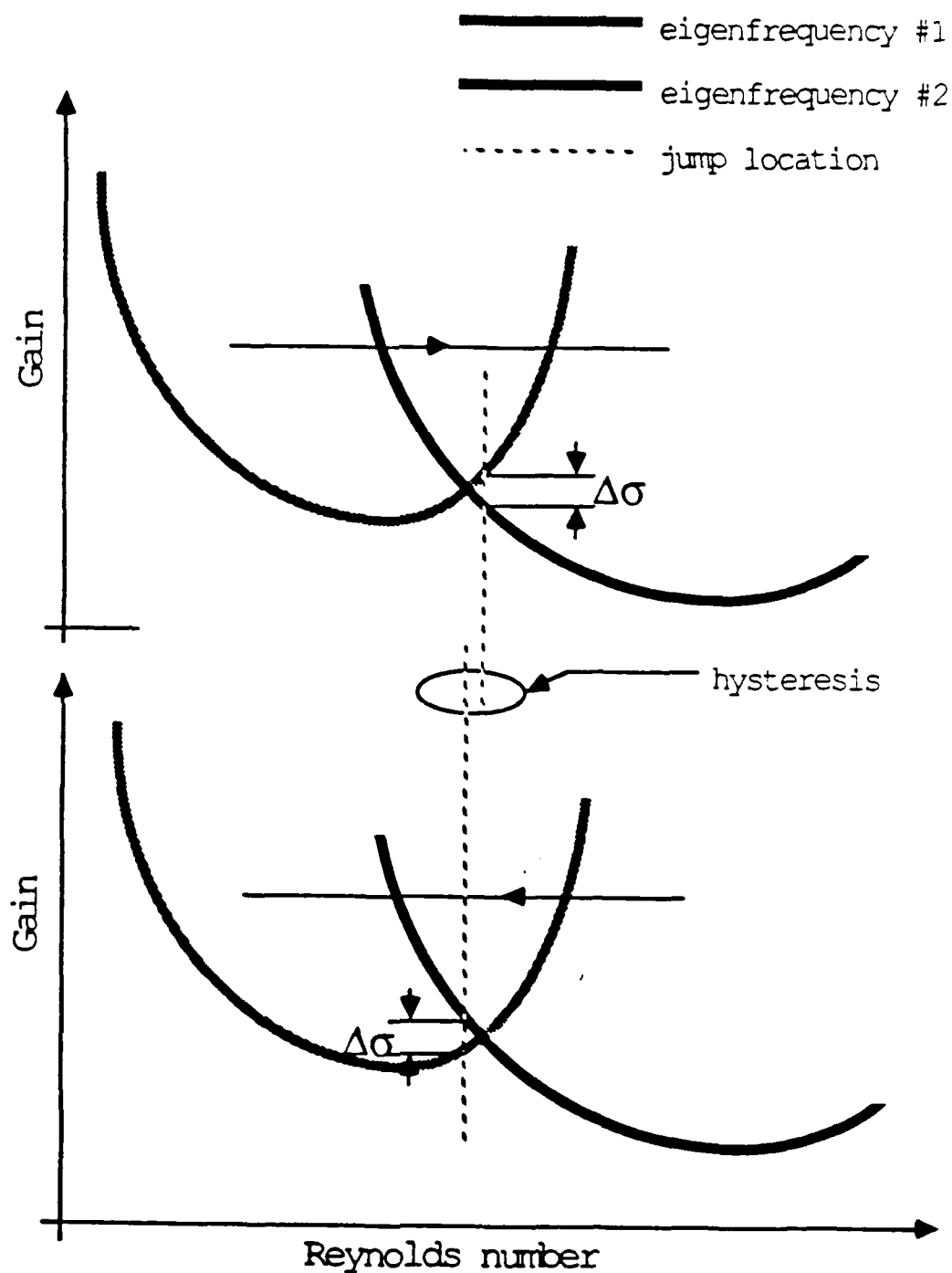


Figure 35. Schematic Illustrating the Frequency Hysteresis Phenomenon Resulting from Reynolds Number Variation at Fixed Gain

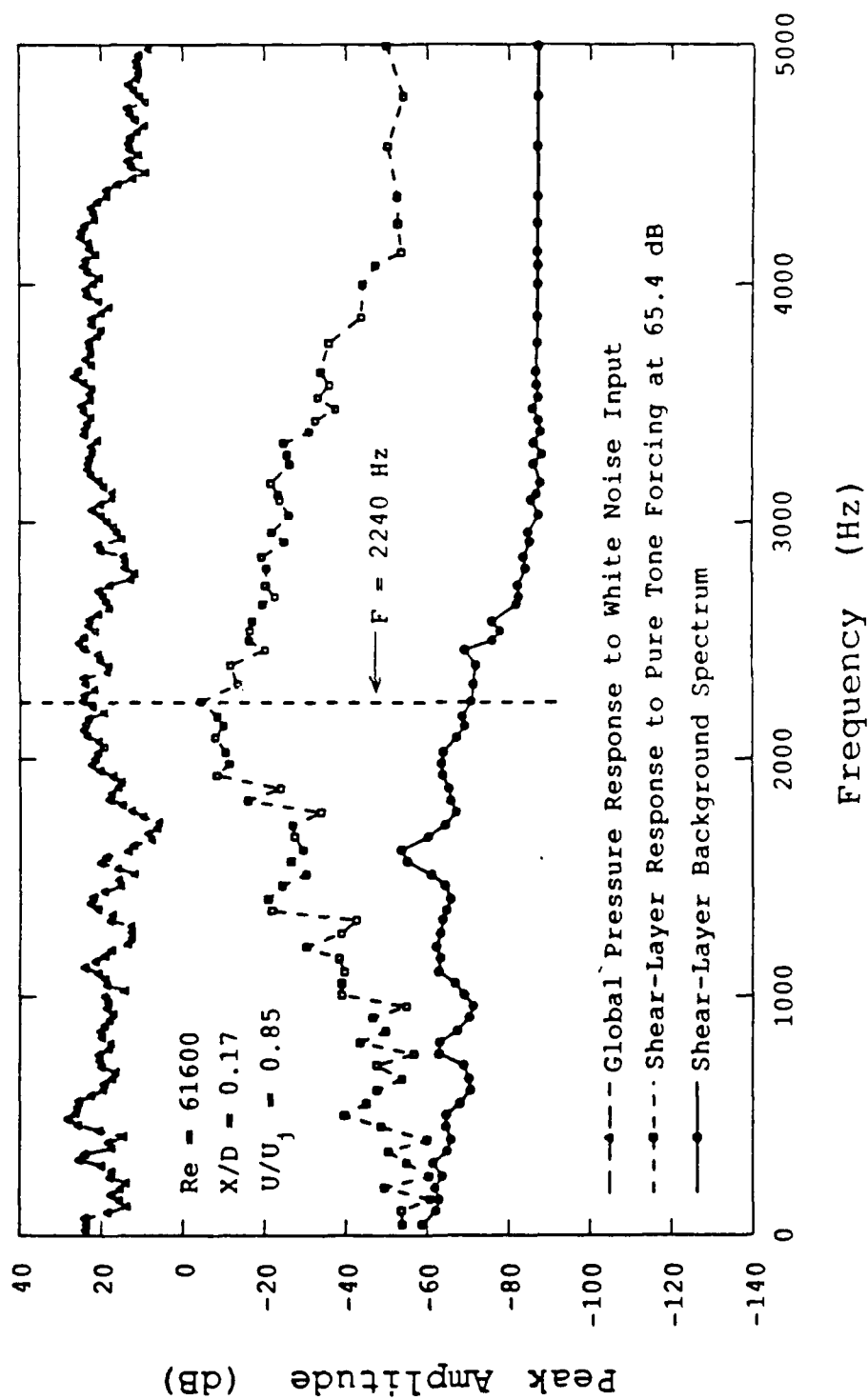


Figure 36. Effect of Acoustic Transfer Function on Shear Layer Response to Monochromatic Excitation at Re = 61,600, X/D = 0.17

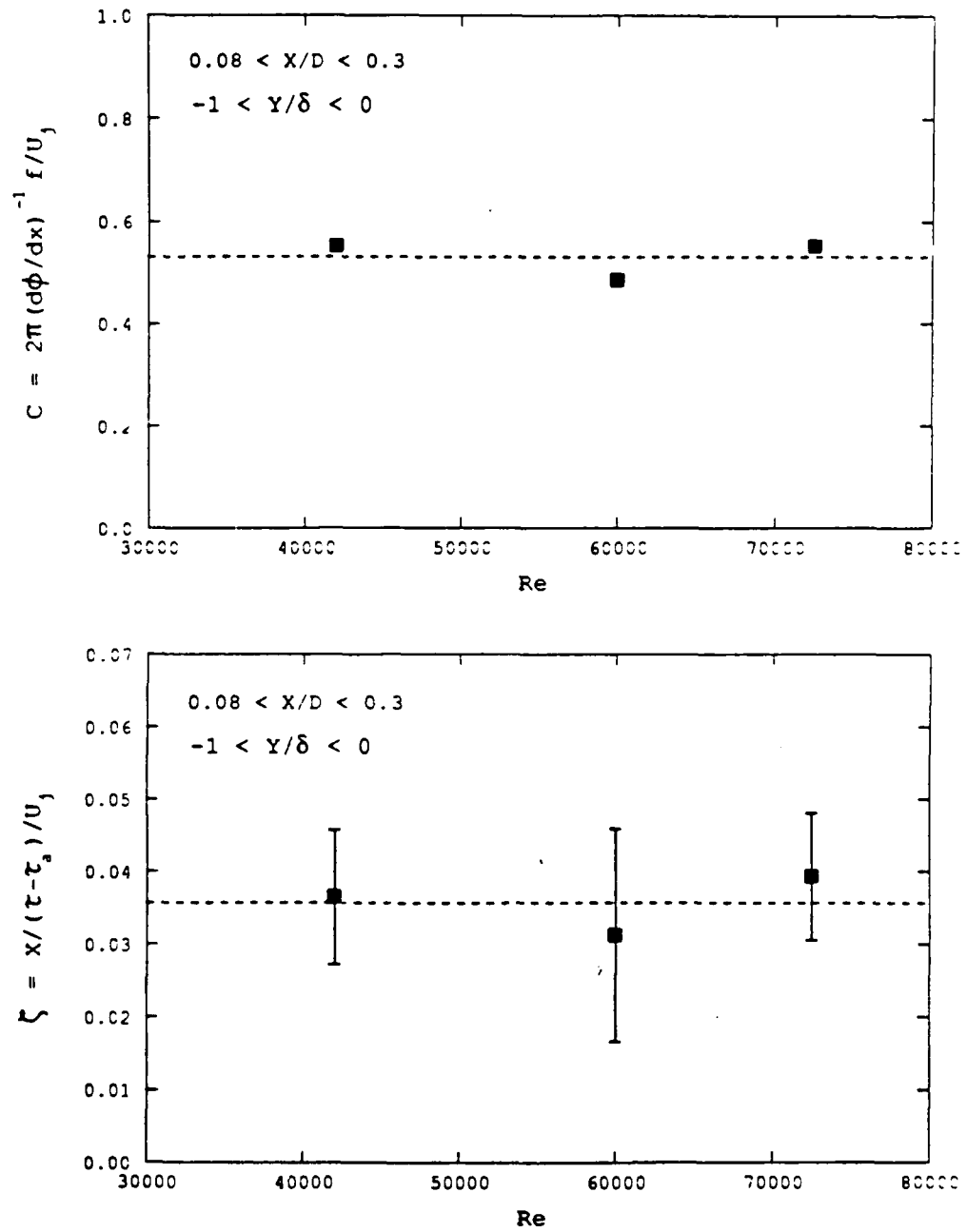


Figure 37. Comparison of Phase Speed and Envelope Convection Speed of the Feedback Frequency, as a Function of Reynolds Number

MODE SELECTION AND RESONANT PHASE LOCKING IN
UNSTABLE AXISYMMETRIC JETS

T. C. Corke, F. Shakib and H. M. Nagib
Fluid Dynamics Center
Mechanical and Aerospace Engineering Department
Illinois Institute of Technology
Chicago, Illinois

(Submitted to Journal of Fluid Mechanics, June, 1989)

Abstract

This paper presents experimental results of the nonlinear phase locking present in the resonant growth of unstable modes in the shear layer of an axisymmetric jet. The initial instability modes scale with the exiting shear layer and grow convectively with downstream distance. Because of the special condition at the exit lip of the jet, the initial growth of modes is very sensitive to local unsteady pressure fields. A part of the unsteady field is stochastic in nature. To a larger extent, the pressure field at the lip of the jet contains the imprint of the downstream developing instability modes, in particular the first unstable axisymmetric mode and its subharmonic. These are felt at the lip of the jet as a result of the energetic processes of the first vortex roll-up and vortex pairing. As a result, a resonant feedback exists which under special conditions makes the initial region of this flow in some sense absolutely unstable. The features of this process are brought out by the normalized cross-bispectrum or cross-bicoherence between the instantaneous unsteady pressure at the lip of the jet and velocity time series measured at the same azimuthal position for different downstream locations. These give a measure of the nonlinear phase locking between the principle modes and their sum and difference modes. Analysis of these show a perfect nonlinear phase locking at the

fundamental axisymmetric and subharmonic frequencies between the pressure field at the lip and the velocity field at the downstream locations corresponding to the energy saturations of the fundamental and subharmonic modes. This resonance process can be suppressed or enhanced by low amplitude axisymmetric mode forcing at the natural preferred frequency or slightly detuned cases. Contrasted with this is the behavior of the fundamental $m = \pm 1$ helical mode. This mode was found to have the same spatial growth rate as the axisymmetric mode and a streamwise frequency approximately 20 percent higher, in agreement with theoretical predictions. However, short-time spectral estimates showed that these two fundamental modes do not exist at the same time or space. This suggests that each is a basin of attraction which suppresses the existence of the other. The apparent nondeterministic switching observed between these modes is likely the result of the response of the jet to stochastic input of axisymmetric or nonaxisymmetric disturbances. This scenario may lead to a low dimensional temporal model based on the interaction between these two modes which captures most of the early random nature seen in our experiments.

I. Axisymmetric Jet

I.1 Introduction

For many years investigations have been conducted to understand the flow processes which occur in jets. One practical purpose of these was to determine the relationship between the observed characteristic velocity fluctuations in the jet and the generation of measured far-field acoustic disturbances associated with these flows. Previous

investigations in naturally and artificially excited jets have determined the importance of two instability length scales: one associated with the initial shear layer thickness at the exit of the nozzle, and the other associated with the jet diameter which governs the shape of the mean velocity profile at the end of the potential core. The instability modes in the first region develop through continuous and gradual frequency and phase adjustments to produce a smooth merging with the second region. This process makes this problem fundamentally interesting, and for that reason it has received a great deal of attention. A more recent excellent review of free-shear flows of the type discussed here was given by Ho and Huerre (1984). As a result, only a short review of past related work is presented here in order to help to focus on the singular characteristic of resonant axisymmetric mode phase locking that can exist in these flows.

1.2 Background

The shear layer development just past the exit edge of a jet is initially dominated by a linear instability mechanism. The vorticity distribution is inviscidly unstable to small perturbations through a Kelvin-Helmholtz instability mechanism. These instability waves grow exponentially with streamwise distance, and when finite amplitudes are reached, roll up into discrete vortices.

In experiments in low disturbance axisymmetric jet flows, a majority of emphasis has been placed on the growth of axisymmetric disturbances in the close vicinity of the nozzle exit. The analysis of Michalke (1971) however, pointed out that the first helical mode has amplification characteristics in this region which are nearly identical to those of the fundamental axisymmetric mode. His analysis further

suggests that as the shear layer thickens or grows, the amplification of the helical mode becomes more dominant over the axisymmetric mode. Mattingly and Chang (1974) performed similar analysis with a different prescribed mean velocity distribution that showed that the amplification of the axisymmetric mode was only approximately 12 percent larger than that for the helical mode, and that the streamwise frequency of the most amplified helical disturbance in that case was approximately 20 percent higher than that of the most amplified axisymmetric mode. Drubka (1981) experimentally verified these results from cross-spectral and azimuthal phase measurements between velocity fluctuations in the shear layer and pressure fluctuations at the lip of a very low disturbance axisymmetric jet flow.

The fact that the growth of the subharmonic of the initial axisymmetric mode leads to the downstream pairing of neighboring vortices is now well established. In a two-dimensional mixing layer, Winant and Browand (1974) concluded that the successive pairing of neighboring vortices was a primary mechanism for the streamwise growth of the shear layer. In a more recent experiment, Ho and Huang (1982) documented for a harmonically forced mixing layer that the first few pairings were accompanied by an approximate doubling of the shear layer momentum thickness. This observation points to the potential importance of this fundamental process in jet mixing and spreading.

Focusing on the growth of subharmonic disturbances, Kelly (1967), in a linear temporal formulation, determined that when the amplitude of a fundamental instability wave reaches a finite value in the presence of a subharmonic wave, another instability mechanism based on a subharmonic resonance can arise. This mechanism requires that both waves have the

same phase speed. This subharmonic resonance is weakly nonlinear and described by the Mathieu equation.

As the initially linear instability grows in amplitude toward a finite value, the shear layer begins to roll up to form discrete vortices. At this point the problem is fully nonlinear and is therefore past the range of validity of the linear model, such as for Kelly (1967). Pierrhumbert (1980) examined the effect of this nonlinearity on the subharmonic resonance. His results predicted that the nonlinearity associated with the rolled-up vortices enhances the growth of the subharmonic instability. The growth of the subharmonic mode is important in the sense of describing the mechanism for the pairing of ring vortices observed in an early experiment by Wille (1963).

Bruun (1977), Peterson (1978), Hussain and Clark (1981) and Laufer and Zhang (1983), among others, documented the effect of pairing on the growth of axisymmetric jets. Acton (1980) modeled discrete vortex ring elements and computationally followed the development of the instability wave into eddies, with and without forcing. Reasonable agreement was observed between this axisymmetric model and the experiments; thereby drawing the speculation that the large-scale structures in the jet are essentially axisymmetric. Ho (1981) based his subharmonic evolution model on this assumption.

External harmonic forcing of the jet has been used by many investigators to organize the streamwise location where the shear layer first rolls up as well as the pairing location. This forcing has invariably been large amplitude and axisymmetric. Kibens (1979) showed that when the initial instability frequency is related to the final "preferred" jet instability frequency by an integer power of two, the

jet becomes organized, vortex pairings were localized and the development of the initial shear layer frequency towards the final preferred jet frequency occurs through an integer number of pairings. Although this was first observed in an externally excited jet, Drubka (1981) documented the same phenomenon for his "low" disturbance unexcited condition at a Reynolds number of 42,000. At this condition, Drubka (1981) also noted the greatest amount of pressure fluctuations at the lip at a frequency corresponding to the subharmonic of the axisymmetric mode. From these results, he suggested a natural self-excitation for this organized pairing state.

Although the exact mechanism of pairing is not completely understood, a number of physical observations associated with this process have been made. When the initial axisymmetric subharmonic mode grows to a certain high amplitude, a secondary instability, the subharmonic resonance, develops. Drubka (1981) reported that during resonance the subharmonic wave attains the same phase speed as the fundamental wave. This occurs after approximately two fundamental wavelengths. Beyond this point, the amplitude of the subharmonic mode increases to grow beyond that of the fundamental and vortex pairing is observed to occur. This point of pairing closely corresponds to the amplitude maximum of the subharmonic mode as shown by Ho and Huang (1982).

The vortex rollup and pairing are not generally expected to occur at a fixed streamwise location. Owing to the doubling in momentum thickness measured by Ho and Huang (1982) at pairing, such behavior would result in a stepwise growth of the shear layer. However, Laufer and Zhang (1983) explained that in general the location of the pairing

moves randomly in time and space which results on the average, in a smooth spreading rate.

Sarohia and Massier (1978) showed that a significant part of the pressure signal in the near field of a jet was generated by the pairing interaction and merging process. Laufer and Zhang (1983) suggest that the induced perturbations at the nozzle exit are the volume integral effect of all the fluctuations existing in the flow, with the largest contribution coming from the subharmonic fluctuation at the pairing location. These pressure fluctuations induced by the unsteady flow downstream can set up an unsteady Kutta condition at the sharp trailing lip of the jet. This phenomenon and the fact that acoustic forcing further organizes the jet suggest that the fluctuations caused by the merging vortices propagate upstream and create a strong feedback loop mechanism in the jet. Ho and Huang (1982) state that the location of the vortex merging can be predicted from the feedback loop evolution. This prediction is made by requiring the number of waves in the feedback loop to be an exact integer.

The organization of the jet flow and feedback accompanying pairing makes it a likely mechanism for acoustic wave generation. Ffowcs Williams and Kempton (1978) from their numerical calculations suggested that the pairing of eddies is the primary mechanism for the production of noise. Since the location of pairing can vary over a distance comparable to one eddy separation, the radiated sound is broadband. Sarohia and Massier (1978) add that the merging process has a statistical distribution of length and life span, so that it is quite probable that the emitted jet noise can appear to be broadband. Kibens (1979) observed, however, that in a forced jet, the resulting increase

in noise consisted of tones at the subharmonics of the excitation frequency, which was accompanied by a reduction of the broadband noise.

I.3 Objectives

The object of this study was to further document the relation between the axisymmetric fundamental and subharmonic modes by following their development and interaction in the velocity field from the lip of the jet to beyond the point of vortex pairing. We hoped to identify the role of the feedback in this process and to locate the region of the maximum shear layer influence. Furthermore, we intended to document the interactions between these and other instability modes, including non-axisymmetric (helical) modes leading to the appearance of other multiple-interaction modes. Such information, we felt, would be necessary to point to efficient and predictable means of controlling these jet flows.

Two Reynolds numbers were examined, one being Drubka's $Re=42,000$ case at which a natural coupling existed between the initial and final jet instability frequencies and, as a contrast, one at which no special coupling existed. The effect of initial conditions on these jets were examined by increasing the broad spectrum turbulence intensity within the jet core and by very low amplitude narrow-band external acoustic forcing. The forcing was intended to favor axisymmetric modes. A level of the forcing was chosen to be comparable to the levels in the natural feedback so as to mutually enhance or compete with that mechanism.

II. Experimental Setup

As in the case of Drubka (1981), this study was conducted in the IIT Jet Facility. A detailed description of that facility and the

characteristics of the jet flow are contained in that reference and will not be presented here. Benchmarking measurements, documented in the thesis by Shakib (1984), were taken to confirm that the flow conditions were the same as for that previous work.

Two of Drubka's flow cases were used in this study. The first of these was his lowest initial disturbance condition ($u'/U_j = 0.05\%$) designated 1L, and the other being his highest initial disturbance jet condition ($u'/U_j = 0.16\%$) designated 3L. A scale drawing of the exit face of the nozzle is shown at the top of Figure 1. The exit diameter of the jet in this figure is 5.14 cm. As shown in this drawing, eight azimuthal pressure taps provide sites for measuring the unsteady pressure field near the separation point at the jet lip.

The data consisted of simultaneously acquired time series of the unsteady pressures at the lip of the jet, and the streamwise velocity fluctuations measured at different spatial locations in the shear layer, up to approximately one diameter downstream. The velocity samples were always taken at the same azimuthal position as the sampled pressure port. This arrangement is schematized at the bottom of Figure 1. A voltage proportional to pressure was obtained from a B&K Type 2209 Precision Sound Level Meter which provided a flat amplitude response up to approximately 4000 Hz. A hot-wire powered by a DISA 55D01 constant temperature anemometer provided a voltage related to the streamwise velocity component. These analog voltages were DC biased and amplified before being digitally sampled and stored on digital magnetic tape.

For the forced jet cases, an upstream-oriented acoustic speaker was placed 4m downstream on the jet centerline. Pure tone oscillations of the speaker were driven by a B&K 1022 Beat Frequency Oscillator. The frequency and amplitude of the forcing sound was set while monitoring the unsteady pressures at the lip using an HP 3582A Real-Time Spectrum Analyzer. This was done with and without flow. The amplitude of the forcing was approximately 0.05% of the dynamic head based on the jet core velocity.

Post processing first consisted of digitally calibrating the pressure and velocity data series. For the case of the velocity data, a fourth order polynomial was used to linearize the anemometer output. Other processing generally involved calculating the mean and rms of the fluctuating quantities, the auto-and cross-spectra and coherence based on long and short time segments using Fast Fourier Transforms and Maximum Entropy Spectral Estimations, respectively, and the auto- and cross-bicoherence. Greater details on the more specialized statistical techniques are presented in the following sections.

III. Mode Energy Distributions

This section documents the streamwise development and the radial dependency of the instability eigenmodes in the initial shear layer of the circular jet. These results encompass the region starting from the lip of the jet, downstream through the first pairing location, and radially across the shear layer. For the dominant instability modes, the modulus of the eigenmodes were calculated from the spectral amplitude of the streamwise velocity fluctuations. The phase of the eigenmodes were determined from the pressure-velocity cross-spectrum.

The phase measurements were relevant since the linear coherence between the velocity fluctuations in the near-field region of the shear layer and the pressure fluctuations at the lip of jet exhibited were high valued for the principle instability modes.

The bulk of the results are presented as two-dimensional contour plots, with x-axis representing the streamwise direction, starting from $x/D = 0.05$, and the y-axis representing the radial direction normalized by either the jet diameter or the local momentum thickness. The contour plots are oriented to show the core of the jet on the top of the plot and the ambient field on the bottom. In order to better obtain a continuous spatial distribution of the plotted quantities, the discrete value points were spline fit first in the radial direction and next in the streamwise direction. A very low damping coefficient was used in the spline fit in order to not alter the actual data values. The constant level contour plots were generated from these spline function fits.

III.1 Jet Mean Characteristics

The two-dimensional contour mapping of the local mean velocity normalized by the jet exit velocity for the low initial disturbance level, 1L case, at $Re = 42,000$ is shown with a physical radial coordinate in Figure 2a. It is apparent from this figure that upstream of $x/D = 0.30$, the shear layer is seen to barely spread from its initial thickness. The first significant growth of the shear layer thickness occurs at approximately $x/D = 0.40$. The rate of spreading further increases at approximately $x/D = 0.60$. We will verify later that these positions correspond respectively to the points of energy saturation of the fundamental and subharmonic axisymmetric modes. We expect that

these x-locations should also coincide with the points of first vortex roll-up and vortex pairing and, that the local changes in the shear layer growth are attributable to these energetic motions.

The iso-mean velocity lines in 2a are reproduced in 2b with the radial coordinate now normalized by the local momentum thickness, $\theta(x)$. This demonstrates that self similar mean flow behavior exists, even well past the point of pairing in this jet.

For the same jet condition, the two-dimensional contour mapping of the total rms of the streamwise velocity fluctuations normalized by the jet exit velocity is shown in 2c. The radial coordinate is again normalized by $\theta(x)$. The rms values are plotted on a logarithmic scale in order to highlight regions of exponential growth.

III.2 Dominant Eigenmodes

The radial spread of the power spectra of streamwise velocity fluctuations for this case at four downstream locations are shown in the contour plots of Figure 3. The amplitude of the spectra are plotted on a logarithmic scale with 5 db difference between the contour levels. To easily differentiate the amplitude levels, the six highest levels are plotted in solid lines and the next five levels in dashed lines. From this and similar plots the dominant instability and interacted modes are identified. The fundamental axisymmetric mode, designated f_0 , occurs at 880 Hz. Although not as apparent in this presentation, the other fundamental mode for this Reynolds number jet occurs at 1050 Hz and corresponds to the $m=1$ helical mode. This frequency is designated f_1 . The other spectral peaks correspond to sum and difference modes derived from the initial fundamental modes. These include $f_0/2$, f_1-f_0 , $2f_0/2-f_1$, $f_1-f_0/2$, $2f_0-f_1$ and $f_0/4$.

We focus on the fundamental axisymmetric and subharmonic modes in Figure 4. These show iso-energy lines in the (x,r) directions, within the shear layer, of u-component fluctuations associated with each mode. This figure and others like it were constructed from the energy in spectral peaks at particular mode frequencies at the different sampled (x,r) -locations. Each mode was defined to fall within a frequency centered bandwidth of 54 Hz (± 27 Hz) which corresponded to 11 points in the spectrum for data acquired at 2500 Hz. Within the frequency bandwidth of a mode, the amplitude and phase were determined at the frequency having the maximum spectral amplitude. The velocity power spectrum at each probe position were closely examined to verify the existence of a spectral peak for each of the primary modes. From these results the regions where spectral peaks existed were identified. On such spatial maps of spectral amplitude, boundaries are plotted as thick solid lines each next to a dotted line pointing to the region where no distinguishable peaks were observed. The contour levels in these plots are in logarithmic, dB, increments so that equally spaced contours denote regions of exponential growth.

In the spectral map of the fundamental axisymmetric mode, Figure 4a, the streamwise spacing between adjacent constant spectral amplitude lines is invariant from $x/D = 0.15$ to 0.40 , marking the linear exponential growth region. Within this x/D , in the region $-0.6 < (r_{.5} - r)/2\theta < 0.6$, the contour spacing is relatively invariant with radial direction. This radial extent corresponds to a range of normalized mean velocity, U/U_j from 0.3 to 0.8 , seen from Figure 2b. The amplitude of the fundamental mode reaches a maximum at $x/D = 0.45$. This is observed to occur on the core side of the shear layer. Beyond the

pairing location, at about $x/D = 0.60$, the amplitude of this mode decreases slowly until it no longer exhibits a spectral peak, as indicated by the solid-dotted line boundary beyond approximately $x/D = 0.7$.

The spectral map of the subharmonic mode for this flow condition is shown in Figure 4b. Examination of this figure shows two regions of constant exponential growth from approximately $x/D = 0.10$ to 0.25 and from $x/D = 0.25$ to 0.50 . Again in the middle portion of the shear layer, $-1.0 < (r_{.5} - 5)/2\theta < 1.0$, the contour spacing in the flow direction is nearly invariant with radial direction. The maximum energy of the subharmonic mode occurs at $x/D = 0.60$. This maximum occurs slightly closer to the centerline of the shear layer than for the fundamental mode maximum.

The eigenfunction moduli for the fundamental axisymmetric and subharmonic modes were extracted from the spectral amplitude spatial maps such as these. This amounted to taking cuts along constant x/D lines to generate the mode shapes shown in Figures 5 and 6. In an effort to collapse these curves, the spectral amplitude $u'_f(x, r)$ was normalized by the square root of the total radial-integral energy at the mode frequency at that streamwise location. Two criteria were set in representing the eigenfunction. First, the eigenfunctions were defined only at streamwise locations where spectral peaks were observed, through the middle region of the shear layer. Second, the mode was to be undergoing exponential streamwise growth, based on values taken along the mode's maximum amplitude line. In the case of the subharmonic and difference modes, two regions of exponential growth were identified. The eigenfunctions in both these regions were included. The second region is

marked in the legend by an asterisk next to its streamwise x/D location.

Based on the above criteria, the eigenfunction moduli of the fundamental axisymmetric and subharmonic modes are shown in the top half of these figures. The corresponding eigenfunction phase distributions are presented at the bottom part. In the central region of the shear layer in Figure 5, the fundamental eigenfunction moduli are reasonably self-similar up to $x/D = 0.40$, which is just upstream of the energy maxima for that mode. Outside the central region, the moduli reach self-similarity past $x/D = 0.25$. This location corresponds to the first emergence of a 180 degree phase change seen in the phase distributions at the bottom. The 180 degree phase shift coincides with the radial position of the minimum mode amplitude. The double peaked behavior of the fundamental mode moduli and 180 degree phase change are consistent with the concept of a developing vorticity wave. In the middle region of the shear layer, the phase lines of the fundamental mode are approximately equidistant indicating a constant wave velocity.

The moduli of the subharmonic eigenmodes, in Figure 6, also exhibit self-similar behavior in the central region of the shear layer. Even at $x/D \geq 0.30$ (asterisked positions) in the region of enhanced resonant growth, the distributions only deviate slightly. The effect of subharmonic resonance can be seen in the eigenfunction phase distribution. There we observe an abrupt increase in the streamwise spacing of iso-phase lines for $x/D \geq 0.30$. This corresponds to a decrease in the phase velocity of this mode, which we will document in a later figure, is an adjustment to match its phase velocity to that of the fundamental mode.

In further statistics, we wish to utilize a single velocity sensor which will follow a similarity line while moving downstream. Drubka (1981) had chosen to follow the constant mean velocity line $U/U_j = 0.6$. A comparison of the streamwise growth rates for the fundamental axisymmetric and subharmonic modes determined by following this line is shown in Figure 7. In this comparison, Drubka's data have been shifted to the level corresponding to a 1 Hz. spectral band width, which is the standard band width for all our results. To investigate the sensitivity of this result to following different lines, we generated similar plots obtained while moving along the center of the shear layer at a constant $U/U_j = 0.5$, as well as along a line which followed the mode streamwise fluctuation maximum. The latter is shown in Figure 8. Neither of these approaches takes into account the radial spreading of the shear layer. In order to capture this effect in the growth of energy in these modes, we also plotted the streamwise development of the energy in streamwise velocity fluctuations in each mode integrated radially across the layer at different x/D locations. The results of this approach are presented in Figure 9.

Comparing these first on a qualitative basis, we observe a number of similar features. Focusing first on the growth of the fundamental axisymmetric mode (open symbols), we observe an initial region of constant exponential growth, which eventually reaches a saturation limit at approximately $x/d = 0.45$. Past this point the energy in the fundamental mode decays. The streamwise growth of the subharmonic mode shows two regions of exponential growth. The first falls in the range from $0.15 \leq x/d \leq 0.25$ and the other from $0.25 < x/D \leq 0.45$. Upstream of $x/D = 0.15$, longer wavelength subharmonic is affected by the close

proximity to the lip. Therefore within the first approximate quarter of the subharmonic wavelength, the amplitude levels are off the expected exponential growth rate observed downstream of this point.

On a quantitative basis, irregardless of the method used, the rate of exponential growth of the fundamental axisymmetric mode is virtually the same. Also, the x/d position of fundamental mode energy saturation does not vary significantly by the four approaches. The significance of the location of the fluctuation maximum is that it marks the position of the first roll-up of the shear layer into a vortex. When scaled on the axisymmetric mode frequency, $x/D = 0.45$ corresponds to three wavelengths from the jet lip.

For the subharmonic mode the rates within both regions of constant exponential growth is also virtually the same between the four methods. Each show the same x/D location of 0.25 for the beginning of the enhanced resonant growth, and except for the similarity line $U/U_j = 0.5$, each mark the location of subharmonic energy saturation to be at $x/D = 0.6$. The first position corresponds to approximately two fundamental or one subharmonic wavelengths from the jet exit. This location coincided with the change in the phase velocity of that mode seen in Figure 6 (bottom). The significance of the point of energy saturation of the subharmonic mode is that it marks the average location of vortex pairing. The characteristic position corresponds to four fundamental or two subharmonic wavelengths from the jet exit.

The streamwise phase development for these modes is shown in Figure 10. These are presented along the mean velocity line $U/U_j = 0.6$ for comparison to Drubka (1981). For the fundamental mode a constant phase velocity of $0.5U_j$ is observed which is predicted well from linear

theory. For the subharmonic mode the phase velocity in the initial growth region is a higher value of approximately $0.8U_j$, which is also in good agreement with linear theory. In the second growth region of the subharmonic, the phase velocity has reduced significantly to match that of the fundamental mode. The matching of the phase velocities is a prerequisite for resonance of the type predicted by Kelly (1967).

III.3 Effect of Initial Conditions on Dominant Eigenmodes

The remaining figures document the effect of mild axisymmetric forcing at the observed natural f_0 , and at a frequency 25 percent higher, on the development of the initial dominant eigenmodes and their interacted modes. In addition to the pure tone forcing, the effect of broad band disturbances obtained by increasing the core turbulence level is also presented. The forcing was performed at $Re = 70,000$ so that in the natural condition it also provides a comparison to the previously documented $Re = 42,000$ case which was known to exhibit the special jet column coupling.

The effects of the mild external acoustic forcing and the initial core disturbance level on the growth of the momentum thickness of the jet at $Re = 70,000$ are shown in Figure 11. The initial momentum thicknesses used to normalize the growth were measured at $x/D = 0.05$. These values are summarized in Table 1.

From Table 1, it is apparent that the initial momentum thicknesses did not vary significantly from one case to the other. This would indicate that even in the presence of these changing initial disturbance conditions, the frequencies of the most unstable modes, which scale with the initial shear layer thickness, remain unchanged.

Table 1. The Effect of External Acoustic Forcing and Initial Core Broadband Disturbance Level on the Initial Momentum Thickness (in cm), for the Jet at $Re = 70,000$.

Case	Natural 1L	Natural 3L	Forced at 2050 Hz 1L	Forced at 2500 Hz 1L
θ_i	0.0136	0.0138	0.0137	0.0142

Figures 12 and 13 document the spatial distribution of fundamental axisymmetric and subharmonic mode energy in streamwise velocity fluctuations within the shear layer to $x/D = 0.6$ for the different initial states. The natural case can be directly compared to its lower Reynolds number counterparts in Figures 4a and 4b. In doing so, one must account for the shorter development length which scales by the ratio of the fundamental frequencies and core velocities. Based on these, the development length for the $Re = 42,000$ 1L case is 1.40 times longer than that of the $Re = 70,000$ 1L case. This has been taken into account in the scaling of the ordinate to allow these two cases to be overlayed for comparison. For such a comparison, the spatial energy distributions for the fundamental and subharmonic modes in the 1L conditions at the two Reynolds numbers are quite similar. Although we expected this based on the linear instability of the initial shear layer, it was not certain if some differences might arise due to the special nature of the $Re = 42,000$ case. Comparison of these two cases shows that the added effect of this final frequency coupling on the global energy distribution in f_0 and $f_0/2$ modes, in the initial region up to the point of first pairing, is minimal.

The immediate effect of pure tone forcing at the natural fundamental axisymmetric mode frequency of 2050 Hz and at a 25 percent higher frequency of 2500 Hz is to increase the initial amplitude of these modes at the jet exit, but not to greatly affect the global energy development. At the higher frequency, the development length shortens by an amount commensurate with the shorter wavelength of the unstable mode.

We do however observe some interesting differences in the subharmonic mode development with the mild pure tone forcing at the natural f_0 . This is manifest in the increase in the size of the region, in the vicinity of the jet exit, where we could not detect a spectral peak (heavy line border) at the subharmonic frequency. In the unforced (natural) cases at both Reynolds numbers, the initial amplitude of the subharmonic had always been larger and more defined than that of the fundamental. This, we will demonstrate, is a result of downstream feedback in the form of acoustic waves produced during pairing. The mild forcing at f_0 appears to inhibit this feedback process. Mild forcing at the higher frequency does not exhibit this characteristic so that the "subharmonic" $5/11f_0$ mode exhibits a strong peak throughout the shear layer near the jet exit. A broad band increase in the core disturbance is observed to mask spectral peaks in the initially weaker fundamental axisymmetric mode at the jet lip, but not that of the subharmonic. The x-development qualitatively follows that of the natural low core disturbance cases.

The eigenfunction modulus and phase of streamwise velocity fluctuations for the fundamental and subharmonic modes at the higher Reynolds number, low initial disturbance condition were quite comparable

to the lower Reynolds number equivalents in Figures 5 and 6, and therefore are not reproduced here. The streamwise growth of these two modes is shown in Figure 14. Here we have chosen to follow the line of maximum streamwise velocity fluctuations of each mode, which was shown to be representative of the whole shear layer in previous figures. Comparing this figure to its lower Reynolds number counterpart in Figure 8, we observe the same stages of development namely, a constant exponential growth region for the fundamental axisymmetric mode, an initial and secondary exponential growth region for the subharmonic mode, and respective saturation locations at x/D values corresponding to three and four fundamental mode wavelengths from the jet exit. The spatial growth rates of the fundamental and initial subharmonic are virtually the same for the two Reynolds numbers when scaled by their wavelengths, although the secondary subharmonic growth is somewhat higher at the higher Reynolds number.

At this higher Reynolds number, a spectral peak at the initial $m = \pm 1$ helical mode frequency was more discernable. We therefore plotted in Figure 15, the streamwise growth of that mode, as well as the difference mode, $f_1 - f_0$. Focusing on the former, we observe a constant valued exponential growth with a spatial rate which is the same as that of the fundamental axisymmetric mode. The comparable growth rates of these two modes had been predicted by Michalke (1971).

The difference mode is observed to exhibit two different regions of exponential growth, like that of the subharmonic mode. The x/D location of the change in spatial amplification of the $f_1 - f_0$ mode also coincides with that point in the subharmonic growth. This would suggest a form of

interaction between these modes which we will expand upon in a later section.

With mild forcing at the fundamental axisymmetric mode frequency, the initial amplitude of that mode, seen in Figure 16, has increased by approximately a factor of ten. The initial amplitude of the subharmonic remains the same. These growth curves show the same characteristic features, although the point of change of slope in the subharmonic growth is not nearly as sharp as in the natural cases. In addition, the location of subharmonic energy saturation has moved slightly downstream. The location of the subharmonic maximum for the natural case is marked on this figure as x_p/D .

When the jet is mildly forced at a frequency 25 percent higher (2500 Hz) an exact fundamental/subharmonic combination was not found to exist. Instead, near-subharmonic modes at frequencies of $5/11f_0$ and $6/11f_0$ were observed, as well as a difference combination at $1/11f_0$. We have speculated that the initial "subharmonic" mode was at the $5/11f_0$ frequency. Part of the basis of that speculation is contained in the eigenfunction magnitude and phase distributions in Figure 17 and in the x -growth of the maximum streamwise velocity fluctuations in Figure 19. In the case of the former, we observe a good comparison to the subharmonic eigenfunctions for the natural jet, such as in Figure 6. The streamwise growth of the $5/11f_0$ mode exhibits the characteristic "subharmonic" development by the presence of two constant exponential regions, with the second having a significantly higher rate. The change in growth rate was also found to coincide with a change in phase velocity, seen in Figure 17.

All this can be contrasted to the spatial characteristics of the

$6/11f_0$ mode. The eigenfunction magnitude and phase distributions in Figure 18 show some early x-similarity which is subharmonic-like, but eventually further downstream it develops two peaks and considerable scatter. This behavior is a primary reason why we chose to present these past growth curves while following the fluctuation maximum, since for this case alone, the other approaches would not be representative. The x-growth of the $6/11f_0$ mode is shown in Figure 20. For that mode we observe a single, constant exponential growth at a rate which is somewhat less than that of f_0 . We observe no change in slope prior to saturation and no change in phase velocity characteristic of subharmonic behavior. Energy saturation occurs at the same x/D location for the $5/11f_0$ and $6/11f_0$ modes.

The streamwise growth of the $1/11f_0$ mode also seen in Figure 20 shows two exponential growth regions, similar to the natural difference mode $(f_1 - f_0)$ in the natural jet. Also similar is that the x/D location for the change in growth of this difference mode coincides with the point of growth rate change of the $5/11f_0$ "subharmonic." We have not verified if the $6/11f_0$ mode is a nonaxisymmetric mode, as in the case of f_1 in the natural jet.

IV. Unsteady Mode Selection

The experimental results of Drubka (1981) had verified that a circular jet is unstable to both axisymmetric and helical modes. He had speculated, based on flow visualization, that in the initial region, $x/D < 1$, the natural jet alternates between these two modes. The answer to this speculation defines a one of the principal objectives of this study. Further, the documentation of the unsteady behavior and the effect of low level harmonic forcing on the unsteady characteristics of

the jet are also addressed with the use of short-time spectral estimations.

The methods used for studying jet instabilities, such as those used by Drubka (1981), are typically based on long-time-average statistics. For example, the spectral estimations determined from Discrete Fourier Transforms (DFT) are usually based on the assumption that the correlation function of each data ensemble asymptotes to zero by the end of the sampling interval. This limits the minimum amount of time lags required for proper spectral estimation. The random band-width noise introduced by the use of DFT also requires averaging of ensemble spectra or frequency smoothing. This creates a major problem. Any alternate switching of the jet instability modes from axisymmetric to helical may occur in an unsteady and non-periodic manner. The long-time statistics required for the convergent estimation of the spectral function using DFT will act to mask this switching process by producing two apparent co-existing peaks at frequencies corresponding to these two modes. In addition, any slight time-variation in the mode frequencies would result in a broadening of the spectral peaks. Because of these manifestations of standard DFT processing methods, we computed short-time single realization spectral estimates using the Maximum Entropy Method (MEM). A description of the method is presented in Appendix A. The discussion of the results for different initial conditions in the jet are presented in the following.

IV.1 Results of Unsteady Mode Analyses

The short-time instability behavior of the three naturally developing and two harmonically forced jets are presented in the following. For each case, a series of short-time MEM power spectra were calculated for the simultaneously sampled pressure and velocity

fluctuation data series in the shear layer at the radial position $U/U_j = 0.6$. The amplitude and phase eigenfunctions of these modes shown previously, documented the x-similarity of that location. For each flow condition, and at each downstream location, consecutive MEM power spectra were calculated from contiguous overlapping short-time-series segments. It was found that 18 time-series points would result in appropriate short-record MEM spectra for the cases in this study. Based on the data sampling frequency, these 18 point records correspond to approximately five to eight axisymmetric wavelengths, (eight for the 2500 Hz forced case), or six to eight helical mode wavelengths.

Each sequential 18 point time-series was formed with a 15 point overlap of the preceding record. That is, each record was advanced by only three new time-series points, corresponding to one axisymmetric wavelength, for each consecutive spectral estimate. This amount was found to produce a smooth transition between contiguous spectra of the type shown in Figure 21. To obtain the most conservative spectrum with emphasis on the frequency content rather than on the amplitude, an 8 point predictive error filter length was chosen for use with the 18 point records. This consistently placed the estimate into region C of our criterion map (see Appendix A), thereby producing spectra which have the correct frequency content but may not display the proper energy content.

As a verification that the correct spectral estimates were obtained from the MEM approach, long-time-averaged spectral distributions were formed by ensemble averaging the consecutive short-time estimates. These were compared to the spectra for the same data properly computed using DFT. In all cases, little difference was exhibited between the spectra from the two methods. Although this is not a guarantee that

every short-time spectral estimate is completely correct in all aspects, it demonstrates that a statistical majority of these have the correct frequency and amplitude information. With this degree of confidence, the results obtained by this approach are presented.

Figure 21 depicts the spectral evolution for the 1L case at $Re = 42,000$ and $x/D = 0.35$. This condition was chosen to demonstrate the alternate switching between the axisymmetric and helical modes ongoing in this jet. These two modes are denoted by f_0 and f_1 at the top of the figure. Following the evolution in this figure, at 0 ms., when the data acquisition was started, the jet was dominated by the helical mode. This is evident by the peak at the frequency f_1 . After approximately 15 ms., the emergence of the peak at f_0 marks the switching from the helical mode to the axisymmetric mode. The jet remains in the axisymmetric mode until approximately 35 ms into the acquisition run where it shifts back to the helical mode. The alternate switching between modes is apparent throughout the time evolution depicted in this figure with both modes appearing to exist nearly an equal amount of time. A quantitative measure of the percentage of time each mode exists follows later in this section.

A similar alternate switching between these two fundamental modes is evident from the time evolution of spectra in Figure 22, at the higher Reynolds number of 70,000, for the low initial disturbance level jet at $x/D = 0.25$. This is contrasted with that evolution depicted in Figure 23, which occurred when the jet was axisymmetrically forced at the frequency f_0 . As expected, this forcing organized the jet instability and effectively suppressed the initial development of non-axisymmetric (helical) disturbances.

To provide a quantitative measure of the percentage of time of occurrence of these dominant modes, a method was developed to detect the existence of spectral peaks (modes). The method defined a peak to be at a frequency in the spectral distribution where its amplitude was higher than at the two neighboring frequencies. The use of such a simple definition was made possible only because of the smooth nature of spectra obtained from the MEM approach. This was meant to detect only the existence and frequency of the spectral peaks (SP). No information or criteria about the amplitude of the peaks was deduced from this method. Employing this method on the consecutive MEM spectra of both velocity and pressure data, such as the ones shown in Figures 21 through 23, the percentage of time a spectral peak exists at any of the resolvable frequencies, irregardless of its amplitude, was deduced. The results are presented in the SP histograms of Figures 24 through 28. These were constructed from 2000 consecutive MEM spectra in order to be representative of the overall spectral peak distribution.

The spectral peak histograms of the pressure fluctuations at the lip of the jet for $Re = 42,000$, 1L condition are shown in the top of Figure 24. The frequencies corresponding to the difference and subharmonic modes are well defined, and have a high value owing to their dominant existence in the spectrum. This mirrors the initial self forcing of the jet due to the coherent feedback at these frequencies.

In the initial shear layer for the same jet conditions, the velocity SP histograms in the bottom part of Figure 24 bring out all of the dominant modes. Since the peak detection does not discriminate on amplitude, we expected the SP histograms to be more sensitive to even low amplitude modes which exist a majority of the time. This was evident in this figure, where as many as 6 modes can be distinguished.

At the location closest to the jet exit, $x/D = 0.15$, the histogram is similar to that for the unsteady pressures at the lip. Following the development downstream, we observe the strong emergence and decay of the dominant modes which reflects their evolution and interactions.

For the same jet disturbance condition at the higher Reynolds number of 70,000, the velocity SP histograms in Figure 25 reveal a more consistent existence of the growing dominant modes. At this higher velocity, the development of the jet by this last station is equivalent to that at $x/D = 1.0$ for the previous figure. As in the lower Reynolds number case, the helical mode appears to exist a majority of the time only downstream of the pairing location, $x/D = 0.8$ for $Re = 42,000$; 0.45 for 70,000.

The effect of low level forcing at the fundamental axisymmetric mode frequency on the $Re = 70,000$ jet is displayed in the velocity SP histograms in Figure 26. From these, the forcing at f_0 is observed to organize the fundamental axisymmetric mode, evident by its significantly higher existence percentage. Near the lip at $x/D = .14$, the SP occurrence of the subharmonic is lower in amplitude and more broadly distributed than in the unforced case in Figure 25. By $x/D = .26$ however, the forcing is observed to better organize the subharmonic mode. As seen in this figure, the helical mode was strongly suppressed by the axisymmetric forcing. Speculation on the continued existence of a mode near the difference frequency in this forced jet is taken up later.

A comparison of the SP histograms for the lip pressure fluctuations in the forced and unforced condition at $Re = 70,000$ was shown in the top part of Figure 26. In the forced case, the SP histograms reflect the additive effects of the acoustic forcing and the downstream influence of

the developing shear layer. As a result, the distribution at the forcing frequency, f_0 , is very sharp and high valued with a strong suppression of adjacent frequencies. The distributions at the subharmonic and difference mode frequencies are, however, relatively unchanged. We contrast this behavior to that for the case of the jet forced at 2500 Hz in Figure 27. In this case the natural f_0 mode at 2050 Hz was strongly suppressed and replaced by a new axisymmetric mode at the 2500 Hz forcing frequency. The pressure histograms at the lip reveal a sharp distribution at the forcing frequency as with the previous forced case. In contrast to that case, the $5/11f_0$ "subharmonic" has been sharply increased in the pressure histograms. In addition, the $1/11f_0$ difference mode is also strongly evident. These lower frequencies are undoubtedly a result of downstream feedback. The high occurrence of $5/11f_0$ in the pressure signal further supports that this is the axisymmetric "subharmonic" mode for this forced jet.

The effect of higher initial disturbance levels in the core at $Re = 70,000$ is presented in the SP histograms in Figure 28. Comparing these to the low disturbance case of Figure 25, the higher broad-band disturbances are observed to lead to less organized axisymmetric modes. In particular, an almost equal predominance of the helical mode at all streamwise locations is observed. A similar sensitivity of the helical mode to initial broadband disturbance levels was reported by Drubka (1981).

In order to form statistics on the occurrence and interaction of the different modes brought out by the MEM spectral estimates, spectral peak indicator functions were generated. For these, the frequencies corresponding to the fundamental axisymmetric mode, its subharmonic, the helical mode, and the difference mode for the jet were focused on. The

frequencies corresponding to the axisymmetric fundamental mode and difference mode were identified from their predominant location in the SP histograms. The subharmonic frequency was then constrained to be half that of the axisymmetric frequency. Similarly, the helical mode frequency was constrained to be the sum of the axisymmetric fundamental and difference mode frequencies. The frequency band width, within which a spectral peak would be accepted to correspond to one of these modes, was chosen as the average of the half width of a Gaussian distribution fit of the axisymmetric and the difference mode velocity SP histograms. These band widths for the different modes are indicated on the SP histograms of Figures 24 through 28.

If a spectral peak was observed within the frequency bandwidth of a given mode on the MEM power spectrum, that mode was considered to be present at that time. This occurrence resulted in a value of one for the indicator function for the period of time that the mode existed. A value of zero indicated the instant over which the mode was not present. The indicator functions for the different modes, at a particular jet condition, were correlated to bring out any interdependence between the evolution of the jet instabilities. The percentage of time an instability mode exists in the total time series will be equal to the average value of the indicator function. Sample indicator functions corresponding to the MEM spectral evolutions in Figure 22 is presented in Figure 29.

Statistic summaries of the occurrence of the four principle jet modes, taken from spectra of pressure fluctuations at the jet lip, are presented in Table 2 for the different jet conditions. These statistics are based on approximately 2000 MEM spectra covering approximately 2 seconds of data acquisition for the $Re = 42,000$ case and 4 seconds for

the $Re = 70,000$ cases. Analysis of the longest continuous data records of 10 seconds for the $Re = 42,000$ 1L case showed no significant differences in these statistics or their distributions.

The results in Table 2 provide information about the disturbance field fed back from the developing velocity field. In the $Re = 42,000$, 1L case, the occurrence of the subharmonic mode is very high. At this Reynolds number, the feedback of the subharmonic mode resulting from

Table 2. Spectral Peak Occurrence of the Instability Modes in the Pressure Field at the Lip of the Jet in Percent of Total Time.

Case	$f_1 - f_0$	Mode $1/2 f_0$	f_0	f_1
$Re = 42,000$ Case 1L	45.4 (2.2)	35.0 (1.5)	6.3 (1.0)	6.3 (1.0)
$Re = 70,000$ Case 1L	38.1 (2.1)	13.0 (1.1)	26.3 (2.9)	3.8 (0.6)
$Re = 70,000$ Forced 2050 Hz Case 1L	27.7 (1.2)	15.3 (1.9)	64.4 (1.6)	1.8 (0.2)
$Re = 70,000$ Case 3L	23.5 (1.3)	6.4 (0.5)	26.9 (2.1)	6.7 (1.2)

Case	$1/11 f_0$	Mode $5/11 f_0$	$6/11 f_0$	f_0
$Re = 70,000$ Forced 2500 Hz Case 1L	52.0 (1.4)	35.5 (2.4)	3.8 (0.6)	48.8 (1.0)

Note: The data in the parenthesis is the standard deviation calculated from several sets of SP indicators.

pairing, is significantly higher owing to the natural coupling of the initial shear layer and jet final Strouhal frequencies. By comparison, we observe that at the higher Reynolds number where the natural coupling is not present, the subharmonic mode is significantly less dominant.

At the higher initial disturbance level condition a significant reduction in the occurrence of the subharmonic mode in the lip-pressure signal was observed. The introduction of broad-band disturbances in this case has also resulted in an increase of the occurrence of the helical mode. One must be careful, however, about trying to infer too much information about the helical mode from the analysis of the pressure fluctuations at the lip, since this mode did not exhibit a strong peak in the lip pressure SP histograms.

The occurrence of the difference mode, which shows a strong existence in the pressure signal, is only slightly reduced by the axisymmetric forcing at f_0 . If the difference mode is the result of the interaction between the axisymmetric and helical modes in the shear layer, the reduction in the occurrence of the helical mode might suggest a similar reduction effect on the difference mode. This, however, was not the case.

The streamwise development of the SP occurrence for the four dominant instability modes in the velocity field of the shear layer is shown in Figures 30 and 31 for the different jet conditions. We focus first on the development of the subharmonic mode in the $Re = 42,000$ 1L case, in Figure 30. There, past the influence of the lip, we observe a decrease in the SP occurrence towards a minimum at $x/D = 0.35$. This location is slightly downstream of the beginning of the subharmonic resonance. Downstream of this location, the occurrence of the subharmonic mode increases, reaching a maximum at $x/D = 0.65$. This

position coincides with the subharmonic fluctuation maximum.

The occurrence development of the fundamental axisymmetric mode is almost the reciprocal to that of the subharmonic. The occurrence of this mode increases from the lip and reaches a maximum at $x/D = .45$, which closely marks the position of maximum energy in that mode. The rapid decrease in its occurrence past $x/D = 0.45$ is associated with the rapid growth of the subharmonic mode and ultimate pairing of the formed vortices. Similar development behavior of these modes occurs for the higher Reynolds number of 70,000, 1L case, shown in Figure 31a.

The external acoustic forcing at the fundamental frequency has interfered greatly with the natural development of the jet as depicted by the velocity SP occurrence development of Figure 31b. As a result of the forcing at f_0 the occurrence of this mode is initially much higher than in the natural case. After a small initial increase, its occurrence decreases towards the natural case behavior. By $x/D = 0.35$, the energy of the axisymmetric mode has reached a maximum. At this location the forced axisymmetric mode has become less organized, evident by a broadening of its SP histograms in Figure 26. These results reflect the diminishing influence of the low level forcing on this mode as it develops downstream.

The forcing at f_0 has moved the maximum occurrence of the subharmonic mode slightly downstream of the natural location. Since this maximum is associated with the pairing process, this low level forcing appears to have slightly impeded that mechanism.

Acoustic forcing at a frequency 25 percent higher than the natural f_0 (31c) has resulted in the occurrence of the forced mode to reach a maximum closer to the jet exit, $x/D = 0.25$, in proportion to the ratio of the forced frequency of natural f_0 . This case is however more

complex than the others in that the occurrence of the $5/11f_0$ "subharmonic" is a maximum upstream of the fundamental mode energy maximum. The occurrence maxima of the $6/11f_0$ and $1/11f_0$ modes bracket the locations of their energy maxima and that of the $5/11f_0$ mode. With the introduction of broad-band disturbances in the 3L case (3ld), the occurrence of the subharmonic mode is initially lower, however its ultimate development as well as the x-development of the other modes is comparable to the lower disturbance condition.

Focusing on the helical mode, we observe for the lower Reynolds number, 1L case that its occurrence development is approximately the reciprocal to that of the subharmonic. The helical mode is only well organized just before the onset of the subharmonic resonance. Past the pairing location its percentage time of occurrence is half the value at its peak. At the higher Reynolds number of 70,000 in both the low and high initial disturbance conditions, the behavior of the helical mode is similar to that of $Re = 42,000$ case. The only difference is in the percentage values, where a greater predominance of the helical mode is observed in the higher disturbance 3L condition. The axisymmetric forcing of the jet has effectively eliminated the occurrence of the helical mode. The curious persistence of the difference mode is also evident here. In general, the streamwise development of the occurrence of the difference mode appears to follow that for the subharmonic mode, and at the furthest downstream measurement location it was the most predominant mode.

In order to better present any interdependence between the fundamental axisymmetric and helical modes, their cross-occurrence was computed from the indicator functions. The streamwise development of that quantity for the unforced jet at both Reynolds numbers is shown in

Figure 32. Also replotted for these cases are the auto-occurrence distributions for f_0 and f_1 . If these two modes were statistically independent of one another, that is, if the occurrence of one mode was not related to the occurrence of the other, their cross-occurrence would be equal to the product of their auto-occurrences. This product signifying statistical independence, is indicated as the small-dashed line in the figure.

It is apparent here that for most of the initial region of the jet, the cross-occurrence of the fundamental axisymmetric and helical modes (indicated by the dashed-dotted line) is zero. This is true in the time series taken from both the velocity and lip pressure data. The only location where their co-existence was not zero was at the x-position of the beginning of subharmonic resonance. The SP occurrence correlation between the axisymmetric and helical modes was also calculated and found to be consistently near zero. These results indicate that the two modes rarely coexist at the same time in the jet.

V. Nonlinear Phase Locking

The first and second order spectral estimates, have been used in previous figures to determine the growth of instabilities in the jet and to document their linear interactions. In this section we are concerned with nonlinear, sum and difference interactions which are documented through the third order spectrum, or bispectrum.

Some early references to bispectral estimates include Hinich and Clay (1968) and Hasselman et al. (1963) in applications to geophysical flows. Lii et al. (1976) used the bispectral estimates, in conjunction with the equation for the rate of increase of energy in a homogeneous turbulent flow field, to show the source and direction of energy

transfer between the frequencies. Other investigators have extended the use of bispectral estimations to study other complex nonlinear flow systems such as transition to turbulence in a two-dimensional wake (Miksad et al., 1982, 1983; and Solis et al., 1986); instability and feedback in an impinging shear layer (Kinsely and Rockwell, 1981); and in a Blasius boundary layer undergoing transition to turbulence (Corke and Mangano, 1987, 1989).

In the present work the bispectral estimates were utilized to measure and document the nonlinear interactions which are a part of the initial shear layer instability, vortex formation, vortex pairing and feedback in axisymmetric jets. Because of the spatially changing energy levels in the modes of interest, the normalized bispectrum, or bicoherence was used. In this manner the emphasis was on the nonlinear phase locking which is necessary for efficient energy transfer between modes. Finally to determine the upstream or downstream influence of the flow, the cross-bicoherence was calculated for the simultaneously samples spatially separated time series. These consisted of velocity fluctuations in the shear layer at different x-locations along a similarity line, and unsteady pressures at lip at the same azimuthal location. A primary emphasis was placed on the interactions of the fundamental axisymmetric and subharmonic modes in order to document the upstream influence of the lip, their cooperative evolution, and the downstream feedback of those quantities which might have a bearing on the subharmonic resonance and pairing processes.

V.1 Cross-Bicoherence

The cross-bicoherence (CBC) is a measure of the nonlinear phase locking between frequencies in three time series. The origins of this statistical quantity is given in Appendix B. Its definition is contained

in equation 24 although the computationally simpler form in equation 27 was used in this study. The time series used in the application of this statistic were the streamwise velocity fluctuations acquired at different spatial locations in jet shear layer, $u(x,r,t)$, and the simultaneous pressure fluctuations at the lip of the jet, $p(t)$ (see Figure 1). The third time series is formed by the sum or difference of these two.

When interpreting the CBC estimates, one finds that the order of the interacting frequencies is an important parameter for determining the direction of influence. For two separate time series, such as are used in these studies, as many as nine (three to the power of two) combination orders are possible, although only six are unique. If for example, a high CBC is observed between frequencies f_1 and f_2 ($f_1 - \omega_1/2\pi$) and their sum or difference frequencies in the time series, three possible interactions could have taken place; namely, that the sum or difference frequencies resulted from the interaction between f_1 and f_2 , or f_1 had interacted with the sum or difference frequency to produce f_2 , or that f_2 had interacted with the sum or difference frequency to produce f_1 . When the origin of a mode frequency is clear, for example if it results from an instability process, this may not be a problem. In the jet however, because of feedback, it is not always clear whether the pressure field at the lip of the jet is the origin of the velocity fluctuations in the shear layer, or if the velocity fluctuations are the origin of the unsteady pressure field at the lip. To clarify this problem, it becomes necessary to look at the streamwise evolution of the CBC while changing the order of processing of spatially separated time series.

The upper frequency limit of the CBC is set by the Nyquist criterion, such that the sum of any two frequencies can not exceed half the sampling frequency. From this frequency limit, the region of validity of a coherence plot for summed interactions takes the form of a right triangle bounded by a -45 degree line, crossing the two Cartesian axes at the half sampling frequency value. The magnitude of the cross-bicoherence is drawn as constant level contours. By our convention, the processing order of frequencies is such that the first frequency is read from the abscissa, the second one from the ordinate, and the third from the point of intersection between the -45 degree line and either of the two axes.

Of the six possible independent processing orders, only three were found to be useful. The order of the processing of the CBC greatly affects the result and is therefore indicated on each plot by the quantity subscripts, p indicating that it was derived from the pressure signal, and u from the velocity signal. The magnitude of the CBC is plotted as contour levels, starting with the lowest level of 10% and increased by 25% up to 85%. Above each of the CBC estimates appears the power spectra of the velocity and pressure signals, plotted in solid and dashed lines, respectively. These are plotted with an arbitrarily shifted origin and with a full dynamic range of 50 db. The pressure spectrum is plotted only as a reference and it does not differ from one figure to another within the same condition. Also included is the linear coherence between the velocity and the pressure signals. This is plotted as a dotted line, and by definition it falls between zero and one.

V.2 Nonlinear Phase Locking for Natural Jet Modes

The initial phase-locking between the modes measured in the unsteady pressure field at the lip of the jet at both $Re = 42,000$ and $70,000$ 1L cases, is depicted in the auto-bicoherence, β_{ppp} , shown in Figure 33. This symmetrical bicoherence exhibits five distinguishable peaks, so-labeled on the figure, which are the result of the interactions between the longer wavelength modes $1/2f_0$ and f_1-f_0 . Peak number 1 signifies the phase-locking between the fundamental axisymmetric and subharmonic modes in the triple form $1/2f_0 + 1/2f_0 = f_0$. This interaction is stronger in the lower Reynolds number case where the initial and final Strouhal numbers are an integer power of two apart. Peak numbers 2 and 3 result from the interaction of the subharmonic mode and the difference mode to produce their sum and difference modes, namely, $1/2f_0 + f_1-f_0 = f_1-1/2f_0$ and $1/2f_0 - f_1-f_0 = 3/2f_0 - f_1$. Peak number 4 results from the interaction of the subharmonic mode with the multiple interacted mode of frequency $3/2f_0 - f_1$ to give their sum at frequency $5/2f_0 - f_1$. Peak 5 results from an interaction of the fundamental axisymmetric mode and the interacted mode f_1-f_0 to give the mode at frequency $2f_0 - f_1$. The nonlinear interactions depicted by the auto-bicoherence distributions in this figure represents the initial self-forced "imprint" resulting from the downstream influence of growing instability and interacted modes in these jets.

In documenting the downstream evolution of the CBC, the emphasis will be placed on the interactions involving only the fundamental axisymmetric and subharmonic modes, peak 1 in Figure 33. The natural behavior of the jet at $Re = 42,000$ will first be used to point out the essential mechanisms involved in fundamental-subharmonic resonance and

feedback. This case will then be used to aid in interpreting the results in jets having different initial disturbance conditions.

A sampling of the cross-bicoherence distributions, β_{ppu} and β_{upp} for the $Re = 42,000$, 1L jet is shown in Figure 34. This was taken at $x/D=0.25$ which corresponds to the point of the beginning of resonant subharmonic growth. A composite of results from similar figures taken at different x/D locations is presented in Figure 35 in order to document the fundamental/subharmonic interaction in this jet. This figure includes the streamwise development of β_{ppu} and β_{upp} for peak 1, of the linear coherence, Γ_{up} , and of the streamwise velocity fluctuations at f_0 and $f_0/2$ (reproduced from Figure 7).

At the closest measurement location, $x/D = .05$ in Figure 35, the linear coherence of the subharmonic mode is approximately 50% whereas for the fundamental it is almost zero. The small peak of approximately 40% in β_{upp} and the lack of a peak in β_{ppu} indicate that the subharmonic mode at this location is phase-locked to the pressure field at the lip, and that no such phase-locking is present for the fundamental mode. The relative difference between the magnitudes of β_{upp} and the linear coherence, Γ_{up} , at the subharmonic frequency indicate that the subharmonic mode velocity fluctuations at this most upstream position are linearly phase locked to the pressure fluctuations at the lip.

At $x/D = .15$, the linear coherence of both modes has increased slightly. The cross-bicoherence magnitudes have also increased to a value approximately the same as for the linear coherence. This indicates the beginning of nonlinear interaction between f_0 and $f_0/2$. By the next location at $x/D = .25$, an abrupt increase in the growth rate of energy at $f_0/2$ marks the beginning of subharmonic resonance. β_{ppu} at this location is approximately 90% which, when accompanied by the

respectively low β_{upp} of approximately 20 percent, indicates a nonlinear phase locking between f_0 in the velocity field and $f_0/2$ in the pressure field at the lip. The arrow pointing downstream in the growth curve in this figure signifies this upstream influence of the lip on the subharmonic mode leading to subharmonic resonance.

At $x/D = 0.45$, β_{upp} is now larger than β_{ppu} suggesting a nonlinear phase locking between $f_0/2$ in the velocity with f_0 in the pressure. At this same location, the energy at f_0 has reached a maximum. We associate this with the first roll-up of the shear layer into discrete vortices spaced at the fundamental wavelength. The larger β_{upp} suggests that this energetic process results in feedback of fundamental mode energy from the velocity field to the pressure field at the lip. This downstream influence is indicated by the upstream facing arrow at the frequency f_0 . It is drawn lightly to signify that fluctuations at f_0 are only weakly felt at the lip.

At $x/D = 0.65$, β_{ppu} is approximately 100% and significantly larger than β_{upp} . At this location, the energy at $f_0/2$ now has reached a maximum. This is associated with approximate point where the formed vortices pair. This indicates that this energetic process results in a nonlinear phase locking between the fundamental mode in the velocity and the subharmonic mode in the pressure. This near perfect phase locking is strong evidence of feedback of subharmonic mode energy from the velocity field to the pressure field at the lip. This downstream influence is drawn as a bold arrow to signify that it is strongly felt at the lip.

V.3 Effect of Initial Disturbances on Nonlinear Development

The effect of forcing the $Re = 70,000$, 1L jet is summarized in Figures 36 through 38 at the fundamentally important x/D locations

corresponding to the beginning of subharmonic resonance, at the point of fundamental mode energy saturation and at the point of subharmonic mode energy saturations. At the first location at $x/D = .15$ in Figure 36, the cross-bicoherence β_{ppu} shows a value at peak 1 indicative of the fundamental-subharmonic interaction resulting from the upstream influence of the lip, seen previously at the lower Reynolds number. At the bottom part of the figure, when the jet was forced at f_0 , we observe that this peak is not present. This suggests that under the conditions of this mild harmonic forcing, the natural initial nonlinear phase coupling between the fundamental and subharmonic modes has been impeded.

At $x/D = .32$ in Figure 37, the high peak 1 in β_{upp} in the unforced jet indicates the feedback of energy at the fundamental mode frequency to the lip, again consistent with the lower Reynolds number case. The broad diagonal shape of this peak for the jet forced at f_0 however suggests that the frequency fed back to the lip in this case is phase locked to a broad range of near-subharmonic frequencies. Such interactions would produce the broad peak in the autospectrum at the subharmonic frequency seen at this x/D in this case. Also observed in the autospectral are the discrete side-band modes to the fundamental in the forced case. The interaction to produce these is seen by the three peaks in β_{upp} centered at the fundamental frequency on the CBC abscissa and aligned to the ordinate frequency of approximately 160 Hz. The 160 Hz frequency may be fundamentally important since it corresponds to a Strouhal number, $fD/U_j = 0.4$, which is value generally associated with the jet column mode (Ho and Huerre, 1984).

By $x/D = .45$ in Figure 38, the high value of peak 1 in β_{ppu} in the

forced jet indicates that the fundamental and subharmonic modes have achieved a concentrated phase locking, comparable to the unforced jet. This subharmonic is fed back and strongly felt at the lip. There also remains some weak nonlinear coupling associated with the fundamental mode side-bands.

The effect of forcing the jet at a frequency 25% higher than the natural f_0 is depicted in Figure 39. This is shown in 39a at the x-position of the beginning of enhanced growth of the $5/11f_0$ mode which was seen from Figure 19. In this case, we now observe a high organization of the jet with strongly coherent nonlinear interactions. Although the linear coherence of the instability modes for the jet forced at f_0 is comparable, a factor of two greater cross-bicoherence levels exists for this 2500 Hz forced condition, demonstrating a much stronger nonlinear phase-locking of these modes in this instance. The interactions involving the $5/11f_0$ mode are apparent in this figure as the band of contour lines at the frequency of 1136 Hz. The source of the non-exact subharmonic is likely a result of the feedback mechanism which acts to select the closest subharmonic frequency that also gives an integer number of wave lengths over the distance from the point of pairing back to the jet lip. This mode interacts with a multitude of other modes to transfer energy to both higher and lower frequencies in discreet fashion to fill the spectrum. The $1/11f_0$ mode although being close to, is distinguishable from the 160 Hz mode seen in the previous forced case.

Further downstream near the location of energy saturation of the $5/11f_0$ mode, the strong nonlinear phase-locking persists. This can be seen in the β_{ppu} distribution in Figure 39b. At this location, the linear coherence, Γ_{up} , of the forced f_0 and interacted

$5/11f_0$ and $1/11f_0$ modes are also still quite high. The large value of β_{ppu} at the frequency intersection of $5/11f_0$ and $1/11f_0$ in the pressure signals suggests that the $6/11f_0$ mode in the velocity fluctuations is a product of that summed interaction. This is also consistent with the insignificant level of the linear coherence at the $6/11f_0$ frequency.

VI. Discussion

VI.1 Pairing Process and Feedback

In the initial region of the jet shear layer, up to four wavelengths of the fundamental mode, the axisymmetric and subharmonic modes grow exponentially in amplitude, evolve, and interact, leading to the formation of vortical structures and finally pairing. Vortex formation and pairing were observed to result in relatively rapid changes in the streamwise growth of the shear layer, and to provide effective sites for downstream influence of the flow on the unsteady pressure field at the jet exit lip.

At the lip of the jet, a degree of nonlinear phase locking between the fundamental axisymmetric and subharmonic modes was found to initially exist. This was seen from the auto-bicoherence distribution in Figure 33. Nonlinear phase locking also existed between other frequencies in the pressure field at the lip as a result of sum and difference interactions with the longer wavelength $f_0/2$ and $(f_1 - f_0)$ modes. These represented a natural tuned self-forced condition to the initial shear layer growth.

Within the first approximately two fundamental wavelengths downstream of the jet exit, the fundamental and subharmonic modes grow independently. Their initial amplitudes are commensurated with the

degree of tuned self-forcing as well as other competing background disturbances. Evidence of their independent growth comes from the difference in their phase velocities (Figure 10), which makes energy transfer inefficient. The lack of intercomponent mode locking was evident in the low levels of cross-bicoherence in this early region at the top of Figure 35.

In this early stage, the fundamental mode is best characterized by a wave representation with a double peaked eigenfunction modulus. the fluctuation minimum between these corresponded to the location of a 180 degree phase shift in the eigenfunction phase. Prior to vortex formation, there existed virtually no growth in the momentum thickness downstream, and the mean profile closely followed a hyperbolic tangent distribution. When you combine these characteristics, one can see the origin of agreement to analysis with linear, spatial, inviscid, parallel stability theory.

At the end of this region (two fundamental wavelengths from the jet exit), the secondary enhanced growth of the subharmonic begins. This was marked by a reduction of the phase velocity of the subharmonic to match that of the fundamental. This change was seen as the rapid shift in the subharmonic eigenfunction phase at $x/D = 0.3$ in Figure 6 requiring less than a quarter of a subharmonic wavelength to make the transition.

In the process of changing phase velocities, the linear coherence, Γ_{up} , is low. This would be expected since this statistic is a measure of linear phase locking and the subharmonic phase development is changing at this location. In contrast to this, the high cross-bicoherence, β_{ppu} , for a fundamental/subharmonic interaction indicates a strong degree of nonlinear phase locking between these

modes. When combined with the lower β_{upp} at this location this documents phase locking between the subharmonic in the pressure field at the lip, and the fundamental in the velocity field at this x/D . We interpret this as the upstream influence of the pressure field at the lip to aid in adjusting the phase velocity of the subharmonic mode, satisfying the resonance condition and leading to its enhanced growth.

The region of influence of the lip is fairly localized, and does not extend far downstream of this point. This was evident by the decreasing β_{ppu} and increasing β_{uup} past $x/D = 0.3$ in Figure 35, prior to fundamental mode saturation.

Fundamental mode saturation occurs one wavelength downstream of this point (three wavelengths from the jet exit). This process is associated with the first roll-up of the shear layer into a vortex ring. The high β_{uup} for a fundamental/subharmonic interaction indicates a strong degree of nonlinear phase locking between these modes which is associated with this event. The direction of the interaction is inferred from the simultaneously low β_{ppu} . These indicate a nonlinear phase locking between the subharmonic in the velocity, and the fundamental in the pressure (at the lip). We interpret this to result from feedback of pure tone acoustic disturbances at the fundamental frequency from the point of vortex roll-up back to the jet lip. This feedback was indicated by the light arrow in Figure 35. The energy in pressure fluctuations at the fundamental frequency at the lip is however relatively small, suggesting that the downstream influence of this mode is weak.

The subharmonic mode continues to grow exponentially for another fundamental wavelength downstream of the point of fundamental mode saturation, four wavelengths from the lip. Since the beginning of its

secondary growth, it had closely grown at the rate of the fundamental. When the subharmonic mode saturates a nearly perfect nonlinear phase locking existed for the β_{ppu} fundamental/subharmonic interaction. When combined with the relatively low β_{upp} , this indicated that the phase locking occurred between the fundamental in the velocity and the subharmonic in the pressure (at the lip). We interpret this to result from acoustic feedback at the subharmonic frequency produced by the energetic process of vortex pairing which is associated with this energy maximum. This process was indicated by the bold arrow pointing in the upstream direction in Figure 35. A larger, dominant peak in the pressure spectrum at the subharmonic frequency indicates that the downstream influence of this mode is relatively strong. The dominance of this mode is similarly seen in the spectral peak histogram of MEM spectral estimates in Figure 24 and 26. The influence is especially strong in the 42,000 Reynolds number jet for which the final frequency coupling existed. However, the importance of subharmonic mode feedback is not restricted to only this extra special condition.

VI. 2 Nonaxisymmetric Modes

Analysis by Michalke (1971) and Mattingly and Chang (1974) had indicated that the initial region of the jet is equally unstable to both axisymmetric and non-axisymmetric (helical) modes. In a previous experiment using the same facility as in this investigation; Drubka (1981) had documented the $m = \pm 1$ helical mode in addition to the fundamental axisymmetric modes. Although his observations were based on long-time averaged spectral estimates, he speculated that the initial region alternates between these fundamental states. In the present experiment, long-time averaged spectra brought out the existence of these two modes. The streamwise frequency of these and the dependence

on Reynolds number was found to be in agreement with Drubka's values. Short-time mode analysis was performed using maximum entropy spectral estimates in order to observe their temporal behavior to answer Drubka's speculation.

Mode detection was based on the existence of spectral peaks in the short-time estimates at the frequencies for the fundamental axisymmetric and $m = \pm 1$ helical modes, respectively. The temporal evaluation of these modes was seen in a qualitative sense in Figures 21 and 22 for the natural jets. These indicated a lack of coexistence and apparent nondeterministic switching between fundamental states. This was quantified in spectral peak occurrence distributions of the type shown in Figures 30 and 31 and in the cross-occurrence distributions in Figure 32.

The spatial exponential growth rate of the helical mode was found to be the same as that of the axisymmetric mode, in agreement with theory. The average initial amplitudes close to the jet exit were also very comparable. In addition, their streamwise extent of constant exponential growth was found to be quite comparable so that their points of energy saturation closely coincided. Presumably then, the dominant mode at any instant is likely to be the one which had the highest initial amplitude forcing due to randomly arriving axisymmetric or nonaxisymmetric disturbances at the jet lip. When the jet was disturbed by far-field harmonic acoustic disturbances which excite axisymmetric modes, the existence of the helical mode was effectively suppressed. In the case of nonaxisymmetric modes, a disturbance which produces a 180 degree azimuthal phase difference around the exit lip would be suitable to produce a $m \pm 1$ helical mode.

One might expect that the percentage of occurrence of each of these fundamental modes would be constant valued throughout the jet initial region. The spectral peak occurrence distributions in Figures 30 and 31 show that this is in fact not the case. This suggests that these modes can overtake and suppress each other through interactions further downstream. For example, the occurrence of the helical mode was observed to reach its maximum at the x/D location associated with the beginning of subharmonic resonance. At this location, the occurrence of the subharmonic is a minimum.

The percentage of time that both the fundamental axisymmetric and helical modes coexist was found to be negligibly small. The only exception was at the beginning of subharmonic resonance where the percentage of their simultaneous occurrence reached approximately four percent. It was only in this region that the cross-bicoherence showed a nonlinear phase locking between the axisymmetric subharmonic and helical modes to produce the difference mode $f_1 - 1/2f_0$. The otherwise general anti-correlation between the occurrence of these two fundamental modes suggests that each might be a basin of attraction which suppresses the existence of the other.

Given this physical picture for the alternate existence of these two fundamental modes, we are left in somewhat of a quandary as to the origin of the difference mode, $f_1 - f_0$. That is, how could these two modes interact to produce their difference mode if they do not coexist?

We have observed the existence of this mode in the pressure and velocity time series. Along with the subharmonic mode, it dominates the lip pressure field to produce a number of nonlinearly phase locked modes formed from sum and difference interactions, which provide a level of initial jet self-forcing. The spatial amplification of the $f_1 - f_0$

mode exhibits two constant exponential growth regions, similar to the subharmonic. The x/D location of the change in exponential growth is at the same point as that of subharmonic. Also, their spatial growth rates are nearly the same. Since the difference frequency is far from the region of maximum linear amplification, this high growth attests to the nonlinear energy transfer to this mode. Since the spatial growth mimics that of the axisymmetric subharmonic, we expect that these two modes are related. If we look to the auto-bicoherence, β_{ppp} , at the lip of the jet in Figure 33, peak 2 documents a nonlinear phase locking between the subharmonic and difference mode in the form $1/2f_0 + f_1 - f_0 = f_1 - 1/2f_0$. This interacted mode in the unsteady pressure is observed to interact with the subharmonic in the unsteady pressure in peak 6 of the β_{ppu} in Figure 34, to produce a nonlinear phase locking with the helical mode at f_1 in the velocity at the beginning of secondary exponential growth. Therefore, we do observe a close link between the $f_1 - f_0$ and $f_0/2$ modes which originates in the fed back unsteady pressures at the jet lip, and through the lip influence, has a downstream effect to produce a nonlinear phase locking between $f_0/2$ and f_1 . Recall that the only point of nonzero coexistence of the f_0 and f_1 modes was at the location of the emergence of peak 6 in Figure 34, which was also the location of the occurrence maximum of the f_1 mode.

When the jet was excited by far-field acoustic pure tones at the axisymmetric mode frequency, f_0 , the helical mode at frequency f_1 is effectively suppressed. But, was it eliminated totally? Examining Figure 31 (b) shows some traces of occurrence of the f_1 mode (dotted) which still contain the same x/D trends as in the natural case, shown in the plot above it. Remember that the acoustic excitation was not meant to totally overwhelm the jet but rather to favor certain modes.

The overall occurrence levels of the $f_1 - f_0$ mode had been reduced by the axisymmetric excitation. This is seen both in the pressure field at the jet lip as well by comparing the distributions in Figure 31a and b (dash-dotted). The reduction is not linearly proportional to the lowering of the f_1 occurrence. However, since the growth of the $f_1 - f_0$ mode is also nonlinearly linked to the $f_0/2$ mode, which has been pointed out is resonantly locked with the f_0 mode, even a trace amount of energy at f_1 could result in a disproportionate energy transfer into the helical mode at the difference frequency. Recall, that the occurrence statistics make no distinction on the amplitude of these modes, only on their existence in the time series. In fact, the amplitude of the $f_1 - f_0$ mode, relative to f_0 , is significantly less with axisymmetric mode excitation.

VI.3 Effect of Initial Forcing

In addition to the pure-tone acoustic excitation at f_0 , acoustic forcing away from the natural axisymmetric mode and broad-band core disturbances had been imposed to study their effects on the initial development of unstable modes in the jet. In the previous section the effect of axisymmetric mode forcing on the helical modes was discussed. A sensitive and consistent indicator of the x-development of the unstable modes is the mode occurrence distributions such as in Figure 31. We therefore look to these to show some of the effects of the weak acoustic excitation. In terms of the axisymmetric modes, the forcing at f_0 gave an expected initial increase in the occurrence of that mode near the lip. The level of occurrence, however, gradually decreased towards the unforced behavior by the location of fundamental mode saturation. Recall that the level of forcing was only 0.05 percent of the dynamic

pressure which would be of the same order as the natural feedback levels.

We observe in Figure 31a and b that the forcing at f_0 had altered the occurrence development of the subharmonic mode (solid). In particular upstream of the location for the beginning of resonant subharmonic growth ($x/D = 0.25$), the occurrence levels are significantly lower for that mode. In the region of secondary growth, the occurrence of the subharmonic increases at a slower rate and reaches a maximum further downstream. Since this maximum is associated with vortex pairing, the low amplitude forcing at f_0 appears to have slightly retarded this process.

To understand this effect better, we look to the fundamental/subharmonic interactions brought out by the CBC in Figures 36 through 38. Recall that the x/D locations for these three figures corresponded to the fundamentally important positions: the beginning of subharmonic resonance aided by the upstream influence of the unsteady pressures at the lip; the saturation of the fundamental mode which provides weak feedback at f_0 to the lip; and the saturation of the subharmonic mode which provides strong feedback at $f_0/2$ to the lip. By interpreting these figures, the low amplitude forcing at f_0 has diminished the upstream influence of the lip by decoupling the nonlinear phase locking between the f_0 and $f_0/2$ modes. In essence, in this initial region, there are two frequency sources feeding the unsteady pressure field at the lip. The first is due to the acoustic input from sine generator and speaker. The second is due to the response of the jet and the closed-loop feedback at $f_0/2$. These two frequencies, being derived from separate sources are therefore not phase locked.

We can observe some subtle effects of the lack of initial phase locking of these two modes. For example, in the beginning of secondary subharmonic growth in Figure 16. Generally, we have observed a sharp change in subharmonic growth which was accompanied by a rapid change of phase velocity of the subharmonic to match that of the fundamental. With the mild forcing at f_0 , we observe a much more gradual change in growth of $f_0/2$, which is also delayed relative to the downstream development of fundamental. This can also be traced to a reduction in the local spreading rate of the jet between $x/D = 0.35$ and 0.45 in Figure 11, which is in the region of secondary subharmonic growth. Past the point of pairing, the spreading rate of the jet forced at f_0 has overcome this early reduction and slightly surpasses that of the natural jet. This behavior might be due to the observed additional nonlinear phase locking with the column mode (160 Hz) that appeared only in this specific forced case.

A recent paper by Monkewitz (1988) predicts subharmonic resonance on the basis of the fundamental mode achieving a minimum amplitude, $u'_f/U_j = 0.015$. Based on this, we can compare the amplitudes of the fundamental axisymmetric modes at the x-position of first enhanced subharmonic growth (x_r/D) for the different cases examined here. In the unforced jet, 1L condition, at both Reynolds numbers, the maximum streamwise velocity fluctuation levels seen from Figures 8 and 14 was roughly the same and equal to 0.0003. This of course is considerably below that predicted by Monkewitz, but in experiments, the absolute levels are somewhat ambiguous since they vary with the spectral band width. For example, Monkewitz's good agreement to Drubka's $Re=42,000$ data is two orders of magnitude off when the amplitudes are converted to

the standard 1 Hz band width, as we had done in the comparison in Figure 7.

Therefore, rather than compare absolute levels, we can look to effects of different initial conditions, most notably between unforced and forced jets. Specifically, this involves our jet at $Re=70,000$, with the spatial growth curves seen in Figures 14 and 16. In this comparison, for the forced jet, we observe an almost order of magnitude increase in the threshold level of the fundamental mode at the x-position of secondary subharmonic growth. Since we have interpreted the effect of our mild forcing to disrupt the natural feedback mechanism and delay subharmonic resonance, this result seems to support that mechanism over one strictly based on amplitude alone.

Forcing the jet at a frequency 25 percent higher than the natural selected f_0 resulted in a more strongly organized jet with strong feedback at $1/11f_0$ and $5/11f_0$ frequencies. The initially shorter wavelength fundamental frequency and strong resonant interaction with the $5/11f_0$ mode resulted in faster spreading in this case.

The nonexact $5/11f_0$ "subharmonic" in this case was likely selected by the flow in order to satisfy a constraint imposed by feedback that there be an integer number of wavelengths from the feedback source, in this case the x/D of pairing, back to the lip of the jet. This selection resulted in a much stronger nonlinear phase locking and a high degree of organization of a broad band of discrete sum and difference modes that was not apparent with weak harmonic forcing. This exercise demonstrates an efficient means of control of the early jet instabilities by making use of the natural upstream influence of the lip and the downstream influence of related modes which are associated with the energetic motions of vortex formation and successive pairings.

Observations such as resonant mode selection and harmonic spectra indicate that a convectively unstable flow (a cold axisymmetric jet) in the presence of feedback appears to share some of the features related to absolutely unstable flows. Such a distinction has profound implications with respect to the possible existence of deterministic chaos in jets as well as issues of flow controllability.

VII. Conclusions

The results documented the existence and exponential growth of the two fundamental modes in the axisymmetric jet shear layer, namely the axisymmetry and $m = \pm 1$ helical modes. In the case of the former, a parametric interaction between it and its subharmonic was found to exist and to be an important factor in the early development of the jet. This interaction was marked by a matching of their phase velocities, requiring a decrease in the phase velocity of the subharmonic, the resonant exchange of energy from the fundamental mode to the subharmonic, and a resulting enhanced exponential growth of the subharmonic mode leading to large amplitudes and eventual energy saturation. A key factor of this process was the recursive feedback of energy from the sites of the first vortex rollup and vortex pairing. These acted to produce a self-forced phase locking of the initial fundamental and subharmonic modes which later led to the early resonant growth of the subharmonic mode, within two fundamental axisymmetric wavelengths. This resonant feedback mechanism gives the jet some of the features attributed to absolutely unstable flows, which may have profound implications on their controllability.

Underlying the resonant organization seen in the axisymmetric modes was the development and growth of the $m = \pm 1$ helical modes. Short-time

spectral estimates had been used to document the temporal evolution of the helical and axisymmetric modes. These indicated a lack of coexistence and apparent nondeterministic switching between these two fundamental states. At any time, the dominant mode was likely to be the one with the higher initial forcing level due to randomly arriving axisymmetric or nonaxisymmetric disturbances at the jet lip. With this scenario in mind, a low dimensional temporal model based on the competition between these two modes may be useful to capture the early random nature which we attributed to spectral broadening at these mode frequencies in the initial jet exit region.

Acknowledgment

This work has been supported by grants from the U.S. Air Force Office of Scientific Research, particularly F49620-80-C-0053 which was monitored by Major Michael Francis, and F49620-86-C-0165 which is monitored by Dr. James McMichael.

References

- Acton, E. 1980. A Modelling of Large Eddies in an Axisymmetric Jet. J. Fluid Mech., 98, pp. 1-31.
- Bruun, H. H. 1977. A Time-Domain Analysis of the Large-Scale Flow Structure in a Circular Jet. Part 1. Moderate Reynolds Number. J. Fluid Mech., 83, pp. 641-672.
- Corke, T. and Mangano, R. 1989. Resonant Growth of Three Dimensional Modes in Transitioning Blasius Boundary Layers. J. Fluid Mech. 209, p. 93.
- Corke, T. and Mangano, R. 1987. Transition of a Boundary Layer: Controlled Fundamental-Subharmonic Interactions. Proceedings of the Symposium on Turbulent Management and Relaminarization, Bangalore, India, Published by Springer-Verlag, pp. 199-213.
- Corke, T. C., Shakib, F. and Nagib, H. M. 1985. Effects of Low Amplitude Forcing on Axisymmetric Jet Flows. AIAA-85-0573, AIAA Shear Flow Control Conference, Boulder, Colorado.

Drubka, R. E. 1981. Instability in Near Field of Turbulent Jets and Their Dependence on Initial Conditions and Reynolds Number. Ph.D. Thesis, Illinois Institute of Technology.

Ffowcs Williams, J. E. and Kempton, A. J. 1978. The Noise from the Large-Scale Structures of a Jet. J. Fluid Mech. 84, p. 673.

Hasselmann, K. Munk, W. and Mc Donald 1963. Bispectrum of Ocean Waves. Proceedings of Symposium on Time Series Analysis, Edited by M. Rosenblatt, John Wiley, New York, pp. 125-139.

Hinich, M. J. and Clay, C. S. 1968. The Application of the Discrete Fourier Transform in the Estimation of Power Spectra, Coherence, and Bispectra of Geophysical Data. Reviews of Geophysical 6 No. 3, p. 347.

Ho, Chih-Ming. 1981. Local and Global Dynamics of Free Shear Layers. Proc. of Symp. on Numerical and Physical Aspects of Aerodynamic Flows, Long Beach, CA, pp.521-533.

Ho, Chih-Ming and Huang, Lein-Saing 1982. Subharmonics and Vortex Merging in Mixing Layers. J. Fluid Mech., 119, p. 443.

Ho, Chih-Ming and Huerre, P. 1984. Perturbed Free Shear Layers. Ann. Rev. Fluid Mech., 16, pp. 365-424.

Hussain, A.K.M.F. and Clark, A. R. 1981. On the Coherent Structure of the Axisymmetric Mixing Layer: A Flow Visualization Study. J. Fluid Mech., 104, pp. 263-295.

Hussain, A. K. M. F. and Zaman, K. B. M. Q. 1981. The Preferred Mode of the Axisymmetric Jet. J. Fluid Mech., 110, p. 39.

Kelly, R. E. 1967. On the Resonant Interaction of Neutral Disturbances in Inviscid Shear Flows. J. Fluid Mech., 31 p. 789.

Kibens, V. 1979. On the Role of Vortex Pairing in Jet Noise Generation. McDonnell Douglas Research Laboratory Report.

Knisely, C. and Rockwell, D. 1981. Self-sustained low-frequency Components in an Impinging Shear Layer. J. Fluid Mech., 116, pp. 157-187.

Laufer, J. and Zhange, J. X. 1983. Unsteady Aspects of a Low Mach Number Jet. Phys. Fluids, 26, p. 1740.

Lii, K. S., Rosenblatt, M., and Van Atta, C. 1976. Bispectral Measurements in Turbulence. J. Fluid Mech., 77, pp. 45-62.

Mattingly, G. E. and Chang, C. C. 1974. Unstable Waves on an Axisymmetric Jet Column. J. Fluid Mech., 65, pp. 541-560.

Michalke, A. 1965. On Spatially Growing Disturbance in an Inviscid Shear Layer. J. Fluid Mech., 23, pp. 521-544.

- Michalke, A. 1971. Instabilität eines Kompressiblen Ruten Friestrahls unter Berücksichtigung des Einflusses der Strahlgrenzschichtdicke, Z. Flugwiss., 9, pp. 319-328.
- Miksad, R., Jones, F. and Powers, E. 1983. Measurements of Nonlinear Interactions During Natural Transition of a Symmetric Wake. Phys. Fluids, 26, 6, pp 1402-1409.
- Miksad, R. W., Jones, F. L., Powers, E. J., Kim, Y. C., and Khadra, L. 1982. Experiments on the Role of Amplitude and Phase Modulations During Transition to Turbulence. J. Fluid Mech., 123, pp. 1-29.
- Monkewitz, P. A. 1988. Subharmonic Resonance, Pairing and Shredding in the Mixing Layer. J. Fluid Mech., 188, p. 223.
- Peterson, R. A. 1978. Influence of Wave Dispersion on Vortex Pairing in a Jet. J. Fluid Mech., 89, p. 469.
- Pierrehumbert, R. T. 1980. The Structure and Stability of Large Vortices in an Inviscid Flow. Ph.D. Thesis, Massachusetts Institute of Technology.
- Reisenthel, P. and Corke, T. C. 1983. Application of Spectral Entropy Methods to Non-stationary Flow Problems. Bull. 36th Amer. Physical Soc. Fluids Division Meeting.
- Sarohia, V. and Massier, P. F. 1978. Experimental Results of Large-Scale Structure in Jet Flows and Their Relation to Jet Noise Production. AIAA J., 16, p. 831.
- Shakib, F. 1985. Evolution and Interaction of Instability Modes in an Axisymmetric Jet, M.S. Thesis, Illinois Institute of Technology.
- Solis, R., Miksad, R. and Powers, E. 1986. Experiments on the Influence of Mean Flow Unsteadiness on the Laminar-Turbulent Transition of a Wake. Proceedings of the Tenth Symposium on Turbulence in Liquids, Rolla, Missouri.
- Wille, R. 1963. Beiträge Zur Phänomenologie der Freistrahlen. Z. Flugwiss., 11, pp. 222-233.
- Winant, C. D. and Browand, F. K. 1974. Vortex Pairing: the Mechanism of Turbulent Mixing-layer Growth at Moderate Reynolds Number. J. Fluid Mech., 63, pp. 237-255.

Appendix A.

Maximum Entropy Spectral Estimates

Recently spectral estimations based on the Maximum Entropy Method (MEM) have been adopted at IIT in the analysis of data series from unsteady fluid dynamics experiments. The main feature of this method is that it allows the determination of spectra for exceedingly short time series where methods based on DFT fail to produce accurate results. Extensive documentation of the characteristics and usage of this method has been done by us on time series derived in this and other fluid flows. The following discussion is meant to provide an overview of the theoretical basis for the method and to document its use in this study.

The maximum entropy time series is determined to be the one in which the entropy, $E(S)$, of the power spectrum, $S(\omega)$, defined as shown below,

$$E(S) = - \int_{-\omega_n}^{\omega_n} \log S(\omega) d\omega \quad (1)$$

is a maximum, under the constraint that the spectrum also be consistent with the first $M+1$ measured lags of the autocorrelation function, R_k . The autocorrelation is defined to be the inverse Fourier transform of the power spectrum, namely

$$R_k = \int_{-\omega_n}^{\omega_n} S(\omega) e^{i\omega k \Delta t} d\omega \quad (-M \leq k \leq M) \quad (2)$$

Here, Δt is the time increment, k is a discrete time index, ω is the angular frequency, ω_n is the angular Nyquist frequency, and i is the square root of negative one.

Defining the Lagrange multiplier λ_k , the solution for $S(\omega)$ which maximizes this variational problem is

$$S(\omega) = \frac{1}{\sum_{k=-M}^M \lambda_k e^{i\omega k \Delta t}} \quad (3)$$

where the λ 's satisfy the constraint equation 2.

The traditional transform notation is obtained by setting

$$z = e^{i\omega \Delta t} \quad (4)$$

where

$$S(z) = \dots + R_{-M} z^{-M} + \dots + R_0 + \dots + R_M z^M + \dots$$

and R_0, R_1, \dots, R_M are known $M+1$ auto-correlation coefficients. The

power spectrum, $S(\omega)$, is related to $S(z)$ by the z transform of the autocorrelation function namely,

$$S(z) \leftrightarrow (z = e^{-i\omega \Delta t}) \quad (5)$$

In factored form,

$$S(z) = \frac{\sigma_M^2}{A_M(z) A_M(z^{-1})} \quad (6)$$

where

$$A_M(z) = 1 + a_1 z + \dots + a_M z^M \quad (7)$$

is a $(M+1)$ length prediction error filter with variance σ_M^2 . Expressing equation 6 in the frequency domain and combining it with equation 3, one obtains the MEM spectral estimate

$$S(\omega) = \frac{1}{\sum_{k=-M}^M \lambda_k e^{i\omega k \Delta t}} = \frac{\sigma_M^2}{(A_M(\omega))^2} \quad (8)$$

The right-hand side of the equality in equation 8 can also be found by modeling the time series as an auto-regressive series of order M .

Such a model therefore maximizes the entropy in the time series.

The problem that remains is to compute the prediction-error

filter coefficients $A_M(\omega)$, and to determine of the "best" order, M , for the auto-regressive model. The approach to the first part is due to Burg (1967) who suggested minimizing the average of the sum of both the mean square prediction and hindsight errors, P_1 , to find the first coefficient a_{11} . For an N -point data series, that quantity is defined as

$$P_1 = \frac{1}{2(N-1)} \sum_{i=1}^{N-1} (x_{i+1} + a_{11}x_i)^2 + (x_i + a_{11}x_{i+1})^2 \quad (9)$$

The remaining coefficients are then found from the Toeplitz recursion formula

$$a_{M,s} = a_{M-1,s} + a_{M,M} a_{M-1,M-s} \quad ; s = 1, \dots, M-1 \quad (10)$$

The order, M , of the prediction-error filter remains to be the key parameter in calculating the most appropriate spectrum. Many empirical studies utilizing synthetic data having known spectral content have been conducted in order to develop measures of determining the proper filter length. Reisenthel and Corke (1983) have studied a number of these and identified four regions of behavior with increasing filter length, M . In the first region, A, with the shortest filter lengths, only a smooth envelope of the distribution having no spectral peaks is obtained. In the next region, B, which starts from the end of the region A, with increased filter length, the spectral peaks that emerge have the correct amplitude and frequency, however, some combining of closely neighboring peaks may occur at lower frequencies. In region C all of the spectral peaks are identified, however, their amplitudes may not be correct. Finally in region D peak splitting is observed to occur, leading to incorrect spectral estimations.

These criteria were used to determine the proper filter length for the analysis of the data series in this study. In its approach here the

method was used to detect the existence of the various modes and to follow their spatial and temporal evolution, without interest in their amplitude. Therefore a prediction-error filter length was chosen which placed us within the above described region C. Due to the nature of the time series, all of the selection criteria had shown a broad C region for all of our flow cases.

Appendix B.

Cross-Bicoherence

The cross-bicoherence is a measure of the nonlinear phase locking between frequencies in three time series. In a general sense, these time series are represented as $u_1(t)$, $u_2(t)$, and $u_3(t)$. For simplicity these are not shown to be a function of their spatial position. The Fourier transforms of these time series are defined as

$$u_i(t) = \int_{-\infty}^{\infty} \tilde{u}_i(\omega) e^{i\omega t} d\omega \quad ; \quad i = 1, 2, 3 \quad (11)$$

$$\tilde{u}_i(\omega) = 1/(2\pi) \int_{-\infty}^{\infty} u_i(t) e^{-i\omega t} dt \quad (12)$$

where (\sim) denotes the transformed function in the wave number domain, ω is the wave number, and i is the square root of negative one.

The first three statistical moments of these time series are given as:

the first order,

$$R_i = \langle u_i(t) \rangle \quad ; \quad i = 1, 2, 3 \quad (13)$$

the second order,

$$R_{ij}(\tau) = \langle u_i(t) u_j(t+\tau) \rangle \quad ; \quad i, j = 1, 2, 3 \quad (14)$$

and the third order,

$$R_{ijk}(\tau_1, \tau_2) = \langle u_i(t) u_j(t+\tau_1) u_k(t+\tau_2) \rangle \quad ; \quad i, j, k = 1, 2, 3 \quad (15)$$

where $\langle \rangle$ is the realizations ensemble average, and τ is a time delay.

The first order moment is the mean of the time series. The second order moment is the correlation. The correlation is a measure of the linear interaction between quantities in the two time series. The correlation can also be determined from the Fourier transform of the time series, namely

$$R_{ij}(\tau) = 1/(2\pi) \int_{-\infty}^{\infty} \langle \tilde{u}_i(\omega) \tilde{u}_j^*(\omega) \rangle e^{i\omega\tau} d\omega \quad (16)$$

where (*) denotes the complex conjugate. The product $\langle \tilde{u}_i(\omega) \tilde{u}_j^*(\omega) \rangle$ is the cross-spectrum between $u_i(t)$ and $u_j(t)$.

The third order moment is a measure of the linear and quadratic interaction between the three time series, as seen in equation 15. In order to better appreciate the origin of the bispectrum it is helpful to derive the relation between the third order moment and the Fourier transform of the time series. The Fourier transform of R_{ijk} is

$$\begin{aligned} \bar{R}_{ijk}(\omega_1, \omega_2) = 1/(4\pi^2) \int_{-\infty}^{\infty} \langle u_i(t) u_j(t+r_1) u_k(t+r_2) \rangle \\ e^{-i\omega_1 t_1 - i\omega_2 t_2} dr_1 dr_2 \end{aligned} \quad (17)$$

Notice that \bar{R}_{ijk} is a function of two wave numbers ω_1 and ω_2 .

In the above equation, replacing the time series by their Fourier integral transform, as defined in equation 12, and interchanging the order of integration and the ensemble average, the following equation can be derived,

$$\begin{aligned} \bar{R}_{ijk}(\omega_1, \omega_2) = 1/(4\pi^2) \int_{-\infty}^{\infty} \langle \tilde{u}_i(\omega) \tilde{u}_j(\omega') \tilde{u}_k(\omega'') \rangle \\ e^{-i\omega_1 \tau_1 - i\omega_2 \tau_2} e^{i\omega t + i\omega'(t+\tau_1) + i\omega''(t+\tau_2)} \\ d\omega d\omega' d\omega'' d\tau_1 d\tau_2 \end{aligned} \quad (18)$$

By taking advantage of Kronecker delta function relations

$$1/(2\pi) \int_{-\infty}^{\infty} e^{i(\omega_1 - \omega_2)\tau} d\tau = \delta(\omega_1 - \omega_2) \quad (19)$$

and

$$\int_{-\infty}^{\infty} f(\omega') (\omega - \omega') d\omega' = f(\omega) \quad (20)$$

equation 18 simplifies to

$$\bar{R}_{ijk}(\omega_1, \omega_2) = \int_{-\infty}^{\infty} \langle \bar{u}_i(\omega) \bar{u}_j(\omega_1) \bar{u}_k(\omega_2) \rangle e^{i(\omega+\omega_1+\omega_2)t} d\omega \quad (21)$$

With the assumption that the series is stationary, rigorous algebra is needed to simplify the above equation. However, in order to avoid these steps, a shorter approach can be adopted. Knowing that the result of the above integral is not a function of time, which requires $\omega+\omega_1+\omega_2$ to be equal to zero, the following relation is derived

$$\bar{R}_{ijk}(\omega_1, \omega_2) = \langle \bar{u}_i(\omega) \bar{u}_j(\omega_1) \bar{u}_k(\omega_2) \rangle \delta(\omega+\omega_1+\omega_2) \quad (22)$$

Defining $\bar{u}^*(\omega)$ as the complex conjugate of $u(\omega)$ then,

$$\bar{R}_{ijk}(\omega_1, \omega_2) = \langle \bar{u}_i(\omega_1) \bar{u}_j(\omega_2) \bar{u}_k^*(\omega_1+\omega_2) \rangle \quad (23)$$

The function $\bar{R}_{ijk}(\omega_1, \omega_2)$ is the cross-bispectrum which will be denoted here as $B_{ijk}(\omega_1, \omega_2)$.

What is the physical interpretation of this quantity? The cross-bispectrum is a measure of the energy transfer resulting from the quadratic interaction of two wave numbers in two time series to produce their sum or difference wave number in a third time series. In the present experiment which dealt with resonant mode interactions, it was more instructive to measure the level of the nonlinear phase-locking rather than the amount of energy transfer. Therefore, the normalized cross-bispectrum, or cross-bicoherence, was utilized.

The cross-bicoherence (CBC) is defined as

$$\beta_{ijk}(\omega_1, \omega_2) = \frac{|B_{ijk}(\omega_1, \omega_2)|^2}{\langle |\bar{u}_i(\omega_1)|^2 |\bar{u}_j(\omega_2)|^2 \rangle \langle |\bar{u}_k(\omega_3)|^2 \rangle} \quad (24)$$

where i , j , and k refer to the time series with wave numbers ω_1 , ω_2 , and ω_3 , respectively, and $(| |)$ is the modulus of the component. These wave

numbers are related to each other such that $\omega_1 + \omega_2 + \omega_3 = 0$. In the experiment in the jet, the time series were the streamwise velocity fluctuations, acquired at different spatial locations in the shear layer, $u(x, r, t)$, and the simultaneous pressure fluctuations at the lip of the jet, $p(r, t)$. The subscripts i, j and k refer to these two measured time series. For the case when i, j , and k are the same, $\beta_{ijk}(\omega_1, \omega_2)$ will be symmetric with respect to ω_1 and ω_2 , and will be referred to as the auto-bicoherence (ABC).

In the above equation, the calculation of the quantity

$$\langle |\tilde{u}_i(\omega_1)|^2 |\tilde{u}_j(\omega_2)|^2 \rangle \quad (25)$$

requires considerable computer time and memory storage for respectively sized transforms. Therefore, it is convenient to replace it by the quantity

$$\langle |\tilde{u}_i(\omega_1)|^2 \rangle \langle |\tilde{u}_j(\omega_2)|^2 \rangle \quad (26)$$

To justify this substitution, several tests had been conducted on synthetic data having a known cross-bicoherence. In order to simulate the types of time series we could expect from this experiment various levels of random noise were also superposed on the tested time series. It was found that for a large enough number of realization averages, the difference between these two quantities was small. Therefore making this simplification, the final form of the cross-bicoherence used was

$$\beta_{ijk}(\omega_1, \omega_2) = \frac{|B_{ijk}(\omega_1, \omega_2)|^2}{\langle |\tilde{u}_i(\omega_1)|^2 \rangle \langle |\tilde{u}_j(\omega_2)|^2 \rangle \langle |\tilde{u}_k(\omega_3)|^2 \rangle} \quad (27)$$

From the Schwarz inequality, the cross-bicoherence falls between the values of zero and one. When, from realization to realization the degree of triple phase-locking

$$\theta_i(\omega_1) + \theta_j(\omega_2) - \theta_k(\omega_3) \quad (28)$$

is high, the CBC will have a value close to one. Here $\theta_i(\omega_1)$ is the instantaneous circular phase angle of $\tilde{u}_i(\omega_1)$. The maximum level of the CBC estimate is however dependent on the signal-to-noise ratio of the data series. When no phase-locking exists it has a value of zero.

List of Figures

- Figure 1. Schematic of Nozzle Face Showing Azimuthal Pressure Taps and Laboratory Coordinate System for Measurements.
- Figure 2. 2D Mean Velocity Mapping, with r Normalized by D (a), and with r normalized by θ (b), and RMS Velocity Mapping in Logarithmic Scale with r normalized by θ (c) ($Re = 42,000$, 1L Case).
- Figure 3. Radial Spread of Velocity Power Spectra, in Logarithmic Scale ($Re = 42,000$, From Top: $x/D = 0.15, 0.35, 0.55$, and 0.80).
- Figure 4. 2D Spectral Amplitude Mapping of Initial Axisymmetric (a) and Subharmonic (b) Modes, with r Normalized by θ ($Re = 42,000$, 1L Case).
- Figure 5. Modulus (top) and Phase (bottom) of Initial Axisymmetric Eigenmodes ($Re = 42,000$, 1L Case).
- Figure 6. Modulus (top) and Phase (bottom) of Subharmonic Eigenmodes ($Re = 42,000$, 1L Case).
- Figure 7. Streamwise Development of Initial Axisymmetric Mode and its Subharmonic with Comparison to Drubka (1981) Performed in Same Facility. ($Re = 42,000$, 1L Case, $U/U_j = 0.6$).
- Figure 8. Streamwise Development of Initial Axisymmetric Mode and its Subharmonic ($Re = 42,000$, 1L Case, Along each Mode's Maximum Amplitude Line).
- Figure 9. Streamwise Development of Radially Integrated Amplitude of Initial Axisymmetric Mode and its Subharmonic ($Re = 42,000$, 1L Case).
- Figure 10. Streamwise Development of Phase of Initial Axisymmetric, its Subharmonic, and Difference Modes ($Re = 42,000$, 1L Case, $U/U_j = 0.6$).
- Figure 11. Streamwise Development of Momentum Thickness for Different Initial Conditions.
- Figure 12. Map of Spectral Amplitude Levels of Initial Axisymmetric Mode for Different Initial Conditions at $Re=70,000$ (From the top; 1L Condition, Forced at 2050 Hz, Forced at 2500 Hz, and 3L Condition).
- Figure 13. Map of Spectral Amplitude Levels of Subharmonic Mode for Different Initial Conditions at $Re=70,000$ (From the top; 1L Condition, Forced at 2050 Hz, Forced at 2500 Hz, and 3L Condition).
- Figure 14. Streamwise Development of Initial Axisymmetric Mode and its Subharmonic ($Re = 70,000$, 1L Case, Along each Mode's Maximum Amplitude Line).
- Figure 15. Streamwise Development of Difference and Helical Modes ($Re = 70,000$, 1L Case, Along each Mode's Maximum Amplitude Line).
- Figure 16. Streamwise Development of Initial Axisymmetric Mode and its Subharmonic ($Re = 70,000$, 1L Case, Forced at 2050 Hz, Along each Mode's Maximum Amplitude Line).

Figure 17. Modulus and Phase of $5/11 f_0$ Eigenmodes ($Re = 70,000$, 1L Case, Forced at 2500 Hz).

Figure 18. Modulus and Phase of $6/11 f_0$ Eigenmodes ($Re = 70,000$, 1L Case, Forced at 2500 Hz).

Figure 19. Streamwise Development of Initial Axisymmetric and $5/11 f_0$ Modes ($Re = 70,000$, 1L Case, Forced at 2500 Hz, Along each Mode's Maximum Amplitude Line).

Figure 20. Streamwise Development of $6/11 f_0$ and $1/11 f_0$ Modes ($Re = 70,000$, 1L Case, Forced at 2500 Hz, Along each Mode's Maximum Amplitude Line).

Figure 21. Time Evolution of MEM Velocity Spectrum ($Re = 42,000$, 1L Case, $x/D = 0.35$, $U/U_j = 0.6$).

Figure 22. Time Evolution of MEM Velocity Spectrum ($Re = 70,000$, 1L Case, $x/D = 0.25$, $U/U_j = 0.6$).

Figure 23. Time Evolution of MEM Velocity Spectrum ($Re = 70,000$, 1L Case, Forced at 2050 Hz, $x/D = 0.20$, $U/U_j = 0.6$).

Figure 24. MEM Spectral Peak Histogram of Pressure (top) and Velocity Time Series ($Re = 42,000$, 1L Case, $U/U_j = 0.6$).

Figure 25. MEM Spectral Peak Histogram of Velocity Time Series ($Re = 70,000$, 1L Case, $U/U_j = 0.6$).

Figure 26. MEM Spectral Peak Histogram of Pressure (top) and Velocity Time Series ($Re = 70,000$, 1L Case, Forced at 2050 Hz, $U/U_j = 0.6$).

Figure 27. MEM Spectral Peak Histogram of Pressure (top) and Velocity Time Series ($Re = 70,000$, 1L Case, Forced at 2500 Hz, $U/U_j = 0.6$).

Figure 28. MEM Spectral Peak Histogram of Velocity Time Series ($Re = 70,000$, 3L Case, $U/U_j = 0.6$).

Figure 29. Spectral Peak Indicator Function Time Series ($Re = 70,000$, 1L Case, $x/D = 0.25$, $U/U_j = 0.6$).

Figure 30. Streamwise Development of Spectral Peak Occurrence of Initial Axisymmetric, its Subharmonic, Helical, and Difference Modes ($Re = 42,000$, 1L Case, $U/U_j = 0.6$).

Figure 31. Streamwise Development of Spectral Peak Occurrence of Initial Axisymmetric, its Subharmonic, Helical, and Difference Modes for Different Initial Conditions at $Re = 70,000$ (From the top; 1L Condition, Forced at 2050 Hz, Forced at 2500 Hz, and 3L Condition).

Figure 32. Streamwise Development of Cross Spectral Peak Occurrence of Initial Axisymmetric and Helical Modes as Compared with Statistical Independent Line for $Re = 42,000$ (top) and $70,000$ (bottom) (1L Case, $U/U_j = 0.6$).

Figure 33. Pressure Auto-bicoherence at $Re = 42,000$ (top) and $70,000$ (bottom) (1L Case, $U/U_j = 0.6$).

Figure 34. Velocity-pressure-pressure (top) and Pressure-pressure-velocity (bottom) Cross-bicoherence at $x/D = 0.25$ ($Re = 42,000$, Case 1L).

Figure 35. Streamwise Development of Amplitude, Coherence, and Cross-bicoherence of Initial Axisymmetric Mode and its Subharmonic ($Re = 42,000$, 1L Case, $U/U_j = 0.6$).

Figure 36. Pressure-pressure-velocity Cross-bicoherence at $Re = 70,000$, $x/D = 0.15$, for Unforced Jet (top) and Jet Forced at 2050 Hz (bottom).

Figure 37. Velocity-pressure-pressure Cross-bicoherence at $Re = 70,000$, $x/D = 0.35$, for Unforced Jet (top) and Jet Forced at 2050 Hz (bottom).

Figure 38. Pressure-pressure-velocity Cross-bicoherence at $Re = 70,000$, $x/D = 0.45$, for Unforced Jet (top) and Jet Forced at 2050 Hz (bottom).

Figure 39. Velocity-pressure-pressure Cross-bicoherence at $x/D = 0.14$ (top) and Pressure-pressure-velocity Cross-bicoherence at $x/D = 0.26$ (bottom) for Jet Forced at 2500 Hz at $Re = 70,000$.

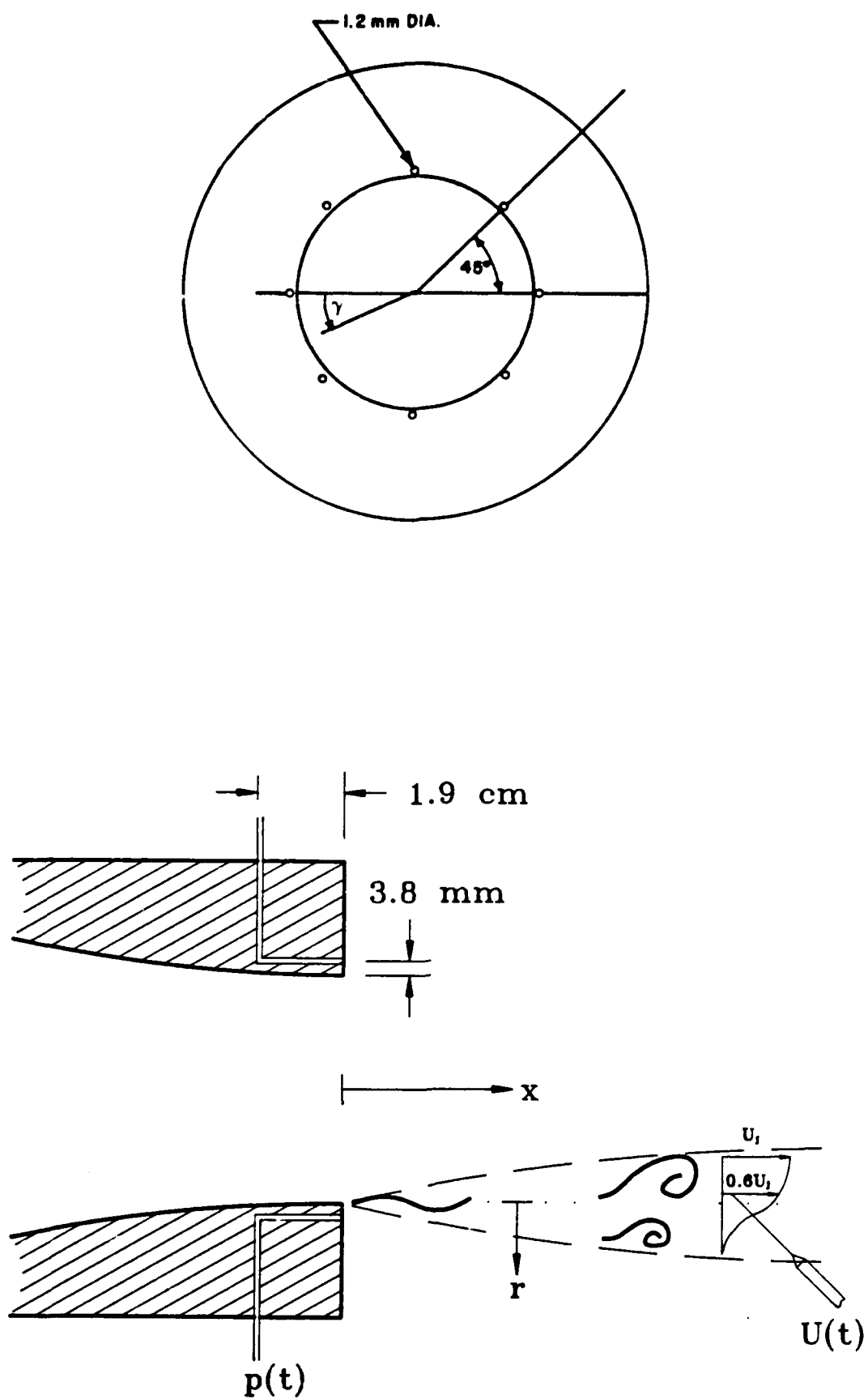


Figure 1.

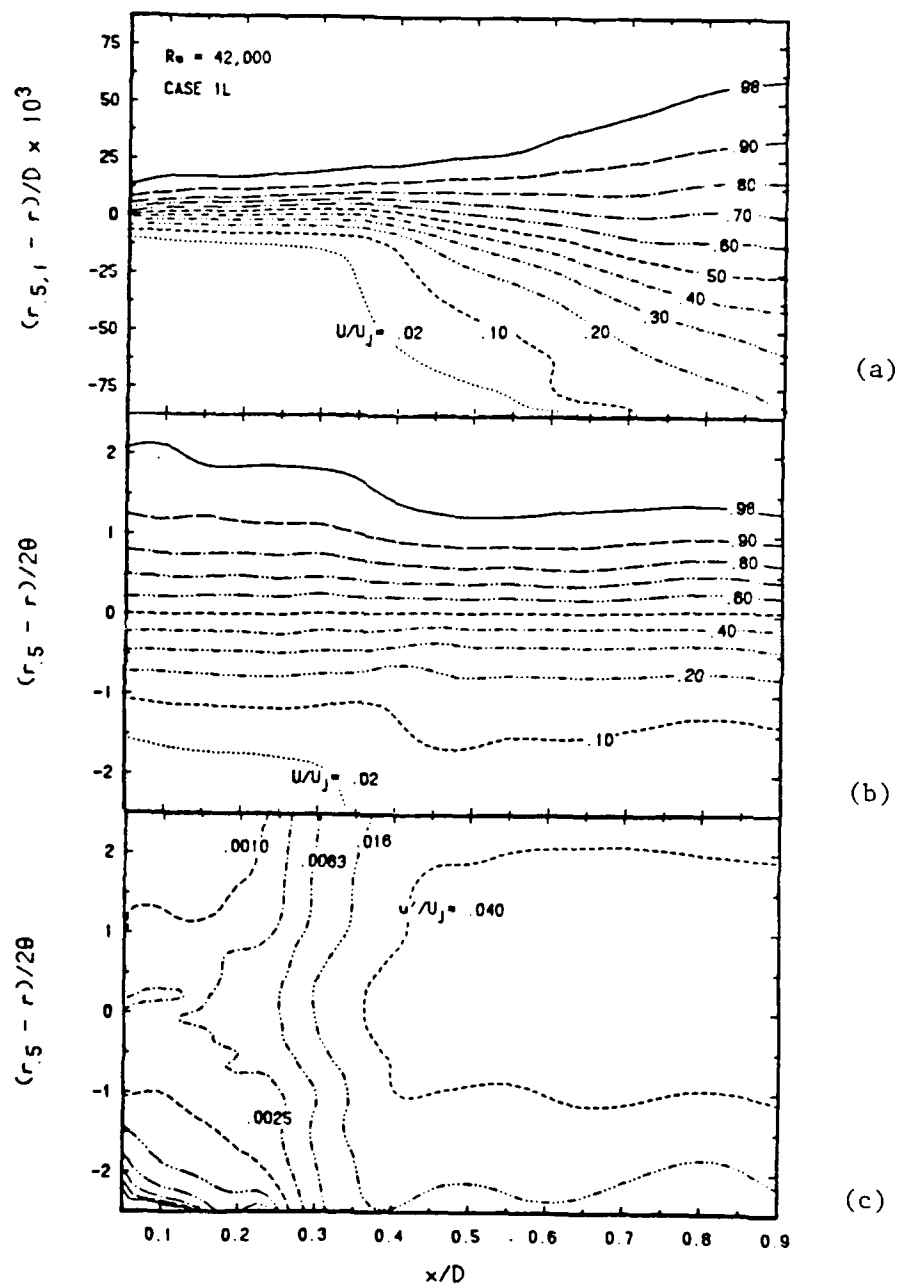


Figure 2.

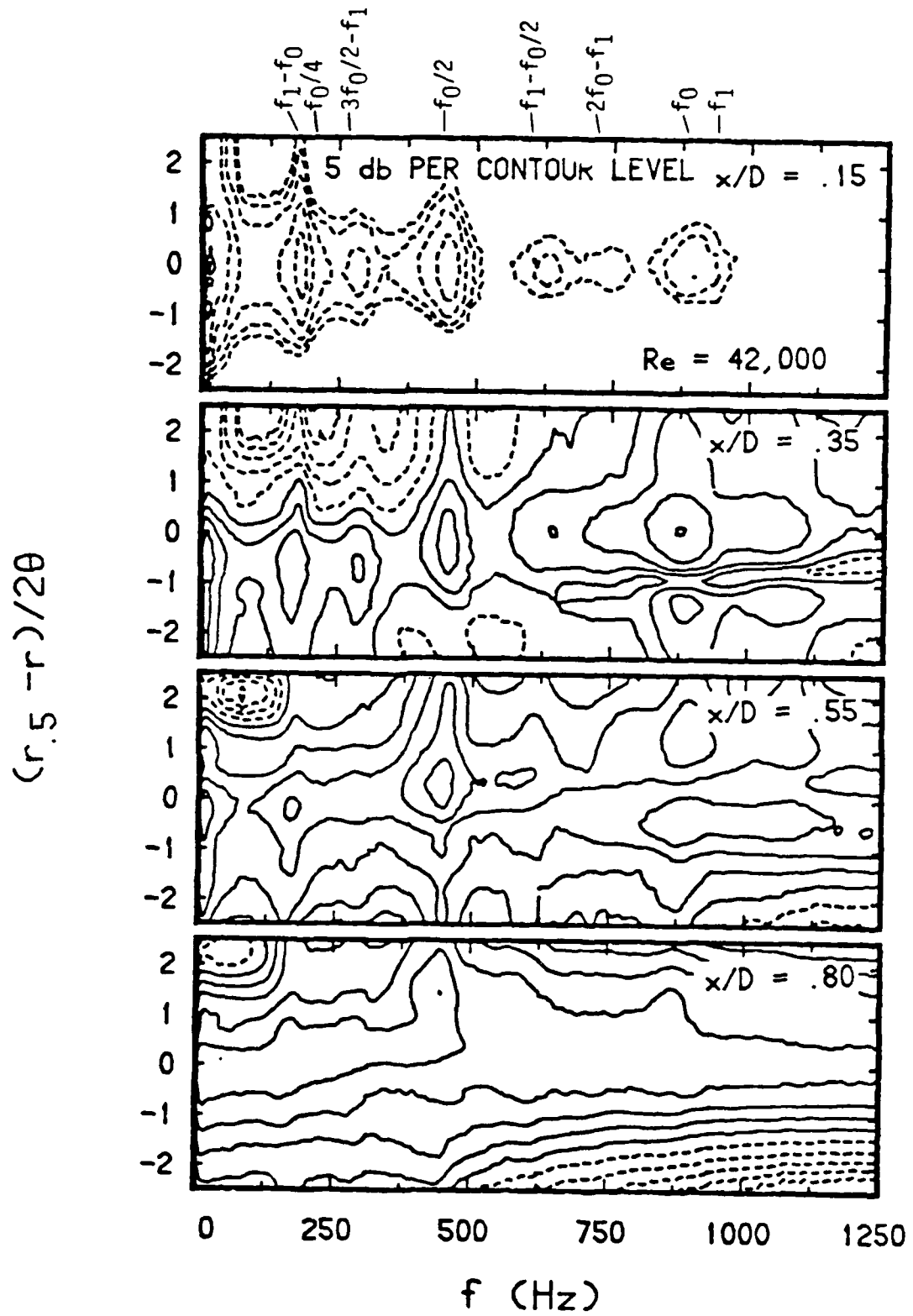


Figure 3.

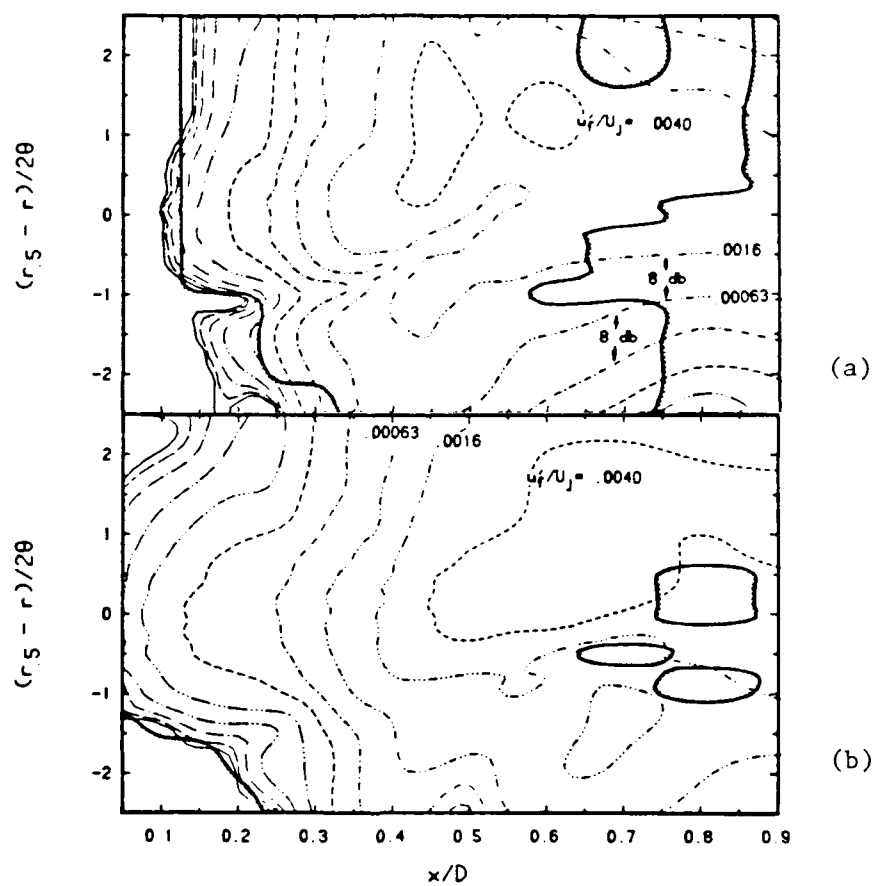


Figure 4.

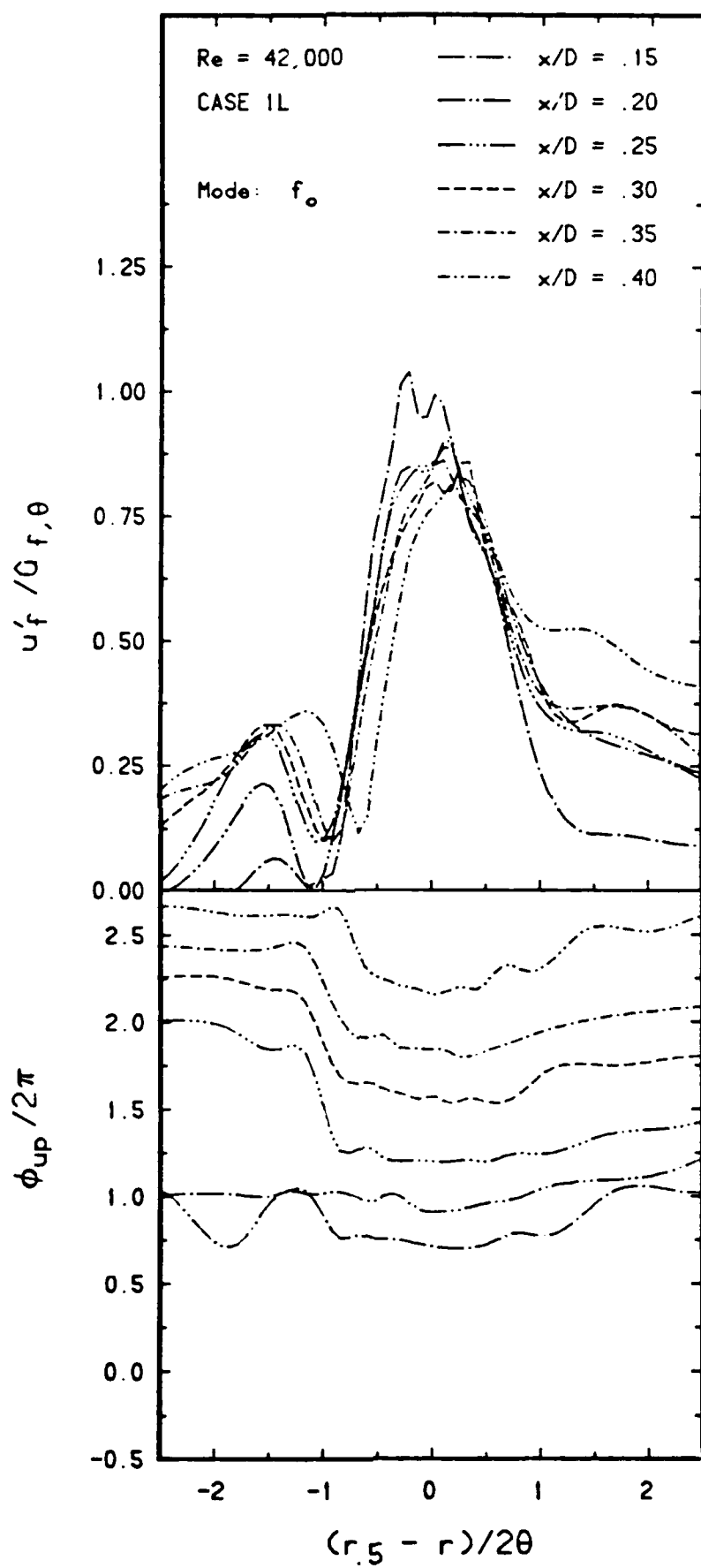


Figure 5.

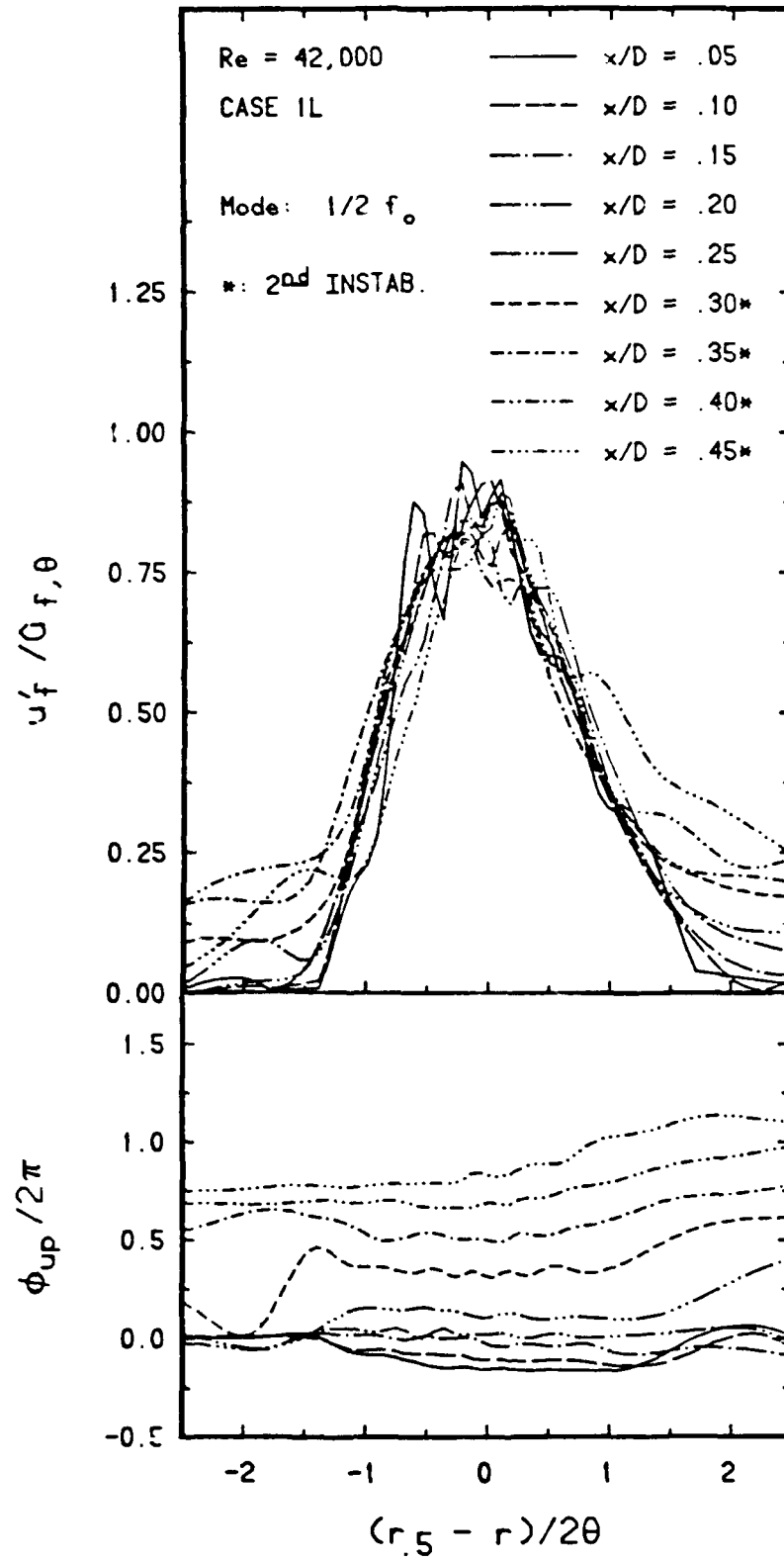


Figure 6

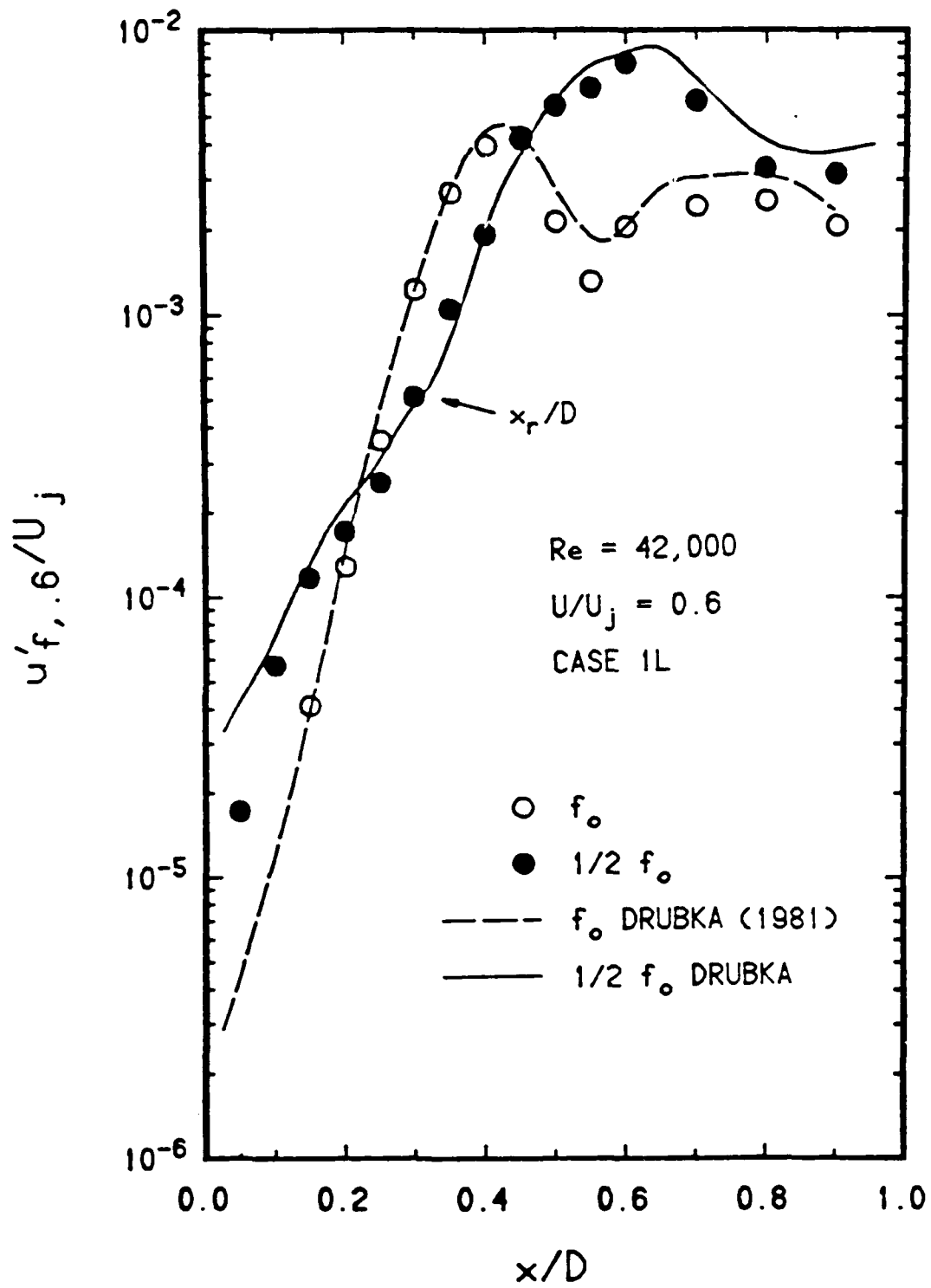


Figure 7.

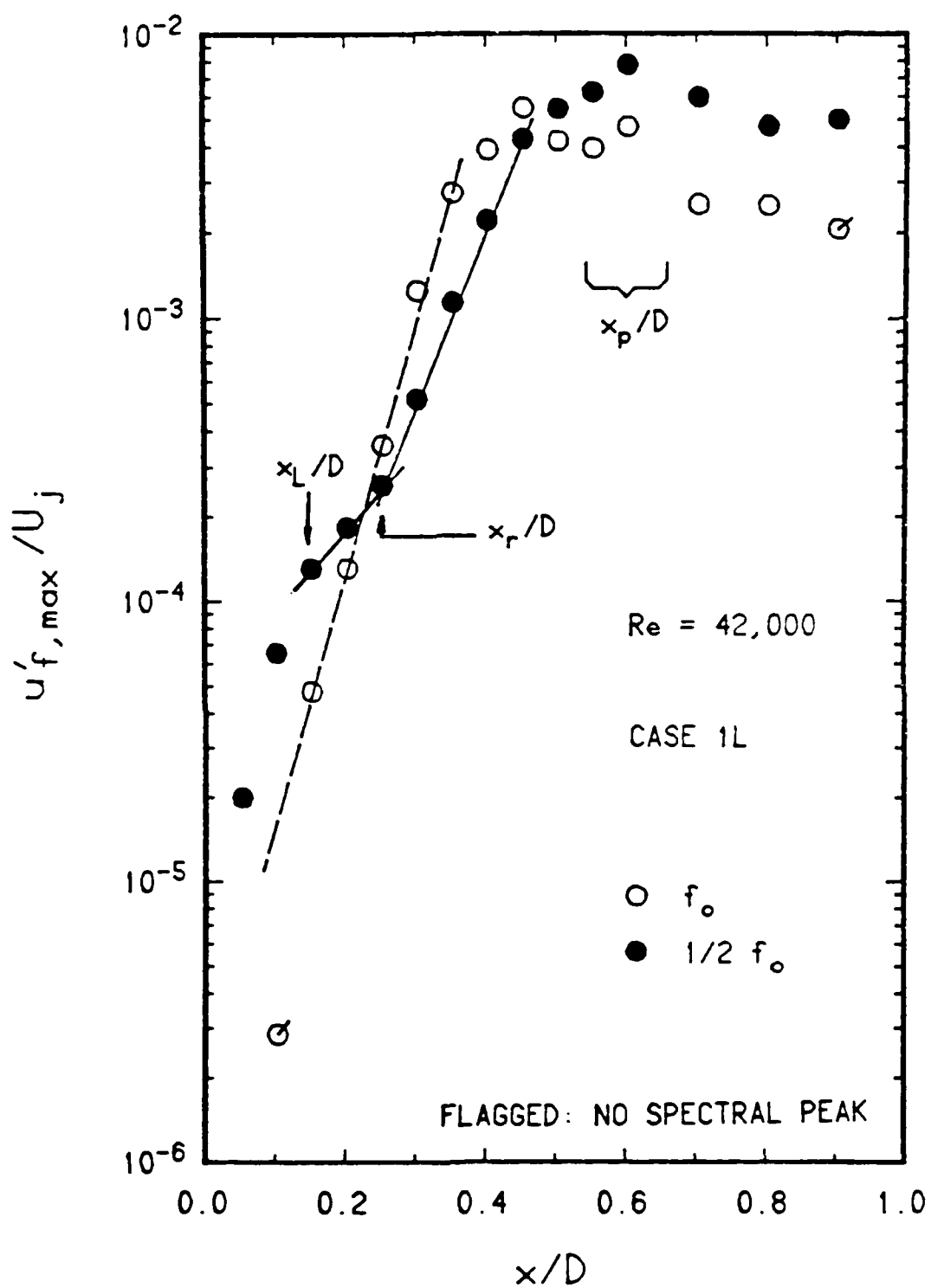


Figure 8.

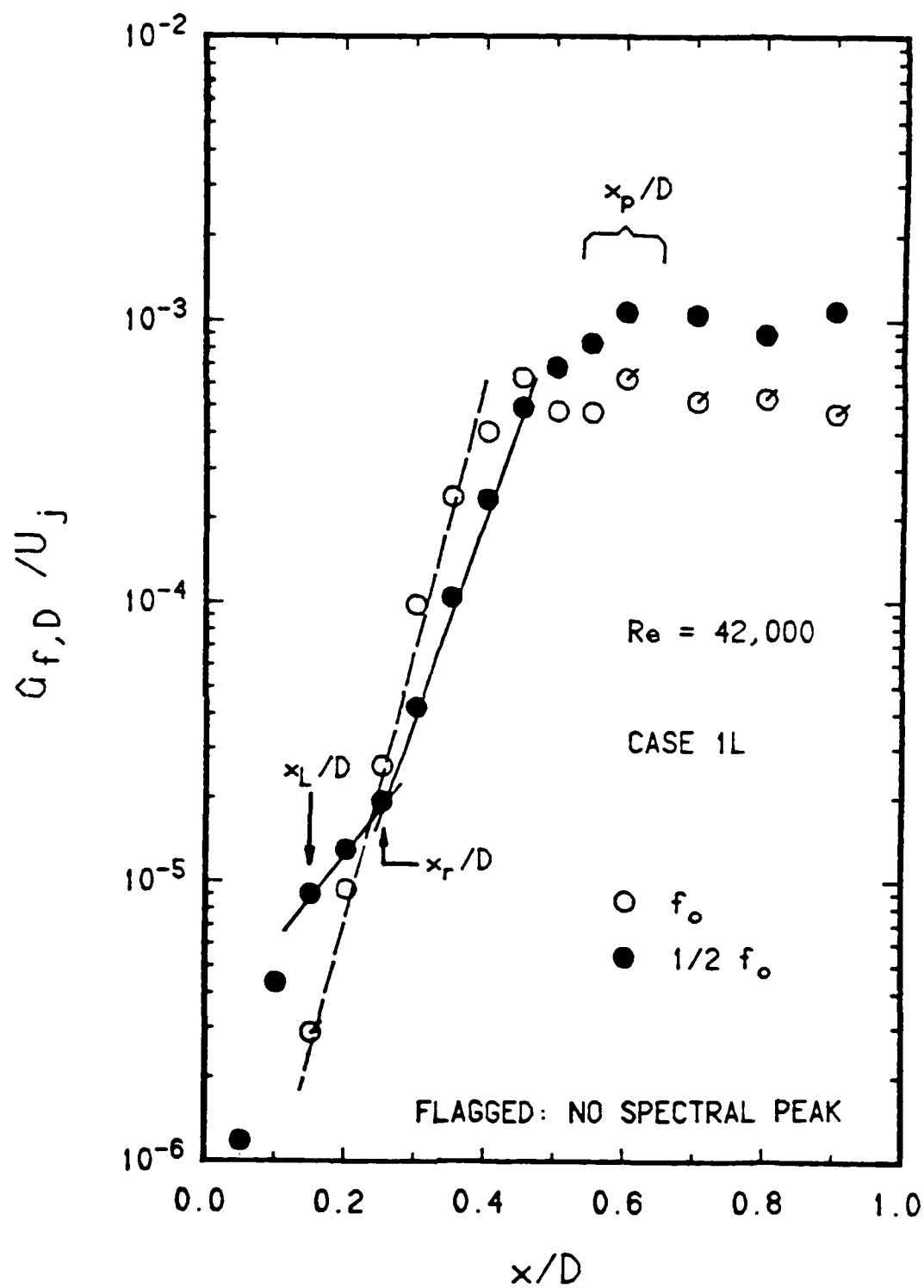


Figure 9.

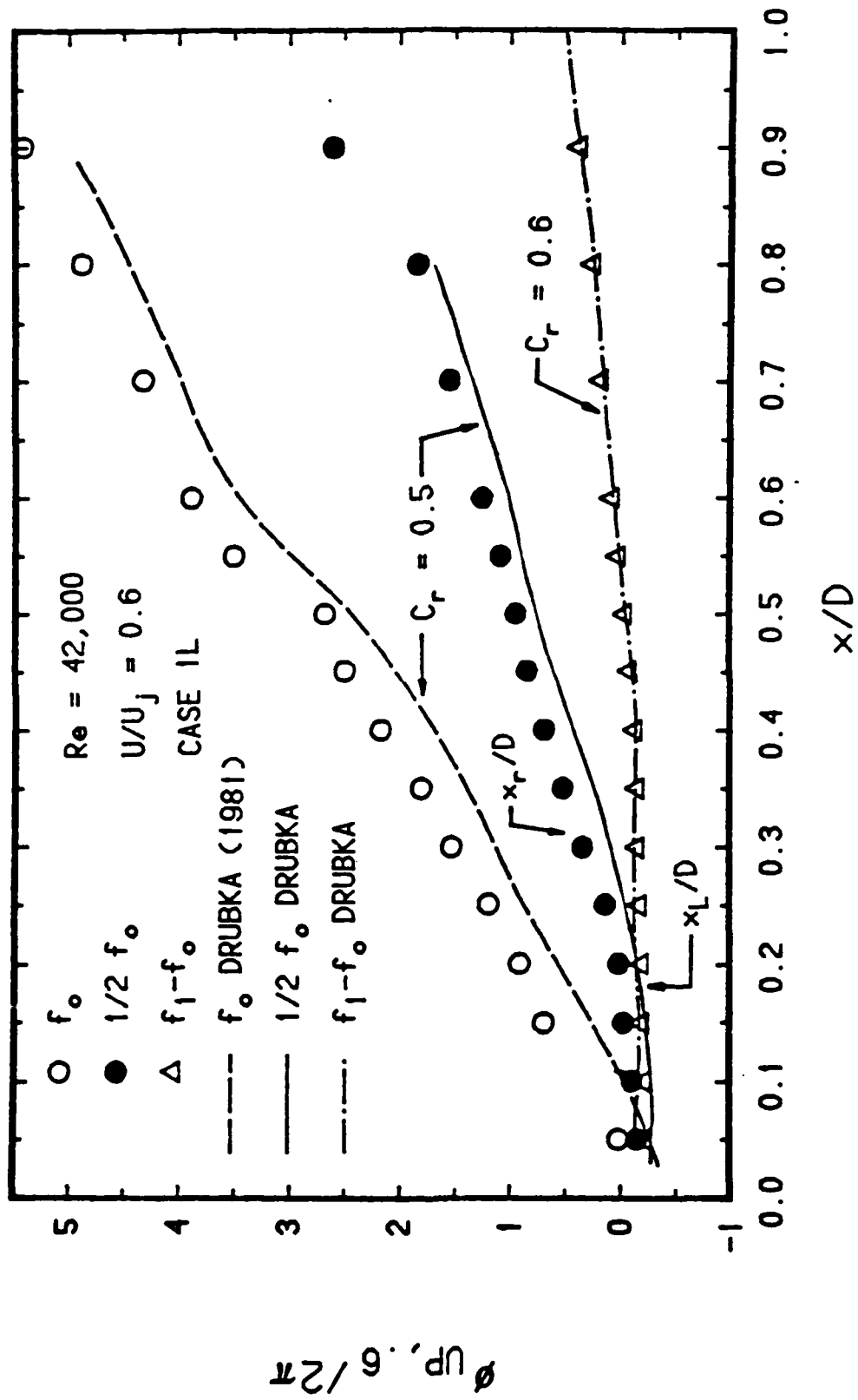


Figure 10.

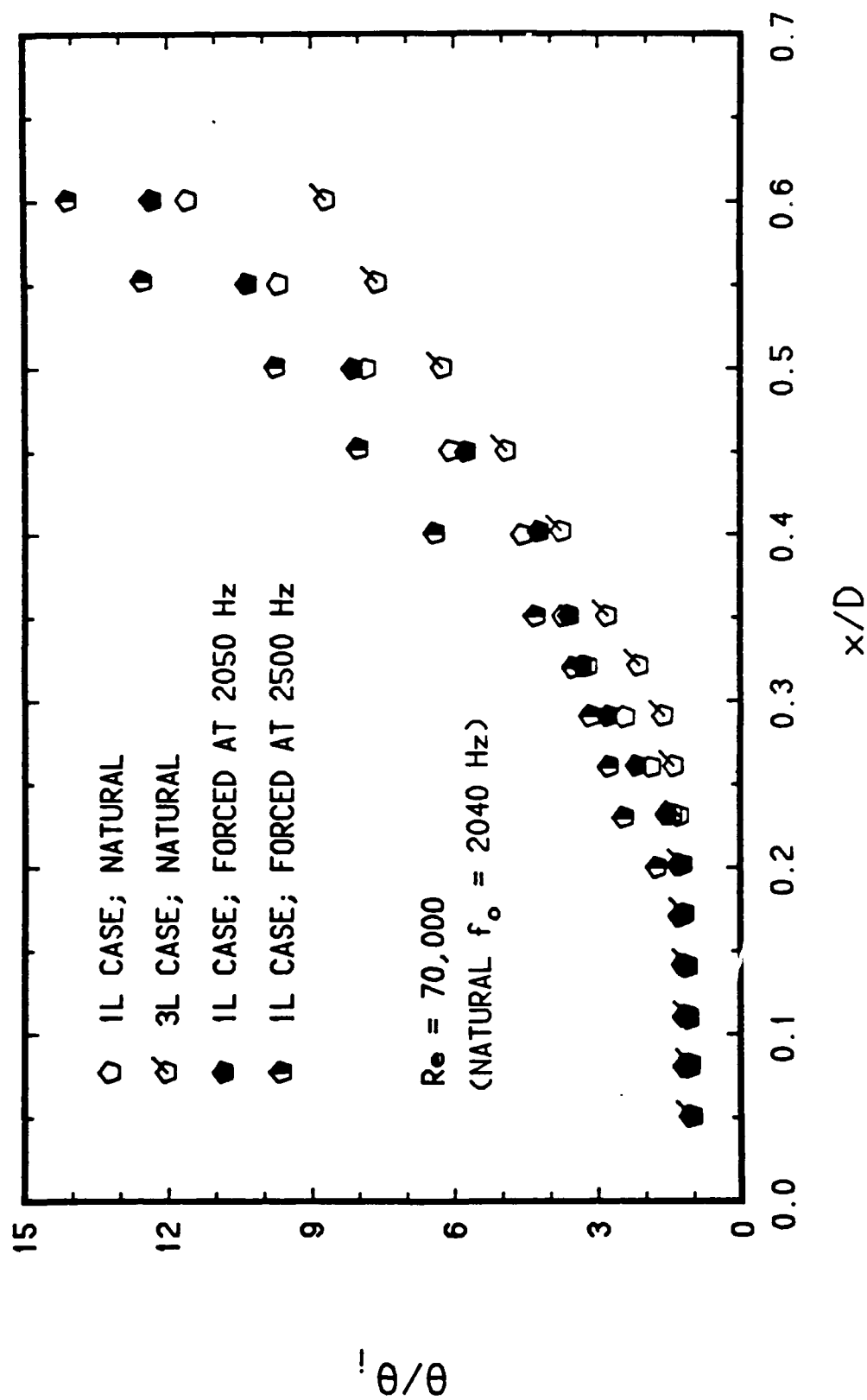


Figure 11.

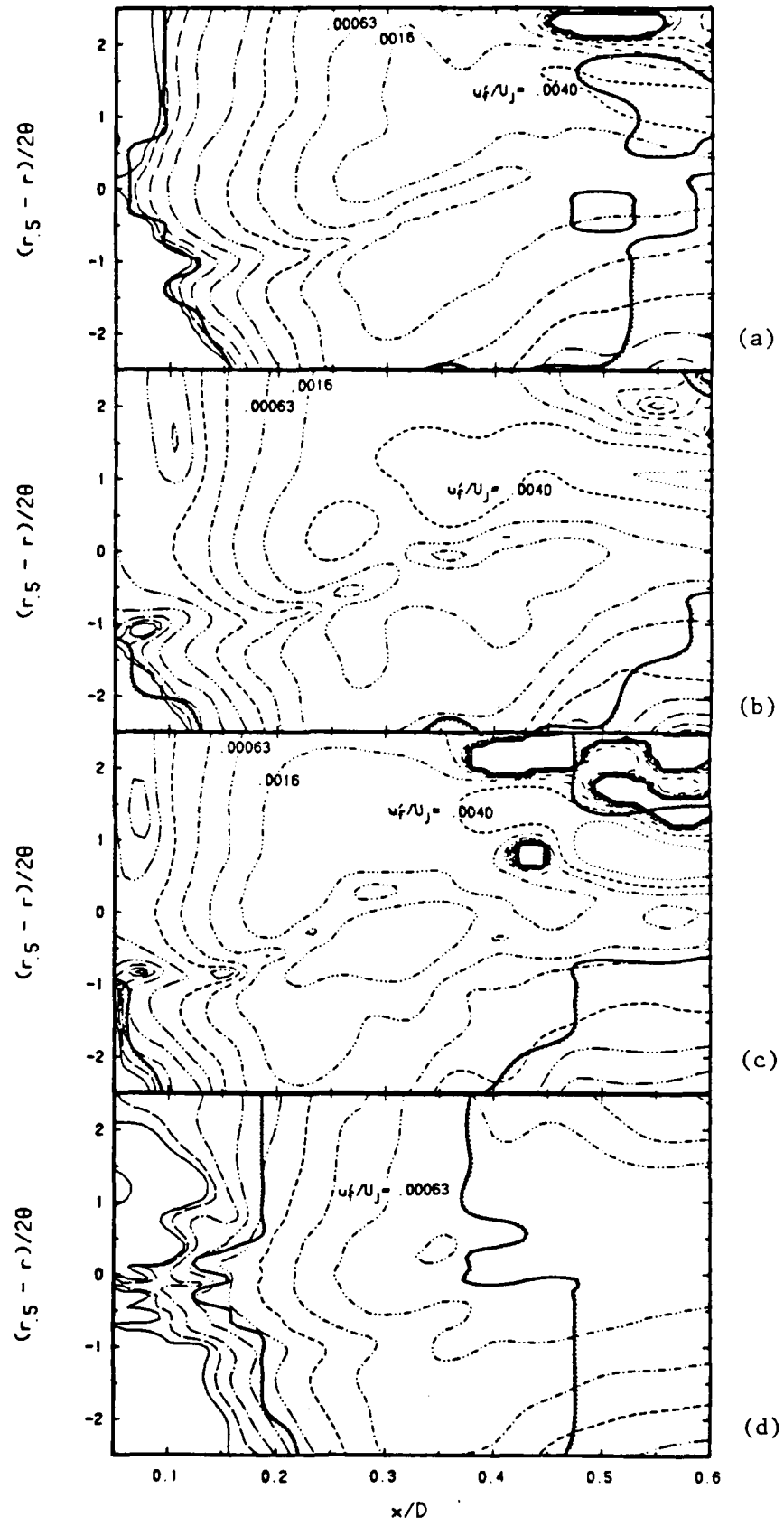


Figure 12.

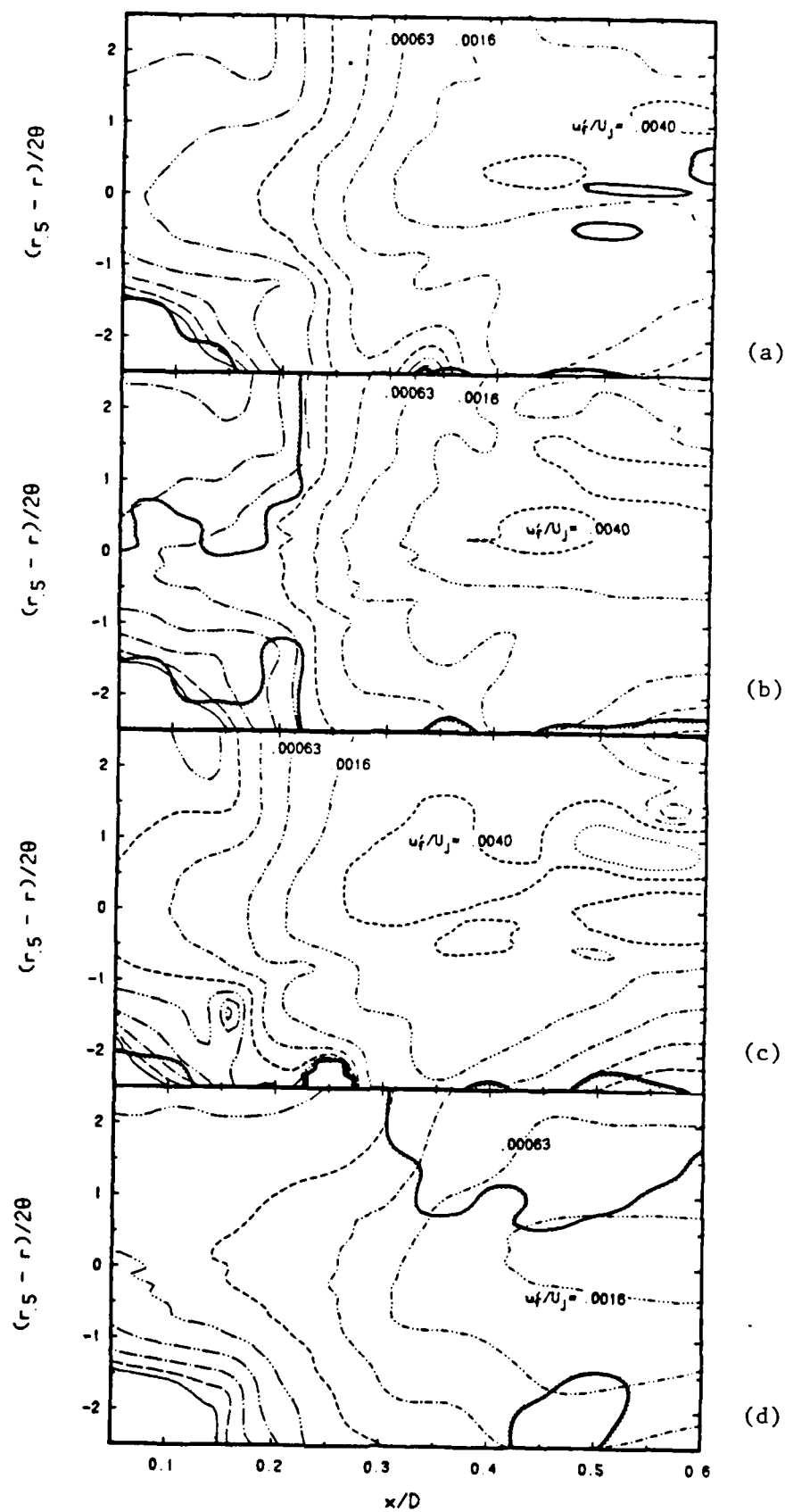


Figure 13.

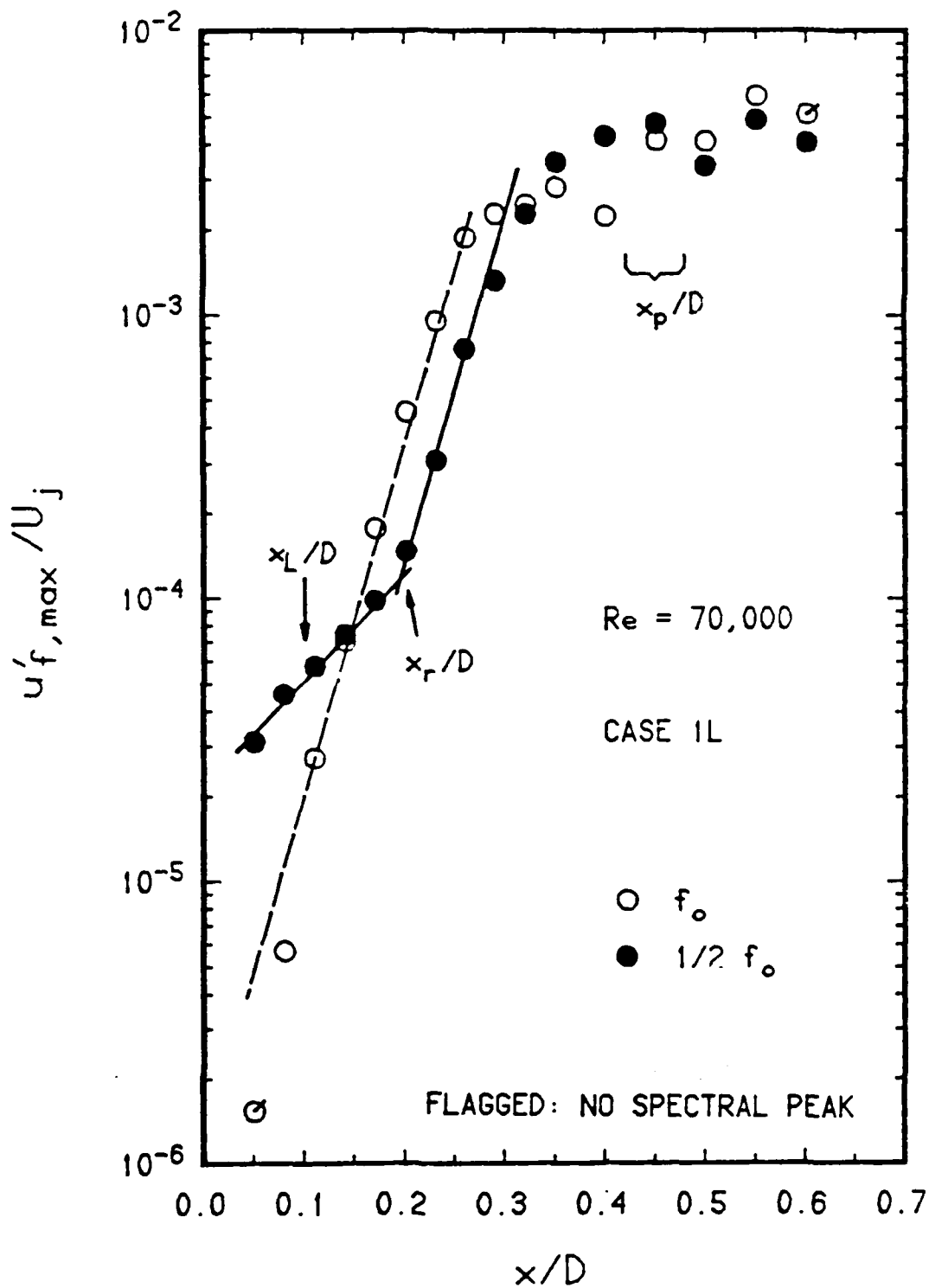


Figure 14.

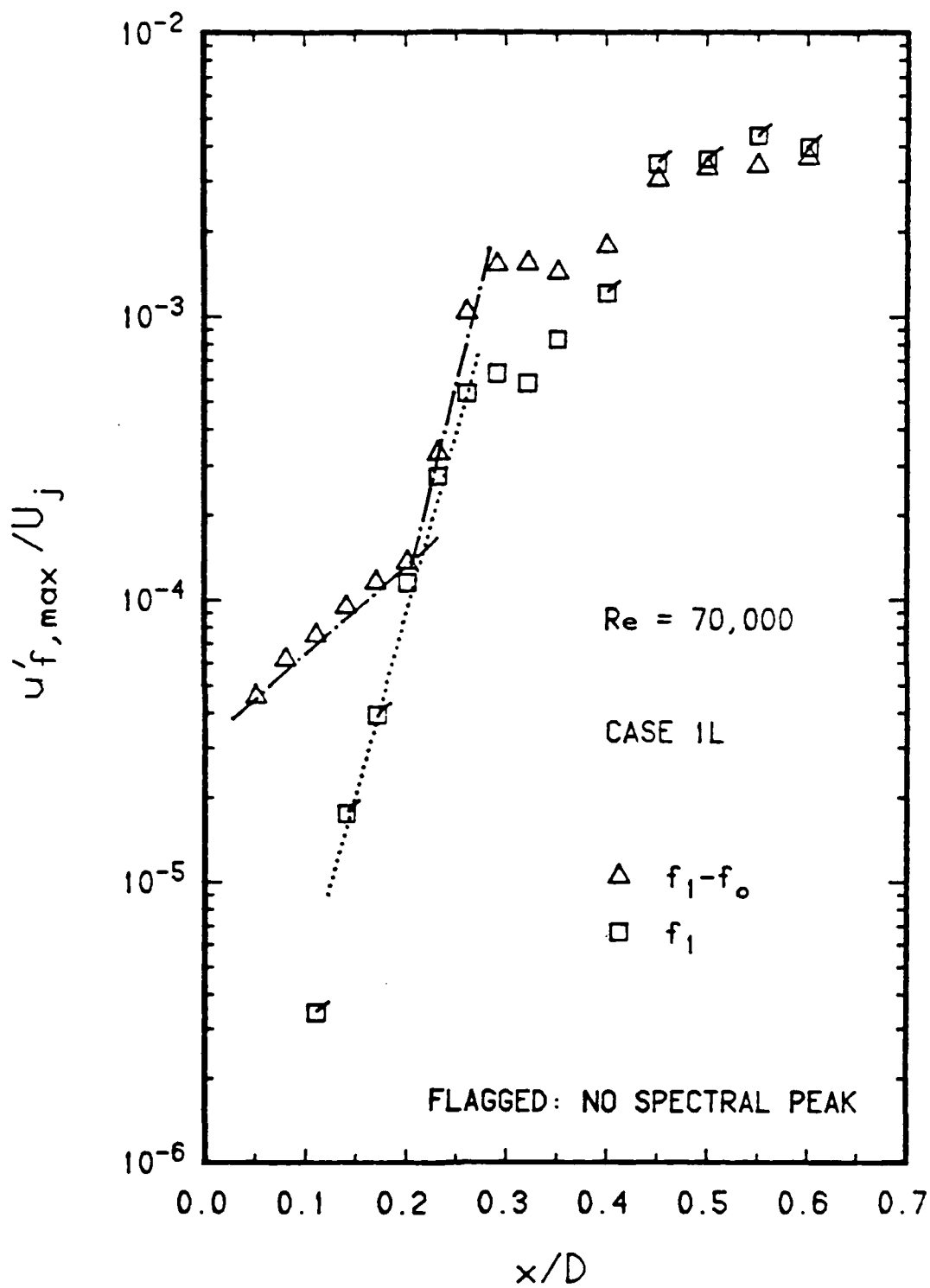


Figure 15.

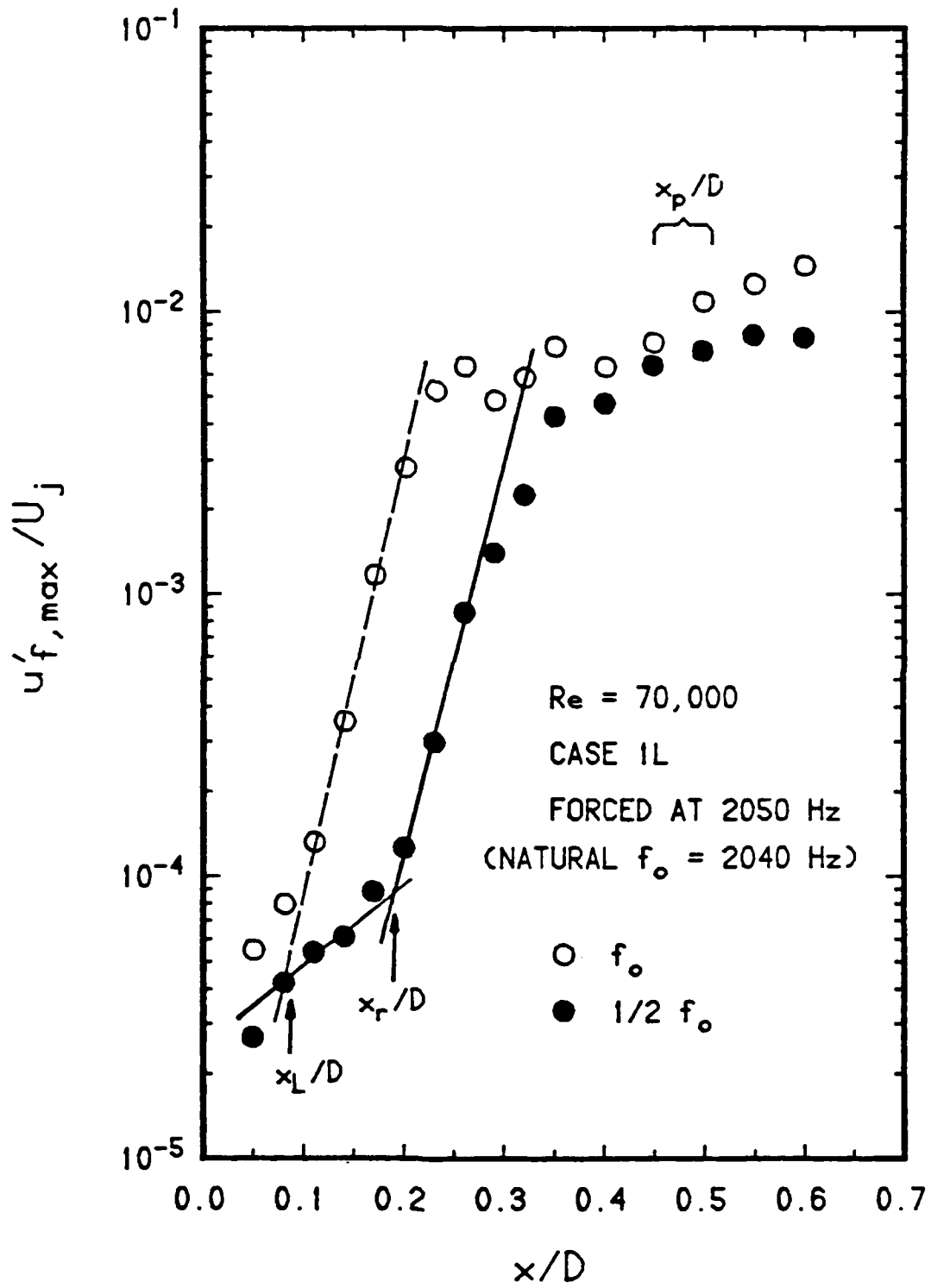


Figure 16.

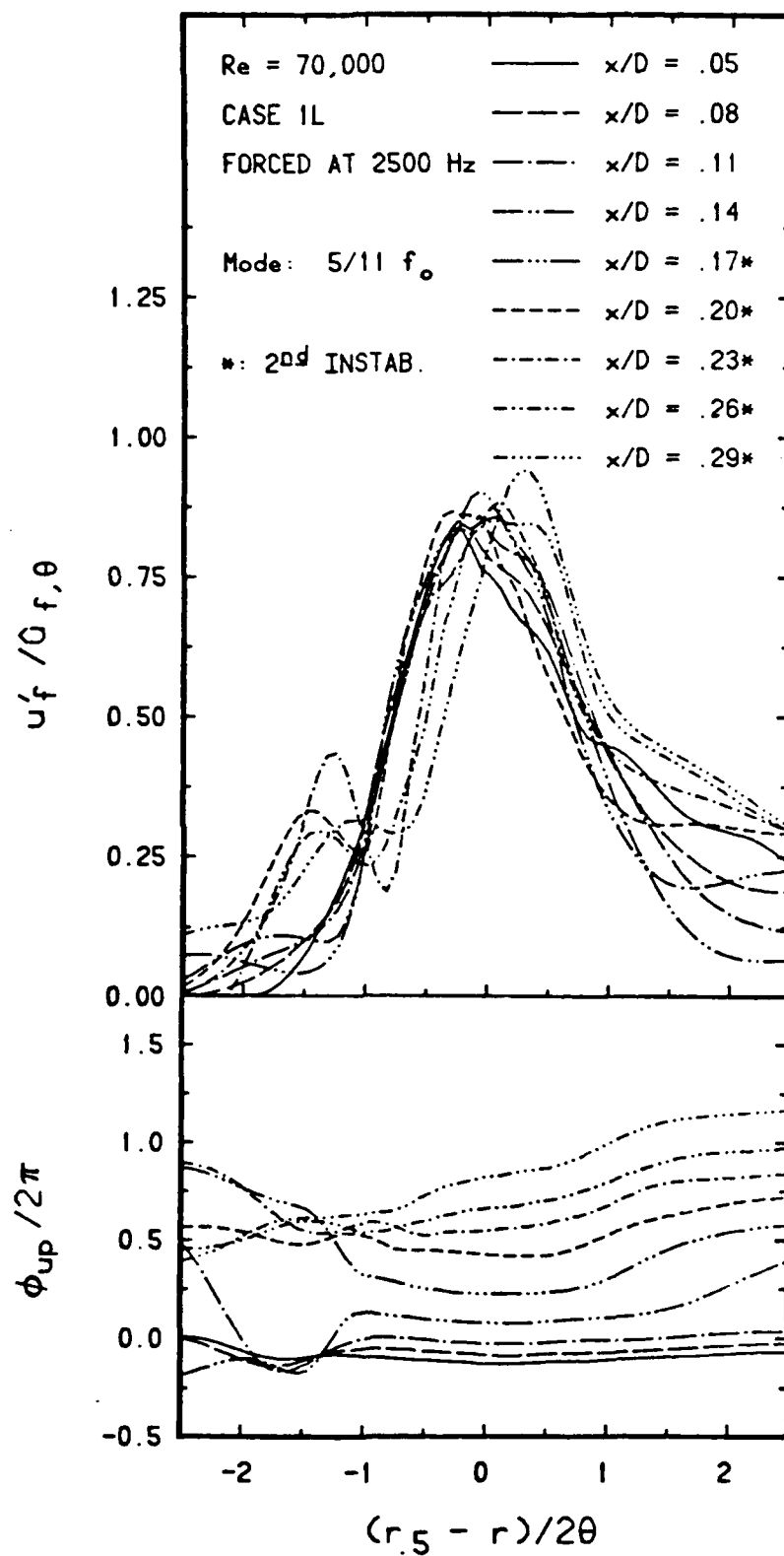


Figure 17.

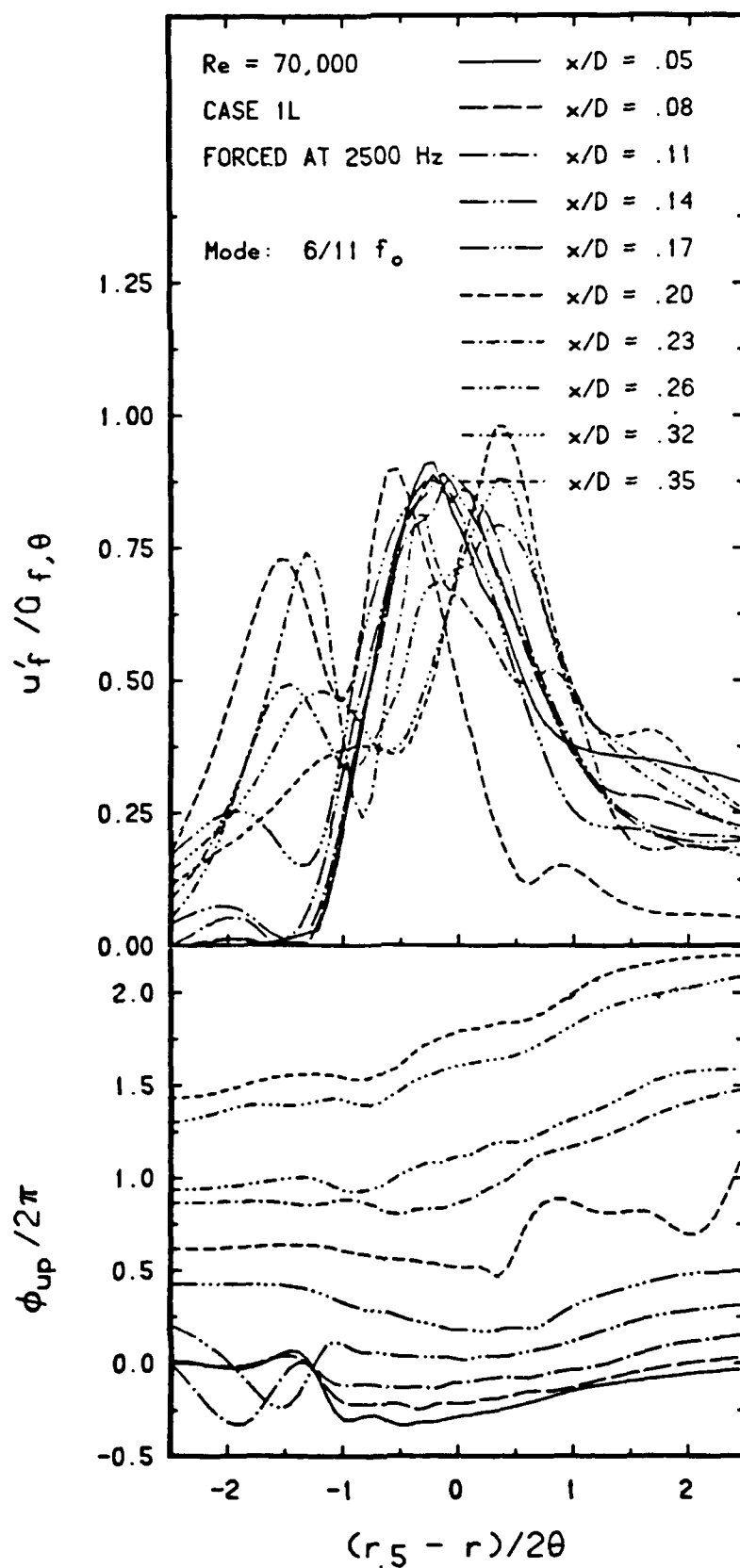


Figure 18.

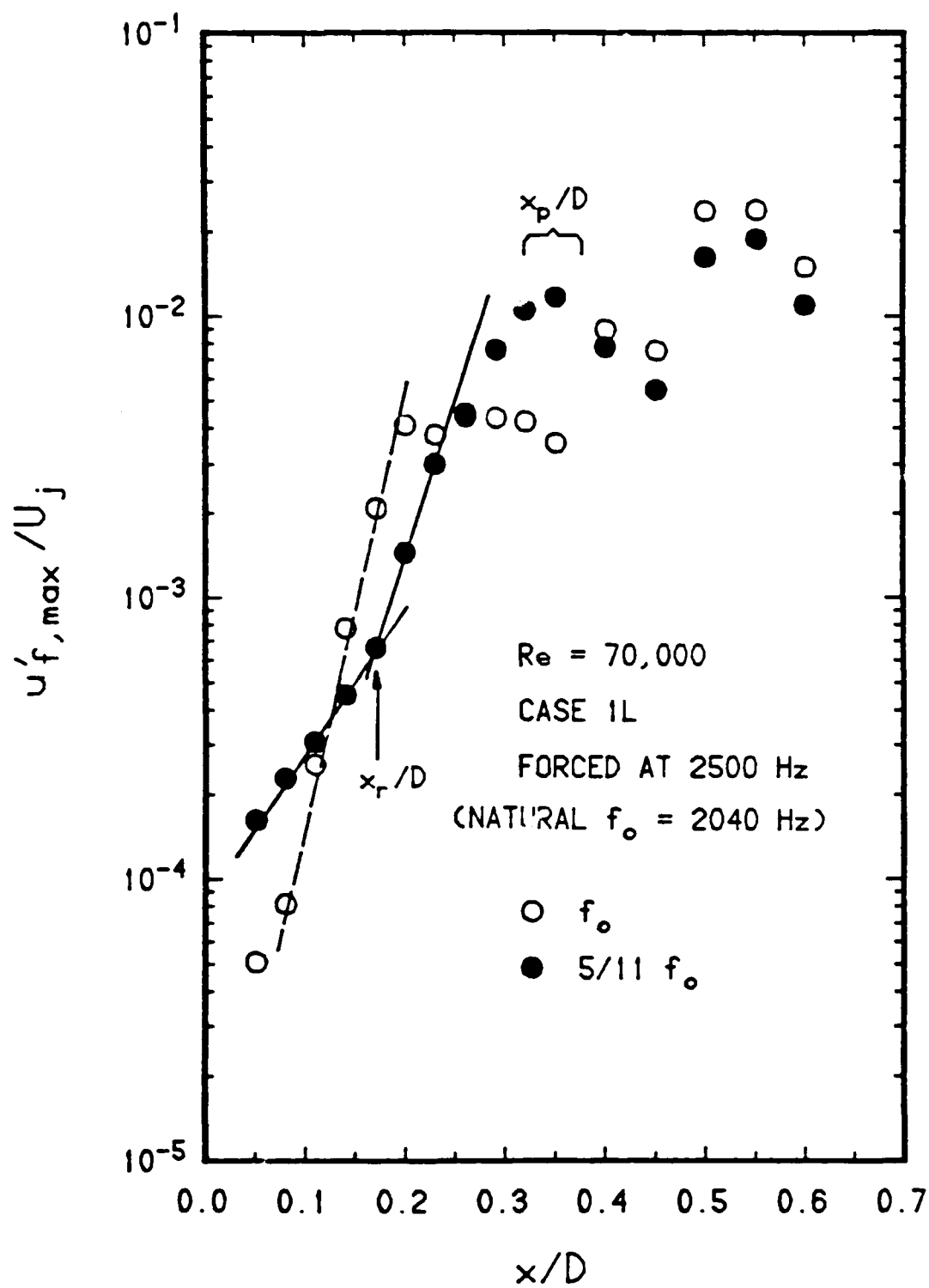


Figure 19.

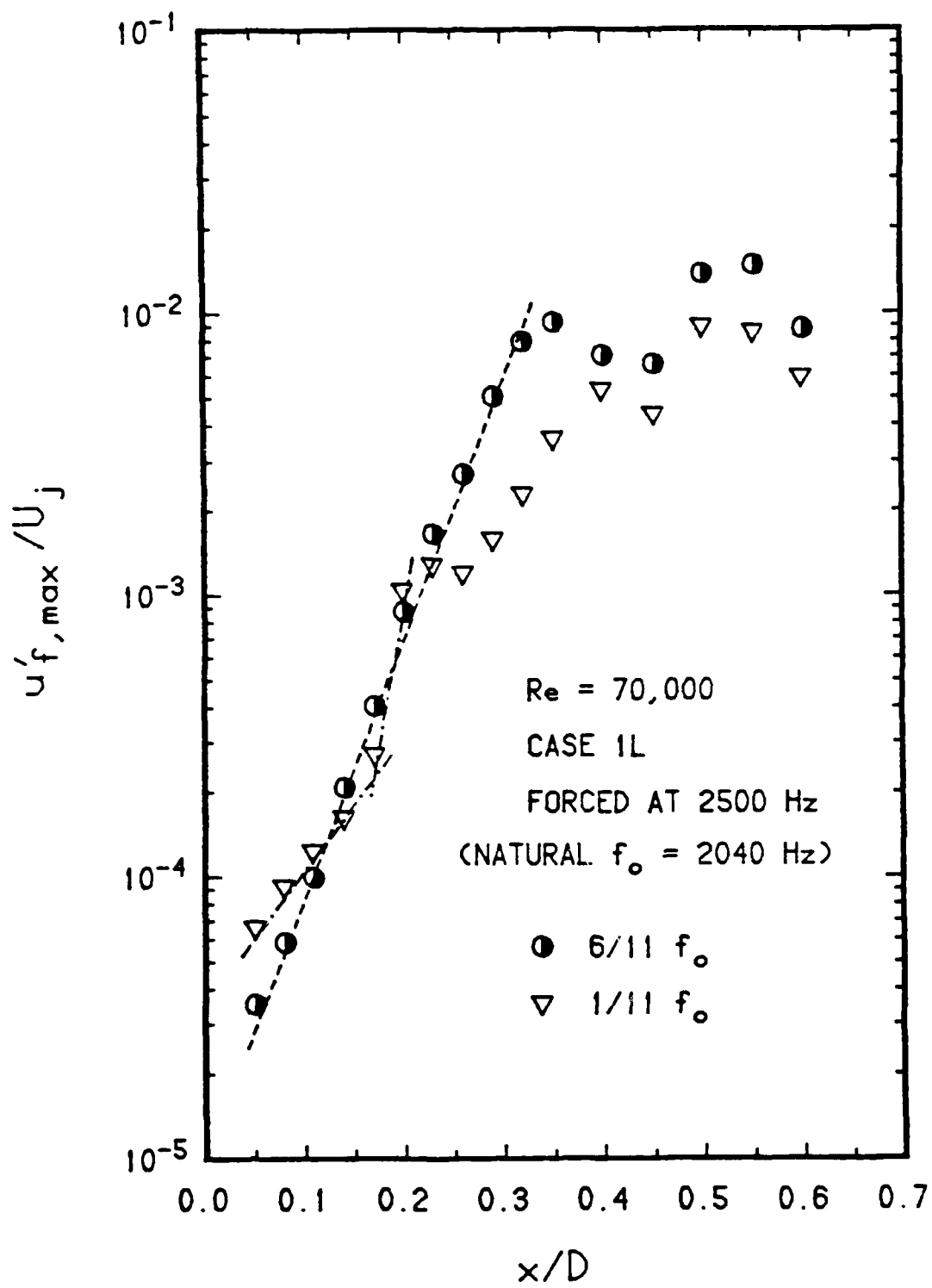


Figure 20.

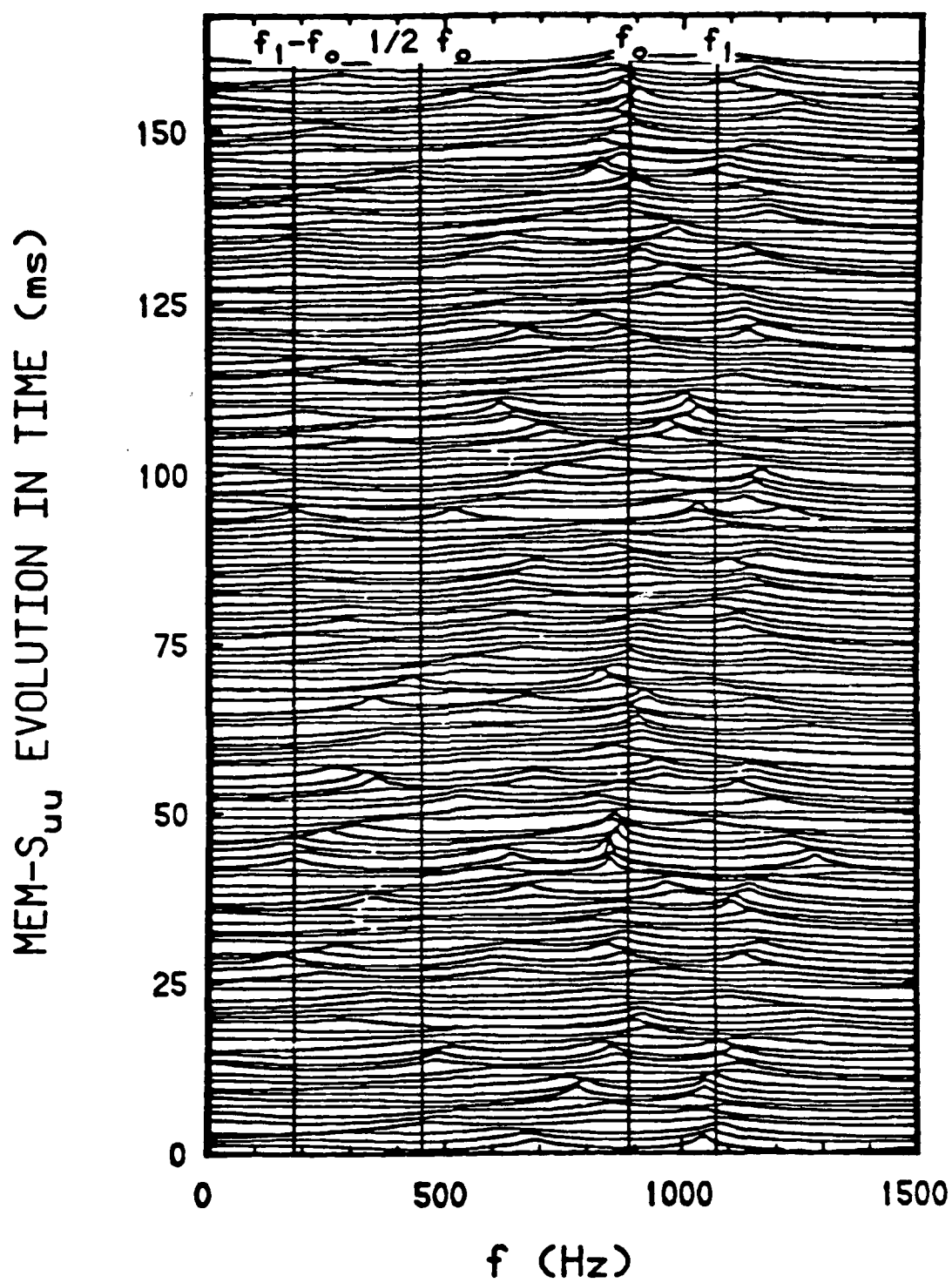


Figure 21.

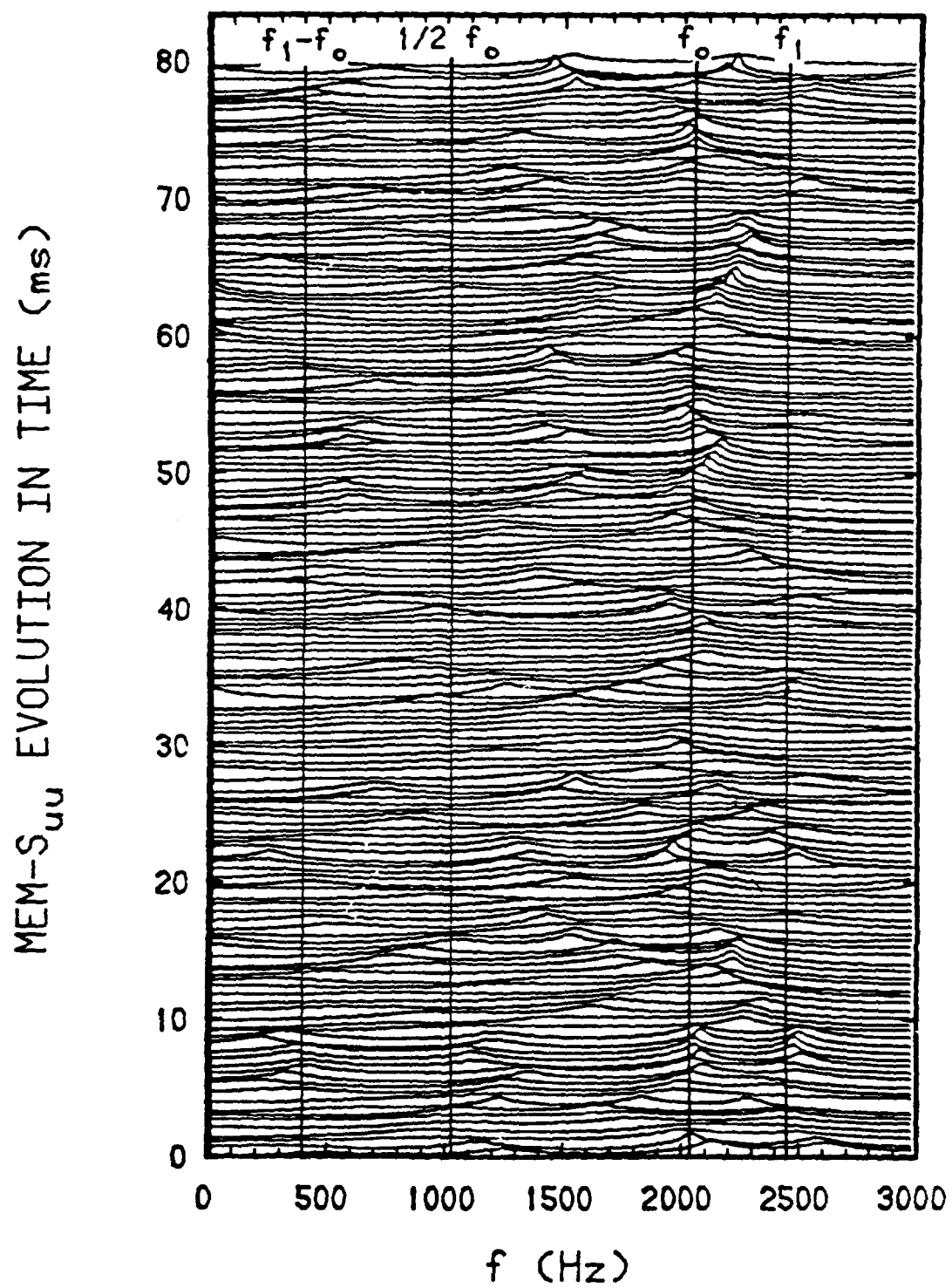


Figure 22.

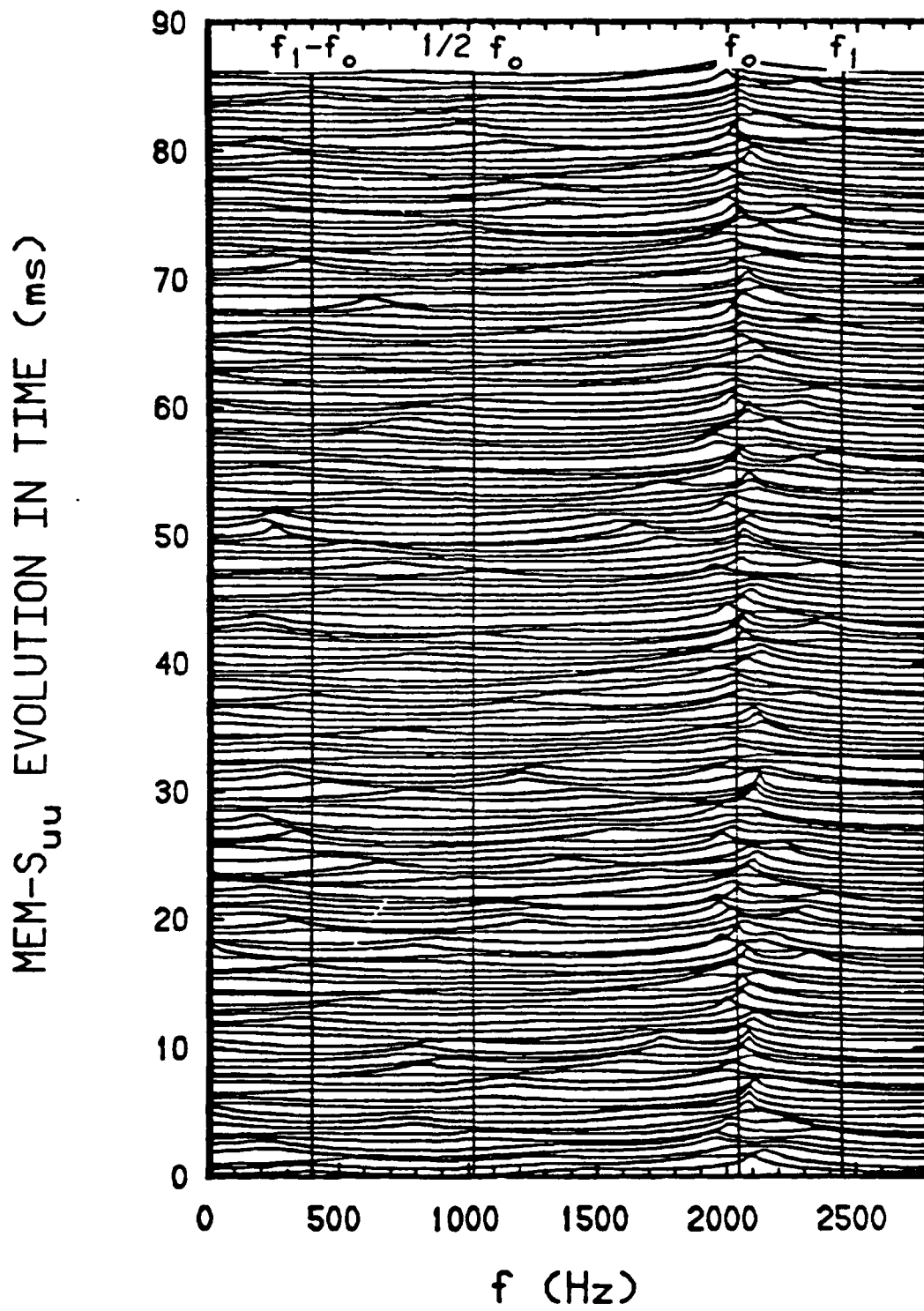


Figure 23.

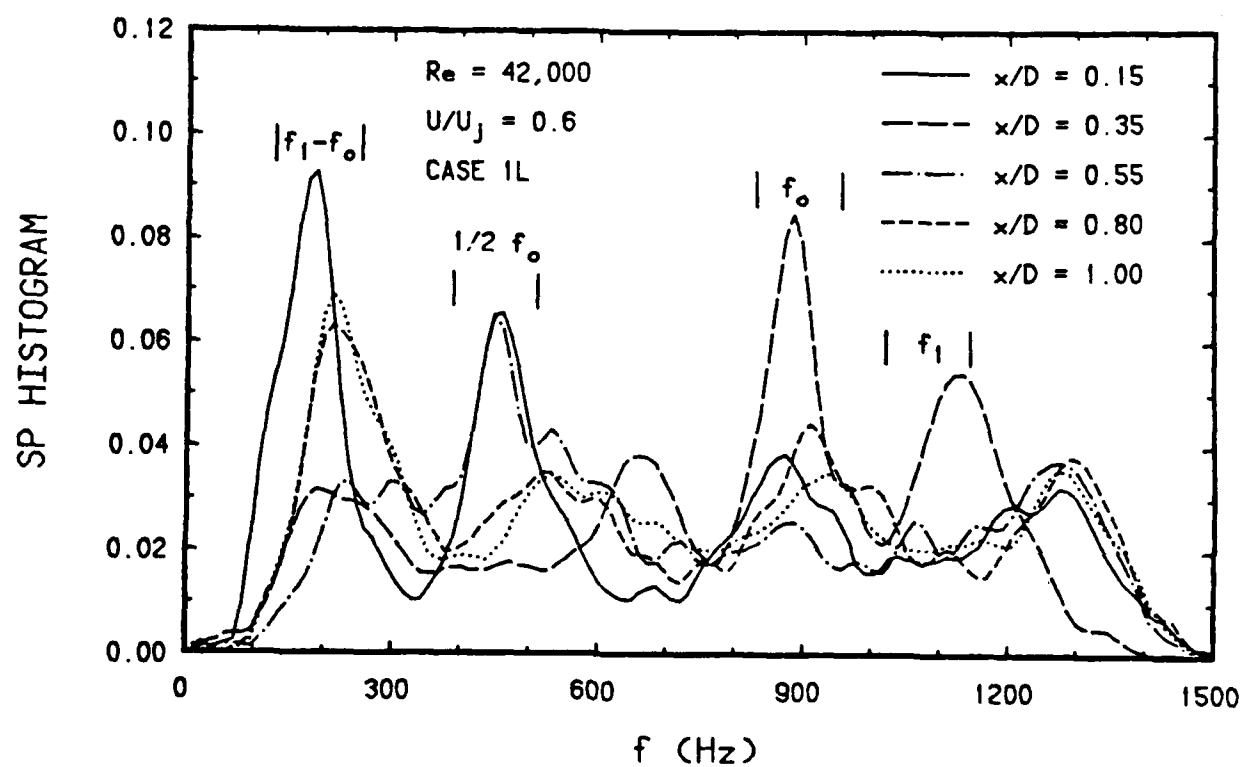
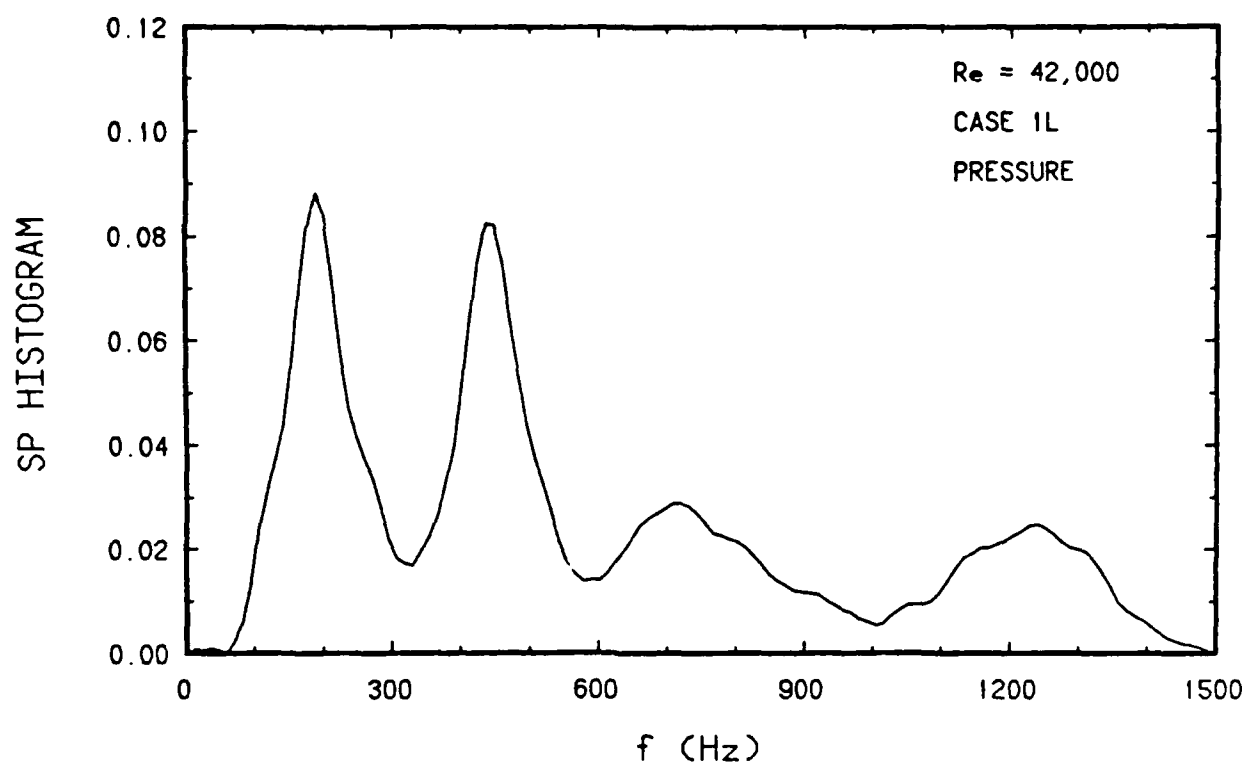


Figure 24.

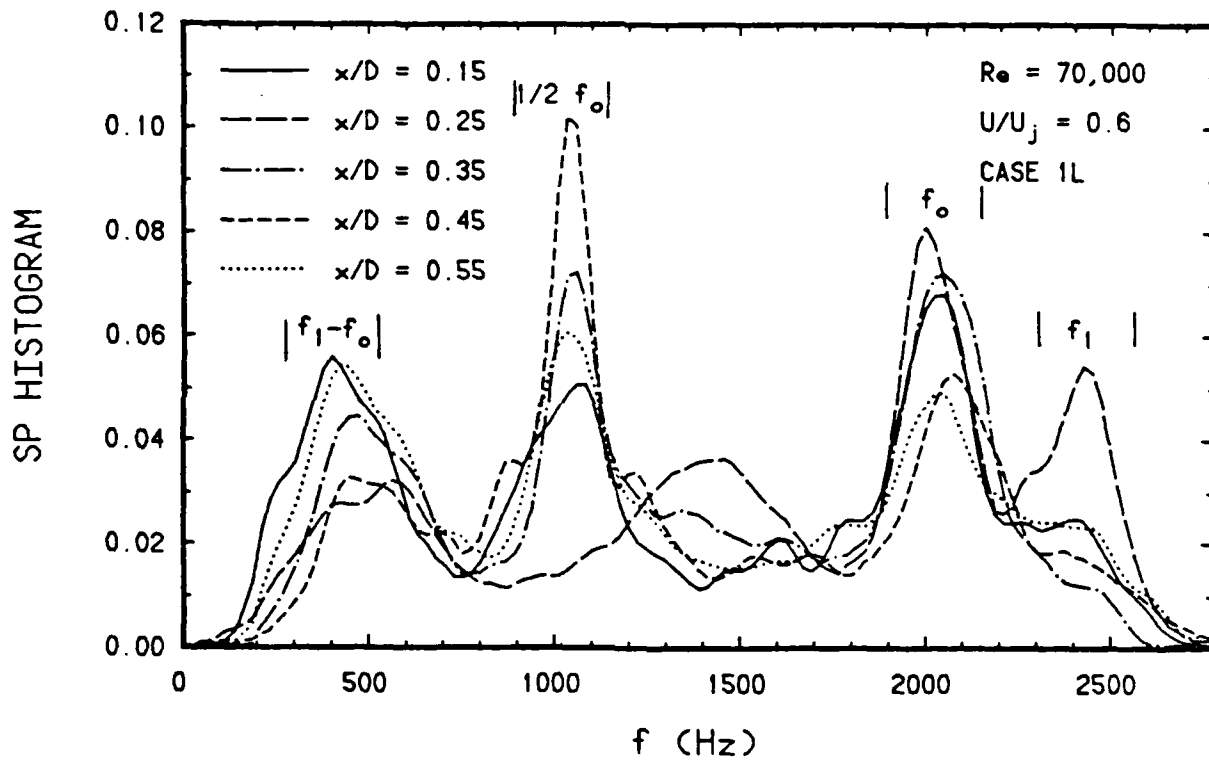


Figure 25.

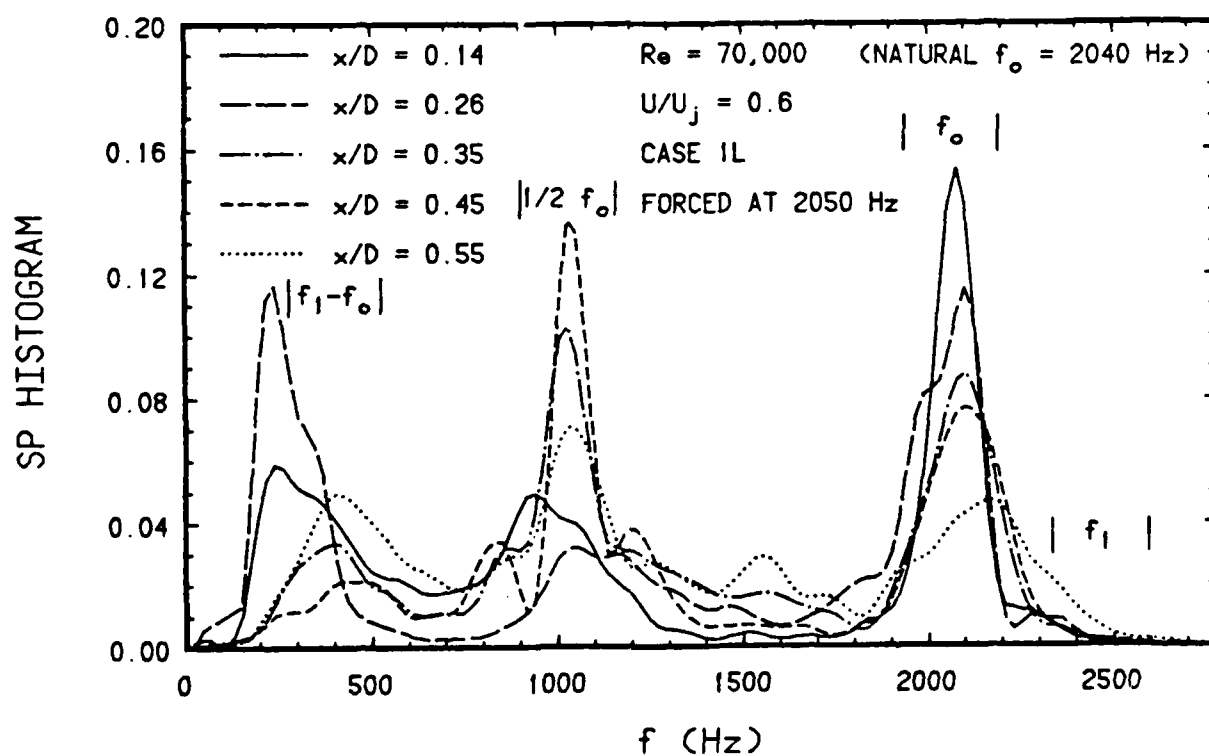
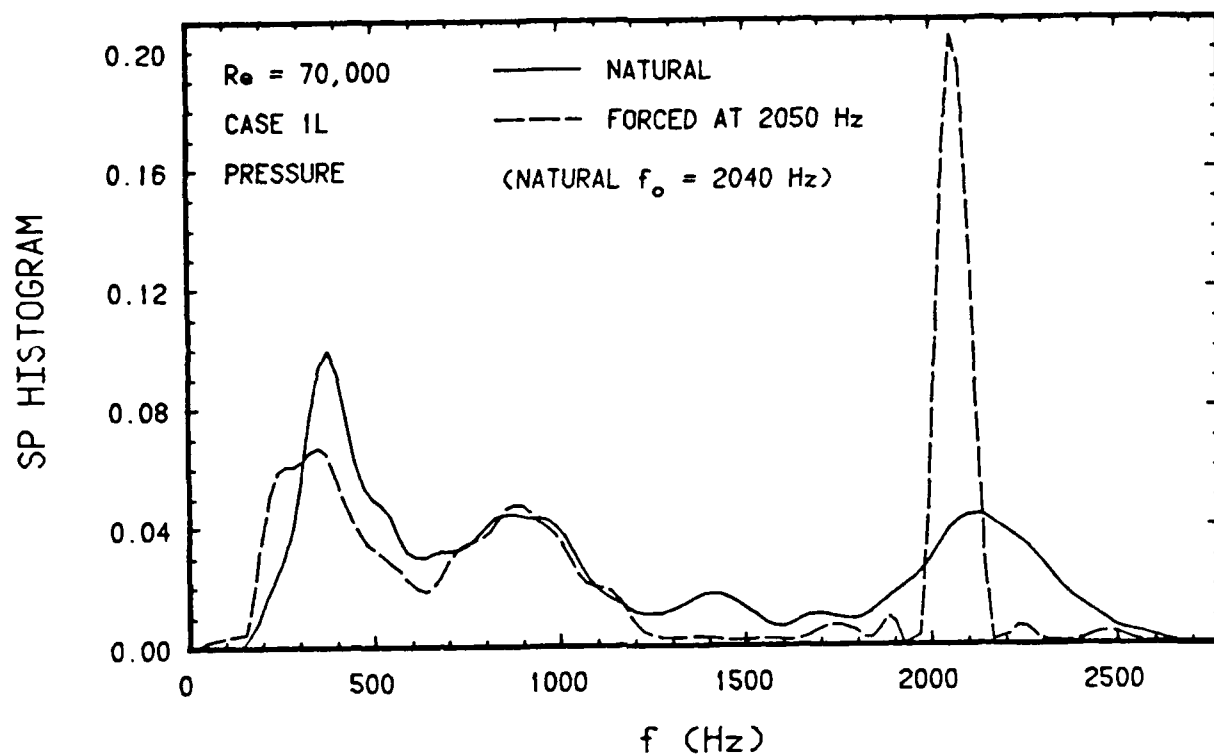


Figure 26.

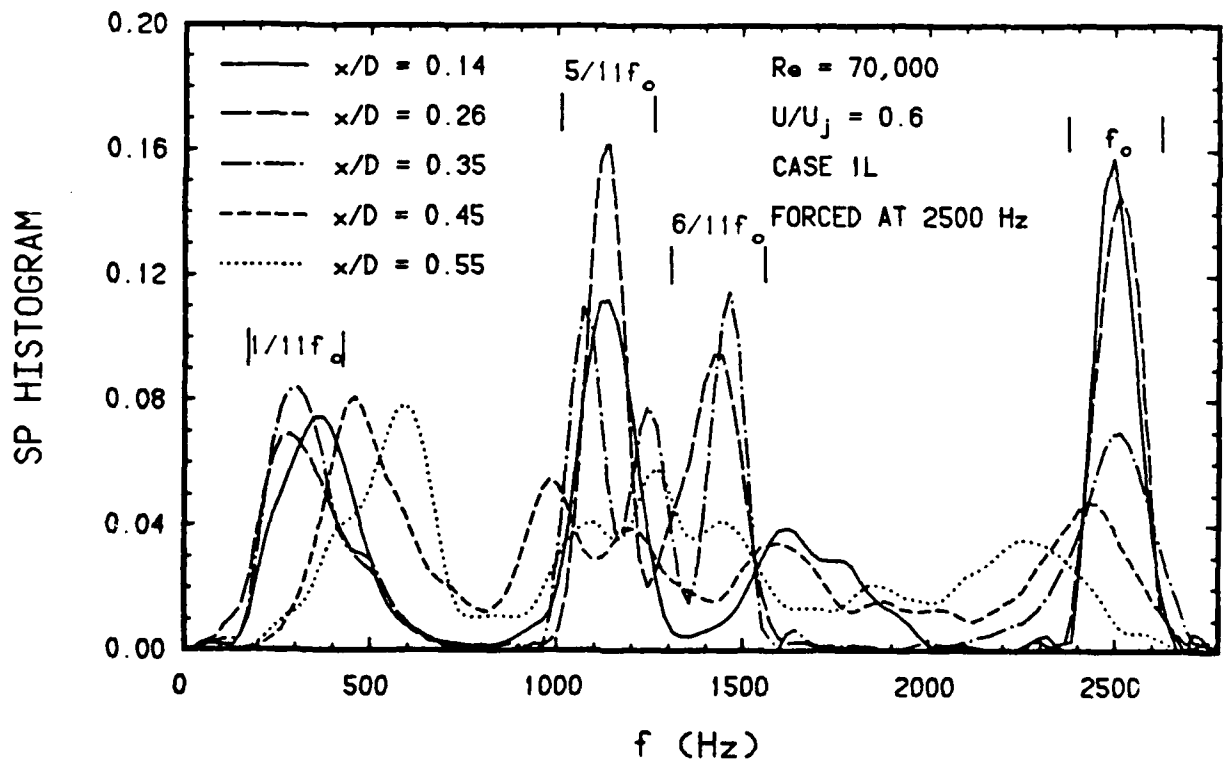
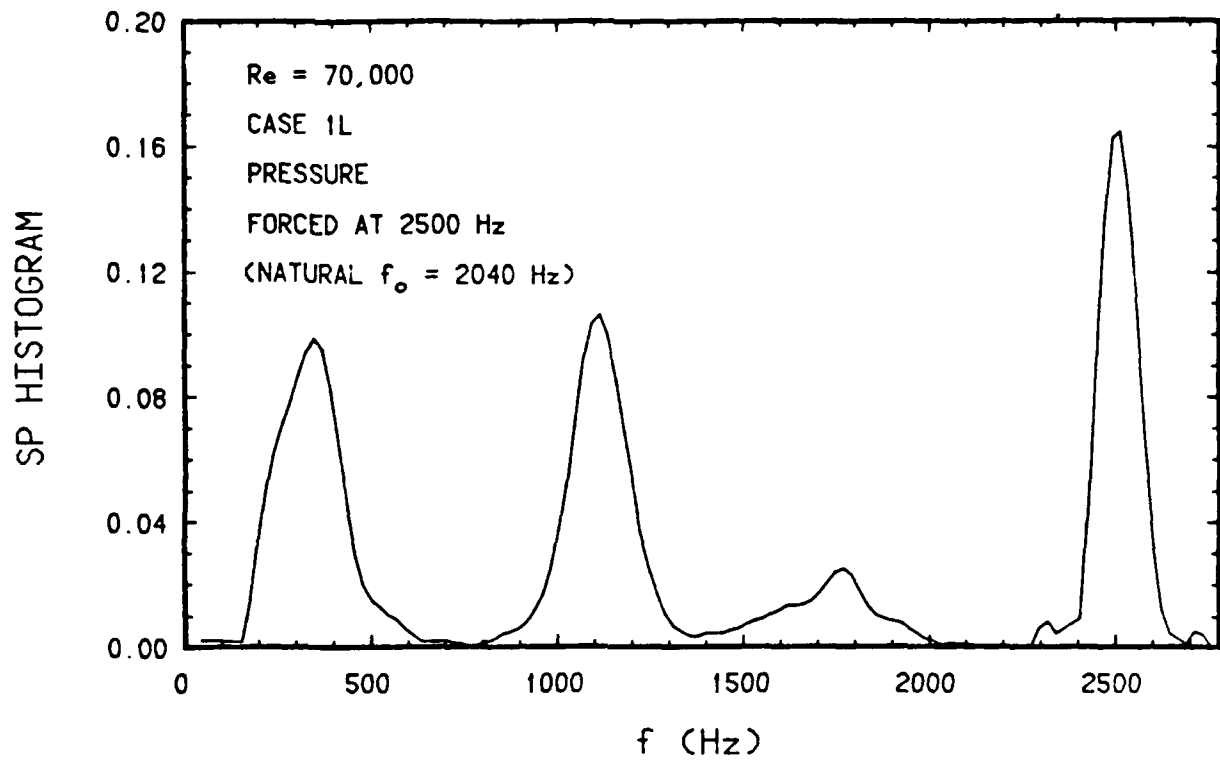


Figure 27.

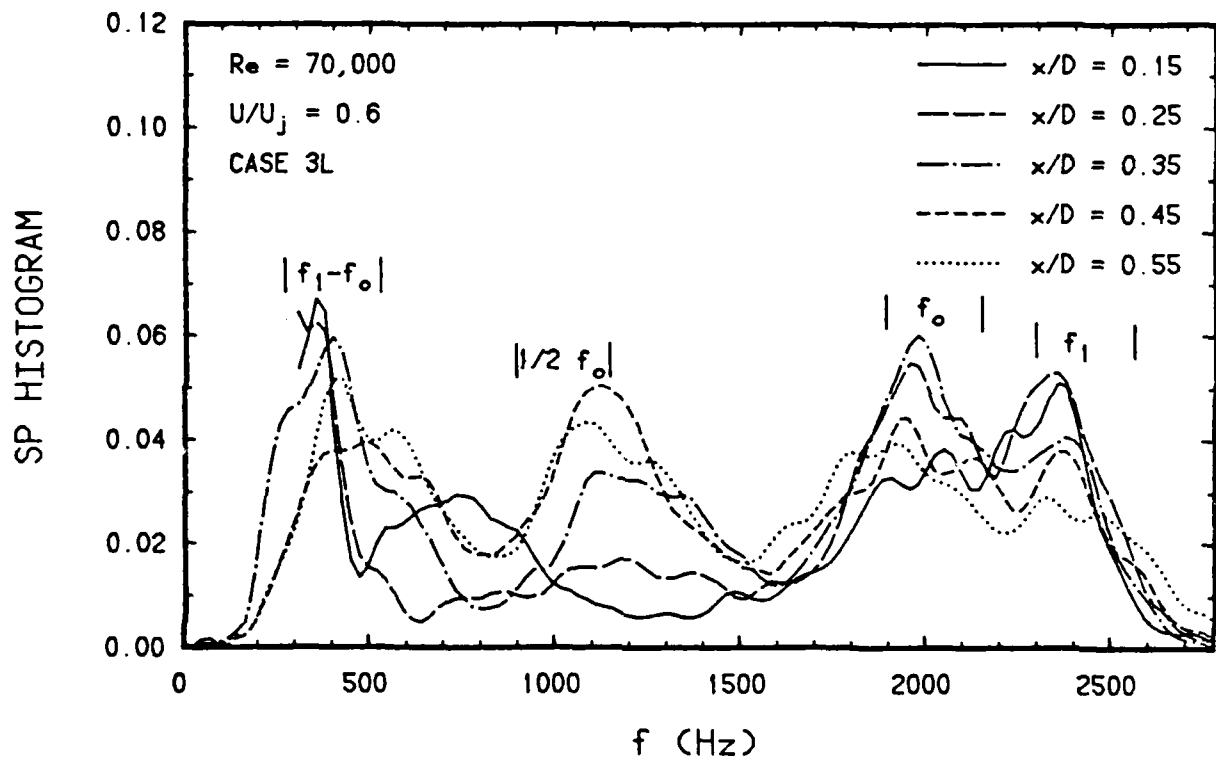


Figure 28.

SP INDICATOR

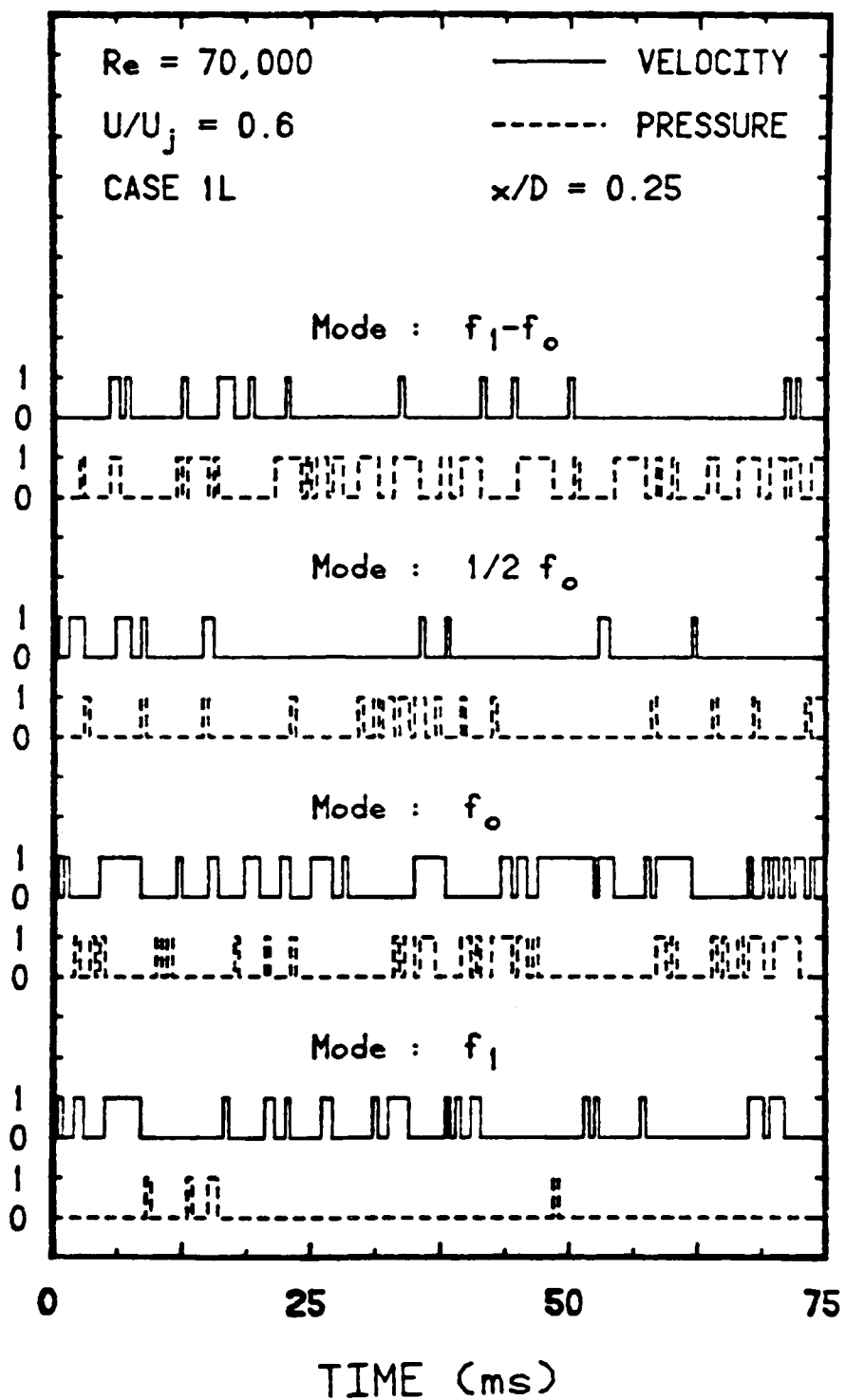


Figure 29.

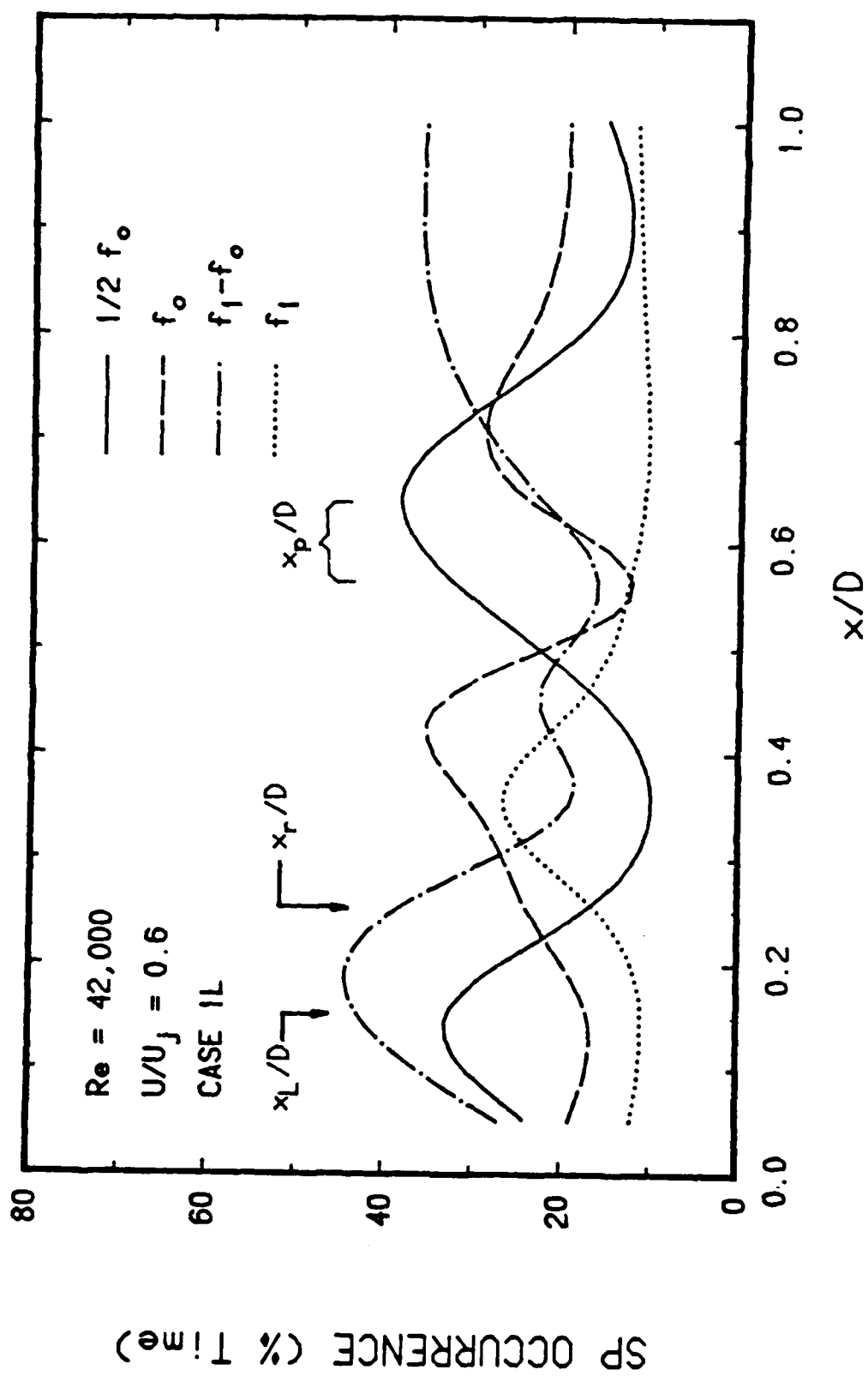


Figure 30.

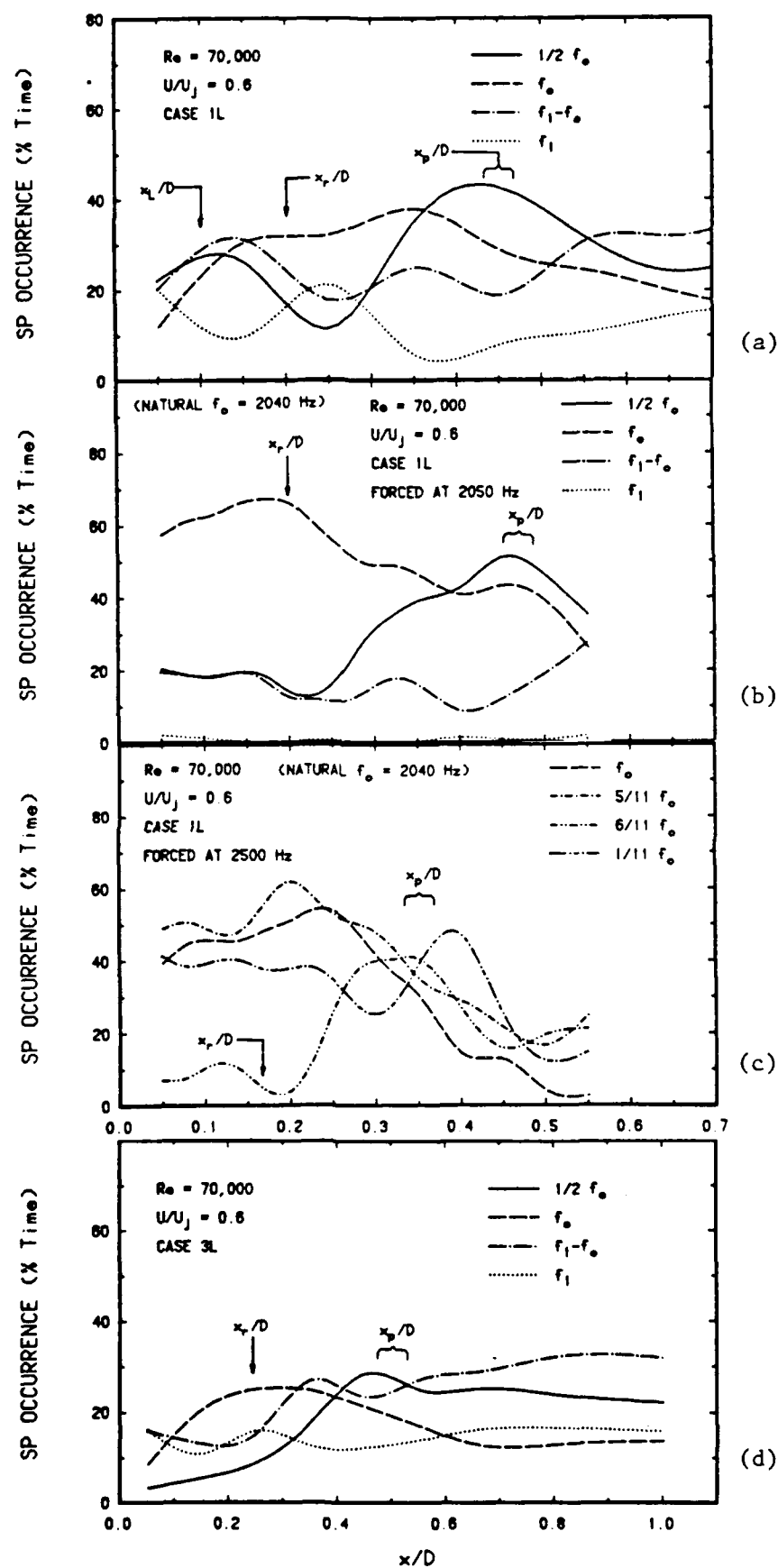


Figure 31.

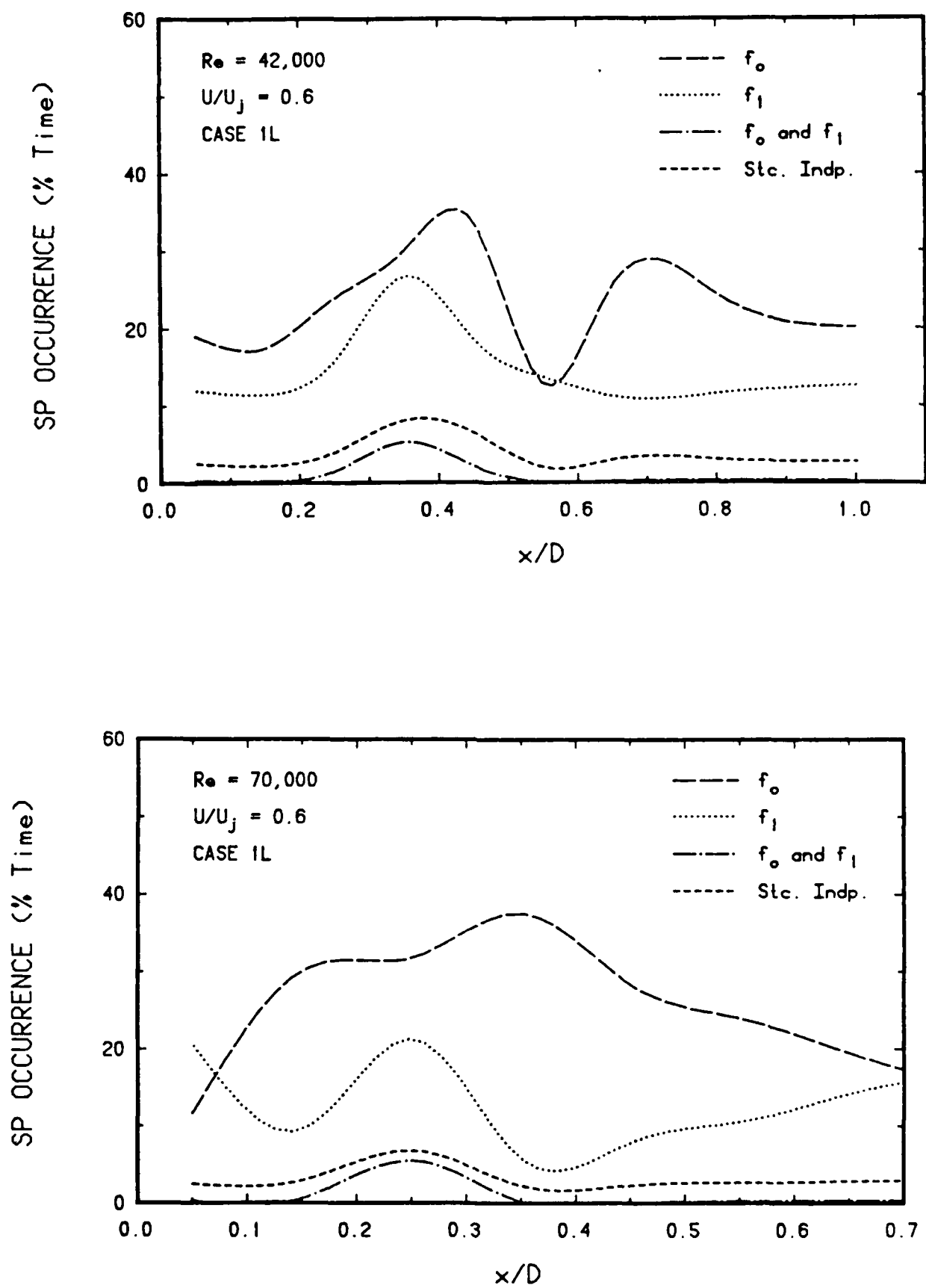


Figure 32.

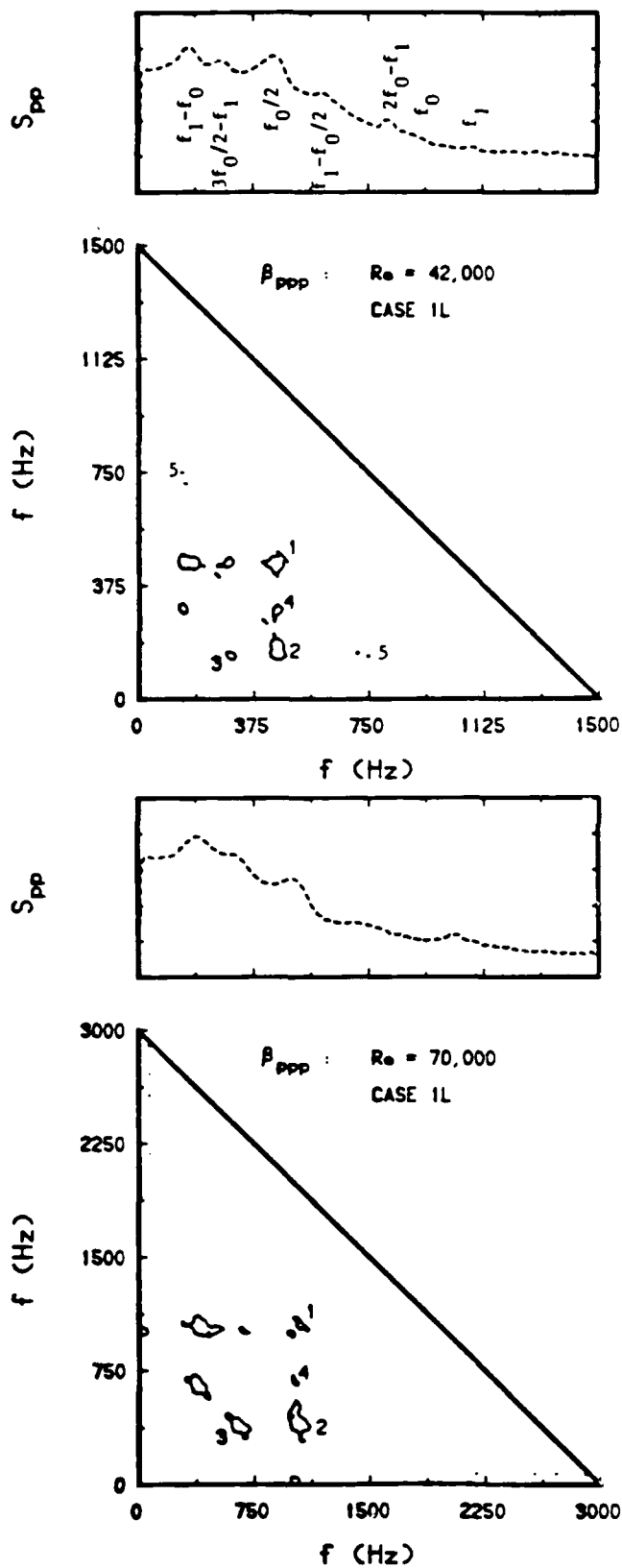


Figure 33.

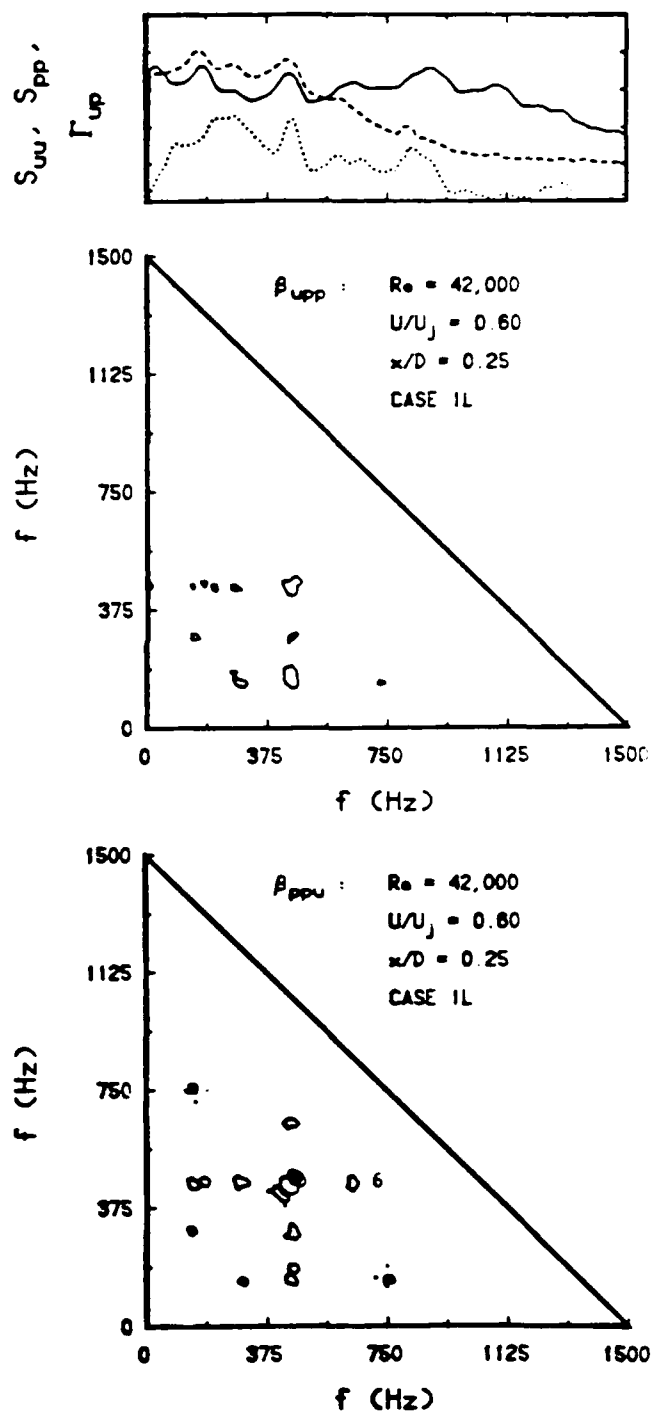


Figure 34.

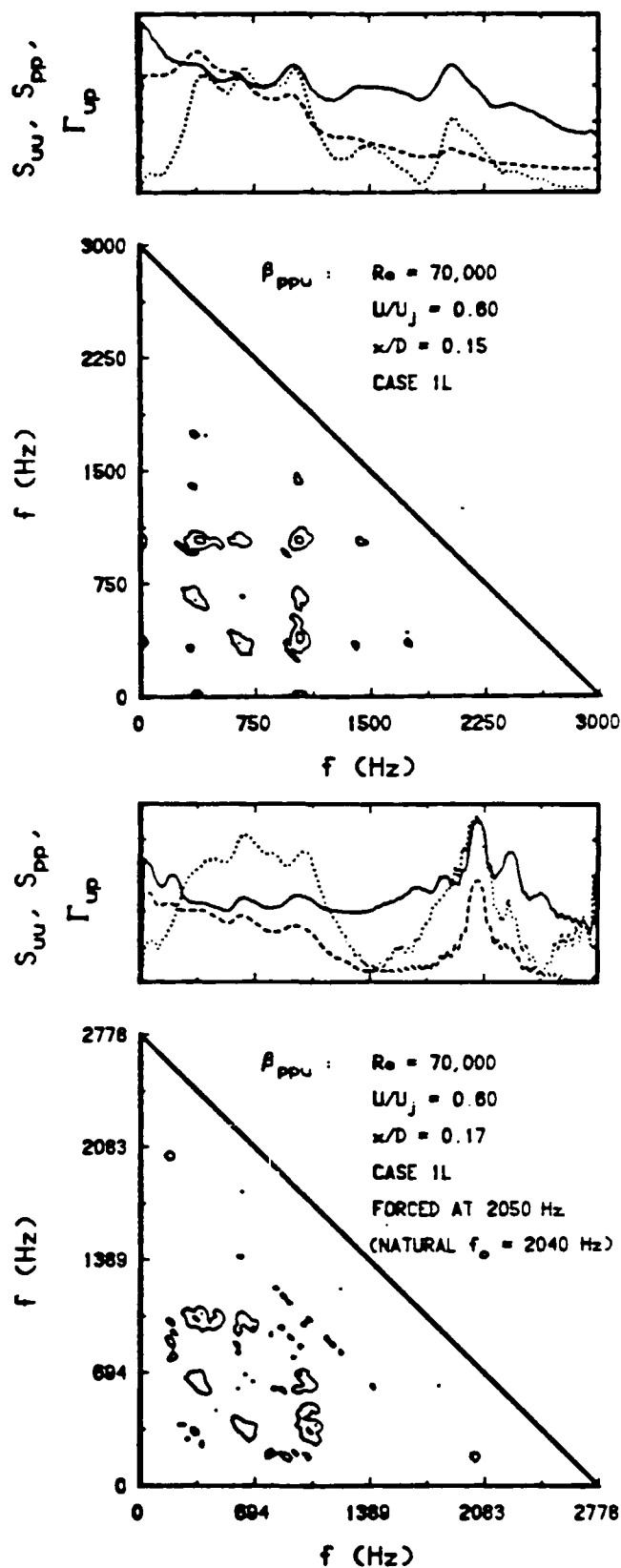


Figure 36.

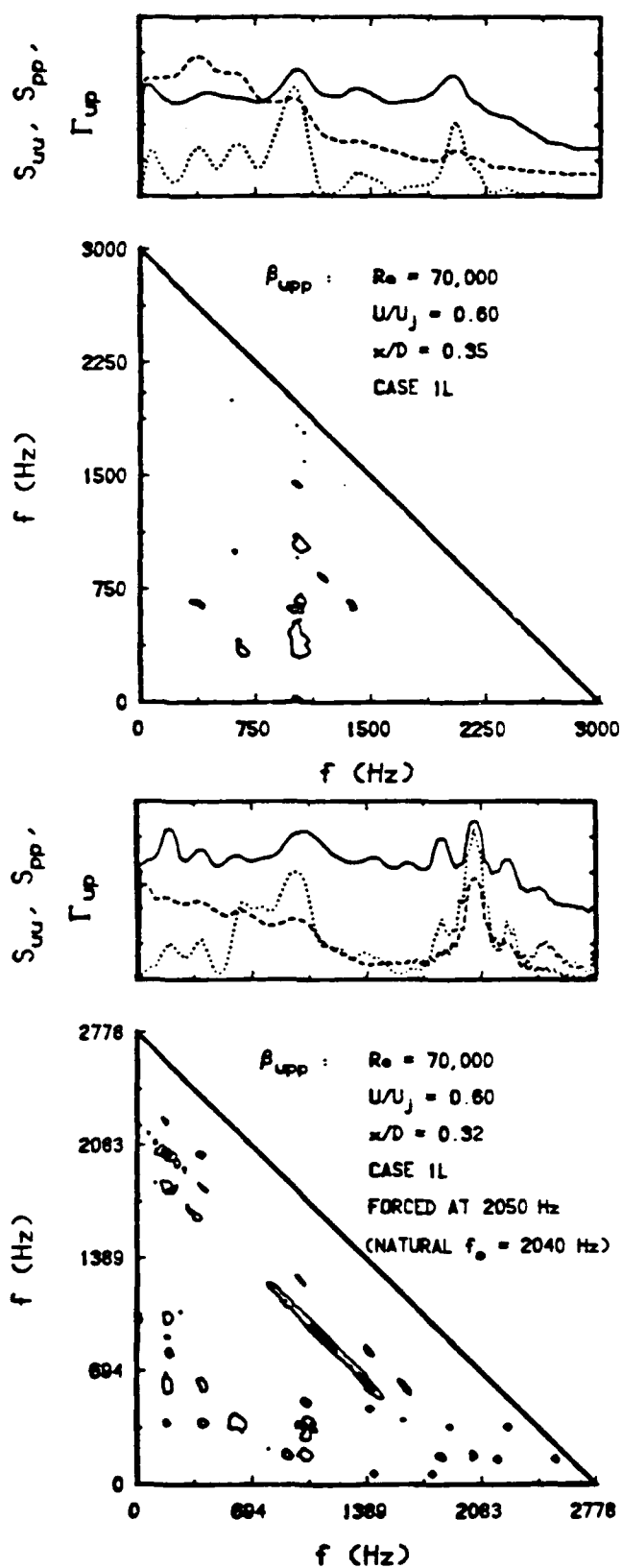


Figure 37.

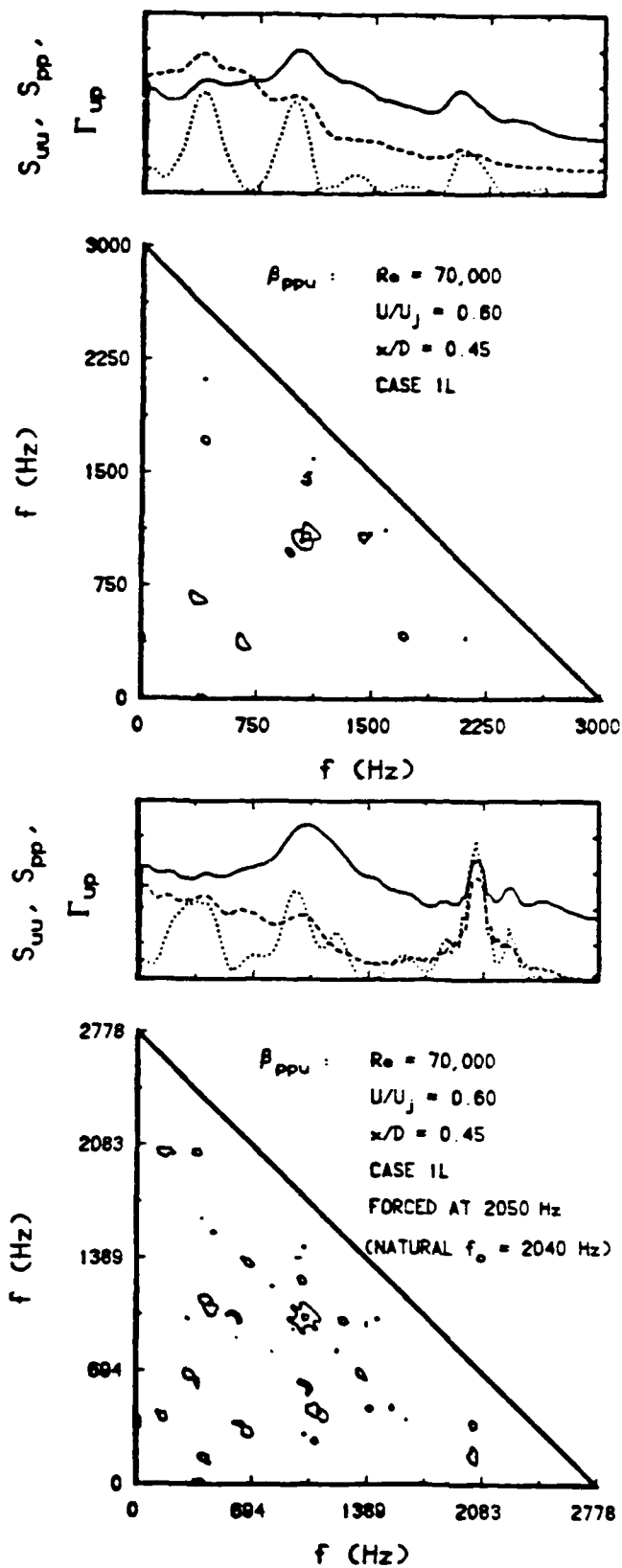


Figure 38.

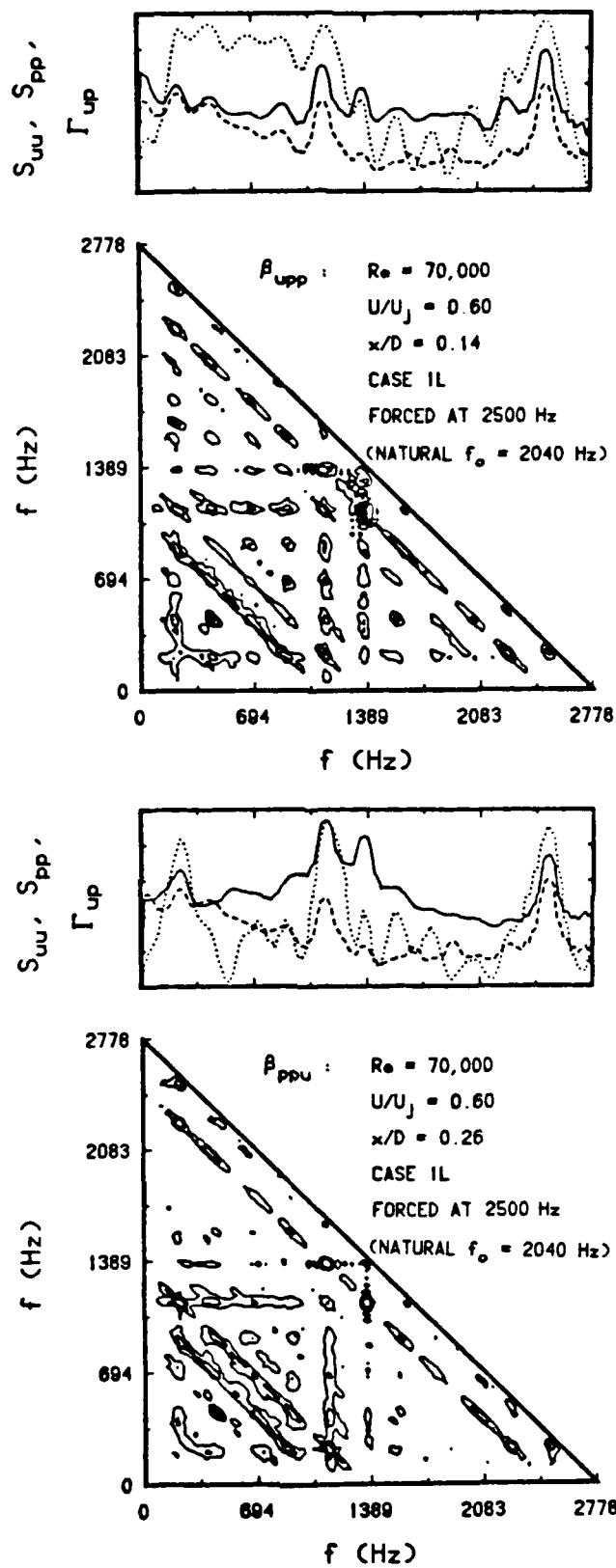


Figure 39.

The dynamics of low initial disturbance turbulent jets

R. E. Drubka

McDonnell-Douglas Corporation, Huntington Beach, California 92647

P. Reisenthel and H. M. Nagib

Fluid Dynamics Research Center, Illinois Institute of Technology, Chicago, Illinois 60616

(Received 28 November 1988; accepted 22 May 1989)

Recent experimental results in axisymmetric free jets are discussed with an emphasis on the dynamics of their self-forced states. The role played by the initial shear-layer instabilities and their coupling with subsequent jet instabilities is examined to reveal key mechanisms and scaling relations.

I. INTRODUCTION

A. Background

The early stages of shear-layer amplification are well predicted by linear stability theory. The mean profile of a jet is inviscidly unstable to small disturbances, which grow exponentially over short distances from the lip. There has been some historical confusion as to which theory (spatial or temporal) was relevant: Whereas the shape of the eigenmodes consistently appeared to be better predicted by the spatial theory, the experimentally measured streamwise growth rates often agreed better with temporal theory. Further insight into the relevance of spatial or temporal approaches was provided by Monkewitz and Huerre,¹ in the context of small velocity ratio asymptotics (i.e., by considering the influence of the velocity ratio of the two streams on the stability properties of the shear layer). The maximally amplified frequency calculated from the Rayleigh equation applied to a hyperbolic tangent profile was found to be $St_\theta = 0.017$ using spatial stability for various velocity ratios.² Later, Huerre and Monkewitz³ used a more general approach by analyzing the behavior of the *impulse response* of a family of parallel (hyperbolic tangent) shear layers, letting both frequency and wavenumber be complex. In particular, they determined that when the velocity ratio is smaller than 1.315, the shear layer is convectively unstable, and hence that if disturbances were continually fed to the system at a given streamwise location (as is the case for acoustically forced shear layers with receptivity at separation), spatial analysis would be the one that is physically meaningful.

Because the momentum thickness grows with downstream distance, the shear layer instability characteristics change with X . Analyses incorporating these nonparallel effects have considered the integrated growth rates of disturbances up to the point of neutral stability. Weakly nonlinear aspects have been analyzed from small perturbations around the neutral point. In particular, the increased growth of a subharmonic frequency leading to pairing has been successfully accounted for by Kelly's subharmonic resonance mechanism.⁴ Drubka⁵ showed that a subharmonic resonance takes place in the jet at approximately two fundamental wavelengths from the lip. Many investigators have recognized the importance of this mechanism in describing the sequence of pairing interactions. In particular, the initial relative amplitudes and phases, especially, of fundamental and

subharmonic frequencies affect the downstream flow development significantly, as discussed recently by Monkewitz.⁶ Cohen and Wignanski⁷ showed that, in addition, when the subharmonic is a helical mode, this interaction can lead to explosive growth, in accordance with Ahmadi-Moghadam's theoretical predictions.⁸

One of the main differences between shear layers and jets concerns the fact that jet flows are characterized by two length scales. While the initial shear-layer instability scales on local momentum thickness, the structure of the jet past the potential core is believed to scale with diameter. Crow and Champagne⁹ used large amplitude periodic surging of a jet and discovered a "large-scale orderly wave structure" that dominated the entire jet column. This so-called "preferred mode" of the jet was found to scale with diameter. The maximum amplification of this mode was obtained for $St_D = 0.3$, independently of exit velocity, and had a wavelength of 2.4 jet diameters. Later, Hussain and Zaman¹⁰ provided a detailed spatial documentation of the large-scale structure associated with the preferred mode. This coherent axisymmetric structure was found to be most dominant at the end of the potential core ($X/D = 4$), and the frequency scaling obtained by Crow and Champagne⁹ was confirmed. These authors also showed that the preferred mode was accompanied by a large increase in jet spreading and sound production. The jet preferred mode was described as a "latent" orderly structure continually excited by background disturbances.

The interaction between shear layer mode and jet column mode was demonstrated by Kibens,¹¹ who managed to force the jet column mode using acoustic shear-layer excitation, such that three successive vortex pairings were observed at fixed streamwise locations. The last of these pairing events coincided with the end of the potential core, providing special coupling conditions with the preferred mode. The "passage" frequency was halved at each pairing interaction and the entire jet column was subjected to axisymmetric large-scale pulsation at one-eighth the excitation frequency. The coupling between the initial shear-layer instability and the final jet structure is presumably optimal for an integer number of pairings within the potential core. In the natural jet, this condition may only be achieved for certain Reynolds numbers forming a geometric sequence. Drubka⁵ was the first to document a natural coupling, for sufficiently low background disturbances. Kibens concluded that shear lay-

er and jet column modes were two independent but interacting mechanisms.¹¹ Under resonant conditions, spectacular changes in the organization of the flow and the spectral content of the radiated sound were observed.

Of importance (among the dominant modes of the jet), however, is the helical ($m = \pm 1$) instability mode, which is initially approximately equally amplified as the fundamental axisymmetric mode. Drubka⁵ showed experimentally the existence of a helical mode having a Strouhal number 20% higher than that of the fundamental axisymmetric mode. Shakib¹² used the maximum entropy method to document the switching between helical and axisymmetric modes, and concluded that the existence of one effectively suppressed the presence of the other. Although a satisfactory explanation of the origin of the temporal switching between these modes has not yet been put forth, it is believed that considerations of the continuing nonlinear competition between these few dominant modes (including subharmonic and jet preferred modes), coupled with feedback to the lip, may provide significant insight into the deterministic nonlinear dynamics of jets.

This paper presents experimental data acquired in a well-documented, very low disturbance axisymmetric jet facility. The characteristics of the unforced initial shear-layer modes are shown to conform closely to spatial linear stability theory. Clear evidence is shown in support of a natural subharmonic resonance mechanism taking place at two fundamental axisymmetric wavelengths from separation. Most importantly, the role of nonaxisymmetric disturbances in the weak coupling between initial shear-layer and final jet instabilities is discussed and contrasted to the case of artificial excitation of the jet "preferred mode."

B. The I.I.T. jet facility

The experiments described in the present paper were all conducted in a low turbulence intensity 5 cm axisymmetric air jet facility. Two jet nozzles (fifth order and matched cubic) of 9:1 area ratio were used in this investigation. The nozzle is attached to the 15 cm diam circular test section of an open circuit wind tunnel. The wind tunnel is powered by a regulated compressed air system that allows the Reynolds

number to be maintained within one percent over extensive periods of time. Its characteristics have been documented extensively by Tan-Atichat.¹³ Because of the low turbulence intensity characteristics of the jet (less than 0.05%) it is possible to simulate the effect of increasingly higher free-stream disturbance levels. These laminar exit boundary layer configurations are referred to as 1L, 2L, and 3L, and were characterized by core turbulence intensity levels of 0.05%, 0.11%, and 0.16%, respectively. A trip could also be used to make the exit boundary layer turbulent (1T case). Unless otherwise specified, the default jet configuration is the 1L case throughout this paper. Finally, a 12 in. speaker placed 70 diameters downstream of the jet exit plane provided the possibility of low-level axisymmetric acoustic excitation of the initial shear layer.

II. DISCUSSION

The detailed documentation of the experimental setup and results presented here, are contained in the Ph.D. theses by Drubka⁵ and Reisenhel.¹⁴ In order to characterize the streamwise flow development of a jet it is customary to establish the centerline decay of the mean velocity. This measurement is presented in Fig. 1, where it is compared to previous data obtained at Reynolds numbers comparable to the highest ones used here. This type of data is useful in characterizing the size of the initial region of the jet as well as the rate of entrainment beyond that region.

A. Profile self-similarity

The variation of the jet shear-layer momentum thickness θ with Reynolds number is examined in Fig. 2. As can be seen from the excellent collapse of the data, the shear-layer profiles display obvious self-similarity over a large range of Reynolds numbers when properly normalized by the local momentum thickness θ . The value of θ is calculated by truncating the integral of the momentum at the location where the velocity is 10% of the maximum (core) velocity. This operational definition of the momentum thickness was introduced to reduce the "rectification error" that results from hot-wire measurement, particularly at the outer edge of the shear layer, where reverse flow is likely to occur. All

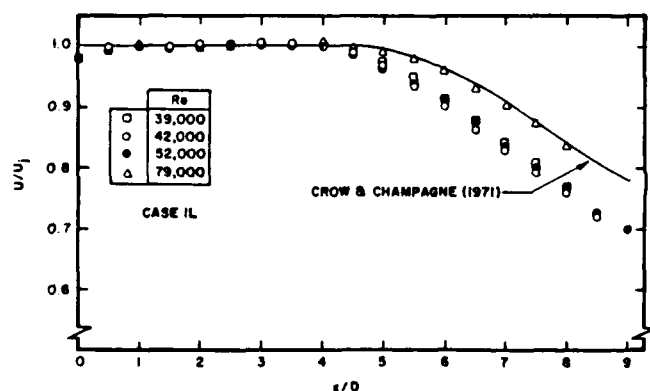


FIG. 1. Effect of Reynolds number on mean streamwise velocity decay along the jet centerline.

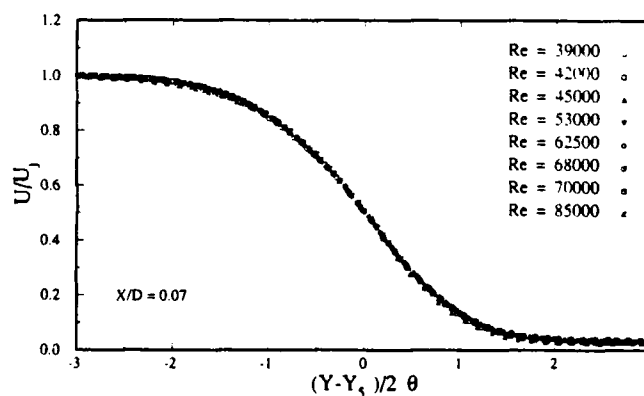


FIG. 2. Self-similarity of mean velocity profiles with Reynolds number at $X/D = 0.07$.

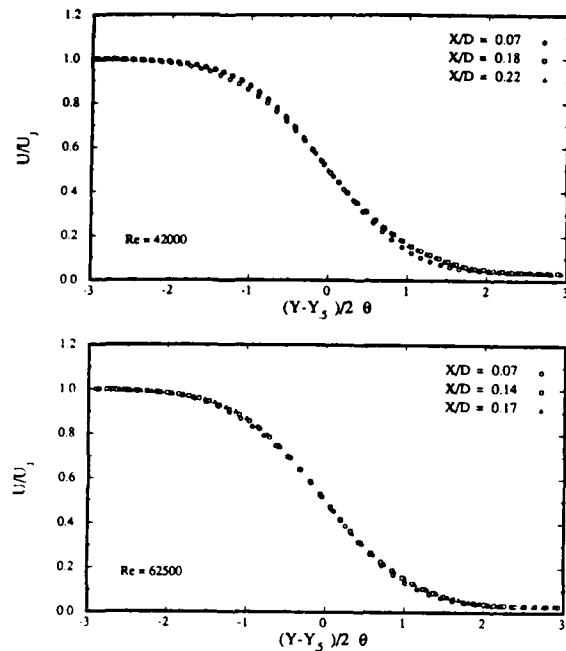


FIG. 3. Self-similarity of mean velocity profiles with downstream distance at $Re = 42\,000$ and $62\,500$.

profiles in Fig. 2 were measured at a fixed downstream location $X/D = 0.07$. The variation of momentum thickness with downstream distance close to the lip is considered in Figs. 3–5. Figure 3 illustrates profile self-similarity with respect to downstream distance at two Reynolds numbers [$42\,000$ (top) and $62\,500$ (bottom)]. In each case, it is clear that profile self-similarity has been achieved for the two most downstream locations. However, there is a noticeable departure from the self-similar profile at the earliest downstream location ($X/D = 0.07$), with a naturally more pronounced departure in the case of longer wavelength shear-layer instability (lower Reynolds number). In Fig. 4 the quasilinear growth of the momentum thickness with downstream distance at $Re = 42\,000$ is described. Of particular interest is the relative increase in θ around $X/D = 0.6$, corresponding to the energy saturation of the subharmonic axisymmetric

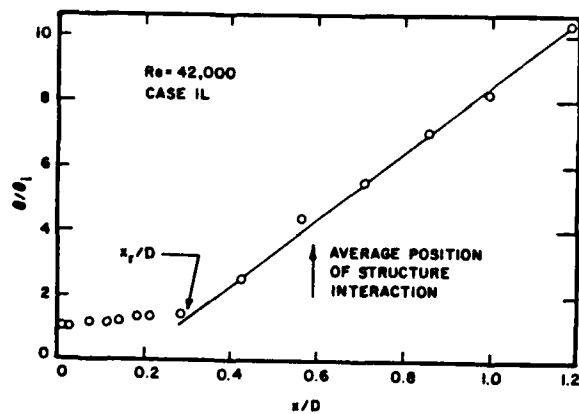


FIG. 4. Development of jet momentum thickness at $Re = 42\,000$.

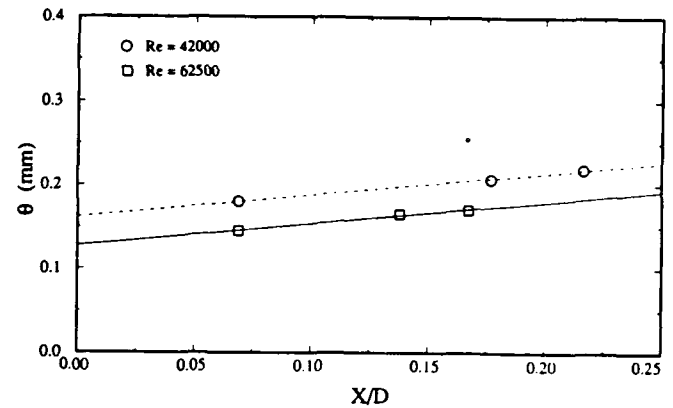


FIG. 5. Initial variation of momentum thickness with downstream distance at $Re = 42\,000$ and $62\,500$.

mode.⁵ The location of subharmonic resonance X_r (to be explained in a later section) is seen to coincide with the onset of strong momentum thickness growth.

The variation of momentum thickness with downstream distance for the two Reynolds numbers presented in Fig. 3 is shown in Fig. 5. At each Reynolds number, three downstream stations were considered, the first location corresponding to the closest practically reasonable position of the hot-wire probe (i.e., that avoided probe feedback). The two farther downstream locations, however, were designed to scale with the wavelength of the natural fundamental axisymmetric instability mode of the jet at each Reynolds number. It is clear from the results of Fig. 5 that to a good degree of approximation, the momentum thickness increases linearly with downstream distance, within the initial region close to the lip. A least-squares fit was calculated at each Reynolds number, yielding virtually identical slopes: $\partial\theta/\partial X = 0.005\,12$ at $Re = 62\,500$, and $\partial\theta/\partial X = 0.005\,14$ at $Re = 42\,000$.

Figure 6 shows the variation of θ with Reynolds number, at $X/D = 0.07$, for the range $39\,000 < Re < 85\,000$. Ideally, one expects the momentum thickness to be inversely proportional to \sqrt{Re} . Consequently, a least-squares fit to the data was calculated and gave $\theta = 33.151/\sqrt{Re} + 0.016$ (mm) at $X/D = 0.07$ (the closeness of the fit to the data

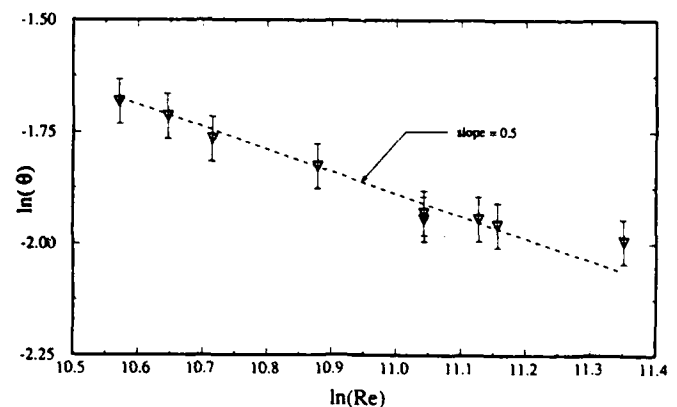


FIG. 6. Momentum thickness variation with Reynolds number at $X/D = 0.07$.

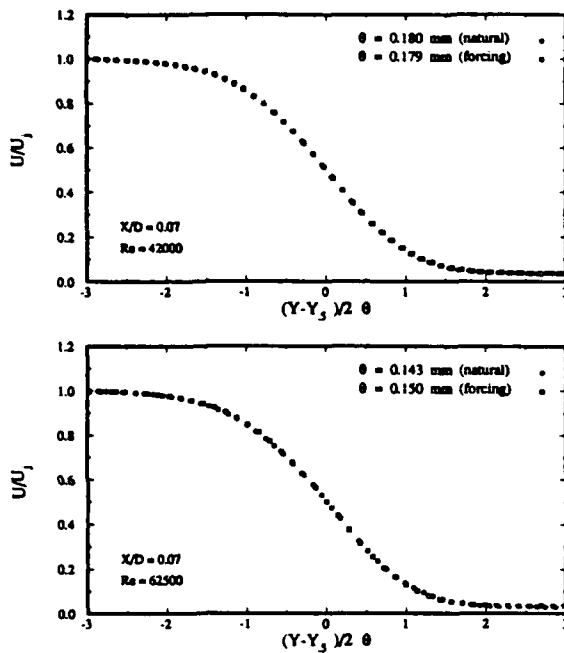


FIG. 7. Comparison of mean shear layer profiles at $X/D = 0.07$, under natural and forced conditions for $Re = 42\,000$ and $62\,500$.

being indicated by the dashed line in Fig. 6). Going one step further, it is possible to use the average slope $\partial\theta/\partial X = 0.005\,13$ to extrapolate θ back to the lip and obtain the following analytical estimate for the initial momentum thickness θ_i : $\theta_i = 33.151/\sqrt{Re} - 0.002$ (mm). The "error" (relative to strict ideal proportionality between θ_i and $1/\sqrt{Re}$) is $2\,\mu\text{m}$, which is to be compared with the average initial momentum thickness of $140\,\mu\text{m}$.

Because some of the work presented here involves shear-layer instabilities driven by acoustic excitation, the effect of forcing on the momentum thickness was also measured at $X/D = 0.07$. A comparison of natural and forced conditions is presented in Fig. 7 for $Re = 42\,000$ and $Re = 62\,500$. In each case, the forcing frequency was chosen to be close to the linearly most amplified frequency (i.e., $870\,\text{Hz}$ at $Re = 42\,000$ and $2200\,\text{Hz}$ at $Re = 62\,500$), and the forcing

acoustic levels were deliberately chosen to be quite large ($74.9\,\text{dB}$ and $78.4\,\text{dB}$ at the lip, at the lower and higher Reynolds number, respectively). As indicated in Fig. 7, a 4.9% increase in θ was measured at $Re = 62\,500$, whereas θ remained practically constant at $Re = 42\,000$. It should be kept in mind, however, that because the physical location of the measurement was fixed, the two Reynolds number cases are not dynamically equivalent, since their wavelength ratio (based on a constant normalized phase speed) is approximately 1.7 . Therefore the conditions at $Re = 42\,000$ may be more representative of true "initial" conditions. Hence the effect of forcing in the present experiments had very little influence on the initial momentum thickness θ_i .

B. Scaling of initial axisymmetric mode

In cases where the boundary layer is laminar, the exit boundary layer momentum thickness is inversely proportional to \sqrt{Re} (see discussion of Fig. 6). This result shows that in this case and when a linear instability mechanism is acting to select the most unstable mode ($St_\theta = \text{const}$), the initial Strouhal frequency St_D is proportional to the square root of the jet Reynolds number.

The work of Mattingly and Chang,¹⁵ which examines the linear stability of axisymmetric jets, brings out a number of enlightening points. Using a family of measured profiles to describe the mean velocity distribution of the jet, it was determined that for initial boundary layers that were thin compared to the jet diameter, both the axisymmetric and first helical modes had nearly the same amplification rate and occurred at frequencies that differed by 17% . The spectrum of Fig. 8, and many others obtained for different Reynolds numbers and exit conditions, indicates that the helical mode ($f_{i,1}$) has a frequency approximately 20% higher than that of the axisymmetric one ($f_{i,0}$). This result clearly shows that the initial jet is equally sensitive to both axisymmetric and helical disturbances.¹⁶ Since both modes were found to have nearly equal growth rates, additional information is necessary to determine the conditions under which one mode may dominate. It was also observed that the growth of the helical mode was tied into the disturbance characteristics in the jet initially.⁵ In the lowest disturbance level case, the helical

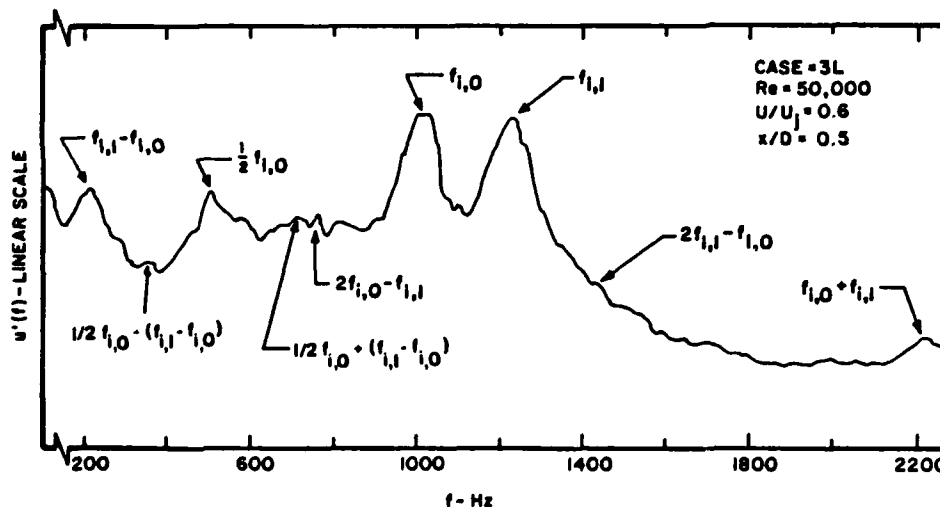
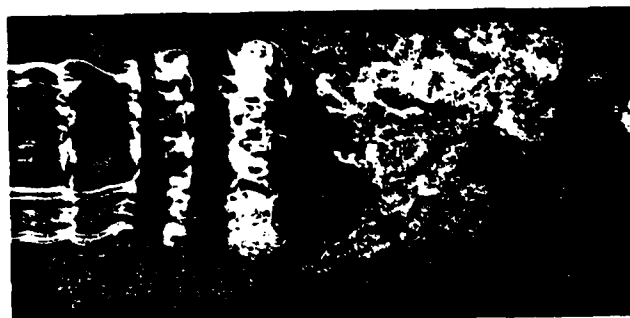
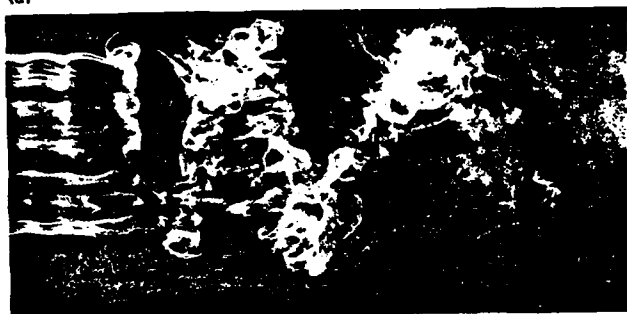


FIG. 8. Velocity spectrum for case 3L at $Re = 50\,000$ detailing nonlinear interactions between $m = 0$, $m = 1$, and subharmonic modes.



(a)



(b)

FIG. 9. Smoke wire flow visualization highlighting both natural axisymmetric (a) and nonaxisymmetric (b) modes at $Re = 10\,000$ (courtesy of S. M. Kusek¹⁶).

mode was only observed through coherence measurement. No large discrete spectral peak was measured. Thus single channel spectra may not always be sufficient to determine these modes.

Visual evidence of the helical mode is presented in Fig. 9, which was obtained using a smoke wire wrapped around the circumference of the jet flow near its exit. The top and bottom photographs depict, respectively, the axisymmetric and helical modes under natural conditions at $Re = 10\,000$.

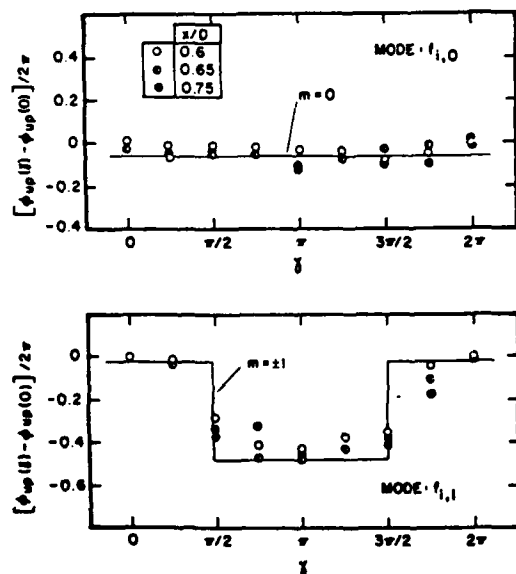


FIG. 10. Azimuthal variation of phase difference between velocity and near-field pressure for initial axisymmetric and helical modes at $Re = 42\,000$ for case 3L.

The two pictures were taken at random phases, a short instant apart, therefore demonstrating the temporal switching between these modes. Quantitative documentation of the phase changes of these two modes is given in Fig. 10. The mean azimuthal phase distribution, as documented by two point correlations, for each of the frequency peaks of the respective modes, provides clear evidence of their shape. The reference curve for the helical mode is based on the superposition of the $m = +1$ and $m = -1$ (i.e., right- and left-handed) helical disturbances.¹⁶

With the restriction that only axisymmetric modes are allowed, then, according to Laufer and Monkewitz¹⁷ and Ho and Huang,¹⁸ the number of waves in a feedback loop should be an integer:

$$0.5f_{i,0}(x_m/c_r + x_m/a) = N, \quad (1)$$

where x_m is the position of the first vortex merging, c_r is the dimensional phase speed of the subharmonic, a is the speed of sound, and $0.5f_{i,0}$ is the subharmonic frequency. For typical experiments in the moderate Reynolds number range, $a \gg c_r$, so that Eq. (1) simplifies to

$$x_m/D = 2Nc_r/f_{i,0}D. \quad (2)$$

In a jet, Gutmark and Ho¹⁹ found N to have a value of 1. The effect of dropping the second term on the concept of a feedback loop was analyzed in detail by Reisenthel.¹⁴ It was also shown by Reisenthel¹⁴ and Drubka⁵ that for high enough frequency $c_r = 0.5U_j$. With this Eq. (2) becomes

$$x_m/D = N/St_{i,0}. \quad (3)$$

This shows that the pairing location is inversely proportional to the initial Strouhal frequency.

The original speculation about the stepwise behavior of the initial instability frequency by Gutmark and Ho¹⁹ centered about the idea that the location of the pairing is fixed in space. If this was the case, from Eq. (3) it is observed that the initial Strouhal frequency would be stepwise. A similar type of behavior was observed with wide-band external excitation by Drubka.⁵ Thus the stepwise behavior of the initial eigenfrequency may be due to an external acoustic forcing. To clarify these views, the variation of the initial axisymmetric instability frequency with Reynolds number was examined for various exit conditions. Results for test flow condition 1L

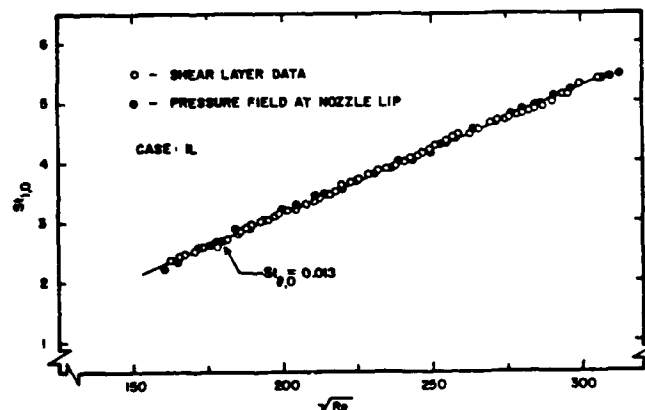


FIG. 11. Variation of initial axisymmetric Strouhal frequency with Reynolds number.

are shown in Fig. 11. Two separate sets of data were taken. One set corresponds to data taken off axis, while the other set corresponds to data taken from one of the pressure taps around the circumference of the jet. Multiple peaks in the streamwise velocity spectrum were observed. Based on the phase measurements around the jet and the off-axis development, the mode which developed a distinct subharmonic frequency was determined to be the initial axisymmetric instability mode. It was carefully checked that the frequency of this mode did not vary in either the downstream or cross-stream direction. To ensure that the probe did not influence the measurements of this mode, the amplitude spectrum of the pressure fluctuations, using one of the pressure taps, was taken with the probe removed from the flow. When these data were plotted in nondimensional form, it was noted that the variation of the initial Strouhal frequency is linear with the square root of the jet Reynolds number. The momentum thickness at the position where a peak in the streamwise velocity spectrum at the initial axisymmetric instability frequency was first detectable was utilized to normalize all cases. In this manner the same relative starting point in the growth of this instability mode can be maintained between test flow conditions.

Normalizing the data of Fig. 11 with this parameter, it was observed that the initial axisymmetric mode scales as $St_\theta = 0.013$. The same value was later repeated by Reisenhel.¹⁴ It should be noted here that for this initially low disturbance level condition, $\theta = \theta_i$ since the first peak is observed very near the jet exit. This value of St_θ agrees with the results of Zaman and Hussain.²⁰ They found that the natural instability occurs at $St_\theta = 0.012$, normalized by the initial momentum thickness of the jet. Surprisingly, this value does not correspond to the maximum amplified mode according to linear theory, $St_\theta = 0.017$. Thus the initial axisymmetric mode is not the most amplified. Similar observations were made by Pfizenmaier²¹ and by Michalke.²²

As the disturbance level in the core of the jet, and hence in the boundary layer, is increased, it is important to determine the effect on the scaling of the initial jet instability. The core disturbance level can be characterized by its fluctuation intensity and also its spectral characteristics. The core dis-

turbance becomes internalized in the boundary layer. If the disturbance level in the boundary layer is low then one would expect that the disturbance would have no influence on the selection of the initial instability frequency since a linear instability mechanism is acting. To examine this, the variation of the initial axisymmetric instability frequency was documented for test flow conditions 2L and 3L. When normalized by the measured momentum thickness using the same criterion as in case 1L, the scaling of the initial Strouhal number was found to be unchanged from that case.⁵ Even though the initial boundary layer disturbance characteristics as observed in Fig. 12 and the downstream evolution of the jet were vastly different for test flow conditions 1L, 2L, and 3L, the selection of the initial axisymmetric instability mode remains the same when properly scaled.

C. Scaling of other instability modes

In the previous section the initial axisymmetric instability frequency was determined in some instances using the near-field pressure, measured at the nozzle exit. A typical pressure spectrum is shown in Fig. 12 for cases 1L, 2L, and 3L at a Reynolds number of 42 000. Also included is a spectrum of the background noise in the laboratory measured 0.3 m behind the nozzle at the same value of exit velocity. The background noise exhibits a uniformly decreasing behavior and contains no discrete spectral peaks for the jet to possibly lock onto. The background pressure spectrum was measured over the entire operating range of exit velocities, flow configurations, and nozzle geometries to ensure that no external peaks were present. Coherence measurements between this pressure signal and the velocity signal in the initial jet near the nozzle lip indicated that the two signals were uncorrelated at all frequencies.

A few basic conclusions can be made from the pressure spectra. First, the effect of the internal disturbance level of the jet, and in particular the exit boundary layer, has a distinct effect on the near-field pressure outside the boundary layer. For low-disturbance levels, peaks exist in the pressure spectrum corresponding to the initial instability modes, the subharmonic mode, and modes which are generated through nonlinear interactions. As the disturbance level increases, there is a broadband decrease in this pressure field. In addition to this, the peaks corresponding to the subharmonic mode and the lower frequency nonlinear modes are no longer distinct, indicating an increase in the randomization due to the increased three-dimensionality. As was noted by Drubka,⁵ the growth rate of the jet also decreased with increasing disturbance level. This was partially attributed to the weakening of the initial developing coherent structures. This weakening caused by the increase of background disturbances is now also observed in the broadband decrease of the pressure field.

Having identified the peaks in the pressure spectrum, the nature of the scaling of these modes is examined next. For each of the test flow conditions, spectra similar to those in Fig. 12 were taken over small increments of Reynolds number. The frequency of each peak was normalized by the jet diameter and jet velocity. Typical variation of this nondimensional Strouhal frequency with Reynolds number is

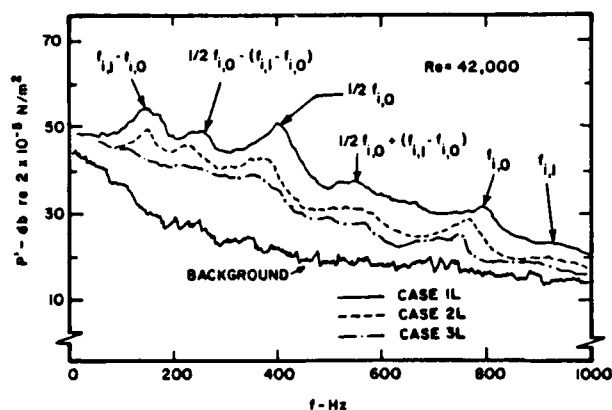


FIG. 12. Effect of initial disturbance level on near-field pressure spectrum at $Re = 42\,000$.

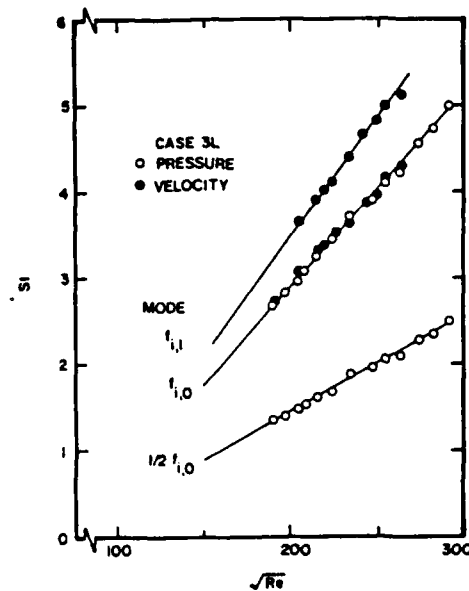


FIG. 13. Variation of Strouhal frequency of axisymmetric, helical, and subharmonic modes with Reynolds number for case 3L.

shown in Fig. 13. It is seen that the Strouhal number of all of the modes that are observed in either velocity or pressure spectra varies linearly with the square root of the Reynolds number. This indicates that all of these modes scale at constant value of St_θ , as was recently confirmed by Kusek, Corke, and Reisenthel.¹⁶

D. Initial instability: Subharmonic resonance and comparison with theory

As shown in Sec. II B, the initial axisymmetric mode grows exponentially until a finite amplitude of approximately 1% of the jet velocity is reached. A subharmonic resonance mechanism, as proposed by Kelly,⁴ then takes place and the growth of this new subharmonic instability leads to the pairing process. The concept that pairing is a result of a subharmonic resonance mechanism was pointed out by Ho and Huang.¹⁸ The growth of this subharmonic mode reaches a maximum value at the pairing location, and this amplitude is larger than the value for the initial axisymmetric mode. It was also shown by Drubka⁵ that at the resonant position both the fundamental and subharmonic waves have the same phase speed (0.5 times the jet velocity), a necessary requirement for a resonance mechanism.⁷ In addition to the equal phase speeds, the fundamental and subharmonic modes must be out of phase for the pairing to occur, as demonstrated by Riley and Metcalfe,²³ and discussed by Monkewitz.⁶

Initially the amplitude of the subharmonic mode is an order of magnitude larger than that of the fundamental. This is due to the natural (self-) forcing of the flow along its downstream development. The subharmonic mode also initially grows exponentially. At one subharmonic wavelength downstream, the subharmonic resonance takes over and the amplification of this mode increases by 40% (see Fig. 14, and a comparison of the present data with Monkewitz's

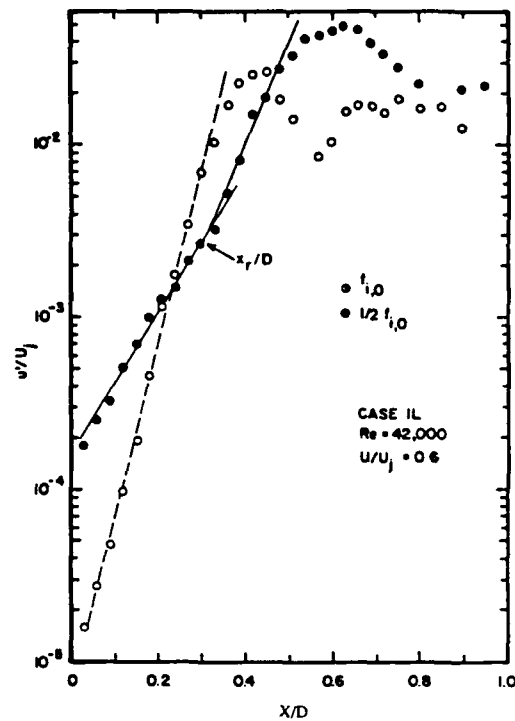


FIG. 14. Development of the initial axisymmetric mode and its subharmonic at $Re = 42\,000$.

analysis⁶). The results indicate that at the coupling Reynolds number condition, the development of the initial axisymmetric mode is not changed. In fact, only the initial amplitude of the subharmonic mode is increased, due to the stronger fed back pressure field. However, as the resonant mechanism progresses, nearly equal maximum amplitudes are observed.

The proper interpretation of the position of subharmonic resonance is not one subharmonic wavelength but rather two initial (fundamental) wavelengths from the lip. The reasoning behind this is clearly evident. For the subharmonic mode there is an initial region where the phase is constant, as explained by Drubka.⁵ After this region the subharmonic has a phase speed of $0.81 U_j$, which was clearly evident in the high Reynolds number cases. Associated with this difference in phase speed between fundamental and subharmonic modes is a difference in wavelength such that $2\lambda_{1,0}$ is smaller than the actual wavelength of the subharmonic in this region. This is simply because the two waves develop initially from linear mechanisms. It is only after the resonance that the subharmonic mode changes phase speed so that the wavelengths are related by a factor of 2. The subharmonic wavelength thus changes as it develops. Since the resonance is actually triggered by the finite amplitude state of the fundamental, the true interpretation of the resonant position is that it occurs at two fundamental wavelengths downstream of the jet lip.

The spreading of the jet with downstream distance for case 1L at a Reynolds number of 42 000 is indicated by the momentum thickness measurements of Fig. 4. At the resonant position of two fundamental wavelengths, the jet begins

its linear growth. From visualizations it is observed that the initial rollup of the jet does occur at this position. The average pairing position, as determined from the visualization, is also indicated on this figure. Near this position there is approximately a 10% increase in the jet thickness as compared to the linear growth. The case illustrated in Fig. 4 is for the natural coupling condition of case 1L, where energy in the subharmonic mode was greatest. In this case pairing is seen to have only a small influence on the linear growth region. For all other cases the effect will be even less. For naturally developing flows, the momentum thickness of the jet does *not* remain constant until pairing occurs, after which it doubles. This is only true in certain axisymmetrically forced conditions, as presented by Ho and Huang.¹⁸

A summary of the measured amplification rates for the initial axisymmetric mode, the initial subharmonic mode (i.e., before subharmonic resonance), and the subharmonic resonant mode (after subharmonic resonance) is presented in Fig. 15. The results demonstrate that the initial amplification of the axisymmetric and subharmonic modes, normalized by the proper momentum thickness, is independent of Reynolds number and the values agree well with those predicted by Monkewitz and Huerre.¹ More scatter is observed in the data for the measured amplification rates of the resonant mode, but it appears that the amplification rates of these modes do not scale with the initial momentum thickness θ_i . Instead, it is expected that this mode should scale with the momentum thickness at the resonant position (see Fig. 14). If this is true then the local momentum thickness of the jet at the resonant position will not scale with the inverse square root of the Reynolds number. This is indicated by the deviation away from the dashed line. There is insufficient data on the momentum thickness at the resonant position to comment further on this conjecture, which indicates that the developing instability is a jet instability, and that viewing the initial shear layer as locally two dimensional on the sole basis of an initially thin boundary layer may be an incorrect assumption.

From the results of Fig. 5 it is observed that over the region of measurements the divergence of the jet, $\partial\theta/\partial X$, is 1.7%. Because of the nearly parallel nature of the flow in this region, it is not surprising that the growth of the disturbances is exponential over the entire region as indicated in

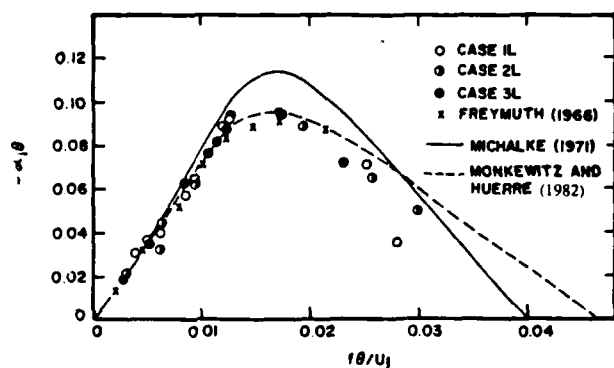


FIG. 15. Summary of mode growth rates with external excitation Strouhal number for all laminar boundary layer cases.

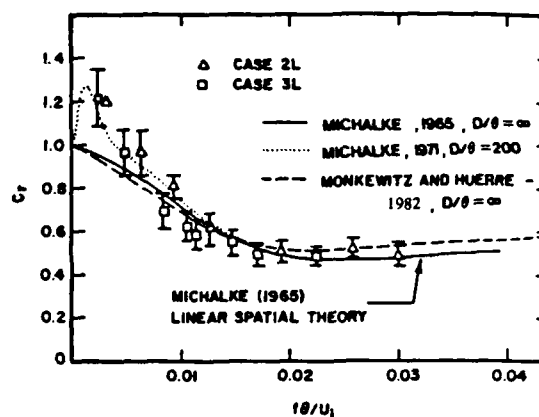


FIG. 16. Variation of mode phase speed with external excitation Strouhal number for cases 2L and 3L.

Fig. 14. This fact is also borne out in the observation of a constant phase speed over the same region, as reported by Drubka.⁵ Some of his results are summarized in Fig. 16. The phase speed clearly follows the trend of Michalke's analysis for a round jet.²² At low frequencies, ultrafast waves are observed just as in the case of Bechert and Pfizenmaier²⁴ and predicted by Michalke.²²

E. Coupling with the jet column mode

A key element in the control of far downstream jet characteristics (such as spreading, etc.) revolves around the transition from an initial length scale θ_i to a terminal jet structure of scale D . The final "passage" frequency was shown to scale with diameter,²⁵ provided that the initial length scale ratio is sufficiently large ($D/2\theta_i > 120$). Because the initial shear-layer instability scales with θ_i , the "initial" and "final" frequencies of the jet are usually unrelated. At certain Reynolds numbers, however, a special coupling can take place between these two instability modes. The mechanistic interpretation of the coupling is that the Reynolds number is such that an integer number of pairing events coincides with the end of the potential core. Because of the possibility of coupling between the shear-layer mode and the preferred mode of the jet, the organization and restructuring of the shear layer is expected to depend on Reynolds number.

It is well known that the long wave instability, commonly referred to as the jet column or preferred mode, develops in all axisymmetric jets. The value of its Strouhal number based on diameter has been found to be typically 0.4, although variations between 0.3 and 0.6 may be found, depending on whether the jet is forced, and depending on the particular facility and jet configuration. This instability is identified on the jet centerline typically two to five diameters downstream of the jet exit. Work by Kibens¹¹ showed that when the exit boundary layer was laminar and the initial axisymmetric Strouhal frequency was an integral power of 2 of the long wave jet frequency (St_j), a small amount of axisymmetric excitation at the initial jet eigenfrequency had a tremendous effect on the organization of the jet. This resulted in a large fraction of the energy being associated with the

coherent structures. Axisymmetric vortex pairings were clearly observed and found to be stationary in space. This mechanism was found to depend on the coupling between the initial axisymmetric mode and the long wave jet instability. Under these conditions, the shear-layer frequency displays a stepwise behavior in X . This is not to be confused with the stepwise behavior of the initial Strouhal frequency with Reynolds number in the presence of spatially coherent external disturbances.²⁵

Based on the above results, a necessary condition for this to occur is that the initial axisymmetric Strouhal frequency of the jet be an integral power of 2 of the long wave jet instability,¹⁷ i.e.,

$$St_{i,0} = 2^n St_f \quad (4)$$

The Reynolds numbers at which this coupling would occur would then be given by

$$Re^* = C(2^n St_f)^2 \quad (5)$$

In the above equation, n is identified as the number of vortex pairings. It must be assumed that the vortex interactions are all axisymmetric for these relations to hold.

The jet Strouhal numbers were first determined along the jet centerline at $X/D = 5$ for five different initial conditions. At this downstream location, the peak in the velocity spectrum is well defined for all cases. In each case, St_D is found to be independent of Reynolds number. The value of St_D , however, is a function of the initial condition, varying from 0.42 to 0.485. For test flow conditions 1L and 2L, St_D has a constant value of 0.42 and only marginally increases to 0.43 for test flow condition 3L. When a thicker turbulent boundary layer was utilized, the value of St_D increased to 0.485. The value of this Strouhal number is a definite function of the initial momentum thickness of the jet. For case 1L, the value of $D/2\theta_i$ is larger than 110. For this case the Strouhal frequency reaches an asymptotic value of 0.42.

With the information provided in Fig. 11, the value of C in Eq. (5) was calculated for test flow condition 1L as $C = 3720$. Knowing this value and the value of $St_D = 0.42$, the Reynolds numbers at which this coupling might take place were estimated from Eq. (5). The resulting resonant Reynolds numbers Re^* form a geometric sequence: 2600, 10 500, 42 000, and 168 000, as the number of pairing events n increases from one to four. This result indicates that this coupling occurs predominately at low and moderate Reynolds numbers. As Re increases this coupling becomes less frequent.

Operation of the present 5 cm jet was limited to Reynolds numbers larger than 30 000. Below this value the pressure field at the nozzle lip was not much larger than the background level and the jet could have been susceptible to external disturbances. The facility could not be continuously run at an exit Reynolds number of 168 000. Therefore if any indication of the coupling mechanism is present in the naturally evolving jet, it would be found at $Re = 42 000$.

If this coupling is to occur, then the jet would become more organized in an axisymmetric sense. This increase in organization would lead to an increase in the observed coherent energy. Some of this energy would be visible in the subharmonic mode but would probably not alter the growth

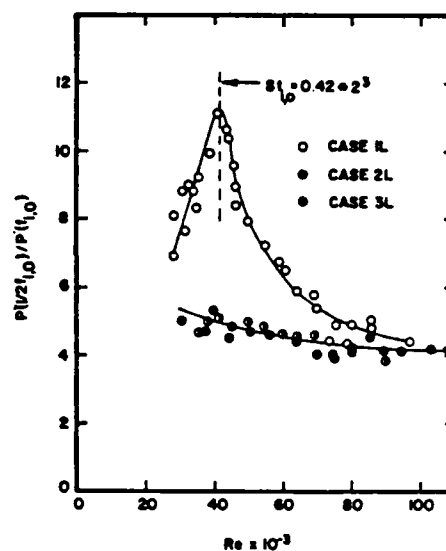


FIG. 17. Reynolds number dependence for normalized amplitude of near-field pressure from the subharmonic mode.

of the initial linear axisymmetric instability. This increase in the subharmonic energy would then be associated with a stronger pressure field for this mode, which would then be felt at the nozzle lip. To examine this, pressure spectra at the nozzle lip were taken at various Reynolds numbers using an alternate pressure measuring system that bypassed the pressure taps for higher accuracy. For each Reynolds number the amplitude of the subharmonic pressure peak was normalized by the magnitude of the peak of the initial axisymmetric mode, $f_{i,0}$. These results are displayed in Fig. 17 for test cases 1L, 2L, and 3L.

For case 1L there is a sharp maximum in the curve that occurs at the exact Reynolds number predicted by Eq. (5). A closer examination of the pressure spectra indicated that the magnitude of the peak at $f_{i,0}$ continuously increased with Re . The peak at the coupling position thus corresponded to an abnormal increase in the pressure field at $1/2 f_{i,0}$. This coupling is *weak*, though, since the increase in the ratio of the pressure amplitudes is only about 2. Another indication of the weak coupling is the observance of only one subharmonic mode in the pressure spectrum. This coupling mechanism was based on the idea of continual vortex pairing until the downstream jet Strouhal frequency was reached. This continual pairing would then lead to the successive development of modes $1/2 f_{i,0}$, $1/4 f_{i,0}$, $1/8 f_{i,0}$, Yet, the second pairing mode ($1/4 f_{i,0}$) is clearly not observed. A third indication of the relatively weak coupling is the lack of any effect this coupling has on the growth rate for the jet at this Reynolds number.⁵

Once the background disturbance level is increased as in cases 2L and 3L, this natural coupling disappears, i.e., the jet is no longer capable of effective self-forcing, via pressure feedback.²⁶ In these cases, the emergence of an initial helical mode was clearly noted. With the competition between this mode and the initial axisymmetric mode, it is not surprising that an axisymmetric coupling is not observed. If initial axisymmetric perturbations of sufficient intensity were added at the proper frequency so that the axisymmetric mode com-

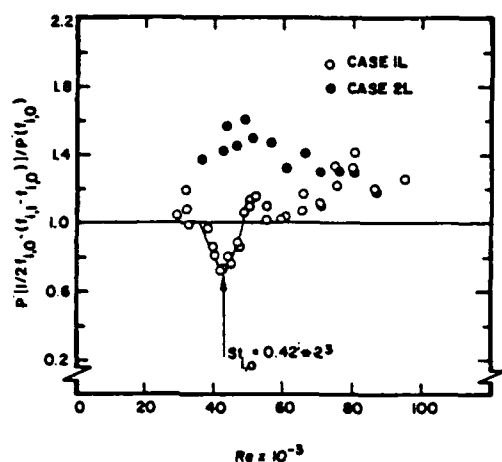


FIG. 18. Reynolds number dependence for normalized amplitude of near-field pressure from nonlinear mode based on interaction between initial helical and axisymmetric disturbances.

pletely dominated the initial helical mode development, then this coupling between long and short waves would be observed at the indicated coupling position. These results suggest that *continual* pairing (in the spatial sense) is not the coupling mechanism between long and short waves as Kibens¹¹ found using external forcing. By externally exciting the jet in the manner of Kibens,¹¹ it is possible to override the effect of the helical disturbances. The *continual* pairing then is a result of the externally imposed axisymmetric forcing. As documented by Corke, Shakib, and Nagib,²⁷ external axisymmetric forcing acts first to *inhibit* the natural coupling mechanism before efficient locking is achieved at higher amplitudes.

To observe the effect of the helical mode on the natural coupling, the peak amplitudes of an axisymmetric-helical nonlinear interaction mode is considered in Fig. 18 as a function of Reynolds number. This interaction mode is the difference between the subharmonic mode $1/2 f_{i,0}$ on the one hand, and the difference mode between helical and axisymmetric frequencies on the other. The choice of this frequency as a sensitive indicator originates from the fact that the interaction modes have lower frequencies than the original modes, and are therefore more efficient radiators at a fixed distance from the jet lip. The amplitude of the interaction mode is suitably normalized by that of the fundamental axisymmetric frequency $f_{i,0}$, so as to indicate the relative importance of the helical to axisymmetric modes. The results of Fig. 18 for the 1L case show that at the coupling Reynolds number, this ratio has a minimum value. This minimum corresponds to the increased axisymmetric field described above. As the Reynolds number deviates from that of natural coupling, the relative importance of the helical mode grows as shown by the trend of the data toward values of this ratio larger than 1. In case 2L no natural coupling was observed. This is demonstrated here by the importance of the helical mode as indicated by this ratio being larger than 1. This value for case 2L is equal to that at the higher Reynolds numbers for case 1L. This further demonstrates that as the disturbance level increases, the helical mode is quite distinct and the flow field

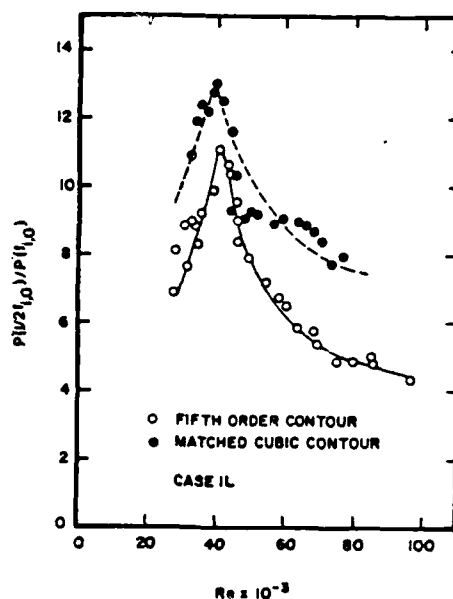


FIG. 19. Effect of nozzle shape on Reynolds number dependence for normalized amplitude of near-field pressure from subharmonic mode.

can no longer be thought of as being fully axisymmetric.

To ensure that this coupling behavior was not influenced by the shape of the nozzle, a similar study was performed using a matched cubic nozzle. These results are displayed in Figs. 19 and 20. The coupling Reynolds number for this case is essentially the same value as for the fifth-order nozzle since the exit boundary layers are nearly identical. The coupling phenomenon is once again displayed in Fig. 19 for test case 1L. The only difference in the behavior of the two nozzles is the larger value of $p'(0.5 f_{i,0})/p'(f_{i,0})$ for the matched cubic nozzle. Upon examination of the values of the peaks in the spectra, it was determined that the increase in this value was due to a decrease in the value of $p'(f_{i,0})$.

The variation of the rms pressure fluctuation associated with the subharmonic nonlinear interactive mode described above is shown in Fig. 20. In this case the behavior of both nozzles is nearly identical and once again demonstrates the

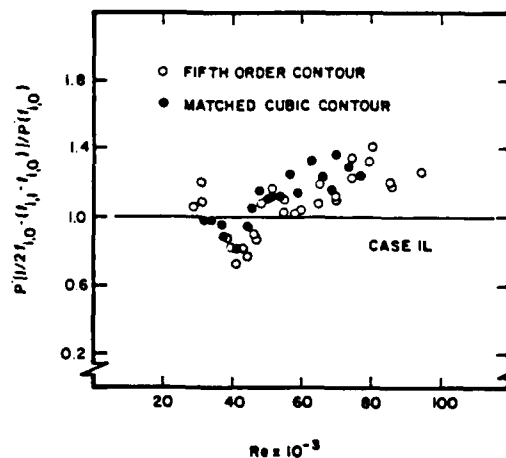


FIG. 20. Effect of nozzle shape on Reynolds number dependence of normalized amplitude of near-field pressure from the nonlinear mode based on the interaction between initial helical and axisymmetric disturbances.

natural coupling position and the emergence of the helical mode when the Reynolds number deviates from the coupling Reynolds number. These results are consistent with those of the previous figures. Thus it appears that the only difference between the two nozzles is the magnitude of the pressure field at the nozzle lip due to the initial development of the axisymmetric instability mode.

In light of these results, it is possible to identify further the existence of the natural coupling on the basis of simple mean velocity measurements such as the centerline decays obtained at various Reynolds numbers and presented in Fig. 1. As documented recently by Reisenthel¹⁴ through sensitivity of such profiles to acoustic forcing, the jet column mode displays a relative insensitivity to excitation, in accordance with the findings of Hussain and Zaman.¹⁰ The weakly resonant jet at $Re = 42\,000$ is in fact "self-forced," which explains the increased difficulty in artificially exciting it, since there is competition between the externally introduced perturbations and the naturally synchronized oscillations in the jet.

Calculations aimed at quantifying the amount of spreading of the jet and based on available centerline decay measurements are presented in Figs. 21 and 22. Figure 21 shows the variation of the spreading estimation S with Reynolds numbers. The quantity S is defined as the integral from $X = 0$ to $X = 8D$ of the variable $(1 - U_{cl}/U_j)$, and therefore represents the area between the line $U_{cl}/U_j = 1$ (no spreading) and $U_{cl}(X)/U_j$. The integral S naturally depends on the location of the last spatial sample and becomes in theory unbounded for large X . This operational definition (truncating at approximately twice the potential core length) is to be regarded only as both a convenient means of reducing the available data and as a consistent method for the estimation of spreading²⁸ for the near region of the jet. Figure 21 shows that S is always greater for the unforced (natural) case. The kink in the curve at $Re = 42\,000$ illustrates the robustness, with respect to external excitation, of the jet column mode. This is made clearer in Fig. 22, which presents the variation of the relative spreading $(S_n - S_f)$ between natural and forced configurations with Reynolds number. The variables S_n and S_f represent the value of S calculated for the natural and forced cases, respectively. Figure 22 therefore illustrates

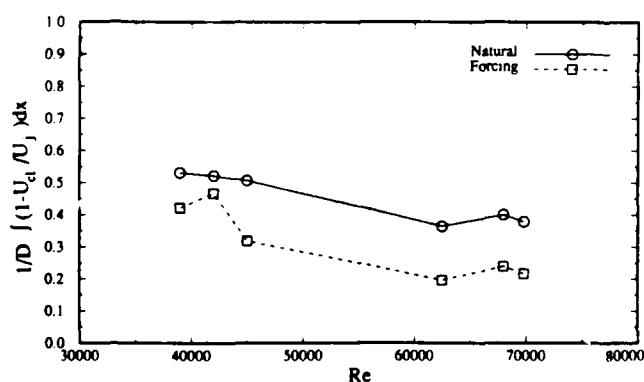


FIG. 21. Variation of spreading estimate with Reynolds number for natural and excited jets.

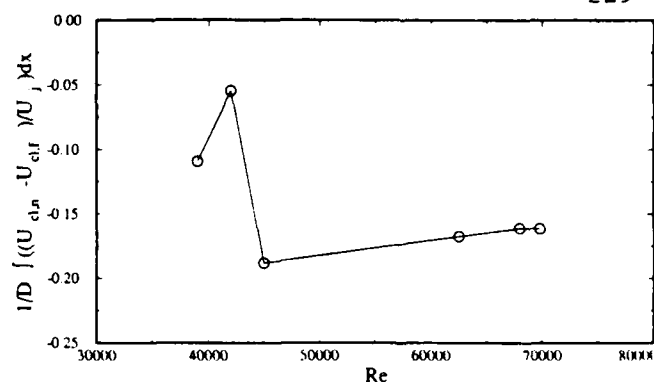


FIG. 22. Variation of relative spreading between natural and forced jets with Reynolds number.

the relative insensitivity to external forcing at the coupling Reynolds number.

Streamwise velocity spectra taken along the similarity line $U/U_j = 0.5$ are shown in Figs. 23–25 under conditions of external excitation at $Re = 66\,000$ and $42\,000$. The complex nonlinear interactions, taking place in the shear layer and depicted in Figs. 8 and 12, are indicated by the multitude and relative broadness of the spectral peaks. The jet column mode ($Re = 42\,000$) corresponds to the flow field with the highest "resilience" to external forcing. Despite this fact, the possibility of "unlocking" the jet is expected, provided that a sufficiently high level of excitation is applied. This hypothesis is tested in Fig. 25. The spatial structure of the shear layer at $Re = 42\,000$ under large amplitude excitation is illustrated by the spectral measurements. As demonstrated recently by Reisenthel,¹⁴ the increased excitation levels also lead to an increase in the centerline decay, as measured by data similar to Fig. 1.

Finally, it is worth mentioning that under resonant conditions, the final Strouhal mode was found to be correlated to the near-field pressure along the entire axial extent of the potential core. The emergence of this mode was most clearly noted in the ultralow disturbance level condition of flow 1L (see Fig. 17). The centerline amplitude development of this mode for this case at $Re = 42\,000$ is shown in Fig. 26. Also

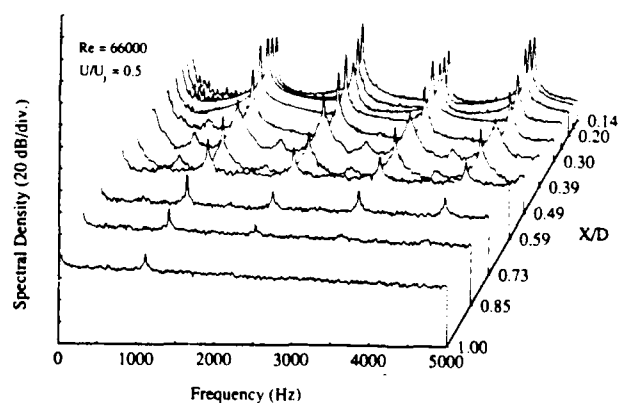


FIG. 23. Variation of velocity spectra with downstream distance under forcing conditions at $Re = 66\,000$.

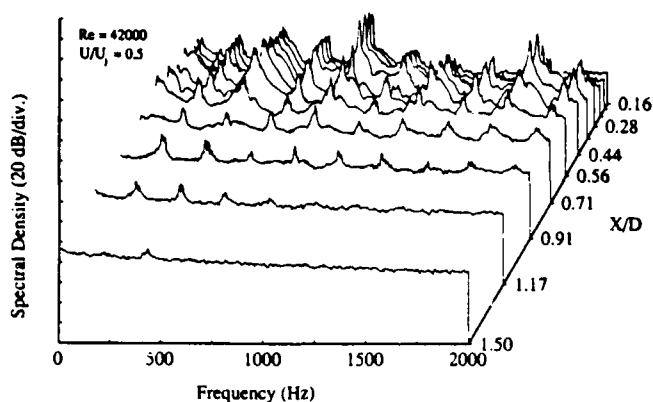


FIG. 24. Variation of velocity spectra with downstream distance under forcing conditions at $Re = 42\,000$.

included in this figure are the results of Crighton and Gaster²⁹ who calculated the centerline spatial amplification rates for an axisymmetric disturbance in a slowly diverging jet flow. Excellent agreement is observed within the first 2.5 diameters even though the measured divergence rate is approximately 25% greater than that used in the theoretical predictions. As the divergence rate increases, the local amplification rate should decrease. This is probably part of the discrepancy between predictions and the measurements beyond 2.5 diameters.

III. CONCLUSION

With the availability of an easily controllable, low disturbance axisymmetric free jet, it has been possible to reveal several important features of the dynamics of turbulent jets. These features were documented by multiprobe velocity and pressure measurements over a range of Reynolds number and initial conditions of the jet. Subharmonic resonance is unequivocally recognized as the precursor to vortex pairing. The details of its evolution are documented and its location is found to be two fundamental wavelengths from the jet lip. The instability characteristics of the subharmonic frequency, even past the point of resonance, appear to conform to local linear stability predictions as long as the appropriate

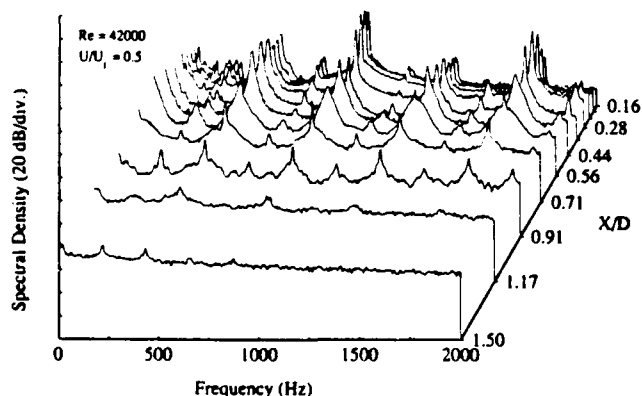


FIG. 25. Variation of velocity spectra with downstream distance under forcing conditions at $Re = 42\,000$, $SPL = 81\,dB$.

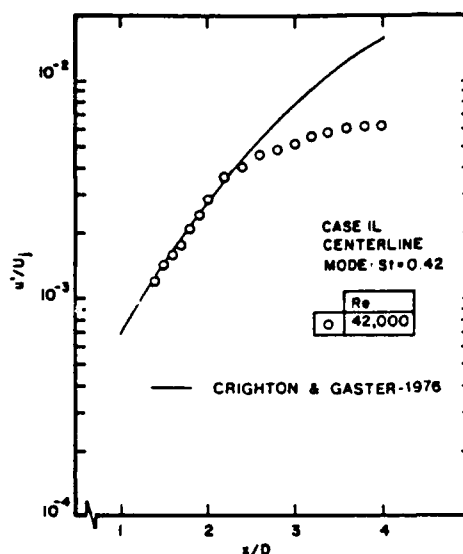


FIG. 26. Streamwise development along the jet centerline of amplitude of the final Strouhal frequency at $Re = 42\,000$.

length scale is used. The existence of previously predicted ultrafast long wave instabilities is confirmed experimentally and the phase speed is found to compare favorably with theory. Finally, a weak coupling between the shear-layer mode and the preferred mode of the jet is revealed at resonant Reynolds numbers, which can be predicted by deterministic arguments about vortex interactions and the scaling of the initial jet instability.

ACKNOWLEDGMENT

P. Reisenthel and H. M. Nagib would like to acknowledge the support of the United State Air Force Office of Scientific Research under Grant No. 86-0165 during preparation of this manuscript.

- ¹P. A. Monkewitz and P. Huerre, *Phys. Fluids* **25**, 1137 (1982).
- ²C. M. Ho and P. Huerre, *Annu. Rev. Fluid Mech.* **16**, 365 (1984).
- ³P. Huerre and P. A. Monkewitz, *J. Fluid Mech.* **159**, 151 (1985).
- ⁴R. E. Kelly, *J. Fluid Mech.* **27**, 657 (1967).
- ⁵R. E. Drubka, Ph.D. thesis, Illinois Institute of Technology, Chicago, 1981.
- ⁶P. A. Monkewitz, *J. Fluid Mech.* **188**, 223 (1988).
- ⁷J. Cohen and I. J. Wygnanski, *J. Fluid Mech.* **176**, 221 (1987).
- ⁸A. Ahmadi-Moghadam, Ph.D. thesis, Illinois Institute of Technology, Chicago, 1986.
- ⁹S. C. Crow and F. H. Champagne, *J. Fluid Mech.* **48**, 547 (1971).
- ¹⁰A. K. M. F. Hussain and K. B. M. Q. Zaman, *J. Fluid Mech.* **110**, 39 (1981).
- ¹¹V. Kibens, *AIAA J.* **18**, 434 (1980).
- ¹²F. Shakib, M.S. thesis, Illinois Institute of Technology, Chicago, 1984.
- ¹³J. Tan-Atchhat, Ph.D. thesis, Illinois Institute of Technology, Chicago, 1980.
- ¹⁴P. Reisenthel, Ph.D. thesis, Illinois Institute of Technology, Chicago, 1988.
- ¹⁵G. E. Mattingly and C. C. Chang, *J. Fluid Mech.* **65**, 541 (1974).
- ¹⁶S. M. Kusek, T. C. Corke, and P. Reisenthel, *AIAA Paper No. 89-0968*, 1989.
- ¹⁷J. Laufer and P. A. Monkewitz, *AIAA Paper No. 80-0962*, 1980.
- ¹⁸C. M. Ho and L. Huang, *J. Fluid Mech.* **119**, 443 (1982).
- ¹⁹E. Gutmark and C. M. Ho, *Bull. Am. Phys. Soc.* **9**, 1102 (1980).

- ²⁰K. B. M. Q. Zaman and A. K. M. F. Hussain, *J. Fluid Mech.* **103**, 133 (1981).
- ²¹E. Pfizenmaier, Proceedings of the Colloquium on Coherent Structures in Turbulence, Southampton, 1974 (unpublished).
- ²²A. Michalke, *Z. Flugwiss.* **9**, 319 (1971).
- ²³J. J. Riley and R. W. Metcalfe, AIAA Paper No. 80-0274, 1980.
- ²⁴D. W. Bechert and E. Pfizenmaier, *J. Fluid Mech.* **72**, 341 (1975).
- ²⁵E. Gutmark and C. M. Ho, *Phys. Fluids* **26**, 2932 (1983).
- ²⁶T. C. Corke, F. Shakib, and H. M. Nagib, submitted to *J. Fluid Mech.*
- ²⁷T. C. Corke, F. Shakib, and H. M. Nagib, AIAA Paper No. 85-0573, 1985.
- ²⁸H. Schlichting, *Boundary Layer Theory* (McGraw-Hill, New York, 1979).
- ²⁹D. G. Crighton and M. Gaster, *J. Fluid Mech.* **77**, 397 (1976).

AIAA '89

AIAA-89-0968

**Control of Two and Three Dimensional
Modes in the Initial Region of an
Axisymmetric Jet**

**S. M. Kusek, T. C. Corke and P. Reisenthel
Fluid Dynamics Research Center,
Mechanical and Aerospace Engineering Department,
Illinois Institute of Technology
Chicago, IL**

AIAA 2nd Shear Flow Conference

March 13-16, 1989 / Tempe, AZ

CONTROL OF TWO AND THREE DIMENSIONAL MODES IN THE INITIAL REGION OF AN AXISYMMETRIC JET

S. M. Kusek[†], T. C. Corke[‡] and P. Reisenthel^{*}

Fluid Dynamics Research Center
Illinois Institute of Technology
Chicago, Illinois 60616

Abstract

Both active and reactive (i.e. enhanced feedback) control of fundamental two- and three-dimensional amplified modes in an axisymmetric jet is presented. This is done by introducing localized acoustic disturbances produced by an azimuthal array of miniature speakers placed in the close proximity of the jet lip on the exit face. The independent control of each speaker output allows different azimuthal amplitude and phase distributions of periodic input pressure disturbances. Under active control, the periodic time series seeding inputs are supplied externally. Under reactive control, the seeding input is derived from the analog time series proportional to the velocity fluctuations taken at a point in space in the developing shear layer downstream of the exit lip. In the case of the latter for axisymmetric modes, Reisenthel (1988) and Reisenthel et al. (1988) have demonstrated that the resulting flowfield is globally unstable and may be modeled using rather simple model amplitude equations. The objective of the present work is to: *i*) examine the linear characteristics of low-level helical seeding, and *ii*) include helical modes into the enhanced feedback concept.

Nomenclature

A	Total forcing amplitude
A^*	Maximum amplitude of single helix
A_1	Forcing amplitude of right-handed helix
A_2	Forcing amplitude of left-handed helix
C	Phase speed
CTA	Constant temperature anemometer
D	Jet diameter
f	Excitation frequency
f_0	Natural axisymmetric mode frequency
f_1	Natural helical mode frequency
HMG	Helical Mode Generator
PMMA	Polymethylmethacrylate
m	Azimuthal wave number
q	Dynamic pressure ($\frac{1}{2}\rho U_j^2$)

r	Radial coordinate
Re	Reynolds number based on diameter ($U_j D / \nu$)
St_D	Strouhal number based on diameter (fD/U_j)
St_θ	Strouhal number based on momentum thickness ($f\theta/U_j$)
u'	Streamwise velocity fluctuation
U	Mean streamwise velocity
U_j	Jet exit velocity
x	Downstream distance measured from the jet lip
α_r	Streamwise wave number
$-\alpha_i$	Spatial amplification rate
δ	Shear-layer thickness
γ	Azimuthal coordinate
γ_0	Arbitrary reference azimuthal coordinate
ϕ	Phase angle
λ	Streamwise wave length
θ	Shear-layer momentum thickness
ν	Kinematic viscosity
ρ	Fluid density
ω	Angular frequency

I. Introduction

The role of three-dimensional disturbances in axisymmetric jets has been the focus of a number of studies in the last two decades. Although most of these studies are theoretical and have addressed the linear stability properties of helical modes, recent attention has been given to the possibility of strong intermodal resonant interactions. The latter mechanism was experimentally demonstrated by Cohen and Wygnanski (1987), and reinforces the need to consider the potential of 3-D modes which may be considered 'dormant' by linear standards.

Perhaps the most recent of theoretical analyses of the stability of azimuthal modes is that of Ahmadi-Moghadam (1986), which considers a thin circular shear layer with a Blasius profile. The use of this self-similar profile is justified on the basis of experiments with laminar exit conditions (see Drubka, 1981). In this study, the effect of curvature was represented by the ratio δ/D .

[†] Graduate Research Assistant

[‡] Associate Professor, Member AIAA

^{*} Visiting Assistant Professor, Member AIAA

Copyright © 1989 by Stephen M. Kusek. Published by the American Institute of Aeronautics and Astronautics, Inc., with permission.

and the results compared to Michalke's (1971) hyperbolic tangent profile: although small differences in the mean velocity profile were found to produce sizable quantitative discrepancies, several general conclusions could be drawn: *i*) the phase speed depends strongly on azimuthal wave number (m) at low frequencies (in particular, the non-dispersive character of the instability waves increases with increasing m), *ii*) the linear growth rates decrease with increasing m , and *iii*) in any event, these effects are accentuated by curvature, and most felt for low Strouhal number. An earlier inviscid spatial analysis by Michalke (1969) for a 2-D hyperbolic tangent profile showed similarly that 2-D modes are always more amplified and that the wave dispersiveness and amplification rate ($-\alpha_i$) both decrease with increasing spanwise wave number.

In contrast to the 'locally parallel' theories, Plaschko (1979) used a multiple scales method similar to the approach of Crighton and Gaster (1976), in order to properly capture the slowly diverging nature of jet flow. A higher gain was found for the axisymmetric mode at higher Strouhal numbers, whereas lower Strouhal numbers promoted higher gain for $m=1$, at farther downstream distances. In addition, Plaschko (1979) showed that the higher order helical modes ($|m| \geq 2$) were always less amplified than their axisymmetric ($m=0$) and first helical ($m=\pm 1$) counterpart.

Mattingly and Chang (1974) reported similar results using inviscid spatial theory applied to a family of experimentally determined velocity profiles in a low Reynolds number water jet. They found that the axisymmetric mode dominates the jet column initially, but that the $m=\pm 1$ mode becomes the most amplified, past $x/D=3$. Their results also indicated that the $m=\pm 2$ mode was never dominant. Recently, Cohen and Wygnanski (1987) also performed an inviscid linear spatial stability analysis of analytically-fitted experimental profiles and obtained good agreement of the mode shapes in the initial region of the jet. The importance of jet divergence was incorporated through the parameter $R_{1/2}/\theta$ (the local ratio of the radius where $U/U_j = .5$ to the momentum thickness). The results of their analysis qualitatively corroborate those of Ahmadi-Moghadam (1986). In particular, they substantiated analytically that when the ratio of spanwise to streamwise wave numbers was small, all modes behave essentially as if the mean flow were two-dimensional.

In spite of the differences in the analytical approaches taken by the above investigators, it is clear that the two linearly dominating modes on a jet column are the fundamental ($m=0$) and first helical ($m=\pm 1$) modes. Although their linear characteristics are virtually indistinguishable at the early stages (i.e. when the shear layer is thin, compared to the jet diameter), there is a greater likelihood to observe and characterize the helical modes at the larger downstream distances (e.g.: $x/D > 3$). This may explain in part why the few available experimental studies of helical mode instability appear to have focused on the non-linear interactions

produced by these modes, rather than on the linear stages *per se*. A frequently used evidence of such interactions is the mean flow distortion produced by the simultaneous forcing of modes with same frequency (see, e.g., Cohen and Wygnanski, 1987, and Long et al., 1988). Admittedly, the concept of resonant interactions (and in particular: subharmonic resonant interactions) appears to be a highly promising avenue of research for controlling jet flows. For example, Ahmadi-Moghadam's (1986) analysis predicts the possibility of a Craik-type (1971) triad interaction in the jet, leading to "explosive growth".

Although it is our goal to investigate this issue experimentally in a forthcoming study (Kusek, 1989), this manuscript describes the results of a preliminary investigation aimed at filling some gaps in the available experimental data dealing with the truly *linear* (i.e. very low amplitude) stages of helical instabilities. The use of very low initial amplitudes to seed non-axisymmetric modes is made possible in part by: *i*) the design of a helical mode generator (described herein) relying on a receptivity mechanism at the lip, and *ii*) by the use of an ultra-low freestream turbulence facility. It should be noted that controlled input levels of acoustic excitation provide us with a means of assessing amplitude threshold effects for non-linear resonances.

In addition, low excitation levels constitute a *realistic* way of seeding instability waves, because these levels are of comparable strength to those generated by the pressure feedback which occurs naturally in jets (Drubka, 1981). Such effects may, in fact, be related to the temporal switching which has commonly been observed between axisymmetric and helical ($m=\pm 1$) modes (Mattingly and Chang, 1974, Shakib, 1984), and for which no satisfactory explanation has yet been provided. An illustration of this switching is provided by the single realization flow visualizations of Figure 1. Both photographs correspond to the natural jet at $Re = 10,000$. The top picture represents a typical axisymmetric instability. However, the bottom one (taken an instant later) shows a long wave length helical instability, past $x/D \approx 1$. In contrast to this 'single helix', Figure 2 illustrates the possibility of two simultaneously occurring helices of opposite azimuthal wave numbers, at $Re = 20,000$. Our primary and long-term objective in this study is to understand the mechanism controlling the temporal switching, coupled with the investigation of new ways in which to alter jets, using controlled two- and three-dimensional excitation. In the present paper, both extrinsic and intrinsic (enhanced feedback) excitations of simultaneous ($m=+1, m=-1$) helical modes are presented.

II. Experimental Apparatus

This experiment was performed in the same jet facility that was used by Drubka (1981), Shakib (1984), Corke et al. (1985, 1989), Reisenhel (1988) and

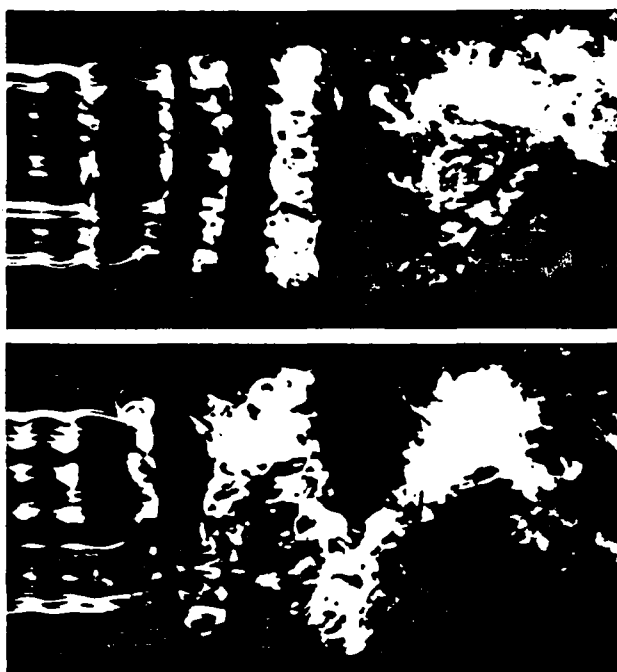


Figure 1. Smoke-wire flow visualization depicting natural axisymmetric (top) and helical (bottom) instabilities at $Re = 10,000$.

Reisenthel et al. (1988). Its very low core turbulence intensity level ($u'/U_j \approx 0.05\%$) makes it well suited for measurements on stability and mode interaction. The characteristics of this jet have been extensively documented in these investigations in terms of eigenmode distributions of the fundamental instability and interacted modes, along with their dependence on changing initial conditions including Reynolds number, initial shear layer thickness and core disturbance level.

In order to benefit from the results of previous measurements, special care was taken in the design of a fixture for holding an array of miniature speakers at the exit plane of the jet. The top of Figure 3 shows a schematic of the exit region of the jet facility. The exit diameter is $D = 5.08$ cm. Close to the exit edge are eight pressure taps which provide time series information on the unsteady pressure field at the jet exit. The speaker fixture (same scale) for holding the 12 downstream-facing, miniature speakers is shown at the bottom of the figure. The fixture assembly (Figure 4) is designed to slip over the exit face of the jet without introducing any additional development length and thereby affecting the initial shear layer momentum thickness. A photograph showing the fixture with 12 speakers mounted on the jet exit is shown in Figure 4.

To excite a helical mode with positive wave number (clockwise moving) m , and frequency ω , the periodic time series to an individual speaker would be $A_1(t, \gamma) = A^* \sin(m\gamma - \omega t + \gamma_0)$. Here, γ_0 is an arbitrary phase shift. The opposite going, equal amplitude helical mode with wave number $-m$, would be produced by the periodic function $A_2(t, \gamma) = A^* \sin(-m\gamma - \omega t + \gamma_0)$. The



Figure 2. Smoke-wire flow visualization depicting the possibility of naturally occurring 'double' helices ($Re = 20,000$).

superposition of these two periodic functions yields $A(t, \gamma) = 2A^* \sin(-\omega t + \gamma_0) \cos(m\gamma)$. Therefore, to produce equal and opposite helical modes with azimuthal wave number $\pm m$ and frequency ω , each speaker will operate with a periodic input $\sin(-\omega t + \gamma_0)$, with an azimuthally stationary modulated amplitude determined by its azimuthal position according to: $2A^* \cos(m\gamma)$. With 12 speakers it may be possible to excite helical modes with azimuthal wave numbers up to $m = \pm 6$. The maximum azimuthal wave number will correspond to a ratio of streamwise to spanwise wave numbers of approximately 2.6 (wave front leaving at $\approx 21^\circ$ from the jet lip). For reference, with the azimuthal wave number $m = \pm 1$, this angle will be approximately 9° , for a streamwise to spanwise wave number ratio of 16.

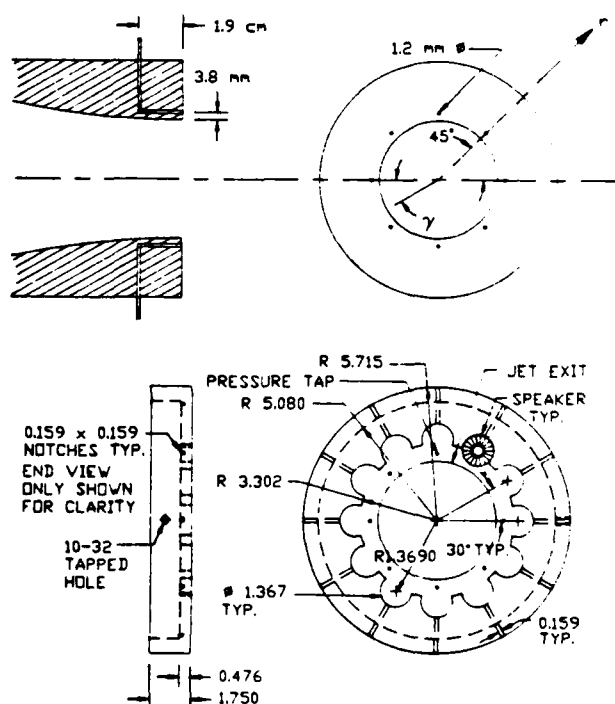


Figure 3. Schematic of jet nozzle (top) and low disturbance fixture (bottom) for holding 12 miniature speakers at jet exit face.

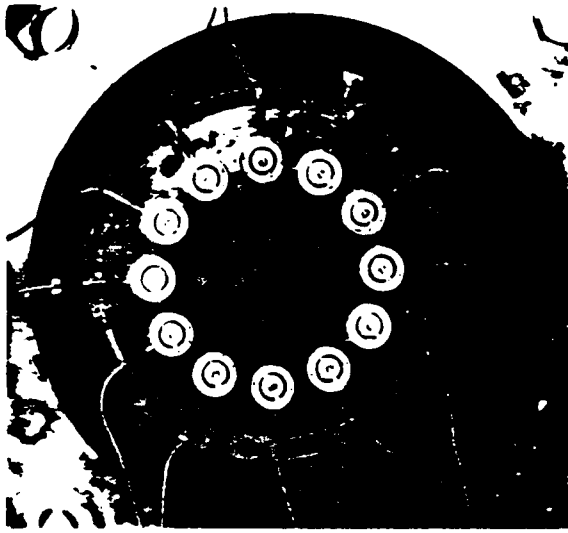


Figure 4. Photograph of helical mode generator mounted on jet nozzle.

Figure 5 shows a simplified schematic for one pair (180° apart) of speakers. To force helical modes, a single time series (with gain factor $\cos(m\gamma)$) originating from a digital/analog output in the case of external excitation, or from an anemometer output, in the case of enhanced feedback control, would be sent to each speaker pair. The speaker pairs operate in phase for even azimuthal wave numbers and with a phase difference of 180° for odd wave numbers. To force axisymmetric modes, a single time series is added at each speaker control circuit. In this case, the axisymmetric mode need not be at the same frequency as (or fixed phase offset with respect to) the helical modes. We therefore can seed directly subharmonic resonance interactions. The speaker control circuit accounts for nonuniformity in sound level output between individual speakers. The ability to add axisymmetric *and* $\pm m$ helical modes will allow the study of modal interaction and/or mode switching.

All flow visualizations were made utilizing a modified smoke wire technique. Traditionally, a stationary stainless steel wire (0.1 mm diameter) is mounted around the periphery of the jet exit at a fixed position close to the jet exit. Between each visualization, the wire is coated manually with smoke-generating oil in a somewhat tedious and time consuming manner. The modification to this technique was to automate the oil coating procedure and create a built-in flexibility to introduce smoke at any desirable x/D location.

Photographs of the new configuration are shown in Figure 6. An outer structural ring (Figure 6a) was made of PMMA for its electrical insulation value and ease of machining. The 16 wire support rods are constructed from 2.4 mm diameter aluminum with tapestry needles (large eyelets) pressed into their ends. A small steel tube (0.2 mm i.d.) is glued to the outer ring at the lower entrance to an oil reservoir cut into the top side of

the lower portion of the outer ring (see Figure 6b). The stainless steel wire is attached to a reel and threaded through the lower end of the steel tube, which causes the wire to pass through the oil reservoir, where droplets adhere to it. The wire is then threaded through the 16 supports and eventually passes through an identical oil reservoir before attachment to the second wire reel. A close-up view of the installed HMG and smoke-wire is shown in Figure 6c. This gives an indication of the relative size of smoke-wire components in the entrainment region.

Presently, a hand crank is turned to move the wire from one reel to the other. In doing so, the wire rises through one oil reservoir where the oil droplets are further distributed to the tapestry needle eyelets to form 16 mini oil reservoirs. These abundant reservoirs decrease the number of turns required to coat the wire completely. Note that the radially adjustable support rods allow the smoke wire shape to be tailored for varying fluid entrainment conditions. For instance, whereas only minor changes are required in the smoke-wire shape when varying the Reynolds number at a fixed x/D , visualization at larger downstream distances requires substantial changes in the smoke-wire circumference. Additional flexibility is provided by the ability to electrically energize the smoke wire between any two support rod locations. This makes it easy to visualize one section of the shear layer when looking at azimuthally varying conditions.

Future modifications to the smoke wire apparatus will include a motor drive (replacing the hand crank) that can be triggered from a typical smoke wire timing device to further automate the visualization process.

III. Results

1. Passive Effects

Any *passive* effect of placing the speaker holder and speakers onto the exit face of the jet is documented in Figures 7 and 8. Figure 7 shows the normalized mean profile through the jet shear layer for the x -position closest to the jet exit, $x/D = 0.11$, at two Reynolds numbers which bracket our general range of operation for measurement (i.e. $30,000 \leq Re \leq 80,000$). Multiple

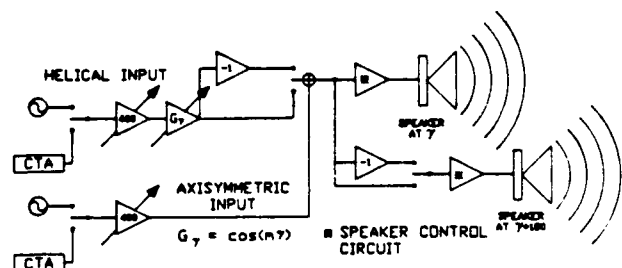


Figure 5. Schematic of the conditioning electronics driving each pair of miniature speakers.

data sets show the degree of repeatability of the mean profile in this initial region of linearly developing modes. When in place, the helical mode generator (HMG) shows no discernible effect. A more sensitive indicator is the Reynolds number dependence of the

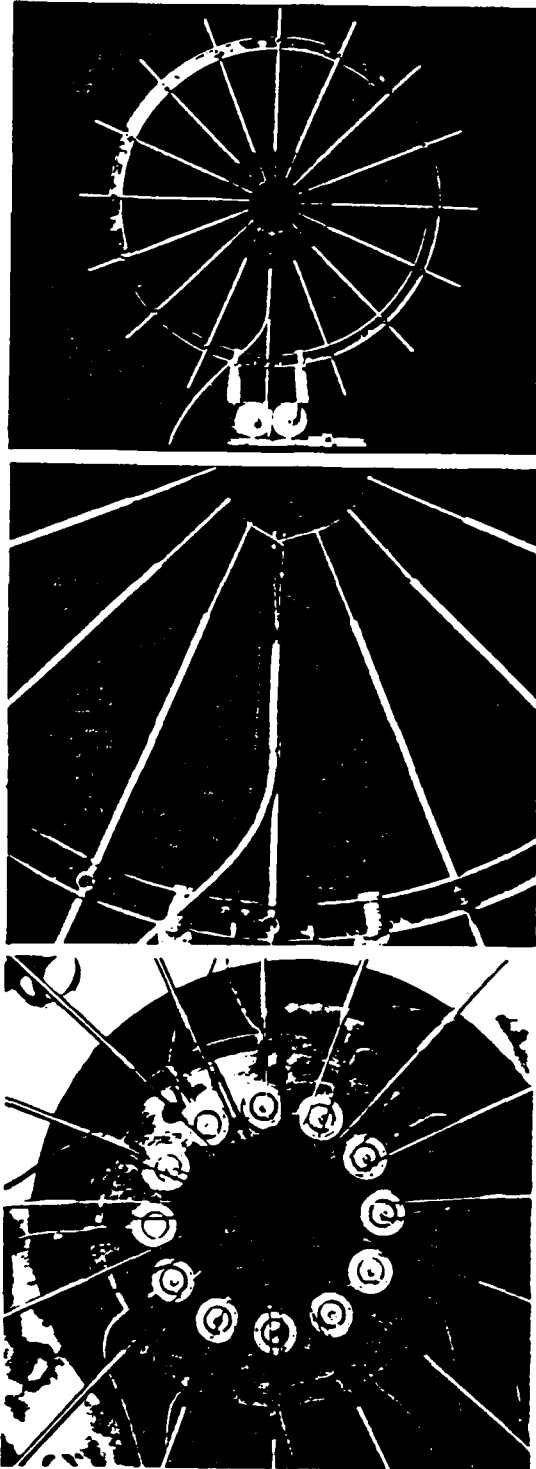


Figure 6. Photographs of the new flow visualization apparatus ; (a) overall view ; (b) close-up of oil reservoirs and smoke-wire path; (c) complete assembly with helical mode generator.

most amplified modes. These are shown in Figure 8 in terms of the fundamental axisymmetric mode at frequency f_0 , its subharmonic, $f_0/2$ and $m = \pm 1$ helical mode at frequency f_1 . For cases when the exit boundary layer thickness is small compared to the jet diameter, inviscid linear stability theory predicts that the instability modes scale with Strouhal number based on local momentum thickness (St_θ). For this particular jet facility, it is shown (Drubka, 1981, Nagib et al., 1989) that upstream of the location corresponding to subharmonic resonance, θ grows less than a few percent. Consequently, the measured θ is approximately equal to the exit momentum thickness. In cases when the exit boundary layer is laminar, such as here, the boundary layer momentum thickness is inversely proportional to Reynolds number (Blasius profile). Since $St_\theta = \text{constant}$, then $St_\theta D / \theta \propto \theta^{-1}$, or: $St_D \propto Re^{1/2}$.

This is seen to be the case without (top) and with (bottom) the HMG for these three natural dominant modes. The slopes of these curves, which is proportional to St_θ , are given in the insets of the two graphs. For the case without the HMG, the St_θ for f_0 is 0.0144. Gutmark and Ho (1983) have tabulated values of St_θ for the fundamental axisymmetric mode from experiments in nine different jet facilities. The values that they report range from 0.012 to 0.018. Drubka (1981) reported a value for this jet of 0.013. Comparing our case with the HMG we observe a slight change in St_θ for both f_0 and f_1 . The difference of course is well within the type of scatter documented by Gutmark and Ho. St_θ for the $f_0/2$ mode remains the same. The velocity distributions and the measured momentum thicknesses showed no

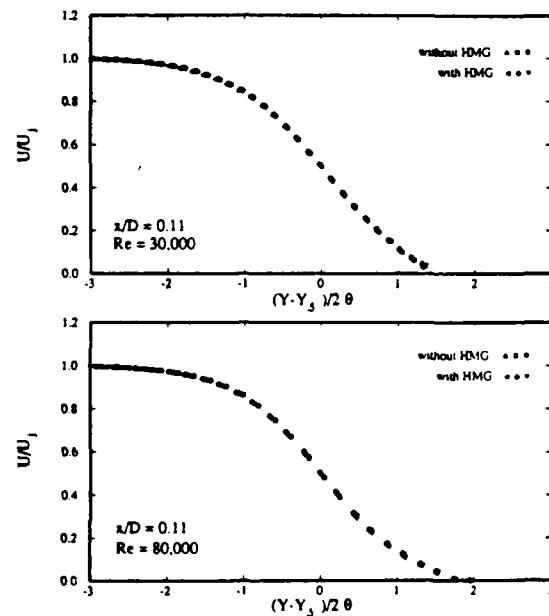


Figure 7. Normalized mean velocity profiles across shear layer without and with helical mode generator (inactive), for $Re = 30,000$ (top) and $Re = 80,000$ (bottom).

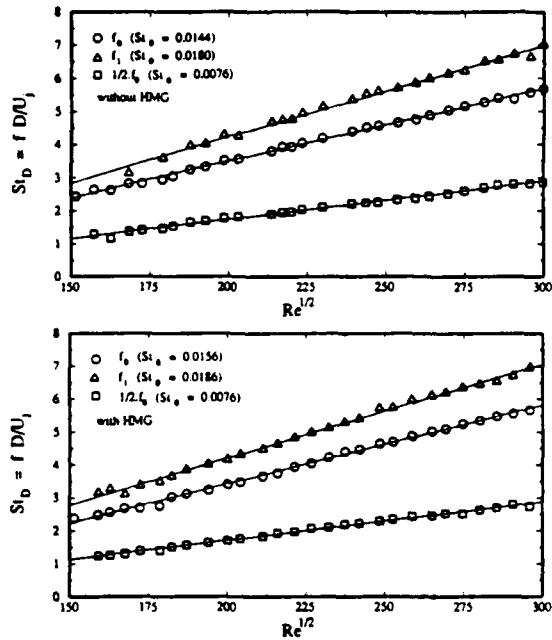


Figure 8. Strouhal number dependence of dominant natural instability modes without (top) and with (bottom) helical mode generator (inactive).

effect to the HMG. We therefore attribute the slight difference in the slopes to a change in the receptivity at the lip, rather than a change in entrainment conditions, which would presumably have changed θ . This is obviously a small effect and otherwise these dominant natural modes develop according to linear theory in either configuration.

2. Active Forcing

As described in Section II, the $\pm m$ helical mode forcing requires an initial prescribed azimuthal amplitude modulation at the lip of the jet. Ideally, this would occur in an azimuthally-continuous fashion. In our situation, the azimuthal initial condition is applied in a discrete fashion from each of the 12 speakers. We therefore were interested in first examining the response of the shear layer to a periodic disturbance produced by a single operating speaker.

The active effect of a single miniature speaker is documented in Figures 9 through 12. Figure 9 documents the streamwise development of amplitude and phase at a fixed Reynolds number, along the similarity line $U/U_j = 0.6$, at a constant azimuthal position. The jet conditions and forcing frequency correspond to the $f_0 = 2500$ Hz case of Shakib (1984) and Corke et al. (1985), produced by a far-field sound source. In Figure 9, we compare the streamwise development between such a far-field source and the single speaker of the HMG. As is evident, the comparison is excellent, especially in the initial linear growth and saturation region. In the case of the far-field sound source, the excited mode will be axisymmetric. We do not expect the same

to be true for excitation with the single miniature speaker at the jet exit. A comparison such as the one provided in Figure 9 also allows to calibrate the true forcing effectiveness of the near-field sound source, as compared to traditional loud-speaker excitation.

For the same conditions, with the single active speaker, the azimuthal amplitude and phase distribution at a fixed x -position ($x = 6$ mm) is shown in Figure 10. The azimuthal position, $\gamma = 0$, marks the center position of the active speaker. These show a localized amplitude effect with noticeable spreading (that is, as early as $x/\lambda \approx 1.2$). The phase distribution documents an approximately 250° phase shift in the azimuthal direction produced by the single small speaker. With the addition of a 180° phase shifted time series at the opposite azimuthal position, we would have the minimum number of speakers (two antinodes) needed to produce the $m = \pm 1$ helical mode. In the direct application, we utilized all twelve speakers to produce a smoother azimuthal variation for this lower order mode. Spectral analysis of the nominal input showed that the energy contained in the first helical mode is approximately 20 dB above the peak value of the next most energetic harmonic introduced by discretization†.

Figure 10 documented the azimuthal variation in phase and amplitude at a single x -location. Similar data taken at different x -positions were used to construct the full 3-D view in Figure 11, using a lower forcing level $p'/q = 0.02\%$. In moving in x , the radial position remained on the same similarity line, $U/U_j = 0.6$, as in Figure 9. In this case, the amplitude and phase are presented as isocontour levels seen as alternating black

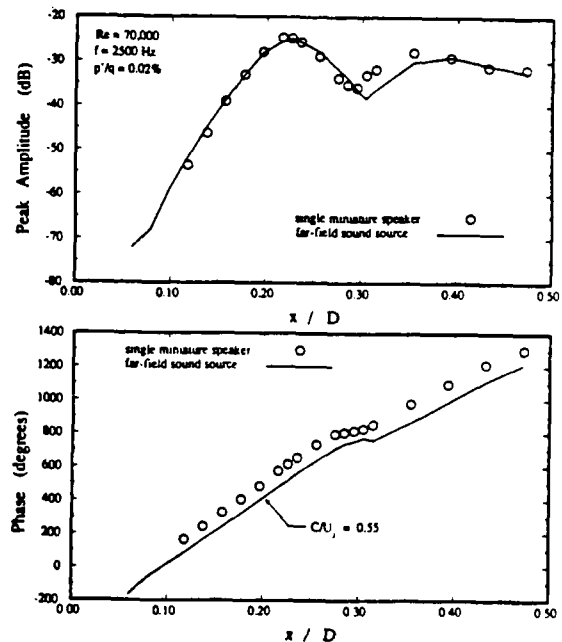


Figure 9. Comparison between near-field and far-field acoustic excitation for the streamwise development of disturbance amplitude (top) and phase (bottom) ($Re = 70,000$; $f = 2500$ Hz; $p'/q = 0.02\%$; $U/U_j = 0.6$).

and white bands. The spatial domain is presented as a flat projection with the azimuthal coordinate γ on the abscissa, and the x -direction, made non-dimensional using the jet diameter, on the ordinate. The white vertical lines in the center mark the location and extent of the single speaker. The white lines at both ends ($\gamma = \pm 60^\circ$) mark the valid region of the phase, where the linear coherence remained above 0.7. Note that this azimuthal region is considerably smaller than in the case of Figure 10, for which the coherence was approximately unity throughout, due to a four-fold increase in the forcing level.

The amplitude is *log* based (dB) so that contour bands spaced equally in x indicate constant linear (exponential) growth. Such a linear growth region is seen to exist in the initial region directly downstream of the active speaker. This extends to approximately $x/D = 0.20$ ($x/\lambda \approx 2.2$), where nonlinear effects result in energy saturation in this mode. For this mode, the point of energy saturation marks the position of the first vortex roll-up (see, e.g., Shakib, 1984). On either side of the speaker, the energy spreads and feeds the same mode. This mode is seen to amplify at approximately the same spatial rate, but because the initial amplitude decays in the azimuthal direction (see Figure 10), the development length, before reaching saturation, is shifted downstream. From the phase distribution at the top of the figure, we observe a constant phase development in the azimuthal direction. The number and width of phase contour bands in the x -direction is indicative of the phase velocity of this mode. Therefore, the phase distribution indicates that the single speaker is exciting a single mode which is traveling at a constant phase speed ($C/U_j \approx 0.54$) everywhere within the valid azimuthal region. Flow visualization which primarily marks the rolled up vortex would show for this case what would appear therefore to be an inclined axisymmetric mode (or so-called "tilted axisymmetric" mode; this question is still under investigation). However, the feature implying the inclination would actually be a result of the azimuthal distribution of the initial amplitude of this mode which provides, away from the active speaker, a longer development length before saturation and vortex roll-up.

The spatial amplitude and phase information from the previous figure can be used to show the reconstituted spatial development of the measured periodic fluctuations excited from the single active speaker. This is presented in Figure 12. In this case, the contours represent pseudo-instantaneous velocity fluctuations, and the surrounding region (grey) corresponds to background amplitude (i.e. 40 dB below maximum). The regions of closed contours have magnitude which are positive (denoted by '+') or negative ('-'). From these we can reconstruct the streamwise growth and azimuthal spreading of the excited periodic mode. These verify that the disturbance excited by the single miniature speaker is planar in nature. The total azimuthal

† This value is to be compared to 15.8 dB, using 8 speakers, and 11.5 dB with 4 speakers.

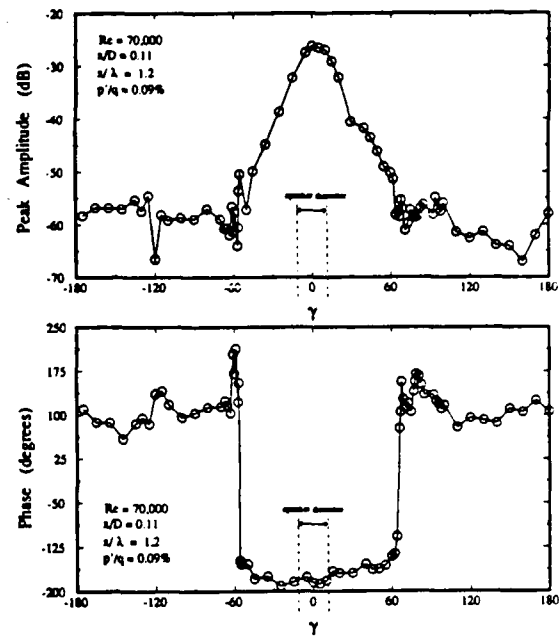


Figure 10. Azimuthal distribution of amplitude (top) and phase (bottom) at $x/\lambda = 1.2$ and $U/U_j = 0.6$, for single miniature speaker ($Re = 70,000$; $f = 2500$ Hz; $p'/q = 0.09\%$).

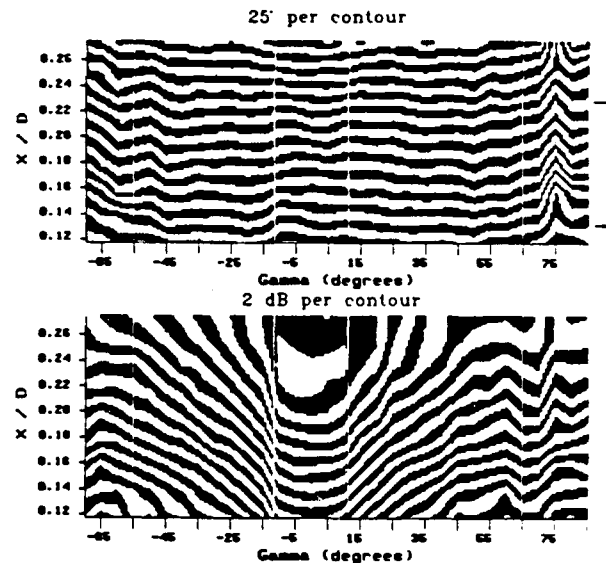


Figure 11. Spatial distributions of phase (top) and amplitude (bottom) as a function of streamwise and azimuthal coordinates for single miniature speaker ($Re = 70,000$; $f = 2500$ Hz; $p'/q = 0.02\%$; $U/U_j = 0.6$).

spreading angle taken from this figure is a quite large value of approximately 160° . The unusually large azimuthal spreading rate could be explained by a quasi-planar response of the thin shear layer, and attests to the high receptivity to disturbances at the exit lip.

Figures 13 and 14 show comparable results for the case of two active neighbor speakers which are of nominally equal amplitude but 180° out of phase. This

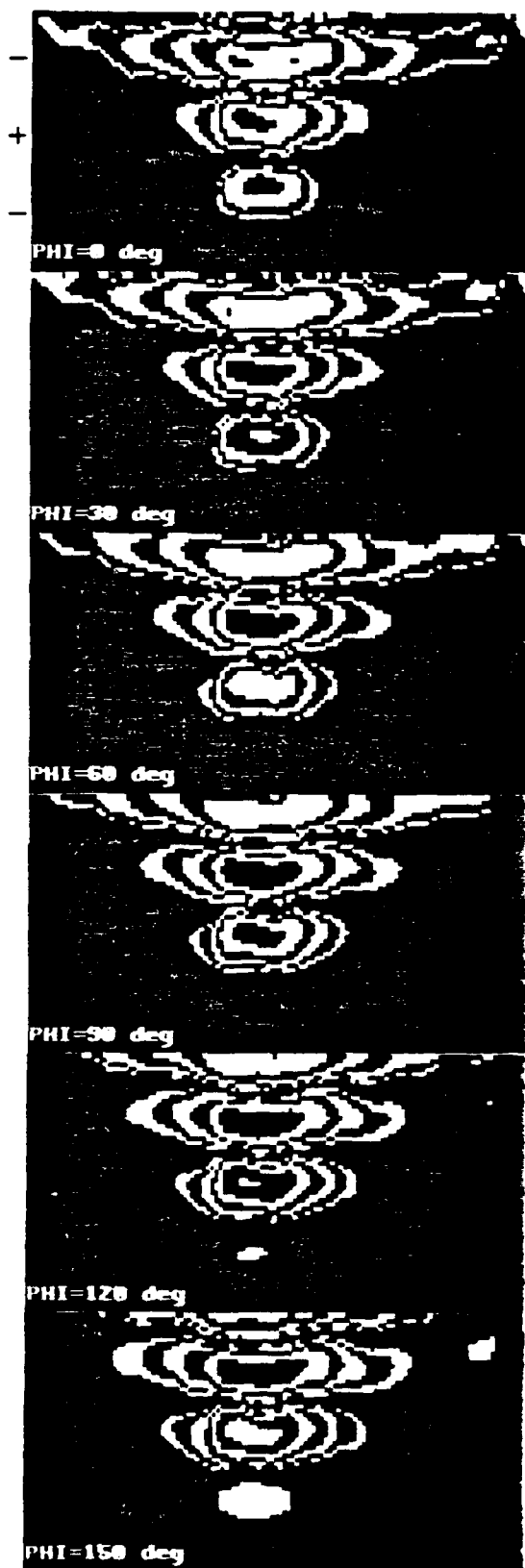


Figure 12. Reconstituted phase-conditioned iso-velocity contours as a function of streamwise and azimuthal coordinates for single miniature speaker ($Re = 70,000$; $f = 2500$ Hz ; $p'/q = 0.02\%$; $U/U_j = 0.6$).

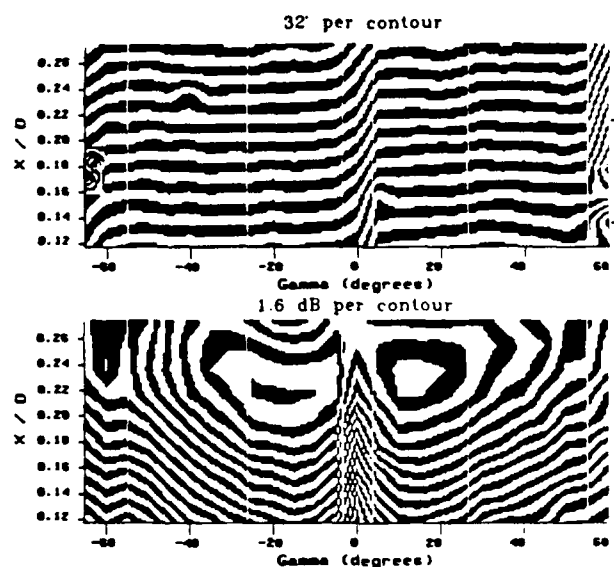


Figure 13. Spatial distributions of phase (top) and amplitude (bottom) as a function of streamwise and azimuthal coordinates for 180° phase-shifted miniature speaker pair ($Re = 70,000$; $f = 2500$ Hz ; $p'/q = 0.02\%$; $U/U_j = 0.6$).

represents a "worst case" scenario which would be required to produce an $m = \pm 6$ helical mode. Again the vertical white lines mark the location and extent of the two speakers. From the amplitude contours, we observe linear growth in the initial region just downstream of the speakers, similar to the single active speaker in the previous case. The phase contours show that the modes downstream of each speaker have the same constant phase speed, but are shifted in phase by 180° with respect to each other. The region where the 180° phase shift occurs is confined to the narrow azimuthal band between the two speakers. Within that region, the amplitude is near the background level. These low levels result initially from the linear phase cancellation of the 180° phase-shifted modes. The phase cancellation region extends the full length of the linear regime and effectively marks the region where nonlinear effects can be neglected.

The pseudo-temporal reconstruction from the amplitude and phase distributions in the previous figure are shown in Figure 14. These clearly show the 180° phase shifted modes which are produced, and the narrow region where phase cancellation occurs. Based on this result, we expect to be able to initially excite the linear growth of helical modes with azimuthal wave numbers as high as $m = \pm 6$. This is essentially consistent with the theoretical results pertaining to thin circular shear layers.

3. Azimuthally Continuous Forcing

In the remaining figures we present flow visualization results for the case with all 12 speakers being operated to produce either axisymmetric ($m = 0$) or $m = \pm 1$ helical modes. The first of these in Figure 15,

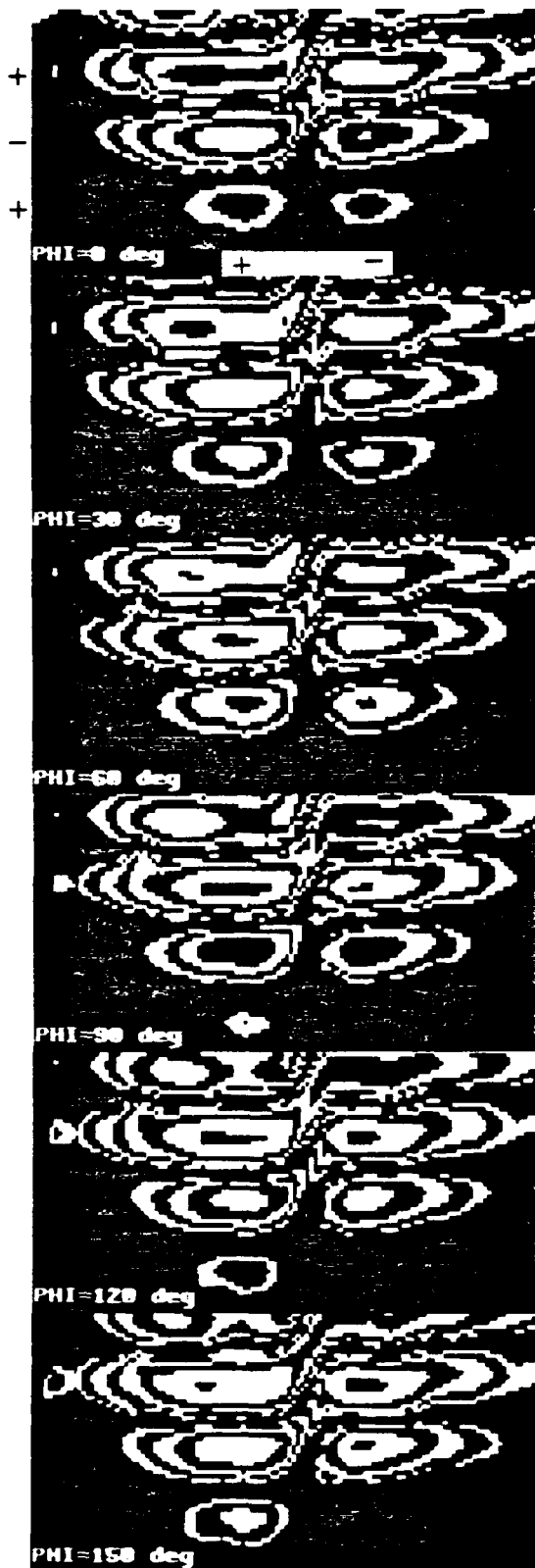


Figure 14. Reconstituted phase-conditioned iso-velocity contours as a function of streamwise and azimuthal coordinates for 180° phase-shifted miniature speaker pair ($Re = 70,000$; $f = 2500$ Hz ; $p'/q = 0.02\%$; $U/U_j = 0.6$).

were performed at a relatively low Reynolds number ($Re = 4000$) and low frequency ($f = 30$ Hz) in order to expand both the linear growth region and mode wave length. Since the use of $m = \pm 1$ helical is aimed at exploiting nonlinear mechanisms, flow visualization to specifically mark the linear amplification region is difficult. At the higher Reynolds numbers of our previous studies (in the range from $30,000 \leq Re \leq 80,000$), that region occupies only the first few millimeters from the exit lip. Within that region we expect to find two to three wave lengths of the fundamental mode. By the time the visualized shear layer has rolled up into more or less discrete vortices, the linear approximations are no longer valid.

In Figure 15, the photographs were taken by flashing the strobe light source in phase with the forcing time series, with the camera lens open. By this approach we are acquiring a phase conditioned average view of the flow field. This provides an indication of the degree of phase locking of the forced modes, especially when compared to single realizations. It also can help to bring out small amplitude coherent modes in their linear stages of development. The photographs in Figure 15 represent an average of 30 realizations. Typical single realizations, taken at the same conditions, are shown in Figure 16.

Focusing first on the $m = 0$ condition (Figure 16a), we observe a good azimuthally uniform wave region and vortex roll-up. As pointed out in the discussion on the mode development from the single active speaker, the x -position of vortex roll-up, for a mode undergoing linear growth, will be sensitive to the uniformity of the initial amplitude distribution. The azimuthally uniform nature of the roll-up for the $m = 0$ condition is an indication therefore that the individual speakers have been properly tuned to yield a uniform amplitude and phase response. The adjustments for these were done in the individual analog circuit stages as explained in Section II. The conditions documented in Figure 16a is one indication that this was successfully performed.

The $m = \pm 1$ helical mode case on the bottom half of Figures 15 and 16 nicely contrast the $m = 0$ case. In this case we have placed the azimuthal amplitude modulation maximum at the top and bottom of the jet (and photograph). The amplitude modulation minima then fall on the horizontal center line of the jet and photographs. This is important for interpreting the flow visualization records. At the azimuthal locations of the maxima (antinodes), we expect to see in the nonlinear region, strong vortex roll-ups which capture a greater percentage of smoke tracer particles. The vortex roll-ups should appear staggered in the flow direction, from one maximum to the other (out of phase) maximum. This corresponds to the top and bottom of the photographs for the present conditions. In the region of the azimuthal amplitude minima, we expect to see weaker filaments of smoke tracer particles. At the nonlinear ("visualizable") locations, these connect the staggered

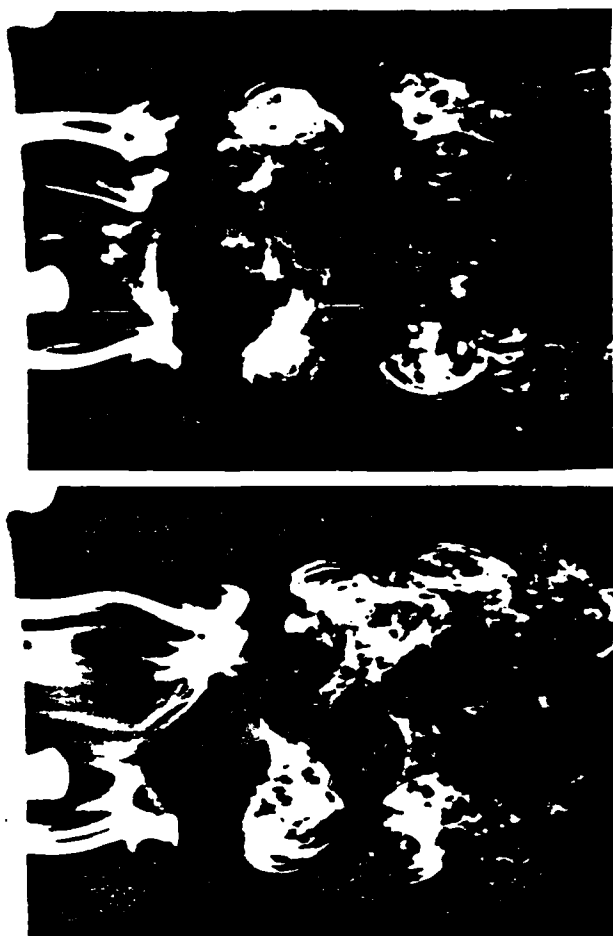


Figure 15. Phase-averaged smoke-wire flow visualizations comparing forced axisymmetric (top) and ± 1 helical (bottom) modes at $Re = 4000$.

vortices at the azimuthal maxima, and cross-over to produce a characteristic 'V' pattern (or 'Y' at the further nonlinear stages). The reconnection of the 'Y' takes place at the azimuthal locations of the minima. This pattern is invariant in the streamwise direction, as opposed to a single $m = +1$ or -1 helix (see for example Figure 1b). Focusing on the photographs at the bottom of Figures 15 and 16, we observe exactly the characteristics we expect for the $m = \pm 1$ helical mode. Except for some fine scale disturbances, we observe little difference between the single and phase averaged realizations, indicating that within this region the flow is phase locked to the initial mode input.

Figure 17 shows single realization flow visualization records for $m = \pm 1$ mode forcing at two higher Reynolds numbers of $Re = 10,000$ (a) and $22,000$ (b). The forcing frequencies in these cases were 150 Hz and 500 Hz, respectively. These are near the most amplified values of the helical mode in the naturally excited jet. As we expect, the nonlinear vortex roll-up region occurs at smaller streamwise distances, and considerable shortening of the streamwise wavelength is observed with increasing Reynolds number. However, in both cases the characteristic staggered vortex pattern from top to

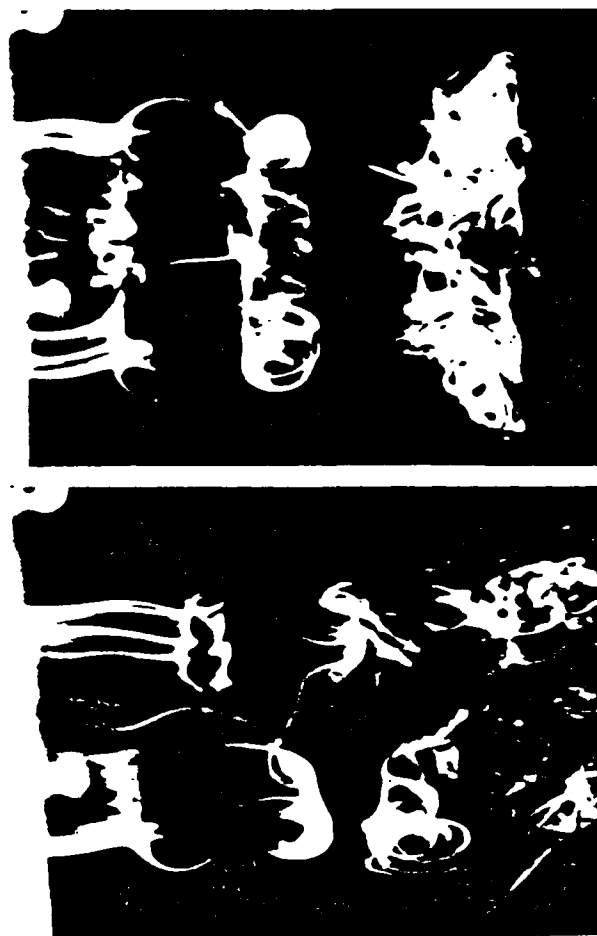


Figure 16. Single realization smoke-wire flow visualizations comparing forced axisymmetric (top) and ± 1 helical (bottom) modes at $Re = 4000$.

bottom is unmistakably present, indicating that although flow visualization may be more difficult at the higher Reynolds numbers, the dynamics of helical excitation appear to be similar in nature. In the case of Figure 17b, the 'Y' pattern is apparently still evident relatively far downstream, although the streamwise wave length is approximately a factor of two larger than the initial wave length. Preliminary results suggest that this comes about from a disconnection of the helical modes near the azimuthal location of the amplitude minimum, and vortex "pairing" at the point of azimuthal amplitude maximum. This observation is consistent with the recent results of intermodal subharmonic resonant interactions obtained by Cohen and Wygnanski (1987).

The previous figures correspond to cases when an extrinsic source provided the mode time series input. The flow visualization records in Figure 18 document the conditions when the time series input to the speakers is provided by an intrinsic source. In this case the time series is provided by a hot-wire velocity sensor placed in the linear amplification region of the exit shear layer. The resulting time series was then amplified and fed back to the input stages of the analog circuits controlling the 12 miniature speakers, using an adjustable gain. The

analog circuits still prescribed the desired azimuthal amplitude variation to promote the simultaneous seeding of ± 1 helical modes, but the eigenfrequency selected by the jet was one which satisfied a resonant feedback condition (see Reisenthel, 1988). As a result of this condition, very pure discrete modes are produced spontaneously.

In Figure 18, the top view corresponds to the case when the azimuthal antinodes are at the top and bottom of the photograph. This is comparable to all the previously shown flow visualization records. In the bottom view, we have interchanged nodes and antinodes to place the minima on the top and bottom of the photograph. In the top photograph, we observe strongly coherent staggered vortex formations indicative of the ± 1 helical mode. This view can be directly compared to that in Figure 17b which is at a comparable Reynolds number although the fluctuation levels of Figure 18 correspond to a saturated limit-cycle. Making that comparison, we observe considerably more organization and spreading of the shear layer. Comparing this view to 18b, we observe that the spreading is disproportionately larger at the sites of the azimuthal maxima. That is the larger amplitude for the resonant jet have resulted in a distortion of the mean flow. The modification of the mean flow is derivable from the nonlinear difference interaction $(\alpha_r, \pm m) - (\alpha_r, \pm m) \rightarrow (0, \pm 2m)$, where α_r is the streamwise wave number. This characteristic is obviously attractive from the point of view of mixing.

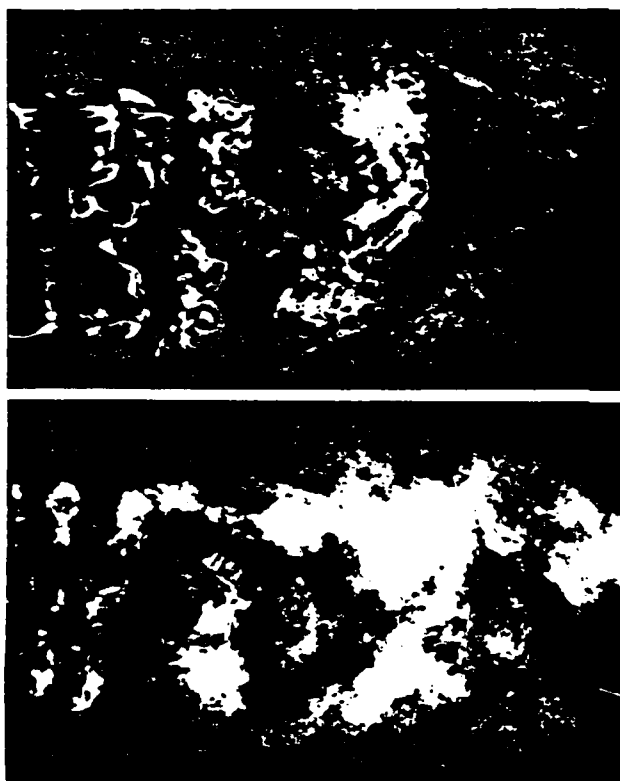


Figure 17. Single realization smoke-wire flow visualizations of forced ± 1 helical modes at $Re = 10,000$ (top) and $Re = 22,000$ (bottom).

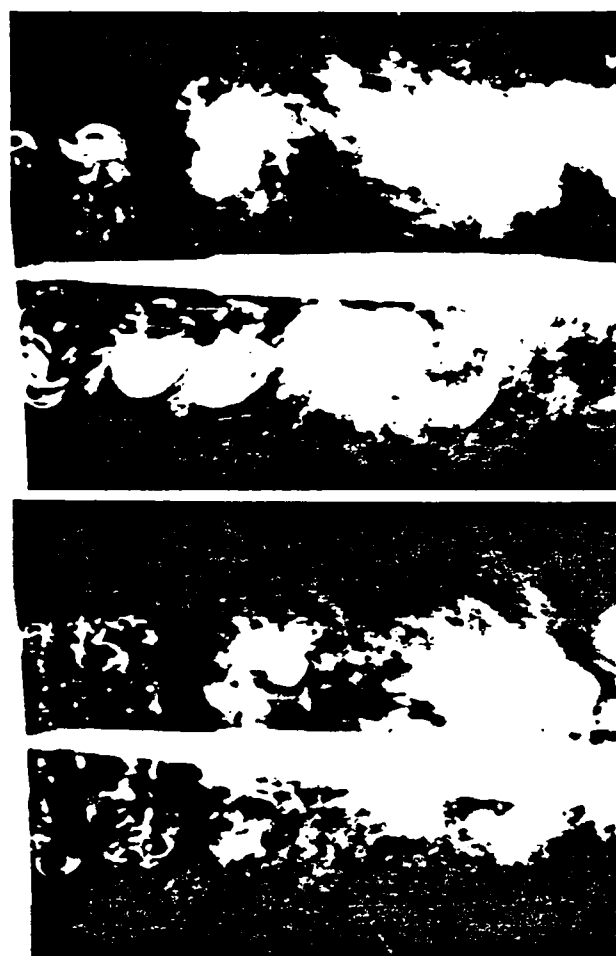


Figure 18. Single realization smoke-wire flow visualizations illustrating asymmetric jet spreading through nodal (top) and antinodal (bottom) views, in the case of helical enhanced feedback at $Re = 20,000$.

Above all, the results of Figure 18 demonstrate the feasibility of using the "enhanced feedback" concept for non-axisymmetric modes.

IV. Concluding Remarks

In this paper we have investigated the ability to seed $\pm m$ helical modes with an azimuthal array of 12 miniature speakers. The speakers were mounted at the face of the jet, in close proximity of the exit lip. Measurements of the mean flow character of the exit shear layer, and of the Strouhal number dependence of the dominant initial instability modes on Reynolds number, showed that our helical mode generator did not introduce any modification of the jet conditions. Forcing from a single active speaker produced, in the linear region, a planar mode of varying initial amplitude around the azimuth. This mode had a constant phase speed of $C/U_j = 0.53$, which compared well to linear theory in a quasi-parallel shear flow. For a forcing amplitude of $p'/q = 0.02\%$, the azimuthal spreading rate had a large value of 160° . This was attributed to the

extreme receptivity at the jet exit.

For two active speakers, operating 180° out of phase, we observed the linear growth of 180° -shifted planar modes. These amplified and reached saturation in a similar fashion to the single active speaker case. The only significant interaction occurred in the azimuthal region between the speakers, where linear phase cancellation took place, and background levels existed. This exercise confirmed quasi-two-dimensional linear theory predictions regarding the relative insensitivity of amplification rates to azimuthal mode number, at least in the limit of infinitely thin shear layers. From this we expect, with our present arrangement, to be able to excite helical modes up to $m = \pm 6$.

Utilizing 12 speakers, we have confirmed through flow visualization our ability to excite $m = \pm 1$ helices in a full range of Reynolds numbers. In these cases, the initial region of the jet was fully phase-locked. From these, we were able to obtain the salient features of the flow, consisting, in the nonlinear stages, of staggered vortices at the azimuthal positions of amplitude maxima, and the formed 'Y' pattern connections to these. The junction of the 'Y' pattern forms at the location of amplitude minima. This pattern is invariant in the flow direction.

We have also shown that intrinsic forcing of the jet through enhanced feedback provides similar dynamics as for the $m = 0$ modes, documented by Reisenthel (1988). This alone or in combination with the $m = 0$ mode offers rich possibilities for exploiting the resonant growth of controllable unstable modes.

Acknowledgment

The authors gratefully acknowledge the support of this work by the Air Force Office of Scientific Research under grant number 86-0165, monitored by Dr. J. McMichael.

References

- Ahmadi-Moghadam, A., 1986. *On the Instability of Thin Circular Shear Layers*. Ph.D. thesis, Illinois Institute of Technology, Chicago.
- Cohen, J. and Wygnanski, I. J., 1987. *J. Fluid Mech.* **176**, 191.
- Cohen, J. and Wygnanski, I. J., 1987. *J. Fluid Mech.* **176**, 221.
- Corke, T. C., Shakib, F. and Nagib, H. M., 1985. *AIAA Paper No. 85-0573*.
- Corke, T. C., Shakib, F. and Nagib, H. M., 1988. *Submitted to J. Fluid Mech.*
- Craik, A. D. D. 1971. *J. Fluid Mech.* **50**, 393.
- Crighton, D. G. and Gaster, M., 1976. *J. Fluid Mech.* **77**, 397.
- Drubka, R. E., 1981. *Instability in the Near Field of Turbulent Jets and their Dependence on Initial Conditions and Reynolds Number*. Ph.D. thesis, Illinois Institute of Technology, Chicago.
- Gutmark, E. and Ho, C. M., 1983. *Phys. Fluids* **26**, 10.
- Kusek, S. M., 1989. M.S. thesis, Illinois Institute of Technology, Chicago. *In progress*.
- Long, T. A., Petersen, R. A. and Wygnanski, I. J., 1988. *Bull. Am. Phys. Soc.* **33**, 2234.
- Mattingly, G. E. and Chang, C. C., 1974. *J. Fluid Mech.* **68**, 541.
- Michalke, A., 1969. *J. Fluid Mech.* **38**, 765.
- Michalke, A., 1971. *Z. Flugwiss.* **19**, 319.
- Nagib, H. M., Drubka, R. E., and Reisenthel, P., 1989. *Submitted to Phys. Fluids*.
- Plaschko, P., 1979. *J. Fluid Mech.* **92**, 209.
- Reisenthel, P., 1988. *Hybrid Instability in an Axisymmetric Jet with Enhanced Feedback*. Ph.D. thesis, Illinois Institute of Technology, Chicago.
- Reisenthel, P., Nagib, H. M., and Corke, T. C., 1988. *Bull. Am. Phys. Soc.* **33**, 2271.
- Shakib, F., 1984. *Evolution and Interaction of Instability Modes in an Axisymmetric Jet*. M.S. thesis, Illinois Institute of Technology, Chicago.

SEEDING OF HELICAL MODES IN THE INITIAL REGION OF AN AXISYMMETRIC JET

S.M. Kusek¹, T.C. Corke² and P. Reisenthel³
Fluid Dynamics Research Center
Illinois Institute of Technology
Chicago, Illinois 60616

Abstract

Active control of fundamental two- and three-dimensional amplified modes in an axisymmetric jet is presented. This is done by introducing localized acoustic disturbances produced by an azimuthal array of miniature speakers placed in the close proximity of the jet lip on the exit face. The independent control of each speaker output allows different azimuthal amplitude and phase distributions of periodic input pressure disturbances. Coupled with this was the development and use of a circular smoke-wire for visualizing shear layer modes around the complete jet circumference.

I. Introduction

The role of three-dimensional disturbances in axisymmetric jets has been the focus of a number of studies in the last two decades. Although most of these studies are theoretical and have addressed the linear stability properties of helical modes, recent attention has been given to the possibility of strong intermodal resonant interactions. The latter mechanism was experimentally demonstrated by Cohen and Wygnanski (1987b), and reinforces the need to consider the potential of 3-D modes which may be considered 'dormant' by linear standards.

Perhaps the most recent of theoretical analyses of the stability of azimuthal modes is that of Ahmadi-Moghadam (1986), which considers a thin circular shear layer with a Blasius profile. The use of this self-similar profile is justified on the basis of experiments with laminar exit conditions (see Drubka, 1981). In this study, the effect of curvature was represented by the ratio δ/D , and the results compared to Michalke's (1971) hyperbolic tangent profile. Although small differences in the mean velocity profile were found to produce sizable quantitative discrepancies, several general conclusions could be drawn: *i*) the phase speed depends strongly on

¹ Graduate Assistant

² Associate Professor

³ Visiting Assistant Professor

a azimuthal wave number (m) at low frequencies, in particular, the non-dispersive character of the instability waves increases with increasing m ; ii) the linear growth rates decrease with increasing m ; and iii) in any event, these effects are accentuated by curvature, and most felt for low Strouhal number. An earlier inviscid spatial analysis by Michalke (1969) for a 2-D hyperbolic tangent profile showed similarly that 2-D modes are always more amplified and that the wave dispersiveness and amplification rate ($-\alpha_i$) both decrease with increasing spanwise wave number.

In contrast to the 'locally parallel' theories, Plaschko (1979) used a multiple scales method similar to the approach of Crighton and Gaster (1976), in order to properly capture the slowly diverging nature of jet flow. A higher gain was found for the axisymmetric mode at higher Strouhal numbers, whereas lower Strouhal numbers promoted higher gain for $m = 1$, at farther downstream distances. In addition, Plaschko (1979) showed that the higher order helical modes ($m \geq 2$) were always less amplified than their axisymmetric ($m = 0$) and first helical ($m = \pm 1$) counterpart.

Mattingly and Chang (1974) reported similar results using inviscid spatial theory applied to a family of experimentally determined velocity profiles in a low Reynolds number water jet. They found that the axisymmetric mode dominates the jet column initially, but that the $m = \pm 1$ mode becomes the most amplified, past $x/D = 3$. Their results also indicated that the $m = \pm 2$ mode was never dominant. Recently, Cohen and Wygnanski (1987a) also performed an inviscid linear spatial stability analysis of analytically-fitted experimental profiles and obtained good agreement of the mode shapes in the initial region of the jet. The importance of jet divergence was incorporated through the parameter $R_{1/2}/\theta$ (the ratio of the radius where $U/U_j = .5$, to the local momentum thickness). The results of their analysis qualitatively corroborate those of Ahmadi-Moghadam (1986). In particular, they substantiated analytically that when the ratio of spanwise to streamwise wave numbers was small, all modes behave essentially as if the mean flow were two-dimensional.

In spite of the differences in the analytical approaches taken by the above investigators, it is clear that the two linearly dominating modes on a jet column are the fundamental ($m = 0$) and first helical ($m = \pm 1$) modes. Although their linear characteristics are virtually indistinguishable at the early stages i.e. when the shear layer is thin, compared to the jet diameter, there is a greater likelihood to observe and characterize the helical modes at the larger downstream distances, e.g. $x/D > 3$. This may explain in part why the few available experimental studies of helical mode instability appear to have focused on the nonlinear interactions produced by these modes, rather than on the linear stages *per se*. A frequently used evidence of such interactions is the mean flow distortion produced by the simultaneous forcing of modes with same frequency (see, e.g., Cohen and Wygnanski, 1987b, and Long et al., 1988). Admittedly, the concept of resonant interactions, and in particular: subharmonic resonant interactions, appears to be a highly promising avenue of

research for controlling jet flows. For example, Ahmadi-Moghadam's (1986) analysis predicts the possibility of a Craik-type (1971) triad interaction in the jet, leading to "explosive growth".

Although it is our goal to investigate this issue experimentally in a forthcoming study (Kusek, 1990), this manuscript describes the results of a preliminary investigation aimed at filling some gaps in the available experimental data dealing with the truly *linear* (initially very low amplitude) stages of helical instabilities. The use of very low initial amplitudes to *seed* non-axisymmetric modes is made possible in part by: *i*) the design of a helical mode generator (described herein) relying on a receptivity mechanism at the lip, and *ii*) by the use of an ultra-low freestream turbulence facility. It should be noted that controlled input levels of acoustic excitation also provide us with a means of assessing amplitude threshold effects for nonlinear resonances.

In addition, low excitation levels constitute a *realistic* way of seeding instability waves, because these levels are of comparable strength to those generated by the pressure feedback which occurs naturally in jets (Drubka, 1981). Such effects may, in fact, be related to the temporal switching which has commonly been observed between axisymmetric and helical ($m = \pm 1$) modes (Mattingly and Chang, 1974, Shakib, 1985, Corke et al., 1990), and for which no satisfactory explanation has yet been provided. Our primary and long-term objective in this study is to understand the mechanism controlling the temporal switching, coupled with the investigation of new ways in which to alter jets, using controlled two- and three-dimensional excitation. In the present paper, our approach to seeding low initial amplitude $\pm m$ helical disturbances, the method for visualizing these, and preliminary results from flow visualization and hot-wire surveys are presented.

II. Experimental Apparatus

This experiment was performed in the same jet facility that was used by Drubka (1981), Shakib (1985), Corke et al. (1985, 1990), Reisenhelt et al. (1988, 1990). Its very low core turbulence intensity level ($u'/U_j \cong 0.05\%$) makes it well suited for measurements on stability and mode interaction. The characteristics of this jet have been extensively documented in these investigations in terms of eigenmode distributions of the fundamental instability and interacted modes, along with their dependence on changing initial conditions including Reynolds number, initial shear layer thickness and core disturbance level.

II.1 Helical Mode Generator

In order to benefit from the results of previous measurements, special care was taken in the design of a fixture for holding an array of miniature speakers at the exit plane of the jet. The top of Figure 1 shows a schematic of the exit region of the

jet facility. The exit diameter, D , is 5.08 cm. Close to the exit edge are eight pressure taps which provide time series information on the unsteady pressure field at the jet exit. The speaker fixture (same scale) for holding the 12 downstream-facing miniature speakers is shown at the bottom of the figure. The fixture assembly is designed to slip over the exit face of the jet without introducing any additional development length and thereby affecting the initial shear layer momentum thickness. (A photograph showing the fixture with 12 speakers mounted on the jet exit is shown in Figure 5.)

To excite a helical mode with positive wave number m (clockwise moving), and frequency ω , the periodic time series to any individual speaker located at azimuthal angle γ would be $A_1(t, \gamma) = A \sin(m\gamma - \omega t + \phi_1)$. Here, ϕ_1 is an arbitrary phase shift. The opposite going, equal amplitude helical mode with wave number $-m$, would be produced by the periodic function $A_2(t, \gamma) = A \sin(-m\gamma - \omega t + \phi_2)$. The superposition of these two periodic functions yields $A(t, \gamma) = 2A \sin(\omega t + (\phi_1 + \phi_2)/2) \cos(m\gamma + (\phi_1 - \phi_2)/2)$. Therefore, to produce equal and opposite helical modes with azimuthal wave number $\pm m$ and frequency ω , each speaker will operate with a periodic input, $\sin(-\omega t + (\phi_1 + \phi_2)/2)$, with each speaker's amplitude determined by its azimuthal position according to: $2A \cos(m\gamma + (\phi_1 - \phi_2)/2)$. With 12 speakers it may be possible to excite helical modes with azimuthal wave numbers up to $m = \pm 6$. The maximum azimuthal wave number will correspond to a ratio of streamwise to spanwise wave numbers of approximately 2.6 (wave front leaving at $\cong 21^\circ$ from the jet lip)⁴. For reference, with the azimuthal wave number $m = \pm 1$, this angle will be approximately 9° , corresponding to a streamwise to spanwise wave number ratio of 16.

Figure 2 shows the circuit schematic for driving the speakers to force simultaneously or separately axisymmetric and $\pm m$ helical modes. The time series for each of these modes are input separately. This allows them to be at different frequencies and initial amplitudes. The first three stages of op-amp circuits for each mode input remove any dc component and amplify the signal up to a factor of 400. This stage is primarily for our experiments with enhanced feedback (Reisenthel et al., 1988, 1990), where the hot-wire anemometer output is fed directly into the forcing input. If the forcing series is supplied by a function generator or computer D/A output, these stages could be omitted.

To force $\pm m$ helical modes, we require the amplitude of the input to the speakers to vary in the azimuthal direction like $\cos(m\gamma)$. This is accomplished with the variable gain amplifier stage marked $G(\gamma)$ on the helical mode circuit path. Each variable gain amplifier feeds a speaker pair which are on opposite azimuthal positions of the jet exit. For the 12 speakers, these pairs are 1 and 7, 2 and 8, ..., 6 and 12. These speaker pairs operate in phase for even azimuthal wave numbers,

⁴ Assuming that the streamwise wave length, λ , is of the order of 10 mm

and 180° out of phase for odd wave numbers. In the former case, the switch setting in Figure 3 is in position 1. In the case of the latter, it is in position 2.

The time series for the axisymmetric mode is added to helical mode input just prior to the outputs to each speaker. This added stage also provides variable gain control to compensate for any amplitude transfer function differences between individual speakers. A unity gain follower is used as a final stage for impedance matching.

We have verified the sound pressure level output from the individual speakers from one of the pressure ports at the jet exit. This was done by rotating the speaker fixture (Figure 1) to sequentially place each speaker above the active port. A small tubulation transferred the pressure fluctuations to the microphone of a sound level meter. The dimensionless output of the sound level meter, on a linear scale, is plotted against the azimuthal angular position in Figure 3. The solid line is the ideal rectified $\cos(\gamma)$ amplitude variation required to seed the $m = \pm 1$ helical mode.

II.2 Circular Smoke-wire

Since we are focusing on the development of three-dimensional modes, we adapted the smoke-wire technique (Corke et al., 1977) to view the shear layer around the complete, or selected portion(s) of the azimuthal coordinate. The method for doing this is shown in the schematic drawings in Figure 4 (a and b).

The basic approach was to suspend in a nonintrusive manner a 0.1 mm diameter stainless steel wire in a circular shape just outside the shear layer of the jet. This was done by passing the wire through the eyes of long tapestry needles pressed into the ends of aluminum support rods. A total of 16 support rods were used as shown in Figure 4a. The rods were held by passing them through radial holes in an outer support ring. This ring was made of plastic acrylic to provide electrical isolation. The rods were fixed in place using thumb screws. The radius of the wire 'loop' was set by adjusting the length of the support rods extending through the ring.

The bottom most support rod in Figure 4a has two needles mounted on its end. These two are slightly offset to allow the wire to pass and close the circle without touching. This can be seen in the side view at the top of Figure 4b. The two needles are also electrically isolated from each other. An electrical lead is attached to one of these, as shown in Figure 4a.

The stainless steel wire passes through holes in the support ring at the bottom, and is held taut on electrically isolated take-up reels (Figure 4a). The holes where the wire passes through the support ring are actually oil reservoirs. To prevent oil from dripping out the bottom, the wire passes through small diameter tubing (0.2 mm inside diameter) glued in as shown in the bottom of Figure 4b. A hand crank is used to move the stainless steel wire from one reel to the other. In doing so, the wire rises through one oil reservoir and carries a coating of oil until the

wire in the circular loop is coated completely. In the process, a small amount of oil will be captured by the needle eyelets. This turns out to be beneficial in that it results in numerous reservoirs and decreases the motion of the wire required to coat the loop. As with the traditional smoke-wire technique, the oil that coats the wire collects in small droplets along the wire due to a surface tension instability. These provide sites for smoke streaks when the wire is resistively heated.

The portion of the wire loop that is resistively heated is determined by the position of the aluminum support rod where the other electrical lead is clipped. For example, clipping to the bottom most rod (Figure 4a) will resistively heat the full 360 degree circle. Clipping to the top most rod will cause the left 180 degree portion to heat. In this manner, we can introduce smoke streaks in any number of the wire sectors between support rods.

For the visualized flowfield presented here, the circular smoke-wire was located as close to the jet exit as possible. The support rods were adjusted to place the circular wire at the outer edge of the shear layer. This placement can be seen in the photograph in Figure 5. When operated, the smoke streak lines are entrained into the shear layer, where they mark the coherent motions as they developed downstream.

The special flexibility of this arrangement is that the apparatus can be located at any downstream position, with the radius of the wire loop being adjusted to account for the jet spreading. In addition, wire shapes other than circular are possible, to accommodate conditions which lead to azimuthal variations in mode amplitude or spreading rate.

III. Results

III.1 Passive Effects

Any *passive* effects of placing the speaker holder and speakers onto the exit of the jet were first documented. Our concern was that by its passive presence in the sensitive region at the jet exit lip, the natural instability character would be altered. Multiple sets of mean velocity profiles through the shear layer over our full range of Reynolds numbers showed no discernible effect (Kusek, 1990). A more sensitive indicator is the Reynolds number dependence of the most amplified modes. These are shown in Figure 6 in terms of the fundamental axisymmetric mode at frequency f_0 , its subharmonic $f_0/2$ and the $m = \pm 1$ helical mode at frequency f_1 . For cases when the exit boundary layer thickness is small compared to the jet diameter, inviscid linear stability theory predicts that the instability modes scale with Strouhal number based on local momentum thickness ($St\theta$). For this particular jet facility (Drubka, 1981, Drubka et al., 1989), upstream of the location corresponding to subharmonic resonance, θ grows less than a few percent. Consequently, the measured θ is approximately equal to the *exit* momentum

thickness. In cases when the exit boundary layer is laminar, such as here, the boundary layer momentum thickness is inversely proportional to the square root of the Reynolds number (Blasius profile). Since $St_\theta = \text{constant}$, then $St_\theta D / \theta \sim \theta^{-1}$, or $St_D \sim Re^{1/2}$.

This is seen to be the case without (top) and with (bottom) the HMG for these three natural dominant modes. The slopes of these curves, which is proportional to St_θ , are given in the insets of the two graphs. For the case without the HMG, the St_θ for f_0 is 0.0144. Gutmark and Ho (1983) have tabulated values of St_θ for the fundamental axisymmetric mode from experiments in nine different jet facilities. The values that they report range from 0.012 to 0.018. Drubka (1981) reported a value for this jet of 0.013. Comparing our case with the HMG we observe a slight change in St_θ for both f_0 and f_1 . The difference of course is well within the type of scatter documented by Gutmark and Ho. The St_θ for the $f_0/2$ mode remains the same. The velocity distributions and the measured momentum thicknesses showed no significant effect due to the HMG. We therefore attribute the slight difference in the slopes to a change in the receptivity at the lip, rather than a change in entrainment conditions, which would presumably have changed θ . This is obviously a small effect and otherwise these dominant natural modes develop according to linear theory in either configuration.

III.2 Active Forcing

As described in Section II, the $\pm m$ helical mode forcing requires an initial prescribed azimuthal amplitude modulation at the lip of the jet. Ideally, this would occur in an azimuthally-continuous fashion. In our situation, the initial condition is applied in an azimuthally-discrete fashion from each of the 12 speakers. We therefore were interested in first examining the response of the shear layer to a periodic disturbance produced by a single operating speaker.

The *active* effect of a *single* miniature speaker is documented in Figures 7 and 8. Figure 7 shows the streamwise development of amplitude and phase at a fixed Reynolds number, along the similarity line $U/U_j = 0.6$, at a constant azimuthal position. The jet conditions and forcing frequency correspond to the $f_0 = 2500$ Hz case of Shakib (1985) and Corke et al. (1985), produced by a far-field sound source. In Figure 7, we compare the streamwise development between such a far-field source and the single speaker of the HMG. As is evident, the comparison is excellent, especially in the initial linear growth and saturation region. In the case of the far-field sound source, the excited mode will be axisymmetric. We do not expect the same to be true for excitation with the single miniature speaker at the jet exit. A comparison such as the one provided in Figure 7 also allows us to calibrate the true forcing effectiveness of the near-field sound source, as compared to traditional far-field loud-speaker excitation.

For the same conditions, with the single active speaker, the azimuthal amplitude and phase distributions at different x-positions are presented in Figure 8. This was sampled at the radial position where $U/U_j = 0.6$, as in Figure 7.

The amplitude and phase are presented as isocontour levels seen as alternating black and white bands. The spatial domain is presented as a flat projection with the azimuthal coordinate γ on the abscissa, and the x-direction, made non-dimensional using the jet diameter, on the ordinate. The white vertical lines in the center mark the location and extent of the single speaker. The white lines at both ends ($\gamma = \pm 60^\circ$) mark the valid region of the phase, where the linear coherence remained above 0.7.

The amplitude is *log* based (dB) so that contour bands spaced equally in x indicate constant linear (exponential) growth. Such a linear growth region is seen to exist in the initial region directly downstream of the active speaker. This extends to approximately $x/D = 0.20$ ($x/\lambda = 2.2$), where nonlinear effects result in energy saturation of this mode. For this mode, the point of energy saturation marks the position of the first vortex roll-up (see, e.g., Shakib, 1985). On either side of the speaker, the energy spreads and feeds the same mode. This mode is seen to amplify at approximately the same spatial rate, but because the initial amplitude decays in the azimuthal direction (see Figure 8), the development length, before reaching saturation, is shifted downstream. From the phase distribution at the top of the figure, we observe a constant phase development in the azimuthal direction. The number and width of phase contour bands in the x-direction is indicative of the phase velocity of this mode. Therefore, the phase distribution infers that the speaker is exciting a single mode which travels at a constant phase speed ($C_r/U_j = 0.54$), everywhere within the valid azimuthal region. Flow visualization, which primarily marks the rolled up vortex, would show for this case what would appear to be an inclined axisymmetric mode. However, the feature implying the inclination would actually be a result of the azimuthal distribution of the initial amplitude of this mode which provides, away from the active speaker, a longer development length before saturation and vortex roll-up.

Figure 9 shows comparable results for the case of two active neighbor speakers which are of nominally equal amplitude but 180° out of phase. This represents a "worst case" scenario which would be required to produce one sixth of the $m = \pm 6$ helical mode. Again the vertical white lines mark the location and extent of the two speakers. From the amplitude contours, we observe linear growth in the initial region just downstream of the speakers, similar to the single active speaker in the previous case. The phase contours show that the modes downstream of each speaker have the same constant phase speed, but are shifted in phase by 180° with respect to each other. The region where the 180° phase shift occurs is confined to the narrow azimuthal band between the two speakers. Within the region, the amplitude is near the background level. These low levels result initially from the

linear phase cancellation of the 180° phase-shifted modes. The phase cancellation region extends the full length of the linear regime and effectively marks the region where nonlinear effects can be neglected.

III.3 Azimuthally Continuous Forcing

In the remaining two figures we present flow visualization results for the case with all 12 speakers being operated to produce either axisymmetric ($m=0$) or $m = \pm 1$ helical modes. These were performed at a relatively low Reynolds number ($Re = 4000$) and low frequency ($f = 30$ Hz) in order to expand both the linear growth region and mode wavelength in physical space. Since the use of $m = \pm 1$ helical modes is aimed at exploiting nonlinear mechanisms, flow visualization to specifically mark the linear amplification region is difficult. At the higher Reynolds numbers of our previous studies (in the range from $30,000 \leq Re \leq 80,000$), that region occupies only the first few millimeters from the exit lip. Within that region we expect to find two to three wavelengths of the fundamental mode. By the time the visualized shear layer has rolled up into more or less discrete vortices, the linear approximations are no longer valid.

In Figure 10, the photographs were taken by flashing the strobe light source in phase with the forcing time series, with the camera lens open. By this approach we are acquiring a phase-conditioned average view of the flow field. This provides an indication of the degree of phase locking of the forced modes, especially when compared to single realizations. It also can help to bring out small amplitude coherent modes in their linear stages of development. The photographs in Figure 10 represent an average of 30 realizations. Typical single realizations, taken at the same conditions, are shown in Figure 11.

Focusing first on the $m=0$ condition (Figure 11, top), we observe a good azimuthally uniform wave region and vortex roll-up. As pointed out in the discussion on the mode development from the single active speaker, the x-position of vortex roll-up, for a mode undergoing linear growth, will be sensitive to the uniformity of the initial amplitude distribution. The azimuthally uniform nature of the roll-up for the $m=0$ condition is an indication therefore that the individual speakers have been properly adjusted to yield a uniform amplitude and phase response. Results from flow visualization such as in Figure 11 are one indication that this was successfully performed.

The $m = \pm 1$ helical mode case on the bottom half of Figures 10 and 11 nicely contrast the $m=0$ case. In this case we have placed the azimuthal amplitude modulation maximum at the top and bottom of the jet (and photograph). The amplitude modulation minima then fall on the horizontal centerline of the jet and photographs. This is important for interpreting the flow visualization records. At the azimuthal locations of the maxima (antinodes), we expect to see in the nonlinear region, strong vortex roll-ups which capture a greater percentage of the smoke tracer. The vortex roll-ups should appear staggered in the flow direction, from one

maximum to the other (out of phase) maximum. This corresponds to the top and bottom of the photographs for the present conditions. In the region of the azimuthal amplitude minima, we expect to see weaker filaments of tracer smoke. At the nonlinear ("visualizable") locations, these connect the staggered vortices at the azimuthal maxima, and cross-over to produce a characteristic 'V' pattern (or 'Y' at the further nonlinear stages). The reconnection of the 'Y' takes place at the azimuthal locations of the minima. Except for some fine scale disturbances, we observe little difference between the single and phase averaged realizations, indicating that within this region the flow is phase locked to the initial mode input.

IV. Concluding Remarks

In this paper, we have investigated the ability to seed $\pm m$ helical modes with an azimuthal array of 12 miniature speakers. The speakers were mounted at the face of the jet, in close proximity of the exit lip. Measurements of the mean flow character of the exit shear layer, and of the Strouhal number dependence of the dominant initial instability modes on Reynolds number, showed that our helical mode generator did not introduce any passive modification of the jet conditions. Forcing from a single or 180° shifted neighbor pair of active speakers were used to confirm quasi-two-dimensional linear theory predictions regarding the relative insensitivity of amplification rates to azimuthal mode number, at least in the limit of infinitely thin shear layers. From this we expect, with our present arrangement, to be able to excite helical modes up to $m = \pm 16$. Coupled with the use of the circular smoke-wire, this provides the basic setup to reach our long-term objective, to study three-dimensional mode resonance mechanisms in jets.

Acknowledgment

The authors gratefully acknowledge the support of this work by the Air Force Office of Scientific Research under grant number 86-0165, monitored by Dr. J. McMichael.

References

- Ahmadi-Moghadam, A., 1986: *On the Instability of Thin Circular Shear Layers*. Ph.D. thesis, Illinois Institute of Technology, Chicago.
- Cohen, J. and Wygnanski, I.J., 1987a: The evolution of instabilities in the axisymmetric jet. Part 1. The linear growth of disturbances near the nozzle. *J.*

Fluid Mech. 176, 191-219.

Cohen, J. and Wygnanski, I.J., 1987b: The evolution of instabilities in the axisymmetric jet. Part 2. The flow resulting from the interaction between waves. *J. Fluid Mech.* 176, 221-235.

Corke, T.C., Shakib, F. and Nagib, H.M., 1985: Effects of low amplitude forcing on axisymmetric jet flows. *ALAA Paper No. 85-0573*.

Corke, T.C., Shakib, F. and Nagib, H.M., 1990: Mode selection and resonant phase locking in unstable axisymmetric jets. To appear in *J. Fluid Mech.*

Craik, A.D.D., 1971: Nonlinear resonant instability in boundary layers. *J. Fluid Mech.* 50, 393-413.

Crighton, D.G. and Gaster, M., 1976: Stability of slowly divergent jet flow. *J. Fluid Mech.* 77, 397-413.

Drubka, R.E., 1981. *Instability in the Near Field of Turbulent Jets and their Dependence on Initial Conditions and Reynolds Number*, Ph.D. thesis, Illinois Institute of Technology, Chicago.

Drubka, R.E., Reisenthel, P. and Nagib, H.M., 1989: The dynamics of low initial disturbance turbulent jets. *Phys. Fluids* 10, 1723-1735.

Gutmark, E. and Ho, C.M., 1983: Preferred modes and the spreading rates of jets. *Phys. Fluids* 26, 2932-2938..

Kusek, S.M., 1990. Helical mode instability in axisymmetric jets. M.S. thesis, Illinois Institute of Technology, Chicago.

Long, T.A., Petersen, R.A. and Wygnanski, I.J., 1988: Azimuthal mode contamination in an axisymmetric jet. *Bull. Am. Phys. Soc.* 33, 2234.

Mattingly, G.E. and Chang, C.C., 1974: Unstable waves on an axisymmetric jet column. *J. Fluid Mech.* 65, 541-560.

Michalke, A., 1969: A note on spatially growing three-dimensional disturbances in a free shear layer. *J. Fluid Mech.* 38, 765-767.

Michalke, A., 1971: Instabilität eines compressiblen runden freistrahls unter berucksichtigung des einflusses der strahlgrenzschichtdicke. *Z. Flugwiss.* 19, 319-

328, (also NASA TM 75190).

Plaschko, P., 1979: Helical instability of slowly diverging jets. *J. Fluid Mech.* 92, 209-215.

Reisenthel, P., Nagib, H.M. and Corke, T.C., 1988: Global oscillations and bifurcations in a jet with enhanced feedback. *Bull. Am. Phys. Soc.* 33, 2271.

Reisenthel, P., Nagib, H.M. and Corke, T.C., 1990: Global instability in an axisymmetric jet with enhanced feedback. *To appear J. Fluid Mech.*

Shakib, F., 1985. *Evolution and Interaction of Instability Modes in an Axisymmetric Jet*, M.S. thesis, Illinois Institute of Technology, Chicago.

FIGURES

- Figure 1. Schematic of jet nozzle (top) and low disturbance fixture (bottom) for holding 12 miniature speakers at jet exit face; as well as measurement coordinate system.
- Figure 2. Schematic of circuits used to condition time-series input to produce axisymmetric and/or ± 1 helical modes from 12 miniature speakers.
- Figure 3. Comparison of azimuthal variation of normalized sound pressure level from 12 speakers to ideal variation for axisymmetric (dashed) and helical (solid) modes.
- Figure 4. Schematic drawing of circular smoke-wire arrangement.
- Figure 5. Photograph of jet exit face with 12 miniature speakers and circular smoke-wire in place
- Figure 6. Strouhal number dependence of dominant natural instability modes without (top) and with (bottom) helical mode generator (inactive).
- Figure 7. Comparison between near-field and far-field acoustic excitation for the streamwise development of disturbance amplitude (top) and phase (bottom) ($Re = 70,000$; $f = 2500$ Hz; $p'/q = 0.02\%$; $U/U_j = 0.6$).
- Figure 8. Spatial distributions of phase (top) and amplitude (bottom) as a function of streamwise and azimuthal coordinates for single miniature speaker ($Re = 70,000$; $f = 2500$ Hz; $p'/q = 0.02\%$; $U/U_j = 0.6$).
- Figure 9. Spatial distributions of phase (top) and amplitude (bottom) as a function of streamwise and azimuthal coordinates for 180° phase-shifted miniature speaker pair ($Re = 70,000$; $f = 2500$ Hz; $p'/q = 0.02\%$; $U/U_j = 0.6$).
- Figure 10. Phase-averaged smoke-wire flow visualizations comparing forced axisymmetric (top) and ± 1 helical (bottom) modes at $Re = 4000$ ($f = 30$ Hz).
- Figure 11. Single realization smoke-wire flow visualizations comparing forced axisymmetric (top) and ± 1 helical (bottom) modes at $Re = 4000$ ($f = 30$ Hz).

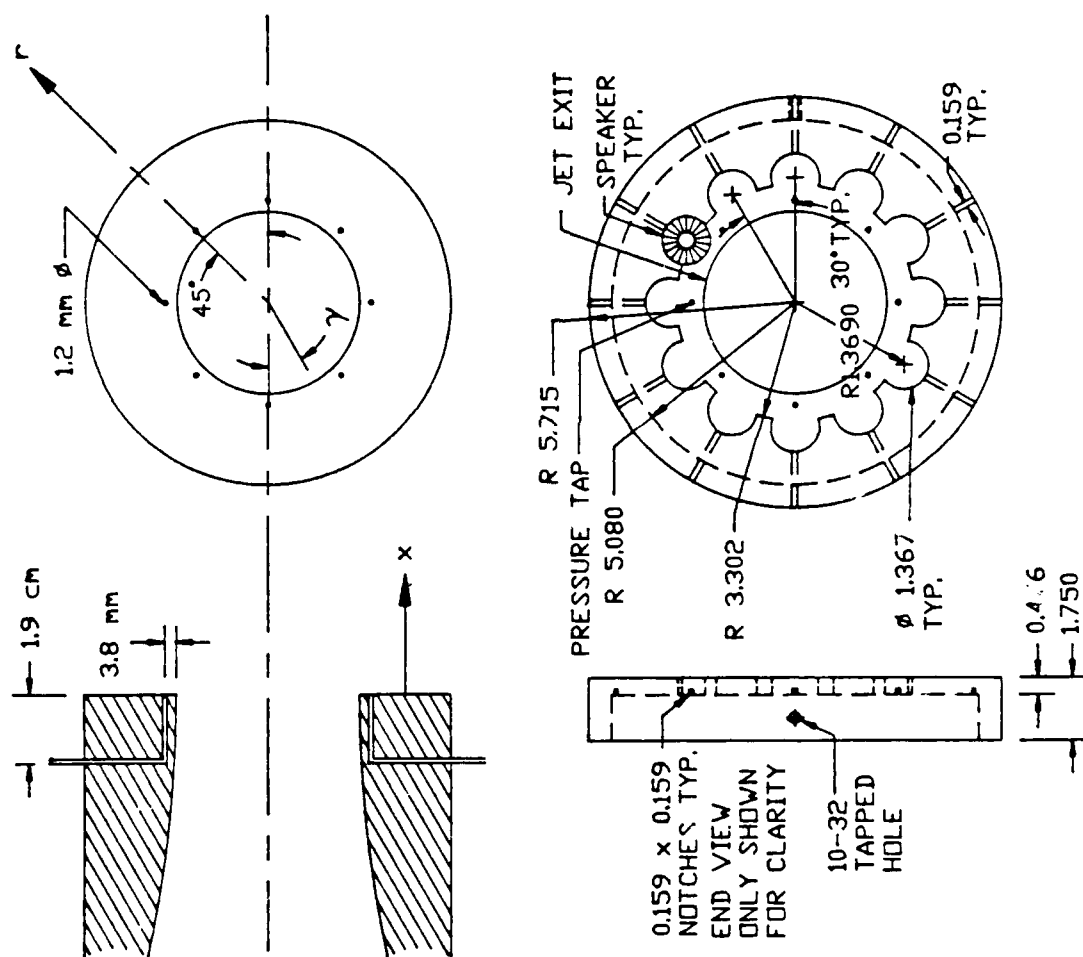


Figure 1.

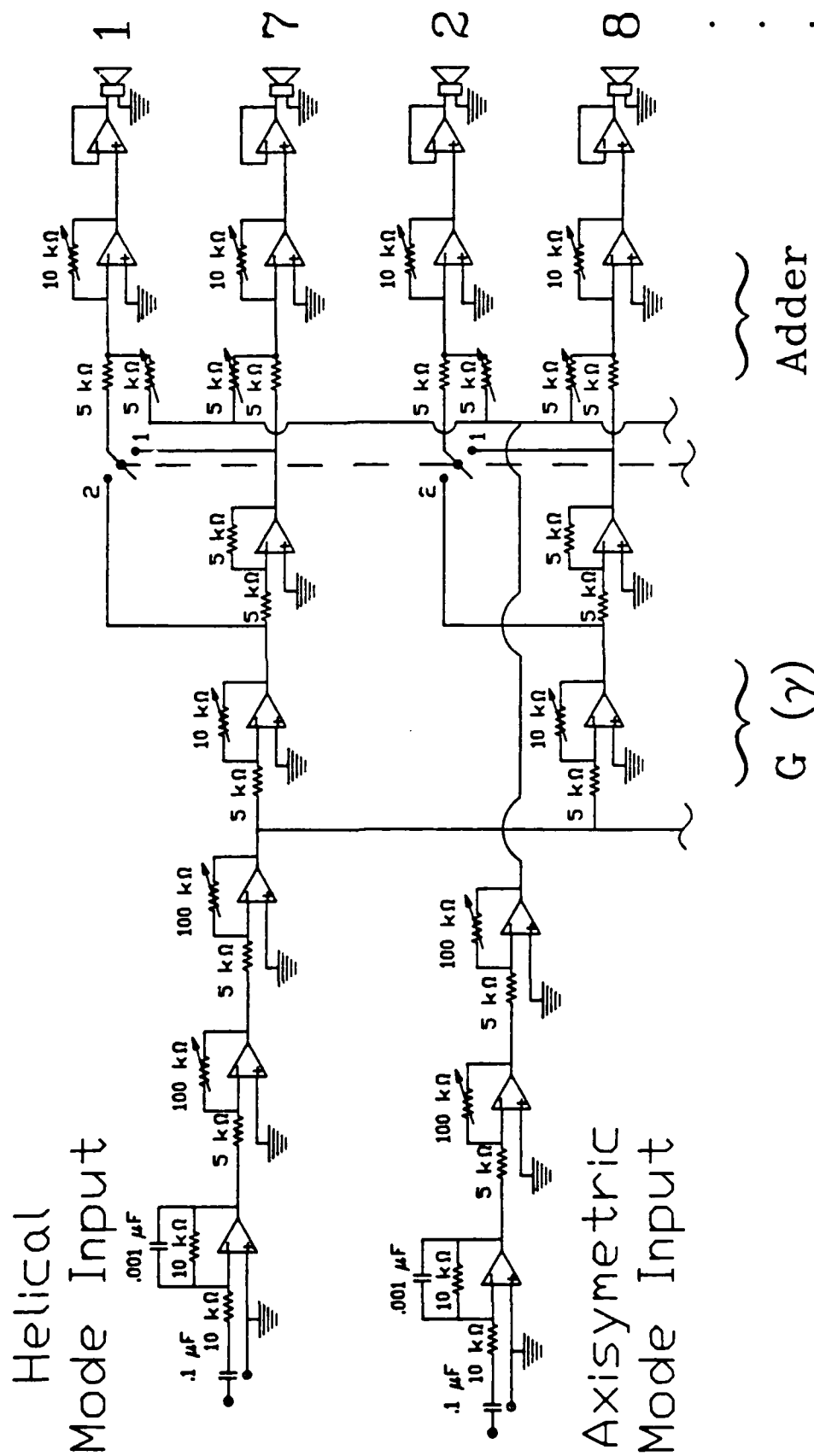


Figure 2.

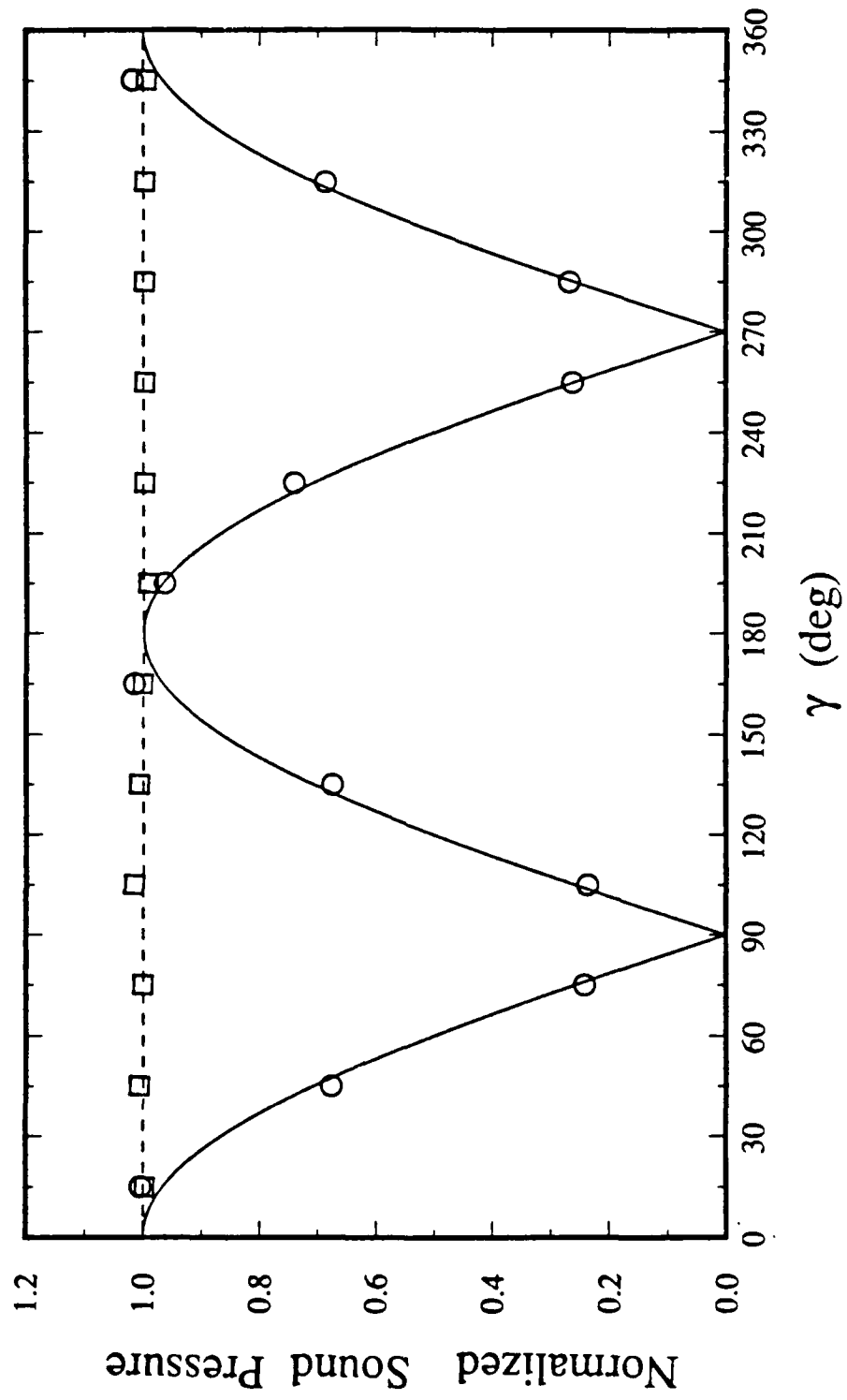


Figure 3.

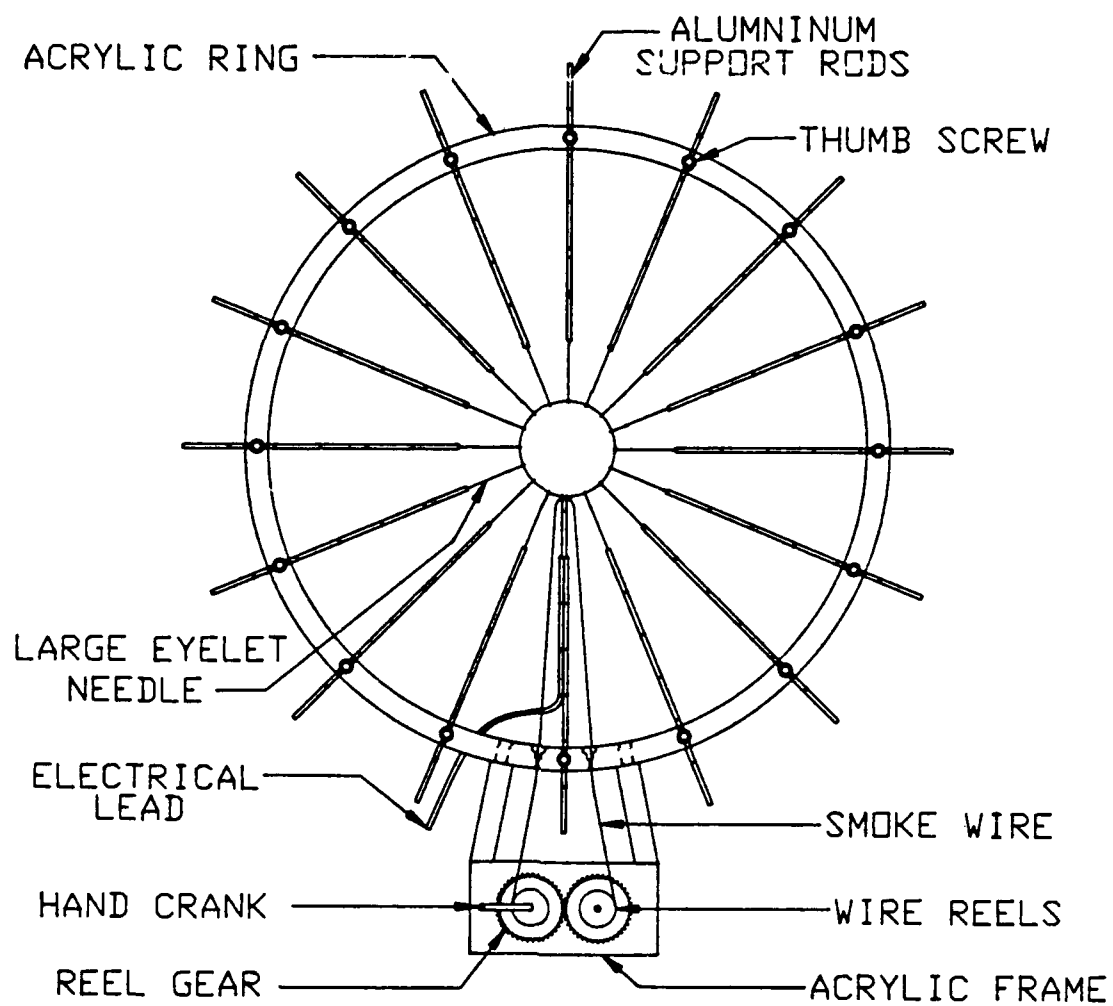


Figure 4a.

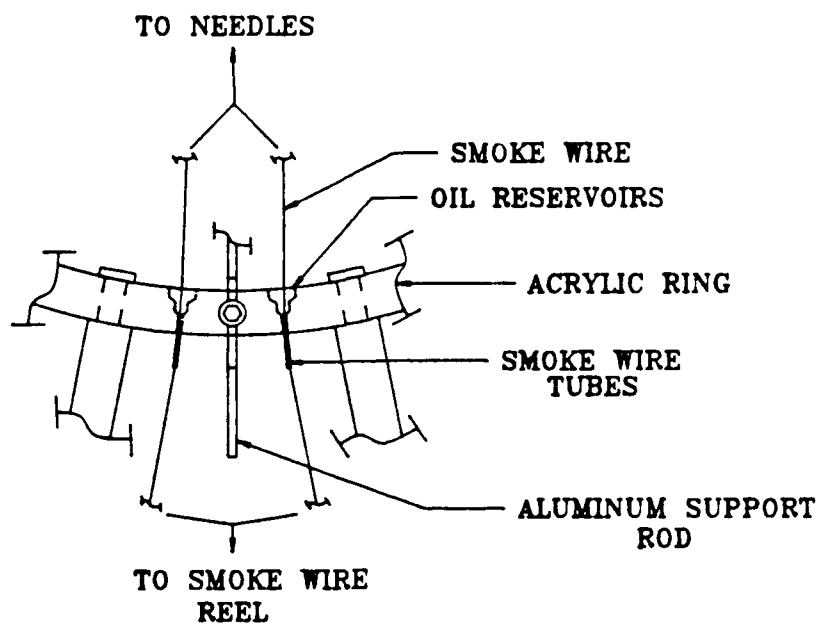
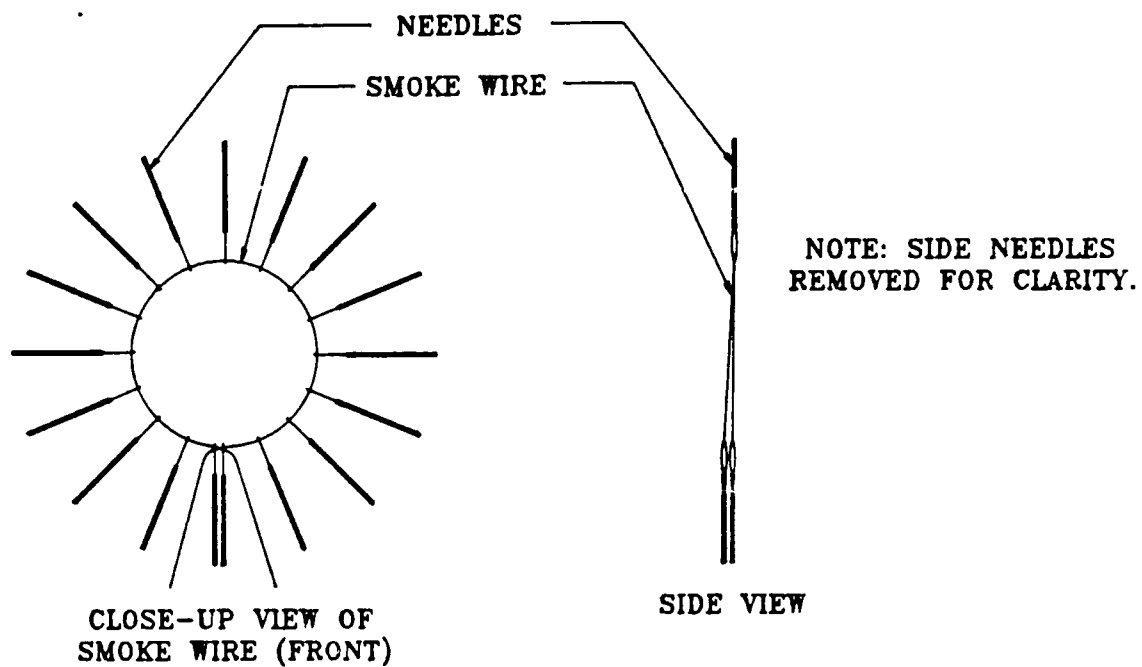


Figure 4b.

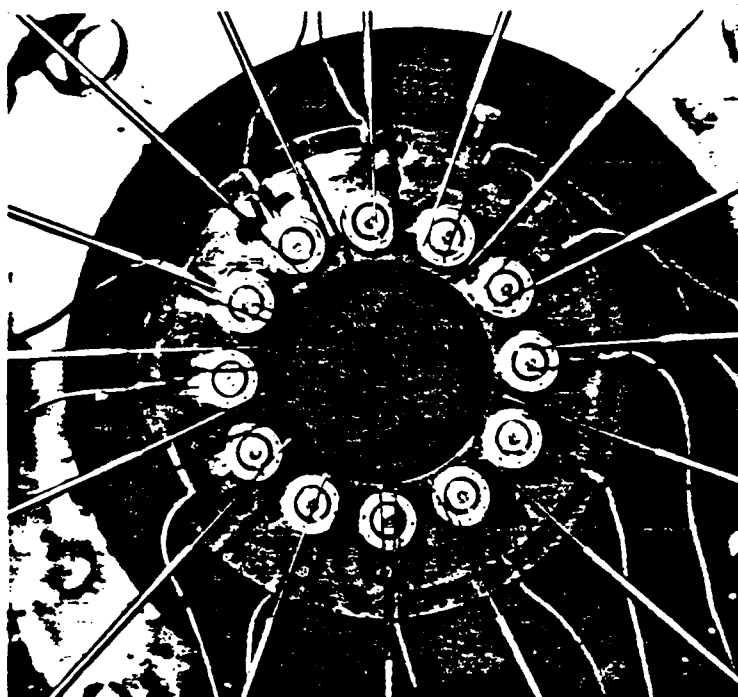


Figure 5.

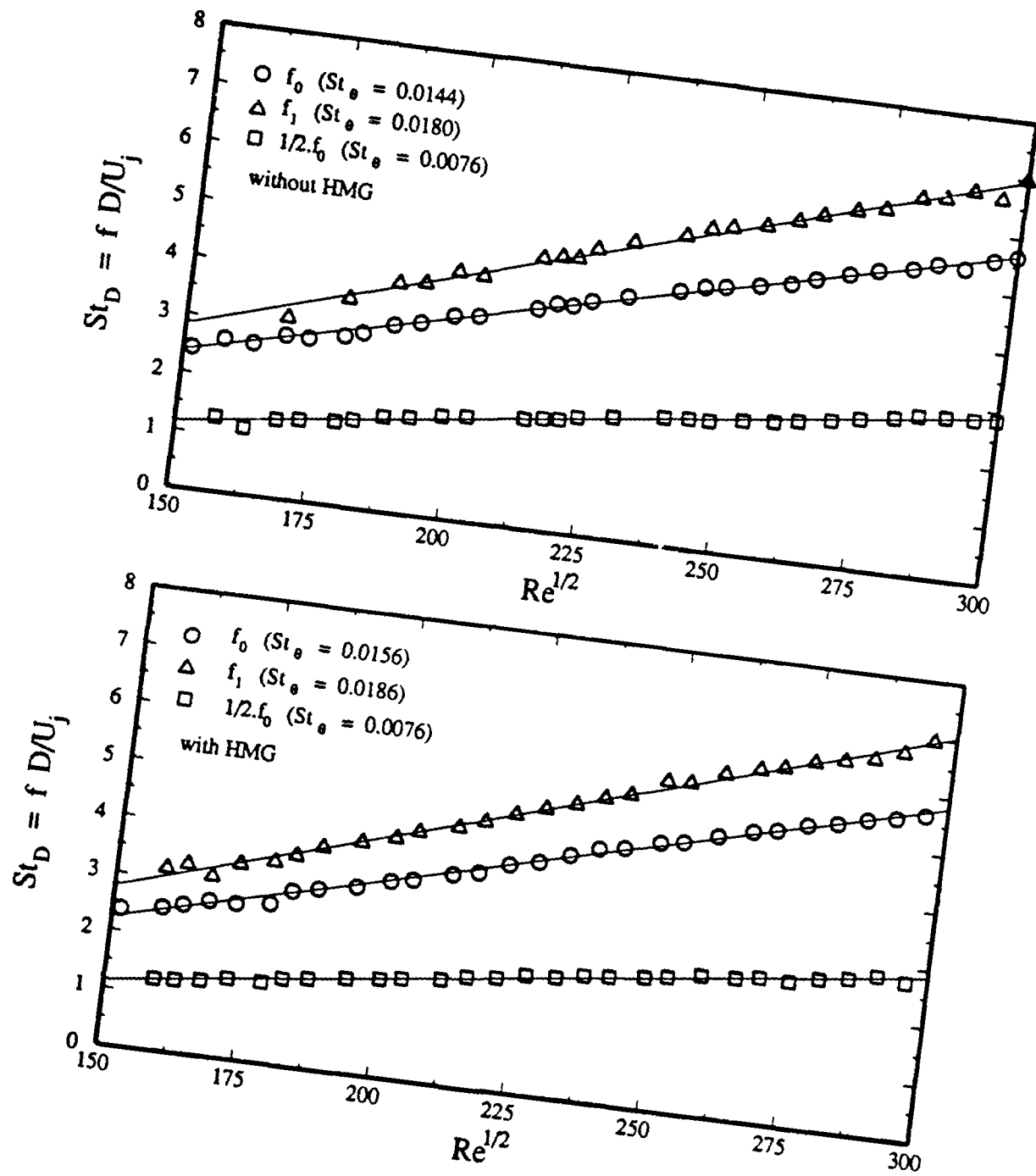


Figure 6.

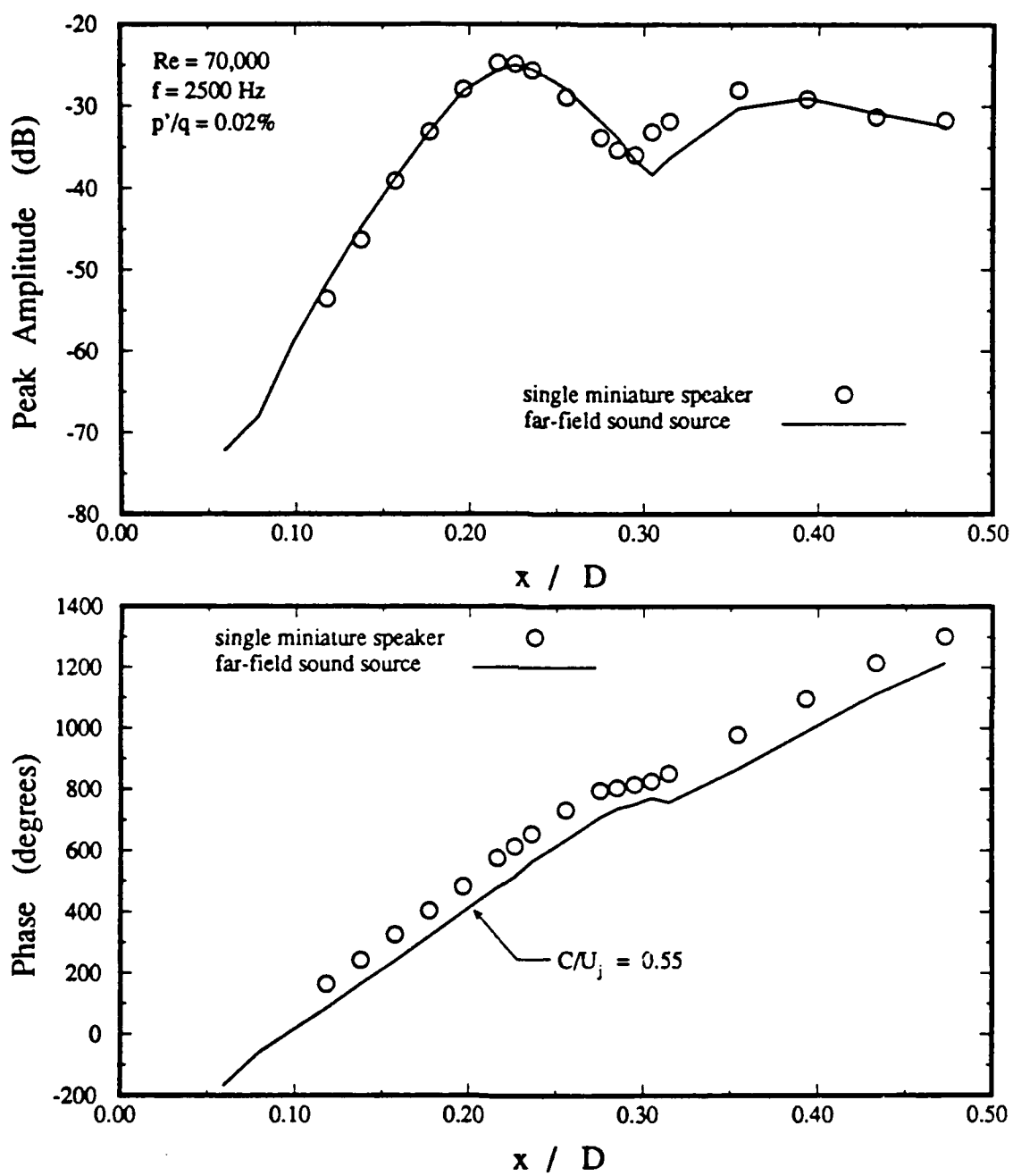


Figure 7.

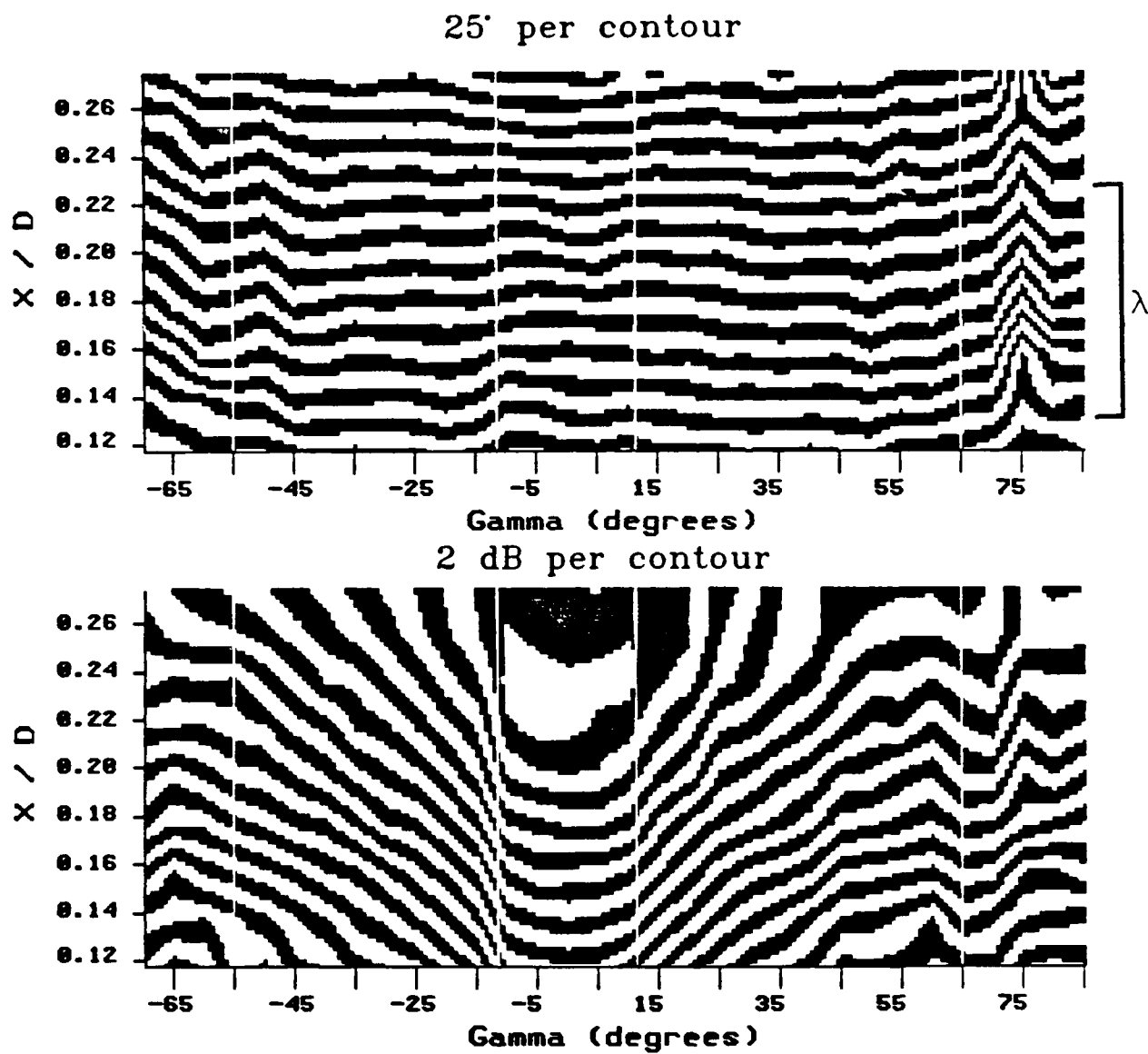


Figure 8.

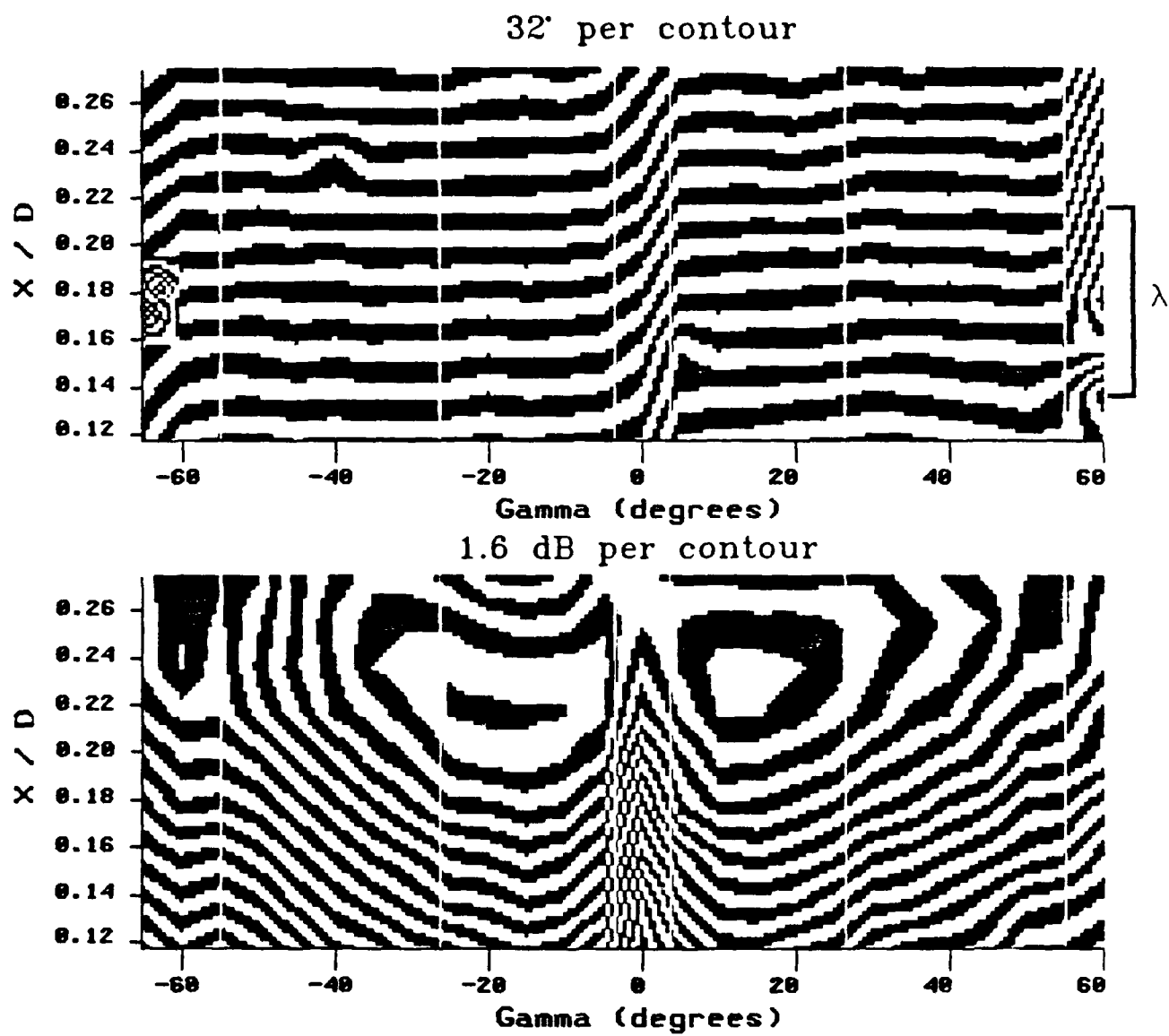


Figure 9.

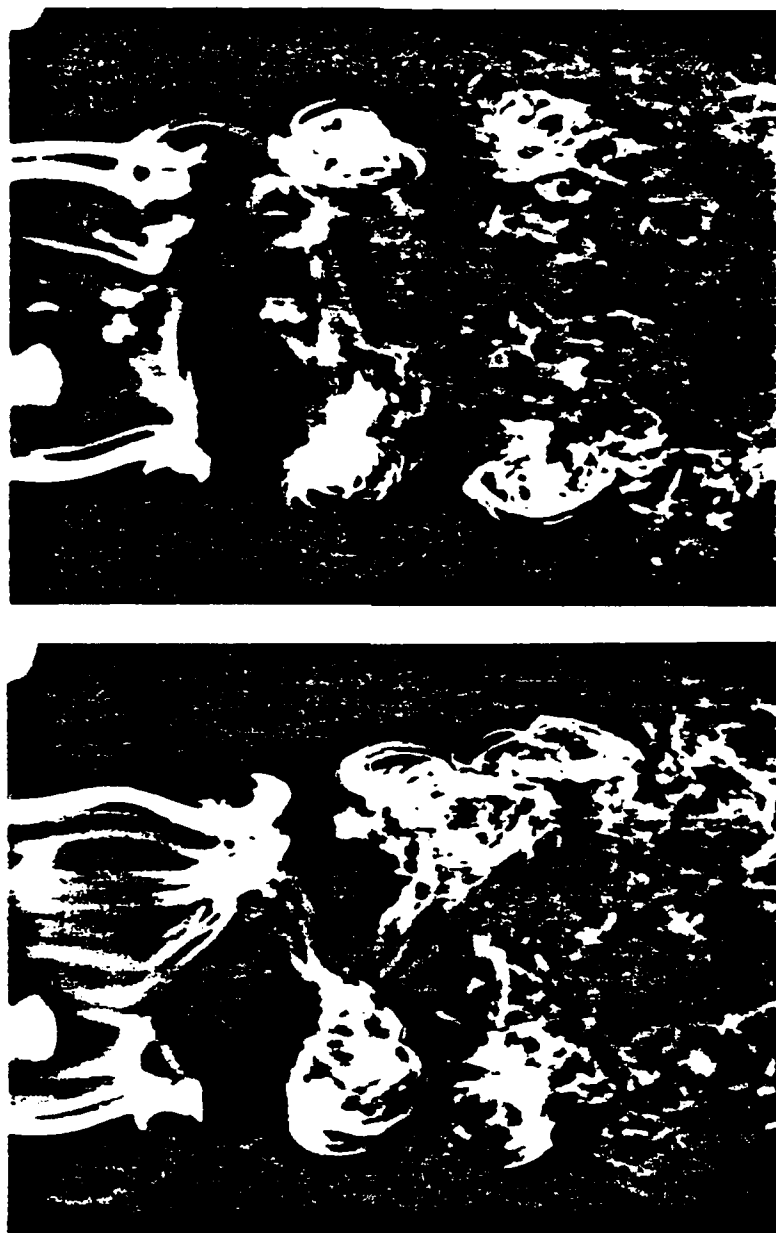


Figure 10.

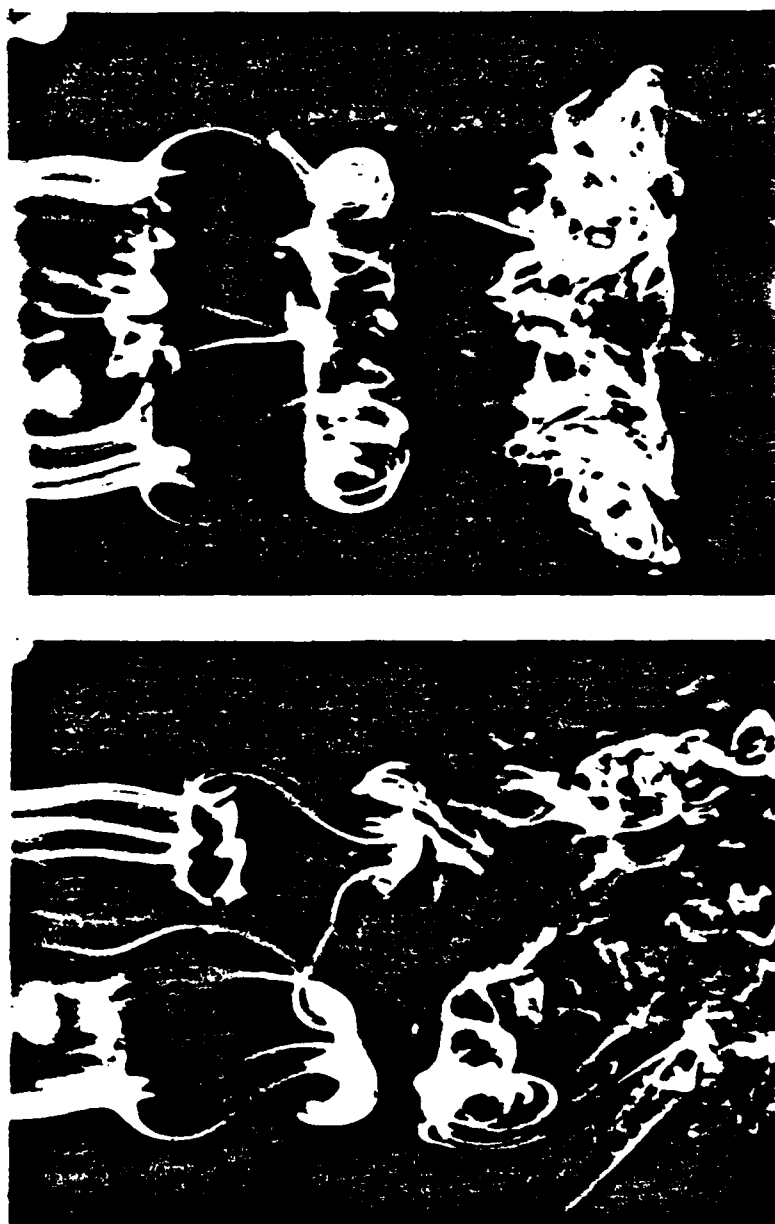


Figure 11.

ECOLE CENTRALE DES ARTS ET MANUFACTURES

RAPPORT DE STAGE DE FIN D'ETUDES

**EXCITATION D'UN JET D'AIR
EN BOUCLE FERMEE**

CLOSED-LOOP EXCITATION OF AN AIR JET

Nathalie NIVELET

**Stage effectué du 13 mars au 8 juillet 1989
à l'ILLINOIS INSTITUTE OF TECHNOLOGY**

Abstract

The existence of a supercritical Hopf bifurcation in Reynolds number is experimentally demonstrated for the case of axisymmetric enhanced feedback. This was achieved by placing a miniature hot-wire probe at a fixed location in the initial shear layer of a low disturbance axisymmetric jet ($60,000 \leq Re_D \leq 80,000$; $Re_{\theta_i} = 170$), and feeding the velocity signal into an array of speakers close to the point of receptivity of the separating shear layer. Quantitative comparisons with the temporal Landau equation at a given streamwise position are presented. Phase averaged measurements using a second 'traveling' probe moving in the range, $1.0 \leq X/\lambda \leq 4.0$, were obtained by repeated opening and closing the feedback loop under computer control. The results indicate that while both real and imaginary parts of the Landau equation appear to be largely independent of space when the flow is almost parallel ($X/\lambda < 1.5$), the Landau coefficient, C_r , decreases by several orders of magnitude within a fraction of the eigenfrequency wave length.

REMERCIEMENTS

Je tiens à remercier le Professeur Naguib de m'avoir accueillie dans son département, des moyens qu'il a mis à ma disposition et de la souplesse dont il a fait preuve.

Je tiens également à remercier tout particulièrement Patrick Reisenthel de toute l'attention et la gentillesse qu'il m'a offertes pendant quatre mois.

Enfin j'aimerais étendre mes remerciements à Sophie Vial, Ahmed Naguib, David Hathway, Edward Nieman, ainsi qu'à tous les membres du groupe de mécanique des fluides qui m'ont accueillie avec tant de gentillesse.

Que tous trouvent dans ce document l'expression de ma gratitude.

SOMMAIRE

INTRODUCTION	1
I. DISPOSITIF EXPERIMENTAL	
I.1.L'écoulement	2
I.2.Instruments de mesure	2
I.3.Equipements informatiques	3
II. EXCITATION DU JET EN BOUCLE FERMEE	
II.1.Description générale	4
II.2.Positionnement de la sonde de feedback	5
II.3.Principaux résultats	6
III.INSTABILITES TEMPORELLES	
III.1.Régime transitoire	10
III.2.Caractéristiques du régime transitoire	10
IV.MOTIVATIONS	
IV.1.Bifurcation de Hopf	12
IV.2.Recherche d'équations de comportement simplifiées	13
IV.3.Validation expérimentale	13
IV.4.Motivations de la présente étude	15
V. PROCEDES EXPERIMENTAUX ET TRAITEMENT DES DONNEES	
V.1.Procédés expérimentaux	16
V.2.Traitements des données	17
VI.RESULTATS ET COMMENTAIRES	
VI.1.Linéarité entre la fréquence propre et le nombre de Reynolds	20
VI.2.Evolution d'un mode dans le temps et l'espace	20
VI.3.Taux de croissance exponentielle	22
VI.4.Coefficient de Landau	23
CONCLUSION	25

Liste des figures

1. Schéma de l'installation	26
2. Schéma de l'expérience	27
3. Variations de la distribution spectrale du signal de vitesse en fonction de la position de la sonde de feedback pour $Re = 70000$	28
4. Exemple de distribution spectrale pour $Re = 75000$ et $x = 5mm$	29
5. Variation de l'amplitude spectrale de la fréquence propre en fonction du gain à $X/D = 0,132$ et $Re = 75700$	30
6. Comparaison entre la structure en bandes de la fréquence propre en fonction du nombre de Reynolds et les résultats théoriques pour $G = 0,132 \text{ Ns/m}^3$ et $X/D =$ $0,17$	31
7. Fonction de transfert en boucle ouverte de la fréquence propre avec courbes de gain pour $X/D = 0,16$ et $Re = 61600$: a) points de fonctionnement mini et maxi b) hystérésis autour du gain critique.	32
8. Régime transitoire, exemple de données brutes	33
9. Illustration de l'évolution temporelle de l'amplitude de la fréquence propre pour $X/D = 0,16$; $Re = 61600$ et $\Omega/\Omega_c =$ $3,25$	34
10. Evolution spatiale de la partie imaginaire du coefficient de Landau à $Re = 68000$	35
11. Bifurcation de Hopf: évolution de l'amplitude spectrale de la fréquence propre en fonction du nombre de Re avec régression parabolique (à un terme)	36
12. Bifurcation de Hopf: évolution de l'amplitude spectrale de la fréquence propre en fonction du nombre de Re avec régression parabolique (à trois termes)	37
13. Bifurcation de Hopf: évolution des valeurs propres paramétrée par le nombre de Reynolds	38
14. Fonctions de transfert des filtres passe bande FIR utilisés pour la démodulation d'amplitude	39

15. Fonctions de transfert des filtres FIR utilisés pour la démodulation d'amplitude	40
16. Illustration de la méthode de traitements des données	41
17. Variations de la fréquence propre en fonction du nombre de Reynolds: a) fréquence mesurée à l'analyseur de spectre en fonction de Re b) fréquence calculée par transformée de Fourier sur les données acquises en fonction de la fréquence mesurée à l'analyseur de spectre	42
18. Variations temporelles de l'amplitude démodulée pour Re = 73000 a) X = 9mm b) X = 15mm	43
19. Variations spatio-temporelles de l'amplitude de la fréquence propre (premier harmonique) pour Re = 76000 (première vue)	44
20. Variations spatio-temporelles de l'amplitude de la fréquence propre (premier harmonique) pour Re = 76000 (seconde vue)	45
21. Variations spatiales de l'amplitude spectrale de l'harmonique et du sous-harmonique du mode axisymétrique	46
22. Diagramme contour des variations spatio-temporelles de l'amplitude de la fréquence propre (premier harmonique) pour Re = 76000	47
23. Diagramme contour des variations spatio-temporelles de l'amplitude de la fréquence propre (premier harmonique) pour Re = 71000	48
24. Diagramme contour des variations spatio-temporelles de l'amplitude de la fréquence propre (premier harmonique) pour Re = 68000	49
25. Variations spatio-temporelles de l'amplitude de la fréquence propre (sous harmonique) pour Re = 76000 (première vue)	50
26. Variations spatio-temporelles de l'amplitude de la fréquence propre (sous harmonique) pour Re = 76000 (seconde vue)	51
27. Diagramme contour des variations spatio-temporelles de l'amplitude de la fréquence propre (sous harmonique) pour Re = 76000	52
28. Variations spatiales du taux de croissance exponentielle pour Re = 71000	53
29. Variations du taux de croissance exponentielle en fonction du nombre de Reynolds (mesures de Reisenhcl)	54

30. Variations du taux de croissance exponentielle en fonction du nombre de Reynolds a) $x = 5$ mm b) $x = 9$ mm	55
31. Variations spatiales de $\ln(1/\beta^2)$	56
32. Détermination de η	57
33. Variations spatiales du logarithme du coefficient de Landau	58

INTRODUCTION

Le but ultime de l'étude que j'ai effectuée à l'Illinois Institute of Technology du 13 mars au 8 juillet 1989 était la détermination des coefficients complexes de l'équation de Ginzburg-Landau dans le développement initial d'un jet d'air excité en boucle fermée par des fluctuations de pression.

Mon stage a comporté les étapes suivantes:

- Une première période de formation et de mise au point de problèmes essentiellement techniques. Cette étape d'environ onze semaines ne sera nullement décrite dans la suite de cet exposé. Sans elle, il eût toutefois été impossible d'utiliser le jet dans de bonnes conditions expérimentales.

- Une seconde étape de préparation et réalisation du travail expérimental d'une durée de trois semaines.

- Enfin les trois dernières semaines, consacrées au traitement des données et à l'analyse des résultats.

Faute de temps, l'utilisation des résultats n'a pu être menée à terme. Seule la détermination spatiale du coefficient de Landau a été possible et non celle de tous les coefficients de l'équation de Ginzburg-Landau. Même si l'objectif initial n'a pas été atteint, l'étude a cependant livré des résultats intéressants qui feront l'objet d'une présentation au 42nd Annual Meeting of the Division of Fluid Dynamics of the American Physical Society.

I DISPOSITIF EXPERIMENTAL

I.1 L'écoulement

L'équipement utilisé est représenté figure 1. La chambre d'uniformisation contient de la mousse qui réalise l'isolement acoustique en aval ainsi qu'une série de grilles en nid d'abeille, d'écrans conçus pour produire en sortie un écoulement uniforme à très faible intensité de turbulence. A la sortie de la chambre, l'écoulement traverse un cylindre de plexiglass de 15,2 cm de diamètre; puis est accéléré dans une contraction du cinquième ordre de rapport 1/9.

Le diamètre du jet est alors de 5,1 cm et la vitesse de l'écoulement est comprise entre 10 et 30 m/s. A la sortie de la contraction, l'écoulement est laminaire avec un niveau de turbulence inférieur à 0,05%.

L'air provient d'un réservoir "basse" pression à environ 3,4 atm. Un système de régulation de pression permet de maintenir le nombre de Re constant à 1% près pendant une longue période. L'arrivée d'air est contrôlée avec précision grâce à une valve équipée d'un moteur électrique. L'écoulement est ensuite amené dans une section de transition par un tuyau d'environ 5 cm de diamètre.

La section de transition contient également de la mousse pour l'isolement acoustique.

I.2 Instruments de mesure

Une sonde à fil chaud est montée sur un mécanisme permettant son déplacement dans les trois directions de l'espace. Deux moteurs pas à pas contrôlent les directions x et y de la sonde (cf figure 2) avec une précision de 10 μm en x et de 5 μm en y. Par comparaison, le diamètre du fil de tungstène qui constitue la partie sensible de la sonde est de 3,8 μm , celui des dents de cette sonde 0,076 mm; l'utilisation d'une sonde miniature permettant naturellement de limiter les interactions avec l'écoulement. Une deuxième sonde miniature, diamétralement opposée à celle de mesure, est utilisée pour la boucle de retour.

Les mesures de vitesse sont effectuées dans la direction de l'écoulement à l'aide de la sonde décrite ci-dessus et d'un anémomètre tous deux "faits maison", c'est-à-dire fabriqués par l'atelier électronique du département. Le signal de sortie de l'anémomètre est recentré sur zéro puis amplifié afin d'augmenter la précision de l'acquisition en utilisant au maximum les possibilités de l'ordinateur ($-5\text{V} < U_{\text{acquis}} < 5\text{V}$).

Le transducteur de pression Validyne DP45 et le démodulateur Validyne CD15 mesurent la vitesse du jet à la sortie de la contraction, ie le nombre de Reynolds. Le transducteur, qui mesure la pression statique en amont de la contraction, est calibré à l'aide d'un manomètre. L'anémomètre est lui régulièrement calibré grâce au transducteur. Un souci particulier a été attaché à la validité de la calibration de l'anémomètre, principal appareil de mesure. Le senseur de la sonde ("le fil chaud") étant très sensible aux variations de température, il a semblé nécessaire d'effectuer des corrections de température dans les divers algorithmes de mesure de vitesse et de calibration. La température de l'écoulement est mesurée à l'aide d'une thermistance et acquise en temps réel par l'ordinateur. La prise en compte de ce paramètre supplémentaire augmente la précision des mesures et la longévité de la calibration du transducteur. Avant chaque expérience, cette dernière se trouvait contrôlée et une recalibration avait lieu le cas échéant.

L'analyse en temps réel des fréquences caractéristiques des deux signaux produits par les sondes et la détermination de leur cohérence sont fournies par l'analyseur de spectre HP3582A à deux voies d'entrée. Le signal d'entrée d'un haut-parleur et le signal de mesure de l'anémomètre sont visualisés sur un oscilloscope Philips PM3055.

Les fluctuations de pression destinées à forcer l'écoulement sont produites par une série de 12 haut-parleurs placés en couronne à la sortie de la contraction (cf figure 2). Un réglage préliminaire des haut-parleurs garantit la symétrie de révolution de leur signal de sortie (à 2,5% près).

Pour éviter les effets de repliement de spectre lors du traitement des données, le signal acquis passe au travers d'un filtre de fréquence analogique Ithaco 4212.

I.3 Equipements informatiques

Deux ordinateurs de type MASSCOMP ont été utilisés pour cette étude:

- Un ordinateur de type DAPS.MCP4 pour l'acquisition des données, capable de conversion A/D à une fréquence de 100000 Hz et de conversion D/A à 330000 Hz. En plus de l'acquisition (vitesse de l'écoulement, température et projection de la vitesse suivant x), ce MASSCOMP assure le pilotage des moteurs pas à pas de la sonde de mesure et du moteur de la valve d'alimentation en air.

- L'ordinateur de traitement (DAPS.MCP1) situé dans la salle informatique reçoit les données à traiter par l'intermédiaire du réseau ETHERNET. Il est équipé d'un microprocesseur 68020 et d'une importante mémoire (500 Mbytes en tout).

II EXCITATION DU JET EN BOUCLE FERMÉE

II.1 Description générale

L'excitation du jet en boucle fermée est un moyen artificiel de réinjecter des perturbations issues du jet dans sa couche-limite initiale (cf figure 2). La "boucle fermée" comprend quatre éléments:

- Le signal de vitesse, mesuré par un fil chaud, est amplifié et injecté comme signal d'entrée dans les haut-parleurs. Les haut-parleurs produisent alors en sortie une fluctuation de pression proportionnelle en première approximation à la fluctuation de vitesse (il est supposé que, localement, il existe une relation linéaire entre la tension du fil chaud et la vitesse). Les haut-parleurs et le circuit électronique constituent la première branche de la boucle. L'amplification du signal de vitesse est à gain variable.

- La deuxième branche est le chemin acoustique des haut-parleurs aux lèvres du jet. Dans le cas présent ce chemin est très court et le temps de transmission de la fluctuation de pression quasi négligeable. Cela constitue une nouveauté par rapport aux expériences précédentes, effectuées par Patrick Reisenthel, dans lesquelles un haut-parleur unique se trouvait à environ 3 m des lèvres du jet.

- La troisième branche est le phénomène de réceptivité qui effectue le couplage entre les fluctuations de pression et les fluctuations de vitesse dans le développement initial de la couche limite.

- Enfin, ces fluctuations de vitesse sont amplifiées de manière sélective lors de leur convection dans l'écoulement.

Il est possible de calculer le gain de la boucle de retour, mais cette donnée est d'un intérêt limité dans l'étude présentée ici puisque le gain est maintenu constant au cours des expériences.

L'intérêt du procédé d'excitation du jet en boucle fermée est qu'il permet d'augmenter l'organisation de la couche limite du jet (apparition d'oscillations harmoniques), renforçant le phénomène naturel d'auto-excitation du jet.

II.2 Positionnement de la sonde de feedback

Le but de l'étude étant de vérifier si le jet excité obéit à des équations dynamiques simplifiées, il est par conséquent souhaitable d'obtenir de "bonnes" conditions expérimentales, c'est-à-dire le développement d'oscillations périodiques.

L'expérience a montré qu'il faut placer la sonde de feedback dans la partie la couche limite où la vitesse est élevée ($U/U_j=0,8$) et à quelques longueurs d'onde des lèvres du jet pour obtenir de telles conditions. Pour mémoire, La figure 3 résume l'évolution de la densité spectrale en fonction de la position de la sonde de feedback (cette série de spectres provient de la thèse de Reisenhel). Pour $0,18 < X/D < 0,28$, il y a une claire dominance d'un mode et de ses harmoniques. C'est naturellement cette configuration qui est intéressante dans le cas présent.

C'est avec le plus grand soin que la sonde de feedback a été positionnée avant le commencement des expériences. L'un des critères de cette opération était l'obtention d'oscillations "pures". La pureté des oscillations provoquées par la boucle fermée est illustrée par la figure 4 qui représente la densité spectrale de la vitesse pour $Re = 75000$ et $x = 5$ mm. Il y a une claire dominance d'un mode (autour de 2900Hz) et de son sous-harmonique.

Il convient de rappeler que toutes les mesures de vitesse sont effectuées par une sonde mobile de mesure, distincte de la sonde de feedback qui, elle, demeure fixe pendant toute la durée de l'expérience.

II.3 Principaux résultats

a) Existence d'un gain, d'une position et d'un nombre de Reynolds critiques

Pour une position correcte de la sonde de feedback, la création d'une boucle fermée provoque l'instauration d'oscillations auto-entretenues harmoniques. L'excitation du jet dépend fortement de la valeur du gain total de la boucle de retour (l'amplification du signal de vitesse est à gain variable). Pour un gain faible, la boucle de retour est sans effet sur la couche limite du jet. Seules des valeurs du gain supérieures à un seuil excitent l'écoulement. La figure 5 illustre la variation de l'amplitude avec le gain. Dans sa thèse de PhD, Reisenthel propose comme valeur du gain critique l'expression suivante:

$$\Gamma_c = \frac{e^{+\alpha_i X}}{R} = \frac{e^{\eta \sqrt{Re} X}}{R} \quad (1)$$

Où:

- R est la fonction de transfert de la réceptivité

$$\frac{u'_e}{U_d} = R \frac{P'}{\frac{1}{2} \rho U_d^2} \quad (2)$$

R peut être supposé constant dans le cas étudié.

- X est la position de la sonde de feedback.

- α_i est le taux d'amplification spatial de la perturbation supposé égal au taux d'amplification maximal et donc proportionnel à la racine du nombre de Reynolds.

En supposant maintenant le gain et le nombre de Reynolds fixes, la condition d'apparition de l'excitation

$$\Gamma > \frac{e^{\eta \sqrt{Re} X}}{R} \quad (3)$$

devient

$$X > X_c, \quad X_c = - \frac{\ln(\Gamma R)}{\eta \sqrt{Re}} \quad (4)$$

Ce qui montre l'existence d'un seuil pour la position de la sonde de feedback.

De même, en supposant la position et le gain fixes, un nombre de Reynolds critique est mis en évidence:

$$Re_c = \left[\frac{\ln(\Gamma R)}{\eta X} \right]^2 \quad (5)$$

b) Existence d'une fréquence propre

Les résultats ci-dessus résument les conditions d'apparition d'oscillations auto-entretenues dans la couche limite du jet. Ces oscillations sont caractérisées par:

- un niveau de fluctuation élevé. Sur la figure 4, le pic de la fréquence fondamentale est à environ 40 dB par rapport au bruit de fond.

- un important degré de déterminisme dans la sélection d'une fréquence unique (accompagnée de ses harmoniques).

Cette fréquence intrinsèque sélectionnée par la boucle fermée est appelée fréquence propre. Dans les conditions de la figure 5, $Re = 75000$ et $x = 5$ mm, la fréquence propre est 2880 Hz.

Le processus de sélection d'une fréquence particulière par la boucle fermée n'a pas été complètement élucidé jusqu'à présent. Cependant de simples considérations sur la phase permettent de conclure à l'existence d'une série discrète de fréquences admissibles. Comme l'a montré Reisenhel, la condition d'apparition d'oscillations (somme des délais de phase de la boucle fermée multiple de 2π) est:

$$2\pi f d / C_0 + 2\pi f x / C + 2\pi f \tau_s + \varphi = 2\pi n \quad (6)$$

où:

- d est la distance des haut-parleurs aux lèvres du jet (quasi négligeable dans le cas étudié).

- C_0 est la vitesse du son.

- C est la vitesse de phase de l'écoulement ($C = U_j/2$).

- τ_s est le retard électronique (négligeable).

- φ est le retard de phase de la réceptivité.

En inversant la relation ci-dessus, il vient:

$$f_n = \frac{n - \frac{\varphi}{2\pi}}{\frac{d}{C_0} + \frac{x}{C} + \tau_s} \quad (7)$$

La figure 6 compare les résultats théoriques de l'équation ci-dessus (φ et τ_s sont pris égaux à 0) avec les fréquences mesurées pour un gain fixe et un nombre de Reynolds compris entre 45000 et 85000. Il apparaît clairement que les fréquences f_n représentent un ensemble de fréquences permises pour l'excitation en boucle fermée; mais ne permettent pas d'expliquer le processus de sélection d'une unique fréquence propre.

c) Hystérésis et structure en bandes

Au cours de l'excitation du jet en boucle fermée et sous certaines conditions (valeur du gain ou du nombre de Reynolds assez importantes), il se développe dans la couche limite du jet des oscillations de vitesse caractérisées par une unique fréquence. En maintenant le gain et la position de la sonde de feedback constants et en faisant varier le nombre de Reynolds, il est possible de déterminer les variations de la fréquence propre de l'oscillation en fonction du nombre de Reynolds. La figure 6 en illustre les principales caractéristiques:

- Les points de mesure s'accumulent suivant des segments de droite très clairement définis. Sur l'un de ces segments de droite, la fréquence propre varie faiblement mais linéairement en fonction du nombre de Reynolds. Les variations de la fréquence propre en fonction du nombre de Reynolds ont donc une structure en bandes.

- Le saut de fréquence d'une bande à une autre s'accompagne parfois d'hystérésis comme il est possible de l'observer autour de $Re = 60000$.

L'équation (7) permet d'élucider la structure en bande décrite ci-dessus, le passage d'une bande à une autre correspondant à un changement de valeur propre.

Les expériences présentées ici nécessitent l'absence de sauts en fréquence intempestifs pour une large plage de nombre de Reynolds. Par conséquent, la sonde de feedback et le gain de la boucle de retour ont été choisis suivant deux critères:

- L'obtention d'oscillations pures.
- L'assurance d'appartenir à une bande assez large.

Le respect de ces critères a permis, au cours des expériences, de faire varier le nombre de Reynolds de 60000 à 78000 sans saut de fréquence.

d) Amplitude de saturation

Les considérations sur la phase ont permis d'expliquer l'émergence d'une fréquence intrinsèque au cours de l'excitation du jet en boucle fermée. Pour élucider le mécanisme de sélection de l'amplitude de saturation de l'oscillation, la boucle fermée est décomposée en deux éléments:

- Une boucle ouverte dont il est possible de déterminer la fonction de transfert (non linéaire) expérimentalement en forçant à diverses fréquences (u'_x/U_j en fonction de $p'_o / \frac{1}{2} \rho U_j^2$).

- Une boucle de retour, constituée du simple étage d'amplification du signal de vitesse issu de l'anémomètre. La condition de feedback s'écrit simplement:

$$\frac{p_o'}{\frac{1}{2} \rho U_j^2} = \Gamma \frac{u_x'}{U_j} \quad (8)$$

La condition de feedback est représentée sur la figure 7 pour différentes valeurs du gain ainsi que la réponse de la boucle ouverte correspondant à la fréquence propre sélectionnée par la boucle fermée à $X/D=0,16$ et $Re=61600$. Pour un gain donné Γ , la boucle fermée impose au point $(p_o' / \frac{1}{2} \rho U_j^2, u_x' / U_j)$ d'appartenir à la courbe C_p et à la courbe de la fonction de transfert de la boucle ouverte. Un point de fonctionnement est ainsi déterminé et donc l'amplitude de saturation de l'oscillation.

III INSTABILITES TEMPORELLES

III.1 Régime transitoire

Des mesures transitoires sont possible grâce à la fermeture d'un interrupteur életronique fermant la boucle de retour à des instants choisis pendant l'acquisition de données (cf figure 2). Cette opération s'appuie sur un interrupteur CD4066 contrôlé par l'ordinateur d'acquisition. Ces mesures de régime transitoire permettent d'obtenir des renseignements sur le caractère temporel des oscillations qui se développent dans le jet excité en boucle fermée. Les caractéristiques spatiales de cette instabilité temporelle sont déterminées grâce à l'usage de deux sondes; une première sonde de feedback fixe et une deuxième sonde de mesure mobile. La figure 8 présente un exemple de données brutes acquises par le MASSCOMP, l'acquisition de deux régimes transitoires successifs et du début d'un troisième s'y trouve illustrée. Les données sont ensuite traitées dans le but de déterminer le taux de croissance temporel de l'oscillation (σ en s^{-1}). Les manipulations nécessaires seront décrites ultérieurement dans le chapitre V.

III.2 Caractéristiques du régime transitoire

Pour un nombre de Reynolds et une position de la sonde de feedback fixes, si à $t = 0$ la boucle de retour (gain Γ) est brutalement fermée et si $\Gamma > \Gamma_c$, l'amplitude de la fréquence propre sélectionnée augmente de sa valeur naturelle de bruit de fond à sa valeur de saturation. Connaissant le comportement en boucle ouverte du système, l'évolution temporelle de la fluctuation de vitesse peut être décrite de la manière suivante. A $t < 0$, la fluctuation de vitesse ($u = u'_x/U_j$) est faible. Le niveau de pression ($p = p'_o / \frac{1}{2} \rho U_j^2$) est inconnu, dépendant certainement du niveau de feedback naturel. A $t = 0$, u a une valeur initial u_0 et l'interrupteur est fermé. Par la boucle de retour, cette fluctuation de vitesse initiale entraîne une fluctuation de pression p_1 . Celle-ci fait ensuite naître une perturbation dans la vitesse aux lèvres du jet par le phénomène de réceptivité. Cette fluctuation initiale (d'un point de vue spatial) de la vitesse est amplifiée dans le sens de l'écoulement provoquant au niveau de la sonde de feedback une nouvelle fluctuation de vitesse u_1 . Le procédé se reproduit jusqu'à convergence; le point de convergence étant le point opérationnel défini ci-dessus (intersection de la fonction de transfert de la boucle ouverte et de la courbe de feedback). La figure 9 illustre la description précédente.

Il a été de plus démontré par Reisenthel que, dans le cas où Γ/Γ_c est proche de 1, la croissance de la perturbation de vitesse est exponentielle dans les premiers instants (ie avant saturation). Le taux d'amplification temporel est donné par la formule suivante:

$$\sigma = \frac{\ln(\Gamma) - \alpha; X + \ln(R)}{\tau} \quad (9)$$

avec $\tau = \tau_a + \tau_n + \tau_s = \frac{d}{c_0} + \frac{x}{c} + \tau_s$ la somme des retards de la boucle.

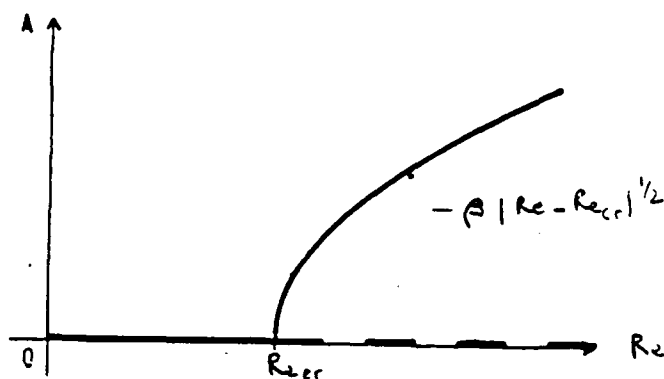
Enfin, il a été prouvé expérimentalement que pour $x < 3\lambda$, la valeur de σ est indépendante de la distance aux lèvres du jet.

IV MOTIVATIONS

IV.1 Bifurcation de Hopf

L'existence d'une bifurcation de Hopf en nombre de Reynolds dans l'excitation en boucle fermée du jet semble probable. Les deux propriétés caractéristiques d'une bifurcation de Hopf sont présentées ci-dessous:

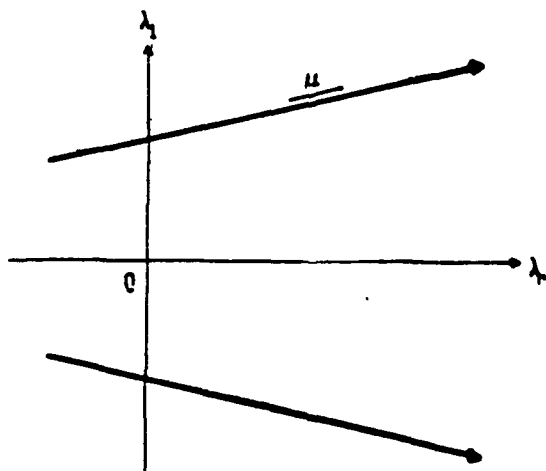
- L'amplitude de saturation de la perturbation au voisinage du point critique doit être proportionnelle à la racine carrée de la "distance" au point. Dans le cas étudié, pour $Re > Re_{cr}$, l'amplitude de saturation de la fluctuation de vitesse doit être proportionnelle à $(Re - Re_{cr})^{1/2}$.



- Appelons u_r et u_i les parties réelles et imaginaires de la fluctuation de vitesse. Si autour du point critique

$$(\dot{\mathbf{u}}) = (\mathbf{A})(\mathbf{u}) \quad (10) \quad (\mathbf{u} = u_r + i u_i)$$

alors il faut que les valeurs propres de $\mathbf{A}(Re)$ soient complexes conjuguées, qu'elles appartiennent au demi-plan complexe gauche pour $Re < Re_{cr}$, qu'elles croisent l'axe imaginaire à Re_{cr} à une vitesse $(d\lambda_r/dRe)$ positive et finie.



Linearized system around Re_c :

$$\mathbf{u} = u_r + i u_i$$

$$\underline{\mathbf{u}} = [u_r, u_i]^T \quad [\dot{\underline{\mathbf{u}}}] = [\mathbf{A}] [\underline{\mathbf{u}}]$$

eigenvalues: $\lambda_r \pm i \lambda_i$

$$\lambda_r < 0 \text{ if } Re < Re_c$$

$$\lambda_r > 0 \text{ if } Re > Re_c$$

$$d\lambda_r/dRe > 0 \text{ and finite.}$$

IV.2 Recherche d'équations de comportement simplifiées

Landau a proposé une équation de modèle simple pour décrire l'état d'un système subissant une bifurcation de Hopf. Il est donc naturel de chercher à déterminer si l'équation de Landau peut décrire l'évolution temporelle du système étudié.

L'équation de Landau s'écrit:

$$du/dt = au - c|u|^2 u \quad (11)$$

où a et c sont deux coefficients complexes.

En cherchant des solutions de la forme $u = A \exp(i\phi)$, l'équation ci-dessus se décompose en:

$$dA/dt = a_r A - c_r A^3 \quad (12)$$

$$d\phi/dt = a_i - c_i A^2 \quad (13)$$

IV.3 Validation expérimentale

a) Détermination des coefficients de l'équation de Landau

Il a été décrit dans le chapitre sur les instabilités temporelles comment, grâce à un interrupteur électronique, il est possible d'enregistrer des régimes transitoires. Dans les premiers instants après la fermeture de l'interrupteur la croissance de l'amplitude de la fluctuation de vitesse peut être considérée comme exponentielle. Comme il sera détaillé par la suite, il est possible d'effectuer des mesures du taux de croissance σ sur des données expérimentales. Considérons l'équation 11, au début de la croissance des oscillations il est possible de négliger A^3 devant A (car A est faible). L'équation (12) devient alors une simple équation du premier degré:

$$dA/dt = a_r A \quad (14)$$

Ce qui montre clairement que le taux de croissance exponentielle σ et a_r sont identiques.

En supposant $\phi = 2\pi f t + \phi_0$, l'équation (13) devient:

$$2\pi f = a_i - c_i A^2 \quad (15)$$

Le coefficient a_i apparaît comme proportionnel à la fréquence initiale. Le coefficient c_i détermine les variations de la fréquence au cours du temps. Connaissant l'évolution temporelle de la fréquence il est possible d'en déduire les coefficients a_i et c_i . Une méthode de détermination du coefficient de Landau c_r sera proposée ultérieurement.

Une première série d'expériences a permis de montrer que:

- $a_r = 0$; $\partial a_r / \partial X = 0$ pour $X/\lambda < 3$ (cf thèse de PhD de Reisenhel)

- $c_i = 0$ et $a_i = 2\pi f$; $\partial a_i / \partial X = 0$ (résultats présentés par Reisenhel à une conférence). La figure originelle à l'appui de ces résultats n'est pas en ma possession. Toutefois ceux-ci ayant été confirmés par la suite, la figure 10 qui représente les variations de c_i (normalisé par A_{\max}^2 / F_{\max}) en fonction de x à $Re = 68000$ démontre clairement que $c_i = 0$.

L'équation de Landau semble donc être un bon candidat pour la description des oscillations temporelles qui se développent dans le jet en boucle fermée pour l'unique position X étudiée ($X/D = 0,17$).

b) Confirmation de l'existence d'une bifurcation de Hopf

Le premier critère à vérifier afin de confirmer l'existence d'une bifurcation de Hopf est que, pour $Re > Re_{cr}$ et Re proche de Re_{cr} , l'amplitude de saturation de la fluctuation de vitesse soit bien proportionnelle à $(Re - Re_{cr})^{1/2}$. N'étant pas en possession des premières mesures effectuées dans ce but, je suis dans l'obligation de présenter ici des résultats postérieurs à ceux obtenus par Reisenhel sur ce sujet.

La figure 11 présente les variations de l'amplitude de saturation de l'oscillation de vitesse en fonction du nombre de Re . Le nombre de Reynolds critique est $Re = 65500$. La position de la sonde de mesure est $x = 5\text{mm}$. Un programme informatique se charge d'effectuer une "régression parabolique" sur les données. Le nombre de points sur lesquels la régression est calculée constitue l'un des paramètres de ce programme. Dans l'exemple proposé, seuls les trois premiers nombres de Reynolds après le seuil semblent appartenir à la branche parabolique et sont pris en compte par la régression. Le coefficient de proportionnalité entre l'amplitude de saturation et la racine carrée de la "distance" au seuil $((Re - Re_{cr}) / Re_{cr})$ est déterminé par le programme d'ajustement et vaut $\beta_1 = 0,57 \text{ m/s}$.

Dans la figure 12, l'ajustement est effectué sur trois termes $([(Re - Re_{cr}) / Re_{cr}]^{1/2}, [(Re - Re_{cr}) / Re_{cr}]^{3/2}, [(Re - Re_{cr}) / Re_{cr}]^{5/2})$ et sur tous les points disponibles. Pour Re proche de Re_{cr} , le premier terme de l'ajustement est prépondérant et donc son coefficient peut être considéré comme le coefficient de proportionnalité recherché ($\beta_1 = 0,50 \text{ m/s}$ dans l'exemple proposé).

Quelque soit la méthode employée pour effectuer la régression parabolique, l'excitation du jet en boucle fermée possède la première caractéristique des bifurcations de Hopf.

Pour vérifier le deuxième critère, il faut au préalable déterminer une matrice A telle que

$$(\dot{\mathbf{u}}) = (A) (\mathbf{u})$$

En écrivant $u = \exp(a_r t) \exp(i\phi)$ (valable au voisinage de la fermeture de l'interrupteur) et comme $d\phi/dt = a_i$, on a:

$$\begin{bmatrix} \dot{u}_r \\ \dot{u}_i \end{bmatrix} = \begin{bmatrix} a_r & -a_i \\ a_i & a_r \end{bmatrix} \begin{bmatrix} u_r \\ u_i \end{bmatrix}$$

La matrice carrée ci-dessus se confond avec la matrice A recherchée pour les instants initiaux.

Les valeurs propres de A(Re) sont alors:

$$\begin{aligned} \lambda_1 &= a_r - ia_i \\ \lambda_2 &= a_r + ia_i \end{aligned}$$

La figure 13 présente l'évolution des valeurs propres paramétrée par le nombre de Reynolds. L'examen de cette figure prouve que le jet excité en boucle fermée vérifie la deuxième caractéristique des bifurcations de Hopf. Ce qui achève de confirmer expérimentalement l'existence d'une bifurcation de Hopf autour du nombre de Reynolds critique.

IV.4 Motivations de la présente étude

Il a été établi qu'il se produit dans le jet excité en boucle fermée une bifurcation de Hopf autour du nombre de Reynolds critique. Pour une position de l'espace ($X/D = 0,17$), l'équation de Landau semble correctement décrire l'évolution temporelle de la vitesse. La recherche d'équations appropriées d'évolution d'amplitude est motivée par leur simplicité par rapport aux équations de Navier-Stokes.

Il est toutefois peu probable qu'une dynamique aussi simpliste qu'est l'équation de Landau (temporelle) puisse gouverner le développement des oscillations de vitesse dans la couche limite du jet. Le but de cette étude est de recommencer la détermination expérimentale des coefficients de l'équation de Landau pour plusieurs positions de l'espace. Les coefficients a_r , a_i et c_i étant indépendants de l'espace, une attention particulière sera accordée au coefficient de Landau c_r . La principale motivation de cette étude est par conséquent de mesurer l'évolution de c_r en fonction de x .

V PROCÉDES EXPERIMENTAUX ET TRAITEMENT DES DONNÉES

V.1 Procédés expérimentaux

Les données sont filtrées analogiquement à 10000 Hz et échantillonnées à 20000Hz dans l'éventualité d'une analyse spectrale par transformée de Fourier. Une difficulté majeure de l'expérience présentée ici a été la répétabilité au jour le jour de conditions expérimentales identiques. En effet, malgré une sonde de feedback fixe, des différences en fréquence et en amplitude de l'excitation ont pu être observées dans des conditions apparemment identiques de gain et de nombre de Reynolds. Pour pallier cette difficulté une table de référence a été établie avant toute mesure associant, à chaque nombre de Reynolds, la fréquence et l'amplitude caractéristiques de l'oscillation. Tous les réglages précédant les mesures ont été établis à l'aide de cette table, la fréquence de référence permettant de sélectionner le nombre de Reynolds et l'amplitude de référence de retrouver le gain. L'acquisition de données s'est divisée en deux parties:

a) L'acquisition de régimes transitoires

Le but des mesures est d'étudier les caractéristiques spatiales de l'instabilité temporelle qui se développe dans le jet à la fermeture de la boucle fermée. Comme décrit auparavant, deux sondes sont utilisées, une sonde de feedback fixe et une sonde de mesure mobile. La sonde de feedback est placée à $X=6,21\text{mm}$ et $U/U_j=0,85$. Pour chaque nombre de Reynolds compris entre 66000 et 77000, la sonde de mesure s'est déplacée de $x=5\text{mm}$ à $x=17\text{mm}$. A chaque position 400 régimes transitoires du type de ceux représentés figure 8 ont été acquis. Chaque mesure est constituée de 2500 points acquis à 20000 Hz. L'interrupteur est synchronisé avec l'acquisition, il se ferme environ au 400ème échantillon et se rouvre après la mesure du dernier point. Etant donné l'importance de la place mémoire requise pour stocker les données acquises, après chaque position un transfert de données de l'ordinateur d'acquisition à l'ordinateur de traitement s'est avéré nécessaire. Puis, après chaque nombre de Reynolds, les mesures ont été sauvegardées sur bandes magnétiques et effacées de l'ordinateur de traitement pour ne pas saturer l'ordinateur. Toute l'acquisition de données s'est produite à la chaîne afin de rationaliser l'occupation du laboratoire. Le traitement n'a débuté qu'après la fin de la phase d'acquisition.

b) L'acquisition de régimes permanents

Les mesures ont été prises à l'aide d'un analyseur de spectre pour un nombre de Reynolds compris entre 61000 et 77000 et pour des positions de la sonde de mesure x comprises entre 5mm et 24mm. le jet est excité de manière permanente par la boucle de retour (il "sonne" indéfiniment). Les mesures relevées à la main sur l'analyseur de spectre sont:

- A_{∞} , l'amplitude de saturation
- φ , la phase entre les deux sondes (celle de feedback et celle de mesure)
- c_0 , la cohérence entre les deux signaux
- F , la fréquence de l'amplitude de saturation.

Le principal problème posé par ces mesures a été leur extrême gourmandise en temps d'utilisation des haut-parleurs dont l'électronique donnait parfois des signes d'essoufflement. Quand la température du laboratoire s'élevait (jusqu'à 28°C), les haut-parleurs semblaient parfois faiblir, impression auditive que confirmait la réduction du pic observé à l'analyseur de spectre. Il a donc été nécessaire d'optimiser l'utilisation des haut-parleurs et parfois de laisser les circuits électroniques se refroidir.

V.2 Traitement des données

a) Démodulation d'amplitude

Le principal outil employé pour le traitement des données est la transformation de Hilbert. Au cours d'une première étape, les données brutes sont filtrées autour de la fréquence propre des oscillations. Elles passent dans un filtre passe bas puis un filtre passe bande afin de se débarrasser des fluctuations indésirables. Tous les filtres de fréquence employés sont des filtres FIR à 65 points. Trois filtres passe bande différents sont utilisés à cause de l'éventail des fréquences concernées (de 2500 Hz à 3000 Hz pour $65000 < Re < 77000$). les trois filtres passe bande sont montrés figure 14 et le filtre passe bas figure 15. Les séries temporelles filtrées en fréquence sont ensuite convoluées avec le filtre de Hilbert digital à 63 points (cf figure 15). L'amplitude et la phase résulte du calcul analytique décrit ci-dessous.

Si $r(t)$ est la série temporelle filtrée et $\hat{r}(t)$ est la transformée de Hilbert de $r(t)$, posons:

$$z(t) = r(t) - i \hat{r}(t)$$

Si $z(t)$ est mis sous forme polaire:

$$z(t) = A(t) e^{i\phi(t)}$$

alors $A(t)$ est l'enveloppe instantannée de $r(t)$ et $\phi(t)$ est la phase instantannée. Les différentes étapes de cette procédure se trouvent résumées dans les deux premiers schémas de la figure 16. Signalons dès maintenant que les deux schémas du milieu de la figure 16 ne sont pas "authentiques" puisqu'ils proviennent de mesures antérieures faites par Reisenhel. ce fait est sans importance puisque leur but est d'illustrer la manière dont le traitement des données s'est déroulé.

Enfin les 400 fonctions $A(t)$ sont moyennées en phase donnant une courbe d'amplitude démodulée moyenne du type de celle représentée au bas de la figure 16.

b) Détermination du taux de croissance

Si $A(t) = \exp(\sigma t)$ alors $\sigma = d(\log(A))/dt$. Le troisième schéma de la figure 16 montre le logarithme de A en fonction du temps. Comme les données sont plutôt bruitées pendant tout le régime transitoire, la pente est déterminée par une méthode des moindres carrés. Etant donné l'importance des données à traiter (12 x 13 x 400 régimes transitoires ont été enregistrés), une méthode de traitement semi-automatique a dû être utilisée.

Pour chaque nombre de Reynolds et chaque position, un programme fait défiler devant un opérateur les 5 premiers régimes transitoires. A chaque échantillon, l'opérateur choisit les limites de l'ajustement, le calcul de la pente s'effectuant entre ces limites. Puis l'ordinateur moyenne les 5 couples de limites proposés et, avec l'accord de l'opérateur, traite les autres échantillons (395) avec les limites moyennes décrites ci-dessus. En cas d'incertitude, l'opérateur peut prolonger l'investigation aussi longtemps qu'il le souhaite.

Les critères en vigueur pour déterminer la longueur de l'ajustement sont les suivants. Le premier critère consiste à maximiser la longueur de la régression afin de diminuer l'erreur. La limite supérieure de l'ajustement est choisi afin de d'arrêter l'ajustement avant la zone de saturation afin d'avoir un taux de croissance strictement exponentiel. Toutefois l'obligation de calculer la régression entre des limites fixes n'a pas permis l'assurance du respect de ces critères pour chaque mesure. En effet, les réalisations d'une même série peuvent présenter d'importantes différences. Le début de la croissance exponentielle ou sa durée peuvent grandement varier d'une mesure à l'autre. Pour $5\text{mm} < x < 11\text{mm}$, le traitement automatique des données s'exécutait correctement. Pour $12\text{mm} < x < 17\text{mm}$, la qualité des données se dégradant, le traitement automatique est apparu comme peu fiable.

Le taux de croissance est obtenu en moyennant les 400 taux de croissance des différentes réalisations. Comme parallèlement, l'amplitude calculée est moyennée, une deuxième méthode d'obtention du taux de croissance exponentielle a été possible. Elle a consisté à faire une régression sur la moyenne en phase des amplitudes.

Les deux méthodes de calcul du taux de croissance ont fourni des résultats similaires bien que différents en valeur, la deuxième méthode donnant des résultats sensiblement supérieurs à ceux de la première. Finalement en dépit de leur incertitude élevée, seuls les résultats de la première méthode ont été utilisés car ils sont apparus comme plus "lisses".

c) Paramètres

A l'issue du traitement des données, pour $66000 < Re < 77000$ et $5\text{mm} < x < 17\text{mm}$, les paramètres suivants ont été calculés:

- σ (ou a_r): taux de croissance exponentiel
- F_i : fréquence initial
- c_i : partie imaginaire du coefficient de Landau
- $A_{\max 1}$: amplitude démodulée asymptotique
- courbes d'amplitude moyennée en phase

Une analyse de Fourier sur les données acquises à d'autre part permis de calculer la fréquence maximum F_{\max} et l'amplitude associée à cette fréquence $A_{\max 2}$. Tous ces résultats ainsi que les résultats de l'acquisition des régimes permanents ont été regroupés dans deux bases de données.

VI RESULTATS ET COMMENTAIRES

VI.1 Linéarité entre la fréquence propre et le nombre de Reynolds

Dans le paragraphe II.3.c est expliqué la structure en bandes de la variation de la fréquence en fonction du nombre de Reynolds. De bonnes conditions expérimentales ont été choisies, entre autres l'appartenance à une large bande. Par conséquent, il doit être possible de vérifier la linéarité entre la fréquence propre et le nombre de Reynolds.

F désigne la fréquence mesurée à l'analyseur de spectre. F_{\max} désigne la fréquence calculée par analyse de Fourier sur les données acquises. La figure 17 présente les variations de F en fonction du nombre de Reynolds et celle de F_{\max} en fonction de F . Comme il apparaît clairement dans le premier graphique, la relation entre Re et F est parfaitement linéaire. Ce résultat est naturel puisque la fréquence mesurée à l'analyseur de spectre tient lieu de référence pour le nombre de Reynolds. La fréquence des données acquises (F_{\max}) présente une certaine dispersion en fonction de F donc du nombre de Reynolds. Pour chaque F (ie nombre de Reynolds) la fréquence de chacune des 13 positions est représentée. La dispersion de F_{\max} est donc normale puisque, l'acquisition d'une série de mesure durant environ deux heures, il se produit inévitablement de légères variations en nombre de Reynolds pendant cette durée. Le contenu fréquentiel des données acquises est donc conforme aux prévisions.

VI.2 Evolution d'un mode dans le temps et l'espace

a) Evolution temporelle de l'amplitude de la fréquence propre.

Comme expliqué dans le paragraphe V.II.a, la moyenne en phase des courbes d'amplitude obtenues après transformée de Hilbert permet d'apprécier l'évolution temporelle de l'amplitude de la fréquence propre. La figure 18 présente deux échantillons de ces courbes pour $Re=73000$, $x=9\text{mm}$ et $x=15\text{mm}$. L'élément le plus frappant de ces deux courbes est l'existence d'un pic en amplitude de taille importante au moment de la fermeture de l'interrupteur. L'examen minutieux des données brutes (cf figure 8) révèle également l'existence d'une impulsion de vitesse à la fermeture de l'interrupteur. Aucune trace d'impulsion de vitesse ne peut être décelée dans les travaux antérieurs de Reisenhel. L'utilisation d'une couronne de haut-parleurs et d'un nouveau circuit électronique en amont de ces haut-parleurs sont les seules différences entre l'installation expérimentale utilisée ici et celle de Reisenhel. Pour une raison à présent inconnue, la fermeture de l'interrupteur sur la boucle fermée semble générer artificiellement une

impulsion électrique dans le circuit électronique des haut-parleurs qui produit ensuite une impulsion de vitesse dans la couche limite du jet. Du fait de l'inévitable feedback, cette impulsion est susceptible de provoquer un écho. Il est possible de d'observer cet écho dans le premier schéma de la figure 18 sous forme d'un deuxième pic en amplitude. Ces fluctuations de vitesse parasites compromettent le caractère exponentiel de la croissance des oscillations à la fermeture de l'interrupteur, rendant plus délicat encore la détermination du taux de croissance exponentielle. Pour $x=15\text{mm}$ (deuxième schéma) le pic en amplitude est moins net à cause du fort niveau d'oscillations naturelles (mode axisymétrique) avant fermeture de l'interrupteur, mais il rend également difficile l'observation de la croissance des oscillations.

b) Diagramme spatio-temporel

A chaque nombre de Reynolds l'évolution temporelle de l'amplitude associée à la fréquence propre est connue pour tout x compris entre 5mm et 17mm. La volonté de comparer ces fonctions pour différents points de l'espace a conduit à une représentation en trois dimensions comme celle de la figure 19. Ce diagramme et les suivants ont été obtenus à l'aide d'un logiciel graphique (SURFER) sur PC. Comme la légende des axes l'indique, il s'agit d'une simple représentation en trois dimensions sans les parties cachées de l'amplitude de la fréquence propre en fonction du temps t et de la position x . Les données sont brutes et n'ont subi aucune manipulation ou lissage (sauf une décimation des points). La résolution en temps étant bien meilleure que celle suivant x , il n'est pas étonnant d'avoir une grille plus dense dans une direction que dans l'autre.

La figure 19 livre d'intéressants résultats qualitatifs:

- L'existence de l'impulsion de vitesse se retrouve naturellement à toutes les positions sous forme d'un pic en amplitude. Le pic semble toutefois se déplacer vers l'arrière à mesure que x augmente. Ce recul est confirmé par les diagrammes contours présentés de la figure 22 à la figure 24. L'allongement de la durée de convection pour une augmentation de x en est l'explication.

- Pour des valeurs "importantes" de la vitesse (à partir de $x = 15\text{mm}$), la couche limite du jet est naturellement excitée. Bien que le filtrage soit effectué autour de la fréquence propre, il est suffisamment grossier pour refléter l'évolution de l'amplitude du mode naturel du jet (le mode axisymétrique). La croissance de ce mode en fonction de x apparaît nettement.

- L'évolution spatiale de la fréquence propre est analogue à celle du mode axisymétrique. Comme le montre la figure 21, le mode axisymétrique ($f_{i,0}$) croît d'abord linéairement en fonction de x puis décroît brutalement au profit de son sous-harmonique avant de connaître une seconde croissance pour des x plus élevés. L'existence d'une "vallée" autour de $x = 13\text{ mm}$ est caractéristique de la décroissance brutale de l'amplitude de la fréquence propre. La figure 20 qui n'est qu'une simple rotation d'axes permet de mieux apprécier la profondeur de la vallée.

- L'évolution du mode propre se produit plus "tôt" (d'un point de vue spatial) que celle du mode axisymétrique. En se reportant au diagramme contour présenté à la figure 22, il est facile d'évaluer la position x à laquelle le maximum du mode propre et celui du mode axisymétrique se trouve. Le premier est à $x/D=0,15$ et le second à $x/D=0,3$ confirmant l'affirmation ci-dessus. La similitude de comportement entre le mode propre et le mode axisymétrique vient renforcer l'idée que l'excitation du jet en boucle fermée accentue l'organisation sous-jacente de la couche limite.

- En filtrant autour du sous-harmonique du mode propre et en retraçant les données par transformée de Hilbert, il est possible d'obtenir les variations spatio-temporelles de l'amplitude du sous-harmonique. Les figures 25 et 26 présentent deux vues en trois dimensions de ces variations. Comme le laissait prévoir le comportement du sous-harmonique du mode naturel (axisymétrique), la croissance du sous-harmonique du mode propre se produit aux alentours de la décroissance brutale de ce mode propre à $x/D = 0,26$ comme il est possible de le déterminer sur le diagramme contour de la figure 27. La similitude de comportement entre le mode propre et le mode naturel se trouve encore renforcée.

- L'examen des différents diagrammes contours ($Re=76000$, $Re=71000$ et $Re=68000$) met en évidence des différences dans l'allure des variations spatio-temporelles de l'amplitude. La torsion des lignes de niveau que l'on distingue nettement pour $Re=76000$ semble changer de courbure à mesure que le nombre de Reynolds décroît. Aucune explication satisfaisante n'a permis d'expliquer cette tendance.

Le principal intérêt des diagrammes spatio-temporels commentés ci-dessus réside peut-être dans leur nouveauté. C'est la première fois que les évolutions dans le temps et dans une direction d'un mode de la couche-limite du jet sont obtenues.

VI.3 Taux de croissance exponentielle

Tous les résultats obtenus jusqu'à présent tant sur l'amplitude des oscillations que sur leur fréquence sont en accord avec les travaux précédents effectués sur le jet. Les premiers points de désaccord sont apparus avec le taux de croissance exponentielle. Comme expliqué dans le chapitre V.2.b, chaque réalisation est unique et le traitement semi-automatique des données ne permet pas de prendre en compte la spécificité de chaque réalisation. La détermination du taux de croissance exponentielle est par nature même très imprécise surtout pour les valeurs importantes de x ($x > 11mm$) pour lesquelles le signal est très bruité. Toutefois, les désaccords constatés se répétant à toutes les positions ou tous les nombres de Reynolds, ils ne peuvent donc être imputés au mode de calcul du taux de croissance exponentielle.

Au cours des mesures effectuées par Reisenhel le taux de croissance exponentielle était apparu comme constant pour $x < 3\lambda$. La figure 28 présente les variations du taux de croissance σ en fonction de x pour $Re = 71000$. Sur ce schéma σ ne semble constant que pour les deux premières positions de la sonde de mesure soit pour $x < 1,5 \lambda$. Ce résultat est confirmé à tous les autres nombres de Reynolds. Pour l'instant il est préférable de se contenter de cette observation.

Bien plus surprenantes sont les variations de σ en fonction du nombre de Reynolds à x fixé. Le calcul et l'expérience ont prouvé, qu'autour du nombre de Reynolds critique, le taux de croissance varie linéairement en fonction du nombre de Reynolds. La figure 29 présente les résultats obtenus sur ce sujet par Reisenhel montre clairement l'existence d'une zone de croissance linéaire. Il est impossible d'observer une telle zone dans la figure 30 qui représente pour $x = 5\text{mm}$ et pour $x = 9\text{mm}$ les variations de σ en fonction du nombre de Reynolds. Aucune explication satisfaisante n'a permis d'élucider cette anomalie. La seule irrégularité constatée est l'excitation du jet par une impulsion électrique du circuit d'alimentation des haut-parleurs à la fermeture de l'interrupteur. En forçant la croissance des oscillations de manière constante, elle pourrait expliquer l'absence de variations de σ en fonction du nombre de Reynolds. Il serait nécessaire de recommencer les expériences en améliorant l'électronique des haut-parleurs pour étudier plus en détail les variations du taux de croissance exponentielle.

VI.4 Coefficient de Landau

Rappelons que la motivation principale de la présente étude est l'examen des variations du coefficient de Landau c_r en fonction de x .

La détermination du coefficient de Landau s'effectue de la manière suivante. L'équation 12 s'écrit:

$$dA/dt = a_r A - c_r A^3$$

En régime permanent ($dA_\infty/dt = 0$), on obtient donc:

$$c_r = a_r / A_\infty^2$$

a_r est égal au taux de variation exponentielle σ . Par conséquent, en se fiant aux résultats de Reisenhel, la relation suivante est vérifiée autour du nombre de Reynolds critique:

$$a_r = \sigma = \eta \left(\frac{Re - Re_c}{Re_c} \right)$$

La relation entre A et Re est également connue. Dans l'hypothèse d'une bifurcation de Hopf, il vient:

$$A_\infty = \beta \left(\frac{Re - Re_c}{Re_c} \right)^{1/2}$$

Les manières de calculer le coefficient β ont été expliquées dans le chapitre IV.3.b (par régression parabolique à un ou plusieurs termes). Deux séries de coefficients ont donc été obtenues pour tout x .

Il vient enfin:

$$c_r = a_r / A_\infty^2 = \frac{\eta}{\beta^2} \quad (\text{en s/m}^2)$$

Le calcul de η s'avère très délicat puisque, comme expliqué au paragraphe précédent, il n'a pas été possible sur les présentes mesures de constater une variation linéaire entre le taux de croissance et le nombre de Reynolds. La première solution consiste à supposer η constant et à représenter $\ln(1/\beta^2)$ en fonction de x . C'est ce que propose la figure 31. Cela permet d'effectuer une comparaison entre les résultats obtenus par les deux différentes méthodes de régression parabolique et de constater que les résultats sont semblables et que leurs variations sont quasi identiques. Dorénavant, seuls les résultats de la régression à trois termes seront pris en considération.

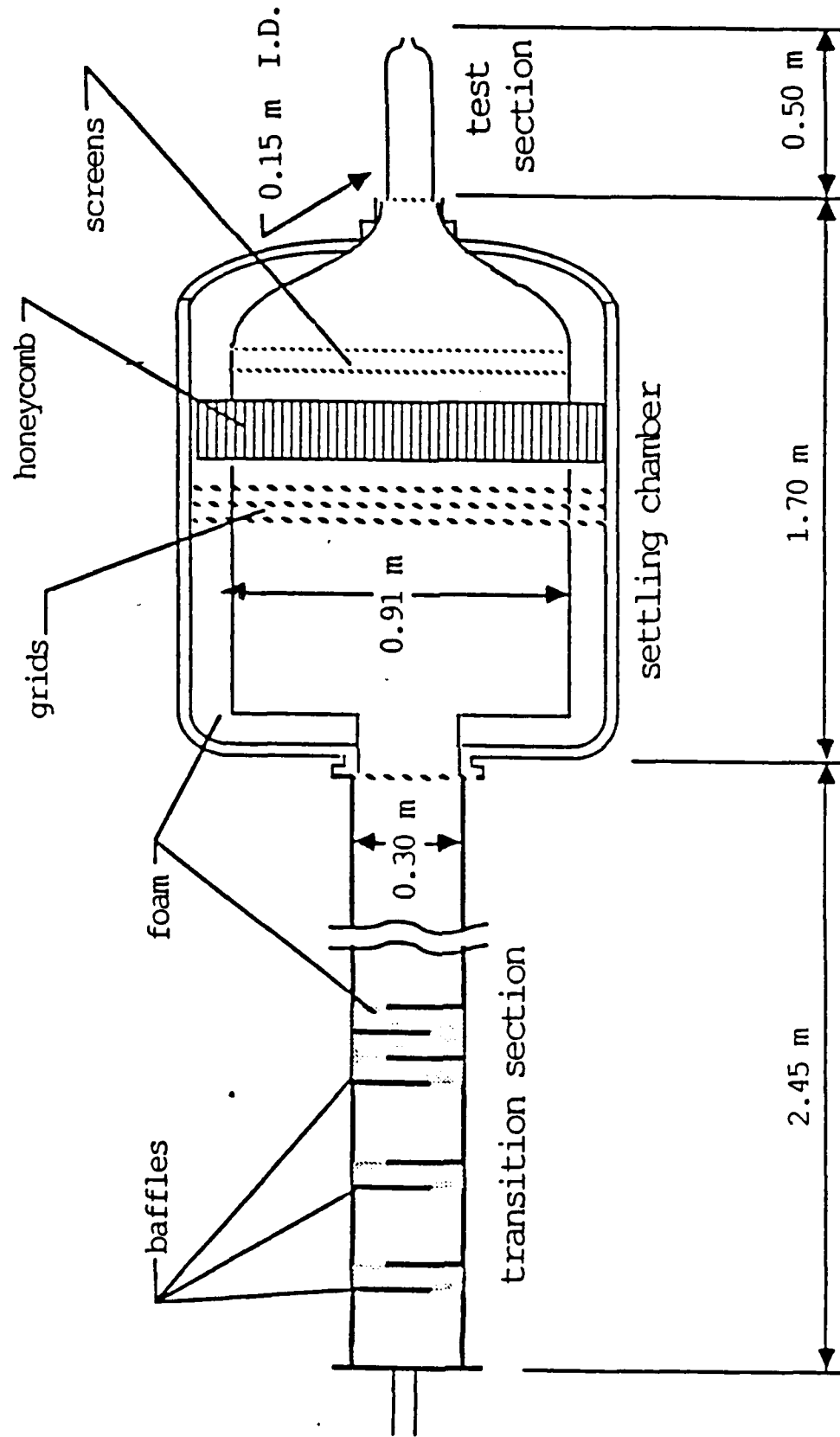
Une méthode d'évaluation de η a été entreprise. Le nombre de Reynolds critique est 65500. En faisant la moyenne des taux de croissance de $Re=66000$, 67000 et 68000 , en déterminant la pente de la droite qui relie le point moyen au point critique, une approximation de η est obtenue (cf figure 32). Il a été ainsi possible de "mesurer" η en fonction de x (η local). Le calcul de c_r peut alors se faire soit avec le η local soit si, en accord avec des résultats obtenus par Reisenethel, on suppose η constant et égal à $\eta(x=5\text{mm})$ (η_{initial}). Les variations de $\ln(c_r)$ en fonction de x sont représentées figure 33. Quelque soit la méthode employée, c_r varie considérablement en fonction de x .

CONCLUSION

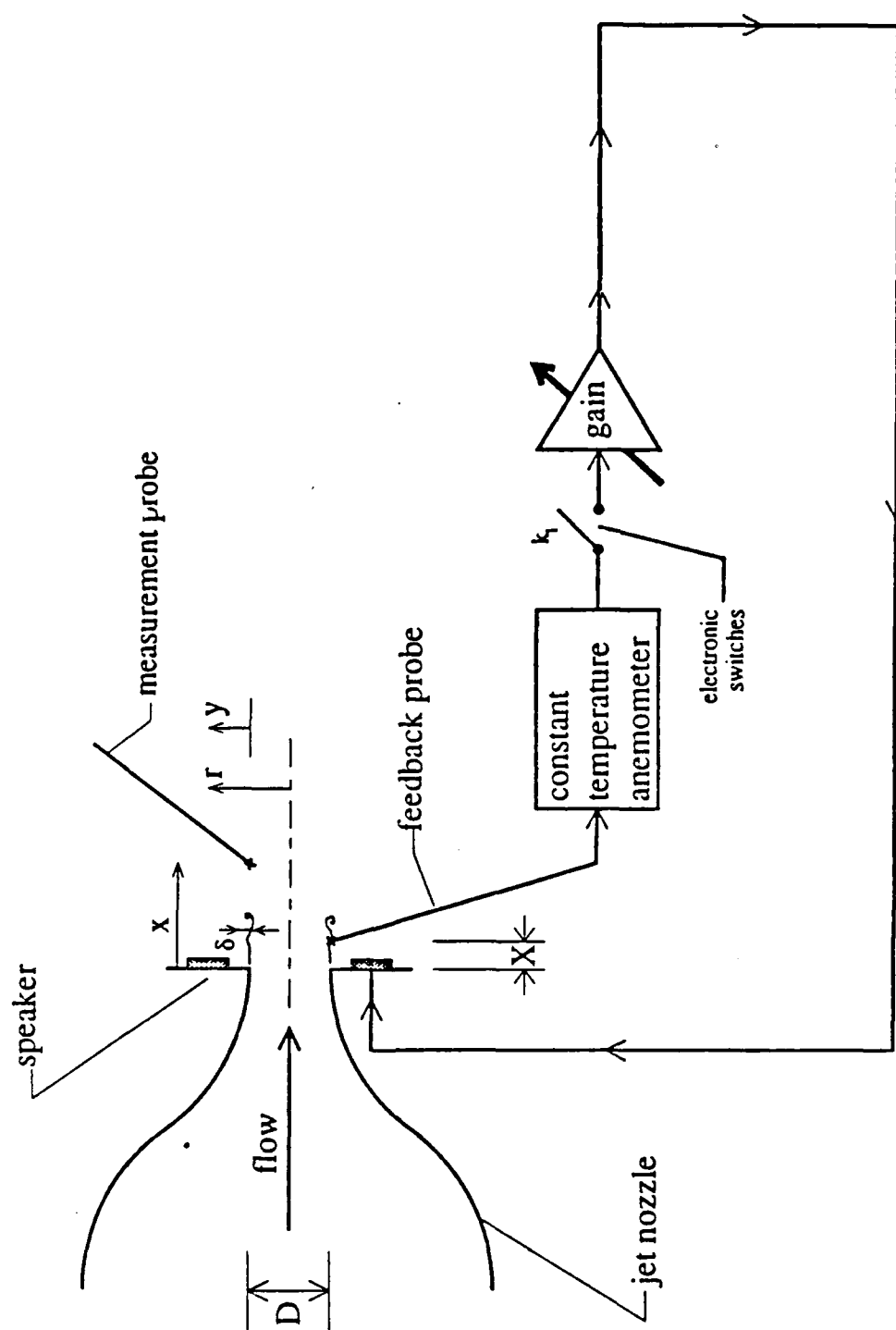
Cette étude a permis de fortifier la conviction que l'excitation du jet en boucle fermée permet de renforcer l'organisation sous-jacente de la couche limite. Grâce à l'utilisation d'un interrupteur synchronisé avec l'acquisition de données et d'une sonde mobile, la mesure de l'évolution spatio-temporelle de l'amplitude du mode propre a pu être réalisée. La modélisation de la dynamique des oscillations de vitesse par l'équation de Landau a été tentée. La forte dépendance du coefficient de Landau en x a montré que l'équation purement temporelle de Landau ne constituait pas une modélisation suffisante.

Des désaccords ont été constatés entre les présentes mesures et des résultats expérimentaux antérieurs qui semblent provenir de conditions expérimentales defectueuses. Pour supprimer le doute, il serait souhaitable d'améliorer l'électronique des haut-parleurs et de ... recommencer. Avec l'expérience acquise et tous les programmes nécessaires déjà écrits, cette opération devrait se réaliser facilement.

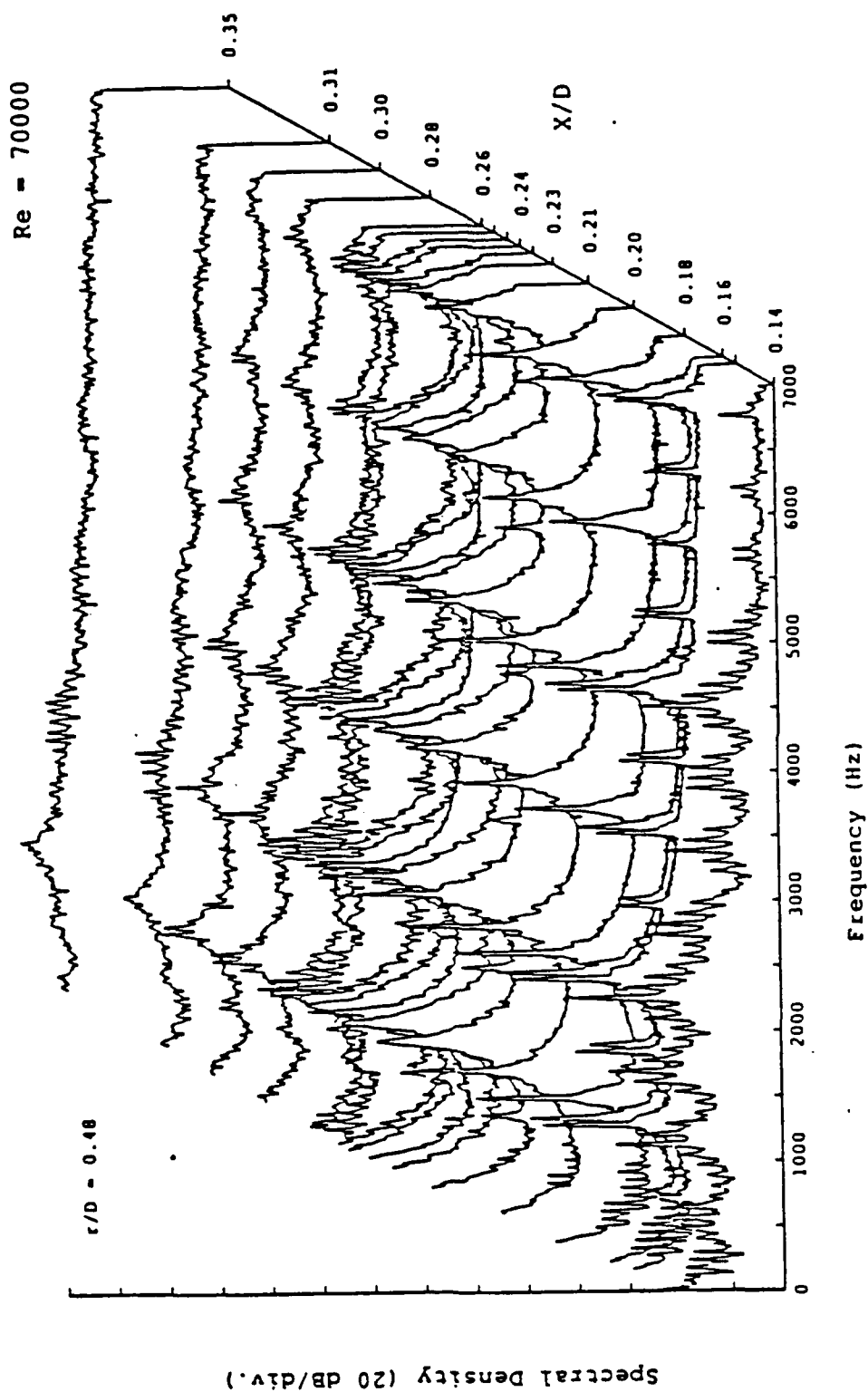
Mes quatre mois à l'Illinois Institute of Technology m'ont beaucoup apporté tant sur le plan linguistique que scientifique. J'ai eu la chance et le bonheur de travailler sous la conduite de Patrick Reisenthel dont les compétences et l'enthousiasme illuminaient chaque journée de travail. Je pense ainsi avoir agréablement et efficacement complété la formation reçue dans l'option Air-Espace et à Centrale.



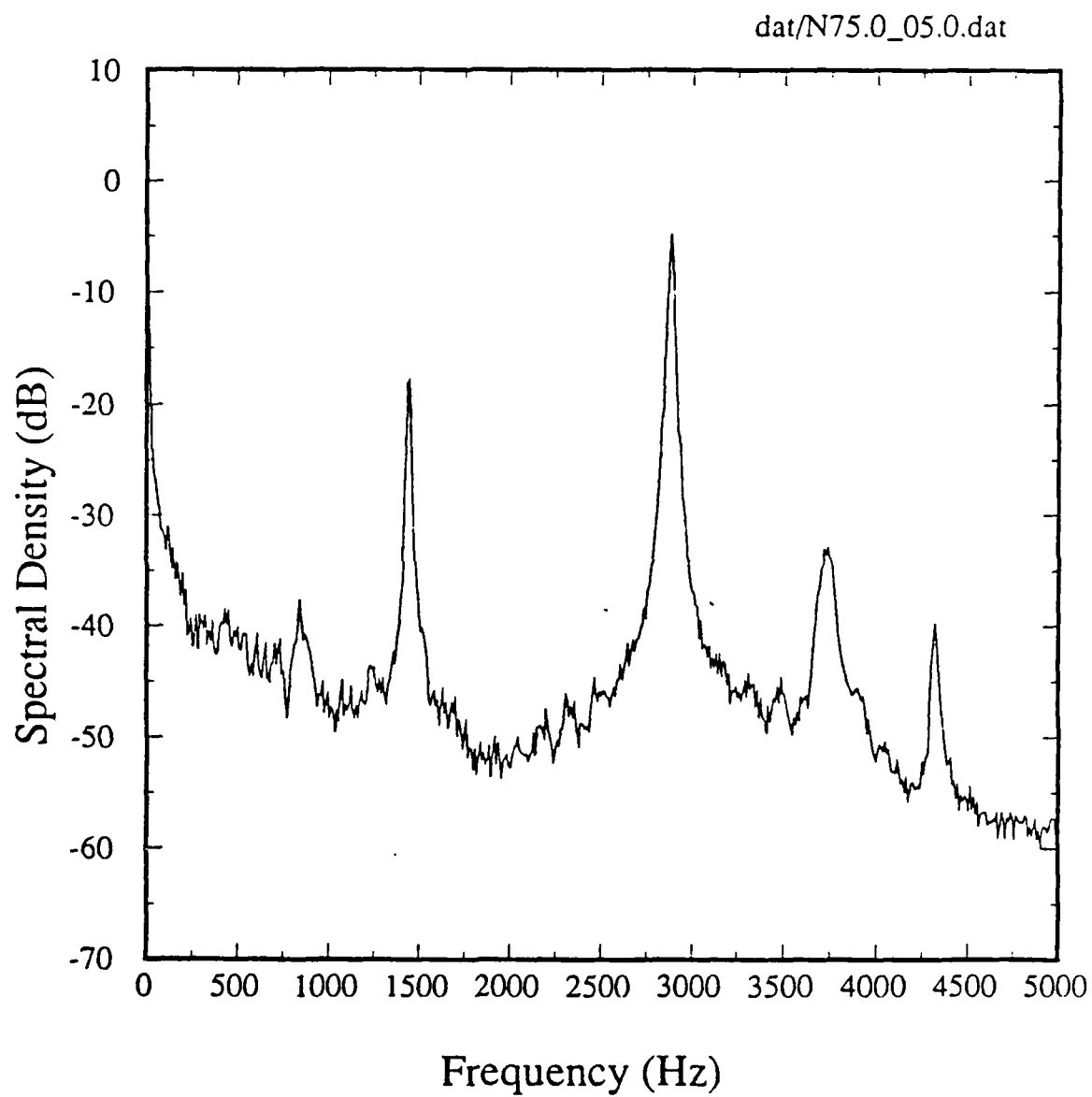
1. Schéma de l'installation



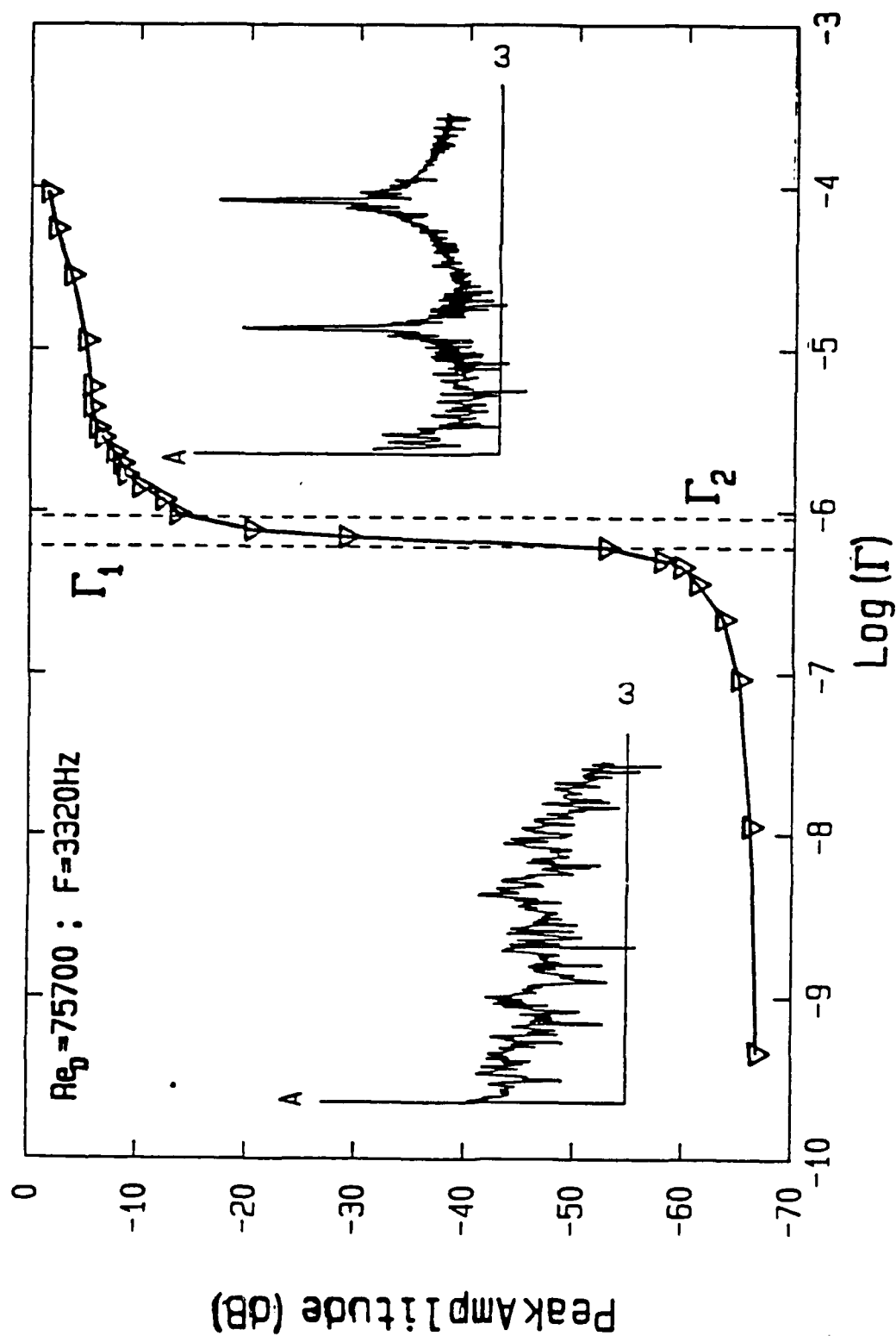
2. Schéma de l'expérience



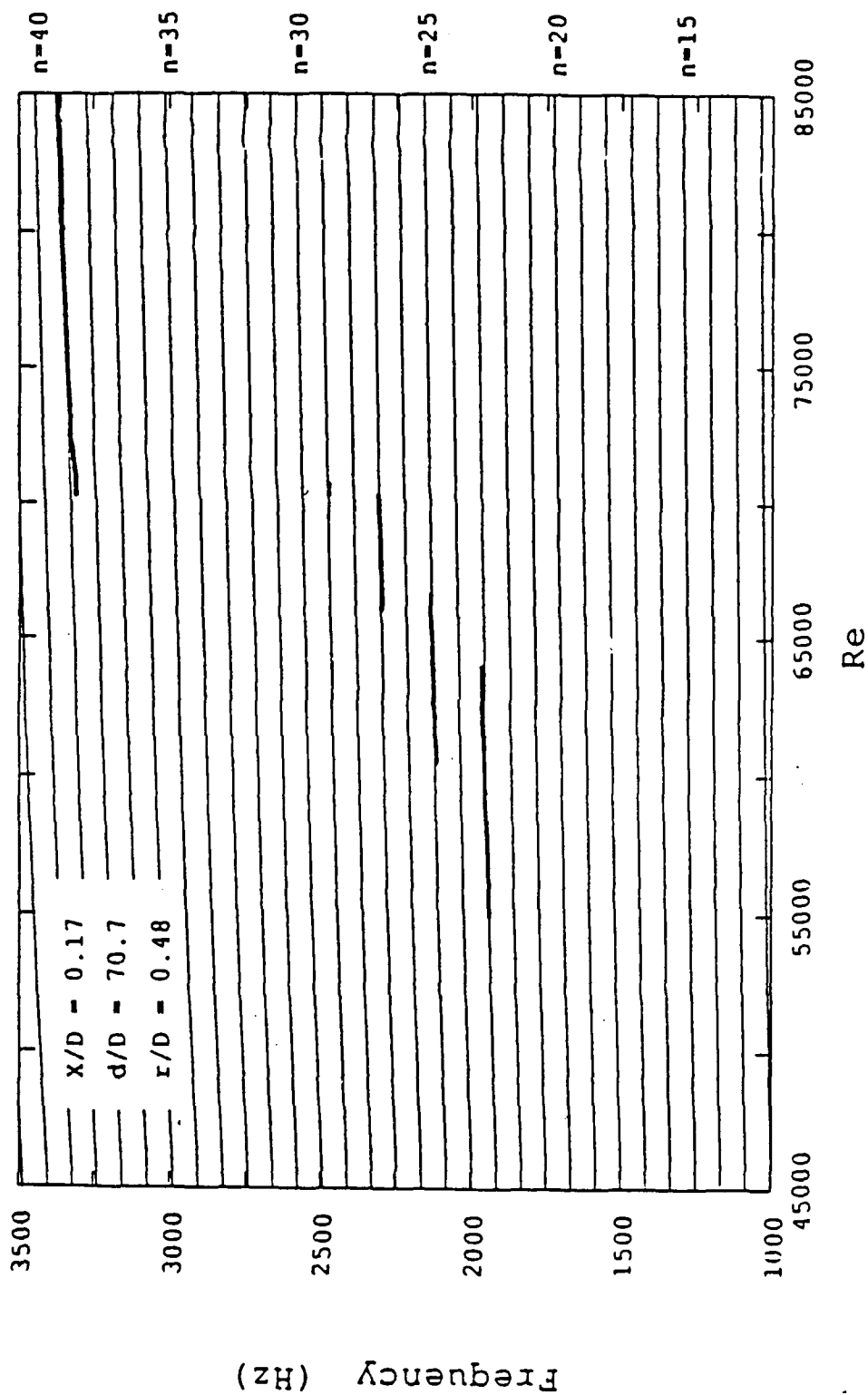
3. Variations de la distribution spectrale du signal de vitesse en fonction de la position de la sonde de feedback pour $Re = 70000$



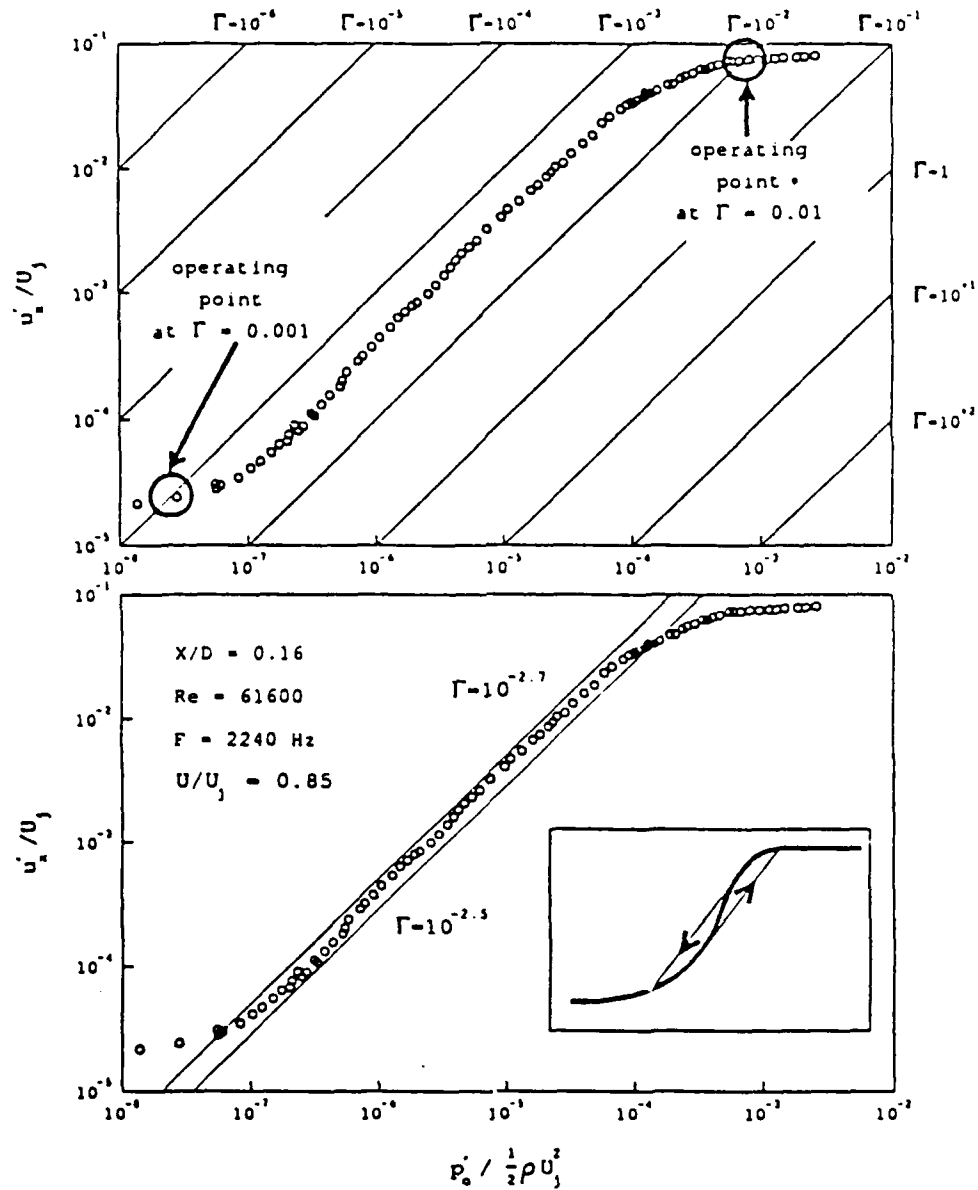
4. Exemple de distribution spectrale pour $Re = 75000$ et $x = 5\text{mm}$



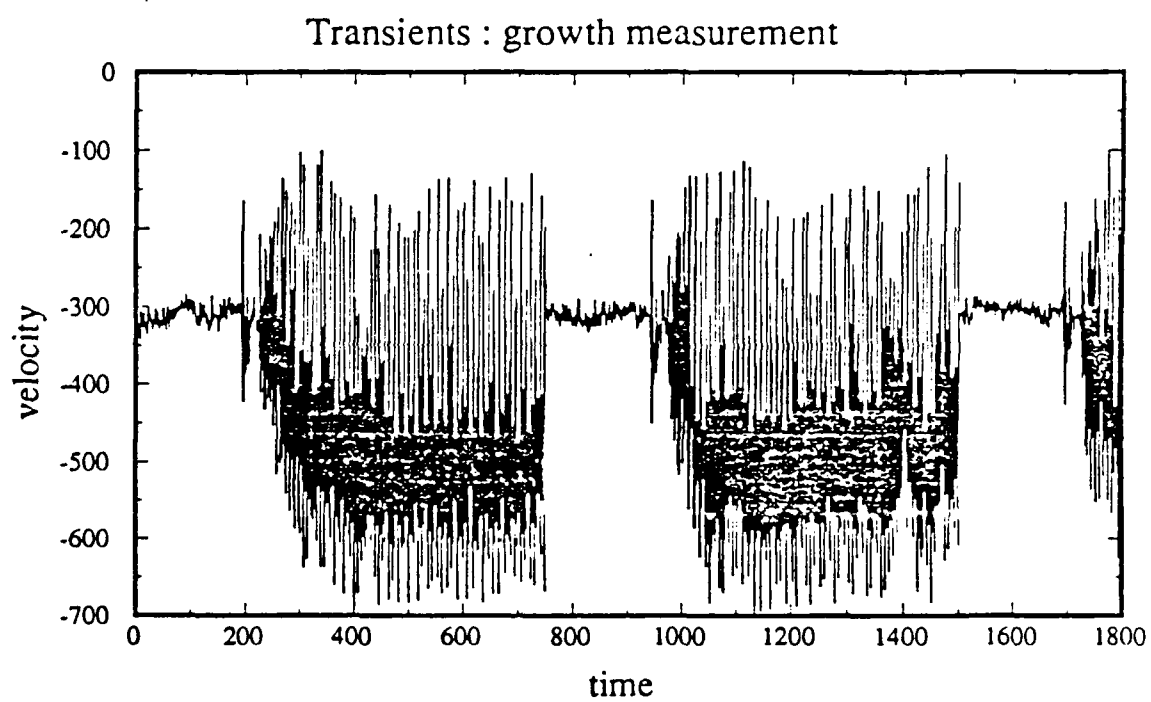
5. Variation de l'amplitude spectrale de la fréquence propre en fonction du gain à $X/D = 0,132$ et $\text{Re} = 75700$



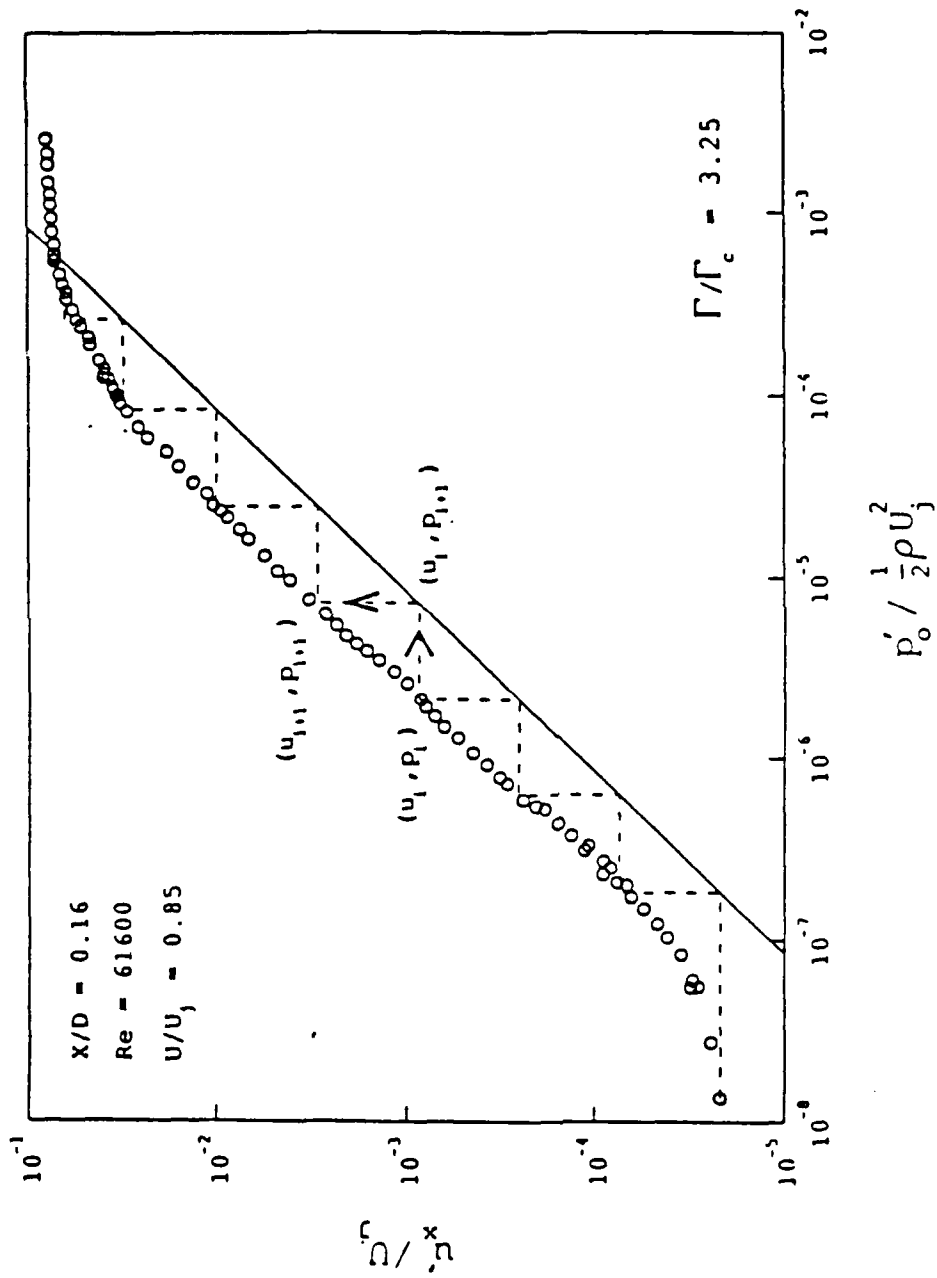
6. Comparaison entre la structure en bandes de la fréquence propre en fonction du nombre de Reynolds et les résultats théoriques pour $G = 0,132 \text{ Ns/m}^3$ et $X/D = 0,17$



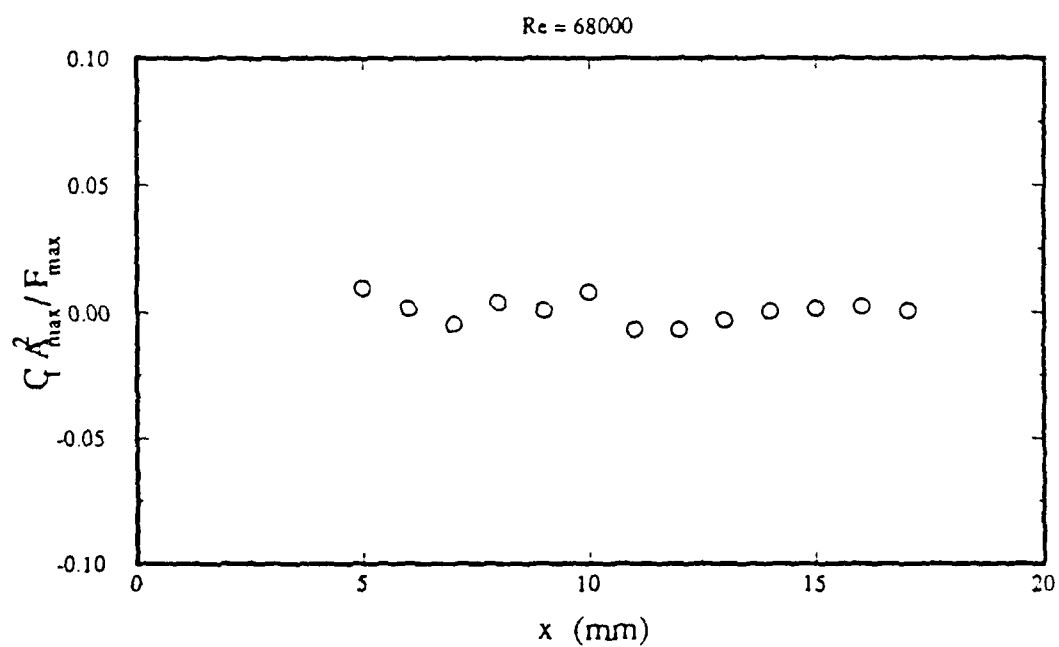
7. Fonction de transfert en boucle ouverte de la fréquence propre avec courbes de gain pour $X/D = 0,16$ et $Re = 61600$: a) points de fonctionnement mini et maxi b) hystérésis autour du gain critique.



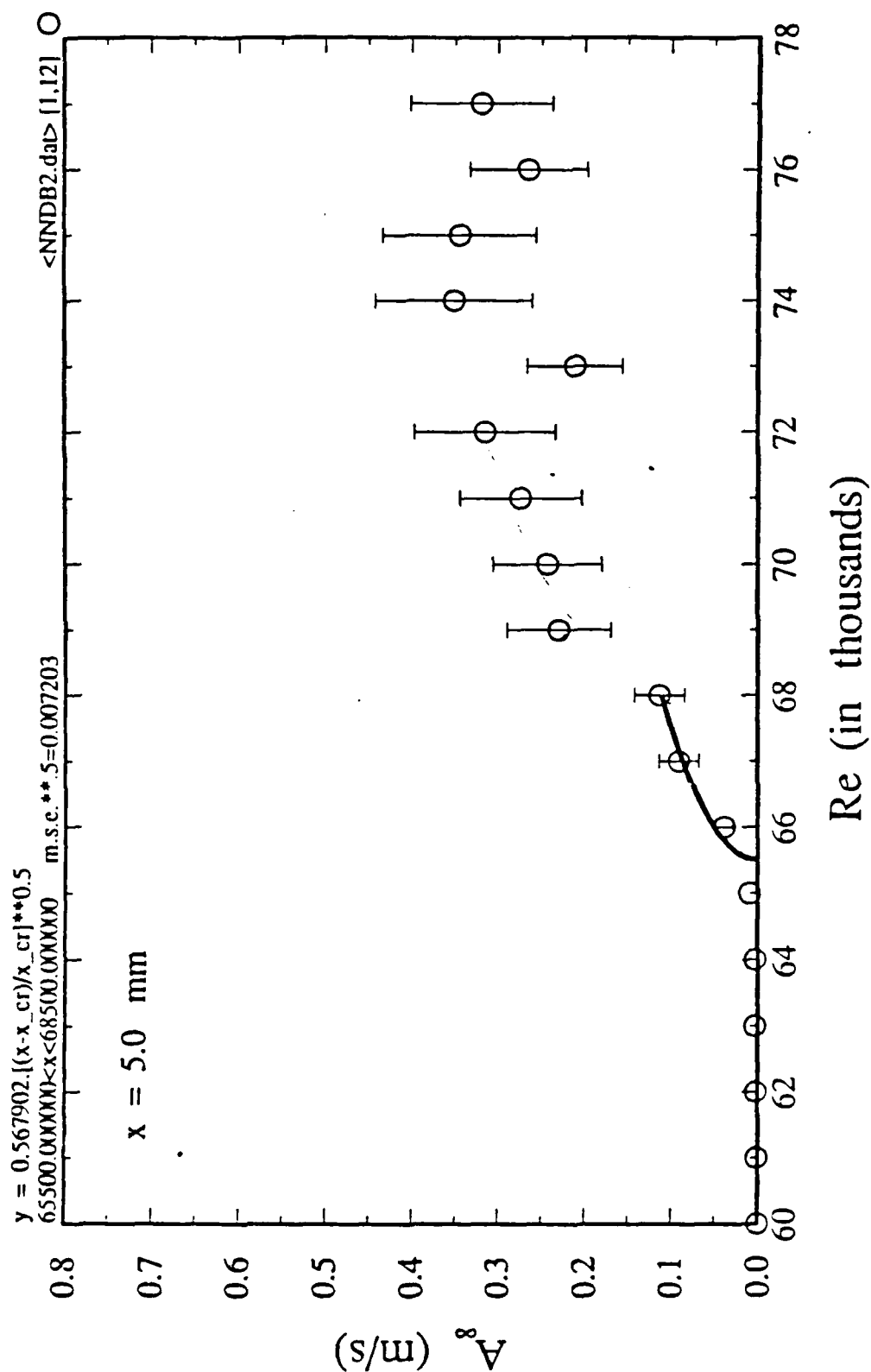
8. Régime transitoire, exemple de données brutes



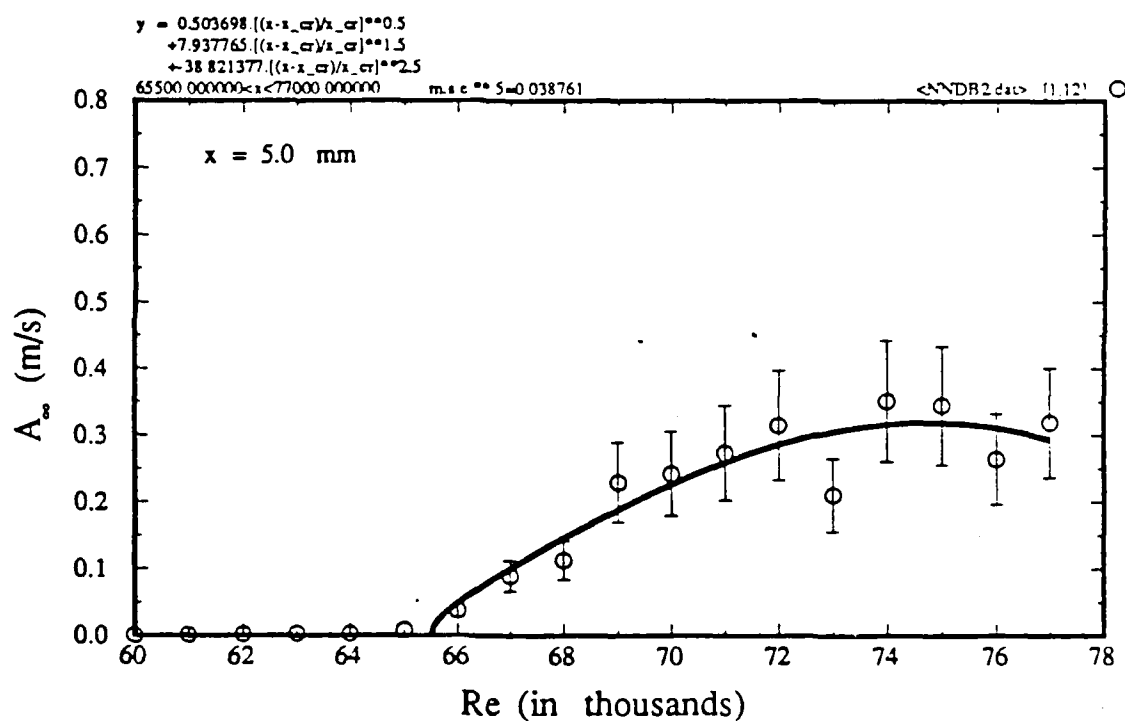
9. Illustration de l'évolution temporelle de l'amplitude de la fréquence propre pour $X/D = 0,16$; $Re = 61600$ et $\Gamma/\Gamma_c = 3,25$



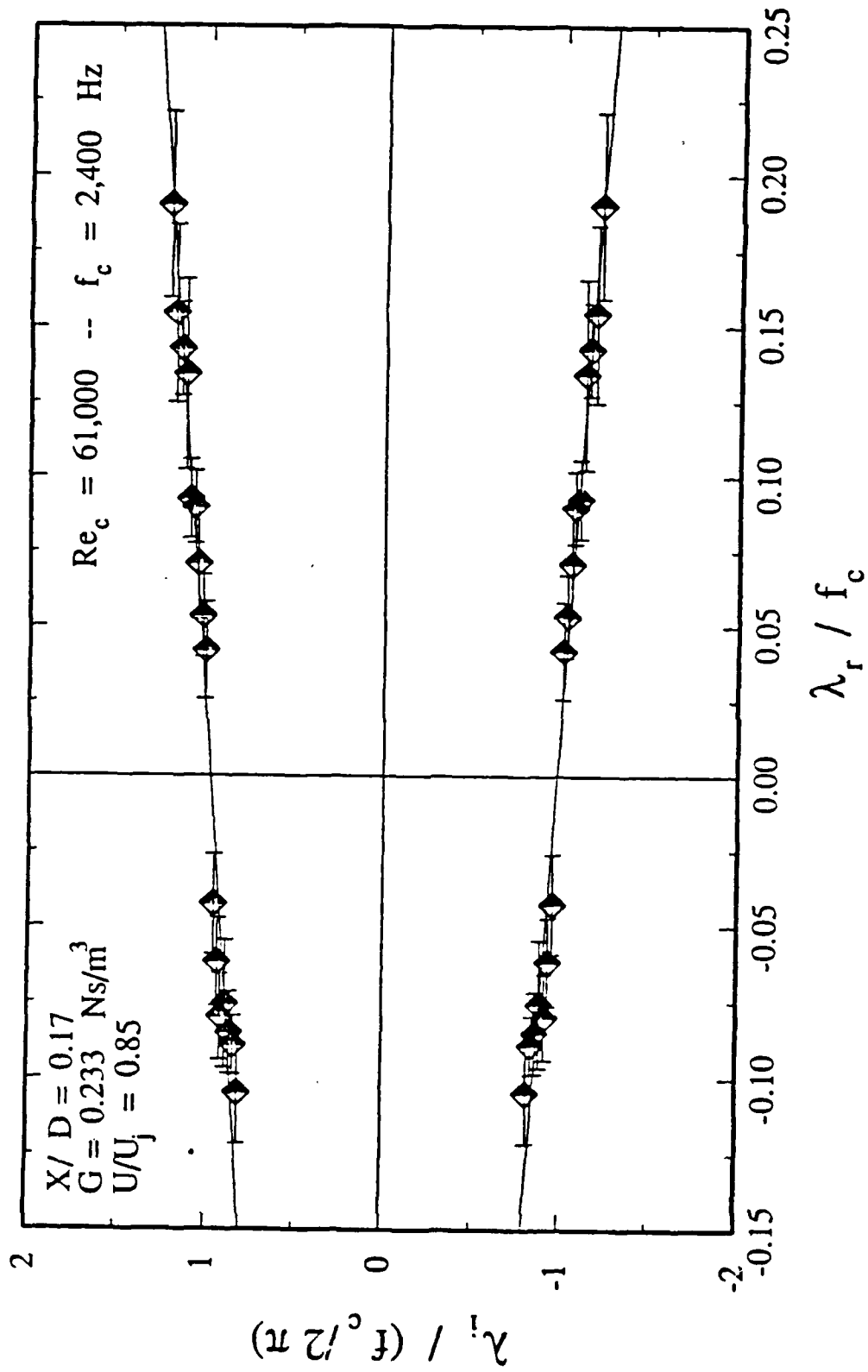
10. Evolution spatiale de la partie imaginaire du coefficient de Landau à $Re = 68000$



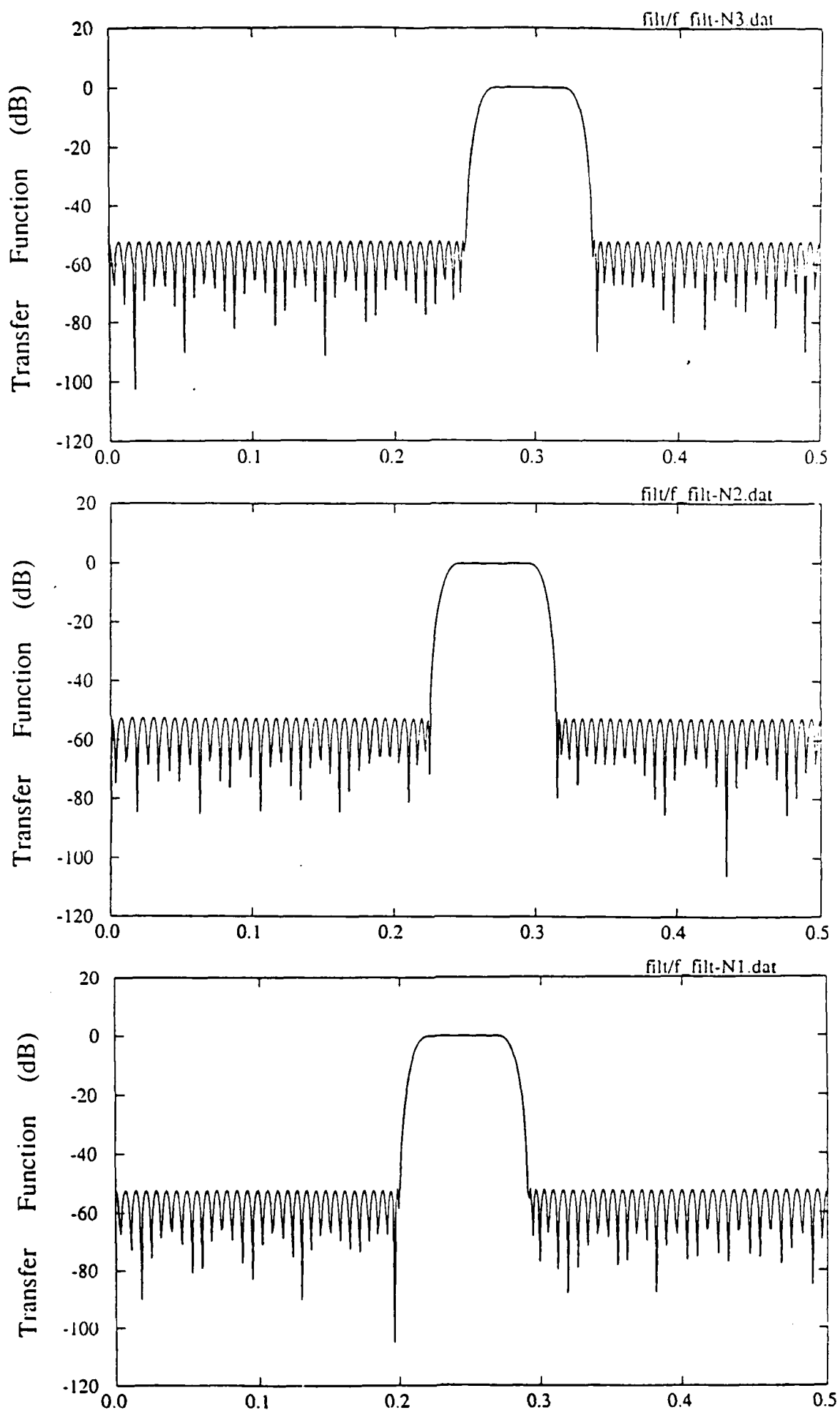
11. Bifurcation de Hopf: évolution de l'amplitude spectrale de la fréquence propre en fonction du nombre de Re avec régression parabolique (à un terme)



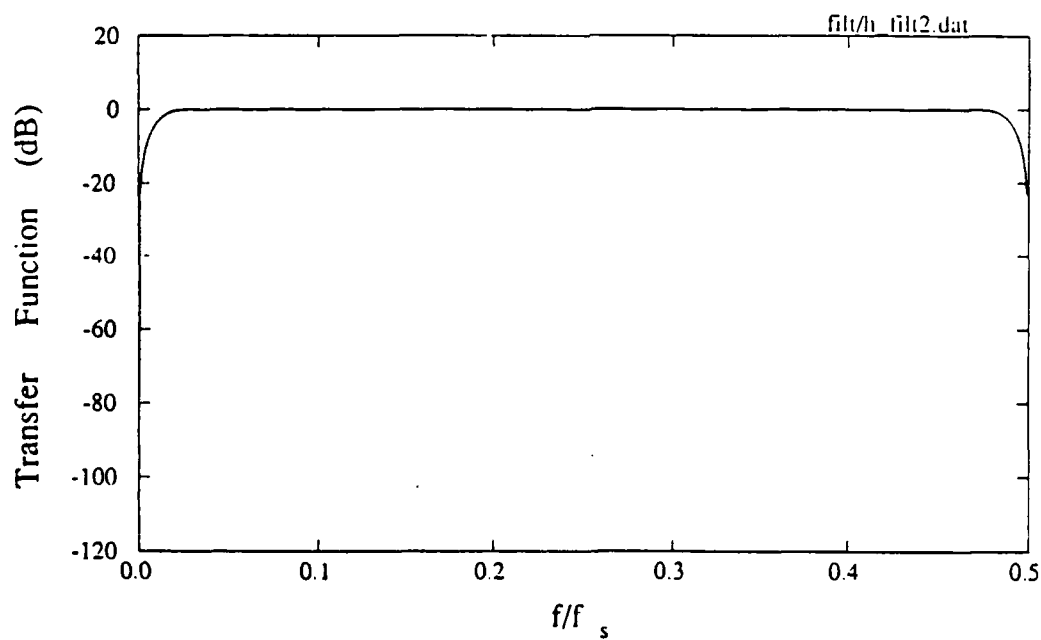
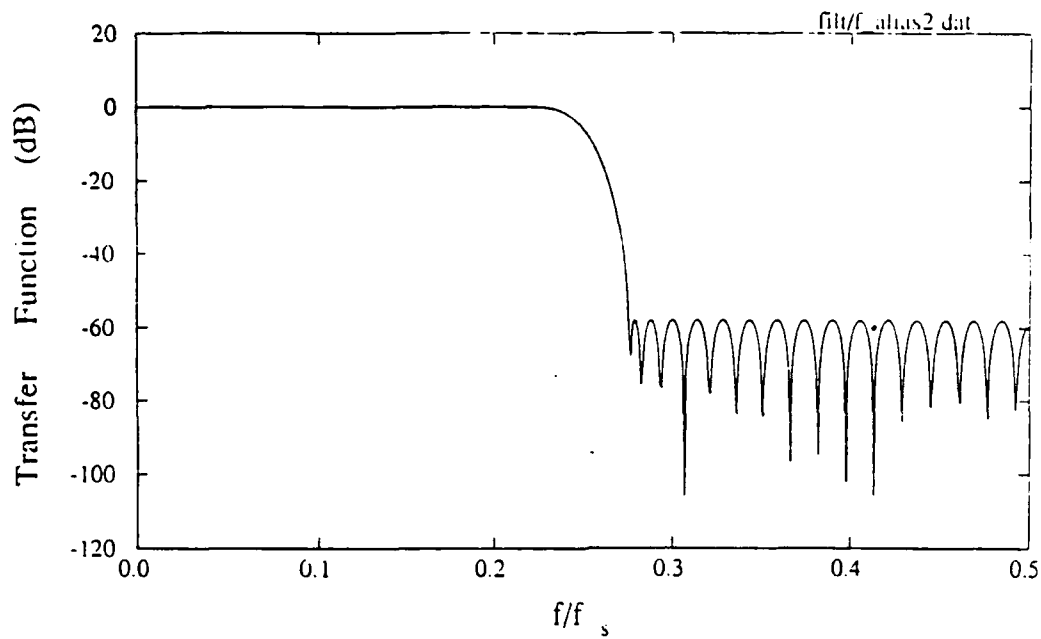
12. Bifurcation de Hopf: évolution de l'amplitude spectrale de la fréquence propre en fonction du nombre de Re avec régression parabolique (à trois termes)



13. Bifurcation de Hopf: évolution des valeurs propres paramétrée par le nombre de Reynolds

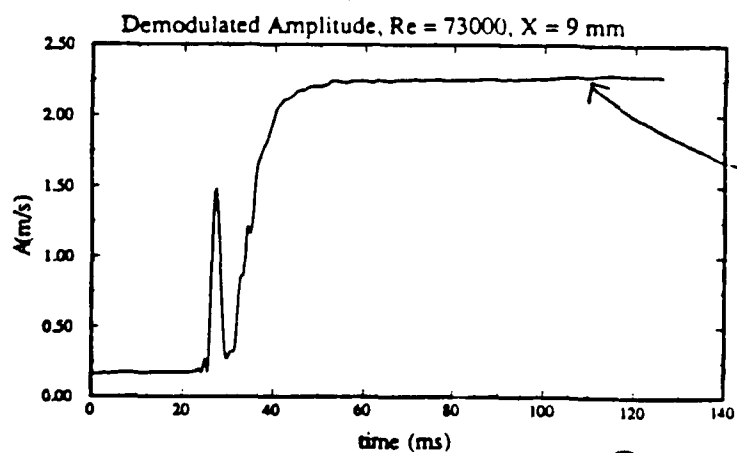
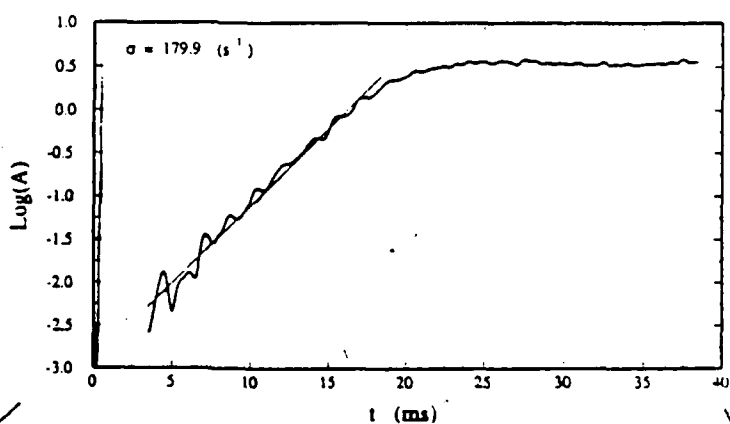
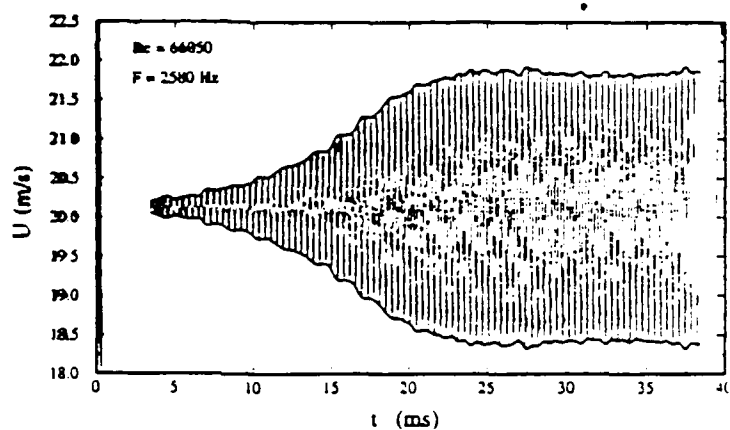
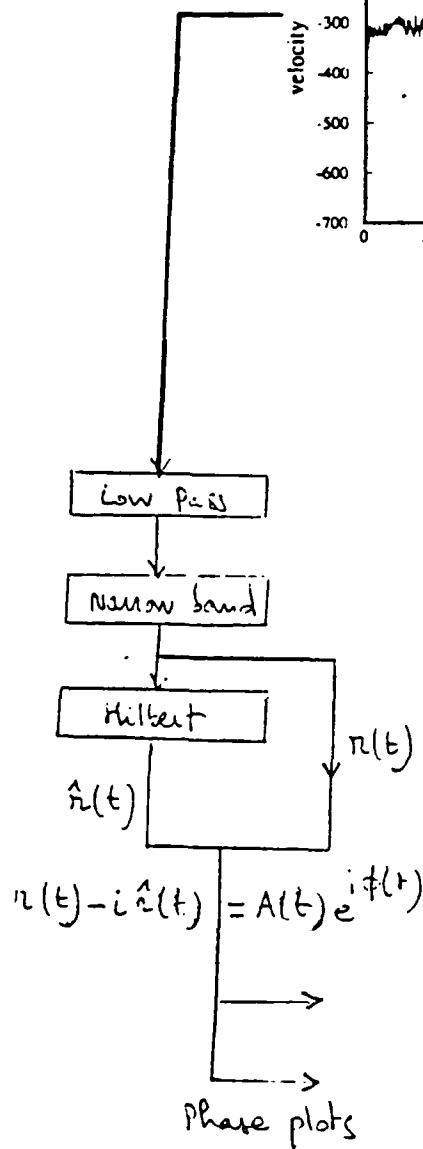
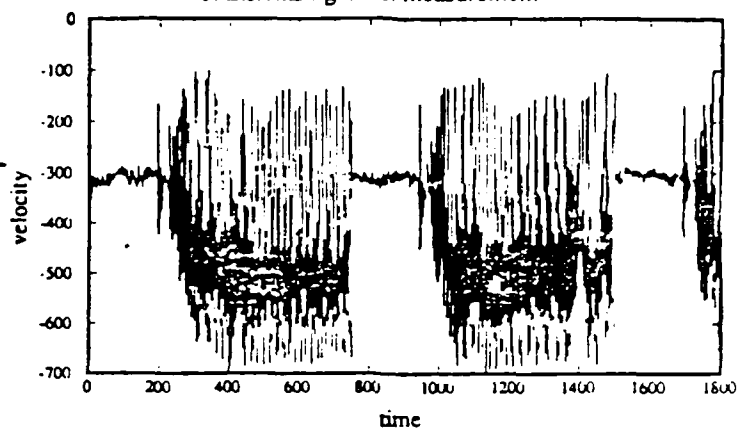


14. Fonctions de transfert des filtres passe bande FIR utilisés pour la démodulation d'amplitude.



15. Fonctions de transfert des filtres FIR utilisés pour la démodulation d'amplitude.

Transients : growth measurement

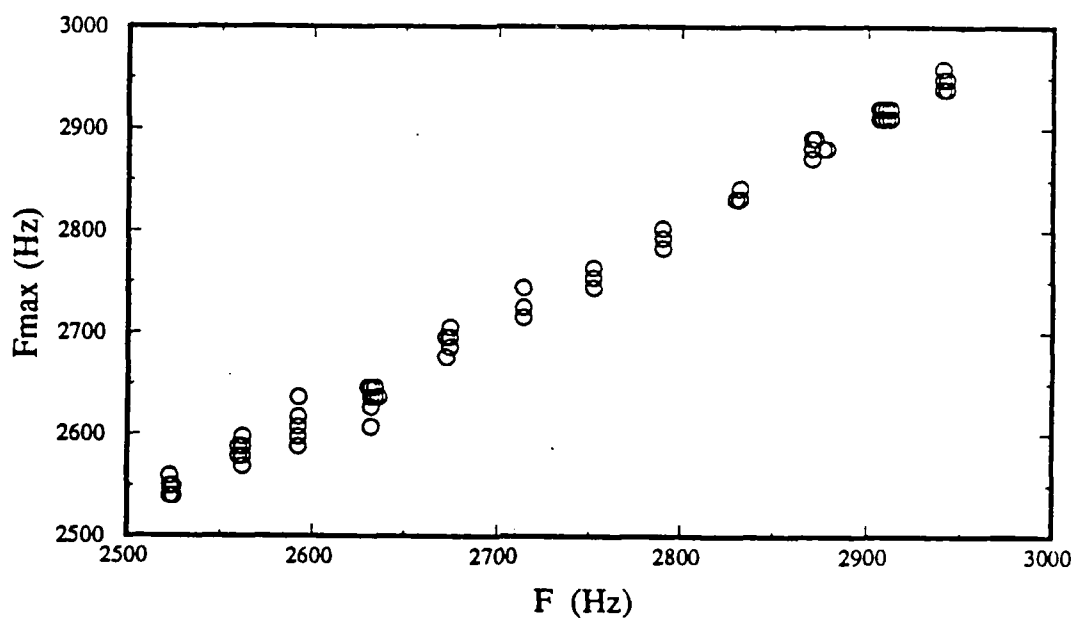
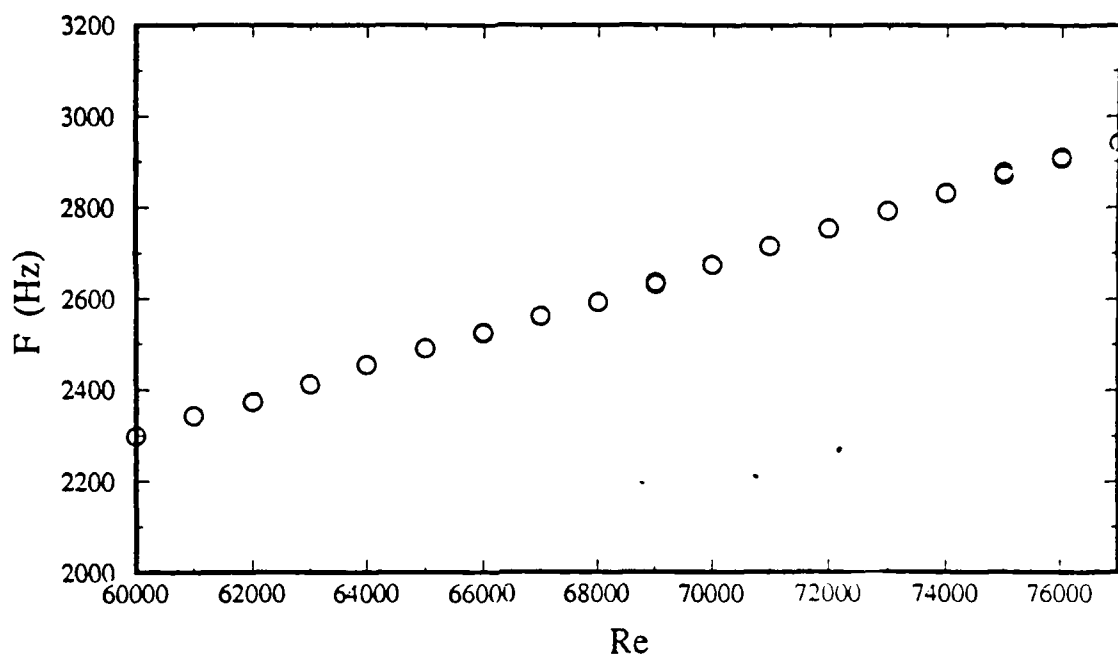


phase information

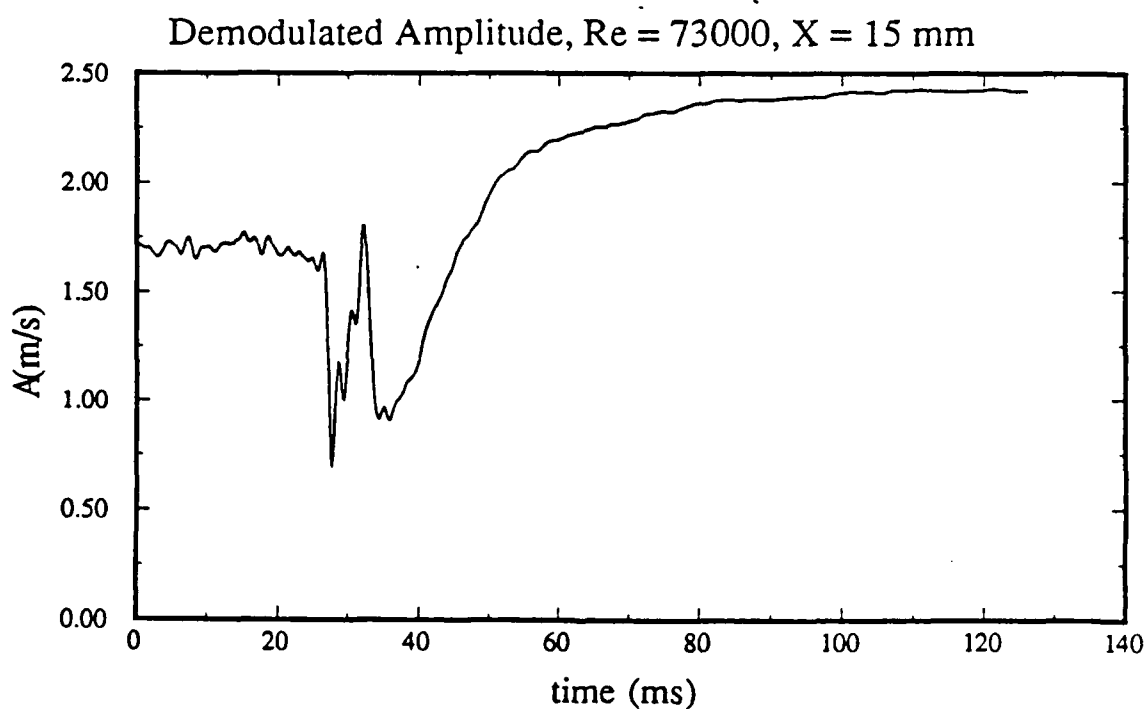
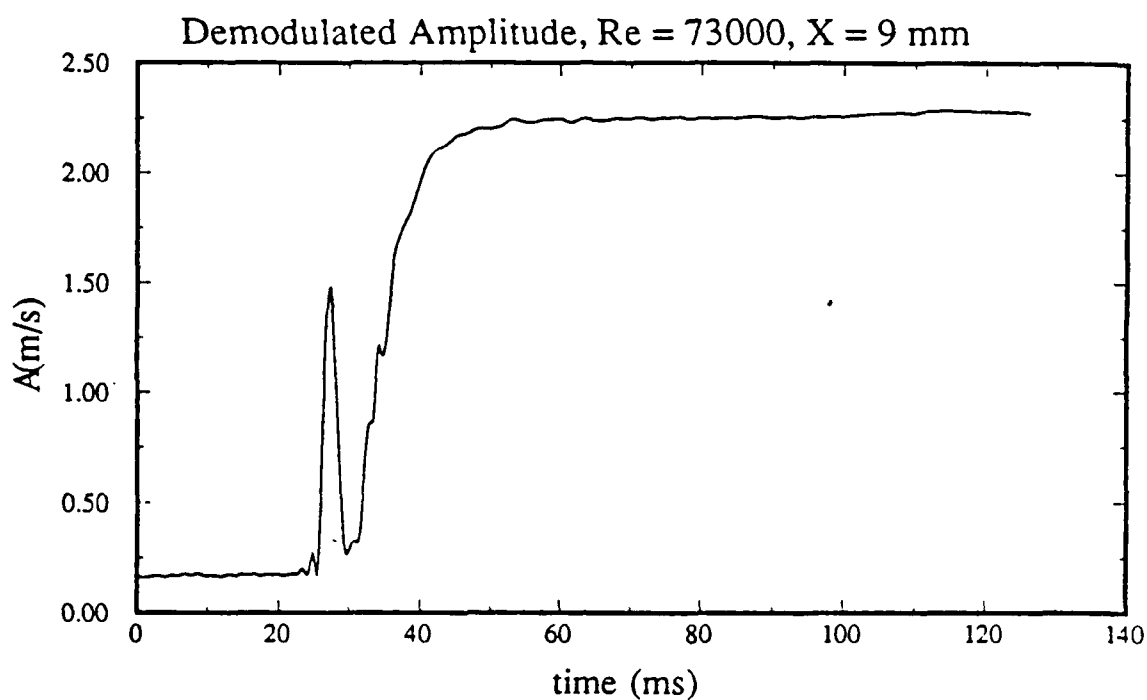
ϕ_i, c_i

A_{max}

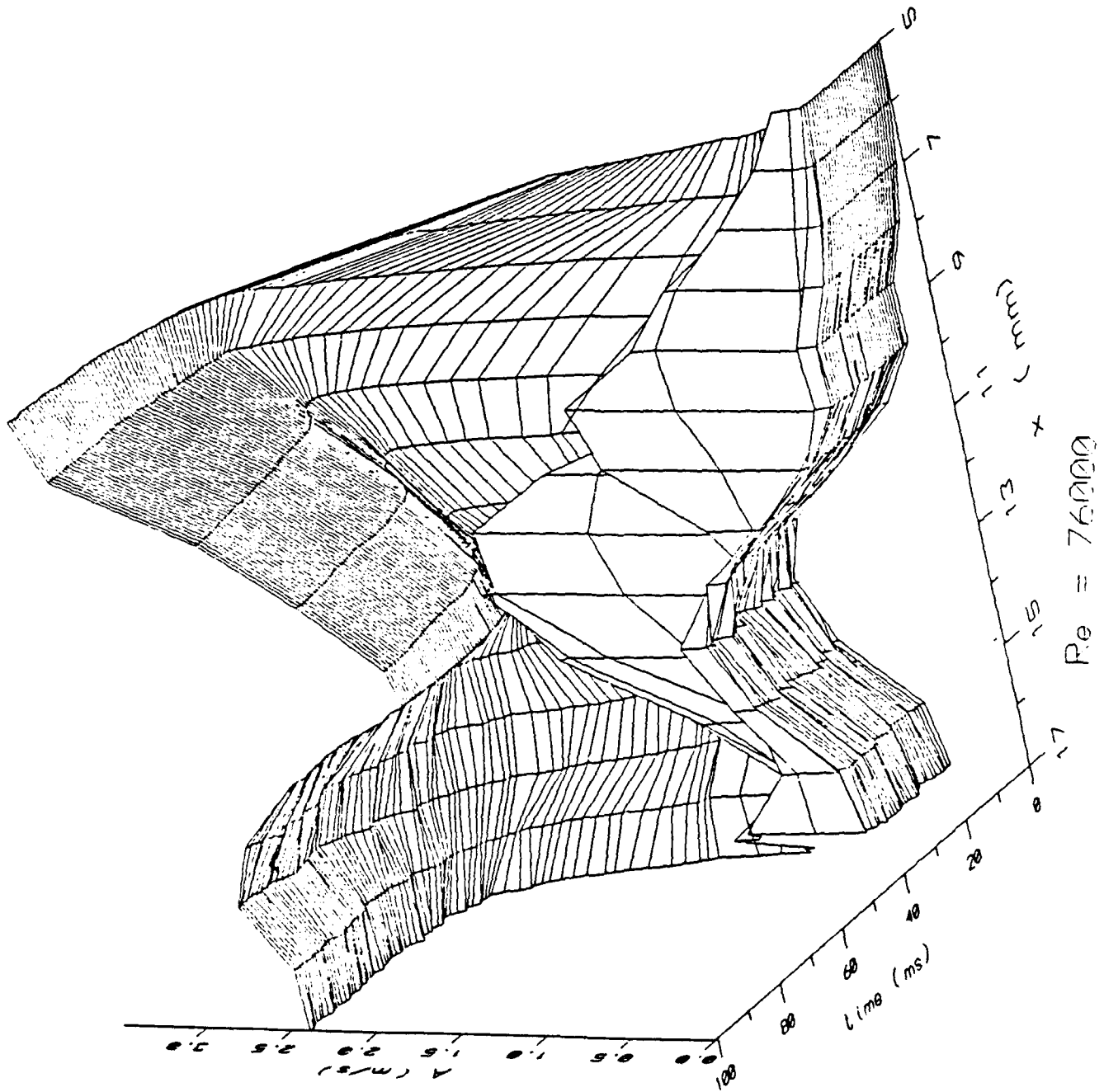
(phase averaged) + σ 41



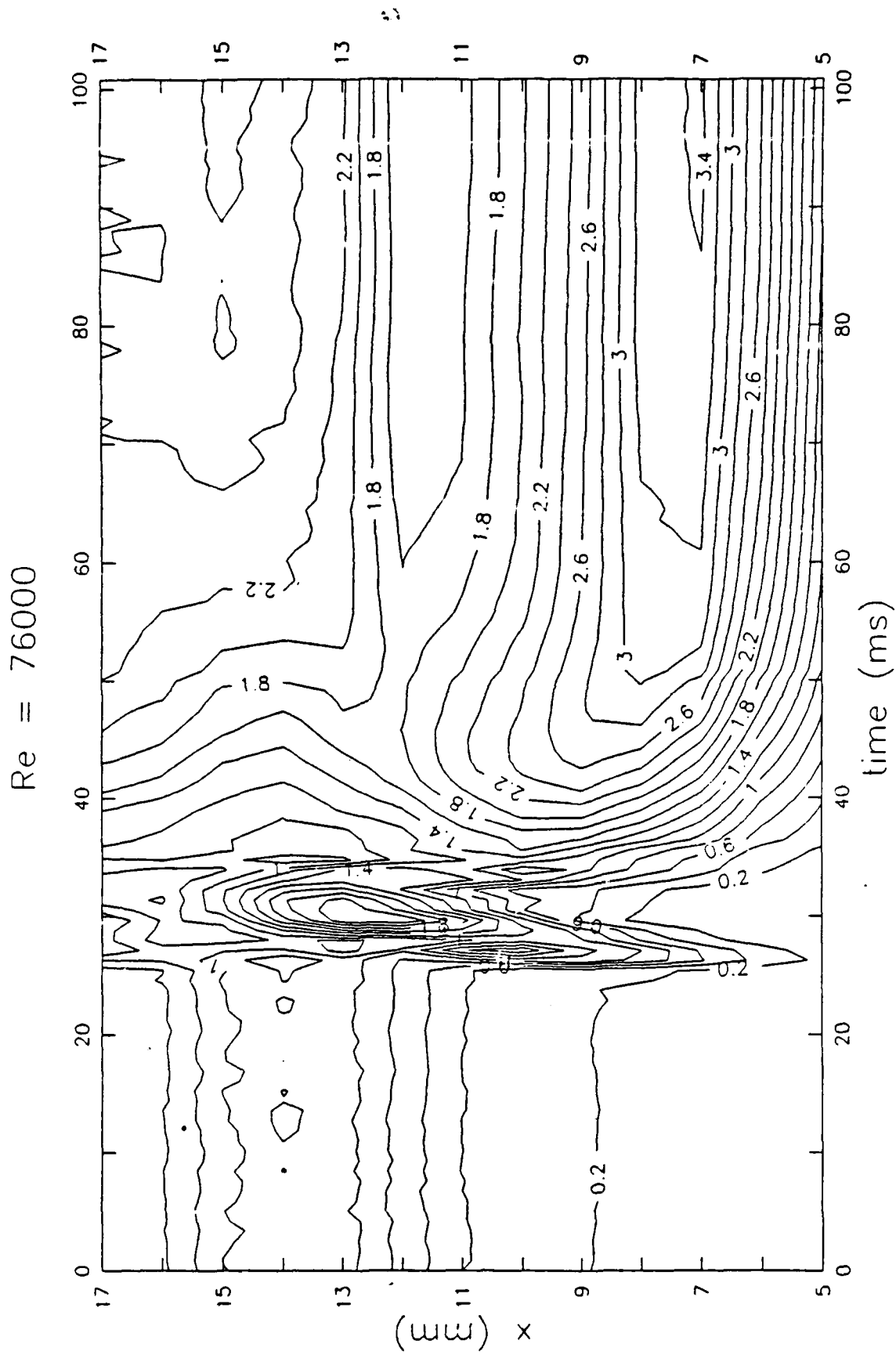
17. Variations de la fréquence propre en fonction du nombre de Reynolds: a) fréquence mesurée à l'analyseur de spectre en fonction de Re b) fréquence calculée par transformée de Fourier sur les données acquises en fonction de la fréquence mesurée à l'analyseur de spectre



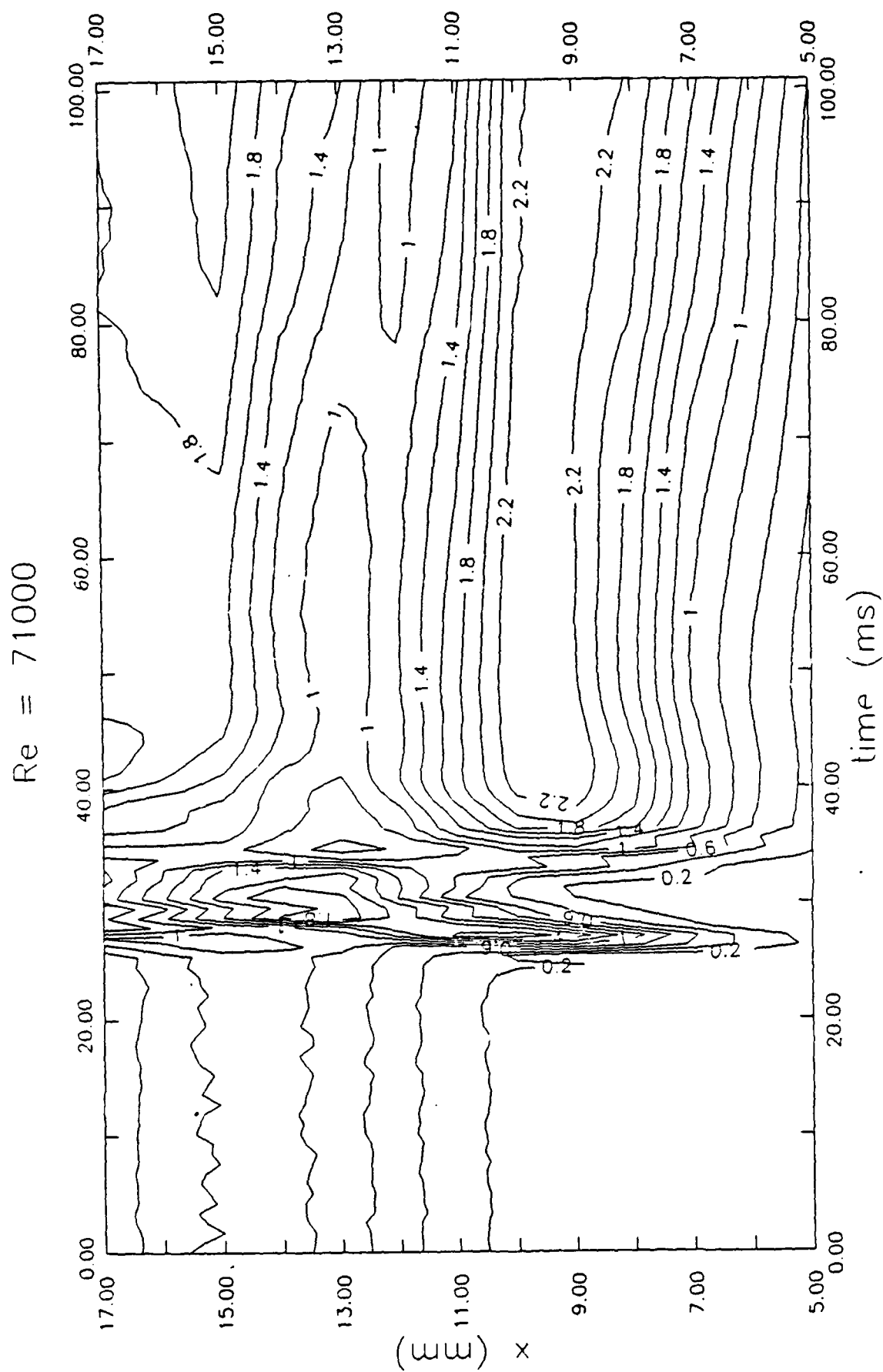
18. Variations temporelles de l'amplitude démodulée pour $Re = 73000$ a) $X = 9$ mm b) $X = 15$ mm



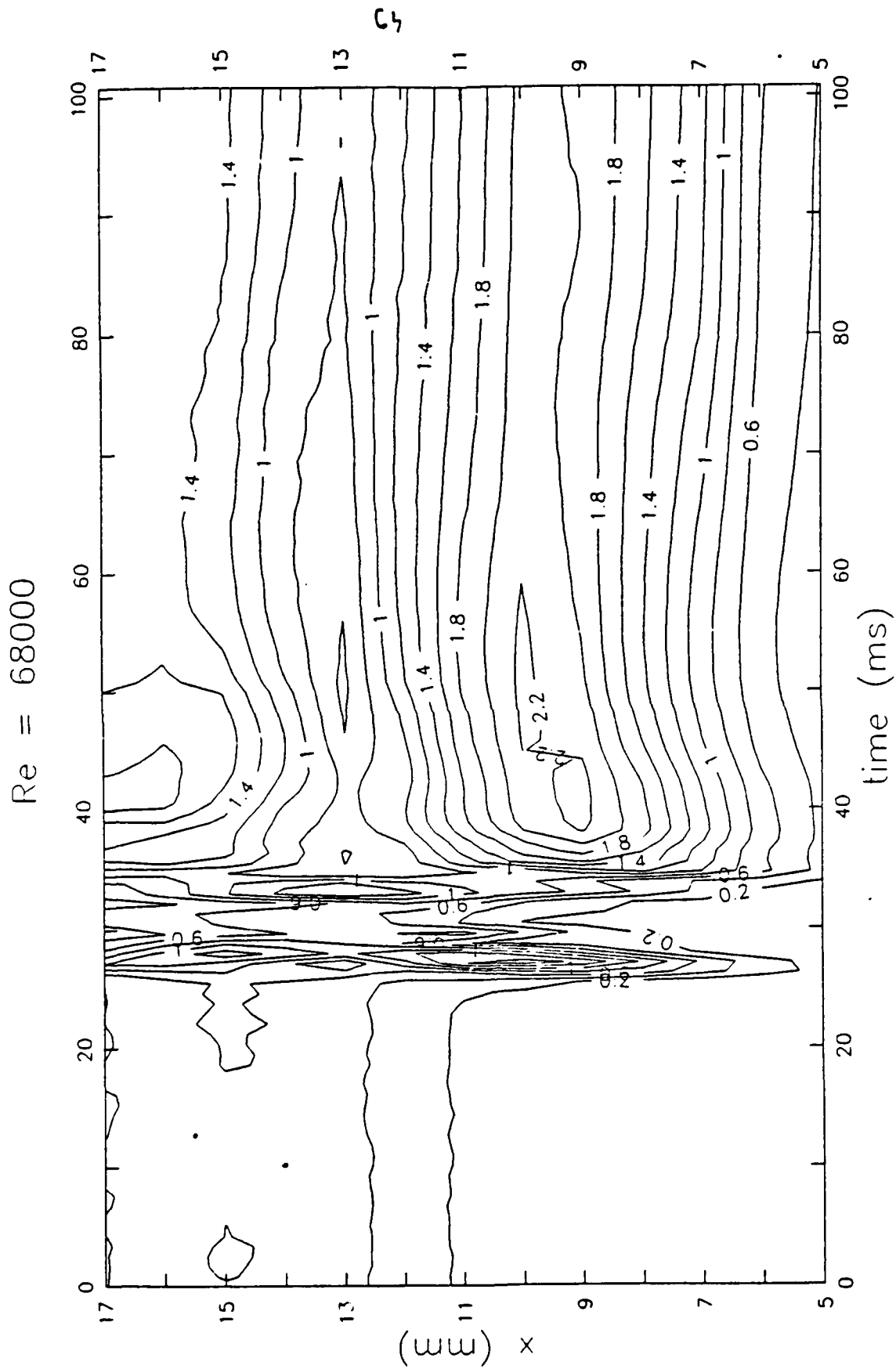
19. Variations spatio-temporelles de l'amplitude de la première harmonique (premier harmonique) pour $Re = 76000$ (seconde vue)



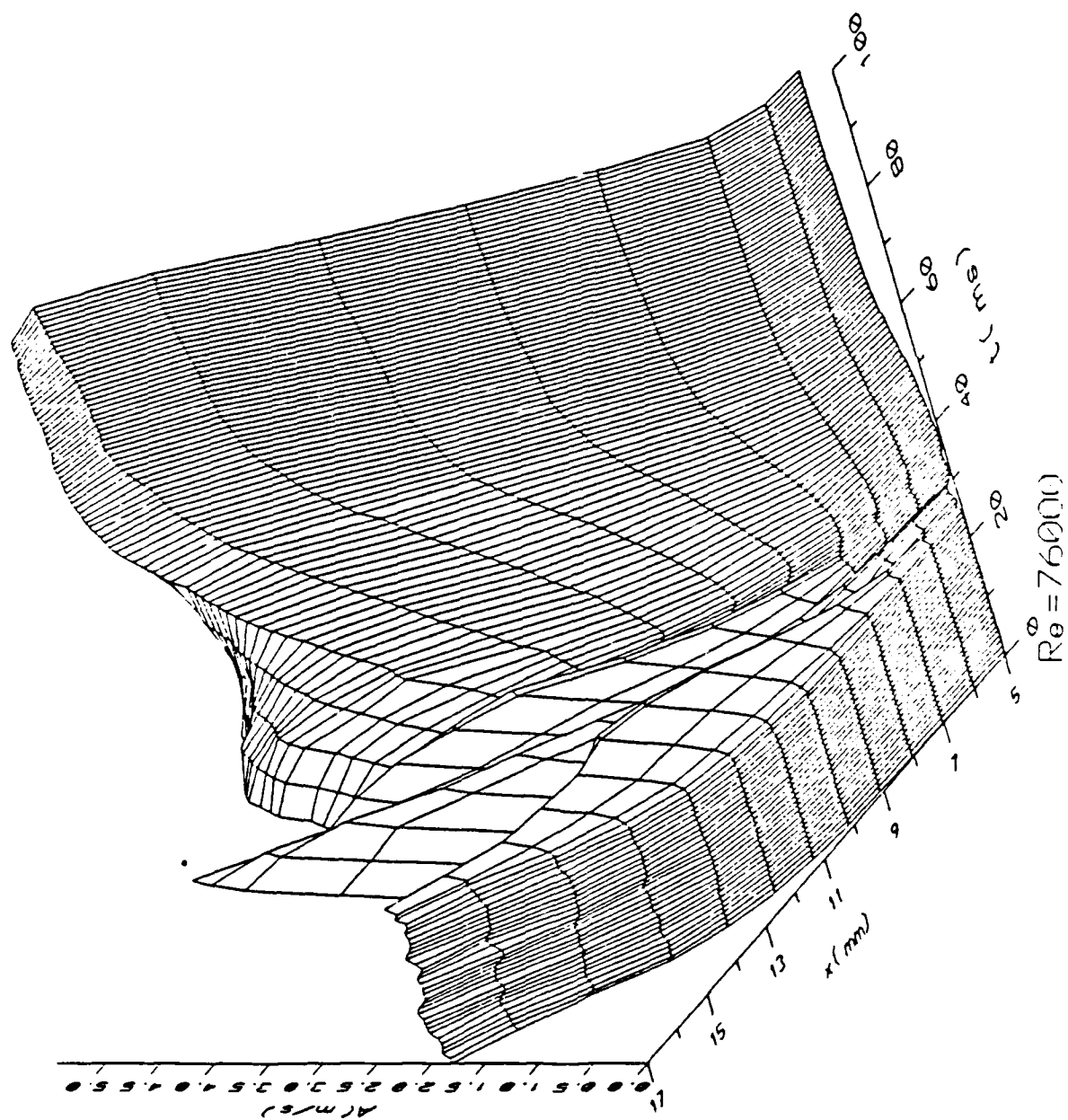
22. Diagramme contour des variations spatio-temporelles de l'amplitude de la fréquence propre (premier harmonique) pour $Re = 76000$



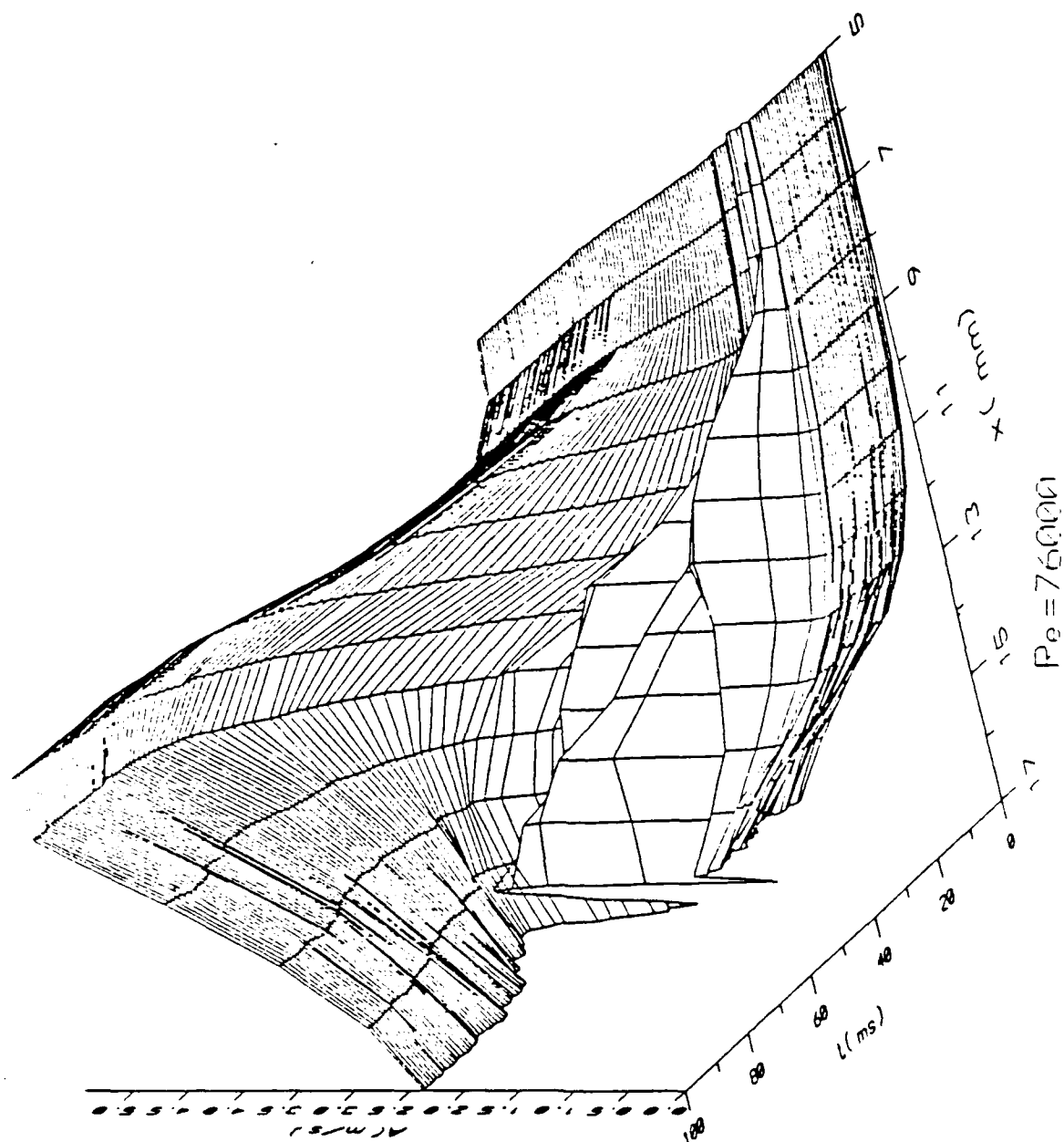
23. Diagramme contour des variations spatio-temporelles de l'amplitude de la fréquence propre (premier harmonique) pour $Re = 71000$



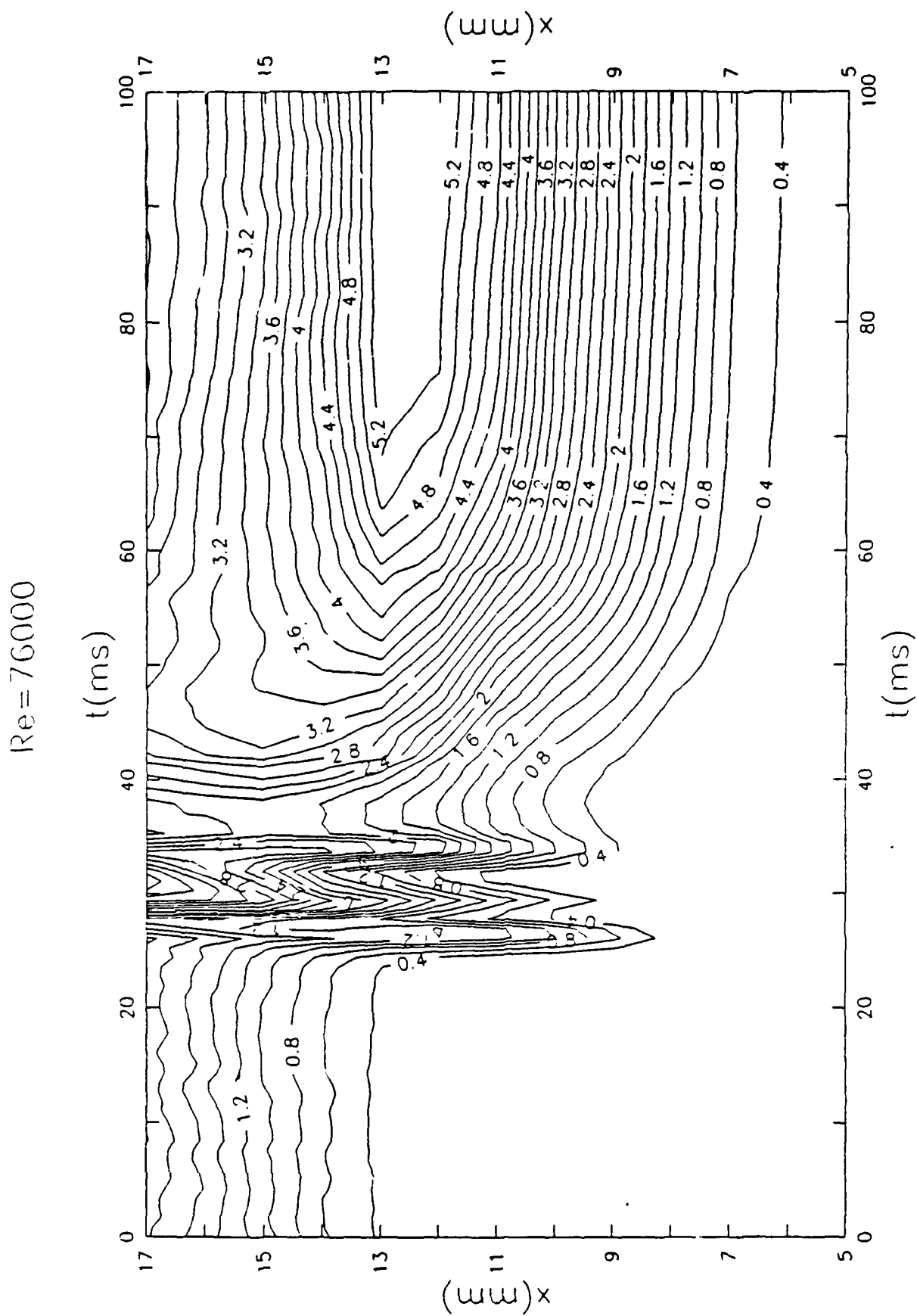
24. Diagramme contour des variations spatio-temporelles de l'amplitude de la fréquence propre (premier harmonique) pour $Re = 68000$



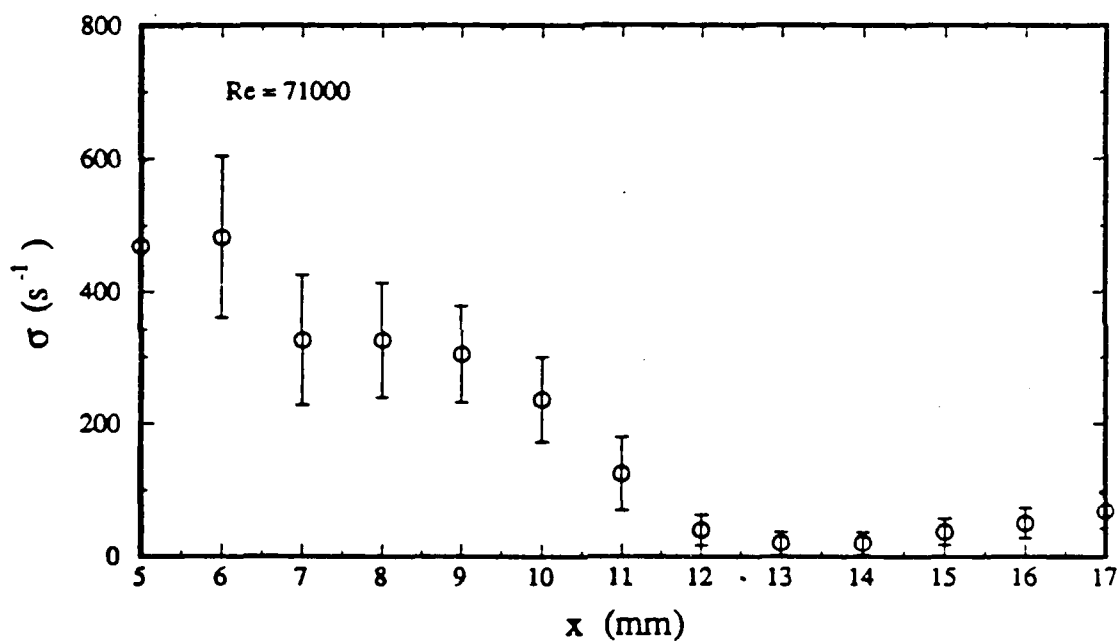
25. Variations spatio-temporelles de l'amplitude de la fréquence propre (sous harmonique) pour $Re = 76000$ (première vue)



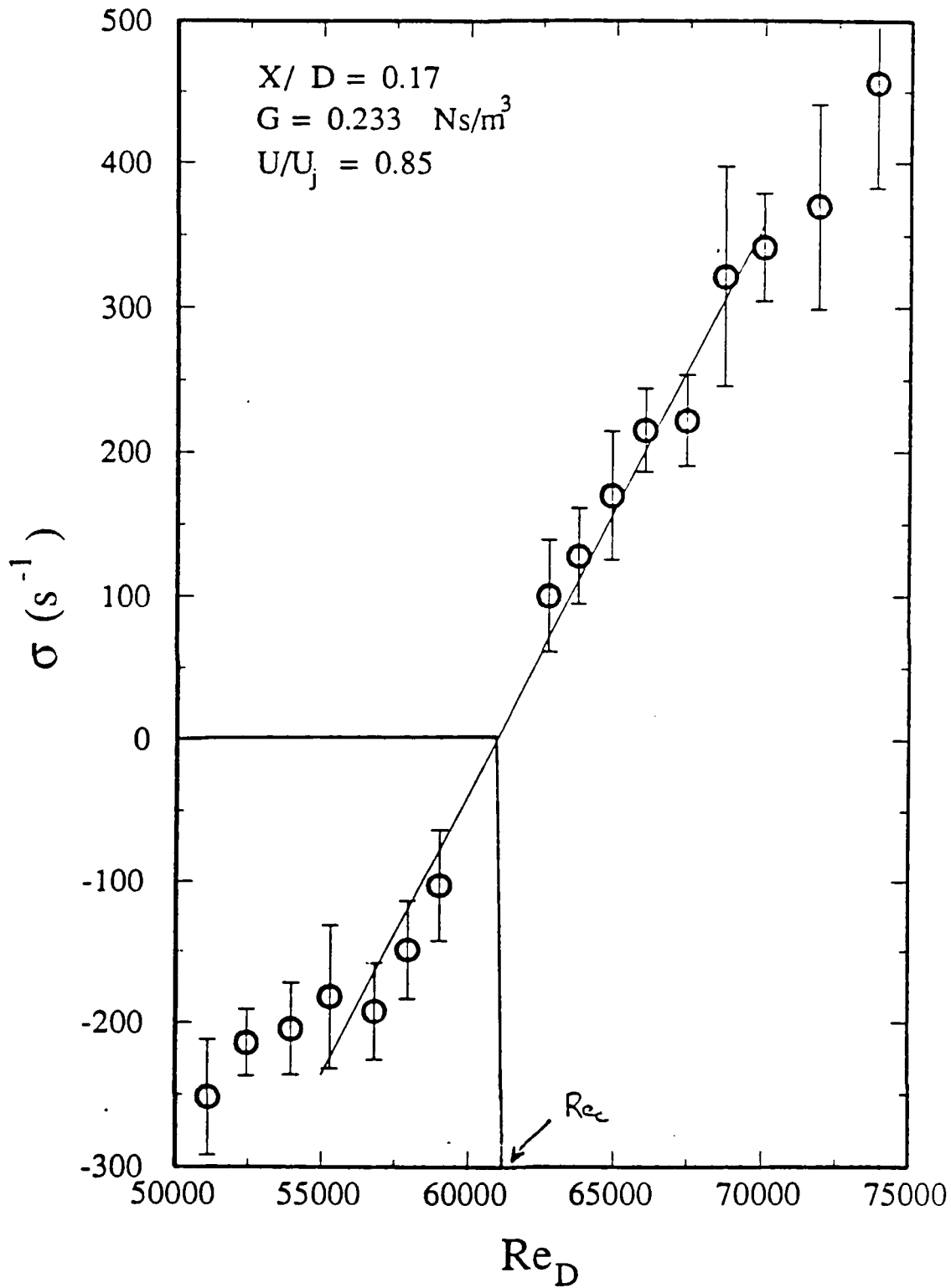
26. Variations spatio-temporelles de l'amplitude de la fréquence propre (sous harmonique) pour $Re = 76000$ (seconde vue)



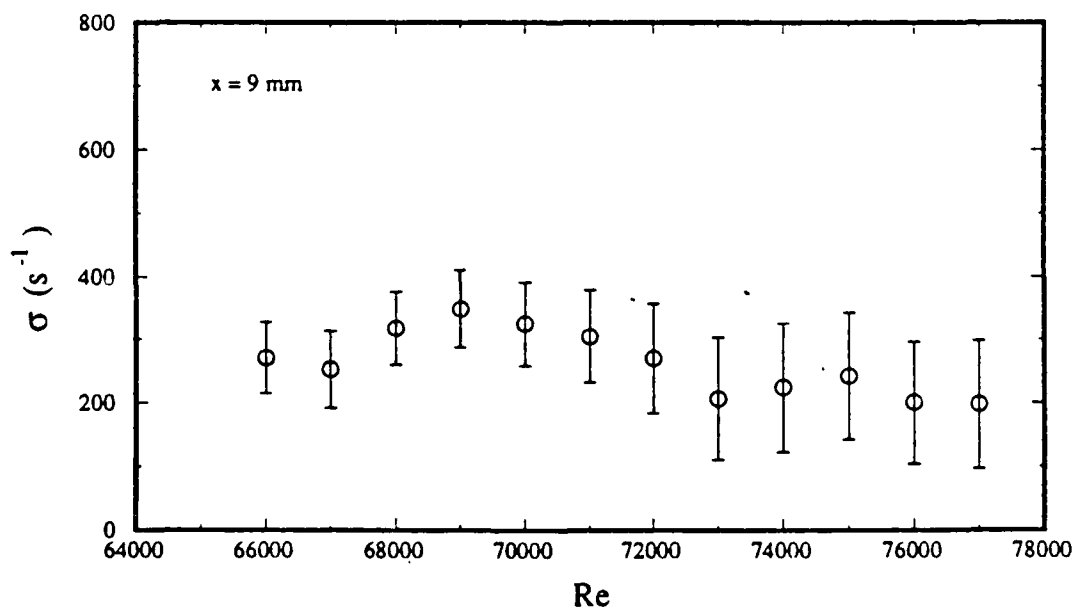
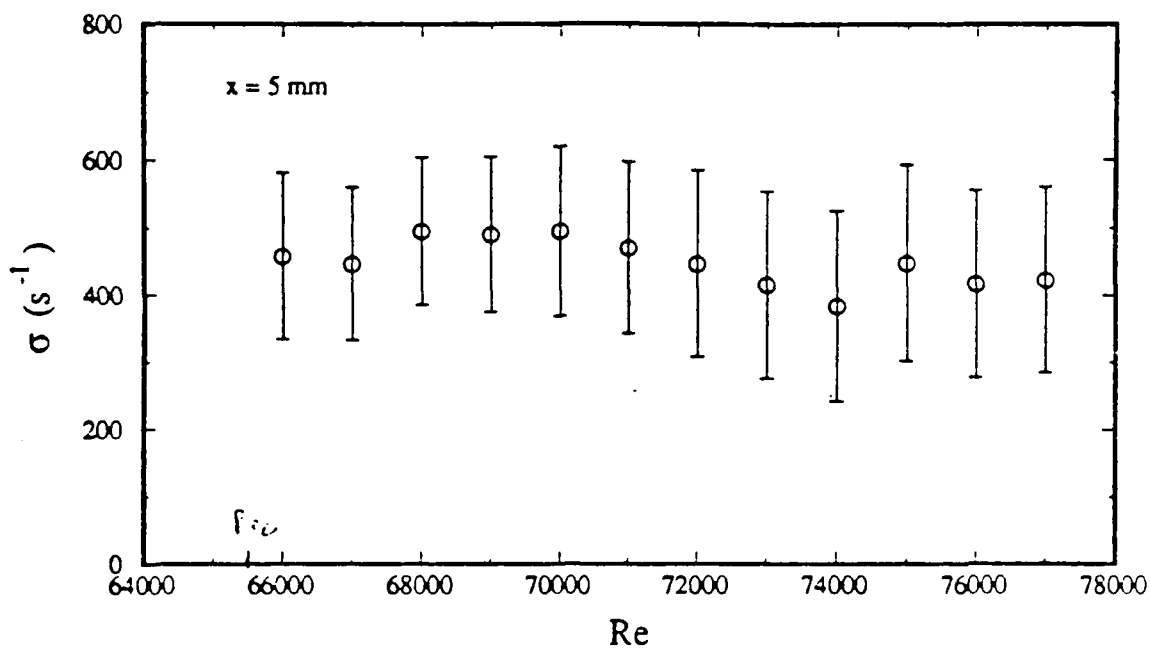
27. Diagramme contour des variations spatio-temporelles de l'amplitude de la fréquence propre (sous harmonique) pour $Re = 76000$



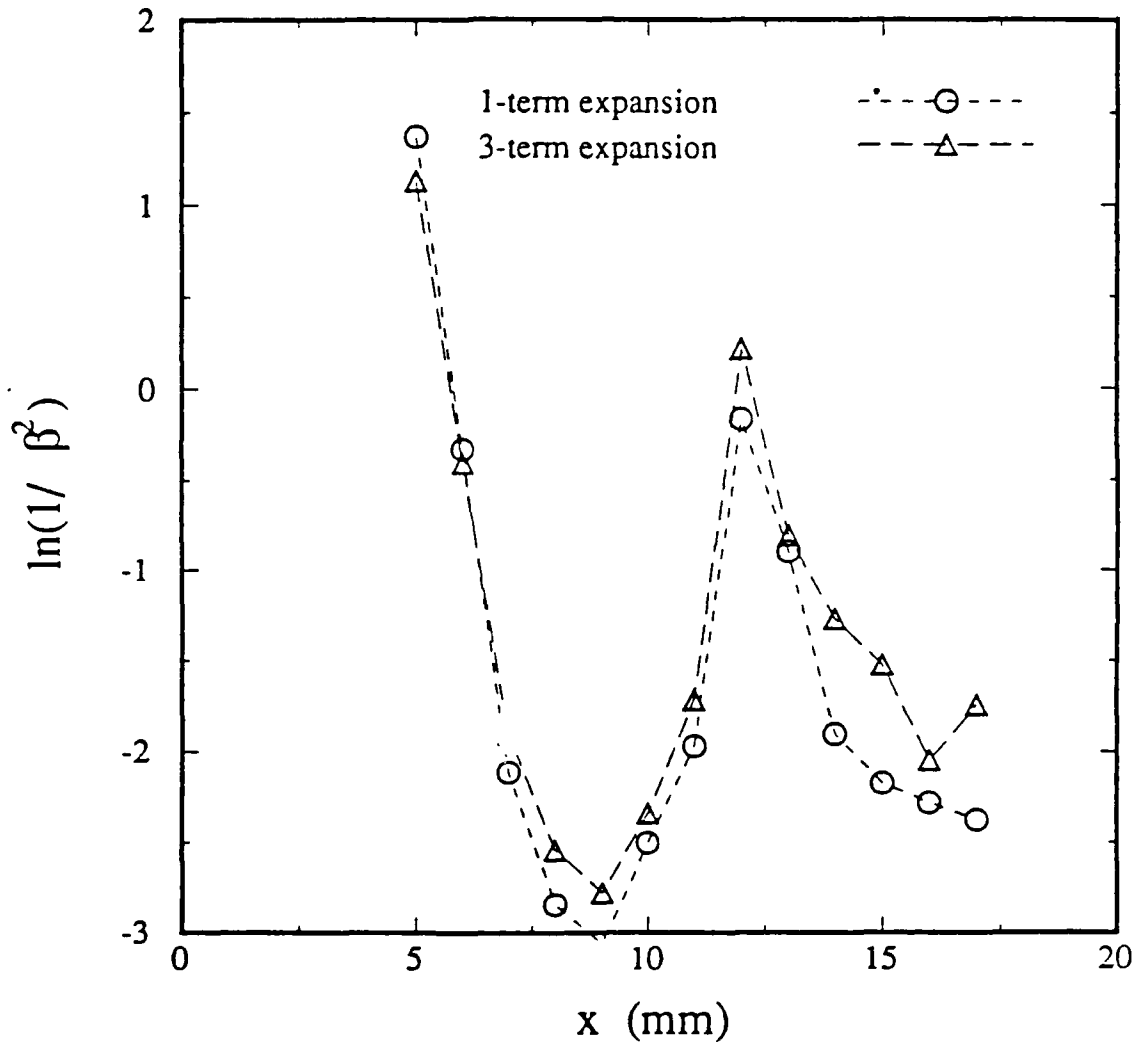
28. Variations spatiales du taux de croissance exponentielle pour $Re = 71000$



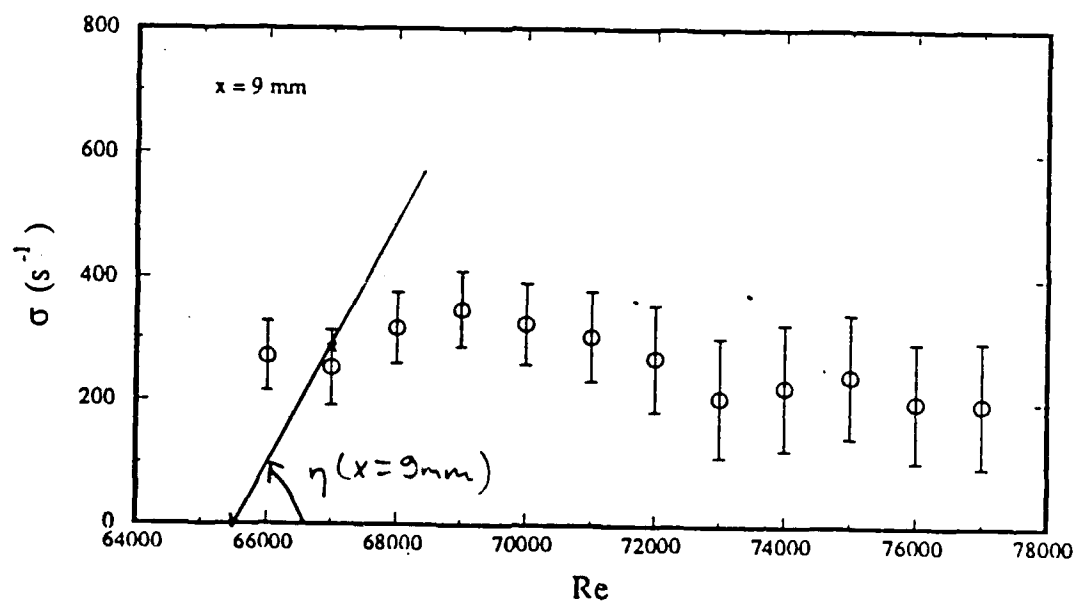
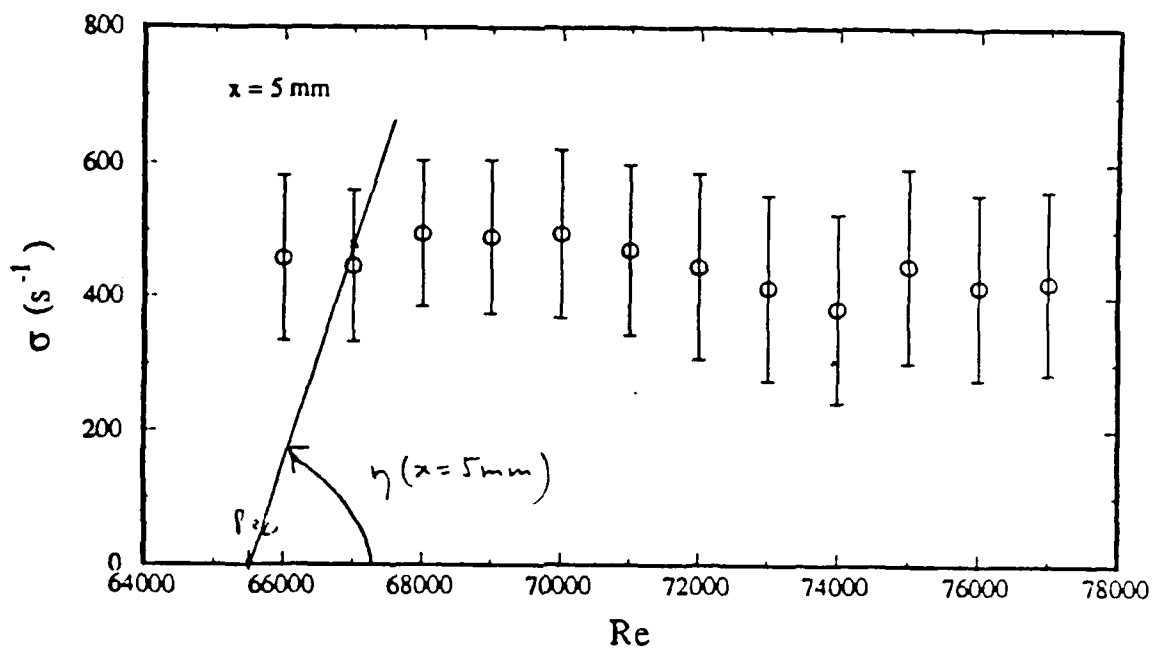
29. Variations du taux de croissance exponentielle en fonction du nombre de Reynolds (mesures de Reisenhel)



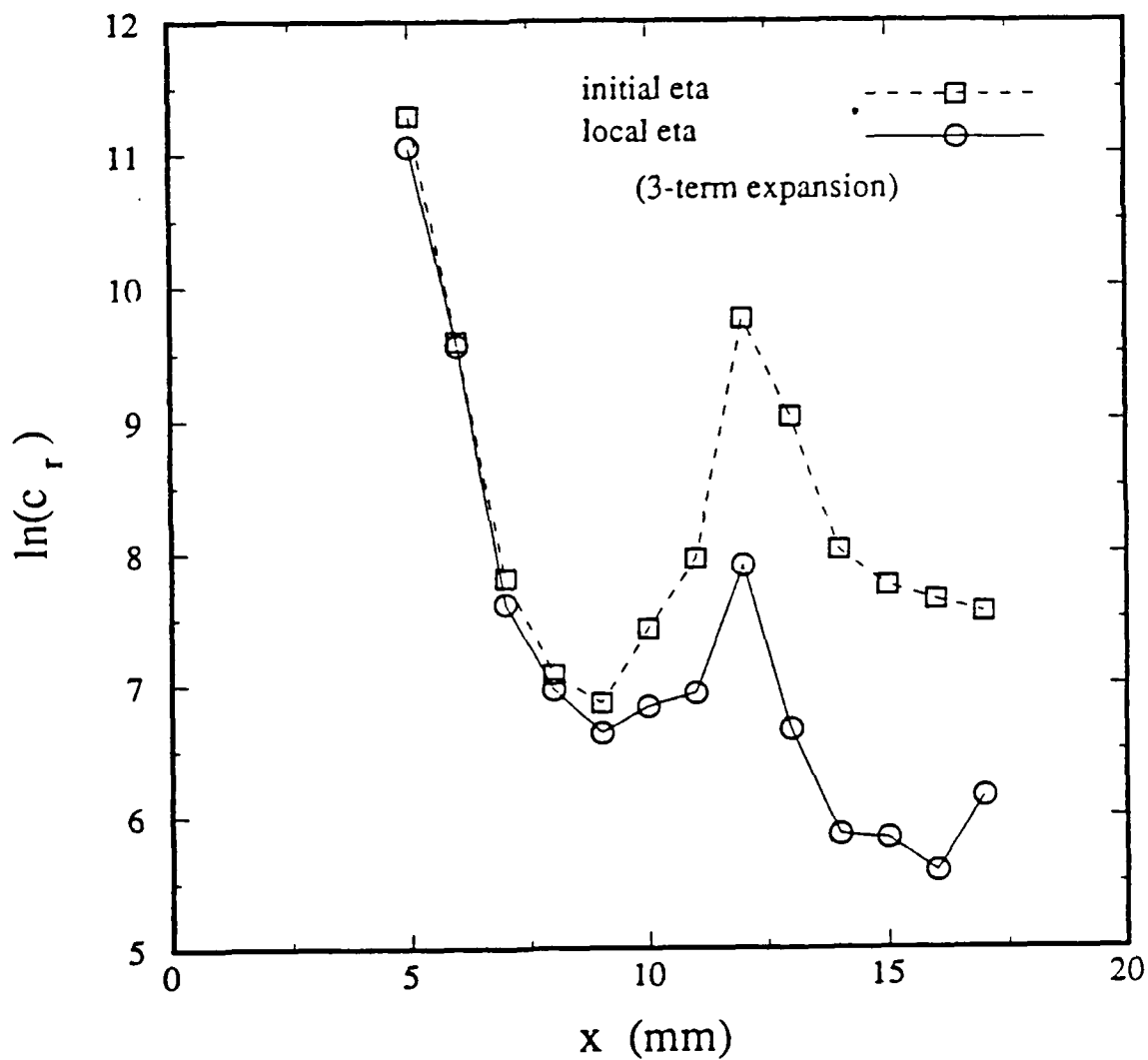
30. Variations du taux de croissance exponentielle en fonction du nombre de Reynolds a) $x = 5$ mm b) $x = 9$ mm



31. Variations spatiales de $\ln(1/\beta^2)$



32. Détermination de η



33. Variations spatiales du logarithme du coefficient de Landau

Abstract Submitted
for the Fortieth Meeting of the Division of Fluid Dynamics
American Physical Society

November 22-24, 1987

Chaos
Sorting Category

9
Category Number

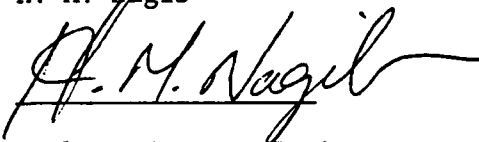
An Experimental Investigation of an Open Flow System with Enhanced Feedback. P. Reisenthel, H.M. Nagib and T. C. Corke, Ill. Inst. Tech. Recent measurements in the shear layer of an axisymmetric jet with and without enhanced feedback are presented for the range of Reynolds numbers $25000 < Re_D < 90000$. In particular, dynamical system analysis and two-probe correlations are used to describe the different routes to turbulence for the cases of natural and harmonically forced jets, as well as jets with mild or enhanced pressure feedback. These measurements document the crucial role of "clean" experimental conditions such as core turbulence intensity (approximately 0.05%), and establish preliminary evidence of "global" absolute instability for true open flow systems in the presence of feedback.

Supported by AFOSR Grant 86-0165.

Audio Visual Needs:

One overhead projector
One slide projector

Submitted by
H. M. Nagib



Mech. and Aero. Engineering
Illinois Institute of Technology
Chicago, Illinois 60616

Abstract Submitted
for the Fortyfirst Meeting of the Division of Fluid Dynamics
American Physical Society

November 20-22, 1988

Physical Review
Analytic Subject Index
Number 47.20

Bulletin Subject Heading in
which paper should be placed
Instabilities in Jets and
Wakes (2g)

Global Oscillations and Bifurcations in a Jet with Enhanced Feedback. P. Reisenthel, H. Nagib and T. Corke, Ill. Inst. of Tech. The role of feedback in a convectively unstable axisymmetric jet is experimentally investigated using a controlled means of enhanced self-excitation. This is achieved by feeding the amplified signal from a hot-wire placed in the initial shear layer to a speaker positioned far away from the jet exit. Under those conditions, it is shown that the exponential amplification or decay of self-sustained oscillations is governed by a global temporal instability, the time constant of which is several orders of magnitude larger than the period of the instability itself. These self-excited, highly organized axisymmetric waves are found to share many of the qualitative features exhibited by a broad class of hydroacoustic phenomena. Based on the present results, the origin of a critical Reynolds number in feedback or resonant systems is explained using the concept of hybrid instability. Finally, experimental evidence is presented in support of a supercritical Hopf bifurcation, and connections with the Landau equation are established. *Supported by AFOSR Grant 86-0165.*

Audio Visual Needs:

One overhead projector
One slide projector

Submitted by
H. M. Nagib

Mech. and Aero. Engineering
Illinois Institute of Technology
Chicago, Illinois 60616

Abstract Submitted
for the Fortyfirst Meeting of the Division of Fluid Dynamics
American Physical Society

November 20-22, 1988

Physical Review
Analytic Subject Index
Number 47.20

Bulletin Subject Heading in
which paper should be placed
Stability

Receptivity of an Axisymmetric Shear Layer to an Azimuthally-Local Sound Source. S. Kusek, T. Corke and P. Reisenthel, Ill. Inst. Tech. The effects of localized acoustic disturbances on the initial growth and development of unstable modes in a high Reynolds number axisymmetric jet are investigated experimentally. These are produced by an azimuthal array of miniature speakers placed in close proximity of the exit lip. For various azimuthal amplitude and phase distributions of periodic input pressure disturbances, the eigenmodes of nonaxisymmetric waves are documented. Comparisons are made to similar results in a jet excited by an axisymmetric far-field acoustic source. The acquired results are used to provide information on the spatio-temporal character of these instabilities, with the goal towards exciting spatially coherent helical modes of higher order.

Supported by AFOSR Grant 86-0165

Audio Visual Needs:

One overhead projector
One slide projector

Submitted by
H. M. Nagib

Mech. and Aero. Engineering
Illinois Institute of Technology
Chicago, Illinois 60616

Abstract Submitted
for the Fortyfirst Meeting of the Division of Fluid Dynamics
American Physical Society

November 20-22, 1988

Physical Review
Analytic Subject Index
Number 47.20

Bulletin Subject Heading in
which paper should be placed
Stability

Receptivity Transfer Function of a Round Jet. M. Ghassemi, Y-M Xiong, P. Reisenthel and T. Corke, Ill. Inst. of Tech. The behavior of an axisymmetric jet under closed-loop excitation is known to depend critically on the phase and amplitude transfer function at the point of receptivity. Specifically, issues of frequency selection in the presence of pressure feedback are contingent on the detailed understanding of pressure-velocity phase relations and their scaling. Measurements of phase and amplitude development of the acoustically forced initial shear layer are combined with results from linear stability theory to infer receptivity transfer functions at the exit lip. The results show only a mild dependence of the amplitude response to Strouhal and Reynolds numbers. However, unexpectedly large phase variations, two to three times those predicted from linear theory, were observed past a critical frequency. Through direct measurements of phase speed, considerations of the coupling between pressure and velocity fluctuations are shown to be responsible for observed local abnormalities in phase. The current results indicate that a clearly more complicated behavior than previously thought may exist in such pressure driven open flows. Supported by AFOSR Grant 86-0165

Audio Visual Needs:

One overhead projector
One slide projector

Submitted by
H. M. Nagib

Mech. and Aero. Engineering
Illinois Institute of Technology
Chicago, Illinois 60616

Abstract Submitted for
The 42nd Annual Meeting of the Division of Fluid Dynamics of the American Physical Society
NASA Ames Research Center, November 19 - 21, 1989.

The rules for submission of abstracts are printed in most issues of the APS Bulletin. In place of the PACS index, please use the sorting categories listed on the right, which are solely for those submitting abstracts to this conference. The size limits are 12 cm (4-3/4 in. wide) x 10.5 cm (4-1/8 in. long) for the portion of the abstract to be reproduced.

Aug 2 1989
 Date

2. Stability
 Sorting Category

f. jets & wakes
 Category Number

SORTING CATEGORIES

Nonlinear Stability of a Viscous Axisymmetric Jet. J. HORWITZ, S. ROSENBLAT, IL INST OF TECHNOLOGY*-
 The temporal stability of a viscous circular jet, assuming a hyperbolic tangent profile for the mean flow, is studied with respect to nonaxisymmetric disturbances. A severely truncated Fourier modal expansion for the disturbance is substituted into the Navier Stokes equation. A projection onto an appropriate subspace leads to a low dimensional system (ten) of nonlinear ODE's for the amplitude of the disturbances where the bifurcation parameter is the Reynolds number (R). There is a Hopf bifurcation on the null solution at $R=21.75$, which leads to a periodic solution, which in turn loses stability at $R=32.5$ and is replaced by a quasiperiodic solution with two incommensurate frequencies f_1 and f_2 . For $32.5 < R < 37$, each peak in the Fourier spectrum of the time series can be indexed by either $q_n = nf_1 - (n-1)f_2$ or $w_n = nf_1 - (n+1)f_2$. As R increases f_2/f_1 increases and as $f_2/f_1 \rightarrow 1/2$, $w_n \rightarrow 0$ indicating a possible homoclinic orbit. No bounded solutions were found for $R > 37$.
 *Supported by AFSOR Grant 86-0165

1. Turbulence
 - a. Theory
 - b. Simulation
 - c. Modeling
 - d. Homogeneous Flows
 - e. Boundary Layers
 - f. Jets
 - g. Wakes
 - h. Free-Shear Layers
 - i. Control
2. Stability
 - a. General Theory
 - b. Boundary Layers
 - c. Taylor-Couette
 - d. Rayleigh-Taylor
 - e. Convective/Buoyant Flows
 - f. Jets and Wakes
 - g. Free-Shear Layers
 - h. Thin Films
 - i. Interfacial
 - j. Control
3. Reacting Flows
 - a. Theory
 - b. Simulation and Modeling
 - c. Experiment
 - d. Control
4. Shock Waves, Detonations, Deflagration
5. Compressible Flows
6. Hypersonic Flows
7. Computational Methods
9. Chaos
10. Vortex Dynamics
11. Laminar Flows
12. Viscous Flows
13. Separated Flows
14. Aerodynamics
15. Waves
16. Acoustics
17. Drops and Bubbles
18. Flows in Porous Media
19. Suspensions
20. Multiphase Flows
21. Rotating Flows
22. Geophysical Fluid Dynamics
23. Biofluids/Non-Newtonian Flows
24. Microgravity
25. Low Density Flows
26. Material Processing
27. Other Topics in Fluid Dynamics:
 Please Specify: _____

Submitted By

David R. Williams
 Signature of APS Member

David R. Williams

Name Typewritten

M.A. E. Dept.

Address

Ill. Inst. of Tech.

Chicago IL 60616

1. Are you willing to chair a session ☐ yes ☐ no

if yes, in what categories? _____ Phone: _____

Suggested Chairperson for session, _____

2. Do you need Audio-Visual Equipment (other than overhead or 35mm projector)? ☐ yes ☒ no

Specify _____

Mail to: Dr. Nagi N. Mansour
 Center for Turbulence Research
 Mail Stop 202A-1
 NASA Ames Research Center
 Moffett Field, CA 94035

Abstract must be received by August 8, 1989.

(Note that a person may speak only once in a contributed paper session at an APS meeting. The first author is the speaker.)

Abstract Submitted for
The 42nd Annual Meeting of the Division of Fluid Dynamics of the American Physical Society
NASA Ames Research Center, November 19 - 21, 1989.

The rules for submission of abstracts are printed in most issues of the APS Bulletin. In place of the PACS index, please use the sorting categories listed on the right, which are solely for those submitting abstracts to this conference. The size limits are 12 cm (4-3/4 in. wide) x 10.5 cm (4-1/8 in. long) for the portion of the abstract to be reproduced.

8/3/89
Date

Stability
Sorting Category

2g
Category Number

Experimental Investigation of Resonant Spatio-Temporal Instability Waves in an Axisymmetric Shear Layer. *P. Reisenthel and N. Nivelet, Ill. Inst. of Tech.* The existence of a supercritical Hopf bifurcation in Reynolds number is experimentally demonstrated for the case of axisymmetric enhanced feedback. This is achieved by placing a miniature hot-wire probe at a fixed location in the initial shear layer of a low disturbance axisymmetric jet ($60,000 \leq Re_D \leq 80,000$; $Re_{\theta_i} \approx 170$), and feeding the velocity signal into an array of speakers close to the point of receptivity of the separating shear layer. Quantitative comparisons with the temporal Landau equation at a given streamwise position are presented. Phase-averaged measurements using a second, 'traveling' probe ($1.0 < X/\lambda < 4.0$) were obtained by repeatedly "opening" and "closing" the feedback loop under computer control. The results indicate that while both real and imaginary parts of the Landau equation appear to be largely independent of space when the flow is almost parallel ($X/\lambda < 1.5$), the Landau coefficient c_r decreases by several orders of magnitude within a fraction of the eigenfrequency wavelength.

Supported by AFOSR grant 86-0165

SORTING CATEGORIES

1. Turbulence
 - a. Theory
 - b. Simulation
 - c. Modeling
 - d. Homogeneous Flows
 - e. Boundary Layers
 - f. Jets
 - g. Wakes
 - h. Free-Shear Layers
 - i. Control
2. Stability
 - a. General Theory
 - b. Boundary Layers
 - c. Taylor-Couette
 - d. Rayleigh-Taylor
 - e. Convective/Buoyant Flows
 - f. Jets and Wakes
 - g. Free-Shear Layers
 - h. Thin Films
 - i. Interfacial
 - j. Control
3. Reacting Flows
 - a. Theory
 - b. Simulation and Modeling
 - c. Experiment
 - d. Control
4. Shock Waves, Detonations, Deflagration
5. Compressible Flows
6. Hypersonic Flows
7. Computational Methods
9. Chaos
10. Vortex Dynamics
11. Laminar Flows
12. Viscous Flows
13. Separated Flows
14. Aerodynamics
15. Waves
16. Acoustics
17. Drops and Bubbles
18. Flows in Porous Media
19. Suspensions
20. Multiphase Flows
21. Rotating Flows
22. Geophysical Fluid Dynamics
23. Biofluids/Non-Newtonian Flows
24. Microgravity
25. Low Density Flows
26. Material Processing
27. Other Topics in Fluid Dynamics:
Please Specify: _____

Submitted By

David R. Williams

Signature of APS Member

David R. Williams
Name Typewritten

M.A.E. Department
Address
Ill. Inst. of Tech.

P. Reisenthel

10 W. 32nd St., Chicago IL 60616

1. Are you willing to chair a session ☒ yes ☐ no

if yes, in what categories? 2g, 2f Phone: (312) 5673192

Suggested Chairperson for session, _____

2. Do you need Audio-Visual Equipment (other than overhead or 35mm projector)? ☐ yes ☒ no

Specify _____

Mail to: **Dr. Nagi N. Mansour**
Center for Turbulence Research
Mail Stop 202A-1
NASA Ames Research Center
Moffett Field, CA 94035

Abstract must be received by August 8, 1989.

(Note that a person may speak only once in a contributed paper session at an APS meeting. The first author is the speaker.)

HYBRID INSTABILITY IN AN AXISYMMETRIC JET
WITH ENHANCED FEEDBACK

BY

PATRICK REISENTHAL

Submitted in partial fulfillment of the
requirements for the degree of
Doctor of Philosophy in Mechanical and Aerospace Engineering
in the School of Advanced Studies of
Illinois Institute of Technology

Approved


Adviser

Chicago, Illinois
May, 1988

ABSTRACT

The present experiment considers an axisymmetric jet as a prototypical open flow system, the organization of which has been enhanced by a strong feedback loop. When the source of feedback signal is located in the initial shear layer, strong self-sustained oscillations were spontaneously produced past critical conditions. Because of the controlled conditions of the experiment, thresholding effects based on velocity and streamwise flow scale were related to the existence of a critical gain. A dual empirical and analytical approach, motivated by observations from this flowfield and based on the concept of "hybrid" instability, was used to explain the origin of frequency selectivity and the existence of a critical Reynolds number in feedback systems.

One of the main results of this study is the demonstration that, close to criticality, open flows with feedback may support global instabilities which grow in time. The temporal growth of the global feedback instability and the spatial amplification in the shear layer, qualify this instability as being "hybrid", in the sense that it is temporal with respect to the amplitude of global oscillations, but convective with respect to the shear layer dynamics. The role of this "hybrid" instability was analysed using phenomenological equations utilizing the results of linear theory to describe in

detail the dynamics of feedback and many of its nonlinear consequences. Finally, it was experimentally demonstrated that, for Reynolds numbers slightly larger than critical, well-defined limit-cycle behaviour is observed. Analytical considerations suggest that an increasing number of potentially excited modes may be involved as the Reynolds number is further increased.

CHAPTER X

CONCLUSIONS

Summary

The role of feedback in a convectively unstable axisymmetric jet has been experimentally investigated using a controlled means of enhanced self-excitation. It was found that under quite general conditions, the upstream propagation of pressure fluctuations and their coupling with the shear-layer instability spontaneously produced strong self-sustained oscillations, past critical conditions. This special open flow configuration was investigated with an eye towards the potential use of dynamical systems in turbulence.

These self-excited, highly organized instabilities were found to share many of the qualitative features exhibited by a broad class of hydroacoustic phenomena. Because of the controlled conditions of the experiment, thresholding effects based on velocity and streamwise flow scale were related to the existence of a critical gain. Furthermore, we have explained, using the concept of "hybrid" instability, the origin of a critical Reynolds number in feedback or resonant systems. Model phenomenological equations utilizing linear stability theory were used to describe in detail the dynamics of feedback and many of its nonlinear consequences. This dual empirical and analytical approach allowed us to

explain the observed frequencies and their inter-relation in more complete and rigorous ways than in previous studies. The present data agree well with the predicted scaling of the critical gain with downstream position of the source of feedback and with Reynolds number. Conditions of mild probe feedback have been used to critically assess the potential importance of the dynamical systems approach as a tool to analyse empirical findings.

Specifically, the demonstration was made that frequency stages are embedded within a band structure. The width of these bands and their possible overlap was determined to bear close ties with phenomena of intermittent switching and hysteresis between competing eigenfrequencies. Clear evidence was presented that these effects should be viewed as being part of a unified structure controlled by the gain of the feedback loop.

Most importantly, the exponential amplification or decay of self-sustained oscillations close to criticality was shown to be governed by a global temporal instability. This instability exhibits a time scale several orders of magnitude larger than the period of the oscillation itself. The growth rates at the onset of resonance were measured experimentally and found to be independent of space. These global intrinsically driven oscillations were found to be insensitive to external disturbances for a substantial range of forcing levels

and initial conditions, although all indications were that the flow remained locally convectively unstable.

The role of the shear layer as a vehicle for the amplification of disturbances within the feedback loop was clearly established by connecting temporal growth rates of the global instability with spatial amplification in the shear layer. These two components of the enhanced feedback effect, qualify the instability as being "hybrid", in the sense that it is a temporal instability with respect to the global amplitude of oscillations, but a convective instability with respect to the shear layer dynamics.

By considering issues of frequency competition based on the temporal growth rates of the global oscillations, an explanation was proposed for the frequency selection process in a closed-loop configuration, and for the observed frequency hysteresis.

Most significantly, it was shown experimentally that, for Reynolds numbers slightly larger than critical, well-defined limit-cycle behaviour is observed, with an increasing number of potentially excited modes of oscillation as the Reynolds number is increased. The related existence of a critical streamwise flow scale for the appearance of self-sustained oscillations in various "tone" experiments was also established.

Greater insight into the role of receptivity in feedback systems has been gained through the examination

of related frequency selection criteria. It is believed that the present measurements of receptivity constitute a wealth of new results that pertain to the excitation of free shear layers, under both steady-state and transient conditions.

Comparison with theoretical estimates based on the application of linear stability theory revealed that while the location and magnitude of frequency jumps only agreed in a qualitative sense, excellent agreement was found in predicting the onset of oscillations.

Recommendations

Based on the results of this investigation, several recommendations can be made. Because feedback systems are ideally suited for dynamical systems analysis (Mees, 1986), and because the global feedback instability was shown to develop temporally, it is felt that the present flowfield might prove to be a viable candidate to establish connections with deterministic chaos. In particular, phase modulations of the eigenfrequency should be analyzed in relation to the lowest eigenvalue of the system, and its possible connection with the jet-column mode. While the amplitude modulations produced by open-loop forcing of the jet are supposedly random (infinite-dimensional) by nature, it is expected that the enhanced feedback constraint will restrict the

dynamics of low-frequency modulations to a finite-dimensional attractor.

It is worthwhile pointing out that the absence of a critical Reynolds number and well-defined bifurcations in (especially high Reynolds number) open flows has been one of the major objections to the applicability of the dynamical systems approach. The present study demonstrates the existence of a critical Reynolds number with respect to global oscillations, and a bifurcation to well-defined limit-cycle behaviour, in a high Reynolds number open flow with feedback. One might speculate that subsequent bifurcations may be found, as the operating point of the feedback loop is nested deeper inside the unstable region of competing eigenfrequencies. From the observations reported in the present manuscript, it appears that moving the feedback probe downstream at fixed gain and fixed Reynolds number might be a more practical approach than an increase in Reynolds number, in order to achieve this goal. In addition, it is foreseen that the analysis of intrinsic aperiodic oscillations and the route to gradual disorder as the streamwise distance of the feedback probe is increased will generate insight into the natural feedback mechanism, with its inherent randomness and loss of phase reference.

It is also suggested that a direct quantification of natural feedback effects is possible by measuring in an

anechoic chamber the decay of velocity fluctuations during on/off transients. In the presence of a feedback loop, perturbations from an organized state (e.g. limit cycle) may yield meaningful flow information (for instance via frequency locking), since even subtle variations of the eigenfrequency convey phase speed information.

Finally, the present findings allow us to speculate that two feedback loops producing axisymmetric and helical ($m = \pm 1$) disturbances could be utilized. Should intermittent switching be observed between these modes (possibly also including the jet-column mode), this would give hope that a low-dimensional model might be formulated for chaotic dynamics in jet flow.

The present findings clearly offer optimistic prospects for the understanding and control of jet flows. In the interpretation of measurements to come, the understanding and functional dependence of the receptivity mechanism will play a crucial role. It is suggested that future theoretical work be directed toward an extension of Bechert's (1982) analysis to finite momentum thickness and moderate Strouhal numbers. Such results would be of great value in the comprehension of (even turbulent) open flows with pressure feedback.

NONLINEAR STABILITY OF A VISCOUS
AXISYMMETRIC JET

BY
JUDITH HORWITZ

Submitted in partial fulfillment of the
requirements of the degree of
Doctor of Philosophy in Applied Mathematics
in the Graduate School of the
Illinois Institute of Technology

Approved 
Adviser

Chicago, Illinois
May, 1990

ABSTRACT

The nonlinear temporal stability of a viscous axisymmetric jet using a hyperbolic tangent approximation to the actual mean flow is studied with respect to axisymmetric and helical disturbances. For the case of axisymmetric disturbances the weakly nonlinear Stuart-Watson perturbation expansion is used to study the self interaction of the fundamental in a neighborhood of the critical Reynolds number (R_c). The Landau constant is positive indicating there is a supercritical Hopf bifurcation. In order to extend these results past $R \sim R_c$, a severely truncated Fourier modal expansion using the Stuart-Watson functions to represent the r dependence, exponentials in z and unknown amplitudes in time is substituted into the Navier-Stokes equation. A projection onto an appropriate subspace leads to a low dimensional (five) system of amplitude equations for the disturbance of the fundamental, harmonic and distortion to the mean flow.

The bifurcation package AUTO and Fourier spectrum are used to characterize the nature of the solutions for various values of R . Numerical results show that the periodic solution is stable for $55.3 < R < 72.3$. There is a secondary bifurcation at $R = 72.3$ to a quasiperiodic solution with 2 incommensurate frequencies (Q_2) f_1 and f_2 . Each peak in the Fourier spectrum can be indexed according to $f = f_1 + nf_2$ for $n = 0, \pm 1, \pm 2, \dots$. As R increases past $R = 78$ there is a transition through another periodic regime and then finally a transition to intermittency for $100 < R < 1000$. In the

case of helical disturbances the ten dimensional system of amplitude equations has a stable periodic solution for $21.75 < R < 33.2$. For $33.2 < R < 37$. there is a Q_2 solution. The Fourier spectrum contains two families of peaks: $q_n = nf_1 - (n - 1)f_2$ for $n = 0, 1, 2, \dots$ and $w_n = nf_1 - (n + 1)f_2$ for $n = 1, 2, 3, \dots$. As R increases f_2/f_1 increases and the limiting frequency $w_1 \rightarrow 0$ as $f_2/f_1 \rightarrow .5$ indicating a possible homoclinic orbit. No bounded solutions exist for $R > 37$.

CHAPTER VI

SUMMARY

The nonlinear stability of a viscous axisymmetric jet having a hyperbolic tangent mean profile has been investigated. A severely truncated form of a Fourier modal expansion has taken either the form of an axisymmetric or a nonaxisymmetric disturbance. The main assumptions leading to the low order models of amplitude equations are

1. parallel flow of mean velocity
2. decomposition of disturbance into separate modes in each of the three spatial directions z , r , and θ
3. severe truncation of an infinite series
4. Stuart-Watson type shape functions in the radial direction.

In an effort to keep the dimension of the system of ODE's low, we have limited the number of terms in the expansion of the perturbation. Only those terms which would arise at first and second order in a Stuart-Watson perturbation expansion have been retained.

In the case of axisymmetric disturbances we were able to obtain the 3-D analogue of the Lorenz equations which includes only the fundamental and mean flow distortion. Unlike the Lorenz system which has chaotic solutions when the Prandtl number is high enough, there are no chaotic solutions for the model of the jet, since there is only a globally stable periodic solution for $R > R_c$. We have also shown that the absence of chaotic solutions is independent of the choice of shape functions. Adding in the harmonic to give

a 5-D system of ODE's causes the periodic solution to lose stability to a quasiperiodic solution with 2 incommensurate frequencies. For one choice of shape functions the quasiperiodic branch eventually goes through a periodic regime and then becomes intermittent. However, a second choice of shape functions leads to a homoclinic orbit and unbounded solutions following the Q_2 regime. The case of nonaxisymmetric disturbances, although more complicated, leads to a similar sequence of bifurcations as the case of axisymmetric disturbances using the second set of shape functions. However, the common feature that distinguishes these low order models which represent an open flow system from the Lorenz system which represents a closed flow system is that the secondary bifurcation leads to a Q_2 regime, rather than to chaos. Of course the range of validity of these expansions remains untested. Thus, the main conclusion is that a very low order truncation does not lead to a model which has chaotic solutions and the model is therefore inadequate to study transition to turbulence. This work represents the first attempt to proceed beyond the linear stability analysis for the axisymmetric jet and the first to include three dimensional disturbances to derive a low order system of amplitude equations.

Possible extensions of this work would retain a higher number of modes. For example, if a_n and $c_{j,k}$ are constants, then the Fourier modal procedure for the axisymmetric case leads to an $N + 1$ dimensional system of ODE's which have the structure

$$\dot{A}_n = a_n A_n + \sum_{\substack{j+k=n \\ |j|, |k| \leq N}} c_{j,k} A_j A_k \quad 0 \leq n \leq N \quad (6.1)$$

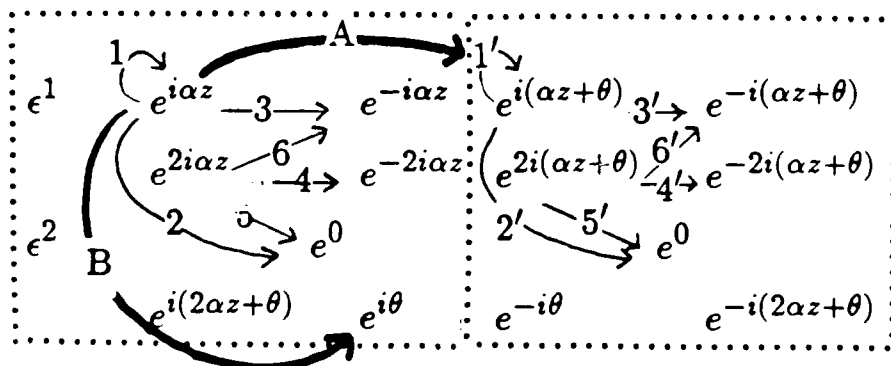
where A_n are the complex amplitudes of the disturbance and $A_j = \bar{A}_{-j}$ when $j > 0$. Since $a_n = (R - R_{cn})$ for $n \neq 0$ and a_0 is a negative constant, (6.1) has a periodic solution bifurcating from R_{c1} , which can be called S_N to denote the order of truncation. It can be shown that the nontrivial solutions of a lower order truncation, say S_{N_1} are not solutions of a higher order truncation, say S_{N_2} where $N_1 < N_2$, although they may be close approximations to it. For example comparisons of the models resulting from the truncations $N = 2$ and $N = 4$ are shown in the diagram below.

This shows that we cannot retain S_2 in going to the higher order solution S_4 since to do so would imply that $A_3 = A_4 = 0$ and the last equation for \dot{A}_4 would not be satisfied since $A_2 \neq 0$.

$N = 4$				
$N = 2$				
$\dot{A}_0 = a_0 A_0 +$	$c_{1,-1} A_1 A_{-1}$	$+ c_{2,-2} A_2 A_{-2}$	$+ c_{3,-3} A_3 A_{-3}$	$+ c_{4,-4} A_4 A_{-4}$
$\dot{A}_1 = a_1 A_1 +$	$c_{1,0} A_1 A_0$	$+ c_{2,-1} A_2 A_{-1}$	$+ c_{3,-2} A_3 A_{-2}$	$+ c_{4,-3} A_4 A_{-3}$
$\dot{A}_2 = a_2 A_2 +$	$c_{1,1} A_1 A_1$	$+ c_{2,0} A_2 A_0$	$+ c_{3,-1} A_3 A_{-1}$	$+ c_{4,-2} A_4 A_{-2}$
$\dot{A}_3 = a_3 A_3 +$	$c_{1,2} A_1 A_2$	$+ c_{2,1} A_2 A_1$	$+ c_{3,0} A_3 A_0$	$+ c_{4,-1} A_4 A_{-1}$
$\dot{A}_4 = a_4 A_4 +$	$c_{1,3} A_1 A_3$	$+ c_{2,2} A_2 A_2$	$+ c_{3,1} A_3 A_1$	$+ c_{4,0} A_4 A_0$

Higher order truncations could verify whether the results obtained in this work still persist or whether they are artifacts of the truncation used and in theory it can be done. However, in view of the large amount of work required to perform even a severe truncation using only three terms it would not be practical to use the Fourier Modal expansion to include higher order terms, especially in the nonaxisymmetric case. A better approach would be to use an entirely different method such as finite differences or finite elements.

Another possible extension would be to incorporate both a two and three dimensional disturbance at leading order as proposed by Craik (1971) for the case of a boundary layer. In this way we could generate a more realistic profile of interactions. For example, the diagram in the dotted boxes below shows the types of interactions studied in this work when only one mode is present at leading order (ϵ^1). In the box on the left we consider the interaction of a z mode, $e^{i\alpha z}$ at leading order. The interactions 1,3,4,6 are all between pure z modes. Similarly in the box on the right, we consider interactions produced by a z, θ mode, $e^{i(\alpha z + \theta)}$ at leading order. The interactions 1',3',4' and 6' are also all between z, θ modes. However, if we consider interactions of a z mode, $e^{i\alpha z}$ and z, θ mode, $e^{i(\alpha z + \theta)}$ at leading order, then we could generate new interactions such as those indicated by A and B which include $z - z, \theta$ and $z - \theta$ interactions.



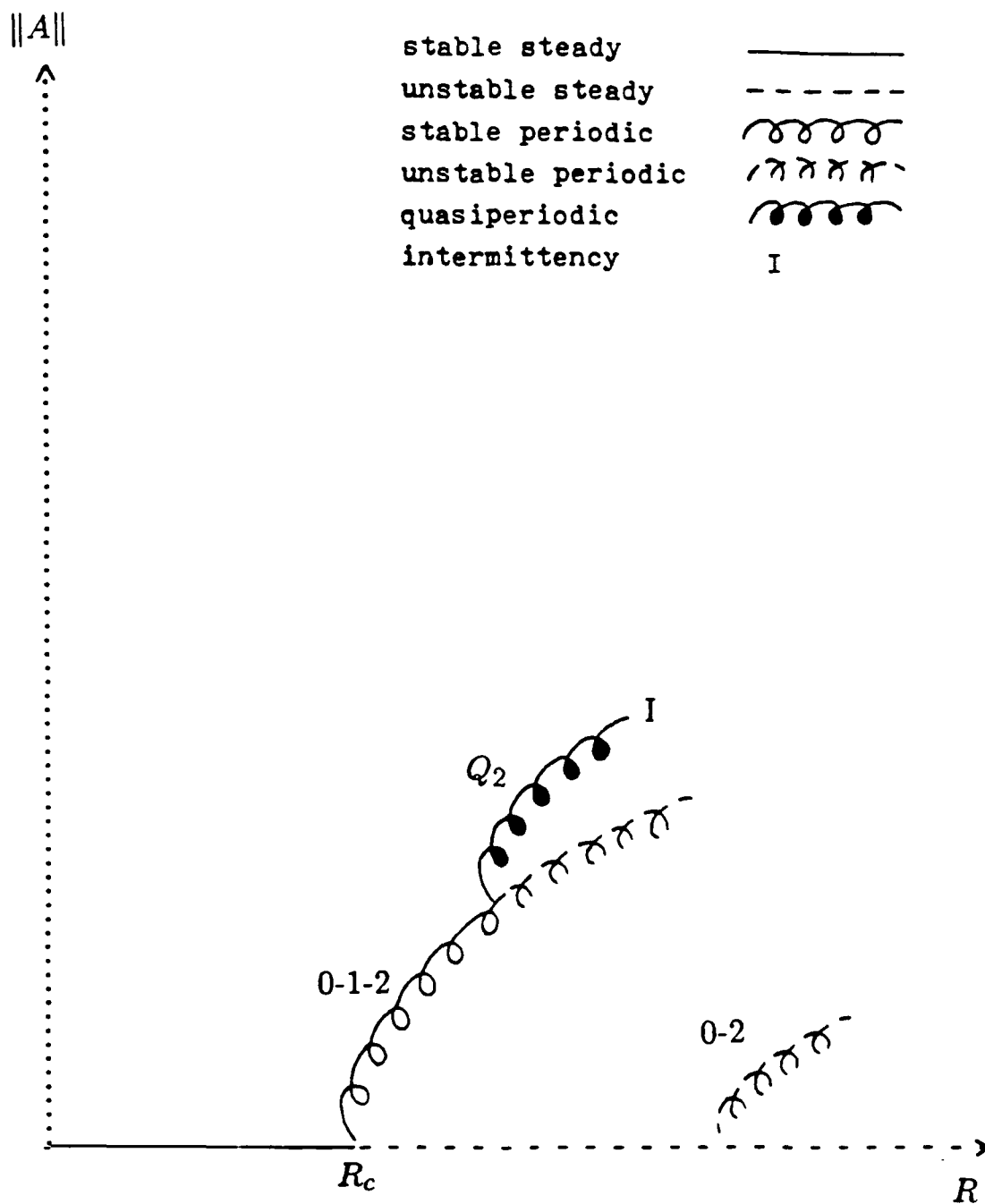


Figure 20. Bifurcation Diagram for Axisymmetric Case: Non-linear Stage (3 modes)

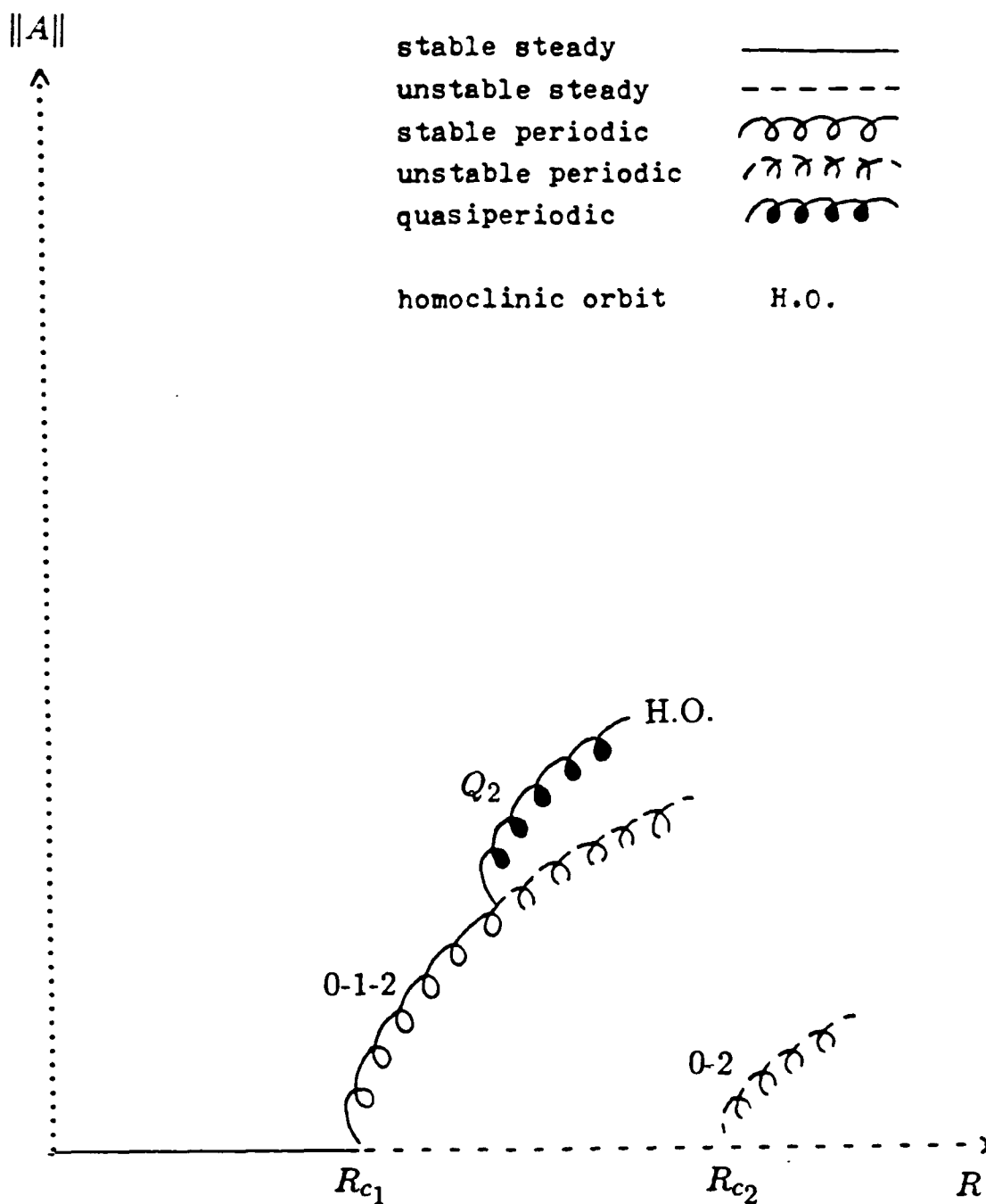


Figure 34. Bifurcation Diagram for Nonaxisymmetric Case: Non-linear Stage (3 modes)

ON THE INSTABILITY OF THIN CIRCULAR SHEAR LAYERS

BY

AZAM AHMADI-MOGHADAM

Submitted in partial fulfillment of the
requirements for the degree of
Doctor of Philosophy in Mechanical
and Aerospace Engineering
in the School of Advanced Studies
Illinois Institute of Technology

Approved _____
Adviser

Chicago, Illinois
December, 1986

ABSTRACT

Temporal and spatial stability calculations of thin circular shear layers, such as would occur in the near-lip region of a large-Reynolds number incompressible jet have been performed analytically and numerically. The linear growth rate in this case decreases in magnitude with both the azimuthal wave number and the ratio of the momentum thickness to the radius of the jet. The long-wave case is also investigated in some detail. Nonaxisymmetric secondary instability through parametric resonance is investigated. The analysis consists of an expansion and a multiple-scaling technique in terms of the amplitude of the primary disturbance. A solvability condition gives the amplitude-evolution equation for the secondary instability. The total growth rate of the secondary instability has two contributions: a linear theory part contribution that, in this case, is always positive and the effect of the parametric resonance. The contribution from the parametric resonance shows the opposite trends of the linear growth rate. A craik-like mechanism is also discussed.

CHAPTER VII

CONCLUSIONS AND SUGGESTIONS FOR FURTHER RESEARCH

The hydrodynamic instability of thin circular shear layers of a large-Reynolds number jet of an incompressible fluid have been investigated analytically and numerically.

The mean flow, to leading order, turns out to be the Blasius shear-layer profile connecting a quiescent external region and a uniform flow in the jet core. The curvature effects for the thin circular shear-layer mean flow are $O(R^{-1/2})$, where R is the Reynolds number based on the jet radius and the core velocity, and could be neglected in the present analysis. The solution was obtained through a numerical integration started in the external region.

As a necessary prerequisite for the secondary-instability analysis which forms the core of this investigation, both temporal and spatial linear inviscid stability calculations have been performed allowing for nonaxisymmetric perturbations. The linearized partial differential equations governing small perturbations on the mean flow were reduced to a second-order ordinary differential equation for the perturbation pressure using, in the usual fashion, the normal-mode assumption. The solution for the perturbation pressure reduces to the modified Bessel function of the first and second kinds in the core region and the external region, respectively. The external-region solution was used to start the numerical integration of the perturbation-pressure equation across

the shear layer and the process was iterated until the numerical solution matched the jet-core solution. This determined the eigenvalue.

For the temporal case both the Blasius shear-layer and a hyperbolic-tangent velocity profile were used in the calculations. The modified Bessel functions involved in the boundary conditions were evaluated using IMSL subroutines and special subroutines written to handle the case of large azimuthal wave numbers (in combination with large arguments). The dominating instability waves, i.e., the ones with the highest growth rates, have wave lengths of the order of the thickness of the shear layer. Both the range of unstable wave numbers and the maximum growth rate are slightly less for the more realistic Blasius shear-layer profile than for the hyperbolic-tangent velocity distribution. For both profiles, the phase velocity is relatively independent of the azimuthal wave number except for small streamwise wave numbers where the difference is substantial, and both the maximum growth rate and the range of unstable streamwise wave numbers are reduced by increasing the azimuthal wave number. This behavior is enhanced by increasing the importance of the curvature effects. It also was found that, for axisymmetric disturbances, the phase velocity is rather sensitive to curvature effects but the growth rate is not and that the opposite is true for nonaxisymmetric disturbances.

For the spatial case, only the Blasius shear-layer profile was used in the stability calculations. Special subroutines were written to evaluate the modified Bessel functions for complex arguments. The results are in general agreement with the calculations of Michalke (1971), who used the hyperbolic-tangent mean-velocity profile and obtained results for the axisymmetric and helical modes. However, the maximum growth rate and the range of unstable frequencies of the axisymmetric mode are somewhat smaller and larger, respectively, than his hyperbolic-tangent results, which led to a good agreement between the results presented here and the experimentally obtained values for the phase velocity and growth rate of Drubka (1981). Furthermore, the phase velocity is strongly dependent on the azimuthal wave number except for large frequencies. The growth rate is relatively independent of the azimuthal wave number for moderate values of that parameter, but as it becomes large both the growth rate and the range of unstable frequencies is drastically reduced. Also, as the azimuthal wave number becomes large the instability waves become increasingly nondispersive, with only a decreasing small-frequency region being dispersive. These effects are amplified with increasing curvature effects.

The linear stability calculations have shown that the azimuthal-wave-number and curvature effects are most strongly felt for small values of the streamwise wave

number or frequency, i.e., when the wave length of the disturbance is large compared to the shear-layer thickness. It was, therefore, of some interest to investigate the case when the wave length is of the order of the radius of the shear layer in some detail. This was carried out for the temporal case only. Two velocity profiles were used in the analysis, namely a broken-line profile with a linear velocity distribution and the continuous hyperbolic-tangent profile. Solutions were constructed in terms of an expansion in powers the ratio of the shear-layer thickness and the jet radius, which is a small parameter in the case under consideration. The lowest-order dispersion relation for both profiles turns out to be the one for the circular vorticity layer studied by Batchelor & Gill (1963). The next-order problem incorporates the effect of the velocity distributions. It was demonstrated that these inner solutions match onto outer expansions as the streamwise wave number (scaled with the jet radius) tends to infinity. In the outer expansions, the details of the velocity distribution enters to zeroth order and the curvature effects are a first-order correction. For the hyperbolic-tangent profile case, where the outer expansion is semi-numerical, it was also demonstrated that both expansions agree with the fully numerical solution in their respective regions of validity.

Nonaxisymmetric secondary instability for the

circular shear layer through parametric resonance has been analyzed. Essentially following Kelly (1967), the theory assumes that the fundamental disturbance, originating from the linear-instability process, has reached a finite amplitude equilibrium through nonlinear effects before the secondary secondary instability occurs. The secondary instability can then be analysed through using linearized equations with periodic coefficients, whose periodicity in space and time is set by the equilibrated fundamental disturbance. Because the coefficients are periodic, several resonance phenomena can occur; the most important one being the principal parametric resonance involving a subharmonic with twice the wave length of the fundamental. These resonances were analysed by using an expansion and multiple-scaling technique in terms of an characteristic amplitude of the equilibrated fundamental disturbance; the latter is assumed to be small but finite. Since the slow time and spatial coordinate involve the amplitude of the fundamental to the first power, the secondary instability process is a faster process than the self-equilibrium process that (presumably) involves the square of that amplitude.

Both temporal and spatial calculations have been carried out. It was found that the most important case, i.e, the one with the strongest contribution to the total growth rate (both temporal and spatial) from the resonance, is the one involving an axisymmetric

fundamental disturbance and two subharmonic modes with opposite, but equal in magnitude, azimuthal wave numbers. For this case, the secondary growth rate increases with both increasing azimuthal wave number and the curvature effects. The linear contribution to the total growth rate shows the opposite effect, however. When the fundamental is nonaxisymmetric, the secondary growth rate decreases with increasing azimuthal wave number and curvature effects.

A Craik-like (1971) triad interaction involving an axisymmetric fundamental and two subharmonic waves with opposite azimuthal wave numbers have also been analyzed. The theory is only an approximate one since the growth rates in this inviscidly unstable flow situation are not necessarily small enough for a strict application of the aforementioned theory. It is felt, however, that even with its limitations the analysis presented here can shed some light upon the transition process in circular shear layers and jets. In particular, it was found that once the subharmonic disturbances have reached a sufficient amplitude so that back-interaction to the fundamental becomes important, an explosive growth will occur within a finite time. This phenomenon was found to be relatively insensitive to the initial conditions. Furthermore, with identical initial conditions, the rapid growth was found to occur earlier for larger azimuthal wave numbers and curvature effects.

As for future research, one of the more important problems still to be resolved is the finite-amplitude equilibration process (or since the mean flow is actually spatially evolving and not a parallel flow, the 'near-equilibrium' process). At present, it is not clear how a theory for this would proceed but in all likelihood it would have to be a fully numerical spatial computation. Second, there is a great need for further experimental work concerning the role of disturbances with higher azimuthal wave numbers in both the early and later stages of the transition process. The receptivity problem for the near-lip region to pressure feedback from the vortex pairing process is also a topic for future research.

NUMERICAL EXPERIMENTS ON CALCULATING ATTRACTOR DIMENSION

The present section documents the optimization and error calibration of a program used to compute attractor dimension based on the Grassberger-Procaccia (1983) algorithm. Dimension is generally considered to be the most basic property of an attractor. It is also the most reliably calculated quantity, as compared to other tools of dynamical systems analysis applied to experimental data. Generally speaking, the dimension of an attractor is indicative of the number of degrees of freedom which play a role in the dynamics of a system. Historically, the interest in dimension calculation came from fractal research ("How long is the cost of Britanny?", Mandelbrot, 1975). More recently, however, the link between fractals and the dynamics of low-dimensional chaotic systems has generated strong incentive to calculate the dimension of attractors in phase space. Farmer et al. (1983) reviewed the various existing measures of attractor dimension, and concluded at the time that computations of fractal dimension were not feasible for attractor dimensions significantly greater than three.

The calculation of attractor dimension started with so-called "box-counting" algorithms. These algorithms

involved the covering of an object with cubes of side ϵ , and counting the number of cubes necessary to cover the object. One would then expect a power law of the type $N(\epsilon) = a \cdot \epsilon^{-D}$ in the limit $\epsilon \rightarrow 0$, where "a" is a proportionality constant and D is the fractal dimension of the object. This concept proved useful to calculate analytically the dimension of self-similar fractals such as Koch's triadic curve, or the one-scale cantor set. However, box-counting algorithms are impractical on a computer, even for low-dimensional calculations.

Grassberger and Procaccia (1983) introduced the "correlation dimension", based on the scaling of a correlation sum over the attractor. The general idea underlying this scaling law is schematically illustrated in Figure 135. For any object topologically equivalent to a line, the number of neighbours contained within a ball of radius R is proportional to the radius. For an object equivalent to a surface uniformly covered with points, the count $N(R)$ becomes proportional to R^2 , etc. Thus, for "classical" objects, the power of R corresponds to our intuitive notion of dimension, based on euclidian geometry. In the general case, though, $N(R)$ is proportional to R^D , where D may not be an integer (lower graph of Figure 135). In this case the dimension is said to be fractal. It should be pointed out that

only for self-similar fractals should one expect the scaling exponent to be identical on all sites of the attractor. In the general case (Hasley et al., 1986), an attractor may be described by a whole distribution of scaling laws over the attractor. In practice, however, one attempts to find a range of radii where one scaling law applies.

The correlation sum is defined as the count of all pairs of neighbours on the attractor, that are within a distance R from each other. The formal expression for the correlation sum is:

$$S(R) = \lim_{N \rightarrow \infty} \frac{1}{N^2} \sum_{\substack{i=1 \\ j=1}}^N H(R - |u_i - u_j|) \quad [45]$$

where H designates the Heaviside step function, and $|u_i - u_j|$ represents the distance between two points u_i and u_j in phase space. The phase diagram (orbits u_i) is constructed according to the method of delays (see Chapter V). In principal, one calculates the correlation sum $S(R)$ for a variety of radii scanning all scales on the attractor. To extract the scaling exponents represented in Figure 135, one displays S versus R on a doubly logarithmic scale, and seeks a linear range, the slope of which is the correlation dimension. Since the actual dimension of the attractor is not known a priori,

and since the calculated dimension is always bounded by the dimension of the embedding space, the slope is plotted as a function of increasing embedding dimension, until convergence is attained.

Because the calculations were performed on a laboratory computer, the following simplifications were used in the numerical implementation of equation [45]. First, the sum was not performed over the entire attractor, but over a fixed number of reference points. The reference points were chosen randomly, and their number was generally chosen to be about one percent of the total number of points on the attractor for real data, and 0.1 % for the test cases described below. Secondly, the norm operator in equation [44] was replaced by the norm one (i.e. sum of coordinate absolute values), in order to avoid any multiplications. It is easy to verify that the scaling arguments of Figure 135 are not altered by replacing the ball by an M-dimensional cube. Thirdly, the correlation sums were calculated for all embedding dimensions and all radii simultaneously. The calculation naturally started for the larger radii so that candidate neighbours can be gradually eliminated from the sorting process. Similarly, by starting with the largest embedding dimension, if a point is not within an

M-dimensional cube of size R , then it is not contained within any lower-dimensional projection of the cube.

Finally, the calculation can be accelerated significantly by integerizing the data prior to any calculation. The advantage of this procedure is that not only is floating point calculation avoided, but in addition any sorting operation is replaced by indirect addressing. The present author's confidence in the validity of this last approximation has been strengthened by our recent awareness of Powell's (1986) results, for which random data integerized on eight bits yielded accurate dimension estimates up to $D = 60$.

Due to these various simplifications, an error calibration of the program was performed in order to empirically establish confidence bounds. Numerous tests were made, involving added sine waves with "incommensurate" frequencies, as well as chaotic attractors with known fractal dimension. Figure 136 shows the variation of the correlation sum with radius and embedding dimension for a one-frequency system, based on 10,000 data points. The slope of Figure 136 converges to 1.03. Figure 137 considers a four-frequency system with 100,000 data points and 100 reference points on the attractor. Possibly because of the poor representation of the attractor, one notices the double power law emanating

from the plot. The determination of the range in which the slope should be considered represents a possible source of arbitrariness for real data. The saturation at the large scales and the presence of a characteristic "knee" in Figure 137 are quite typical of such plots. For scales smaller than the knee location, the error is generally random (truncation, digitization), and the local slope equals the embedding dimension. Thus, the dimension associated with the largest scales of motion is the first plateau encountered when plotting the slope starting from the largest radii. The calculated dimension for this test signal made of four incommensurate frequencies is $D = 4.2$.

Figure 138 represents an error calibration for the calculation of attractor dimension using the program described above. Up to nine "incommensurate" frequencies were generated. The number of samples varied from 10,000 to 100,000, depending on the dimension, and the number of reference points on the attractor varied from 9 to 100. Two chaotic attractors were considered. For the Henon map (dimension 1.26), the result was $D = 1.20$. For the Lorenz attractor (dimension 2.06), the calculated dimension was 2.03 using true X, Y, and Z coordinates, and 2.01 using the method of delays. The error between measured dimension and expected dimension was found to be

smaller than 0.5 up to attractor dimensions of five. For more than five incommensurate frequencies, the error was found to be quite large (e.g. $D = 11.3$ for the nine-frequency system). It was noticed that the error was consistently positive with quasi-periodic systems, and negative with fractals. It is not clear whether there is any significance to this observation. The main conclusion of Figure 138 is that the dimension estimates using the current program appear to be accurate within 0.5 for dimensions smaller than five.

It is interesting to notice that the "representation error" mentioned by Guckenheimer (1986) leads to error estimates which fit quite well the data of Figure 138. It is not clear why these estimates appear to predict the expected error, since Guckenheimer's argument concerned the resolution of small scales on an attractor, and not the attractor dimension. According to this calculation, however, the expected error would be:

$$\epsilon = D.N^{-\frac{1}{D}} \quad [46]$$

A 10 % error was obtained for the dimension calculation of a five-frequency system using 100,000 points. By multiplying the number of points by five, the theoretical improvement according to equation [46] was predicted to yield a 7.2 % error. The actual error from a 500,000 data

point calculation was 7.6 %. Similarly, one run with 3,200,000 data points was predicted to yield a five percent error ; the resulting calculation (nine days of running time on the Masscomp computer) was accurate within four percent of the expected dimension. Clearly, the amount of data needed to improve the accuracy of dimension estimates increases exponentially. This additional deterrent precludes any attempt to efficiently calculate pointwise dimensions above five with any reasonable accuracy.

Figure 139 illustrates the use of the dimension program on real data (see Chapter V) acquired in the jet shear layer at $X/D = 0.35$ and $Re = 70,000$. The calculations were done with 100,000 data points and 1000 reference points on the attractor. The top graph (correlation sum versus radius) shows the presence of a "knee" below which the slope continues to increase with embedding dimension. The range of scaling is more clearly illustrated by the region of constant slope $d(\text{Log}(S))/d(\text{Log}(R))$ in the bottom graph. The result of this calculation (see Figure 53) yielded a dimension equal to 1.1 for the large scale motions of the attractor.

It is worthwhile mentioning that new measures characterizing the geometry of attractors at the onset of

chaos have made their recent appearance (see Hasley et al., 1986). The concept that an attractor can be statistically characterized by a single number is overly simplistic. Despite its widespread calculation, the existence of a single scaling exponent over the attractor is the exception more than the rule.

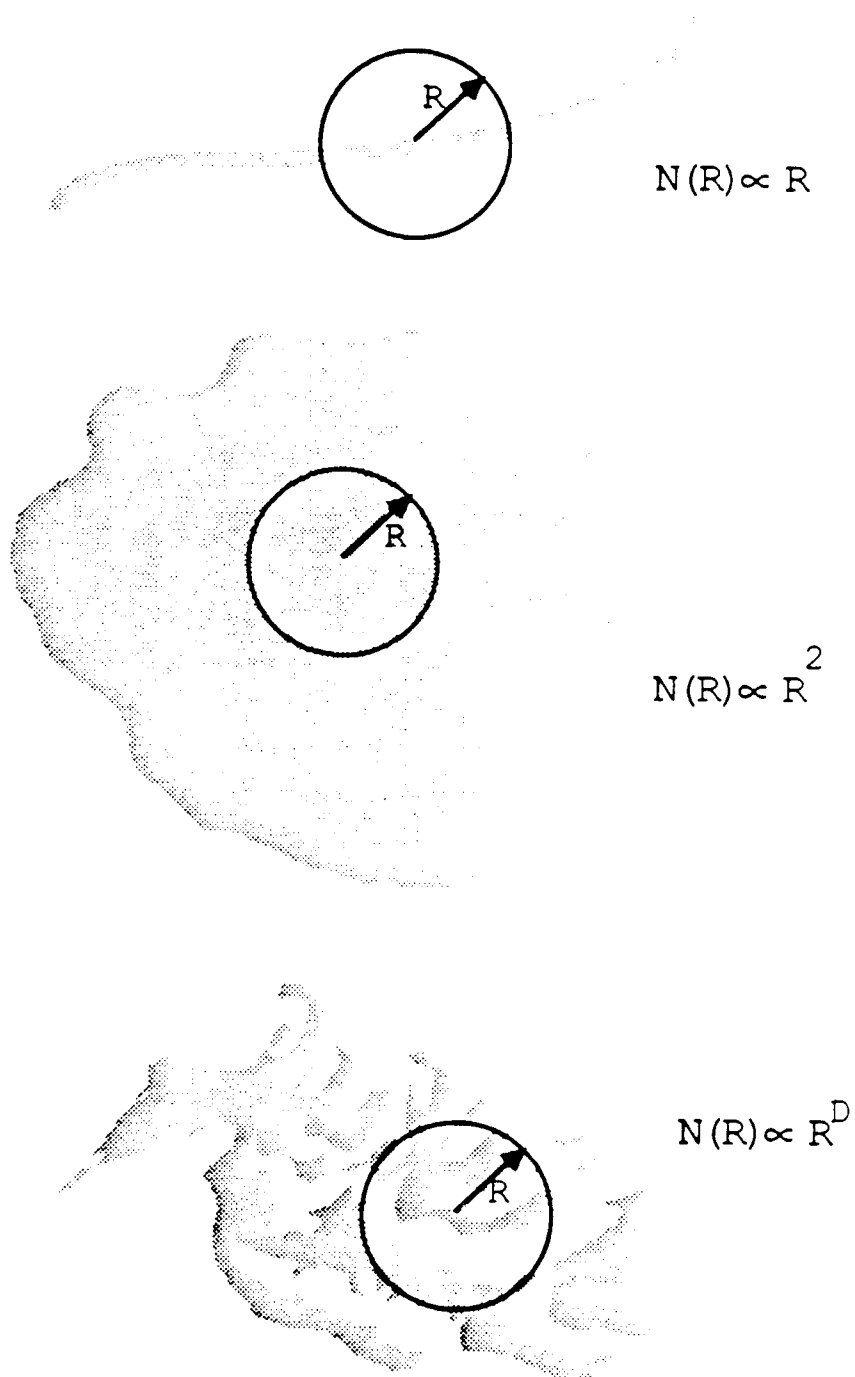


Figure 135. Schematic Illustrating Local Scaling Laws for Various Geometries

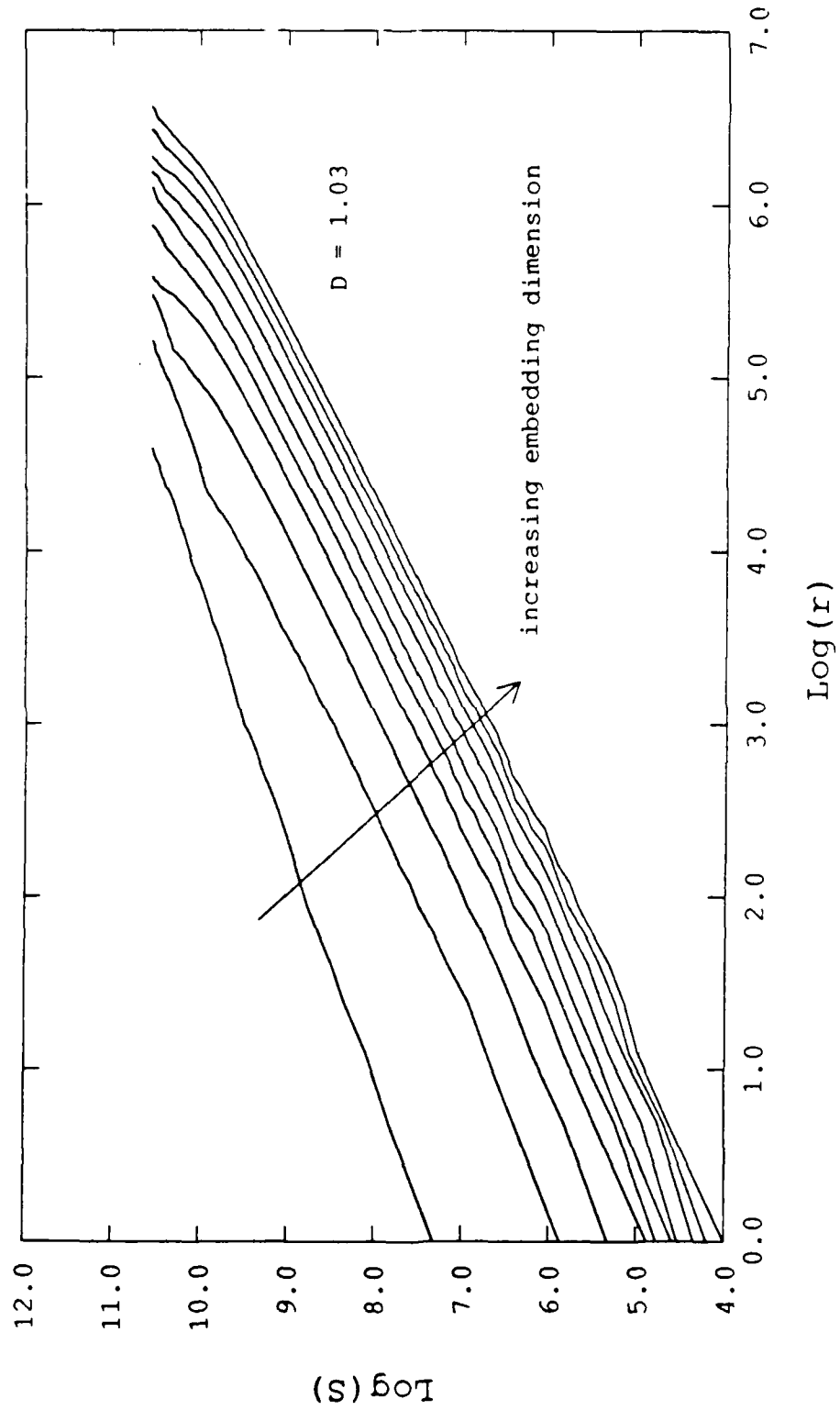


Figure 136. Variation of the Correlation Sum with Radius and Embedding Dimension, Based on 10,000 Data Points of a One-Dimensional System

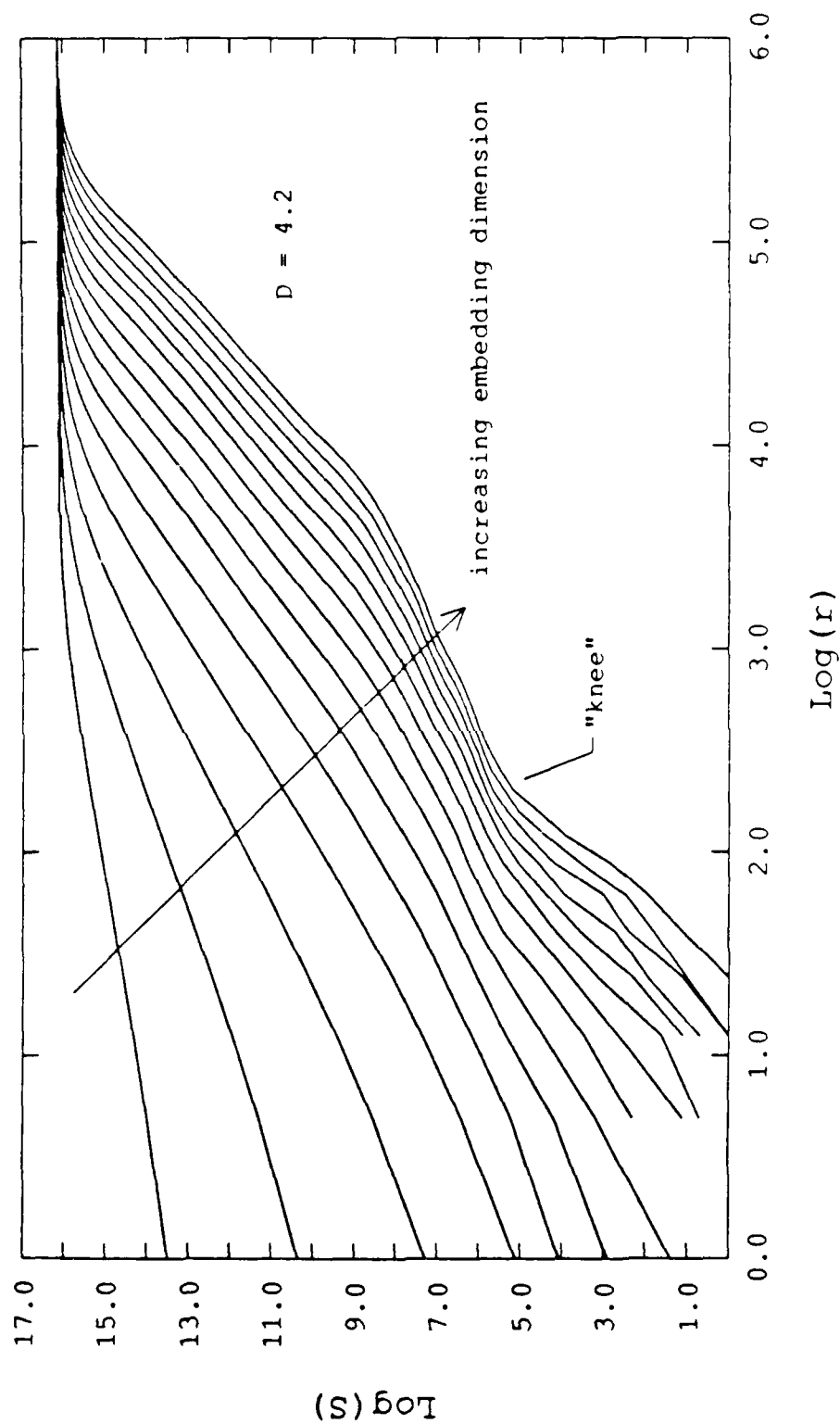


Figure 137. Variation of the Correlation Sum with Radius and Embedding Dimension, Based on 100,000 Data Points of a Four-Dimensional System

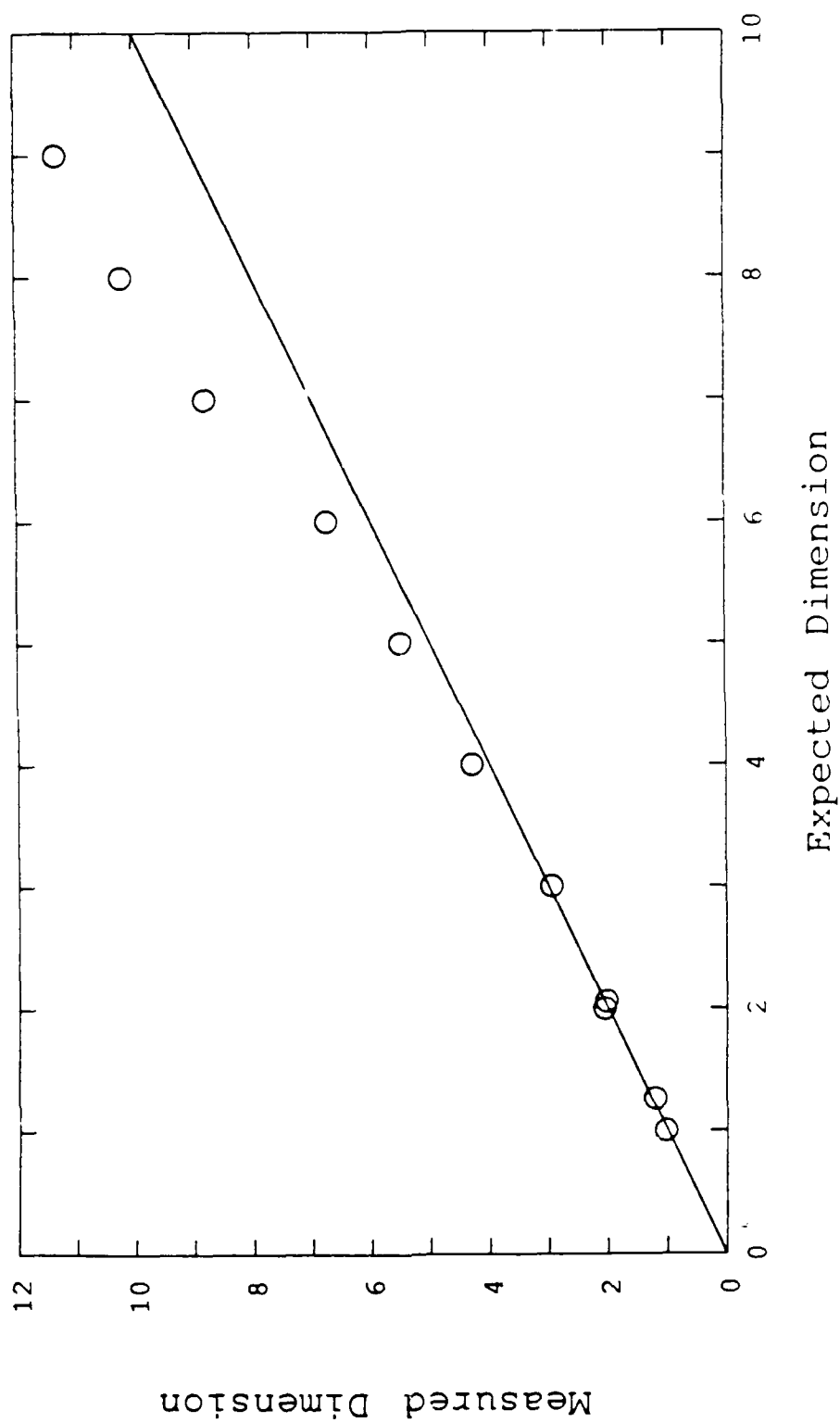


Figure 138. Error Estimation of Calculated Attractor Dimension, Using the Simplified Grassberger-Procaccia Algorithm

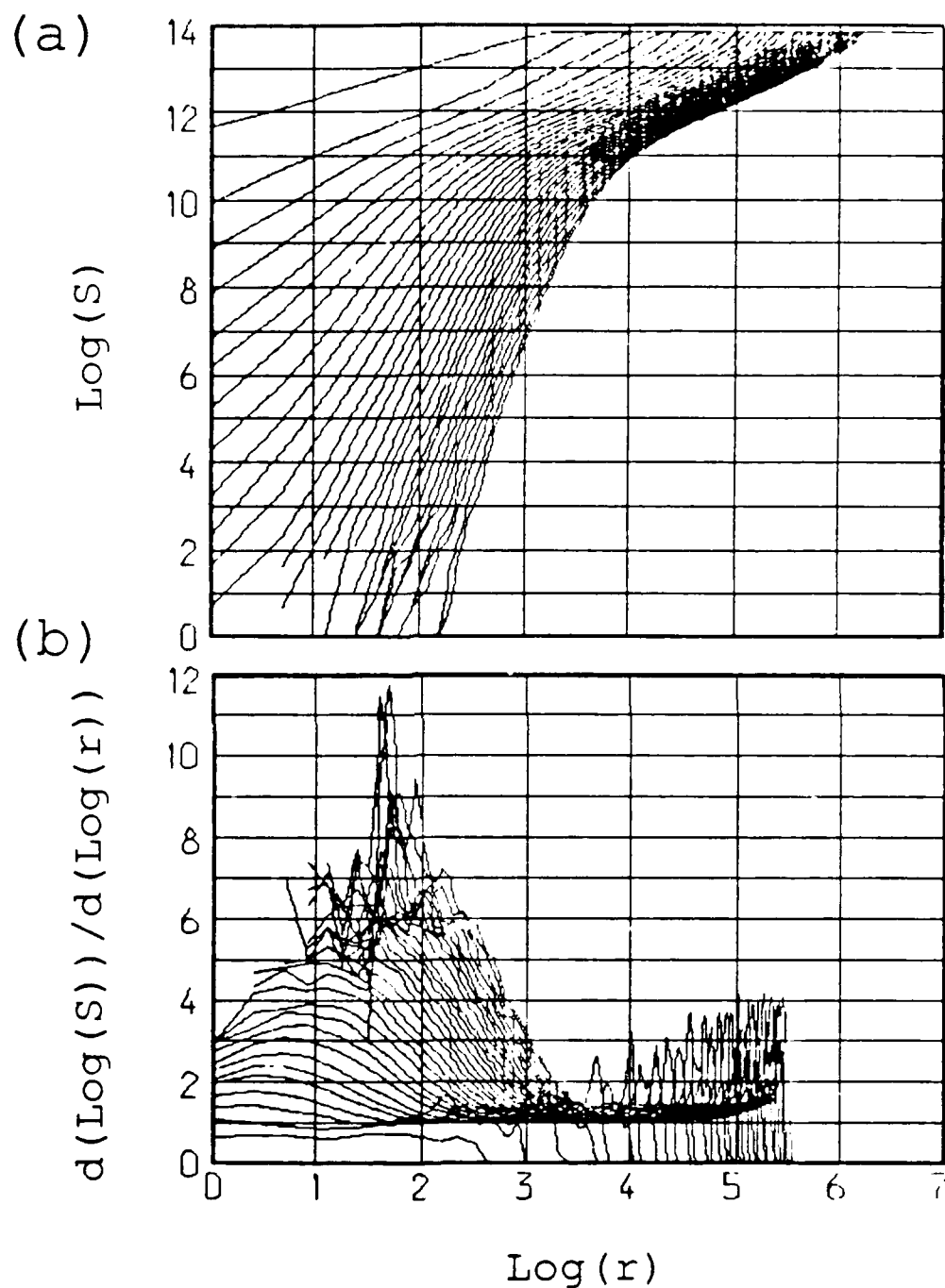


Figure 139. Illustration of the Determination of Attractor Dimension Using: (a) Correlation Sum as a Function of Radius, (b) Slope, with Increasing Embedding Dimension (Jet Data at $X/D = 0.35$ and $Re = 70,000$)